Design & Development of Innovative Proton Exchange Membrane Fuel Cells

By

J. G. Carton, BSc. Eng, M. Eng.

Supervisor

Dr. Abdul Ghani Olabi

School of Mechanical and Manufacturing Engineering

Dublin City University

DCU

Ph.D.　　　　　　　　　　　　　**March 2011**

DESIGN & DEVELOPMENT OF INNOVATIVE PROTON EXCHANGE MEMBRANE FUEL CELLS

James G. Carton B. Eng.

Student No: 56116705

School of Mechanical & Manufacturing Engineering

Dublin City University, Dublin 9, Ireland

Supervisor:

Dr. Abdul Ghani Olabi

March   **2011**

Declaration

I hereby declare that this material, which I now submit for assessment on the programme of study leading to the award of Ph.D. is entirely my own work, that I have exercised reasonable care to ensure that the work is original, and does not to the best of my knowledge infringe upon any law of copyright, and has not been taken from the work of others, save and to the extent that such work has been sited and acknowledged within the text of my work. I also certify that it has not been submitted in whole or in part to any other University or Institution.

Signed: _____.   Student Number: 56116705.

James G. Carton

Date: September 1st 2011.

Acknowledgements

I would like to firstly and fore mostly thank my supervisor, Dr. Abdul Ghani Olabi, for his continuous help, support and encouragement throughout the duration of this work. Without his kind support this achievement would not have been possible.

I would like to thank Dr. Vincent Lawlor for his advice throughout the past number of years.

I would also like to thank the technicians of the school of mechanical and manufacturing engineering, especially: Liam Domican, Martin Johnson, Michael Tyrell, Alan Meehan and Michael May who aided me during my time in Dublin City University.

I would like to acknowledge Prof. Dr. Christoph Hochenauer and Dr. Gerald Zauner of the Upper Austrian University of Applied Sciences for the use of some of their specialised equipment.

I would like to a acknowledge Sergie Albino of the Space Life Science Lab, Florida for his advice over the past few years.

I would also like to acknowledge fellow postgraduate students: Sabawoon Shafaq, Evans Chikarakara, David Clarke, David Moore, Ali Saood, Kevin Sheridan, Adele Petrone, Abdulaleem Albadawi, Kamrul Hasan, Hussam Achour and Walid Smew, who I had the pleasure to work beside in the last number of years.

Finally, I would like to thank my family for their continued support throughout the duration of this thesis. I also want to thank my girlfriend Tina for her love and strength and I look forward to all their continued encouragement in future endeavours.

Abstract

The research undertaken in this thesis is concerned with the design and development of Proton Exchange Membrane (PEM) fuel cells and provides a body of information for continued PEM fuel cell development, which will ideally aid in the future commercialisation of these electrochemical devices.

Through a combination of numerical analysis, computational fluid dynamic modelling and experimental work, effective flow plate designs, flow field configurations and materials are analysed and new innovative designs are proposed.

The flow plate of a PEM fuel cell is one of the most important structures in these devices. Effective design of the flow plate will aid in the optimisation of PEM fuel cell technology. Due to the low operational temperature of PEM fuel cells, water species can form in the flow field and this can affect their performance. Two phase flow models were used to study this phenomena. These models show how the water flooding in flow field channels can hinder the mass transport if these are not properly designed, leading to reduced performance, increased heat and reduced fuel utilisation. A high speed camera technique in an ex situ apparatus was used to validate the model and water mitigation methods are proposed.

From the culmination of the analysis performed a novel application of open pore cellular metal foam as a flow plate material is proposed in this thesis. A model is developed, to simulate this relatively new material and extensive pressure analysis and flow modelling has been completed using this model. Computational fluid dynamic modelling, with an additional electrochemical PEM fuel cell module, has been carried out on conventional double channel flow plates and open pore cellular foam flow plates. Flow regimes, pressure analysis, water accumulation, oxygen concentration, fuel utilisation, current & voltage curves and cell temperature profiles are analysed.

The PEM fuel cell model with open pore cellular metal foam flow plate performs in excess of a 55% improvement on the current density of the bench mark double serpentine flow plate under the same operating conditions at 0.7 volts.

All of the above multi physical phenomena match very well to the experimental results. This information is new to the area and should help optimise PEM fuel cell performance.

Contents

Design & Development of Innovative Proton Exchange Membrane Fuel Cells: J. Carton

Nomenclature

PEM   Proton Exchange Membrane

MEA   Membrane Electrode Assembly

GDL   Gas Diffusion Layer

MPL   Micro-Porous Layer

ORR   Oxygen Reduction Reaction

DMFC   Direct Methanol fuel Cell

SOFC   Solid Oxide Fuel Cell

ATP   Adenosine Tri-phosphate

CFD   Computational Fluid Dynamics

VOF   Volume of Fluid

ppi   Pores Per Inch

DOE   Design of Experiment

FEA   Finite Element Analysis

DAQ   Data Acquisition System

R&D   Research & Development

fps   Frames Per Second

ISS   International Space Station

ESA   European Space Agency

EO   Electro-osmotic

PTFE   Polytetrafluoroethylene

MF   Porous Metal Foam

RVCF   Reticulated Vitreous Carbon Foam

SLIC   Simple Line Interface Calculation

PLIC   Piecewise Linear Interface Calculation

UDF   User Defined Function

Design & Development of Innovative Proton Exchange Membrane Fuel Cells: J. Carton

RUCS	Representative Unit Cell Structure
SME	Small & Medium Enterprises
MRI	Magnetic Resonance Imaging
NMR	Nuclear Magnetic Resonance
η_{act}	Activation losses
η_{ohmic}	Ohmic losses
η_{conc}	Concentration losses
T	Temperature (°C or specified if K)
ΔG	Free Gibbs energy change (J)
ΔH	Enthalpy (J)
E_{rev}	Ideal fuel cell voltage (V)
F	Faraday constant (94685 C/mole)
E_{cell}	Fuel cell operating voltage (V)
i	Current density (A/m^2)
i_o	Exchange current density (A/m^2)
i_1	Limiting current density (A/m^2)
A	Area (m²)
R	Gas constant
$\dot{m}$	Mass transfer
Ca	Capillary number
We	Weber number
M	Morton number
Eo	Eotvos number
Δx_{cell}	Grid dimension
s	Liquid water saturation
λ	Water content
ϕ	Electrical potential (V)
R	Volumetric transfer current (A/m^3)

Design & Development of Innovative Proton Exchange Membrane Fuel Cells: J. Carton

γ	Concentration dependence
D_i	Mass diffusivity of species i
r_w	Condensation rate
C_2	Pressure jump coefficient
G	Gravity (m/s)
μ	Fluid Viscosity (Ns/m^2)
ρ	Density (kg/m^3)
ΔP	Pressure Drop (Pa)
L	Distance (m)
K	Permeability (m^2)
C	Form Coefficient
v	superficial velocity (m/s)
d_p	Particle diameter (m)
ε	Porosity
ξ	Constant
m	Constant
α	Thermal Diffusivity (m^2/s)
d_L	Ligament Diameter (m)
Θ	Contact Angle (°)
P	Pressure (Pa)
P_{vap}	Vapour partial pressure (Pa)
p_{gas}	Gas partial pressure (Pa)
$\dot{m}$	Mass flow rate (kg/s)
m_v	Mass of the droplet (kg)
r	radius (m)
D	Diameter (m)
Re	Reynolds number
Γ	Diffusivity (m²/s)

X

R_0	Universal gas constant (8.314472 x10-15) J/K.mol
$\dot{m}$	Mass flow rate (kg/s)
δ	Area (m²)
V	Velocity (m/s)
V̶	Volume (m³)
t	Time (s)
m	Molar Mass (mol)
η	Efficiency / Loss
A_p	Surface area of the particle (m²)
σe	Conductivity of electrons (S/m)
σi	Conductivity of ions (S/m)
N	Nernst potential (V)
V	Volts (V)
I	Current density (A/m²)
φ	Electrical potential (V)
σ	Electrical conductivity (ohms-1)

R_0 Universal gas constant (8.314472 x10-15) J/K.mol

$\dot{m}$

Design & Development of Innovative Proton Exchange Membrane Fuel Cells: J. Carton

List of Figures

Design & Development of Innovative Proton Exchange Membrane Fuel Cells: J. Carton

Design & Development of Innovative Proton Exchange Membrane Fuel Cells: J. Carton

Design & Development of Innovative Proton Exchange Membrane Fuel Cells: J. Carton

Design & Development of Innovative Proton Exchange Membrane Fuel Cells: J. Carton

Design & Development of Innovative Proton Exchange Membrane Fuel Cells: J. Carton

Design & Development of Innovative Proton Exchange Membrane Fuel Cells: J. Carton

Design & Development of Innovative Proton Exchange Membrane Fuel Cells: J. Carton

Design & Development of Innovative Proton Exchange Membrane Fuel Cells: J. Carton

Design & Development of Innovative Proton Exchange Membrane Fuel Cells: J. Carton

List of Tables

1

Chapter 1- Introduction

1.1 Fuel Cells

Fuel cells are energy conversion devices that produce electricity, electrochemically, from a catalytic aided reaction of a fuel with an oxidant, see Figure 1. Molecular hydrogen is the most commonly used fuel, but other hydrogen containing fuels can be used also, depending on the fuel cell type, see Table 1. Oxygen is the most frequently used oxidant for fuel cells and this can be simply obtained from ordinary air, for most fuel cell applications.
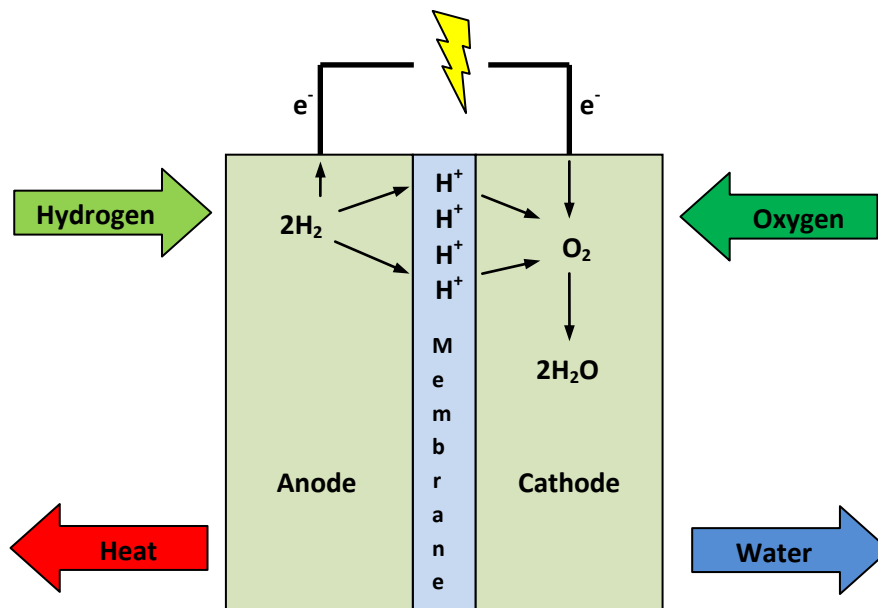
Figure 1 Schematic of a fuel cell.

Fuel cells have advantages over heat engines and batteries. Most conventional power generation methods use intermediate steps of producing heat and mechanical work to generate electricity; these steps are avoided with fuel cells, for example fuel cells are not limited by thermodynamic limitations of heat engines, such as the Carnot efficiency and can be switched on and off relatively fast compared to large thermal power stations. Unlike batteries, fuel cells do not suffer cyclic charge/discharge

deterioration and if continuously supplied with a fuel, the electrical power of a fuel cell can be sustained indefinitely [1]

Fuel cells offer a promising alternative to traditional power sources; achieving power generation with high efficiency and low environmental impact. Fuel cells have the advantage of being clean, only producing water and heat as by products. The efficiency of a fuel cell can be quiet high but varies depending on the type and system application. In addition, fuel cells have high power density, have no moving parts, have proven durability and robustness, operate silently and can be designed into many shapes and are modular, to obtain the desired amount of electrical power, individual fuel cells are combined to form a fuel cell stack.

Table 1 Fuel cell typology [2]**.**

Type	Electrolyte	Operating Temperature (°C)	Fuel	Oxidizer	Sensitivity	Electric Efficiency (%)	Application	Technology
Alkaline fuel cell (AFC)	Potassium hydroxide fluid	50-200	Hydrogen (industrial grade)	Oxygen (Air)	CO_2, CL, S	60-65	Stationary/ Mobile/ Portable	Mature
Direct Methanol fuel cell (DMFC)	Solid polymer	20-90	Methanol	Oxygen (Air)	S, FL	20-30	Stationary/ Mobile/ Portable	Early commercial/ Under development
Phosphoric Acid fuel cell (PAFC)	Phosphoric acid	100-220	Hydrogen (high grade)	Oxygen (Air)	CO_2, C, S	35-40	Stationary	Commercially available
Molten Carbonate fuel cell (MCFC)	Molten carbonate	600-700	Hydrogen (or any hydrogen containing fuel with internal reforming)	Oxygen (Air)	CL, S	50-60	Stationary	Under development
Solid Oxide fuel cell (SOFC)	Solid oxide	600-1000	Hydrogen (or any hydrogen containing fuel with internal reforming)	Oxygen (Air)	CL, S	50-66	Stationary/ Mobile	Under development
Proton Exchange Membrane fuel cell (PEMFC)	Solid polymer	30-100	Hydrogen (high grade)	Oxygen (Air)	CO_2, CL, S, CO, FL	40-50	Stationary/ Mobile/ Portable	Early commercial/ Under development

Fuel cells bear significant resemblance to electrolysers and electrolytic capacitors. All three devices have similar components; a central electrolyte, which carries ions or electrons from one electrode to the other; two electrodes, one each side of the electrolyte, one positive (cathode) and one negative (anode), where the electrochemical reactions occur; and a catalyst (fuel cell and electrolyser), which speeds the reactions at the electrodes.

Various types of fuel cells have been developed depending on their electrolyte type, ion flow or temperature range, see Table 1. This thesis focuses on low temperature fuel cells, particularly the Proton Exchange Membrane (PEM) fuel cell. These fuel cells are in a transition between development and early commercialisation, because of their suitability to mobile and transport applications, which allows a healthy environment for researchers to solve important, fundamental problems. PEM fuel

cells also require less complicated Balance of Plant (BOP) or expensive laboratory facilities to begin research. Many issues with PEM fuel cells are elated to material cost and manufacturability of components which can be solved given enough support and focused research.

The PEM fuel cell will be introduced in the next section and a full description of PEM fuel cell technology and current research is reviewed in Chapter 2. The reader is referred to [1, 3-5] for further information about all other types of fuel cells; their technology, their application and current research.

1.2 Proton Exchange Membrane Fuel Cell Overview

Proton Exchange Membrane (PEM) fuel cells are low temperature fuel cells that get their name from the unique electrolyte it uses, a solid phase proton conducting membrane about 0.020mm thick. These fuel cells are almost universally of the planar bipolar type and operate effectively between 60°C - 80°C.

1.2.1 PEM Fuel Cell Components

Two major components make up the essence of a PEM fuel cell, a Membrane Electrode Assembly (MEA) and flow plates. A MEA which consists of a proton exchange membrane, an electrically conductive porous gas diffusion backing layer and an electro-catalyst at the interface between the backing layer and the membrane is the heart of the PEM fuel cell and is responsible for the electrochemical reaction. The flow plates distribute the fuel and oxidant to the reactive sites of the MEA via flow channels (flow fields) and electrically connect the cells. Supplementary components of a PEM fuel cell include gaskets, gas connectors, current collectors and backing plates, see Figure 2. These additional components are not of major importance in PEM fuel cell research because of the low operating temperature sealing, corrosion, shielding or leaking concerns are minor.

1.2.1.1 Proton exchange membrane

The most common material used for the membrane of a PEM fuel cell is Nafion. It was developed by Dr. Walther Grot at DuPont by modifying Teflon. Nafion was the first synthetic polymer ever developed with ionic properties, and it started an entirely new class of polymers called Ionomers [1]. The membrane is located between the cathode and anode layers which allow the flow of hydrogen ions and stops electrons. Electrons then must flow through an external circuit producing electricity.

1.2.1.2 Catalyst layer

Due to the low operational temperature of these fuel cells (far below the ignition temperature of hydrogen in air) a very effective catalyst electrode has to be incorporated to ensure the electrochemical reaction takes place. Platinum or platinum alloys are most frequently used [6].
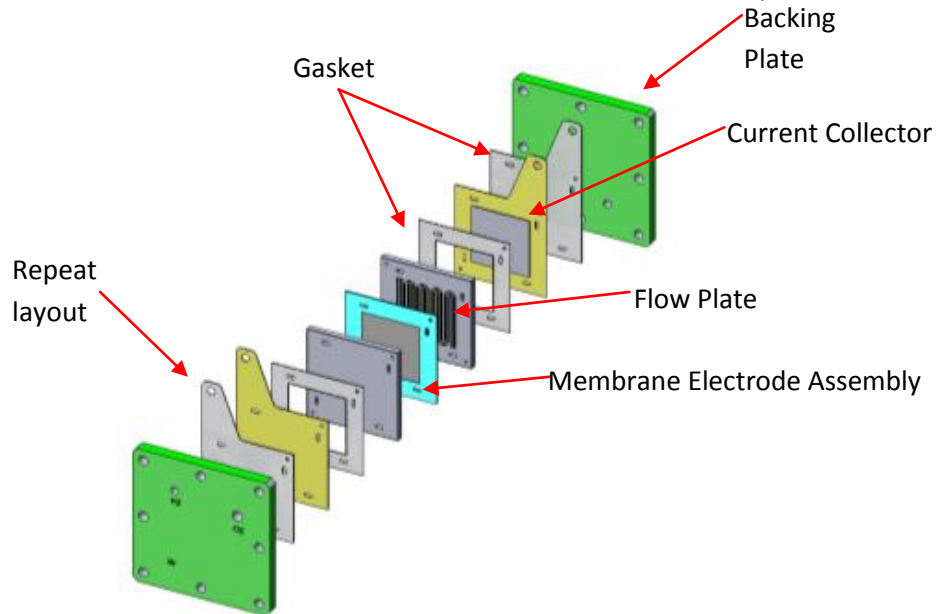
Figure 2 Exploded view of a PEM fuel cell.

1.2.1.3 Gas diffusion layer

The Gas Diffusion Layer (GDL) is a conductive carbon fibre cloth or paper which aids the dispersion of the gases from the flow plates to the catalyst. It is manufactured from carbon cloth or paper material that has been processed through a heat treatment process to toughen it and aid its conductivity [7].

1.2.1.4 Flow plates and flow fields

The gas flow plate has many different descriptive names; interconnect; bipolar plate; flow plate; electrode; with respect to the type and the design of the PEM fuel cell. The flow plate is a vital component of a PEM fuel cell, it distributes fuel and oxidant to reactive sites, collects produced current, removes reaction products, manages water through the cell and provides mechanical support for the cells in a stack. Specially designed flow plates, with intricate flow fields imbedded, have to meet the conflicting requirements, of providing good electrical contact and allowing easy passage of the gases concerned, distribute hydrogen to the surface of the anode and air to the surface of the cathode [8]. The flow plate design is very important and it is the main theme of this thesis. The interaction of this component with other components of the PEM fuel cell is profound and reviewed in Chapter 2 and the scope of this thesis with relation to the flow plate design is summarised in section 1.3.

1.2.2 PEM Fuel Cell Applications

PEM fuel cells offer several advantages over the use of other fuel cell types; including low temperature operation, high power density, fast start up, system robustness, flexibility of fuel type (with reformer) and no sealing, corrosion, shielding or leaking concerns [8]. PEM fuel cell technology may be a leading candidate technology for the application to portable electronic devices, remote

systems including space applications and for light-duty transportation applications. With fuel reformers, conventional fuels such as natural gas or gasoline can be used in the absence of a hydrogen source. Fuel cell systems have been demonstrated by major automobile companies mainly as a public relations campaign to show a zero emission vehicle, but still they have not taken to this market due to cost, infrastructural and policy reasons [6].

Many industries are pushing for fuel cells to be used in portable electronic devices. These devices are getting smaller and more powerful, with; internet /phone /messaging /radio /music /TV /video /camera /photos /games /documents /3G /Bluetooth /GPS /; these devices need a lot of power, to last an acceptable period of time, in a small space. PEM fuel cells are not readily available in the market place but Direct Methanol Fuel Cells (DMFC), have been pioneered by some companies due to the availability of their fuel, methanol. Angstrom Power Inc. [9] is one of many new companies and has demonstrated 'Better than Batteries' performance at scales equivalent to today's mobile lithium ion batteries. Toshiba launched a direct methanol fuel cell in Japan in October 2009 as an external power source for mobile electric devices [10].

In the past, the limiting factors of intermittent renewable energy (especially wind power) have been storage, transport and control of that energy. With the use of fuel cells and hydrogen technology, electrical power from renewable energy sources can be delivered where and when required, cleanly, efficiently and sustainably. Wind/hydrogen hybrid systems use the benefits of renewable energies with the benefits of hydrogen and fuel cells, negating most of the limitations of both technologies. Fuel cell systems offer high efficiency, high power to weight ratio, small size, scalable, silent, clean, green technology to compliment renewable energy systems. A PEM electrolyser can produce hydrogen from water when excess energy is available from the renewable energy source. The hydrogen is then stored. The PEM fuel cell can transform this stored energy into electricity, on demand, effectively and efficiently when there is limited renewable energy available [11]. Remote devices that use electricity, far from power lines or human intervention that need a constant supply of energy; buoys, remote stations, houses and bases, etc or those facilities that need a backup power supply; hospitals, factories, computer servers, etc could be the starting point for these systems. In addition the system design can be applied to satellites. Hundreds of satellites orbit the Earth every 90 minutes with 45 minutes of darkness and 45 minutes of an enormous amount of solar radiation. Satellites can be in space for longer than 10 years. With the increased telecommunications market it is imperative that energy systems of these satellites is small and light and reliable over a long period of time. Solar panels used in conjunction with batteries have been used since the earliest days of space travel. These systems have some issues including, weight, heat generation, power density, cycle life. PEM fuel cells in conjunction could be used in a similar manor as wind/hydrogen system described.

1.2.3 PEM Fuel Cell Outlook

Despite many potential benefits, the PEM fuel cell still faces many challenges such as crossover losses, flooding, inadequate fuel utilisation and problems with low temperature start-up. However the largest constraint of PEM fuel cells is their cost (between $1500 and $3000/kW), this is due to the amount of precious metals used, low volume production, infancy of the technology and immature manufacturing processes used. Large volume production of fuel cells, with reduced and efficient use of precious metals, should reduce the cost of a PEM fuel cell to under $100/kW in the next 5 years [12]. The hydrogen economy holds great promise for the future of power generation and transport industry and fuel cells provide the most effective, efficient device for converting hydrogen into electricity. Potential markets are being established in the energy world and as a result focus is being placed on the fuel cell design and engineering for better performance. Some of the first hydrogen pipelines have been constructed and many more are planned. In the interim hybrid engines and fuel cells using fossil fuels or alcohols may bridge the current fossil fuel based power and transport industry to a clean hydrogen based power and transport industry.

Security of energy supply, global climate change, carbon taxes, CO_2 fines and costly carbon credits, as well as economic implications of rising fuel prices, will create financial drivers for renewable, carbon free or neutral energy for domestic users, Small and Medium Enterprises (SME's) and larger industries alike. We not only need energy from sustainable sources, we also need clean energy.

1.3 Thesis Scope

PEM fuel cells still need to solve basic problems including, a reduction of cost, weight, complexity and optimal component material selection, but they must ensure to sustain a robust, efficient and easy to manufacture product, before they are an everyday device in cars or phones. The materials currently being used in PEM fuel cells have essentially remained the same for the last 25 years [13]. In spite of all the industrial R&D efforts, the time-effective design and optimization of the flow fields and flow plates remain one of the important issues for the cost reduction and performance improvement of PEM fuel cells. Flow plates constitute between 60% & 80% of the weight and 30% of the total cost in a fuel cell stack. Therefore widespread applications of PEM fuel cells rely heavily on both cost and weight reduction of the flow plate [14].

The ultimate goal of this body of work is to improve the performance of PEM fuel cells (i.e. increase the energy efficiency and power density). This can be achieved by PEM fuel cell flow plate development. The focus of the thesis is to develop low-cost lightweight construction materials, enhance the design, layout, configuration, water mitigation and fabrication methods of the PEM fuel cell flow plate.

1.4 Thesis Goals & Scientific Objectives

The objectives of the following work are:

- To create a body of information of current PEM fuel cell flow plate research and view gaps in literature.
- To increase the effectiveness of PEM fuel cells flow plates, in relation to design, layout, configuration, water management, gas transport to achieve a better performing PEM fuel cell.
- To investigate the methods and issues associated with water accumulation and water transport through flow plate and flow field designs.
- To develop a computer model of channels of flow plate flow fields that would aid in the design and mitigation of water flooding in PEM fuel cells and to validate this model by visualisation techniques.
- To investigate the use of innovative open pore cellular foam materials as a flow plate material in a PEM fuel cell.
- To develop a Representative Unit Cell Structure (RUCS) of the above foam material and create a model to simulate this material, in relation to design, layout, configuration, water management, gas transport to achieve a better performing PEM fuel cell.
- To develop a PEM fuel cell electrochemistry model with a conventional flow plate design and porous foam flow plate design and to validate both models by experimentation.

1.5 Thesis Layout

Chapter two is a review of the literature relevant to this study. The literature review is divided into nine different sections. The present global energy outlook is viewed in Section 2.1. Section 2.2 examines the possibility of a future energy carrier, hydrogen, and hydrogen production methods such as electrolysis and bio hydrogen production are briefly reviewed. Section 2.3 introduces the PEM fuel cell including its operation and electrochemistry, this section is structured to introduce the reader to PEM fuel cell technology. Section 2.4 details PEM fuel cell design: the membrane, catalyst, GDL and flow plates are examined and design issues reviewed. Section 2.5 reviews water management of PEM fuel cells. This section describes water flooding and the effects on the PEM fuel cell performance. The interaction of water droplets with gravity is briefly reviewed and the final sections review methods and component designs that help manage or mitigate water flooding issues. Section 2.6 reviews PEM fuel cell modelling and introduces the reader to this topic. Section 2.7 describes open pore cellular foam material, structure, current applications and characteristics, which may be beneficial to PEM fuel cells. Section 2.8 reviews the current status of PEM fuel cells and potential

benefits and obstacles to the success of fuel cells. Section 2.9 summarises the literature review and conclusions and gaps in literature are identified. A very important gap in the literature was found in the literature review and this forms a major part of the research in this thesis.

Chapter three describes the model and simulation methods used in the course of this thesis. The aim of this chapter is to introduce the reader to the Computational Fluid Dynamic (CFD) modelling, which was the main tool used to complete the modelling and simulation and to obtain an overview of the models used to complete the analysis and development of the PEM fuel cell.

Chapter four details the layout, design, setup, methods and procedures in the PEM fuel cell testing and flow visualisation experiments. This brief chapter is an overview for the reader and informative for future researchers that may need guidance and advice in this area of the subject.

Chapter five details flow plate model development, simulation and experimental results with relation to the design and development of effective flow plates. The simulation results include the CFD flow plate model simulation results, the mini channels Volume of Fluid (VOF) model simulation results, the open pore cellular foam CFD results and the PEM fuel cell electrochemistry model results. The experimental results include the PEM fuel cell electrochemistry results and high speed camera visualisation results.

Chapter six presents a clear concise discussion of the results of this body of research. The developed models have been very effective to aid in the successful development and improved performance of innovative flow plates for PEM fuel cells, which were validated by experimentation.

Finally, Chapter seven summarises the conclusions from this thesis and presents recommendations for future research. The future research includes expanding the current studies to simulate a complete PEM fuel cell stack utilizing the open pore cellular foam material.

2

Chapter 2 - Background & Literature Review

2.1 Present Energy Outlook

The industrial revolution in the 18th century introduced social and technological benefits such as jobs, money, technology, electricity, large cities, a rise of living standards and increased life span. However industrialisation also brought exploitation, population boom, urban squalor and pollution. Fossil fuel pollution was on a scale never seen before, which has had long-term effects on planet Earth. Today the world's economies and first world, twenty first century life style, are heavily energy dependent, the majority of which is oil, gas and coal derived. Burning remarkable amounts of fossil fuels since the industrial revolution has manifested itself into global warming [15]. Anthropogenic green house gases continue to be released into the atmosphere at a rate of 3.5 million tons per hour [16]. Over the past decades alarming concerns indicating air pollution is causing the green house effect has been evident and moreover the effects on planet Earth profound, Figure 3.

The world's fossil fuel reserves are finite, eventually becoming a thing of the past, and peak oil production will be reached within the near future. However, it seems for the moment that oil is being found as much as it is being used. As the main oil reserves deplete and technology improves, new oil fields are being discovered and furthermore small fields and oil sands are becoming more economically exploitable, if not without environmental concern. The behaviour of the energy system is expected to be markedly different after oil peak is passed: the energy system will lose resilience, the price of energy will be higher, but the pattern of supply may be both more rational and predictable. Physical shortages have been experienced before, where fuel station queues become rampant. Wars and disputes may fester between regions or countries, in order to obtain the last barrels of oil, but that will increase oil prices rapidly and oil's fate will be sealed. The exact date for oil to be knocked from its position as the primary energy source is left to debate, conjecture or speculation of others.
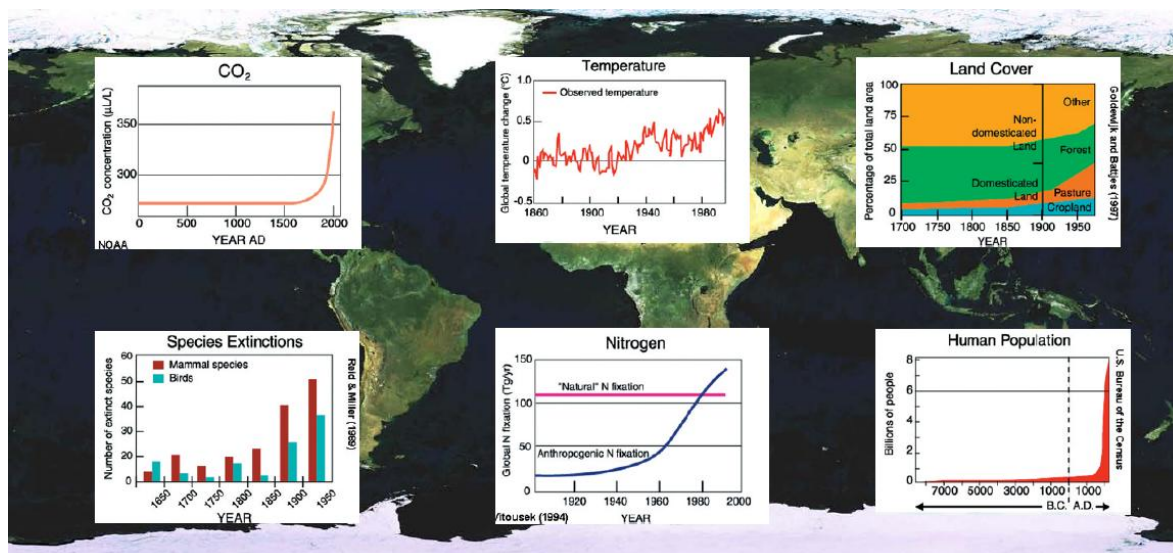
Figure 3 Climate change index 2010 [17]**.**

It is acknowledged that renewable energy technologies have a massive role to play in the coming years in order to secure energy supply, fill the cheap oil gap, ensure sustainable economies, provide sustainable human population growth, control green house gas emission and ensure a cleaner healthier environment for every being on the planet. The latest edition of world climate summits, representing over 192 countries; Cancun 2010 and Copenhagen 2009 [18], progressing from the Kyoto-protocol [19] has shown clearly that worldwide green house gas emissions must be decreased and a global temperature increase of 2°C must not be exceeded.

The European Union (EU) has decided to stimulate an increase in Europe's use of renewable energy sources. By 2020, twenty percent of Europe's energy is to be derived from renewable energy [20]. Ireland sits on the periphery of Europe with the calm Irish Sea to the east and the force of the Atlantic Ocean to the west. Weather systems travel across the Atlantic heading east. One of the first obstacles to these weather systems is the island of Ireland. Strong south westerly winds penetrate the whole country the majority of the year. The potential for electricity generated by wind power is enormous for Ireland. In 2008 the Irish government set a target of 40% electricity consumption from renewable sources by 2020. In the 2001 Ireland was set a target of moving from 3.6% to 13.2% renewable electricity by 2010 by a European directive. Ireland achieved 14.4% in 2009 and is on track to exceed the national target of 15% in 2010. The significant electricity production growth from renewable sources in recent years is largely attributable to onshore wind [21,22].

Renewable energy sources, such as wind, solar, wave and biomass, are starting to establish themselves in energy markets and in the near future, circa 2050, clean nuclear fission and nuclear fusion are expected. With existing renewable technologies and new complimentary technology developments, new energy carriers and new energy markets are being developed. Furthermore over a

period of years renewable energy will provide advantages over and reduce the need for fossil fuels. One of these energy carriers is hydrogen and the complementary technology is the fuel cell.

2.2 Future Energy Carrier: Hydrogen

Composed of a single proton and a single electron, hydrogen is the simplest and most abundant element in the universe. It is estimated that 90% of the visible universe is composed of hydrogen. Hydrogen is the raw fuel that most stars 'burn' in a fusion process to produce energy. The Sun's hydrogen supply is expected to last another 5 billion years. On earth molecular hydrogen (H_2) can be used as a fuel in order to power engines, produce heat or produce electricity directly [23].

Scientists had been producing hydrogen for years before it was recognized as an element. Written records indicate that Robert Boyle produced hydrogen gas as early as 1671 while experimenting with iron and acids. Henry Cavendish first recognized hydrogen as a distinct element in 1766.

Hydrogen is found naturally on earth combined with other elements, for example in water it is combined with oxygen and in fossil fuels it is commonly combined with carbon. Hydrogen combines with other elements also forming numerous compounds. Some common compounds are: water (H_2O), ammonia (NH_3), methane (CH_4), table sugar ($C_{12}H_{22}O_{11}$), hydrogen peroxide (H_2O_2) and hydrochloric acid (HCl).

Hydrogen possibly has a great future. When it is used in energy generation the only by-products are water and heat, no green house gases and no harm full waste. Hydrogen can have the benefit of being a clean non-toxic renewable fuel source. If it can be produced cheaply and transported safely it may replace fossil fuels as an energy carrier [24]. Hydrogen has to be produced or processed for it to be used as a fuel. The challenge is to separate hydrogen from other naturally occurring compounds in an efficient and economic manor [25].

2.2.1 Hydrogen's Commercial Importance

Ironically, the main use of hydrogen in today's economy is for fossil fuel purification, but it is also used throughout many industries across the world [26].

- Refineries use hydrogen in chemical processes in order to remove sulphur and to convert heavy hydrocarbons to gasoline and diesel.
- Large amounts of hydrogen are combined with nitrogen from the air, in order to produce ammonia (NH_3), a major component of fertilizer and a familiar ingredient in household cleaners, through a process called the Haber process.
- Hydrogen is also used as an additive in the food industry, such as peanut oil, through a process called hydrogenation.

- Liquid hydrogen is used in the study of superconductors and when combined with liquid oxygen it makes an excellent rocket fuel.

- Hydrogen can be used to power internal combustion engines or to make electricity directly using fuel cells.

2.2.2 Hydrogen Production

Hydrogen is not an energy source, rather an energy vector or carrier [26]. This means that it has to be produced from one of the primary energy sources: fossil fuels, nuclear or renewable [27,28]. The term renewable has been defined to include solar, wind, biomass, hydro, geothermal and urban waste resources [29]. There are many technologies that can be used to produce hydrogen and three of these methods are discussed in the next section.

2.2.2.1 Hydrogen production by electrolysis

In chemistry and manufacturing, electrolysis is a method of using an electric current to drive an otherwise non-spontaneous chemical reaction. Electrolysis is commercially highly important as a stage in the separation of elements from naturally occurring compounds such as ores using an electrolytic cell.

Water electrolysis is the splitting of water molecules into its simpler elements, hydrogen and oxygen gases, by applying a DC voltage higher than a thermo neutral voltage (1.482 V) to electrodes. Molecular hydrogen is produced at the negative electrode (cathode) and molecular oxygen is produced at the positive electrode (anode). Alkaline and PEM electrolysis are the most popular methods for water electrolysis and a detailed review was carried out by Zeng and Zang [30].

Alkaline electrolysis uses an electrolyte solution added to pure water. The added electrolyte solution reduces the resistance of pure water, resulting in a faster more efficient electrochemical process that reduces waste heat. The necessary charge exchange occurs through the flow of OH-ions in the electrolyte and current (electrons) in the electric circuit. Strong bases such as potassium hydroxide (KOH), and sodium hydroxide (NaOH) are frequently used as electrolytes.

PEM electrolysis is the reverse process of a PEM fuel cell and the electrolyte is a membrane. Oxygen is produced at the positive electrode (anode) while the protons pass through the membrane and combine on the opposite electrode (cathode) with electrons to form hydrogen.

Water electrolysis is currently around 75% energy efficient and could be theoretically increased to more than 90% in the future [26]. Therefore this process appears to be an efficient method of producing high purity hydrogen in large quantities with little or no environmental impact, if the electrical energy required is from a renewable power source [31].

2.2.2.2 Hydrogen production by steam reforming of fossil fuels

Hydrogen may be obtained from fossil fuels such as methanol, petroleum or coal. However natural gas is commonly used, as it is the most economically viable at present. The process is called steam reforming of fossil fuels and combines high temperature steam with the hydrocarbon in a catalytic chemical reaction that removes the carbon element, producing hydrogen but also large quantities of carbon dioxide. At elevated temperatures the metal catalyst is usually nickel. The hydrogen produced through steam reforming is not as pure as electrolysis production as it contains impurities such as sulphur [32].

2.2.2.3 Biological hydrogen production

In 1939 a German researcher named Hans Gaffron [33], while working at the University of Chicago, observed that the algae he was studying, Chlamydomonas reinhardtii (a green-algae), would sometimes switch from oxygen production to hydrogen production. Gaffron never discovered the cause for this change and for many years other scientists failed in their attempts at its discovery. Cyanobacteria and micro algae along with higher plants are capable of oxygenic photosynthesis according to the following reaction:

$$CO_2 + H_2O \Rightarrow 6\ [CH_2O] + O_2 \qquad\qquad Eqn.\ (2.2.1)$$

In the late 1990s professor Anastasios Melis [34] found that under certain conditions, a few groups of micro algae and Cyanobacteria consume biochemical energy instead of reducing CO_2. The algae, with its internal oxygen flow interrupted allowed the enzyme responsible for hydrogen production, hydrogenase, an environment to react. The algae produce molecular hydrogen by the following reaction:

$$2H^+ + 2X_{reduced} \Rightarrow 6\ H_2 + 2X_{oxidized} \qquad\qquad Eqn.\ (2.2.2)$$
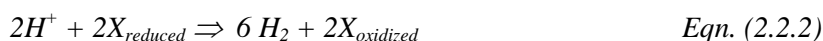
where the electron carrier, X, is thought to be ferredoxin.

Phototrophic purple bacteria, Rhodospirillum rubrum & some Cyanobacteria, when exposed to sunlight can be used for hydrogen production on the basis of bacterial growth [35]. In such a photo-fermentation process, the microorganisms produce hydrogen and carbon dioxide under anoxic conditions by using the chemical energy of organic acids and additional light energy of the sun. Hydrogen evolves as the final product from hydrogenase and nitrogenase activity. Nitrogenase is an enzymatic complex, which enables fixation of atmospheric nitrogen. Molecular nitrogen is reduced to ammonium with consumption of Adenosine Triphosphate (ATP):

$$N_2 + 6H^+ + 6e^- \Rightarrow 2HN_3 \qquad\qquad Eqn.\ (2.2.3)$$
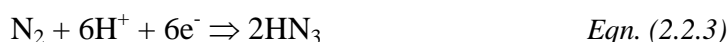
However Nitrogenase catalyzes proton reduction in the absence of nitrogen gas.

$$2H^+ + 2e^- \Rightarrow H_2 \qquad\qquad Eqn.\ (2.2.4)$$
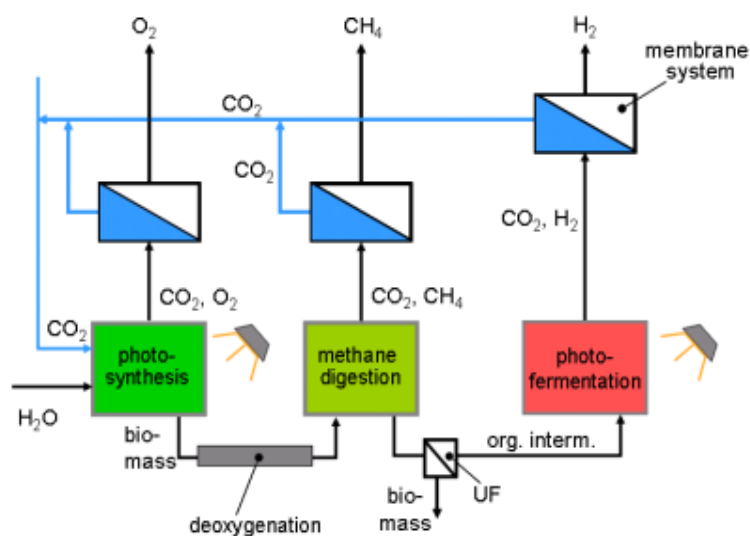
Figure 4 Bio-hydrogen production system using three types of hydrogen producing organisms [36]**.**

To date the bio-hydrogen production process has only been investigated in laboratory experiments, Figure 4 [36]. However first estimations have shown, that a ground-area of around 400 m² has to be covered by photo-fermentation reactors in central Europe to produce hydrogen containing approximately 1.6 kW of annual mean thermal energy. Hydrogenase is however too oxygen-labile for sustainable hydrogen production. Biological hydrogen production is the most challenging area of biotechnology with respect to environmental problems.

The future of hydrogen production depends not only on research advances, i.e. reactor efficiency improvement in or through genetically engineering micro-organisms, but also on economic considerations (the cost of fossil fuels), social acceptance and the development of energy systems that can utilize hydrogen e.g. fuel cells [37].

2.3 Proton Exchange Membrane Fuel Cells

Fuel cells present the most efficient, most effective and cleanest device to convert hydrogen fuel directly into electricity. A Proton Exchange Membrane (PEM) fuel cell, Figure 5, offers a low temperature, high power, robust, practical, scalable fuel cell to power everything from portable electronic devices to vehicles to space craft.

DuPont originally developed a solid phase acid supported proton conducting membrane, an ionomer, in the late 1960's [1]. This proton conducting membrane allows the flow of hydrogen ions and can stop electrons. However the membrane needs to be saturated with water so that the transport of ions can proceed. This Teflon based solid electrolyte was exploited by many applications. The membrane reduced the complexity and resistance issues associated with liquid electrolytes of electrochemical

devices at the time. The idea of a low temperature, liquid electrolyte free fuel cell, a PEM fuel cell, was created. PEM fuel cells operate at low temperatures providing instant start-up and require no thermal shielding to protect personnel. The use of a solid polymer electrolyte eliminates the corrosion and safety concerns associated with liquid electrolyte fuel cells. About 50% of maximum power is available immediately at room temperature. Full operating power is available within about 3 minutes under normal conditions [5].
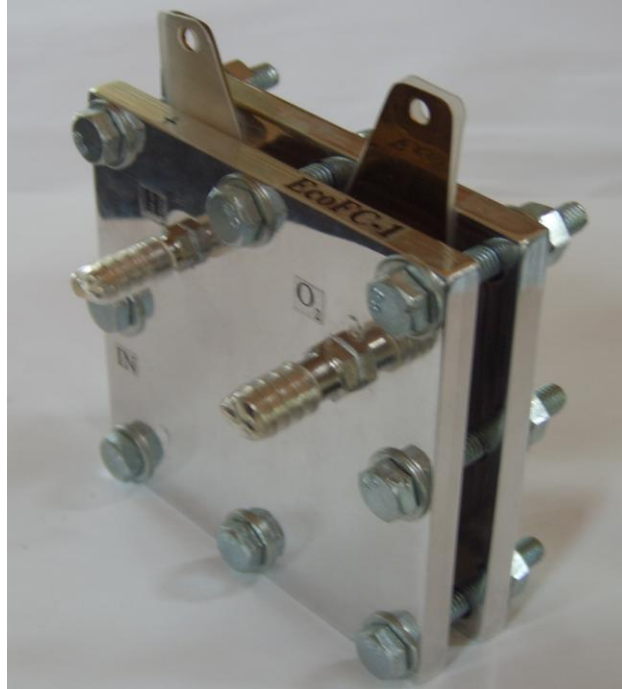
Figure 5 Proton Exchange Membrane (PEM) fuel cell.

2.3.1 PEM Fuel Cell Layout & Operation

A single PEM fuel cell is almost universally of the layered, planar, unipolar type (for individual cells) or bipolar type (for stacks), and operates effectively between 60°C - 80°C, Figure 6. To obtain the desired amount of electrical power, individual fuel cells are combined to form a fuel cell stack. Increasing the number of cells in a stack increases the voltage, while increasing the surface area of the cells increases the current.

The membrane, which allows the conduction of hydrogen ions, is located at the centre of each cell. On either side of the membrane, the cathode and anode layers, which consist of soot like carbon particles with nano-meter-size platinum particles, as the catalyst bonded to them, initiate the electrochemical reaction. The electrodes on each side of the membrane are porous, allowing the respective gasses to diffuse through them. These three layers can be combined into one unit known as the Membrane Electrode Assembly (MEA) [5]. The Gas Diffusion Layer (GDL) is attached to either side of the MEA to allow even spread and uniform diffusion of the gases concerned to the electrode/membrane interface. The next layer has specially designed bipolar plates (also called field

flow plates or gas diffusion plates) to distribute hydrogen to the anode surface and air to the cathode surface.
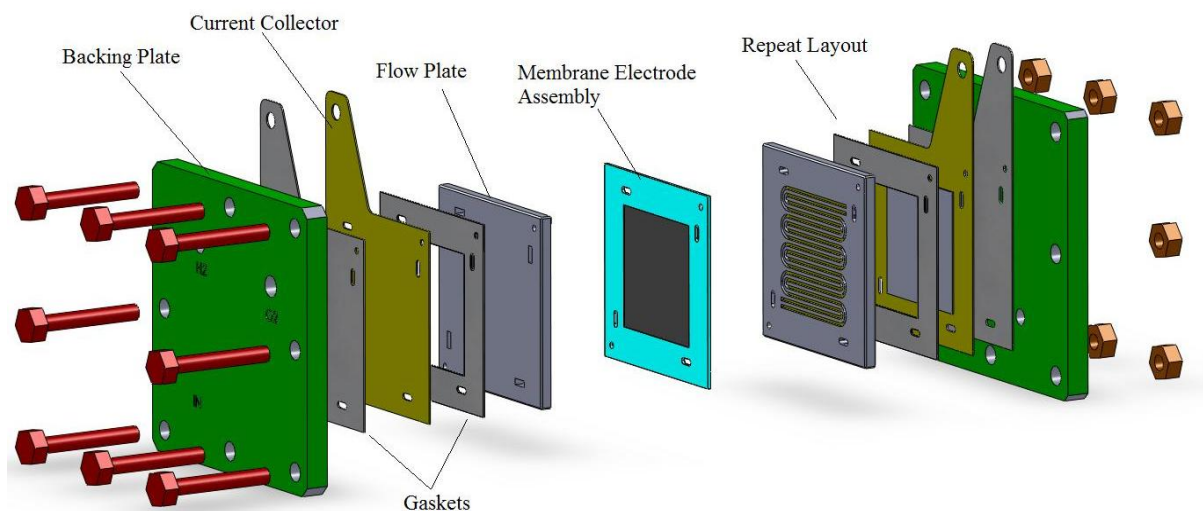
Figure 6 Proton Exchange Membrane (PEM) fuel cell model (exploded view).

PEM fuel cells operate on the principal of an electrochemical reaction between hydrogen and oxygen with the aid of a catalyst. Hydrogen fuel is channelled to the anode, on one side of the fuel cell, while oxygen from the air is channelled to the other cathode side of the cell. The hydrogen diffuses through the GDL to the anode catalyst. At the anode, the hydrogen molecules first come into contact with the platinum catalyst on the electrode surface. The hydrogen molecules break apart, bonding to the platinum surface forming weak H-Pt bonds. As the hydrogen molecule is now broken the oxidation reaction can proceed. Each hydrogen atom releases its electron, which travels around the external circuit to the cathode (it is this flow of electrons that is referred to as electrical current). The remaining hydrogen proton bonds with a water molecule on the membrane surface, forming a hydronium ion (H_3O^+). The hydronium ion travels through the membrane material to the cathode, leaving the platinum catalyst site free for the next hydrogen molecule. At the cathode, oxygen molecules come into contact with a platinum catalyst on the electrode surface. The oxygen molecules break apart bonding to the platinum surface forming weak O^-Pt bonds, enabling the reduction reaction to proceed. Each oxygen atom then leaves the platinum catalyst site, combining with two electrons (which have travelled through the external circuit) and two protons (which have travelled through the membrane) to form one molecule of water. The redox reaction has now been completed. The platinum catalyst on the cathode electrode is again free for the next oxygen molecule to arrive.

2.3.3 PEM Fuel Cell Electrochemistry

This section examines PEM fuel cell electrochemistry and identifies how power is generated within a fuel cell. Electrical losses within fuel cells are recognized and issues with PEM fuel cells are

identified. It is important to understand how factors such as temperature, material, design and configuration affect the electrochemistry efficiency of a fuel cell.

In fuel cells chemical energy contained in a fuel can be directly converted into electricity at theoretically higher efficiencies than all other common fuel conversion methods. The Carnot efficiency limit that affects combustion and heat engines does not apply to fuel cells. When chemical energy is converted to electricity as in combustion for example, the heat of the maximum theoretical efficiency is limited by the operating temperatures [1]. This fact is expressed below in equation 2.3.1.

$$\eta = T_{max} - T_{min} / T_{max} \qquad\qquad Eqn.\ (2.3.1)$$

The theoretical efficiency for fuel cells can be expressed as a relationship between the mechanical energy available, free energy change of the fuel cell reaction ΔG in the higher heating value of the fuel cell reaction, and the enthalpy change of the fuel cell reaction ΔH [38].
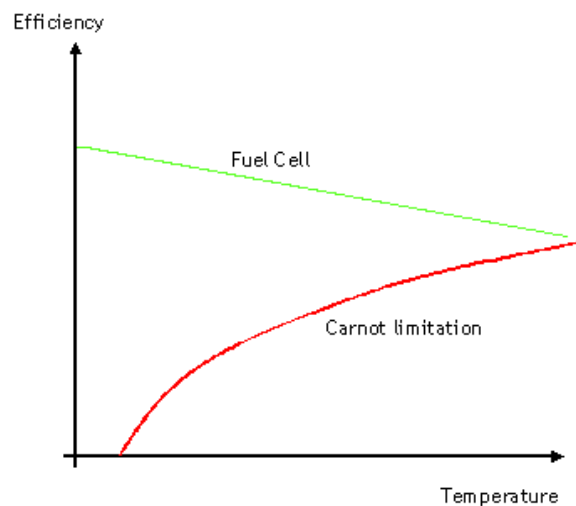
Figure 7 Comparing fuel cell and Carnot efficiency as a function of temperature [38]

Fuel cells potentially have a higher efficiency and over a large temperature and power range as shown in Figure 7. Combustion and heat engines are well suited for operation under constant conditions because they have a limited maximum power range. Should this range be exceeded their efficiencies drop quite fast. This is where fuel cells have a large advantage, because they have a high efficiency over a high a range of powers and temperatures. This makes fuel cells perfect for dynamically load cycles [38].The high efficiency at very low loads is particularly useful.

2.3.3.1 PEM fuel cell voltage & efficiency

If the PEM fuel cell was perfect at transferring chemical energy into electrical energy, the ideal cell voltage (thermodynamic reversible cell potential) of the hydrogen fuel cell would be 1.23 volts, at 25ºC and one atmosphere [1]. However this is not the case for a practical cell, the formation of water from hydrogen and oxygen gases is an exothermic reaction, which has an enthalpy of -286 kilojoules

of energy per mole of water formed. The free energy available to perform work decreases as a function of temperature. At 25ºC and one atmosphere the free energy available to perform work is about -237 kilojoules per mole. This energy is observed as electricity and heat. As the fuel cell heats up to operating temperature, around 80ºC the ideal cell voltage drops to about 1.18 volts. However there are many limiting factors that reduce the fuel cell voltage further. The voltage out of the cell is a good measure of electrical efficiency; the lower the voltage, the lower the electrical efficiency and the more chemical energy is released in the formation of water and transferred into heat [1]. The fuel cell's performance is summarised with the graph of its current and voltage characteristics, polarisation curve (I-V curve) shown in Figure 8 and explained in detail in the next sections.
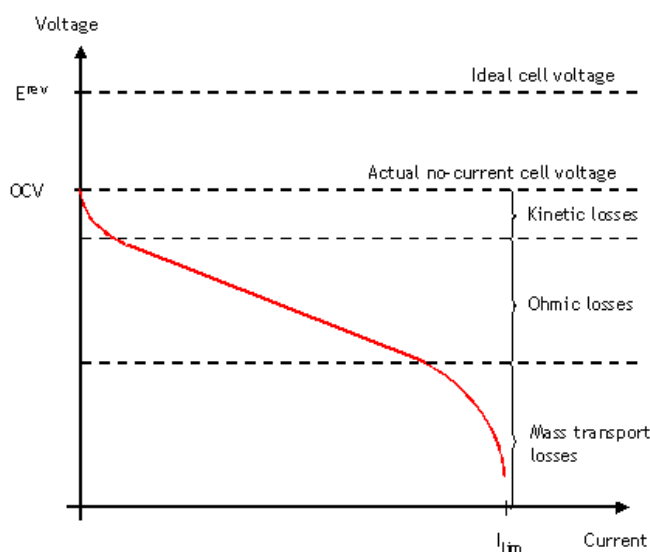
Figure 8 A typical current voltage diagram for a fuel cell indicating the points on the I-V curves that correspond to different losses [38]**.**

2.3.3.2 Energy losses in PEM fuel cells

The losses in fuel cells are a very important concept to understand for the following sections in this work. The losses in fuel cells are related to the power produced by the cells. The more current that is drawn from a cell, the higher the losses from the cell would be. This is the reason why the voltage of the cell reduces as more current is drawn from the cell. This ideal cell voltage (E_{rev}) of a fuel cell can be calculated from the available free energy, ΔG [1].This equation is shown below in equation 2.3.2:

$$E_{rev} = \Delta G / nF \qquad\qquad Eqn.\ (2.3.2)$$

Where ΔG is the free Gibbs energy, n is number of electrons transferred in the electrochemical reaction and F is the Faraday constant (94685 C/mole) [1]. The E_{rev} is also dependent on operating conditions like temperature, pressure and concentration of reactants.

The term overvoltage refers to the difference between the ideal cell voltage and the operating cell voltage. This, in due course, represents the losses in the cell. The relationship between the theoretical

E_{rev} and the actual operating voltage (E_{cell}), expressed in equation 2.3.3, is a more correct way to express the efficiency (η) of a fuel cell [1].

$$\eta = E_{cell} / E_{rev} \qquad \textit{Eqn. (2.3.3)}$$

In general there are four main sources of potential drop in PEM fuel cells:

- Activation over potential
- Ohmic over potential
- Mass transport (concentration) over potential
- Fuel crossover and internal currents losses

Understanding these fundamental concepts of losses in the fuel cell and the terminology used to describe them is essential for understanding the following sections of this work.

2.3.3.3 Activation over potential

Activation losses are a result of the energy required to initiate the reaction and losses due to the slowness of the electrochemical reactions taking place on the surface of the electrodes. This is a result of the catalyst. The better the catalyst the less activation energy required. Platinum forms an excellent catalyst however there is much research underway for cheaper materials. A limiting factor to power density available from a fuel cell is the speed at which the reactions can take place. The cathode reaction, (the reduction of oxygen) is about 100 times slower than that of the reaction at the anode, thus it is the cathode reaction that limits power density. The losses depend on factors such as electrode material properties, ion intersection and electrolyte characteristics. These losses can be reduced by increasing the operating temperatures however increasing the temperature may cause other losses. Electrochemical reaction kinetics cause the voltage to decrease and these losses can mainly be seen in an I-V curve as the cell begins to produce current, as seen on the left-hand side of Figure 8. The Tafel equation is used to model the losses, it is simplified as:

$$\eta_{act} = A\ln(i/b) \qquad \textit{Eqn. (2.3.4)}$$

where, i is the current density, $A = A_a + A_c$, which are constants depending on the electrodes (slope of the Tafel equations) and $b = i_{oa}{}^{Aa/A} + i_{oc}{}^{Ac/A}$ where, i_o is the exchange current density [1].

2.3.3.4 Ohmic over potential

Ohmic losses are a result of the combined electrical resistances of the various fuel cell components that produce heat. These include the electrode material resistance, the electrolyte membrane resistance and the various interconnection resistances. The major proportion of the losses within a fuel cell occur as more current is drawn from the cell, as seen in Figure 8 (middle part of the plot). The voltage drop is linearly proportional to current density (or the current taken from the cell) therefore the loss can be modelled using [38]:

$$\eta_{ohmic} = iR \qquad\qquad \textit{Eqn. (2.3.5)}$$

where, i is the current density given in Acm^{-2} and R is the specific resistance given by:

$$R = L/A\sigma \ \Omega cm^2 \qquad\qquad \textit{Eqn. (2.3.6)}$$

where L is the length of the electrode, A is the area of electrode and σ is the conductivity. The resistance can be reduced by using electrodes with a high conductivity, appropriate flow plate material and making the electrolytes as thin as possible [39].

2.3.3.5 Mass transport over potential

Mass transport (concentration) losses result from the reduction of the concentration of hydrogen and oxygen gases at the electrodes. For example, following the reaction new gases must be made immediately available at the catalyst sites. With the build up of water at the cathode, particularly at high currents, catalyst sites can become clogged, restricting oxygen access. This is responsible for the sharp decline in the potential at high current densities and can be seen at the tail end of the I-V curve in Figure 8. Using the Nernst Equation, the loss can be modelled by the following equation [38]:

$$\eta_{conc} = (RT/2F)\ln(1-i/i_1) \qquad\qquad \textit{Eqn. (2.3.7)}$$

where R is the specific gas constant for hydrogen, T is the operating temperature i_1 is the limiting current density. If R and T are known, equation 2.3.7 is further simplified to:

$$\eta_{conc} = m \exp(ni) \qquad\qquad \textit{Eqn. (2.3.8)}$$

where m is $3e^{-5}V$ and n is $8e^{-3}\ cm^2 mA^{-1}$ [40].

2.3.3.6 Fuel cross over and internal currents

This loss is typically small compared to others therefore its effect can be negligible in correctly sealed and supported cells [39]. It is the energy loss due to the waste of fuel passing through the electrolyte and from electron conduction through the electrolyte. The electrolyte is only supposed to transport ions; however a certain amount of fuel diffusion and electron transfer will always be possible.

2.3.3.7 Combining PEM fuel cell losses

It is these combined losses that characterise the I-V graphs and indicate the performance of the PEM fuel cell. The real voltage output of the cell can therefore be obtained by starting with the thermodynamically predicted voltage (1.23V) and then subtracting the voltage losses:

$$E_{cell} = V = E_{rev} - \eta_{act} - \eta_{ohmic} - \eta_{conc} \qquad\qquad \textit{Eqn. (2.3.9)}$$

therefore

$$V = E_{rev} - A\ln(i/b) - iR - m \exp(ni) \qquad\qquad \textit{Eqn. (2.3.10)}$$

E_{rev} is the reversible OCV given by 1.23V.

A is the slope of the Tafel line {0.03V}

R is the area-specific resistance {2.45 e−4}

m {3e-5V} and n {8e-3 cm^{2}mA^{-1}} are the constants in the mass-transfer overvoltage. These values are taken from Ballard Inc. [40].

2.4 Proton Exchange Membrane Fuel Cell Design

This section reviews the most important materials under development for PEM fuel cells in relation to flow plates, electro-catalysts, GDLs and ion conducting membranes. This section also examines the designs and configurations of flow plates and flow fields and their interaction with other PEM fuel cell components. It is acknowledged that the PEM fuel cell is composed of additional components such as backing plates, gaskets, interconnects etc and these serve to ensure a correct operational robust PEM fuel cell. However for the purposes of design aspects covered in this thesis the major areas will be discussed and additional components will be discussed as necessary.

Depending on the fuel used in the PEM fuel cell, the requirements for these materials are completely different. For this thesis the PEM fuel cell is considered to operate with pure hydrogen and oxygen from air, unless otherwise stated.

The main requirement for the future of PEM fuel cells is to achieve a reduction in the capital cost of the system. Attention to materials selection is the main goal of researchers while fabrication and scaling-up the production volume is the main goal of industry trying to commercialise PEM fuel cells. These efforts may cause a complete review of all the materials used up to now [13].
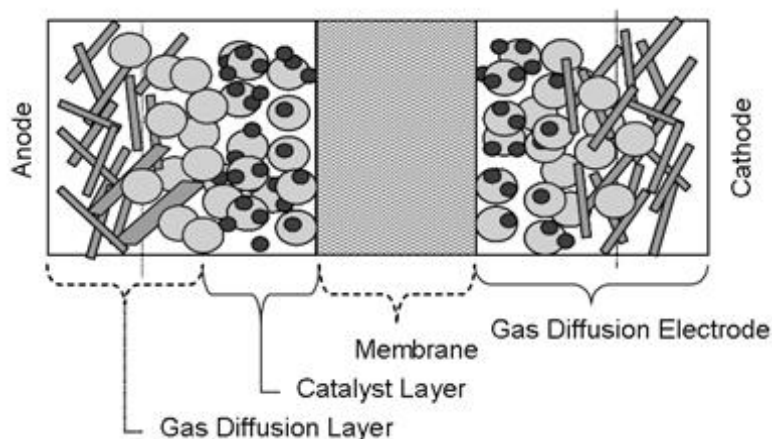
Figure 9 Membrane Electrode Assembly (MEA) [42]**.**

2.4.1 Membrane Electrode Assembly (MEA)

At the heart of the PEM fuel cell is a membrane electrode assembly (MEA), comprising of a proton exchange membrane sandwiched between two electrodes (the anode and the cathode), which contain

the electro catalyst, Figure 9. Attached to each electrode is a gas diffusion layer. This configuration is referred to as a 5 layer MEA. A 3 layer MEA can be manufactured also, but in this configuration the GDL is not attached [41].

2.4.1.1 Proton exchange membrane

The membrane material used in PEM fuel cells is mainly polymer based and it is located between the cathode and anode layers. The membrane functions as an electrolyte, allowing the flow of hydrogen ions but it stops electrons. Electrons then must flow through an external circuit producing electricity. The membrane should have the following properties:

- Resistant to chemical attack

- Durable & robust

- Wide operating temperature range -30°C to 200°C

- Highly ion-conductive

- Have minimal thickness

The most common material used for the membrane of a PEM fuel cell is Nafion. Nafion combines the physical and chemical properties of its Teflon base material with ionic characteristics that give the final material the correct parameters for use in PEM fuel cells.

$$-[(CF_2 - CF_2) - CF_2 - CF]- \qquad\qquad H^+$$
$$| \qquad\qquad\qquad\qquad\qquad |$$
$$[O - CF_2 - CF -] O - CF_2 - CF_2 - SO_3^- \quad \downarrow$$
$$| \qquad\qquad\qquad\qquad\qquad$$
$$CF_3 \qquad\qquad\qquad\qquad H^+$$
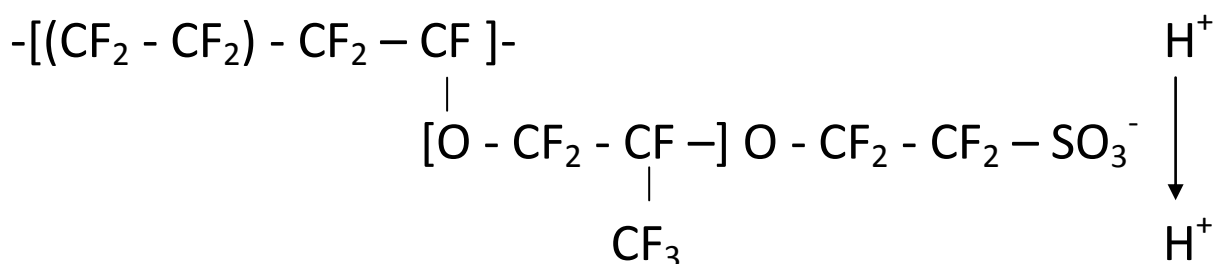
Figure 10 Long chains of PTFE (Teflon) with side chain ending with sulphonic acid.

Nafion consists of Polytetrafluoroethylene (PTFE) chains, commonly known as Teflon forming the backbone of the membrane. Attached to the Teflon chains, are side chains ending with sulphonic acid (HSO$_3$) groups, Figure 10. A close-up view of the membrane material shows long, spaghetti-like chain molecules with clusters of sulphonate side chains. An interesting feature of this material is that whereas the long chain molecules are hydrophobic, the sulphonate side chains are highly hydrophilic. For the membrane to conduct ions efficiently the sulphonate side chains must absorb large quantities of water. Within these hydrated regions, the hydrogen ions of the sulphonic acid groups can then move freely, enabling the membrane to transfer hydrogen ions, in the form of hydronium ions from one side of the membrane to the other.

Once extruded into its final form (typically sheet or tubing), Nafion is a translucent plastic that is similar in appearance to Teflon, but clearer and less opalescent. Once activated, Nafion immediately

begins to react with its surrounding environment. Moisture is absorbed and exchanged with the surroundings. The original colour of the Nafion changes gradually from translucent to yellow, then brown, then even black.

One major issue with Nafion membranes is that the proton conduction mechanism is based on the migration of hydrated protons. Above 100°C, pressurized operation is required to ensure the presence of liquid water. Support equipment such as humidifiers need to be added to the PEM fuel cell system to ensure correct humidification. Mechanical stresses such as fatigue due to the swelling and shrinking of membranes as a result of changes in water uptake during humidity and thermal cycling have a negative effect on membrane durability. Chemical degradation is another concern related to Nafion membranes and this can occur over long term operation of the PEM fuel cell. Chemical degradation can be mainly attributed to peroxide formation that attack the membranes structure by contaminant transition metal ions forming reactive peroxyl and / or hydroxyl radicals. This weakens the polymer and reduces its ability to handle mechanical stress. Chemical degradation can be intensified if the membrane is operated over 150°C with the added issue of the release of harm full gases such as fluorine [43].

There is much effort being applied to the development of cheaper, usually fluorine-free, less water dependant membrane materials [6,13,44]. These include; partial fluorine polymers, sulfonated aromatic polymers, polymer/acid complexes and inorganic composite membranes reviewed by Suo et al. [45]. Kaneko et al. [46] suggest the use of hydrocarbon polymers even though they had been previously abandoned due to low thermal and chemical stability. However hydrocarbon membranes provide some definite advantages over nafion membranes, including low cost, high water uptake, wide temperature range and they are recyclable. A fullerene-based membrane enables high-temperature PEM fuel cell operation [47]. This membrane is not water based, so the need for humidification is redundant and when operating over 100°C liquid water from the Oxygen Reduction Reaction (ORR) is not an issue. Higher temperature operation (>150°C) means carbon monoxide poisoning would be minimised, it would eliminate the need for fuel processors or reformers for some fuels and it would increase the electrode kinetic rates, improving the fuel cell performance and minimising the use of expensive catalysts.

2.4.1.2 Electro-catalyst layer

The electro-catalyst layer is the heart of the PEM fuel cell. On the hydrogen side (anode) of the PEM fuel cell the catalyst initiates dissociation of the hydrogen into protons and electrons. The electrons then travel through an external circuit while the hydrogen protons travel through to the cathode side of the membrane. This catalyst initiates the combination of the protons with oxygen from the air and the electrons from the external circuit to produce water and heat.

For fuel cell operation with pure hydrogen and air, platinum (Pt) is the most active material and it is extensively used in PEM fuel cells. However, the electro-catalyst layer is the most expensive part of PEM fuel cell. To reduce the cost, nano-particles of platinum on a carbon support have been developed. When the unit diameter of transition metals is in the nano realm, catalytic properties are dramatically enhanced and the materials are known to have increased reactivity compared to their micron counterparts. Some manufacturers can produce nano-nickel and nano-cobalt particles with just a few hundred atoms to help replace or reduce platinum content in fuel cells.

The electro-catalyst layer is made from a mixture of a catalyst, soot like carbon powder and membrane powder, a porous electrode material is produced with the nano-meter-size particles of the catalyst embedded in it, which is bonded to the gas diffusion layer on one side and pressed against the membrane on the other side. It is also noted that, cost effective fabrication of porous electrode structures was achieved for the first time only about 50 years ago when improvements in performance were obtained during the 1960s by depositing small crystallites (2–5 nm) of the electro-catalyst (usually platinum or Pt alloys) onto carbon powder or paper. This accomplishment was probably the first manifestation of an engineered nanostructure, and it is not surprising that its implementation more than 40 years ago was so difficult [13].

Today the reduction in noble-metal content without degrading the cell performance has been, and continues to be, an important R&D activity. The platinum loading has been significantly reduced from 2 mg cm^{-2} of electrode to values below 0.5 mg cm^{-2} without significant impact on performance and lifetime [6].
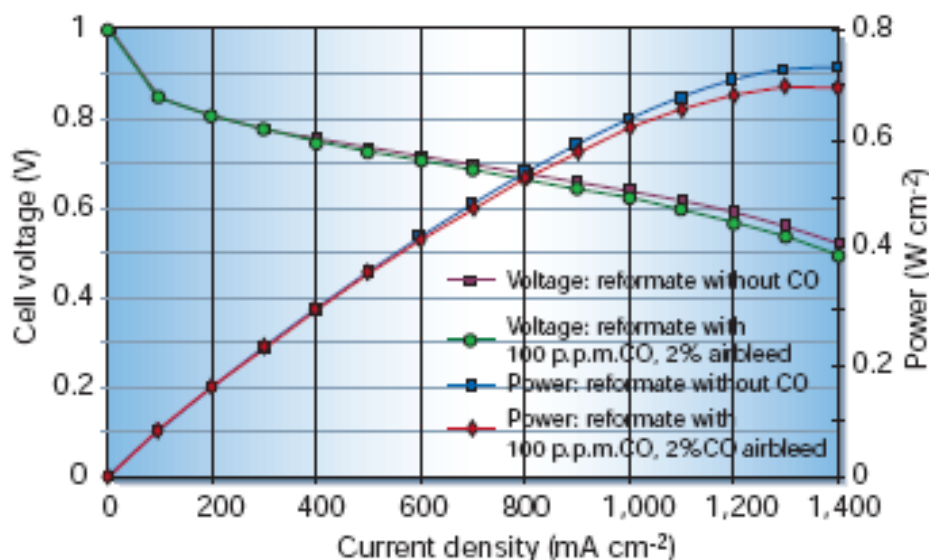
Figure 11 CO tolerance on Pt/Ru anode electrodes [13]**.**

For fuels containing traces of carbon monoxide (CO) a CO tolerant catalyst is required. This remains one of the most challenging tasks for the successful development of commercial PEM fuel cell systems. For reformate electrodes as well as for methanol oxidation, the removal of absorbed CO

species is the rate determining step. The oxidation of absorbed CO on platinum is slow, and is facilitated by adjacent absorbed OH species. This is the reason why Ruthenium (Ru), with its low potential for OH formation, is the most efficient component of the binary catalysts. Pt/Ru and other binary and ternary alloys with these noble metals have been investigated intensively and performance values have increased significantly [13]. The loss in performance is usually expressed in mV for a certain CO content, as shown in the I-V curves in Figure 11.

2.4.1.3 Gas diffusion layer

The outer most layer of the MEA is the porous electrode and gas transport layer, commonly referred to the Gas Diffusion Layer (GDL). The GDL is thicker than the catalyst layer, it is generally between 100-400μm thick, whereas the catalyst layer is between 10-50μm thick [1]. It is composed of a conductive carbon fibre, which typically consists of a fibrous structure in the form of a thin paper or woven cloth, see Figure 12.

The GDL provides many key functions for a PEM fuel cell:

- Mechanical support for the catalyst structure and membrane
- Electronic conductivity
- Heat removal
- Dispersion of the gases from the flow plates
- Reactant access to catalyst layers
- Product water removal
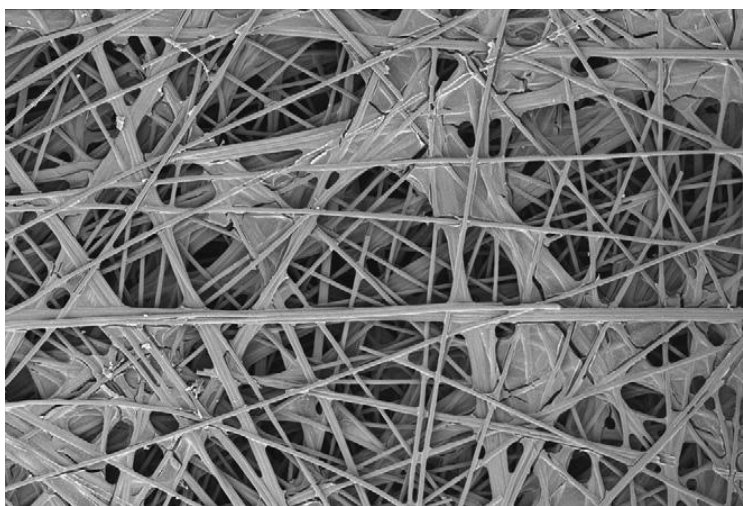
Figure 12 SEM image of a Toray GDL [12]

The porous nature of GDL micro structure makes it necessary to define an effective thermal conductivity, a transport parameter that plays an important role in fuel cell performance analysis. GDL's are manufactured from carbon cloth or a carbon paper material that has been processed through a heat treatment process to toughen it and to aid its conductivity. Since electrons flow through

the GDL heat is produced on this layer and furthermore water can stagnate on the fibres [48]. A thin GDL provides better gas access but it reduces mechanical strength and increase electric resistance.

A Micro-Porous Layer (MPL) is the inner layer of the GDL with smaller porosity than the outer layers of the GDL. Pasaogullari et al. [49,50] and Weber et al. [51] have investigated the effect of a MPL on water transport. Similar work was completed by Jin et al. [52]. The researchers showed that an MPL enhances the liquid water removal and therefore decreases flooding. They have suggested that an MPL placed at the cathode side enhances the water transport through the membrane towards the anode. Increased water removal from the cathode and increased water flow across the membrane may improve the cell performance by reducing the flooding at the cathode and by enhancing the membrane hydration and therefore increasing the conductivity of the membrane. However, Pasaogullari et al. [49,50] only used a serpentine flow channel; other flow channels may exhibit different results.
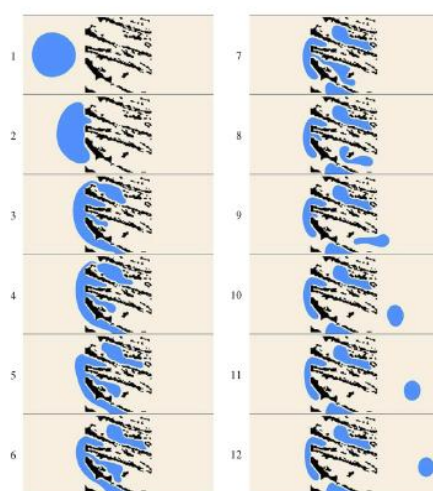
Figure 13 Unsteady two-phase simulation results using LB binary fluid model simulating two-phase flow through fibrous structure of carbon paper GDL; blue area is the liquid drop and black coloured area indicates porous GDL [53]**.**

Simulation results from multi-phase flow simulations of various fibre distributions indicate that the permeability of the medium is strongly influenced by the effect of fibre orientation. The model by Park et al. [53], Figure 13, successfully simulated the complicated unsteady behaviours of liquid droplet motion in the porous medium providing a useful tool to investigate the mechanism of liquid water accumulation/removal in the GDL of a PEM fem fuel cell. Park et al. [53] concluded that a thin GDL with small porosity results in good electrical conductivity; however efficient mass transport requires large pores. The amount of cross flow is strongly correlated with the thickness and permeability of the GDL in a PEM fuel cell. It seems that the effect of the fibre orientation on the permeability of the medium can be dominant over that of porosity within the given range of porosity.

Zang et al. [54] analysed the distribution of liquid water phase saturation for different GDL structures including GDL with uniform porosity, GDL with sudden change porosity (GDL with MPL) and GDL with gradient porosity distribution using a one dimensional model. It was noted that for uniform

porosity GDL, the gas diffusion increases with the increase of porosity and contact angle and increases with the decrease the GDL thickness. For the GDL with a MPL, the larger the MPL porosity and the thinner the MPL thickness are, the stronger the gas diffusion is and for a gradient change porosity GDL with the same average equivalent porosity, the larger the porosity gradient is, the more easily the gas diffuses.

(a)   (b)
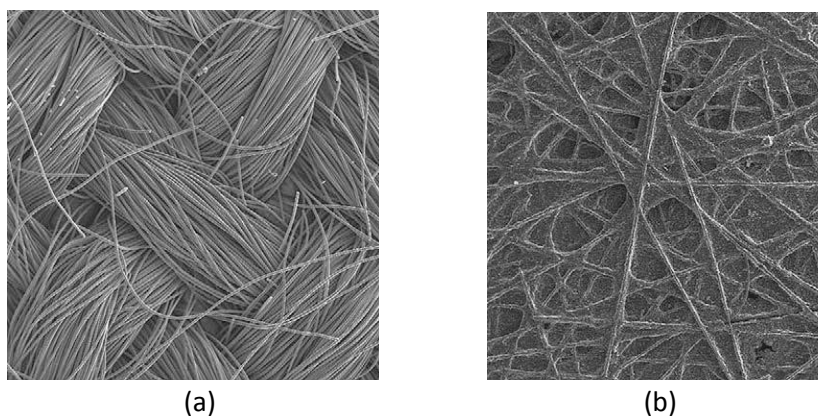
Figure 14 Microscopic pictures of the carbon gas diffusion media:(a) Carbon cloth (b) Carbon paper [55]**.**

According to Maher et al. [56] who studied of the effect of the GDL porosity, the GDL porosity has some effects on the fuel cell performance. Higher porosity improves the mass transport within the PEM fuel cell; it evens out the local current density distribution; mass-transport limitations may occur at higher current densities; the molar oxygen fraction at the catalyst layer increases with more even distribution; however higher porosity increases the contact resistance. For a lower porosity a much higher fraction of the total current is generated at the cathode catalyst layer. This can lead to local hot spots inside the MEA that can increase electrical resistance and damage the membrane.

Benziger et al. [57] examined water flow through carbon cloth and carbon paper GDLs, Figure 14, treated with Teflon. Due to the hydrophobic nature of the treated media no water flowed through the media until pressures of 5–10 kPa were applied in order to overcome the surface energy of the water/Teflon interface in the largest pores. The largest pore sizes ranges from 250 μm in the carbon cloth and 40 μm in the Toray carbon paper. The largest pore size in the catalyst layer applied to the carbon cloth was 20 μm. Increasing the applied hydrostatic pressure permitted water to flow through smaller pores in the GDL. It was noted that water flows through less than 1% of the void volume in the GDL; the small pores remain free of water to permit gas to the catalyst layer.

Zhang et al. [58] developed a metallic porous medium, with improved thermal and electrical conductivities and controllable porosity, based on micro/nano technology for its potential application in PEM fuel cells. The gas diffusion medium, as shown in Figure 15, was made of 12.5μm thick copper foil and it was tested in an operational PEM fuel cell. The small thickness and straight-pore feature of the material provided improved water management. Results indicated that the performance

did not decline at lower flow rates, unlike conventional gas diffusion layers. It was also shown that the performance can be further enhanced by increasing the in-plane transport.
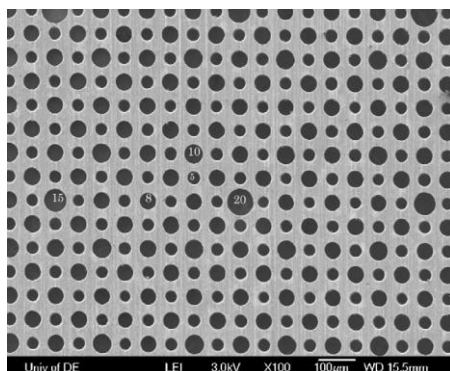
Figure 15 Image of copper GDL [58]

2.4.2 PEM Fuel Cell Flow Plates

The flow plate has many functions within the PEM fuel cell (listed below) but its main aim is to act as a manifold to supply fuel and oxidant gases to the MEA reactive sites and this makes the flow plate a vital component for the PEM fuel cell.
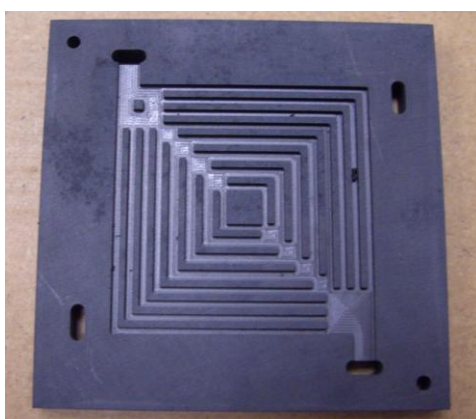
Figure 16 Flow plate with intricate flow field design.

The flow field plate acts as a gas distributor and allows for the supply and control of fuel and oxidant. At the same time it allows for an exit for waste water through the open channels and waste heat through the conductive flow plate material. In existing flow plate designs it is important to create intricate flow field structures within the flow plate, as shown in Figure 16. These flow fields can contain many channels in order to reduce gas transport losses. By incorporating this design the reactants are kept flowing across the MEA contact area. Intricate designs encourage uniform convection, mixing and homogenous reactant distribution. Comparing this method to just feeding the gas into a corner or a single chamber assembly, where the gas would tend to stagnate leading to poor reactant distribution [1]. However the necessity of an intricate design has an effect on the cost of the fuel cell; compatible materials and machining costs escalate prices.

The hydrogen and oxygen flow plates are conventionally mirror images of each other. It is noted, however that the flow plate configuration is usually designed and optimised for the oxygen side as oxygen is the limiting factor or the electrochemical reaction and liquid water is produced on this side of the cell. This methodology can also reduce manufacture and assembly complexity, thereby reducing cost. This design methodology has been adapted in this study also.

The main functions of the flow plate in a PEM fuel cell are to [59-61]:

- Separate oxidant and fuel gases.
- Distribute gases uniformly over the active areas of the MEA.
- Collect electrons and provide a conductive medium between the anode, cathode and adjacent cells.
- Ensure a solid structure for the stack.
- Remove heat from cells.
- Removal of excessive water & prevent dehydration of the membrane.
- Prevent leakage of reactant gases and/or coolant.

Flow plates constitute between 60 & 80% of the weight and 30% of the total cost in a fuel cell stack. For this reason, the weight, volume and cost of the fuel cell stack can be reduced significantly by improving the design, layout and configuration of the flow plate, the use of low-cost lightweight construction materials & optimal fabrication methods [14]. For a given PEM fuel cell the power density can be significantly increased by reducing the profile of the flow plate. As much as a 50% increase in the output power density has been reported [62,63] just by appropriate distribution of the gas through the flow plate alone. In spite of all the R&D efforts, a cost effective design and optimal operation of flow plates remains one of the important issues for the cost reduction and performance improvement of PEM fuel cells [8].

The following sub sections introduce existing state of the art flow plate designs and reviews problems and possibilities for this component in PEM fuel cells. The aim of this section is to assess current state of the art flow plates & flow fields and acquire ideas for the design and development of new innovative flow plate and flow fields.

2.4.2.1 Flow plate materials

Graphite materials are a preferred material for flow plates, because of their corrosion resistance and thermal stability. However, the conductivity of graphite materials is much less than those of metallic materials see Table 2. Higher contents of graphite produce better electrical conductivity values, but the associated mechanical properties become more undesirable, as the increased brittleness not only reduces the toughness, but also makes manufacturing more difficult and expensive. In addition, the fabrication costs of graphite plates incorporating gas flow field distribution channels are high, making

such components too expensive. Also as graphite materials are porous, a binder or resin has to be added in order to produce the necessary impermeably.

Table 2 Conductive values for different materials.

Graphite	10^3 S cm^{-1}
Carbon Polymers	1 to 10^3 S cm^{-1}
Aluminium	100 – 300 10^3 S cm^{-1}
Stainless Steel Alloys	5,300 x 10^3 S cm^{-1}
Titanium	2,400 x 10^3 S cm^{-1}
Copper	63,000 x 10^3 S cm^{-1}
Silver	59,000 x 10^3 S cm^{-1}
Gold	45,000 x 10^3 S cm^{-1}

Much effort is being expended on the development of cost-effective materials for the flow plates. Table 3 lists the characteristic of a suitable material for flow plates.

Table 3 Optimal flow plate characteristics [59-61]**.**

High electronic conductivity and low contact resistance
High thermal conductivity
High mechanical strength
Impermeable to gases
High corrosion resistance
Balance between conductivity, strength, size, weight, cost
Integrated uniform cooling channel
Easy to manufacture in large quantities

Due to the properties listed in Table 3, the overall efficiency of the fuel cell depends extensively on the fuel cell flow plate performance. Several types of materials are suggested for the development of flow plates [64,65]:

- Polymer-coated metal sheet.
- Electro graphite.
- Flexible graphite.
- Carbon–carbon composite.
- Graphite–polymer composite.
- Advanced (graphite–carbon–polymer) composite.

- Thin metallic sheets.
- Stainless steels.

Polymer/graphite compound flow plates have been developed. Polypropylene, for example, can be mixed with graphite to achieve sufficient electrical conductivity (10 Scm^{-1}) [13]. This reduces the flow plate resistivity to a value well below the membrane resistivity. Polymeric materials can be machined more easily and cheaply by hot pressing or injection moulding.

Metallic flow plates may counter graphite flow plates draw backs. The gaseous flow structure can easily be fabricated in thin metal foils by pressing, but only a few metals are sufficiently corrosion-resistant in the acidic membrane environment. The most promising materials are stainless steels, as the other candidate metals such as titanium, chromium, niobium, tantalum and gold (including gold-plated metals) are too expensive. Stainless steels can provide satisfactory performance for several thousand hours. The steel is protected by a passive layer at the cathode side, but the anode side becomes contaminated by corrosion products [13]. Peng et al. [66] researched the possibility of using hydro formed metal sheets as a cheaper alternative and they concluded that the design dimensions are notably different than for graphite plates. They conclude that the optimal dimensions for hydro formed metal sheets are 0.5, 1.0, and 1.6mm for channel depth width and rib width respectively. Abo El-Enin et al. [67] investigated the use of aluminium, coated with different nickel alloys, as a flow plate instead of graphite in order to reduce the cost and weight and ease the machining. The electroplated nickel alloys on aluminium substrate produced a new metallic flow plate for PEM fuel cell with a higher efficiency and longer lifetime than the graphite bipolar plate due to its higher electrical conductivity and its lower corrosion rate.

2.4.2.2 Flow field design

Parameters for flow field design include width and depth of the channel and rib width. Channel width is generally chosen on the need to distribute the reactant gas over the active cell surface, the rib width (distance between channels) is based on the need for current collection. Li et al. [68] have noted that the channel depth is determined based on the consideration of the flow regime and the flow condition in the channel, the channel length and the pressure drop in the channel. In most cases the ratio between the rib width and channel width is around 0.8-1 because the reactant gas transport is relatively slower that the electronic conductivity of the flow plate materials. According to research carried out by Peng et al. [66] there is a small debate as to what the optimal dimensions for flow channel design. The channel width should be in the region of 1.5mm thick, rib width should be between 0.5mm and 1.4mm and the depth should be no deeper than 2.04mm in order to maintain optimum hydrogen consumption on graphite flow plates, which are traditionally used on PEM fuel cells. Spiegel et al. [69] investigated the performance of a micro electromechanical based fuel cell with different channel feature sizes. Fuel cell performance should improve as the channel feature size

decreases and gas flow velocity increases since the increased flow velocity enhances mass transport, as shown in Figure 17. However, it was found that a drawback, of the smaller feature size, is the increased pressure drop in the flow channels.
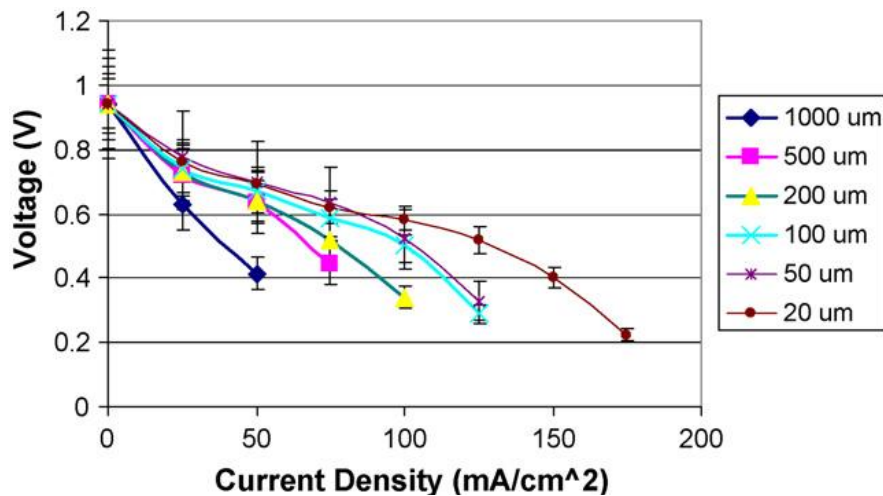
Figure 17 I–V curve of the cell performance tests with different flow field channel widths [69]

2.4.2.3 Flow field configuration

As briefly mentioned already, the flow field is the region that the gas is allowed to flow inside the flow plate. With the structure and material set out by the flow plate, the flow field is necessary to allow the gases to flow over the MEA to ensure efficient mass transfer and reduce mass transport (concentration) losses in the PEM fuel cell from the hydrogen and oxygen concentration reduction at their respective electrodes.

The key characteristic when designing a flow field are:

- Even distribution of pressure on the GDL and membrane.
- Even distribution of temperature on the GDL and membrane.
- Low pressure drop through the PEM fuel cell.
- Convective flow and mixing within the PEM fuel cell.
- Maintain high reactant concentration over the entire active area of the GDL and membrane.
- Enhance membrane hydration.
- Aid in the mitigation of water flooding.
- Low cost and simple design for manufacturing.

PEM fuel cell performance improvement is based on minimization of all transport resistances, which largely depend on flow field designs. Improvement in these designs will lower costs, create higher efficiency and better power density on both volume and weight basis. Flow plate and flow field design and development is necessary, in order to get an optimal layout or configuration, which can give maximum output from the cell. In existing flow fields, intricate flow field structures are common and

a variety of the most common practical flow plate and flow field designs are reviewed in the next section.

2.4.2.4 Serpentine flow field

A double serpentine flow field, Figure 18, is one of the most common and practical channel layouts for existing PEM fuel cells and it is often referred to as an industrial standard. Continuous fluid flow through the channel forces the gases to flow over the entire active area of the MEA, which eliminates areas of stagnant flow and also overcomes flooding in the channel.
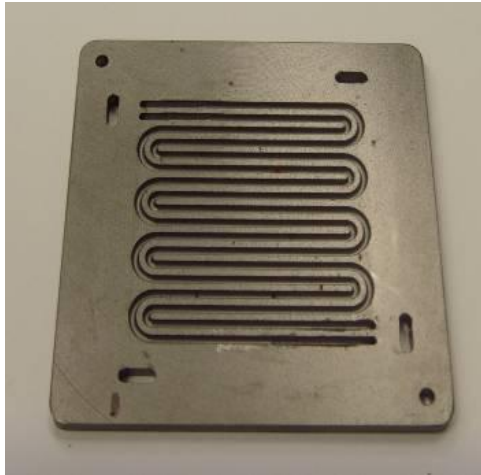
Figure 18 Serpentine flow plate

Carton and Olabi [70] performed a design of experiment (DOE) study on three PEM fuel cell flow plate configurations. It was concluded that over all the serpentine flow plate performed best, due to its continuous flow and water flooding mitigation design. Li et al. [48] also concluded that the serpentine plates offer the best results for water removal, since it ensures the removal of water produced from a cell with acceptable parasitic load. However, a substantial pressure drop due to the long flow path results in concentration gradients from inlet to outlet. To solve this issue several continuous separate flow channels might be used to limit pressure drop and for a low voltage operation the greater number of bends in the plate the greater the cell performance. But Wang et al. [71] proved that the greater the amount of bends the greater the pressure drop in the cell which can reduce the cell performance as shown in Figure 19. Low flow pressure requires more power to deliver the reactant gases which decreases cell efficiency, up to 35 % of the of the PEM fuel cell stack output in some tests [68].
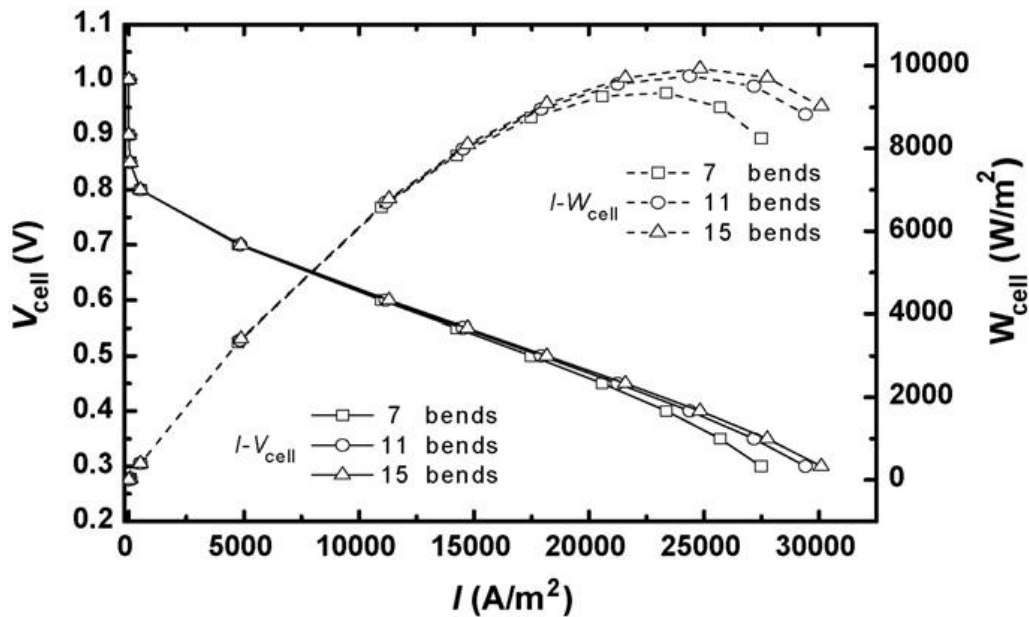
Figure 19 Quantity of bends in a flow plate affecting pressure drop and performance [71]

2.4.2.5 Straight or parallel flow field

The straight or parallel flow field is shown in Figure 20. This design contains a number of separate parallel flow channels connected to inlet and exhaust headers. Shorter channel lengths with no directional changes result in a low pressure drop within the cell.
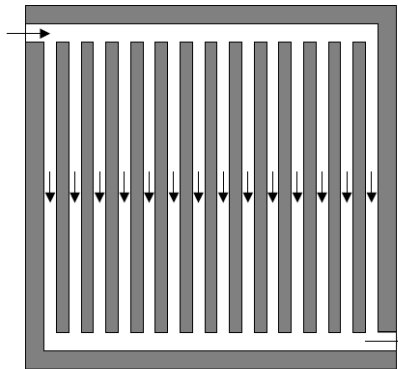
Figure 20 Straight or parallel flow field.

However, low and unstable voltage is associated with this design after long periods of operation. Water may block some channels due to gas flow distribution which is a result of the quantity and size of water droplets within the cell. The gases then tend to follow the least resistant path. Also non-uniform compressive load across the fuel cells can be noticed within the stack when the anode and cathode plates are aligned in parallel. Overlapping the flow plate ribs makes the contact area and smoothness of the ribs dependant on manufacturing. Variation in contact areas results in variation in local stress, which may lead to damage and premature failure of cell components [8].

2.4.2.6 Pin-type flow field

The Pin-type flow field design, as shown in Figure 21, utilizes a circular or rectangular array of pins protruding from the plates. Reactant gases flow through the grooves formed by pins, which is actually a network of series and parallel flow paths.
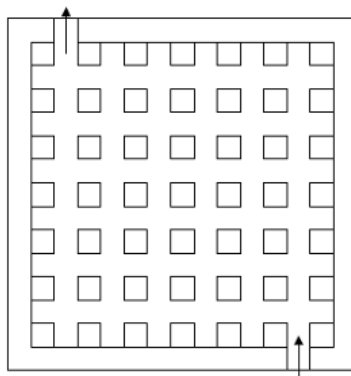
Figure 21 Pin-type flow field.

This design results in low reactant pressure drop. Reactants through this design tend to follow a path of least resistance, which may result in channelling and formation of stagnant areas within the PEM fuel cell. This may lead to uneven reactant distribution, inadequate product water removal and poor PEM fuel cell performance. Relatively stable recirculation zones may arise behind each pin as the flow is very slow in such a small channel and concentration may be depleted in these stable recirculation zones [8].

2.4.2.7 Integrated flow fields

Both reactant and cooling flow fields are on the same plate surfaces. The gas flow field faces the active area of the MEA and the cooling flow field surrounds the gas field. This eliminates a separate cooling layer; however this type of plate is unable to maintain a uniform temperature distribution over entire PEM fuel cell surface.

2.4.2.8 Bio-inspired flow fields

Kloess et al. [72] investigated two new bio-inspired flow field patterns: a leaf design and a lung design, as shown in Figure 22. Numerical simulation and experimental testing were completed which concluded that both designs allow for uniform gas flow and lower pressure drop compared to serpentine or interdigitated flow fields increasing the peak power density by 30%.
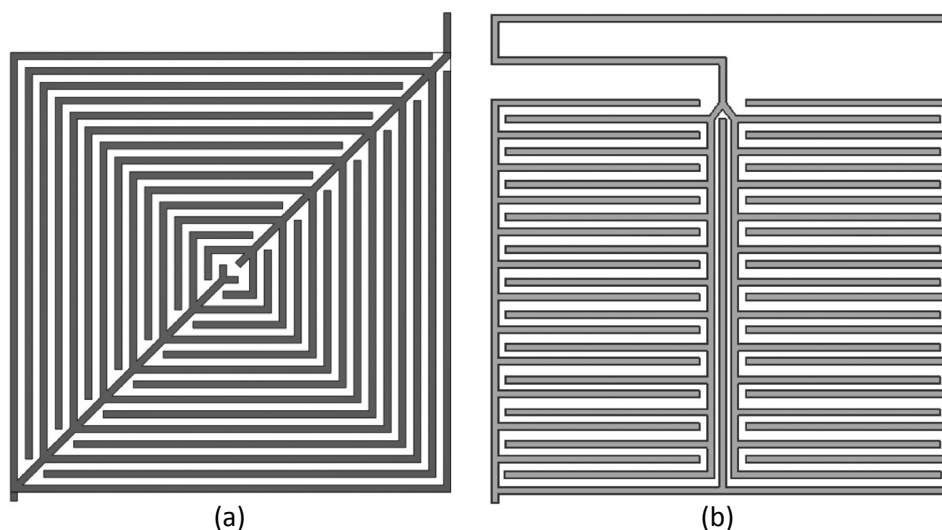
Figure 22 Bio-inspired flow fields (a) Leaf flow field (b) Lung flow field [72]**.**

2.4.2.9 Interdigitated flow field

An interdigitated flow field consists of dead-ended flow channels machined in to the plate. The flow channels are not continuous from the cell inlet to the cell exit and as a result the reactant flow is forced under pressure through the GDL to reach the flow channels connected to the exit, Figure 23.
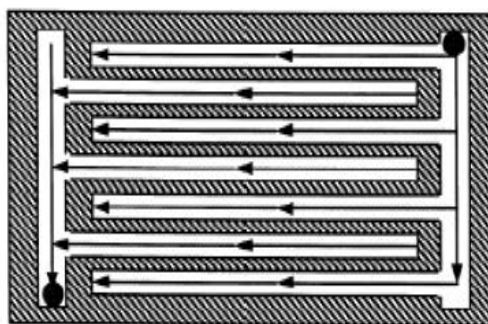
Figure 23 Interdigitated type flow field.

This forced convection is normal to the catalyst layer and allows for good mass transfer of species without gas diffusion limitations. In addition water accumulated in the GDL is forced with the gas stream towards the exit, relieving flooding issues. However, parasitic losses may be encountered due to the increased pressures needed by the supply gases to push fluid through the GDL. A generalised numerical model of a PEM fuel cell with interdigitated design was presented by Le et al. [73]. The model was able to show the movement and transport of drops and slugs of water from inlet to outlet and their effect on oxygen concentration in the GDL, which can relate to the efficiency of the cell.

2.4.2.10 GDL & flow plate interface

It is noted that in conventional flow fields such as serpentine and parallel flow fields, the dominant reactant flow is in the direction parallel to the electrode surface, Figure 24. In this configuration the reactant flow to the catalyst layer is predominantly by molecular diffusion through the GDL. This can

lead to large concentration gradients across the GDL and mass transfer limitations because of the small channel dimensions, laminar gas flow and the inherent slow molecular diffusion process.
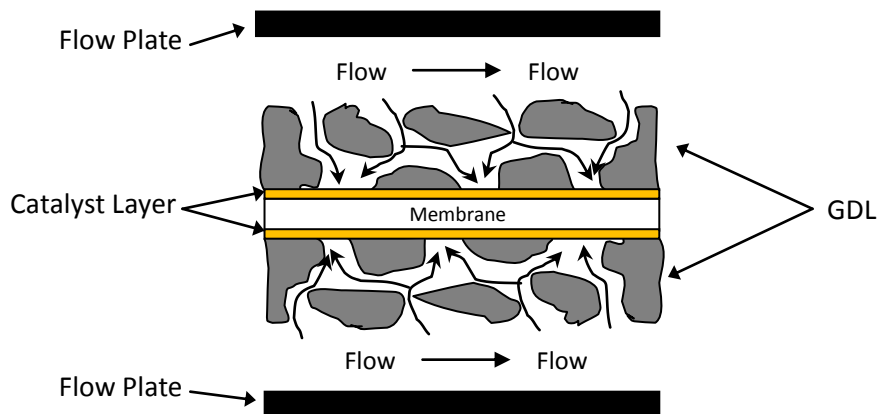
Figure 24 Conventional flow-field design mechanism, taking from [74]**.**

Interdigitated flow fields, as shown in Figure 25, provide convection velocity normal to the electrode surface for better mass transfer and enhanced water removal from the channels and GDL. This design consists of dead ended flow channels, which are not continuous from inlet manifold to exit, so that the reactant flow is forced under pressure to go through the GDL. This provides enhanced performance at high current density operation. However large pressure losses and high parasitic power (due to increased gas flow pressure) are characteristics of this type of flow field, which may limit this application to smaller stack sizes.
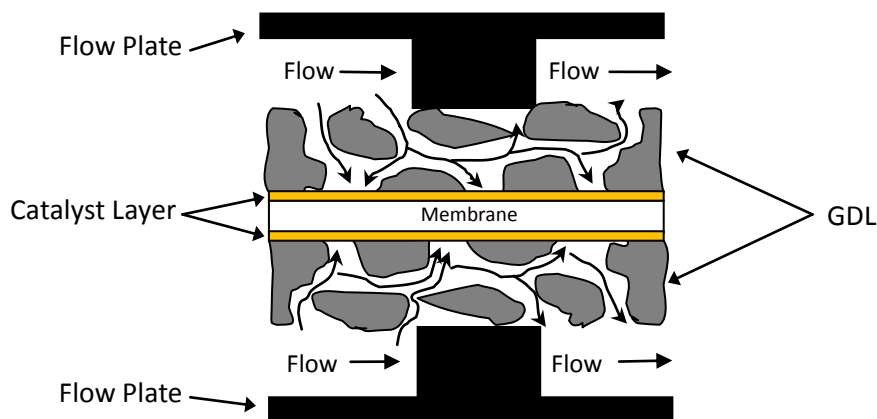
Figure 25 Dead ended flow-field design mechanism, taking from [74]**.**

All components in a PEM fuel cell are held tightly together in order to prevent gas leaks. There are two types of contact between the GDL and the flow plate, mechanical and electrical. The more compressed the fuel cell the higher the electrical conductivity of the fuel cell. Lin et al. [75] investigated the compression effect on the fuel cell performance; compression reduces gas permeability and contact resistance which increases the difficulty of water removal and gas transport because the pore volume reduces. In addition, excessive compressive pressures will cause the

membrane to deform and may cause cell leakages resulting in an internal short. The contact resistance in the fuel cell is determined by various material properties such as surface topology, clamping pressure and operation conditions. It is important to get the ratio of conductivity and pore volume correct for optimal PEM fuel cell performance. Lai et al. [76] produced a study using a Finite Element Analysis (FEA) model to predict the contact resistance of a PEM fuel cell; it was found that the contact resistance decreases rapidly with increased pressure, unfortunately this study did not note cell performance with the various pressures.

2.5 PEM Fuel Cell Water Management

At present many barriers still persist in PEM fuel cell design that suppress or restrain their development and full commercialisation potential. One of these barriers is water management within the PEM fuel cell. To design effective flow fields and flow plates water management has to be understood. This section describes water flooding issues in relation to its source, transport and affects within a PEM fuel cell. In addition water management and mitigation methods are reviewed.

2.5.1 Water Flooding

Liquid water accumulates mainly at the cathode especially at high current densities. This is as a result of the Oxygen Reduction Reaction (ORR), remembering that the electrochemical result of combining hydrogen and oxygen at a temperature below 100°C forms liquid water. Water can also be transported from the anode to the cathode through the membrane via electro-osmotic drag and local pressure, temperature and concentration gradients [77]. In addition, if a nafion membrane is used it must be fully hydrated for it to be a good proton conductor, as mentioned in Section 2.4.1.1, and in order to maintain the membrane hydration level, especially at start up, the reactant and oxide gases are often fully humidified with water, which can condense in the cell.

2.5.1.1 Mechanism of water flooding

Many factors affect how water is transported from the catalyst layer to the flow plate and how droplet formation occurs, grows and ultimately how water flooding occurs within the PEM fuel cell flow plates or channels. These factors include the membrane, flow plate or flow field channel design, air flow rate, temperature, power density, gas humidification as well as cell orientation and force of gravity acting on the PEM fuel cell.

In an optimal PEM fuel cell humidified feed gases enter the cell. On the hydrogen side (anode) water molecules diffuse through the GDL and attach to protons on the anode catalyst layer. During the electrochemical reaction the protons move through the membrane dragging the water molecules with them (electro-osmotic drag). The moisture content in the hydrogen can begin to decreases along the

flow channel because of this process. However, on the air side (cathode) water molecules diffuse through the GDL into the catalyst layer to hydrate the membrane. In addition, due to a concentration gradient from anode to cathode, because of the ORR, water begins to diffuse back through the membrane to the anode.

For operational PEM fuel cells at low current densities, the above process is mainly true and neither membrane dehydration nor flooding occurs. The problem arises when high current densities are required. At high current densities a large amount of water is produced by the ORR and the humidified air can add condensed water to the cathode resulting in cathode flooding. In addition at high current densities, the membrane can dry out on the anode side because water transport from the anode by electro-osmotic drag exceeds its transport to the anode by back diffusion from the cathode. This results in the dehydration of membrane and shrinking of the pores, thus further limiting the back diffusion of water. It can be seen that the net water flux from the anode to the cathode is directly proportional to the current density. At high current densities, the large electro-osmotic drag from the anode dries out the anode and floods the cathode. The key to understanding membrane hydration is the balance that has to be struck between the electro-osmotic drag and back diffusion [77]

2.5.1.2 Water transport in PEM fuel cells

When the cathode layer floods, water needs to be transported from the electrode, through the GDL and into the flow plate channels and then exhausted out of the cell to mitigate the flooding problems. The water transport mechanism from the GDL into the flow plate channels has been explained by two theories; converging capillary tree water transport mechanism proposed by Nam and Kaviany [78], Figure 26 and channelling liquid water transport mechanism proposed by Litster et al. [79], Figure 27.
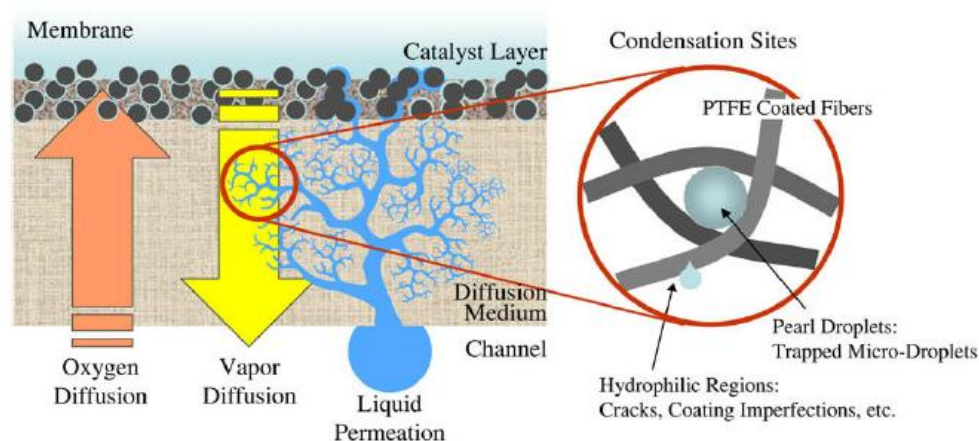
Figure 26 Water transport from catalyst layer by capillary tree mechanism [78]

Both theories have their differences but they do concur that water droplets can form on the GDL. These droplets, mainly originate from the electro-catalyst layer. They join and grow in the GDL and squeeze out into the channels due to capillary action within the GDL, GDL hydrophobic nature and

due to pressure and temperature forces in the flow plate channels [71,80-82]. These droplets grow or combine and consequently, liquid water flooding occurs in the flow fields of the flow plate [68].
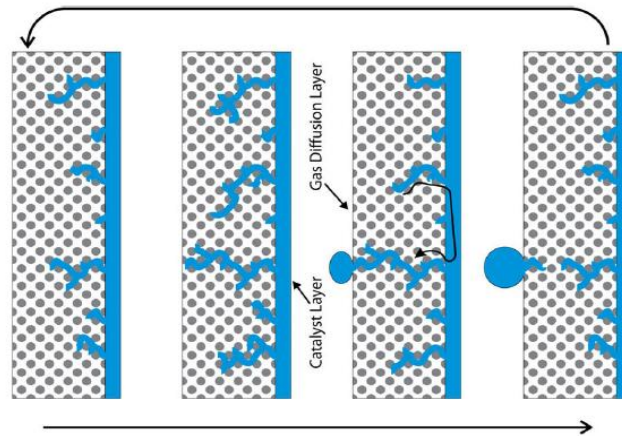
Figure 27 Channelled liquid water transport mechanism[79]

2.5.1.3 Flow Regimes in PEM fuel cells

As described above, water droplets can form in the flow plate's channels on the GDL surface. The presence of water droplets causes many issues within the PEM fuel cell and their mitigation is necessary. However due to the operation of a PEM fuel cell water droplets move, collide evaporate and grow within the flow channel flow path. It is necessary to understand the flow pattern of air and water (two-phase flow) in PEM fuel cells so that mitigation of water droplets and flooding is achieved successfully.
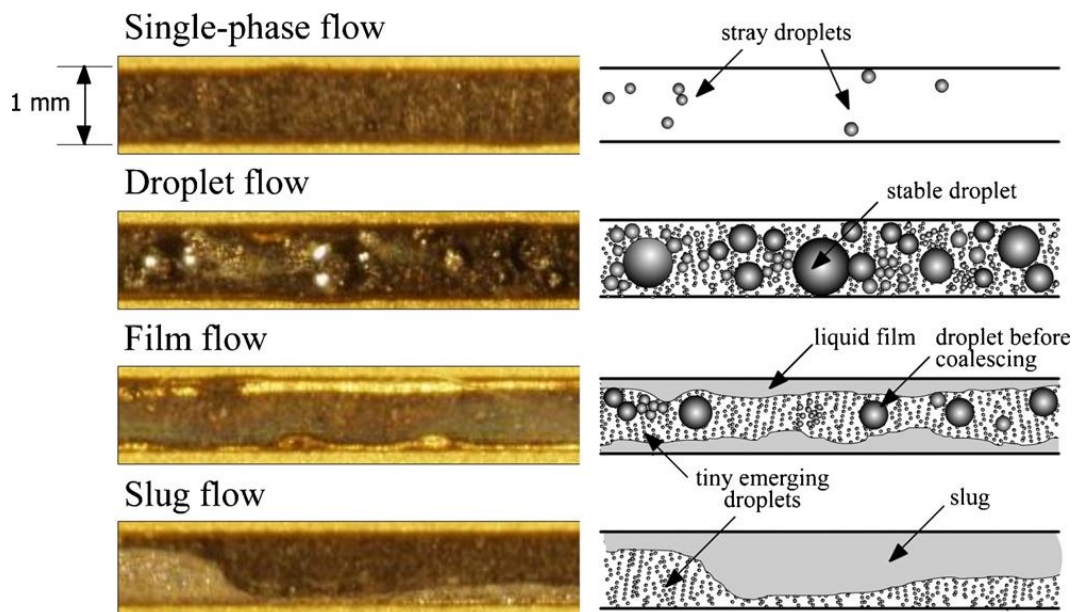
Figure 28 Water transport through channels of an operational PEM fuel cell [83]

Hussaini et al. [83] presented actual images corresponding to the most common flow patterns in operational PEM fuel cells, Figure 28, and a brief description of the different flow patterns as observed from these channel images are given next.

Single phase flow: In this regime, hardly any water droplets are observed on the GDL surface and the flow is mostly in the form of partially humidified gas. Water droplets may appear sporadically on the GDL surface but tend to be quickly evaporated by the flowing air stream.

Droplet flow: This region is dominated by water droplets that emerge from the GDL surface and remain adhered to the surface by surface tension forces. Mass transfer occurs at the interface with the flowing gas. Due to the hydrophobic nature of the GDL surface, droplets are circular in shape and do not spread out laterally on the surface. The maximum radius that a droplet can grow to is limited either by its detachment size (under shearing action by gas flow) or the channel depth.

Film flow: Further downstream, the influx of liquid water through the GDL is sufficiently high so that the droplets, on contact either with neighbouring droplets or channel walls, coalesce and are wicked into the walls and form a liquid film of growing thickness. A wavy motion is observed on the film surface due to the continuous influx of water and coalescence of droplets. Large droplets are no longer observed. Tiny droplets may appear and are generally confined to a narrow region at the centre of the channel.

Slug flow: Further growth of the film causes it to accumulate into a slow-moving slug. This results in pressure drop oscillations and causes an internal flow rate adjustment among the channels. Clogging of channels may occur when the slugs stagnate near a channel's exit region and completely stop gas flow through it.

Lu et al. [84] have observed three different types of water to air flow regimes in their study, slug flow, annular/film flow and mist flow. Slug flow and intense annular flow cause an increased pressure drop due to liquid water build-up and this is a key cause of flow misdistribution that dramatically reduces the PEM fuel cell performance and durability. For further information on flow patterns the reader is referred to a review that was carried out by Cheng et al. [85] on two phase flow pattern maps.
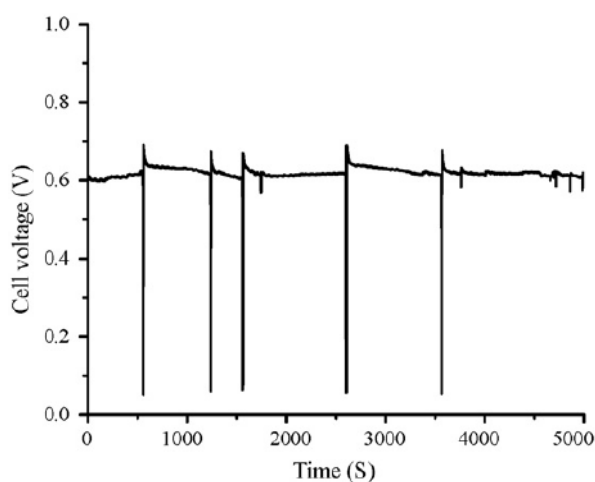
Figure 29 A typical water flooding pattern in a PEM fuel cell operated at constant current density [48]

2.5.1.4 Water flooding effects

When a PEM fuel cell accumulates too much water at high current density, about one-third of the electrode surface area may not be utilised [86,87]. In addition, with large droplets forming and being moved downstream by the airflow, the cell voltage may be affected, which can be viewed as uneven cell voltage operation, see Figure 29.

The phenomenon of flooding is a well established problem at the cathode electrode where both the catalyst layer or/and the GDL may be mass transport-limited due to condensed water. This water flooding increases the internal resistance of the cell, blocks the ORR reaction, disrupts cell pressure and gas flow, making the cell voltage and current unpredictable and unrepeatable, reducing the PEM fuel cell performance dramatically. It is noted that if low temperature operation or Nafion based membranes continue to be used, good PEM fuel cell performance depends on good water management [88].

2.5.2 Observing Water Movement in PEM Fuel Cells

In low temperature PEM fuel cells, two phase flow is common, a mixture of gas (air, hydrogen or water vapour) and a liquid (water). As discussed in Section 2.5.1, effective water management is one of the key strategies for improving the performance and durability of low temperature PEM fuel cells. Phenomena such as membrane dehydration, catalyst layer flooding and two-phase flow in flow channels are all determined by water distribution and movement in the GDL porous layers and the design of the fuel cell flow plates flow field. In order to understand two phase flow and help design more effective PEM fuel cells it is valuable to physically view the operational activity of a fuel cell. However this may not always possible due to the design of the cell or difficulty in viewing the microscopic scale of the phenomena. Other methods can involve using ex situ apparatus to better view a more controlled model of an operational PEM fuel cell.

The next section reviews the in situ and ex situ approaches completed in literature to help view water movement in PEM fuel cells, focusing on optical visualisation methods, as this method is incorporated in the present work.

2.5.2.1 Liquid water visualisation

Several new methods for liquid visualisation, in PEM fuel cells, have been reported in literature in the past decade, including nuclear magnetic resonance (NMR), magnetic resonance imaging (MRI) and neutron imaging [89,90]. These methods can penetrate deep into the fuel cell, view liquid transport in operational PEM fuel cells and provide high contrast images. However these techniques are extremely expensive, limited in availability and somewhat limited in temporal resolution. For this study, direct optical imaging was performed as it was readily available, cost effective and provided the necessary

resolution for flow field investigation and so most reviewed literature is focused on optical imaging techniques.

There are many studies in literature relating to water movement in channels, from early in this century to this present day, encompassing a range of disciplines (electronic cooling/heating, conditioning systems, nano materials/fluids and electro-fluidic systems such as batteries and fuel cells). Since a huge information base was available, a range of studies were reviewed from many disciplines, but the focus was placed in previous studies of fluid (mainly water) movement in PEM fuel cells.

In relation to fluid flow and flow regime analysis an early study by Bhaga and Weber [91] studied bubble movement in viscous liquids in relation to shapes, wakes and velocities. More recently Harirchian and Garimella [92] performed visualisations of flow boiling regimes in micro channels relevant for electronic heat-sinks. This study utilised a high speed camera in order to observe flow regimes in micro channels ranging from 400 μm to 5850 μm. It was noted that fundamental knowledge of boiling mechanisms, micro-channel dimension and flow regime maps were not readily available in literature for such devices.
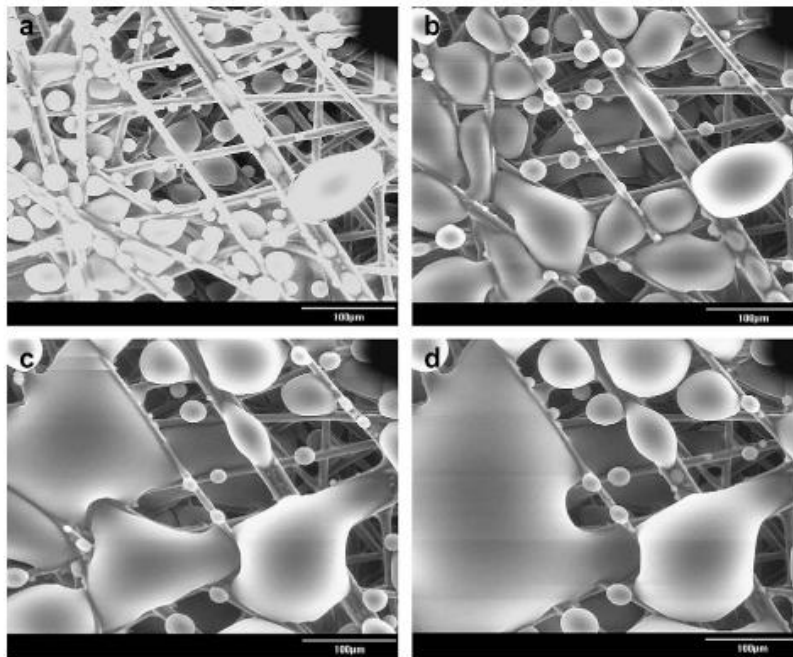
Figure 30 Time-sequenced ESEM images of smaller liquid water droplets agglomerating to form larger droplets in a GDL [52]**.**

With regard to PEM fuel cells a detailed review of liquid water visualisation was recently conducted by Bazylak [93]. Many liquid water visualisation techniques including nuclear magnetic resonance (NMR), beam interrogation and direct optical imaging techniques were mentioned. The reviewer concluded that even with the difficulties posed by direct optical imaging such as opaque materials or in situ apparatus and limitations of magnification and speed of the camera used, direct optical

visualisation of liquid water in micro channels of PEM fuel cells can provide high temporal and spatial resolution information and can be easier and cheaper to implement than other techniques.

Kumbur et al. [94] employed an ex situ simulated flow channel apparatus in order to study the effects of hydrophobicity, channel geometry, droplet chord length and height and air flow rate on droplet formation and instability. They also presented an analytical force balance model to predict the droplet characteristics at instability. Lu et al. [84] also employed an ex situ apparatus, but they investigated the water transport in a test section composed of eight flow field channels. The effects of air flow rates on the two-phase flow and flow regime maps were presented. At low flow rates (1.7m/s) slug flow dominated and at high flow rates (7.9m/s) annular/film flow and at highest flow rates (24.6m/s) mist flow was observed.

Other researchers such as Hussaini et al. [83] viewed the water transport through channels of an operational PEM fuel cell. Tuber et al. [95] visualized liquid water transport in the cathode gas channel of a transparent PEM fuel cell at low operating temperatures (30°C). They found that using a hydrophilic cathode GDL resulted in increased current density, which they attributed to a more uniformly hydrated membrane. This was also noted by Ge and Wang [96] who visualized water droplet formation in the anode flow channels. They observed that droplets tended to form on the gas channel walls when a hydrophobic GDL was employed, whereas a hydrophilic GDL tended to wick water from the channel into the GDL.

Spernjak et al. [97] investigated the effects of varying GDL materials and hydrophobicity. They found that PEM fuel cells with an untreated GDL was more prone to film and slug formation in the cathode gas channel. Kimball et al. [98] measured the critical hydrostatic pressure head for liquid water breakthrough for various GDL materials, and they obtained photographs of the GDL at breakthrough. They also varied the orientation of a single channel fuel cell to observe liquid water motion and its effect on the local current density.

Yang et al. [99] employed a flow field to image water droplet transport through a GDL into a flow field. These authors observed a variety of phenomena in the gas channel, including the intermittent emergence of droplets from the GDL surface, film formation along the channels, and channel clogging. It was observed that droplets can emergence at preferential locations. However, an explanation of these phenomena was not provided. Hakenjos et al. [100] employed a transparent fuel cell and attempted to correlate the appearance of flow field flooding with the spatial temperature distribution. Gao et al. [101], using con-focal microscopy, also observed preferential GDL flow locations and the recession of water pathways upon breakthrough. The authors proposed that liquid water flows in the GDL are similar to flows in soils.

Ous and Arcoumanis [102] viewed the formation of water droplets emerging from an operational PEM fuel cell, Figure 31. A transparent proton exchange membrane fuel cell was again used to

visualise the water droplet formation during its operation. Results show that water accumulates first in the middle flow channels and that no accumulation takes place at the bend areas. Measurement of the fuel cell current during water production showed that the current gradually declines as more water fills the channels, but that this has no effect on the droplet formation on the surface. The shrinking of the droplet seems to be due to its increased cross-sectional area in the direction of the airflow, which may push the droplet back into the GDL. It was also noted that increased airflow rate prevented droplet formation but reduced current due to membrane dehydration.
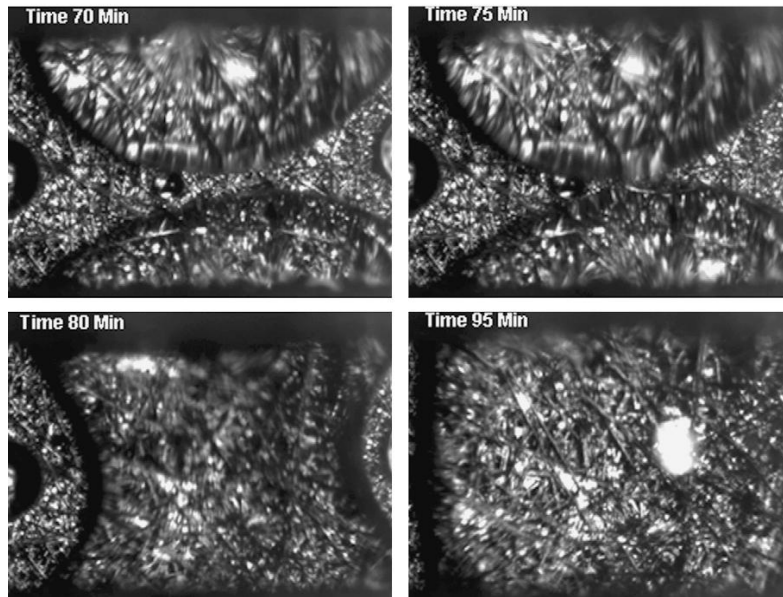
Figure 31 Formation of water droplets emerging from an operational PEM fuel cell [102]

Again, Weng et al. [103] confirmed the beneficial effects of high cathode gas flow rates for water removal; however un-humidified cathode gas streams at high stoichiometry resulted in membrane dehydration. Liu et al. [104] investigated the liquid water accumulation in PEM fuel cells cathode flow channels with three different flow field configurations: parallel, interdigitated, and cascaded. At low operating temperatures (25°C) and ambient pressure, they observed that the parallel flow field was the most unsuitable flow field design for water removal, resulting in the worst performance of the PEM fuel cell.

2.5.2.2 Water droplet interaction with gravity and flow plate orientation

Many factors affect how droplet formation occurs, develops and how it is transported through the PEM fuel cell channels. One of these factors is simply the orientation of the cell. However, a more important issue is to understand to what extent the force of gravity has on fluid inside the PEM fuel cell. A review was completed in order to understand how gravity interacts with fluid flow specifically applicable to PEM fuel cells. Microgravity investigations serve as a tool, which can help to study fluid flow being much better understood in microgravity studies, eliminating the masking effects of gravity. Microgravity experiments can be performed in orbit or on the International Space Station (ISS)

however a parabolic flight or drop towers also offer 0g (microgravity). The benefits of parabolic flights for researchers are that microgravity lasts longer, than drop towers for example, periods of 2g (twice normal gravity) are also experienced and between each parabola manoeuvre 1g (normal gravity) is resumed. An added advantage is that the experiments can be controlled directly by the operator and the cost of a parabolic flight is much cheaper than a space borne experiment.

The European Space Agency (ESA) has over 25 years of parabolic flight experience and over 400 experiments have been performed in microgravity. Pletser [105] reviewed the first thirty campaigns and fluid flow in microgravity has been popular. Examples of fluid experiments carried out include; capillary channel fluid flow analysis; annular flow in pipes; diffusion effects; Marangoni effects; solidification of liquid metals; heat exchanger designs; etc.

However few dedicated PEM fuel cell experiments have been found in literature. Some literature was found that could be applicable to fuel cell systems and certain fluid dynamic regimes. These include a study by Xie et al. [106] who investigated carbogal-air two-phase flow regimes in microgravity in a 10mm diameter tube and fluid flow regime analysis that was completed by Valota et al. [107]. Separation of fluids was investigated by Weislogel et al. [108] while Yuan and Frederking [109] investigated vapour-liquid separation of HE II, which was more interesting from a fluid flow point of view than applicable to PEM fuel cells. Luciani et al. [110] performed an experiment on flow boiling in micro-channels in an ESA sponsored parabolic flight and Zhao [111] conducted a study on two-phase flow and pool boiling heat transfer in microgravity. These experiments are applicable to heat exchanger systems, but the results may be suited to PEM fuel cell systems also.

An application of porous substrate liquid/gas separation in heat exchangers for space applications was investigated by Balasubramaniam et al. [112] and Chen et al. [113]. Both groups studied micro-porous wicking structures that may have applications in microgravity environment. These materials may be beneficial for PEM fuel cells operating in a space environment.

Guo et al. [114-118] published many papers on an in-situ visualization regarding two-phase flow inside the anode flow channels of a small liquid fed direct methanol fuel cell in normal and reduced gravity, conducted in a drop tower. From these studies it was noticed that the flow regimes at microgravity can be different but may be explained by viscous drag also the size of bubbles of CO_2 in microgravity are larger than at 1g but these bubbles can hinder performance due to the loss of bouncy effects which occur at 1g. It was also noted that dead zones due to water accumulation at the bottom of vertical channel in 1g does not occur in 0g which enhances the performance of the fuel cell.

Chen and Wu [119], Pien et al. [120] and Wu et al. [121] relate their publications to gravity experiments by placing the PEM fuel cell cathode and anode in horizontal and vertical positions, but these experiments do not clearly show the interaction of gravity with the PEM fuel cell behaviour and

they have not been compared to microgravity experiments. These experiments simply view the PEM fuel cell in different orientations in 1g.

Benzinger et al. [122], while also using this gravity analogy, show that the orientation of the reactant gas flows relative to gravity plays a key role in the long-term stability of the PEM fuel cell operation. When the reactant flows are assisted by gravity in draining liquid water from the GDL and flow channels, the currents are stable. However if the fuel cell is oriented so the liquid water must be pushed from the flow channel by gas flow against gravity, the local current densities fluctuate. The current density fluctuations appear periodic, where the period is 1 second for vertically oriented fuel cells and 104 seconds for horizontally oriented fuel cells. These fluctuations are undesirable because they reduce the efficiency of the fuel cell.

Guaru et al. [123] have shown that where the water exits the GDL/flow channel interface, water accumulates in pending or sessile droplets. These droplets detach when the gravity and the shear forces generated by a two-phase drag exceed the maximum force available to support them. Changing the value of gravity should then, change the size that the droplet must be, before it is released into the flow regime. Large droplets are undesirable and zero gravity could cause large droplets that soon clog up the flow PEM cathode flow channel.

Finally, Kimball et al. [98] explain that the slugging phenomenon is very complex and highly dependent on the orientation of the fuel cell with respect to gravity. If the fuel cell is oriented such that gravity assists the removal of liquid from the cathode gas flow channel, the fuel cell will operate stably if the feed flows are in excess to the ORR. When the fuel cell is oriented such that the gas flow must push the liquid slugs against gravity, water slugs form spanning the gas flow channel and temporary block the flow of gases which creates large fluctuations in the current density along the length of the flow channel. This group present a formula for estimating the size of a drop before it is released from a pore, as shown in equation 2.5.1:

$$r_{drop} \geq (3\gamma_{water}\, r_{pore}\, /\, 2\rho_{water}\, g\,)^{1/3} \qquad\qquad Eqn.\ (2.5.1)$$

where g is a variable. It would be interesting to investigate if such formulas hold up to 0g and 2g conditions.

2.5.3 Managing water in PEM fuel cells

Over the last 15 years, extensive research work has been carried out on water flooding, including prediction through numerical modelling, detection by experimental measurements and mitigation through the design of cell components and the manipulation of operating conditions [48]. The following section investigates water mitigation methods, techniques and components to aid in the effective design of PEM fuel cells.

2.5.3.1 PEM fuel cell operating conditions

Recent work on water management have shifted from water transport in the MEA to water transport in the gases, which can be controlled by manipulating operating variables of the PEM fuel cell stack such as the temperature, humidity and pressure of the gases. Suhaimi et al. [77] has shown that by saturating the hydrogen feed and using dry air, in a PEM fuel cell with an active area of 200cm^2, successful prevention of water droplet formation in the cathode and hence flooding was avoided. Unfortunately, if either dry gases or fully humidified saturated gases are used, complicated balance of plant systems have to be incorporated to the PEM fuel cell stack.

A sufficient pressure loss in the anode flow channels can draw water through the membrane from the cathode side, and remove the excess water by the anode stream. However, reactant pressure losses through the flow plate can increase the parasitic load and the degree of difficulty for hydrogen recirculation. If the reactant gas temperature is increased along the flow direction from the inlet to the outlet of the fuel cell, the capacity of the gas stream to absorb water also increases [8], but this can be difficult to control, again needing balance of plant devices.

A very common flooding mitigation strategy is simply increasing cathode gas flow rate in order to remove liquid water via evaporation and advection. Effective operation is typically achieved by increasing operating air flow rate well above stoichiometric levels or periodically flushing the cathode with momentarily high air flow rates (2-60 times above stoichiometric levels) [124].

Jiao et al. [125] has noted that due to the weak wall adhesion of hydrophobic GDL surfaces, liquid water from the gas flow channel could take away some liquid water inside the GDL, and such splashing of liquid water is good for water drainage. However if liquid water from the electrode moves too fast into the gas flow channel, part of the water could be pushed back into the electrode due to the high air flow in the channel.

2.5.3.2 Micro Porous Layer

Micro Porous Layers (MPLs) can help with water management within PEM fuel cells as mentioned by Chen et al. [113]. Pasaogullari et al. [49] and Weber et al. [51] have investigated the effect of a micro-porous layer (MPL) on water transport. They showed that an MPL enhances the liquid water removal and therefore decreases flooding. They have suggested that an MPL placed at the cathode side enhances the water transport through the membrane towards the anode. Increased water removal from the cathode and increased water flow across the membrane may improve the cell performance by reducing the flooding at the cathode and by enhancing the hydration of the membrane and therefore increasing the conductivity of the membrane.

Holmstrom et al. [80] have identified that the gas humidity of the anode may also significantly affect the flooding of the cathode, as the net flow of water through the membrane is dependent on the

humidity difference between the sides as well as on the current density. Since more water is accumulated at the cathode side during high current densities, flooding of the GDL is greater. Comparison of Holmstrom et al. results from the anode and the cathode investigation, at high inlet humidity, shows that the hydrophobic properties of the GDLs are much more important at the cathode than at the anode. This implies that it is more important to have the MPL at the cathode to enhance oxygen and water transport and might not be necessary at all at the anode. The MPL may in some situations act as an extra mass transfer resistance at the anode. This in turn suggests that GDLs with low thermal and contact resistances but poor water management properties could be used at the anode side.

2.5.3.3 Electro-osmotic pumping

Several groups have examined the Electro Osmotic (EO) pumping technique to mitigate cathode channel flooding [48]. In Buie et al. [124] experiment two porous glass EO pumps are placed against the wall of the cathode channels. During fuel cell operation, water formed at the cathode is forced out of the GDL by means of hydrophobic forces, and then allowed to transform into water droplets. Liquid water droplets are wicked into the hydrophilic porous glass structure of the EO pump. Once the EO pump structure is adequately saturated with water, EO pumping actively drives water through the porous glass structure into the integrated water reservoirs in the acrylic top plate. It was reported that the EO pumps were able not only to prevent cathode flooding but also to remove water from a flooded cathode to recover the fuel cell, with less than 15%, consumed as a parasitic loss. However 15% could be a very substantial percentage of the PEM fuel cell power and the intricacy of placing EO pumps into stacks may not be feasible.

2.5.3.4 Hydrophilic and hydrophobic GDL's

Annular flow and slug formation within flow plates causes problems with the mass transport in a fuel cell as described by Lu et al. [11] and Benziger et al. [12]. A hydrophilic GDL retains liquid water on its surfaces and along the catalyst layer as a result of strong wall adhesion. A hydrophilic layer could also attract liquid water from the gas flow channel into the electrode, which makes the problem worse. The contact angle, as shown in Figure 32, between the liquid water and the surface plays a role in water management. A few proposed water management schemes have involved the integration of additional or replacement materials into the MEA. Hydrophobic gas diffusion layers, integrated with polytetrafluoroethylene (PTFE), as described by Buie et al. [124] and Jiao et al. [125] and capillary action can aid in effective water removal from fuel cell. Jiao et al. [125] noted that the hydrophobic level of the electrode must be carefully controlled, and the catalyst layer must have higher or equal hydrophobic level compared to the GDL resulting in one directional expulsion of liquid water (from catalyst layer to GDL).
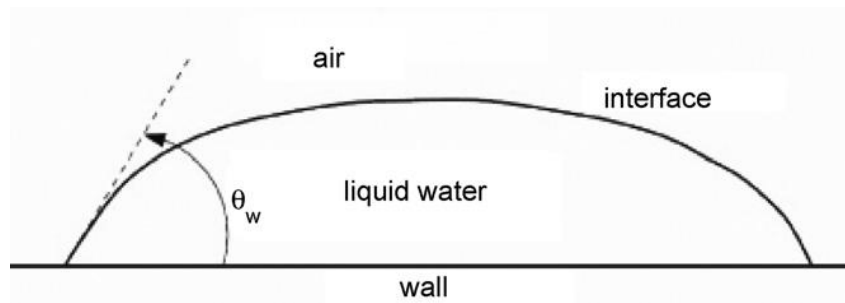
Figure 32 Contact angle between liquid water and surface plays a role in water management [125]**.**

2.5.3.5 Thinner membrane

Other suggestions regarding means to improve water management include manufacturing thinner membranes, because it shortens the water back diffusion process and catalyst layers which would result in easier water removal.

2.5.3.6 The 100°C mark

Ion conduction is a thermally activated process and its magnitude varies dramatically from one material to the next. The type of electrolyte, which may be either liquid or solid, determines the temperature at which the fuel cell is operated. Higher temperature operation is preferred for reasons of electrode activity (higher system efficiency & fuel flexibility). However, for portable or intermittent power applications, lower temperature operation is typically favoured as it enables rapid start up and stress is minimised due to thermal cycling.

Li et al. [48] discuses some solutions to water management problems such as the development of PEM fuel cells that operate at temperatures above 100°C ,so water would not be an issue, however as discussed in Section 2.4.1, nafion membranes will only operate efficiently at temps under 120°C which leaves a narrow window for operating temperatures and more importantly the transport of protons through the membrane relies on the protons forming hydronium ions with water molecules. The aim then is to produce a PEM fuel cell with an alternative membrane, as discussed in Section 2.4.1, that operates above 150°C. This would enable the PEM fuel cell to operate without the issue of flooding, humidification and complex Balance of Plant (BOP) components would not be necessary. In addition, precious metal catalysts would be reduced, electrode poisoning would be minimised and kinetic rates improved. There is however much work to be completed on membranes and catalysts to ensure robust durable higher temperature PEM fuel cells.

2.5.3.7 Flow plate design

The flow field design is critical in the effective water management of PEM fuel cells operating below 100°C. Liquid water accumulation is a typical problem in PEM fuel cells and this can be tackled by the proper design of flow fields.

As mentioned in Section 2.5.3.4, a hydrophilic layer on the GDL can make flooding worse; a hydrophilic layer retains liquid water on its surface and can also attract liquid water. However, a hydrophilic layer can be only micro metres thick and aid water transport from the PEM fuel cell if positioned correctly in the flow channel; this will be revisited in the discussion in Chapter 6.

Holmstrom et al. [80] studied the interplay between the GDL and the flow plate and flow field design. It was noted that a porous GDL with an open structure (a high in-plane permeability) may improve the utilisation of the catalyst layer and smoothen the local current distribution over the ribs and channels, however the use of a GDL with a high in-plane permeability in combination with a flow field design makes it possible to have relative high pressure drop between adjacent channels. Such a cross flow leads to a larger effective flow area altering reactant flow in the flow channel so that the resultant pressure and flow distributions are substantially different from that without considering this flow. Li et al. [126] investigate the cross flow in a PEM fuel cell, with a serpentine flow plate, by a numerical and experimental study. Experimental measurements revealed that the pressure drop in a PEM fuel cell is significantly lower than that without cross flow. Three-dimensional numerical simulation were performed for wide ranges of flow rate, permeability and thickness of gas diffusion layer in order to analyze the effects of those parameters on the resultant cross flow and the pressure drop of the reactant streams. Considerable amount of cross flow through gas diffusion layer was found in flow simulations and its effect on pressure drop became more significant as the permeability and the thickness of gas diffusion layer increased.

High pressure losses through the flow fields increase the parasitic load, increase the difficulty for hydrogen recirculation and high pressure drop between adjacent channels can be disadvantageous for membrane hydration, however small pressure drops are actually helpful for the removal of product water in vapour form. Assuming ideal gas behaviour, the total reactant gas pressure is

$$P = P_{vap} + P_{gas} \qquad\qquad Eqn.\ (2.5.2)$$

where P_{vap} and P_{gas} are the partial pressure of the water vapour and reactant gas in the reactant gas stream. The molar flow rate of the water vapour and the gas is related as follows:

$$\dot{N}_{vap}/\dot{N}_{gas} = P_{vap}/P_{gas} = P_{vap}/P - P_{vap} \qquad\qquad Eqn.\ (2.5.3)$$

The total pressure loss along a flow channel will increase the amount of water vapour that can be carried and taken away by given amount of reactant gas flow if relative humidity is maintained. In addition if the gas temperature is increased along the flow direction from the inlet to the outlet of the fuel cell, the capacity of the gas stream to absorb water also increases [8]. These approaches can be used to enhance water removal by both oxidant and fuel streams, as a sufficient pressure loss in the anode flow channels can draw water through the membrane from the cathode side, and removes the excess water by the anode stream. The fuel cell performance at high current operations can be improved significantly, as shown by [68].

The pressure drop is a significant issue to be considered in choosing the flow field designs in addition to the I–V cell curve. The cathode pressure drop can be converted to a power density using [127]:

$$WP = \Delta PA_{channel}V/A_{total} \qquad \qquad Eqn. \ (2.5.4)$$

where WP represents the cathode pressure drop loss, ΔP the total cathode pressure drop in the fuel cell, $A_{channel}$ the cathode cross-sectional flow inlet area, V the fuel velocity at the cathode inlet and A_{total} represents the total reaction area.

2.6 PEM Fuel Cell Modelling & Simulation

As discussed in Section 2.2, PEM fuel cell operation involves simultaneous, complex processes and hence, the development of a model for a complete PEM fuel cell that considers all parts, all components and all phenomena is a big challenge. Fortunately, the developments of high performance computing and advanced numerical algorithms, has allowed researchers to model PEM fuel cell systems as well as individual components with greater fidelity than ever before.

A large number of flows encountered in nature and technology are a mixture of phases. In multiphase flow, a mixture of a gas, a liquid or a solid, or any combination, is conceived. Section 2.4 discussed the experimental and visualisation techniques used in literature to understand water formation and movement in PEM fuel cells. However, when a more detailed or faster and less expensive method is needed, modelling the PEM fuel cells two phase environment in a microscopic scale can prove invaluable.

Section 2.6.1 reviews the modelling work conducted to understand flow interface tracking and growth and distribution of water droplets and species inside PEM fuel cells, mainly focusing on volume of fluid methods as this method was used in this thesis.

Section 2.6.2 looks at the interaction of fluid flow and gravity and investigates the affect that gravity has on droplets or water management in PEM fuel cells.

Section 2.6.3 reviews the 3-D electro-chemistry modelling work in literature and PEM fuel cell models that takes into account all aspects of species transport and electrochemical reactions.

2.6.1 Modelling two-phase flow in PEM fuel cells

In this study, fluid flow in mini channels relevant to PEM fuel cells is studied using suitable Computational Fluid Dynamic (CFD) software. Volume of fluid (VOF) method was applied for the simulations of fluid motion in mini channels in this study. The VOF method is detailed in Chapter 3. This section reviews phenomena, models and modelling techniques that have been completed in relation to understanding two phase flow in PEM fuel cells.

Recently, three-dimensional CFD models have been developed by taking full advantage of different commercial CFD software packages such as Fluent, Open-Foam, CFX, Star-CD and CFDRC, etc. Two-phase flow is a very complex phenomena and its simulations play important role in understanding fuel cell water management. The complications are mostly attributed with the interfaces between fluids and different layers of the PEM fuel cell during the detachment and motion of droplets from the GDL into the channel and through the channel.

An early review by Hyman [128] looked at many different numerical methods for tracking multi-phase interfaces, including surface tracking, volume tracking (VOF) and moving mesh. Cerne et al. [129] used VOF method to simulate bubble motion through a viscid fluid due to buoyancy forces and compared the results to experimental results from literature. Annaland et al. [130] used VOF to create a model that would accurately represent gas bubbles rising in liquids. The results matched results from the Grace bubble diagram. Lai et al. [131] used VOF to study thermo-capillary induced flow in a micro-channel. Using slugs of water in micro-channels they were able to generate a capillary pressure gradient for liquid propulsion by applying a difference in temperature between the front and back ends of the micro-channel. Theodorakakos et al. [132] utilized a flow field to capture side-view droplet detachment images for input to their CFD VOF simulations. Horvath et al [133] compared VOF methods of open source solver (OpenFOAM) and commercial solver (Fluent) with a bubble column experiment. The results of the solver predictions match well with experiment, but it was noted that a higher grid and refinement around interfaces would produce better results especially for the smaller bubble interactions.

Recently, Fei et al. [134] used VOF and other techniques to help derive a model that can be used for CO_2 bubble transport in a liquid methanol solution for a direct methanol fuel cell (DMFC). In another study, Du et al. [135] used VOF method to study two phase flow in a PEM fuel cell. The results from this study show that the surface wet-ability of the channel wall can greatly affect the flow pattern, especially when the channel walls and the GDL surface possess different contact angles. When the channel walls are more hydrophobic, more water is accumulated on the GDL. An increase in the surface tension results in a slight increase of slug frequency and a slight decrease in slug length. The onset of slugging along the channel is determined by the gas-liquid mixture velocity, gas-to-liquid flow ratio and the way water is introduced into the gas flow channel. Furthermore, the calculated pressure drop fluctuations show a strong dependence on the channel liquid content and the slug length.

Park et al. [53] modelled fluid flow through GDLs. It was concluded that a thin GDL with small porosity results in good electrical conductivity; however efficient mass transport requires large pores. The amount of cross flow is strongly correlated with the thickness and permeability of the GDL in a PEM fuel cell. It seems that the effect of the fibre orientation on the permeability of the medium can

be dominant over that of porosity within the given range of porosity. However, this study only used a serpentine flow channel; other flow channels may exhibit different results.

Zhu et al. [136] modelled liquid water entering a PEM fuel cell channel through a GDL pore. A 2-D VOF model was employed to view the effects of flow channel size, droplet coalescence and pore size on the emerging water droplet dynamics. It was found that in large micro channels (0.5mm) droplet deformation slows down and droplet breakup may not occur. This can result in a film of water forming against the GDL downstream of the pore. In another study by Zhu et al. [137], the effect of micro-channel geometry on water droplet dynamics in a PEM fuel cell using a 3-D VOF model, was investigated. They compared many different micro channel designs; rectangular, trapezoid, upside down trapezoid, triangular, rectangular with curved bottom wall and semicircular (aspect ratios in the range of 0.1 - 2) with respect to evolution and motion of the droplets, flow resistance, saturation and coverage ratio. This study concluded that the geometry and the micro-channels wet-ability drastically affect water droplet movement which should help design better flow channels for more effective water removal.

Zhou et al. [138] studied water behaviour in the cathode side of a PEM fuel cell, with a serpentine micro channel using VOF, as shown in Figure 33. Water droplets and films were introduced into the micro channel at varying positions, to simulate different operational conditions of the PEM fuel cell and air at 10m/s was used. Detailed results show droplet evolution and breakup and movement of water films through the serpentine micro-channel.
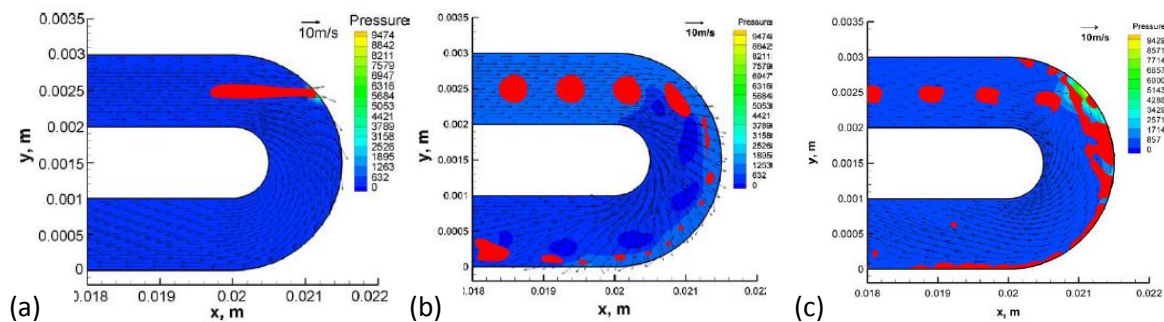
Figure 33 VOF model showing micro droplets initially (a) Suspended at channel inlet (b) Suspended in channel bend (c) Attached to channel wall [138]**.**

Quan et al. [139] also studied the water management in a PEM fuel cell flow channel. This study focused on hydrophilic effects on channels, channel geometry, air inlet velocity and pressure drop in relation to water behaviour. It was concluded that sharp corners inside the channel with the aid of hydrophilic surfaces may aid in water transport and due to increased spreading of the liquid, pressure drop is increased in the flow channel.

2.6.2 Models of fluid flow in microgravity

Gravity is a strong force that acts on everything on earth, its interaction with water droplets, water movement or water flooding mitigation in PEM fuel cells is of interest in this study. Minimal information was found in relation to specific modelling of PEM fuel cells; systems or components in different gravity environments. However, fluid models incorporating gravity were found and a brief review was able to be completed.

Dushin et al. [140,141] studied two phase flow through porous media, in microgravity, because it was noted that gravity may mask instability effects of viscous fluids. Scovazzo et al. [142] introduced an early model that can be applied to two phase flow through porous media in microgravity. Guo et al. [143] developed a mathematical model to predict distribution of fluid flow in confined porous media under microgravity but more recently Lakehal et al [144] performed numerical simulations to study the effect of gravity on two-phase flow heat transfer in small diameter pipes. They suggest that microgravity experimental campaign dealing with air water systems can be performed by the European Space Agency on its space Fluid-Lab facility. However, Stanic et al. [145] developed a mathematical model for a gravity/water management relationship. It was concluded from the model that gravity has a negligible effect on pressure drop and water removal which is mainly affected by gas flow.

2.6.3 CFD 3-D electro-chemistry modelling in PEM fuel cells

It is extremely complex to observe and measure the transport phenomena of chemical species in the PEM fuel cells and implementing CFD modelling gives a more accurate description of the reactions within the fuel cell. Good interpretation of CFD models allow the designer to build a more efficient and reliable fuel cell. This is an effective approach in studying the fuel cell and of great benefit in the development of the PEM fuel cells [146].

The first computational models of PEM fuel cells were recorded in the early 1990s, with most models being one dimensional, isothermal and focusing on the electrode, catalyst layer and membrane [147] [148]. The late 1990's saw the dawn of more advanced and complex PEM fuel cell modelling, 2-D models were first studied and then 3-D models with multiphase flow followed. The first model incorporating two-phase flow and transport of reactants and products in the air cathode of a PEM fuel cell was studied analytically and numerically by Wang et al. [149]. Single and two phase flow regimes were classified by current density according to the appearance of water at the MEA interface.

Berning [150] developed a model that focused on the single phase and multiphase flows in straight channel. In particular, the single-phase model accounts for many important transport phenomena in a complete assembly of gas channels, porous gas diffusion electrodes, and thin catalyst layers. Heat transfer is also considered in this model and the physical structure of the fuel cell is split into four computational domains. The main computational domain accounts for gas flow, heat and mass

transfer inside the flow channels and gas diffusion electrodes. Sub domain I consists of the Membrane Electrode Assembly (MEA), Sub domain II also consists of the MEA and is used for solving liquid water flux through the membrane. Sub domain III consists of the membrane only and is used for calculating the electric potential drop. In this model, the electrode kinetics are modelled by a simplified version of the Butler-Volmer equation which only accounts for the dependence of current density on oxygen concentrations. This is one of the major limitations of this modelling approach.
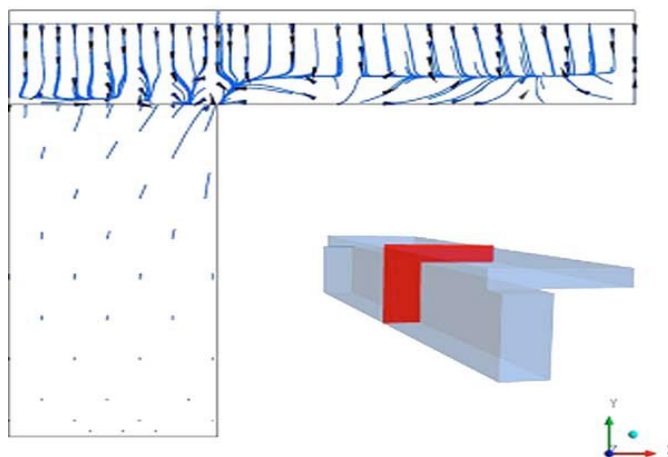
Figure 34 The liquid water streamlines after 20seconds of operation in PEM fuel cell model.

Most CFD based models presented still do not resolve the three-dimensional nature of the catalyst layer and use simplified electrochemical kinetics in which constant activation over potential is assumed. This fact was highlighted by Gurau et al. [123], who argue that to date, multiphase CFD models for PEM fuel cells fail to provide even a qualitative depiction of the fuel cell water management. They emphasize that this is due to the inability to capture two-phase phenomena in the cathode catalyst layer and the water saturation equilibrium at the interface between the fuel cell components. They argue that a model without the cathode catalyst layer cannot capture dominant mechanisms of water transfer and cannot explain correctly the fuel cell performance. Gurau et al. [123] presented their model, Figure 34, which did account for the cathode catalyst layer and developed transport equations for describing the production and transport of water in this layer. Their study identified possible new mechanisms of water transport in the catalyst and GDL layer and predicted that water starts to accumulate at the rib of the flow field. Their model however focused on water transport and could be developed further. A general numeric model was recently presented by Le et al. [151] and a numerical model for interdigitated flow fields was also presented by Le et al. [73]. The liquid water transport on a PEM fuel cell with interdigitated design was investigated in the later study. The behaviour of liquid water was understood by presenting the motion of liquid water droplet in the channels and the porous media at different time instants. The numerical results show that removal of liquid water strongly depends on the magnitude of the flow field. Due to the blockage of liquid water, the gas flow is unevenly distributed, the high pressure regions takes place at the locations where water liquid appears. In addition, mass transport of the species and the current density

distribution is significantly degraded by the presence of liquid water, as shown in Figure 35 (a). Highest current density was noticed at the channel interfaces of the serpentine model, Figure 35 (a), this is mainly due to the contact with the flow plate and fuel readily available. On the interdigitated flow field a more distributed current density is apparent, however water accumulation is seen at the top right of the interdigitated flow field, Figure 35 (b).
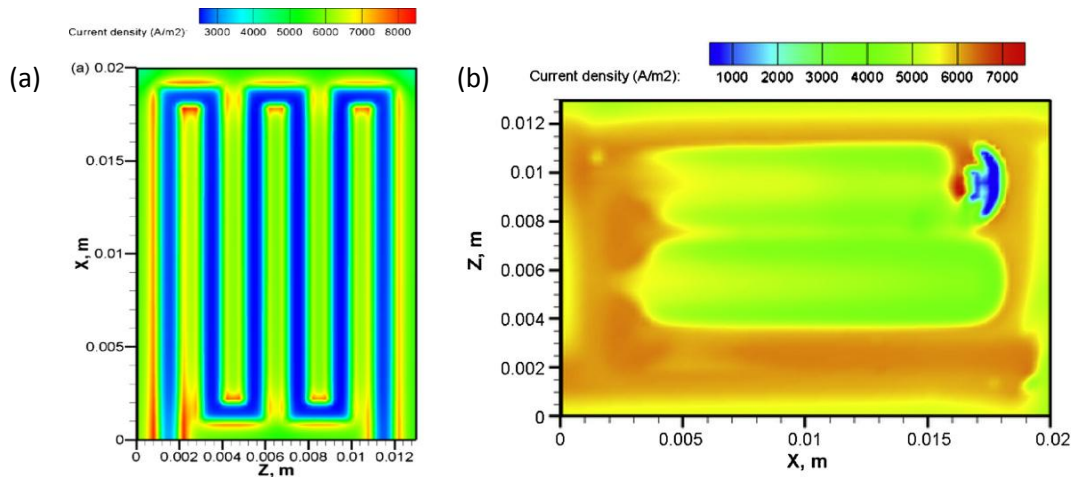
Figure 35 The distribution of local current density at the catalyst/GDL interfaces at the cathode and anode (a) Serpentine flow field [152] **(b) Interdigitated flow field** [73]**.**

2.7 Open Pore Cellular Foam Material

Open pore cellular foam, Figure 36, is a relatively new class of cellular material with the ability to be manufactured with tailored mechanical, thermal, acoustic and electrical properties by varying the material's relative density and cell morphology. Open pore foam material can provide great benefits to solve many engineering problems and at present it has many applications in filter systems, heat exchangers and more recently in the electrodes of some electrochemical devices; super capacitors, batteries and electrolysers.
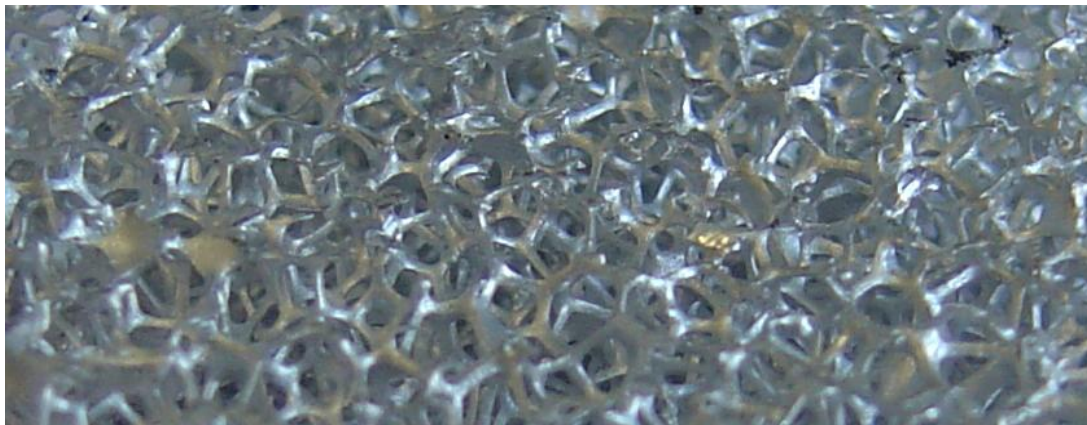
Figure 36 Open pore cellular foam structure

Open pore cellular foam material was described in literature and was identified to be of interest for use in fuel cells. This section describes open pore cellular foam material and reviews its uses and applications in relation to PEM fuel cells and the possibilities of using it as a flow plate material in PEM fuel cells.

2.7.1 Open pore cellular foam structure

As the name suggests these materials have an open pore structure composed of isotropic pores which are connected to each other by ligaments. The array of pores forms a solid homogonous matrix, having the same properties of the parent material but at the fraction of the weight. These materials are mainly manufactured by casting or foaming [153], leaving the final open pore foam material, Figure 36. Foam manufacturers usually classify foam in terms of the number of pores per linear inch (ppi) and this is an important characteristic of the material, which will be discussed in the following sections.

The foam structure provides several unique properties, which can be tailored at manufacture. These include [108,154-158]:

- Independently variable porosity from 5 to 100 ppi
- Independently variable density from 3 to 12 percent
- High (and variable) surface area to unit volume
- High strength-to-weight ratio
- Completely isotropic load response
- Variable stress-strain characteristics
- Low resistance to fluid flow
- Low pressure drop for fluid flow
- Thermal & electrical conductive
- Large surface area (up to nine times with compression)
- Inert & temperature resistant (RVCF in a non oxidising environment)
- Isotropic & rigid geometry (RVCF)

2.7.2 Open pore cellular foam material

Porous Metal Foam (MF) & Reticulated Vitreous Carbon Foam (RVCF) materials are two common classes of open pore cellular foams, Figure 37. A variety of metals including; aluminium, copper, tin, zinc, nickel, silicon, inconel (nickel-chromium-based super-alloy), silver and gold, can be made to produce an open pore MF. Aluminium foam is one of the most popular MF, followed by copper foam. Advanced combinations can be achieved through secondary coating processes [159].

RVCF is an open pore foam material composed solely of vitreous carbon [154,155]. As its name implies, vitreous carbon is a form of glass-like carbon that combines some glass properties with those

of normal industrial carbons. It has isotropic material properties unlike other carbon-based materials such as graphite coatings and carbon fibres.
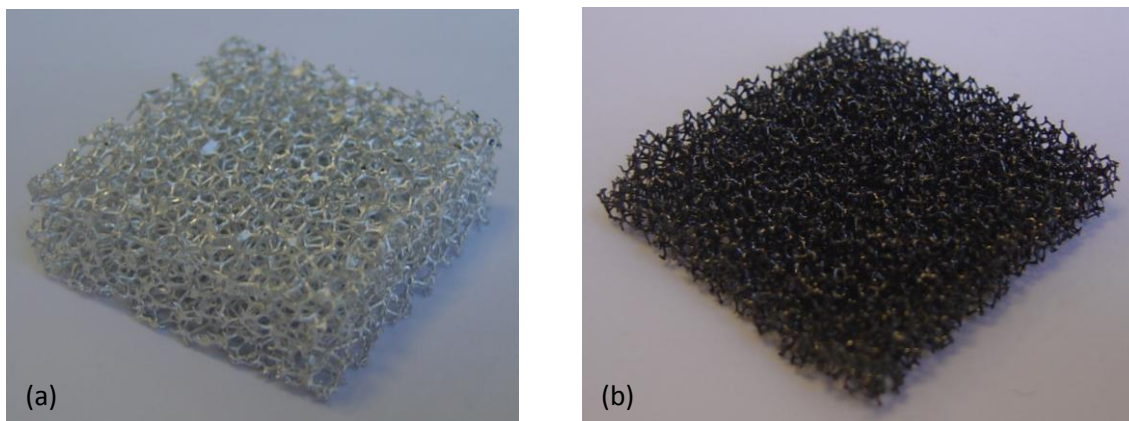
Figure 37 Open pore foam (a) Aluminium metal foam (b) Reticulated vitreous carbon foam.

2.7.3 Applications of MF & RVCF

An early review on RVCF, by Wang, appeared in 1981 [154] and predicted increasing applications in analytical chemistry, particularly in sensor development. Today MF & RVCF have many applications [158,160-163]:

- RVCF can be used in electrochemical processes that require very high current distribution areas and low electrical and fluid flow resistance. The extremely high void volume of RVC means that it can be used in applications where the cell volume loss to electrodes must be minimized. Blaedel et al. [164] described a flow-through electrolytic cell which contained a working electrode composed of a variable number of RVCF disks.

- The self-supporting nature, low density, low out gassing, low heat capacity and excellent K value of RVCF makes it suitable for use in inert gas and vacuum furnaces.

- RVCF can be used for filtration in a variety of environments including but not limited to molten metals, corrosive chemicals and high or low temperature gases and liquids.

- RVCF is non-toxic and biologically inert, and can be used in pollution control systems for biological growth. Specifically, it can be used as a catalyst or as a support matrix for a catalyst, in tower packings, or in any other structure where low pressure drop, large available surface area and chemical inertness are necessary.

- Foam products can all be densified. MF & RVCFs can be used in extreme conditions in order to absorb noise with frequencies between 250 Hz and 3 kHz and absorb impacts.

- Thermal applications, phase change materials, heat exchangers etc [165-167]

- Heat exchanger microgravity/space applications [112].

- Electrochemical applications [168,169].

10ppi   **45ppi**   **100ppi**
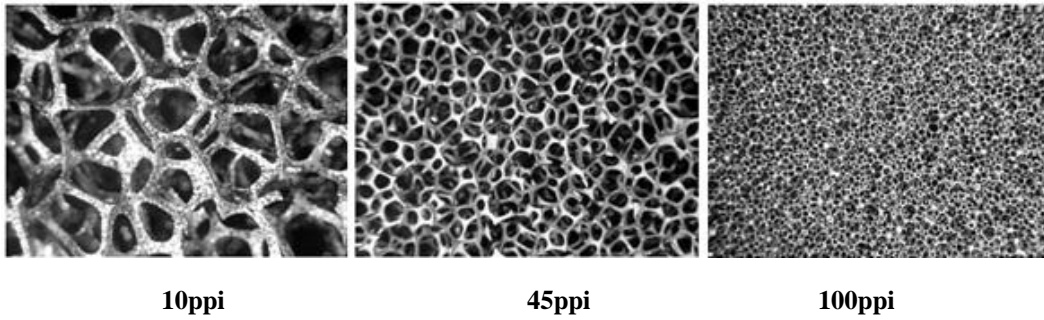
Figure 38 RVCF structure with different pore size [170]
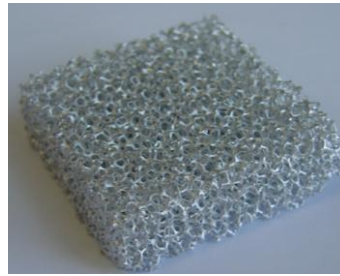
Figure 39 Aluminium metal foam flow plate

2.7.4 MF & RVCF materials for PEM fuel cells

Friedrich et al. [156] reviewed the physical structure and properties of RVCF (in terms of ppi, strut length, strut thickness and area of the triangular strut) for 10, 30, 60 and 100 ppi grades using scanning electron microscopy. It was noted that 100ppi grade RVCF had a surface area of approximately $65cm^2$. The pressure drop of a flowing stream across an RVCF structure is small. It was concluded that due to the properties of the open pore foam it would be suitable for use with a number of technologies including fuel cells. SEM micrographs are seen in Figure 40.
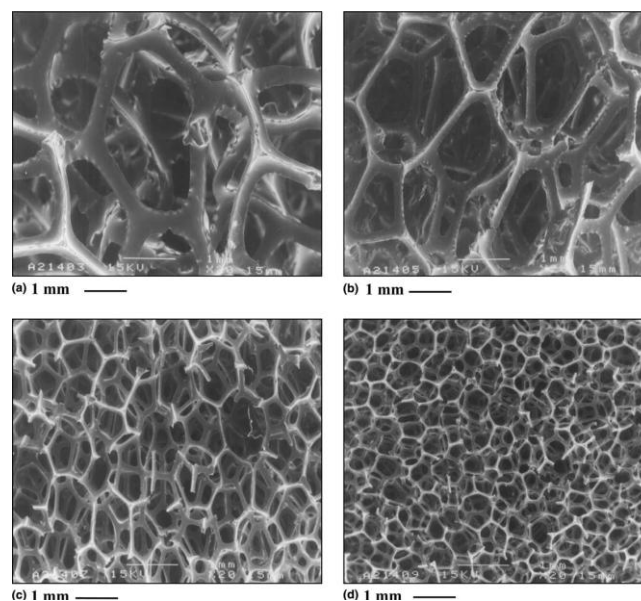
Figure 40 SEM micrographs of: (a) 10, (b) 30, (c) 60 and (d) 100 ppi RVC samples [156]

A porous flow plate with an interdigitated flow field was proposed by Yi et al. [171] to enhance mass transport in the gas diffusion layer and to eliminate excess liquid water along the gas flow path. Benefits of this flow plate configuration were discussed, including demonstration of performance and stability improvement. However the structure and design of the porous flow plate was not discussed and it is unknown what type of porous material was used in the construction of the plate. Lister et al. [172] completed a study of the performance of two PEM fuel cell designs with dry inlet gases: a standard, non-porous graphite cathode plate design and a porous hydrophilic carbon plate version. Results showed that the porous plate yields significant improvements in performance and robustness of operation with a maximum power density 3.5 times greater than that achieved with the non-porous plate at the same operating conditions, also membrane resistance and air pressure drop was reduced. They credited the advantages of the porous plate to passive water redistribution and internal air humidification. Kumar et al. [173] proposed a prototype PEM fuel cell with the flow plate made out of stainless steel porous material, the performance of which was compared to the conventional channel type flow plate designs. Initial results showed the feasibility of such flow plates, but it also showed that further improvements may be achieved by decreasing the permeability of MF in the channels. In a separate study by Kumar et al. [14], three different porous materials were investigated; Ni-Cr MF (50 PPI), stainless steel MF (20 PPI), and carbon cloth. It was seen that the performance of the PEM fuel cell with Ni-Cr MF was highest and decreased in the order of stainless steel (SS-316) MF, conventional parallel flow field channel design and carbon cloth. This trend was explained based on the effective permeability of the gas channels in the flow plate. The use of MFs with low permeability values resulted in an increased pressure drop across the flow field, which enhanced the cell performance, Figure 41.
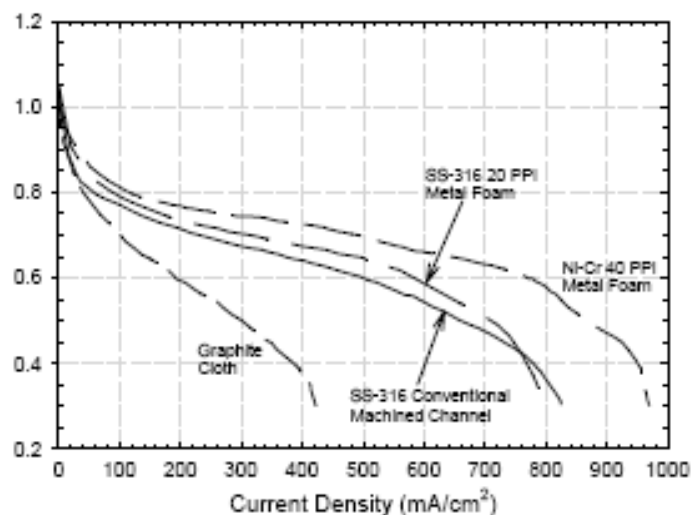
Figure 41 Polarization curves for different porous flow plates [14].

Chen et al. [174] placed open pore foam insets into the flow field of a flow plate. Results from the operational cell indicated that flow mal-distribution had been reduced with the inserts. 10% water was

retained in the porous inserts and the inserts featured a self-adjusting capacity for water management in flooding and drying conditions.

2.7.5 Open pore cellular foam models

Flows in porous media may be modelled using a macroscopic approach, where volume-averaged semi-empirical equations are used to describe flow characteristics, or a microscopic approach, where small-scale flow details are simulated by considering the specific geometry of the porous medium [175]. This study used a microscopic approach to model open pore cellular foam so that small-scale flow details of specific porous geometry could be simulated and analysed. In addition averaging affects produced by macroscopic approach would be eliminated. To aid the development of an idealised structure to represent the foam cells a review of literature was completed to view existing models and indicate gaps in literature.

Lu et al. [176] took the approach of modelling the fluid flow through open pore cellular MFs as a system of cylinders in their combined flow and heat convection model. Krishnan et al. [163,175] simulated thermal transport in open pore cellular MFs using different periodic unit-cell geometries, Figure 42. The periodic unit-cell structures were constructed by assuming the pore space to be spherical and subtracting the pore space from a unit cube of the metal. Different types of packing arrangement for spheres were considered including; body centred cubic, face centred cubic and A15 lattice, which give rise to different foam structures. Effective thermal conductivity, pressure drop and Nusselt number are computed by imposing periodic boundary conditions for aluminium foams saturated with air or water. The computed values compare well with existing experimental measurements and semi-empirical models for porosities greater than 80%.
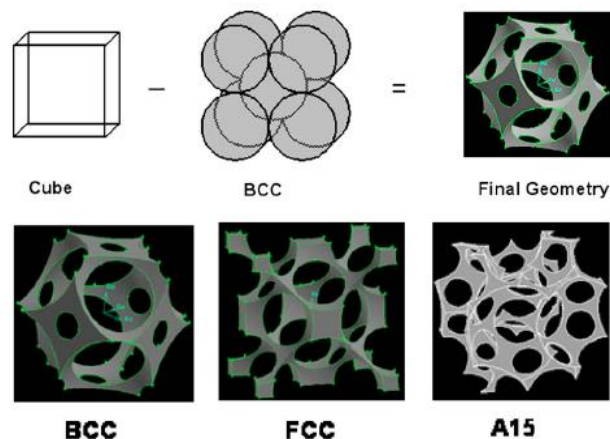
Figure 42 Schematic representation of foam geometry creation of Krishnan et al. [163]

Early work by Du Plessis et al. [177] attempted to capture the relevant characteristics of open pore cellular MF based on a set of rectangular prisms. They used the results of an analytical flow analysis on this model to solve the flow through open pore cellular foams on a larger scale with relatively good results. But a later study by Fourie and Du Plessis [178], have used a 14-sided tetrakaidecahedron,

Figure 43, to simulate pressure drop and flow in open cell metal foam model. Boomsma et al. [179] also simulated flow through open pore cellular MF using the tetrakaidecahedron cell which has long been considered the optimal packing cell first proposed by Lord Kelvin in1887. A historically popular experimental approach was the pea-packing experiment. In this experiment, peas were compressed inside a container. The resulting packed peas were then carefully observed and the number and shape of the flattened sides were recorded. From these and similar experiments Lord Kelvin postulated that the ideal packing cell shape was the so-called ''tetrakaidecahedron''. The 14 sided tetrakaidecahedron cell was decided upon mainly through experimentation, and has never been mathematically proven to be the optimal packing cell.
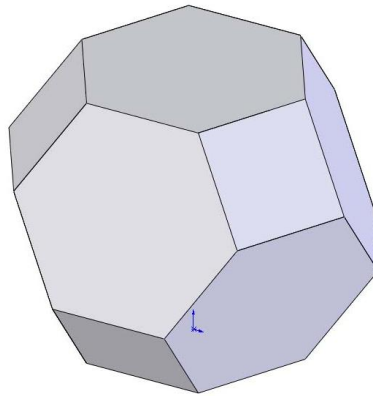
Figure 43 Tetrakaidecahedron cell.

However other researchers, [167], have noted in literature that the isotropic open pore cellular foam consists of randomly oriented polygon shaped cells that could be approximated by a dodecahedron Figure 44.
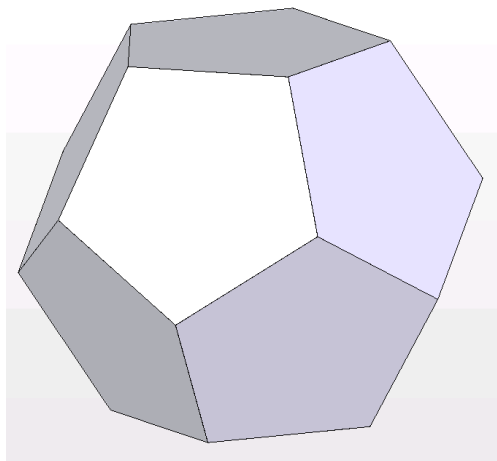
Figure 44 Dodecahedron cell.

Ozmat et al. [167] reviewed the structure of MF and concluded that some geometric characteristics of the dodecahedron are related to the physical structure of the metal foams, such as ligament size, surface area, cell density, and relative density. Figure 45 shows a comparison between a dodecahedron cell model developed during this thesis and a real open pore foam structure. This will be described and analysed in Chapter 4.
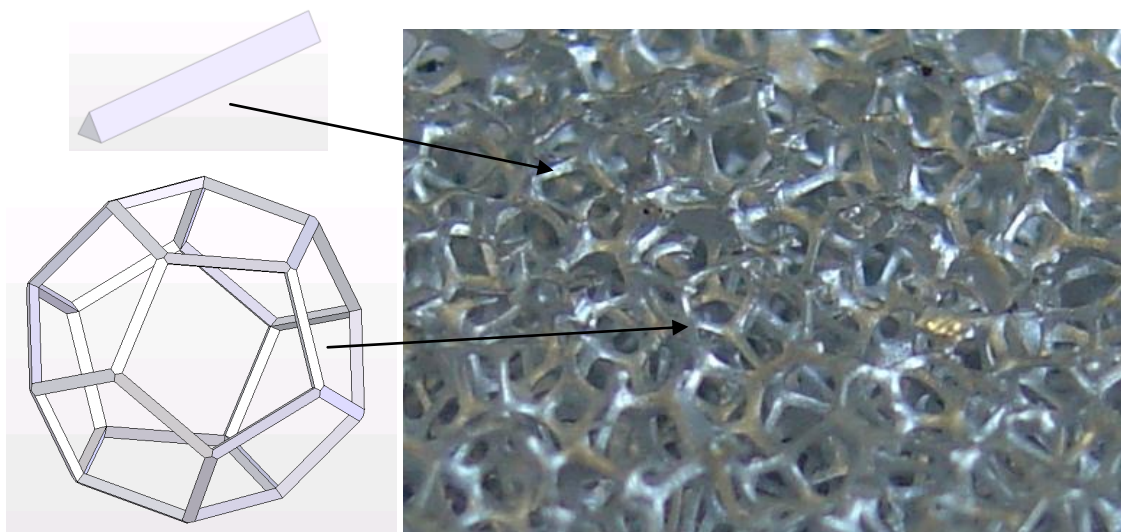
Figure 45 Comparing ligament and pore models to a real open pore foam structure.

2.7.6 Open pore cellular foam characteristics

Properties such as electrical conductivity, thermal conductivity and pressure drop are important to know for a material that may be used as a flow plate in a PEM fuel cell. The outline of the characteristics of open pore cellular foams are presented in the following sections and a full discussion is completed in Chapter 6 with relation to the suitability of these materials as flow plates for PEM fuel cells.

2.7.6.1 Electrical & thermal conductivity of foam materials

Lemlich [180] was one of the first people to propose a theory for the electrical conductivity of polyhedral foam with sufficiently low bulk density. Lemlich proposed that conduction occurred effectively only through a random lattice of very narrow plateau borders. Dharmasena et al. [181] developed a tetrakaidecahedral unit-cell approach to represent open pore cellular aluminium foam and a simplified electrical resistor network derived to model low frequency current flow through the foam. The analysis indicates that for the range of relative densities studied (4–12%), the conductivity of tetrakaidecahedral foams has a linear dependence upon relative density. The distribution of metal in the cell ligaments was found to significantly affect the conductivity. Increasing the fraction of metal at the ends of the ligaments resulted in a decrease in electrical conductivity at a fixed relative density. Low frequency electrical conductivity measurements of open pore cellular aluminium foam confirmed the linear dependence upon density, but the slope was smaller than that predicted by the unit-cell model. The difference between the model and experiment was found to be the result of the presence

of a distribution of cell sizes and types in real samples. This effect is due to the varying number of ligaments, ligament lengths, and the cross-sectional areas available for current conduction across the cellular structure. It was noted that compression can increase the thermal and electrical resistance of the foam material by increasing the number of resistive elements that are in series in the direction of compression. Ma et al. [182] also completed electrical conductivity measurements of a number of aluminium foams with different densities and pore diameters. Their results are shown in Table 4.

Table 4 Open pore cellular foam conductivity values [183].

Pore Diameter (um)	Conductivity (S/cm) [[182]]	Corresponding foam sample (ppi)
2540 - 2880	0.06171	10
1270-1210	0.21873	20
850-920	0.15957	30
640-700	0.19318	40
560-510	0.19318	45
320-290	-	80
250-230	-	100

2.7.6.2 Pressure drop of porous foam materials

It was noted that even pressure distribution within the flow plate can ensure a more effective fuel cell performance. But in conventional flow fields, as the flow field length increases, the pressure decreases across the GDL from inlet to outlet, this can lead to the effectiveness of the fuel cell decreasing rapidly from inlet to outlet. Increasing the inlet pressure can increase cell performance, however it may reduce the efficiency of the system as BOP equipment are needed to power this pressure increase.

Understanding pressure gradients across the GDL and providing an acceptable pressure drop in the PEM fuel cell's flow plate can ensure good PEM fuel cell performance. Pressure drop equations and testing has been performed on numerous kinds of foams by many researchers. Experimental pressure drop results of 10ppi, 20ppi and 40ppi open pore cellular foams, from ERG Aerospace [159], are shown in Figure 46. However in order to build and develop models and determine the benefits and to characterise open pore cellular foam material for PEM fuel cells it was necessary to view literature and analyse if measurements and calculations of pressure drop are applicable to PEM fuel cells.
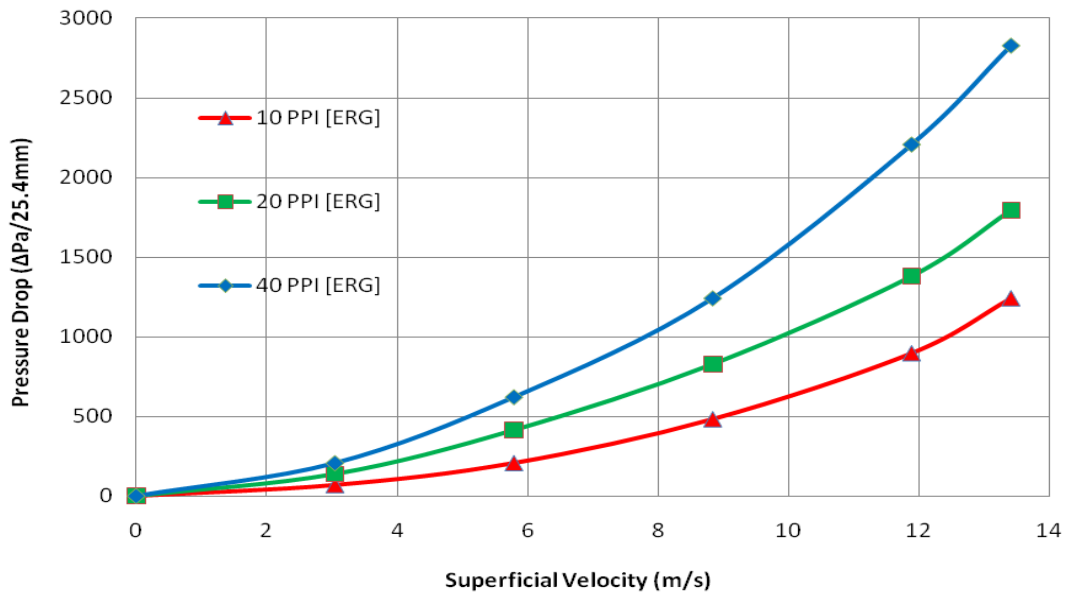
Figure 46 Pressure drop in a range of open pore cellular foams [159]**.**

Pressure drop through porous materials can be determined from Darcy's law:

$$\Delta P/L = (\mu/K)\, v \qquad\qquad Eqn.\ (2.7.1)$$

where ΔP is the pressure drop over length, L, μ is the fluid viscosity, v is the superficial fluid velocity and K describes the permeability of a porous medium i.e. how easy it is for fluid to flow through it. However, Darcy's law is only applicable for Reynolds number less than one (Re < 0.1). For high enough flow velocities (> 0.1 m/s) form drag (constant related to material that would hindering flow e.g. ligaments of the foam) becomes important and the hydraulic properties that now characterise a porous medium are its permeability (K) and form coefficient (C). To describe the pressure drop in the foam or simultaneously determine K and *C* for a porous medium at these velocities the Hazen-Dupuit-Darcy model (also known as the Forchheimer-extended Darcy model) is used:

$$\Delta P/L = (\mu/K)\, v + \rho C\, v^2 \qquad\qquad Eqn.\ (2.7.2)$$

where ρ is the fluid density.

Medraj et al. [184] conducted an experimental analysis on the pressure drop across simple structure metallic foams at different velocity ranges using air as the working fluid. They observed that pressure drop characteristics fit the polynomial model of Hazen-Depuit-Darcy where K and C are important values. A study performed by Dukhan [185] also found that the pressure drop increased with increasing Darcian velocity following the Hazen-Depuit-Darcy model and that the lower-porosity foam produced significantly higher pressure drop. Both K and C correlated well with the porosity. The correlations predicted the results of some previous studies reasonably well, especially for the low-pore-density foam. Wilson et al. [186] also looked at permeability and form drag coefficient of porous

inserts in an experiment using rod and holes with water as the working fluid they show that their experimental data correlates to Hazen-Dupuit-Darcy model.

The Ergun equation describes flow of a fluid past a collection of uniform spherical particles of diameter d_p:

$$\Delta p /L = A v + B \rho v^2 \qquad\qquad Eqn. (2.7.3)$$

where

$$A = 150\mu(1 - \varepsilon)^2 / \varepsilon^3 d_p^2 \qquad\qquad Eqn. (2.7.4)$$

and

$$B = 1.75(1 - \varepsilon) / \varepsilon^3 d_p \qquad\qquad Eqn. (2.7.5)$$

where ε is the void space or the porosity of the material. This equation is most commonly used in flow through a packed bed; however for the purposes of correlating models and that this equation allows input of many variables that are available for open pore cellular foam materials, this equation will be tested.

The pressure drop inside metal foams is described by the equation developed by Ashby et al. [183]:

$$\Delta p /L = \xi \ 1/ d_p [\mu^m \rho/(1 - \alpha)^{2-m}] \ v^{2-m} d_L^{-m} \qquad\qquad Eqn. (2.7.6)$$

where α is the thermal diffusivity, d_L is the MF ligament diameter and ξ and m are determined experimentally. Some ξ and m values are shown in Table 5. This equation is in the context of pressure drop in relation to heat transfer, but for the purposes of correlating models, this equation will be tested.

Table 5 Open pore cellular foam ξ and m values [183]**.**

Foam ppi	ξ	m
80	4	0.19
30	4	0.37
20	4	0.43
10	4	0.44

The pressure drop inside metal foams is described by the equation developed by Fourie and Du Plessis [178].

$$\Delta p /L = (3-\tau) \ x \ (\tau-1) \ x \ (\rho \tau^2 v^2/\varepsilon^3 d_p) \ x \ (3C_{dv}/2 + C_{df}//4) \ x \ \varepsilon \qquad Eqn. (2.7.8)$$

where

$$C_{dv} = 24\mu\varepsilon/\rho \tau(3-\tau) \ d_p \ v \qquad\qquad Eqn. (2.7.9)$$

and

$$C_{df} = 1 + 10 \; (\rho v^2 d_p(\tau \text{-}1)/ \; 2\mu\varepsilon)^{-0.667} \qquad\qquad \textit{Eqn. (2.7.10)}$$

where τ is the tortuosity (relation to ligament structure) and C_{df} and C_{dv} are drag and frictional coefficient respectively as described by Fourie and Du Plessis [178]. This equation correlated well with experiments completed by Bastawros et al. [187] and described by Lu et al. [176] and shown in Figure 47. These equations are quiet complex introducing new terms and coefficients to describe flow and pressure drop through open pore cellular foam materials.
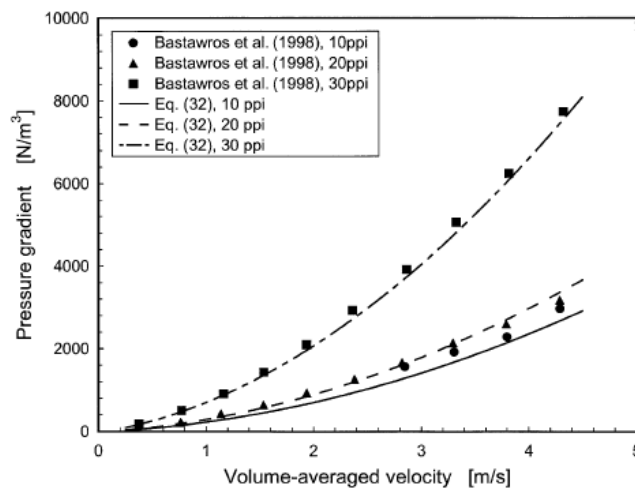
Figure 47 Pressure drops in foam material [178]**.**

From reviewing the literature for values of permeability (K) & form coefficient (C) many different values were found even looking at the same material samples researches produce different values, as shown in Table 6. It is noted that K and C values depend on the porous media type and thickness, fluid type and fluid velocity. To ensure accurate open pore metal foam K and C values for the test samples used in this thesis data would have to be provided from the manufacturer, ERG Aerospace [159].

Table 6 Permeability & form coefficient of porous media, according to various researchers.

Sample	Pore Ø (mm)	Permeability (K) m^2	Form coefficient (C) m^{-1}	Reference	Notes
Powder metallurgy foam	0.36	3.51E-10	6.95E+03	Loya et al. [188]	-
Powder metallurgy foam	0.69	1.34E-10	1.07E-02	Loya et al. [188]	-
10ppi	-	1.00E-07	2.10E-02	Dukhan (2006) [185]	-
10ppi	-	1.67E-07	9.30E-02	Haack et al. [189]	-
10ppi	-	1.76E-07	4.91E+01	Dukhan (2010) [190]	0-15vel discrepancy
20ppi	-	6.30E-08	2.90E-02	Dukhan (2006) [185]	-
20ppi	-	1.32E-07	7.91E+01	Dukhan (2010) [190]	0-15vel discrepancy
30ppi	-	1.00E-07	1.50E-01	Haack et al. [189]	-
40ppi	0.63	4.70E-08	3.80E-02	Dukhan (2006) [185]	-
40ppi	0.63	4.80E-08	7.50E-02	Cavallini et al. [191]	-
40ppi	0.63	1.21E-07	1.01E+02	Dukhan (2010) [190]	0-15vel discrepancy
Rods	1	1.72E-09	1.92E-01	Wilson et al. [186]	-

The pressure drop analysis including a comparison of the above equations for pressure drop in open pore cellular foams and experimental results of the open pore cellular foam samples and the representative model of different open pore cellular foams developed in this work (introduced and developed in Chapter 4) are discussed in Chapter 6.

2.8 Status of PEM Fuel Cell Technology

Hydrogen and fuel cells are medium and long term energy technology options. Because fuel cells are not yet mass produced, for several reasons, mentioned throughout Chapter 1 and Chapter 2, the near term mass commercialisation of this technology is predicted to occur at a time period that ranges from the year 2012 to anything beyond 2020 [6,12,38]. A common phrase used in the fuel cell field is that in many areas the technology, infrastructure and policies, need not an evolution but a revolution to make them a feasible commercial mass market product. Table 7 shows the status of PEM fuel cell technology. The cost per kW is the limiting factor for PEM fuel cells and in order to become commonplace in the open market PEM fuel cells need to meet the cost margins dominating each of the power sectors where it should be utilised.

Table 7 Status of PEM Fuel Cell Technology [37]

Parameter	Current Status (2010)	Theoretical / Ideal	Unit
Operating temperature	70 – 80	@ 25	°C
Operating pressure (relative to atm)	200,000-300,000	atm	Pa
Open circuit voltage	1	1.18	Volt
Optimal operational voltage	0.6 – 0.7	1.18	Volt
Power density (Cell)	1	10	W/cm^2
Power density (Stack)	120	1000	W/Kg
Efficiency [37]	40 - 65	83	%
Precious metal requirements (Cell)	0.017	0	g/cm^2
Precious metal requirements (Stack)	17	0	g/kW
Fuel cell cost [21]	3,000	< 50	$/kW
Maintenance cost	0.005- 0.010	0	$ / kWh
Cell operating lifetimes [12]	7300 - 13,000	>100,000	hours

2.8.1 Benefits & obstacles to the success of fuel cells

As our demand for electrical power grows, it becomes increasingly urgent to find new ways of meeting it both responsibly and safely. Table 8 summarises the benefits, obstacles and possible solutions to the commercialisation of fuel cells.

Table 8 Benefits & obstacles to the success of fuel cells [192]**.**

Benefits	Obstacle	Comment
Fuel cells are efficient. Co-generation of heat, cooling and electrical power from the one source.	Fuel cells are expense. Low lifetime. Technology is not proven.	Platinum catalyst is used and is a rare earth element. Platinum and other precious metals can be recycled.
Fuel cells are clean (low emissions, potentially zero CO_2, environmentally safe)	Fuel cell infrastructure	No fuel cell infrastructure or hydrogen supply is available. Existing fuel-chain infrastructure could be utilised.
Fuel cells are quiet	Mass market acceptance	The public have to buy fuel cells.
Fuel cells are modular and flexible to system needs. Systems are fast to install with minimal maintenance is required.	Combustion Engines	ICEs are still cheap and the fuel is still relatively cheap & accessible.
Jobs & economy.	Governments policy	Potential to nurture or destroy fuel cell & hydrogen technology development. Distributed power generation supports many national energy strategies. Government support and grants.

While at first glance this list of barriers may seem pessimistic, it actually means that a massive opportunity in research, to develop new intellectual property to make this technology feasible. During the last century some progress has been made in fuel cell technology but all the technological problems have not been solved. There is certainly room for new companies and new research activities in the fuel cell field. It should be noted that the drive for fuel cell technology and the advantages it offers far outweighs the barriers and it is certain that they will be overcome. A further examination of current research in PEM fuel cell technology is discussed in Appendix A.

2.9 Conclusions & Indication of Gaps in Literature

If hydrogen is to become an energy carrier in the future, fuel cells present the most efficient, most effective and cleanest device to convert hydrogen fuel directly into electricity. The Proton Exchange Membrane (PEM) fuel cell offers a low temperature, high power, robust, practical, scalable fuel cell for many stationary and mobile power applications.

PEM fuel cells still need to solve basic problems including, a reduction of cost, weight, complexity and optimal component material selection, but they must also ensure and sustain a robust, efficient and easy to manufacture product. PEM fuel cell problem areas include:

- Membrane: Water based membranes are limited to low temperature operation and they need humidification leading to over hydration or dehydration issues.
- Catalyst: The electro-catalyst layer is the most expensive part of PEM fuel cell relying on precious metals mainly platinum in their construction but platinum can be poisoned by contaminants reducing its performance.
- Flow plate: Material selection and flow plate design and configuration affect the PEM fuel cell's operation and performance. (This is the topic in which the emphasis of this thesis is focused.)

From the literature review completed, some conclusions are evident:

1. Higher temperature PEM fuel cell operation (>150°C), using non water based membranes, means that humidification would be redundant, catalyst poisoning would be minimised, fuel processors or reformers would be unnecessary (for some fuels) and the electrode kinetic rates would increase, improving its performance and minimising the use of expensive catalysts.
2. Even if PEM fuel cells operate at high temperatures mass transport, ohmic resistance, material cost and complexity issues will still exist and have to be resolved.
3. For portable or intermittent power applications, lower temperature PEM fuel cell operation is typically favoured, as this enables rapid start up and stress, due to thermal cycling, is minimised.

4. Membrane and catalyst issues do pose a barrier to the emergence of low temperature PEM fuel technology, however, mass transport, water flooding, ohmic resistance issues must be dealt with.

5. Effective water flood mitigation, effective mass transport, increased efficiency, reduced ohmic resistance, weight, cost and complexity of PEM fuel cell stacks can be achieved by optimal flow plate properties and design.

From the PEM fuel cell flow plate design and development review some gaps in literature are visible:

1. Many materials and designs have been proposed in the construction of flow plates but optimum design, configuration and flow field layout has not been satisfactorily demonstrated. Flow plate mass transport, water flooding, ohmic resistance and other issues still remain. It is the aim of this thesis to increase the effectiveness of PEM fuel cells flow plates, in relation to design, layout, configuration, water management and gas transport to achieve a better performing PEM fuel cell.

2. Water flooding depends on many factors including the effect of gravity; few models have taken gravity into account in literature. This may inhibit some effects of water flood mitigation. A full review of water flooding, gravity and water mitigation is completed in this thesis and conclusions are drawn.

3. Water droplet formation and release from GDL pores have been studied in literature however droplet coalescence and slug formation due to air flow and pressure gradients in the flow channels has not been studied to the same degree. It is the aim of this thesis to investigate the methods and issues associated with water accumulation and water transport through flow plate and flow field designs. To develop a computer model (validated by visualisation techniques) of flow plate flow fields and analyse droplet coalescence and slug formation and impacts on PEM fuel cell performance.

4. Open pore cellular foam materials including Metal Foam (MF) and Reticulated Vitreous Carbon Foam (RVCF) and their potential as a flow plate material has not been investigated to a satisfactory degree in literature. It is the aim of this thesis to investigate the use of innovative open pore cellular foam materials as a flow plate material in a PEM fuel cell.

5. A satisfactory Representative Unit Cell Structure (RUCS) model for open pore cellular foam material has not been developed in literature. A RUCS is proposed and developed in this thesis.

6. A model of open pore cellular foam materials, that can correlate pressure and flow regimes, has not been demonstrated in literature. It is the aim of this thesis to develop a model to simulate the above foam material, in relation to design, layout, configuration and gas transport to achieve a better performing PEM fuel cell.

7. An electrochemistry PEM fuel cell model demonstrating open pore cellular foam flow plates has not been simulated or developed in literature. It is the aim of this thesis to develop a PEM fuel cell electrochemistry model with a RUCS of open pore cellular foam flow plate.

8. An effective optimum design, configuration and layout of possible open pore cellular foam flow plates have not been described in literature and a determination of voltage, current, power and efficiencies of open pore cellular foam flow plates in an operational PEM fuel cell is not available in literature. It is the aim of this thesis to validate the simulation results by experimentation and obtain an optimum design of open pore cellular foam flow plates.

3

Chapter 3 - Modelling & Simulation Methods

3.1 Introduction to Modelling & Simulation

A model is a simplified representation used to understand the interaction of parts in a system. Since all models are simplifications of reality, there is always a trade off as to what level of detail should be included in the model. If too little detail is included in the model then relevant information or interactions may be missing and the resultant model does not fit reality. If too much detail is included in the model the model may become too complex, complicated and computationally intensive.

A simulation generally refers to a computerized version of the model, which is run over time to study the implications of the defined interactions. Simulations are generally iterative in there development. A model is developed, it is simulated, results obtained, the model is revised and the iterations continues until an adequate result is obtained.

From the literature review, Chapter 2, it was clear that models are essential in order to understand PEM fuel cells and PEM fuel cell systems. Modelling allows the researcher to delve deep into problem areas and solve many issues saving time, without the trouble of completing numerous tedious experiments. However, experimentation is an integral part of the simulation validation process that will be described in Chapter 4 and 5. The development of all the models used in this work as well as the simulation and experimental results are described in Chapter 5. The simulation and experimental results are discussed in Chapter 6.

Section 3.2 of this chapter introduces Computational Fluid Dynamic (CFD) modelling which was the main tool used to complete the modelling and simulation activities carried out in this thesis.

Section 3.3 of this chapter introduces three main modelling methods are used in this thesis:

> Section 3.3.1: 2-D & 3-D laminar flow single phase CFD
> Section 3.3.2: 2-D & 3-D laminar flow two phase (volume of fluid) CFD
> Section 3.3.3: 3-D PEM fuel cell electrochemistry

3.2 Computational Fluid Dynamics

Computational fluid dynamics (CFD) is a numerical code that contains equations within various models to describe various multi-physics phenomena. As the name suggests the software is mainly used to model fluid motion including gases and liquids, but it may also be used to model heat transfer, species transport, chemical reactions, multi phase flows, solidification and melting and various other multi-physical phenomena. These models may be coupled together in order to solve physical problems simultaneously. The simulation of many models has been completed during the course of this thesis and these are described in this chapter.

The main three benefits provided by the CFD analysis are insight, foresight and efficiency. CFD modelling provides an insight to how interactions, such as gas flow, can take place. The software enables for the virtual analysis of a design and therefore helps to view problems that may not be visible through other means. If the system has been modelled and somehow validated, an engineer can adapt the model geometry or boundary conditions to and improve or analyze a design or system and therefore many test variations can be used to obtain the best possible result. When the device or system being studied is difficult to build or analyze for economic, logistic, time or difficulties in making measurements. CFD allows engineers to model and often very accurately predict what occurs in the system or design. The insight and foresight that CFD offers can allow the engineer to design equipment or systems to be more efficient, ensure industrial compliance, and may increase the design cycle of products. The CFD analysis produces a better design quickly and also saves money.

As a summary CFD is a tool for compressing the design and development cycle of a product for future rapid prototyping. However, CFD is not only a useful tool for industry it may also be used by researchers in order to study various systems and indeed fundamental science questions. In this study CFD was used to model single and two phase fluid flow, mass transfer and the electrochemical reactions within a PEM fuel cell. For more information on CFD modelling with regards to PEM fuel cells the reader is pointed to [193].

3.2.1 The Navier-Strokes equations and CFD

The Navier-Stokes equations are named after L.M.H Navier (1778-1836) a French mathematician and an Irish-English scientist, G.G. Stokes (1819-1903). These equations are based upon equations for motion and mass conservation and can provide a complete mathematical description of the movement of incompressible Newtonian fluids. The beauty of the equations is that they have only four unknown terms u, v, w (which are the velocity components in the x, y and z directions) and ρ the density. The equations deal with the following key points.

- Conservation of mass.
- Conservation of linear momentum.

- Conservation of angular momentum.

- Symmetry of the stress tensor.

- Conservation of energy.

- Conservation of mechanical energy.

- Conservation of internal energy.

- Hydrostatic and viscous stress tensors.

The Navier-Stokes equations are nonlinear, second-order, partial differential equations and are generally quite complex. Exact mathematical solutions except in a very few instances are not one hundred percent possible. However in the cases where solutions have been obtained and compared experimental results the results have been in close agreement. The Navier-Stokes equations are quite complex and the reader is pointed to the following texts for more information [193].

3.2.2 Outline of the CFD simulating process

The CFD process for any model exercise is tedious and sometimes frustrating. For this reason this section will very briefly introduce the reader to the CFD process but focus more concisely on the skills that an operator should be aware of when using CFD software. Once the user is use to and has developed many models the modelling and simulation procedure becomes faster and basic information such as setup and procedure are trivial. However, to aid any future research this section may be invaluable.

3.2.2.1 The computer

An Intel Core 2 Quad CPU operating at 2.4GHz. with a windows XP operating system was utilized. Solid Works, Pro-Engineering, Ansys 12 Workbench, Mesh & Fluent software were all used in the model development and simulation process. Fluent software operated using serial processing on the local machine.

3.2.2.2 Generating geometry

The geometry of the model was created using a mixture of CAD programs (Ansys 12, Solid Works or Pro-Engineering) depending on the complexity of the geometry that was to be modelled. These 2-D and 3-D solid modellers allow intricate structures that were necessary for some of the models, to be created.

3.2.2.3 Meshing

The models were imported in to a modeller platform called Ansys Workbench where a work profile is created. A computational mesh is generated, which is downloaded into the CFD software and boundary conditions and appropriate models are applied to the problem.

The geometry is divided into small grids using the mesh tool embedded in the modeller platform. The grid designates the cells or elements on which the flow is solved. Care is taken while meshing since it can affect the results to a great extent. The effects that meshing has on the design include; rate of convergence (or even lack of convergence), solution accuracy and CPU time required. If the mesh meets an acceptable standard (i.e. skew, aspect ratio, volume change etc) it is then exported into the CFD analysis software.

A point to note is that there are several methods of discretization that may be applied to CFD modelling. These include the finite difference method, the finite volume method and the finite element method. The finite element method is often used in solid mechanics because of the considerable geometric flexibility that it allows and because general-purpose codes can be used for a wide variety of physical problems. The finite volume method (used in this study) however is used most often in CFD because it rigorously enforces conservation, it is flexible in terms of the geometry, the variety of physical phenomena it can handle and it is directly related to both the physical quantities such as mass flux. Figure 48 shows different stages within a finite volume method.

In the finite-volume method ...

(1) A flow geometry is defined.

(2) The flow domain is decomposed into a set of *control volumes* or *cells* called a *computational mesh* or *grid*.

(3) The *control-volume* equations are *discretised* – i.e. approximated in terms of values at *nodes* – to form a set of *algebraic* equations.

(4) The discretised equations are solved numerically.
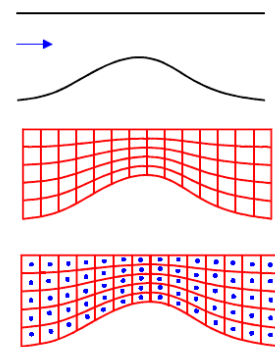
Figure 48 Illustration and commentary showing the different stages involved in the finite volume discretization method [113].

Fluid motion can be described by applying the fundamental laws of mechanics including the conservation of mass and momentum equations to the motion of a fluid. Coupled governing equations are used within a discrete gridded domain to solve a continuous problem as shown below in Figure 49. If it is taken, for example, that between X=0 and X=1 is a space that contains physical property such as pressure, velocity, temperature etc. in a continuous domain. If pressure is taken as an example the domain could be described as:

$$p = p(x), \ 0 < x < 1$$

<div align="right">*Eqn. (3.2.1)*</div>

Correspondingly in a discreet domain the pressure would be defined at each grid point thus:

$$p = p(x_i), \ i = x_1, x_2....N$$

<div align="right">*Eqn. (3.2.2)*</div>
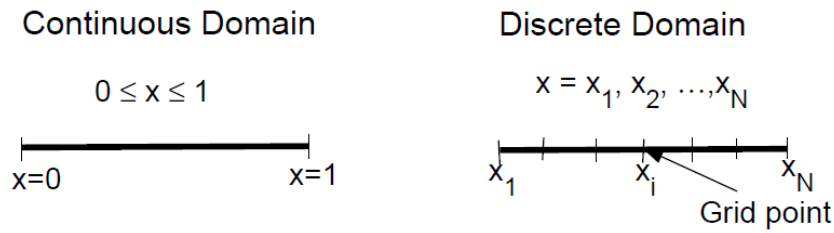
Figure 49: A 1-D example showing the concept of a gridded domain [114].

Ansys 12 Mesh software was used to mesh the models. A mixture of mesh types was used, quadrilateral, hexahedral and tetrahedral, depending on the complexity of the geometry. Each model had between 100,000 and 500,000 discrete cells.

3.2.2.4 Simulation

These meshed models are then exported in to a commercial software Fluent to complete the CFD analysis. The commercial Fluent licence of Dublin City University has a limitation of 512,000 cells allowed per model and because of this limitation all models had to have less than this amount of cells. This limitation made the overall task of meshing very difficult. The model size and complexity had to be reduced to the minimum acceptable level to accommodate this limitation.

The fundamental elements of the CFD simulation are:

- The model is discretized where variables such as density pressure and velocity are approximated by their values as a finite number of nodes within the modelled zone.
- The equations of motion are discretized where the continuous control volume or differential equations are converted to discrete algebraic equations.
- The resulting system of algebraic equations are solved in order to give values at the nodes within the model.

The double-precision version of Fluent is used. This solver type enables more accurate calculations of node coordinates when the geometry has features of very disparate length scales, the geometry has multiple enclosures via small diameter connections or where there may be high aspect ratio grids. The model scale and then the input parameters are specified. The input parameters include the solver model, operating conditions, material used, boundary conditions and residuals that provide convergence checking. When all inputs have been specified, the iterations are set and the solver is left to run. Models took between 30 minutes to 15 hours to complete each simulation, depending on the modelling method used. Several key phenomena were monitored and checks were made to ensure the changes per iteration were not too large. Flux reports were also analysed; the sum of the flux at the inlet should closely match the flux at the outlet. If the model did not converge, iterations are updated or inputs restructured depending on the fault. When convergence occurs, the post-processing stage is

initiated. The post-processing involves analysing the results obtained (i.e. pressure distribution, velocity, temperature, turbulence, etc). The flowchart of the algorithm is shown in Figure 50.
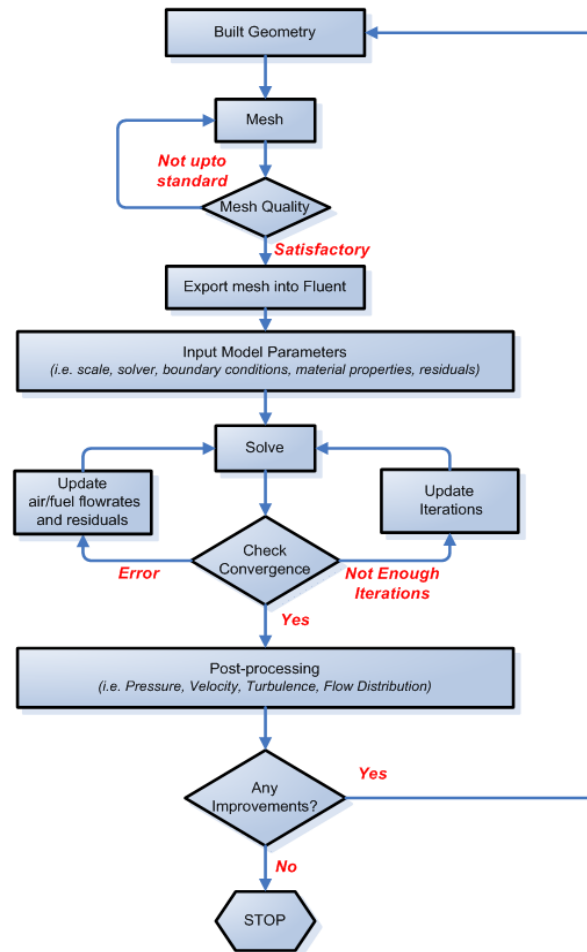
Figure 50 Flow chart highlighting all the main steps of the CFD modelling.

3.2.2.5 Post-processing

Reports provided by the CFD software in the form of contour plots, vector plots and flux reports are used to analyse if the solution is correct or not. Often the CFD software results are loaded into a separate post-processing program that allows more advanced post-processing techniques to be applied to the results, thus allowing better visualization or analysis not provided by the CFD software.

3.2.2.6 Model validation

Only a basic knowledge of the working equations in CFD software may be useful for engineers using CFD software. It would be more important for developers of the code for researchers involved in the fundamental researching of fluid flow and fluid properties to have a much more detailed understanding. Having said this it is commonly said in the CFD field that without validation of CFD models, instead of having "Computational Fluid Dynamic" results the engineer or operator may just have "Colourful Fluid Dynamic" results [193]. Without a skilled user who can make concise educated

guesses and apply learned reasoning to any set of CFD results the results may be wrong and indeed unphysical.

Modelling is only as good as compared to what it can be verified against. Simulation results were verified against different models, experiments and results from literature. Pressure drop experiments, polarisation curves and visualisation techniques were all used to assist in validation and analysis of simulation results in this study. Model development, simulation results and analysis is detailed in Chapter 5. A complete discussion of all the results is presented in Chapter 6.

3.2.2.7 Mesh comparison / grid independence

To check for grid independence each grid was adapted with about twice and then with about half the number of elements. This mesh comparison analysis was undertaken to determine the best mesh to use for the 2-D & 3-D models. As mentioned in Section 3.2.2.3 a mixture of mesh types were used depending on the model. Figure 51 (a) is a mapped quadrilateral (quad) mesh with a low node density and Figure 51 (b) is a paved triangular mesh with a high node density. The parameters compared can be outlet velocity, convergence rate, outlet pressure, equi-angle skewness and the aspect ratio. Velocity and pressure at the outlet were mainly used in this study as these are paramount factors in the analysis. In the following sections grid independence is shown where it is deemed necessary.

(a)   (b)
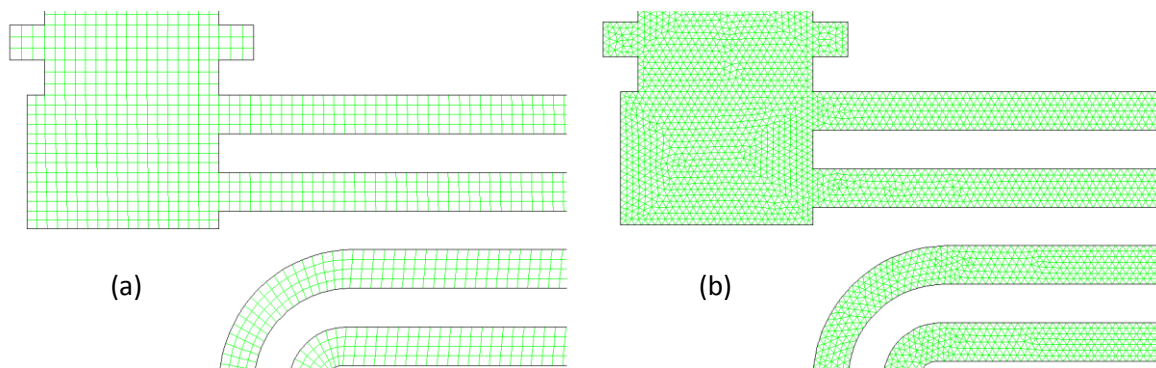
Figure 51(a) Quadrilateral mesh (b) Tetrahedral mesh.

3.3 Modelling & Simulation of PEM Fuel Cells

PEM fuel cells operate in a fluid / electrochemical environment and to understand various process and design better fuel cells it is necessary to complete fluid based studies and electrochemical simulations. CFD modelling (using Fluent software) was the main tool used to complete the modelling and simulation. Within Fluent three main modelling methods are used in this thesis:

- 2-D & 3-D laminar flow single phase CFD
- 2-D & 3-D laminar flow two phase (volume of fluid) CFD
- 3-D PEM fuel cell electrochemistry

These correspond to four main models used and or developed in this thesis:

- 2-D & 3-D modelling of single phase flow in flow plate flow field designs. Flow field designs are taken or modified from literature and others are developed in this thesis. Information on the flow pattern and pressure can be predicted using the CFD software. This aids in geometric design of flow plates and flow fields and their suitability for a PEM fuel cell. Section 3.3.1 of this chapter introduces the single phase fluid flow CFD and the design and development of these models is described in Chapter 5, Section 5.2.1.

- 3-D modelling of the new open pore foam material as a flow plate material. A representative cell structure of open pore cellular foam material is developed and the model is built because this relatively new material has not been characterised satisfactorily in literature. This model investigates information on the flow pattern and pressure analysis through seven different types of open pore cellular foam using CFD software. Section 3.3.1 of this chapter introduces the single phase fluid flow CFD and the design and development of these models is described in Chapter 5, Section 5.2.3.

- 2-D & 3-D modelling of two phase flow within channels and bends of flow fields to understand water mitigation and flooding in conventional flow fields. Information on water transport, droplet movement, accumulation and water flooding in channels and bends under different operating conditions can be observed and this can aid in the design of PEM fuel cell components that mitigate water flooding. Section 3.3.2 of this chapter introduces the two phase fluid flow CFD and the design and development of these models is described in Chapter 5, Section 5.2.2.

- 3-D modelling of the electrochemistry within the PEM fuel cell using conventional and new flow plate designs. This model takes into account all aspects of an operational PEM fuel cell. It uses many variables and parameters to accomplish its objective to verify if the designs and models discussed earlier are valid and whether they can improve the performance of a PEM fuel cell. Section 3.3.3 of this chapter introduces the electrochemistry CFD and the design and development of these models is described in Chapter 5, Section 5.2.4.

3.3.1 Single phase fluid flow in flow plates & new open pore foam material

PEM fuel cells operate in the laminar flow region due to the slow flow rates of oxygen/air and hydrogen, necessary for the electrochemical reaction, as described in Chapter 2, Section 2.2. The flow of air/oxygen or hydrogen and pressure distribution over the GDL should be evenly spread and pressure from inlet to outlet minimised.

The main focus of the single phase CFD modelling is to assist in the optimisation of the flow plate and flow field design. Optimisation is carried out through the analysis of velocity, flow regimes and

pressure distribution through the PEM fuel cell flow plate. From the analysis of the model a number of conclusions can be drawn, including;

- Velocity & pressure distribution through the flow plates.

- Pressure drop from inlet to outlet.

- Prediction of the flow of the fluid through the flow field of various flow plate designs.

- Areas inside flow plates prone to possible water blockages can be identified and redesigns completed to reduce these possible blockages.

- Dead zones (eddy currents or recirculation zones, related to the utilisation of the GDL by the fluid.) can be identified and redesigns completed to reduce these issues.

- Geometric anomalies may be identified that hinder fluid flow.

- Various complicated geometric designs may be tested to see if they aid fluid flow.

- Model development from idea to result is very fast (as short as days, depending on the complexity).

Single phase flow is very suitable to view these phenomena. The most suitable flow plate designs that give the best results after the modelling process is complete can be manufactured. The predictions, conclusions and results obtained from the model simulations can be validated from literature and by experiment. The development of flow plate, flow field and open pore cellular flow plate designs and all modelling and experimental results are detailed in Chapter 5. A complete discussion of all the results is presented in Chapter 6.

3.3.2 Two phase fluid flow in flow field channels
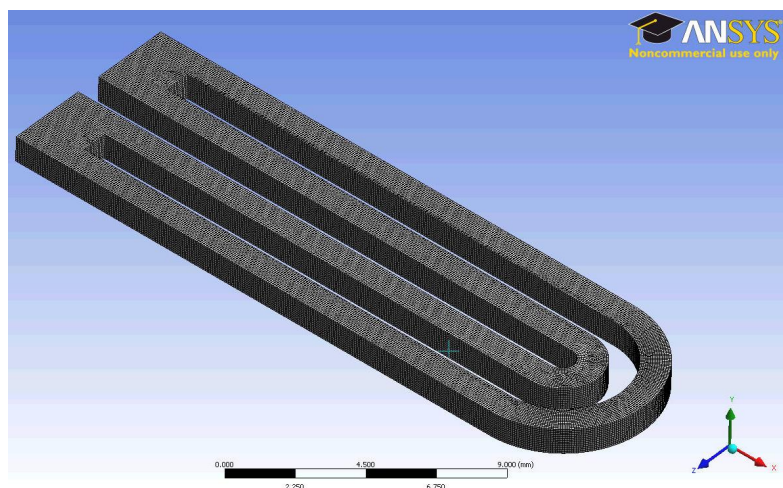
Figure 52 3-D model with a double serpentine layout.

Because of the complexity of the model and significant computational efforts involved, the numerical calculations, for two phase flow in mini channels, were performed using commercial CFD software, Fluent. Figure 52 shows the PEM fuel cell flow plate channel structure of one of the 3-D models used in the study. In Fluent, three different Euler-Euler multiphase models are available: the Volume of

Fluid (VOF) model, the mixture model, and the Eulerian model. From determining the flow regime that best represents the multiphase system being investigated, the appropriate model is selected. VOF is one of the well examined and established interface tracking algorithms and successfully handles the problems with the surface topological changes like separation or unification of several parts of the surface. Table 9 shows the limitations of using VOF method and their affect on the models in this study.

VOF method was applied for the simulations of fluid motion in mini channels without heat transfer in this study. Using CFD modelling techniques a two phase flow model is developed and investigated under a number of probable scenarios, including accumulation of droplets and slugs (elongated water droplets) in the mini channels. In addition with the aid of imaging techniques, visualisation of the water is recorded in a simulated PEM fuel cell to ensure a correct model and results are compared.

Table 9 Limitations of the VOF model.

VOF Limitation Description	Affect on Model
You must use the pressure-based solver. The VOF model is not available with either of the density-based solvers.	This does not affect the investigated problem.
All control volumes must be filled with either a single fluid phase or a combination of phases. The VOF model does not allow for void regions where no fluid of any type is present.	All control volumes are filled with air and water slugs or droplets
Only one of the phases can be defined as a compressible ideal gas. There is no limitation on using compressible liquids using user-defined functions.	Compression is not an issue.
Stream-wise periodic flow (either specified mass flow rate or specified pressure drop) cannot be modelled when the VOF model is used.	This does not affect the investigated problem.
The second-order implicit time-stepping formulation cannot be used with the VOF explicit scheme.	This does not affect the investigated problem.
When tracking particles in parallel, the DPM model cannot be used with the VOF model if the shared memory option is enabled.	This does not affect the investigated problem.
A drawback of VOF methods is the so-called artificial (or numerical) coalescence of gas bubbles which occurs when their mutual distances is less than the size of the computational cell [130].	Models have a fine mesh.
Momentum Equation: One limitation of the shared velocity field's approximation is that in cases where large velocity differences exist between the phases, the accuracy of the velocities computed near the interface can be adversely affected.	Fluids are travelling at relatively close velocities in the investigated problem.
Energy Equation: the accuracy of the temperature near the interface is limited in cases where large temperature differences exist between the phases.	Temperatures are relatively close in the investigated problem.

3.3.2.1 Volume of fluid method

The VOF model is a surface-tracking technique applied to a fixed Eulerian mesh. It is designed for two or more immiscible fluids where the position of the interface between the fluids is of interest. In the VOF model, a single set of momentum equations is shared by the fluids, and the volume fraction

of each of the fluids in each computational cell is tracked throughout the domain. Applications of the VOF model include stratified flows, free-surface flows, slug flows, filling, sloshing, the motion of large bubbles in a liquid, the motion of liquid after a dam break, the prediction of jet breakup (surface tension), and the steady or transient tracking of any liquid-gas interface [193].

The VOF formulation relies on the fact that two or more fluids (or phases) are not interpenetrating. For each additional phase that is added to the model, a variable, the volume fraction of the phase in the computational cell, is introduced. In each control volume, the volume fractions of all phases sum to unity. The fields for all variables and properties are shared by the phases and represent volume-averaged values, as long as the volume fraction of each of the phases is known at each location. Thus the variables and properties in any given cell are either purely representative of one of the phases, or representative of a mixture of the phases, depending upon the volume fraction values.

3.3.2.1.1 VOF equations

The tracking of the interface(s) between the phases is accomplished by the solution of a continuity equation for the volume fraction of one (or more) of the phases. For the qth phase, this equation has the following form:

$$\frac{1}{\rho_q} \left[\frac{\partial}{\partial t}(\alpha_q \rho_q) + \nabla \cdot (\alpha_q \rho_q \vec{v}_q) = S_{\alpha_q} + \sum_{p=1}^{n}(\dot{m}_{pq} - \dot{m}_{qp}) \right]$$

Eqn. (3.3.1)

where $\dot{m}_{qp}$ is the mass transfer from phase q to phase p and $\dot{m}_{pq}$ is the mass transfer from phase p to phase q. The volume fraction equation will not be solved for the primary phase; the primary-phase volume fraction will be computed based on the following constraint:

$$^n\Sigma_{q=1}\, \alpha_q = 1$$

Eqn. (3.3.2)

Roughly two important classes of VOF methods can be distinguished with respect to the representation of the interface, namely Simple Line Interface Calculation (SLIC) and Piecewise Linear Interface Calculation (PLIC). The accuracy and capabilities of the modern PLIC VOF algorithms greatly exceeds that of the older VOF algorithms [130].

The VOF model can include the effects of surface tension along the interface between each pair of phases. The model can be augmented by the additional specification of the contact angles between the phases and the walls. This can be completed by specifying a surface tension coefficient as a constant, as a function of temperature, or through a User Defined Function (UDF). The solver will include the additional tangential stress terms (causing what is termed as Marangoni convection) that arise due to the variation in surface tension coefficient, but variable surface tension coefficient effects are usually important only in zero/near-zero gravity conditions.

Surface tension effects near the curved meniscus of a discrete drop, results in a pressure jump across the liquid and gas phases. This jump is given by the Young-Laplace equation:

$$P_g - P_l = G \sigma cos\Theta / d \qquad\qquad Eqn. (3.3.3)$$

where P_g and P_l represent the pressure on the gas and liquid side, respectively; σ is the surface tension; Θ is the contact angle; and d is the height of the channel. The factor G is a geometrical constant of the channel. For parallel plate channels $G = 2$. The pressure drop depends upon the surface tension coefficient, σ, but also the surface curvature as measured by two radii in orthogonal directions, R_1 and R_2:

$$P_2 - P_1 = \sigma(1/R_1 + 1/R_2) \qquad\qquad Eqn. (3.3.4)$$

where P_1 and P_2 are the pressures in the two fluids on either side of the interface. The importance of surface tension effects is determined based on the value of two dimensionless quantities; the Reynolds number, Re, and the capillary number, Ca; or the Reynolds number, Re, and the Weber number, We. For Re << 1, the quantity of interest is the capillary number:

$$Ca = \mu U / \sigma \qquad\qquad Eqn. (3.3.5)$$

and for Re >>1, the quantity of interest is the Weber number:

$$We = gLU^2 / \sigma \qquad\qquad Eqn. (3.3.6)$$

where U is the free-stream velocity. Surface tension effects can be neglected if Ca >>1 or We >> 1. For this study, the Reynolds number Re is small, thus capillary effects are of greater importance. Rather than impose this boundary condition at the wall itself, the contact angle that the fluid is assumed to make with the wall is used to adjust the surface normal in cells near the wall. This so-called dynamic boundary condition results in the adjustment of the curvature of the surface near the wall. If Θ_w is the contact angle at the wall, then the surface normal at the live cell next to the wall is:

$$\hat{n} = \hat{n}_w cos\Theta_w + \hat{t}_w sin\Theta_w \qquad\qquad Eqn. (3.3.7)$$

where $\hat{n}_w$ and $\hat{t}_w$ are the unit vectors normal and tangential to the wall, respectively. The contact angle Θ_w is the angle between the wall and the tangent to the interface at the wall, measured inside the phase. If setting the contact angle between the oil and air phases as shown in Figure 53, Θ_w is measured inside the oil phase.
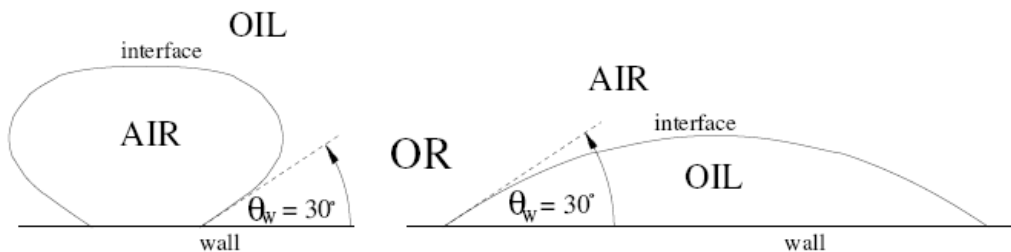
Figure 53 Wall adhesion of oil & air [193]**.**

The shapes and rise velocities of bubbles in quiescent viscous liquids can be related by the dimensionless Morton (M), Eotvos (Eo) and Reynolds (Re) numbers [194] where:

$$M = \frac{g \mu_l^4 \Delta \rho}{\rho_l^2 \sigma^3}$$

Eqn. (3.3.8)

$$Eo = \frac{g \Delta \rho d_e^2}{\sigma}$$

Eqn. (3.3.9)

$$Re = \frac{\rho_l v_\infty d_b}{\mu_l}$$

Eqn. (3.3.10)

where the effective diameter d_e is defined as the diameter of a spherical bubble with the same volume as the bubble [130]

3.3.2.1.2 VOF discretization

The volume fraction equation may be solved either through implicit or explicit time discretization as described above. Explicit scheme has been chosen for this model, specifically geometric reconstruction (piecewise-linear) scheme, Figure 54. This scheme requires the volume fraction values at the previous step, rather than at the current time step as for the implicit scheme.
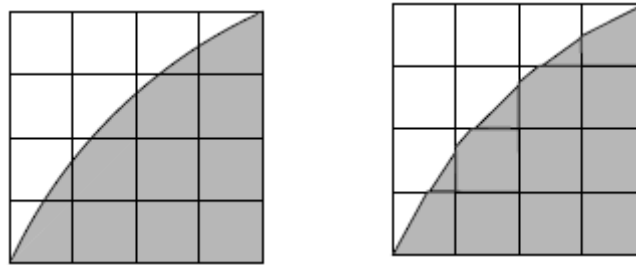
Figure 54 Discretization (a) Actual Interface (b) Interface shape represented by the geometric reconstruction (piecewise-linear) scheme.

3.3.2.1.3 VOF time step

The calculation of the time step, Δt, can be completed by estimating the maximum possible velocity of the interface and the grid cell dimension, Δx_{cell}. As shown below:

$$\Delta t = \Delta x_{cell} / v$$

Eqn. (3.3.11)

where v is the velocity of the fluid flow. A lower time step can be chosen from the calculated time step as this would provide more accurate results, but a higher time step may cause divergence of the model. A Time step of $5e^{-6}$ seconds was selected for this study as this ensured the simulation converged and effective data could be obtained in a reasonable time period.

3.3.2.2 Flow channel CFD model assumptions

A real flow field within a PEM fuel cell may have an intricate geometric structure. In addition, the attached GDL may feature both micro- and macro-pores as well as a distribution of pore sizes. Also, the liquid water distribution and the effective surface tension of the gas / liquid interface within the flow plate may depend on the hydrophobic or hydrophilic nature of the flow plate material. This makes the two phase flow and distribution of water and air species through mini channels complex. It is therefore necessary to simplify the model using certain assumptions that are commonly made in literature: [73] [149]

- The fluid flow in the channel is laminar due to the low velocities and the small size of the micro channels.
- The cell temperature remains constant.
- The gas phase is an ideal mixture.

3.3.3 3-D Electrochemistry Modelling of the PEM Fuel Cell

3-D electrochemistry aims to gain a more detailed understanding, prediction, control and optimisation of the transport effects, liquid formation and electrochemical activities in PEM fuel cells. It is interesting to understand the basic electrochemical equations that the software uses in its approach to PEM fuel cell analysis and voltage and current results. This information will also be useful for others who will continue with future PEM fuel cell modelling.

Electrochemistry of a fuel cell involves the chemical reactions within the fuel cell. The purpose of the 3-D model is to gain understand of electrochemical reactions occurring within the cell and from this understanding determine the optimal operating conditions using polarisation curves. It also allows geometric flexibility meaning that as long as the model is set up in the correct way almost every type of geometry can be solved for. The computational models will also be validated by making a comparison to the experimental data (polarisation curves obtained experimentally).

3.3.3.1 Fuel cell theory and the fluent fuel cell module

The PEM fuel cell module is provided as an add-on module with the standard Fluent licensed software for the modelling of PEM fuel cells. The PEM fuel cell module is an extra set of equations, to the normal CFD equations, that have been defined by Fluent Inc., for the modelling of PEM Fuel cells. The Fluent PEM fuel cell model is comprised of several UDFs and a Graphical User Interface (GUI). The electrochemical reactions occurring on the catalyst are modelled through various source terms while other model parameters are handled through the user interface.
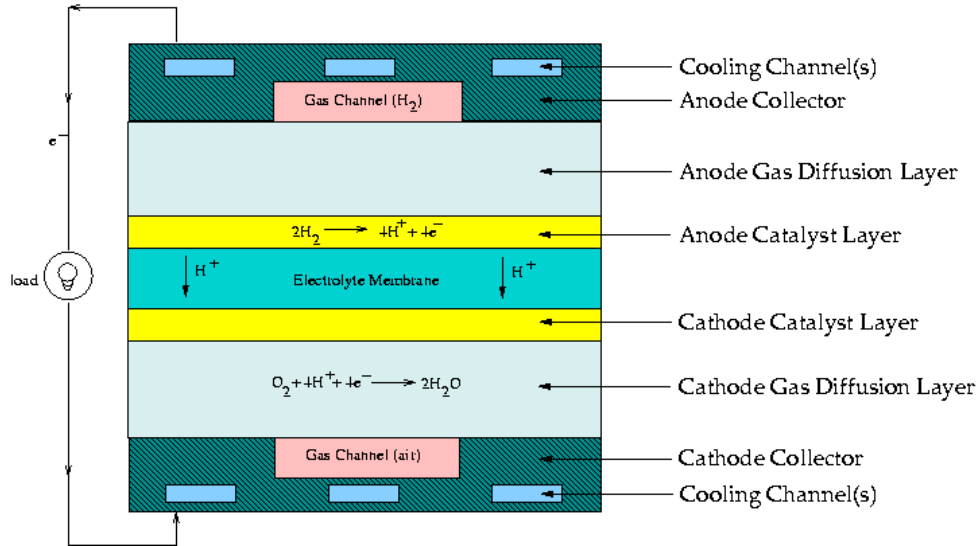
Figure 55 General PEM fuel cell model.

In the PEM fuel cell model, as shown in Figure 55, two electric potential fields are solved. One potential is solved in the membrane and catalyst layers. The other is solved in the catalyst layers, the diffusion layers and the current collectors. Surface reactions on the porous catalyst region are solved and the reaction diffusion balance is applied to compute the rates. Based on the cell voltage that the user defines, the current density value is computed. Alternatively, a cell voltage can be computed based on a user defined average current density. The liquid water saturation, s, and the water content, λ, are also solved as user-defined scalars.

3.3.3.1.1 PEM fuel cell potential

At the centre of the electrochemistry is the computation of the rate of the hydrogen oxidation and the rate of oxygen reduction. These electrochemical processes are treated as heterogeneous reactions that take place on the catalyst surfaces inside the two catalyst layers on both sides of the membrane. The driving force behind these reactions is the surface over-potential, the difference between the phase potential of the solid and the phase potential of the electrolyte/membrane. Two potential equations are first solved for in the PEM model:

$$\Delta(\sigma_{sol}\,\phi_{sol}) + R_{sol} = 0 \qquad\qquad Eqn.\ (3.3.12)$$

accounts for the electron transport e^- through the solid conductive materials and:

$$\Delta(\sigma_{mem}\,\phi_{mem}) + R_{mem} = 0 \qquad\qquad Eqn.\ (3.3.13)$$

represents the protonic transport of H^+ where σ is the electrical conductivity (1/ohm-m), ϕ is the electric potential (volts) and R is the volumetric transfer current (A/m^3). External boundary conditions must be added to the model to solve for ϕ_{sol} and ϕ_{mem}. There are two types of external boundaries; those which pass an electrical current and those that do not. No protonic current leaves the PEM fuel cell through any external boundary, and therefore there is a zero flux boundary condition for the membrane phase potential, ϕ_{mem}, on all outside boundaries. For the solid phase potential, ϕ_{sol}, there

are external boundaries on the anode and the cathode side that are in contact with the external electric circuit. Only through these boundaries does electrical current generated in the fuel cell pass. On all other external boundaries there is a zero flux boundary condition for ϕ_{sol}. Fixed values for ϕ_{sol} (potentiostatic boundary conditions) are used. If the anode side is set to zero, the (positive) value prescribed on the cathode side is the cell voltage.

The source terms in Equations 3.3.12 and 3.3.13 are also called the exchange current density (A/m^3), and have the following general definitions:

$$R_{an} = j_{refan} \, ([H_2]/ \, ([H_2]_{ref})^{\gamma an} \, (e^{\,\alpha an F \eta an/RT} - e^{\,-\alpha cat F \eta an/RT}) \qquad \textit{Eqn. (3.3.14)}$$

$$R_{cat} = j_{refcat} \, ([O_2]/ \, ([O_2]_{ref})^{\gamma cat} \, (-e^{\,+\alpha an F \eta cat/RT} + e^{\,-\alpha cat F \eta cat/RT}) \qquad \textit{Eqn. (3.3.15)}$$

where j^{ref} is the volumetric reference exchange current density (A/m^3), [O2] & [H2] are the local species concentration, reference value ($kgmol/m^3$), γ is the concentration dependence, α is the transfer coefficient and F is the Faraday constant. The above equation is the general formulation of the Butler-Volmer function. A simplification to this is the Tafel formulation that reads:

$$R_{an} = j_{refan} \, ([H_2]/ \, ([H_2]_{ref})^{\gamma an} \, (e^{\,\alpha an F \eta an/RT}) \qquad \textit{Eqn. (3.3.16)}$$

$$R_{cat} = j_{refcat} \, ([O_2]/ \, ([O_2]_{ref})^{\gamma cat} \, (e^{\,-\alpha cat F \eta cat/RT}) \qquad \textit{Eqn. (3.3.17)}$$

By default, the Butler-Volmer function is used in the Fluent PEM fuel cell model to compute the transfer currents inside the catalyst layers. The driving force for the kinetics is the local surface over-potential, η, also known as the activation loss. It is generally the difference between the solid and membrane potentials, ϕ_{sol} and ϕ_{mem}. The gain in electrical potential from crossing from the anode to the cathode side can then be taken into account by subtracting the open-circuit voltage V_{oc} on the cathode side:

$$\eta_{an} = \sigma_{sol} - \phi_{mem} \qquad \textit{Eqn. (3.3.18)}$$

$$\eta_{cat} = \sigma_{sol} - \phi_{mem} - V_{oc} \qquad \textit{Eqn. (3.3.19)}$$

From these equations the two potential fields can be obtained. For a full review of these equations the reader is referred to [193].

3.3.3.1.2 Current and mass conservation

The following reactions occur, respectively, at the anode and the cathode:

$$H_2 = 2H^+ + 2e^- \qquad \textit{Eqn. (3.3.20)}$$

$$O_2 + 4H^+ + 4e^- = 2H_2O \qquad \textit{Eqn. (3.3.21)}$$

The electrochemical reactions that take place inside the catalyst layers are considered heterogeneous reactions and take place on the catalyst surfaces in the porous media. The volumetric source terms for the species equations (kg/m^3-s) and energy equation (W/m^3) are given as:

$$SH_2 = (-M_{w,}H_2/2F)R_{an} \qquad\qquad Eqn.\ (3.3.22)$$

$$SO_2 = (-M_{w,}O_2/4F)R_{cat} \qquad\qquad Eqn.\ (3.3.23)$$

$$SH_2O = (M_{w,}H_2O/2F)R_{cat} \qquad\qquad Eqn.\ (3.3.24)$$

Additional volumetric sources to the energy equation implemented in the Fluent PEM model include ohmic heating, heat of formation of water, electric work and latent heat of water.

$$S_h = I^2R_{ohm} + h_{reaction} + \eta R_{an,cat} + h_{phase} \qquad\qquad Eqn.\ (3.3.25)$$

The species concentrations of hydrogen and oxygen in the rate calculation are the surface values. The reactions are treated as surface reactions in the two catalyst layers, and it is assumed that the diffusive flux of any reacting species is balanced by its rate of production.

$$\rho D_i/\ \delta(y_{i,surf} - y_{i,cent})r = M_{w,i}/\eta F)\ R_{an,cat} \qquad\qquad Eqn.\ (3.3.26)$$

where D_i is the mass diffusivity of species i (m^2/s), r is the specific reacting surface area of the catalyst layer or surface-to-volume ratio (1/m), $y_{i,surf}$ is the mass fraction of species *i* at the reacting surface, $y_{i,cent}$ is the mass fraction of species *i* at the cell centre, $\delta = 1/r$ is the average distance between the reaction surfaces and the cell centre (m). The left hand side of this equation represents the diffusive flux at the reacting surface and the right hand side represents the rate of mass generation. This equation can be used to obtain the surface values of H_2 and O_2 concentrations, applying a Newtonian solution procedure. These surface, or wall, values are then used to compute the rates in Equation 3.3.22 through to Equation 3.3.24. For a full review of these equations the reader is referred to [193].

3.3.3.1.3 Liquid water formation, transport & effects

PEM fuel cells operate less than one hundred degrees Celsius and water vapour may condense to liquid water, especially at high current densities, as mentioned in Chapter 2, Section 2. To model the formation and transport of liquid water, including various physical processes such as condensation, vaporization, capillary diffusion, and surface tension, Fluent PEM model uses a saturation model. In this approach, the liquid water formation and transport is governed by a conservation equation for the volume fraction of liquid water, s, or the water saturation:

$$\frac{\partial(\epsilon\rho_l s)}{\partial t} + \nabla \cdot \left(\rho_l \vec{V}_l s\right) = r_w \qquad\qquad Eqn.\ (3.3.27)$$

where r_w is the condensation rate.

The electrolyte membrane of the fuel cell is modelled as a porous fluid zone. Properties such as membrane phase electrical conductivity, osmotic drag coefficient, back diffusion flux and membrane water diffusivity are evaluated as functions of the water content, λ.

$$\lambda = 14 + 1.4\ (\alpha - 1)\ (\alpha > 1) \qquad\qquad Eqn.\ (3.3.28)$$

where α is the water activity that is calculated from the water vapour pressure and saturation pressure of water. For a full review of these equations the reader id referred to [193].

3.3.3.1.4 Accounting for advection and diffusion in the PEM fuel cell.

It is important to also have a basic understanding of species transport and how CFD accounts and calculates specie concentrations. A basic concept for the movement of species is that a specie within a gas volume will tend to spread evenly within the gas. When a higher quantity of a specie is located in one part of the volume than another, a potential is generated measured by the partial pressure of the specie. This potential drives some of the specie at the higher concentration into the zone where the species is at a lower concentration. This is referred to as pure diffusion mass transfer. In reality this may also occur in a fluid in motion and then the diffusion potential must be combined with the forces causing the fluid to move which will aid or hinder the diffusion of the species and this is referred to as advection. A similar equation to 3-2-32 may be derived for any physical quantity that is advected or diffused by a fluid flow. For each such quantity an equation is solved for the concentration (i.e. amount per unit mass), for example, the concentration of salt, sediment or chemical constituent. Diffusion occurs when concentration varies with position. It typically involves transport from regions of high concentration to regions of low concentration, at a rate proportional to area and concentration gradient. For many scalars it may be quantified by Fick's diffusion law [113] as seen below:

$$rate\ of\ diffusion = -\ diffusivity\ x\ gradient\ x\ area \qquad Eqn.\ (3.3.29)$$

or

$$rate\ of\ diffusion = -\Gamma \times \frac{\partial \phi}{\partial n} \times A$$
$$Eqn.\ (3.3.30)$$

Equation 3.3.30 is often referred to as gradient diffusion. A common example is heat conduction or in the case of fuel cells partial pressure gradients in the oxidant and fuel channels. For an arbitrary control volume the mass of specie inside a PEM fuel cell can be described as the mass inside the cell multiplied by the concentration inside:

$$Amount\ in\ cell = \rho\ x\ V\ x\ \phi \qquad Eqn.\ (3.3.31)$$

The advective flux of a specie inside a PEM fuel cell can be described by multiplying the mass flux by the concentration of the specie:

$$Advective\ flux = C\ x\ \phi \qquad Eqn.\ (3.3.32)$$

The diffusive flux of a specie inside a PEM fuel cell can be described by the diffusivity of the specie in the mixture times the gradient of the concentration of the specie within the mixture multiplied by an area as seen in Equation 3.3.33:

$$Diffusive\ flux = -\Gamma \times \frac{\partial \phi}{\partial n} \times A \qquad Eqn.\ (3.3.33)$$

The quantity of a species produced or removed in a PEM fuel cell can be determined by multiplying the source/sink density by the volume as seen in Equation 3.3.34:

$$Source = S \times V \!\!\!\!/ \qquad\qquad Eqn. \ (3.3.34)$$

Balancing the rate of change against the net flux through the boundary and rate of production yields the scalar-transport or (advection-diffusion). Please refer [193] for further information.

3.3.3.1.5 Porous jump boundary conditions

Porous jump conditions are used to model a thin "membrane" that has known velocity (pressure-drop) characteristics. It is essentially a 1-D simplification of the porous media model available for cell zones. Examples of uses for the porous jump condition include modelling pressure drops through screens and filters and modelling radiators when you are not concerned with heat transfer. This simpler model is whenever possible, instead of the full porous media model, because it is more robust and yields better convergence. The thin porous medium has a finite thickness over which the pressure change is defined as a combination of Darcy's Law and an additional inertial loss term:

$$\Delta p = -(\mu/\alpha \ v + 0.5C_2 \rho v^2)\Delta m \qquad\qquad Eqn. \ (3.3.35)$$

where μ is the laminar fluid viscosity, α is the permeability of the medium, C_2 is the pressure-jump coefficient, v is the velocity normal to the porous face, and Δm is the thickness of the medium. Appropriate values for α and C_2 can be calculated using the techniques described in [193].

The design and development of the models that use these CFD methods is described in Chapter 5.

BLANK PAGE

4

Chapter 4 - Experimental Apparatus

4.1 Introduction to Experiments

Before any practical experiments could be conducted, a laboratory to test PEM fuel cells had to be designed, suitable equipment purchased and the system setup. In addition a hydrogen gas source had to be obtained. Also, during the course of this work, the evolution process of the PEM fuel cell investigations changed and the experimental setup was modified to suit these advances.

The following Section 4.1.1 briefly describes the final laboratory setup and some safety measures taken while using hydrogen gas in the experiments.

Section 4.1.2 describes the experimental setup and experimenting procedures for standard flow plate and porous media flow plate testing, since both use similar testing system and procedures.

Section 4.1.3 describes the visualisation experimental setup.

4.1.1 Laboratory Setup to Test PEM Fuel Cells

The test equipment used to test the PEM fuel cell, comprised of pressure gauges, gas humidifying chambers, hydrogen input, air input, flow meters, multi-meters, a resistive load and a desk top computer with a Data Acquisition (DAQ) system using lab view and National Instruments instrumentation.
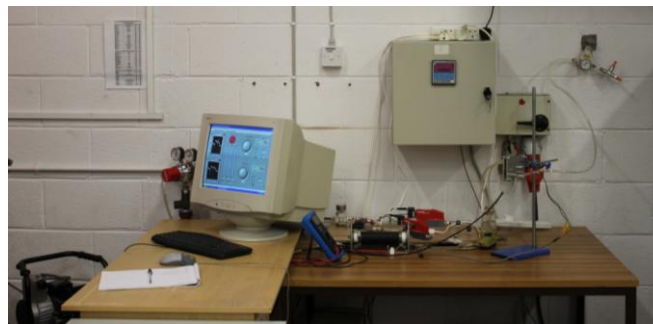
Figure 56 Fuel cell laboratory.

The PEM fuel cell testing system is capable of monitoring and regulating the oxidant (air) and fuel reactant (hydrogen) streams into and out of the fuel cell, as well as providing constant data to the DAQ device for later compilation.

4.1.1.1 System layout

The fuel cell can be split into two parts the inputs and the output. The inputs are fuel (hydrogen) and oxidant (air) gases, the outputs are the unused fuel and the electric power.

Figure 57 Hydrogen gas bottle (Supplied by BOC Ireland).

The reactant gas, hydrogen, is stored in a compressed cylinder, see Figure 57, as this was the safest easiest and cheapest method to store the correct amount and correct grade of hydrogen for PEM fuel cell testing. The hydrogen bottle was purchased from BOC Gas in North Dublin. The hydrogen costs about €25 per 1 m^3 or per a small bottle fill and there is rent paid on the bottle per month of about €15. Since the PEM fuel cell only uses small quantities of hydrogen per test (millilitres), a small portable bottle suited very well.

Figure 58 Hydrogen regulator.

A specialised hydrogen regulator (BOC series 8500 hydrogen pressure regulator), see Figure 58, was purchased for safe and easy use of the hydrogen gas. The regulator is attached to the gas bottle by a left hand threaded nut and it was tightened securely. The gas is turned on by using the specialised tool and tuning a square bolt anti clockwise on the top of the gas bottle. Gas enters the right hand gauge

and the bottle pressure is displayed, a pressure between 100 and 150 bar is displayed when the bottle is full. The large red knob is then rotated clockwise to start the flow of gas through the hydrogen lines and to control the hydrogen line pressure. A line pressure of about 200000 Pa is used, which is displayed in the left hand gauge. The pressure regulator was necessary to test different pressures in the PEM fuel cell and to avoid pressures greater than 300000 Pa that could damage the PEM fuel cell.

Figure 59 Hydrogen & Oxygen/Air flow meters/controllers.

To successfully and correctly measure all the information from the PEM fuel cell, it was important to measure the flow of hydrogen flowing in to the fuel cell accurately. Accurate measurement devices, volumetric flow meters/controllers (Voegtlin red-y series flow controller), Figure 59, had to be installed at this point so that the correct information could be collected. Each hydrogen rated and air rated flow controller was calibrated for each gas and each flow controller was controlled by the data acquisition (DAQ) software (Lab View).

Figure 60 Precision air regulator.

The oxygen is obtained from normal air through a compressor. The oxidant gas, oxygen, enters the test-system from the compressor at a line pressure of 200000 Pa. This pressure is controlled by a standard precision air regulator, see Figure 60. The pressure regulator was necessary to test different pressures in the PEM fuel cell and to avoid pressures greater than 300000 Pa that could damage the PEM fuel cell.

It is important to note that the pressure regulators for hydrogen and air had to be placed before the volumetric flow meters/controllers, as the regulator itself imposes a back pressure on the pressure regulator, and the pressure regulator can also affect the flow rate. In the set up if the pressure dropped for any reason, the volumetric flow meters/controllers can adjust itself automatically.
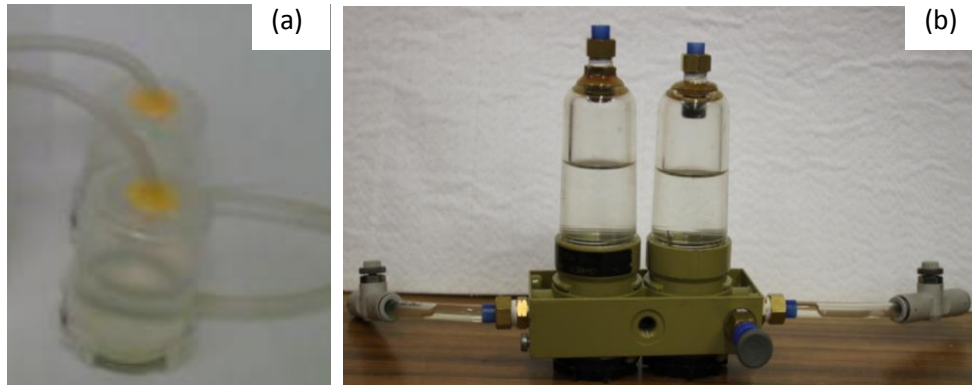
Figure 61 Hydrogen & air humidifiers (a) Simple flow through humidifier designs (b) Temperature regulated humidifiers.

The membrane of the PEM fuel cell needs to be humidified as stated by the manufacturer of the MEA (Model: ECOFC-1 - H2Economy, Armenia). In the test system a number of designs of humidifiers were tried and tested and the final design is shown in Figure 61 (b). Both air and hydrogen gases can be separately humidified using the in house temperature controlled humidifiers. Saturator temperature was set equal to the fuel cell temperature to ensure full gas humidification. The humidified hydrogen and/or air streams were passed through the fuel cell until the temperature of the fuel cell steady stated. During testing humidification was kept constant; therefore not affecting the experiments.

The following components and systems include the outputs from the PEM fuel cell being tested or unused products from the PEM fuel cell test system that must be captured or released in a controlled manner. The voltage & current are picked up by the DAQ hardware and analysed through the software. The voltage and current is also double checked by a multimeter. The current and voltage values from the fuel cell are used to define the power of the cell, the percentage of fuel used and eventually the practical efficiency can be calculated.

Figure 62 DAQ device used to collect PEM fuel cell data.

The Lab View software and its data acquisition (DAQ) components, Figure 62, are crucial for data reading and analysis. Lab View is used to control the flow of hydrogen and oxygen and to obtain the

current, voltage and temperature produced by the cell. With this information mathematical calculations produce results of power, electrochemistry activity, cell efficiency and gas utilisation. Please refer to Appendix C for details of the LabView program that was designed and implemented for this study.

Figure 63 Back pressure exhaust pressure regulator.

After the hydrogen gas reacts in the PEM fuel cell by combining with oxygen, generating electricity, a percentage of the gases exits the system without being used. A back pressure can be used to reduce the amount of unused hydrogen that escapes from the cell. The back pressure can be controlled by a hydrogen rated pressure regulator as shown in Figure 63. A back pressure is not used on the air exit the output pressure is assumed to be the atmospheric pressure. However, a water trap is positioned on the exit of the air and hydrogen lines of the PEM fuel cell through which exhaust water may be collected and this ensures that the exit lines do not get blocked with water. The excess unused gas is extracted to the extractor as shown in Figure 64.
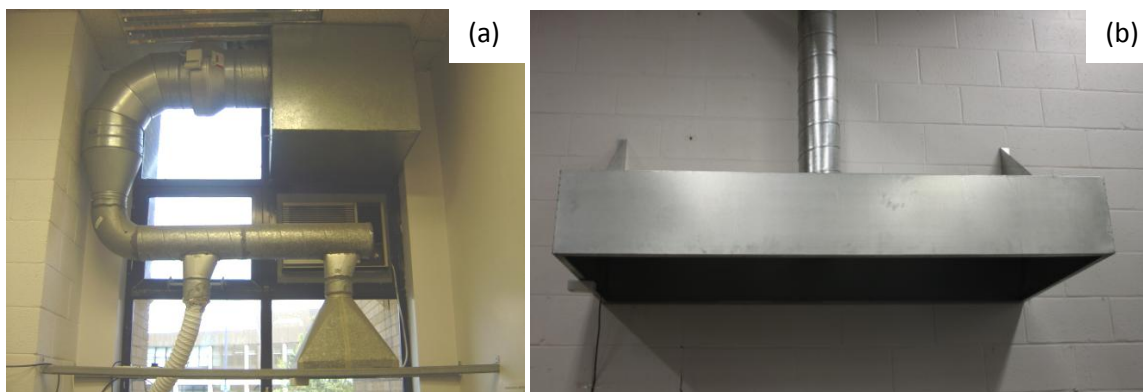
Figure 64 Extraction system (a) Initial extractor (b) Final extractor.

4.1.1.2 Reading current & voltage

A load is connected to the PEM fuel cell. The load that is used in the experiments is a variable resistor, a rheostat that simulates the working environment of the fuel cell device. The DAQ device is connected in parallel with the load and this can record voltage. A multimeter is connected in series with the positive wire from the fuel cell and this records current travelling through the load. The apparatus is set up as shown in Figure 65.
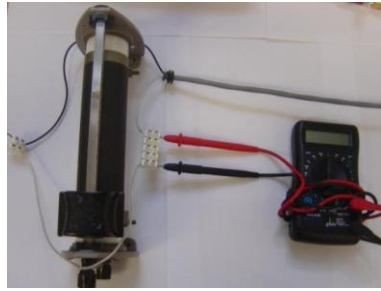
Figure 65 Load (Rheostat) configuration.

When the experiment begins, the leaver of the rheostat is positioned fully to the left as shown in Figure 66 (a). (Note: when the leaver is positioned fully left, maximum resistance of approx 12.7Ω is achieved.) The first reading of the current and voltage are taken at this point. (Note: Voltage will be maximum and current will almost be minimum (almost zero) at this position) As shown in Figure 66 (b) & Figure 67 (a) the leaver of the rheostat is slowly moved to the right to decrease the resistance. By decreasing the resistance the voltage will drop and the current will increase (V=RI or R=V/I).
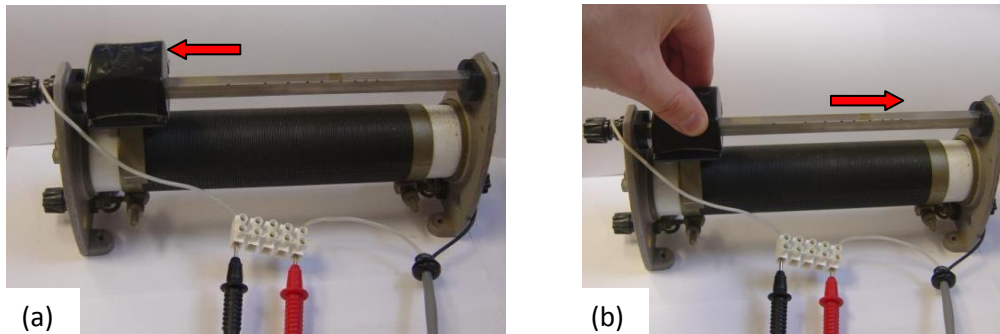
Figure 66 Taking readings of voltage & current from the PEM fuel cell (a) Maximum resistance (b) Reducing resistance

The resistance is continually reduced in small increments and the voltage and current are allowed to settle before readings are taken. The leaver of the rheostat is moved until it is positioned fully to the right as shown Figure 67 (b). (Note: when the leaver is positioned fully right minimum resistance of approx 0.25Ω is achieved.)
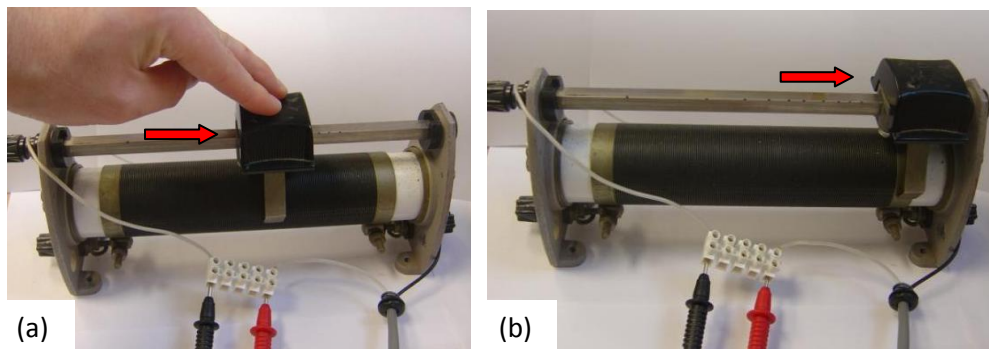
Figure 67 Taking readings of voltage & current from the PEM fuel cell (a) Reducing resistance (b) Minimum resistance

The final reading of the current and voltage are taken at this point. (Note: Voltage will almost be zero and current maximum at this position).

4.1.1.3 Safety

The molecules of hydrogen gas are smaller than all other gases, and it can diffuse through many materials considered airtight or impermeable to other gases. This property makes hydrogen more difficult to contain than other gases. Hydrogen leaks are dangerous in that they pose a risk of fire where they mix with air.

PEM fuel cells are considered safe devices because the electrochemical reactions take place within the PEM fuel cell. The electrolyte within the cell allows an electrical current to flow in an external circuit from the hydrogen to the oxygen reaction, and suppresses the normally explosive reaction when hydrogen and oxygen are brought together and ignited to form water [1].

In order to monitor the hydrogen, a hydrogen leak detector as shown in Figure 68 (a) was incorporated in the experiment set-up. The detector is sensitive to any traces of combustible concentrations of hydrogen in the air. It also allows for the experiments to be shut down in the case of hydrogen leaks.

Figure 68 Safety measures: (a) Hydrogen leak sensor (b) Air extractor.

Another safety mechanism used in the experiment is the extractor as shown in Figure 68 (b). The small hydrogen molecule size, that increases the likelihood of a leak, also results in very high buoyancy and diffusivity. Leaked hydrogen rises and becomes diluted quickly outdoors, resulting in a very localized region of flammability that disperses quickly. Indoors, the hydrogen diffusivity and buoyancy is reduced and the tendency for the hydrogen to continue to rise decreases. Therefore an extractor is needed. The purpose of the extractor is to dispense all the exhausted gases from the room. This reduces the concentration of harmful gases in the room, thus minimising the likelihood of asphyxiation or fire.

Additional safety precautions:

- Much of the apparatus and containers are manufactured from soft plastics and glued together, reducing the possibility of leaks and shrapnel in the case of an explosion.

- Low pressures (1 to 3 Bar gauge) and extremely low flow rates (20 ml/min to 150 ml/min) are used in the experiments.

- Hydrogen rated, fittings, piping, gauges are used flow controllers and pressure fittings are used throughout the experimental apparatus.

- Protective glasses and gloves are used at all times during experimentation.

- The PEM fuel cell testing laboratory is in a large room to minimise the risk of high concentrations of hydrogen in the room.

- The PEM fuel cell testing laboratory has special access, away from classrooms, so students would not enter the room.

- Safety signs were erected in the PEM fuel cell testing laboratory.

- Fire extinguishers and fire blankets were readily available in the PEM fuel cell testing laboratory.

- A risk assessment was completed on the PEM fuel cell testing laboratory.

Figure 69 Hydrogen rated fittings and safety equipment.

4.1.2 PEM Fuel Cell Testing System

The initial step of the experimentation was carried out to obtain the input parameters of a purchased industry standard PEM fuel cell. The parameters were obtained from the manufacture's specification of the fuel cell under certain operation conditions. Please refer to Appendix G for full specifications of the purchased industry standard PEM fuel cell.

4.1.2.1 Experimental setup for PEM fuel cell testing

The experimental setup is shown in Figure 70. The reactant gas, hydrogen, is stored in a compressed cylinder. A specialised hydrogen pressure controls the hydrogen gas flow pressure. The gas then passes through volumetric flow meters. The flow controllers are calibrated for the hydrogen gas and air. The flow controllers are controlled by the data acquisition (DAQ) software (Lab View). Both air and hydrogen gases were humidified as stated by the manufacturer of the MEA using in house temperature controlled humidifiers. Saturator temperature was set equal to the fuel cell temperature to ensure full gas humidification. The humidified hydrogen and air streams were passed through the fuel

cell until the temperature of the fuel cell steady stated. During testing humidification was kept constant; therefore not affecting the experiments.
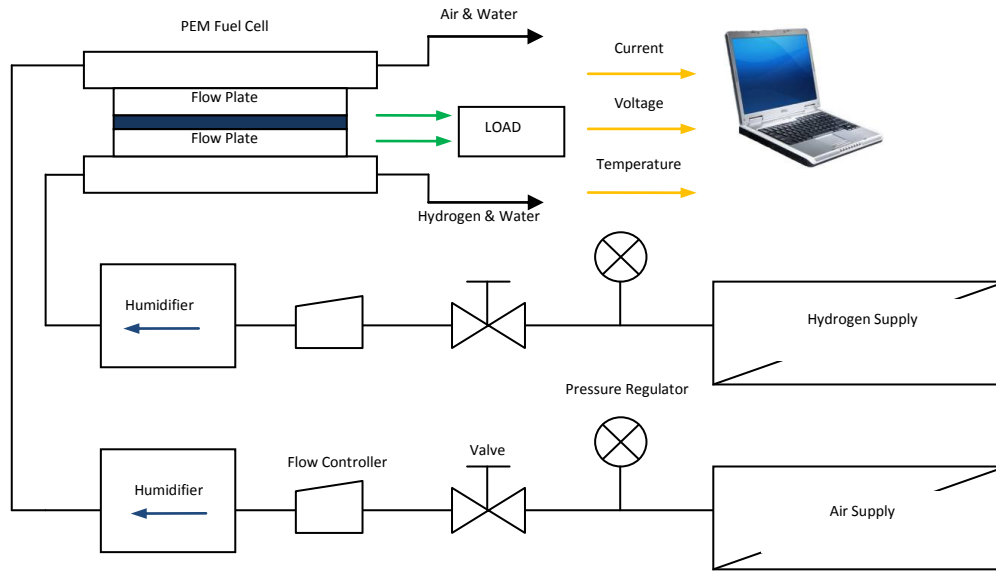
Figure 70 PEM fuel cell experimental setup.

The open circuit voltage and the fuel cell operating voltage are detected by the DAQ hardware and analysed through the software. The open circuit voltage reading is also double checked at the anode and cathode using a multimeter (Fluke 8808A digital multimeter). The fuel cell current is measured using a multimeter (Fluke 8808A digital multimeter) in series with the external load. A 12.7 Ω variable rheostat supplied the variable resistive load.

A hole was drilled at the centre of each back plate of the fuel cell to position the K-type thermocouples as close to the centre of the fuel cell as possible. The thermocouples were placed into the fuel cell backing plate, against each flow plate, and the temperature values recorded through the DAQ system. The location of the thermocouples in the fuel cell indicated that the cell was operating between 55°C and 60°C for all experiments. This was chosen to be a steady state region and fluctuations were minimised.

4.1.2.3 PEM fuel cell experimental procedure

All safety procedures are firstly and fore mostly adhered to before, during and after all experiments. Safety precautions are described in Section 4.1. Each experiment lasts between 20 to 25 minutes, after about 20 minutes warm up time. At the end of the experiment readings are checked and repeat test are carried out if necessary. The procedure for flow plate testing is as follows:

- The PEM fuel cell to be tested is positioned and hydrogen and air pipes are connected.
- All parts of the test system are checked for leaks or damage.
- The hydrogen sensor is switched on.
- The extractor system is switched on.

- The DAQ system is loaded and switched on.

- Temperature readings from the humidifiers and the PEM fuel cell are checked.

- The air compressor is primed and the air pressure regulator is set to the required pressure.

- The hydrogen bottle is turned on and the pressure regulator is turned to the required pressure.

- The hydrogen and oxygen flow controllers are switched on. The readings take about 3 seconds to level and then an accurate flow for hydrogen and an accurate flow for air are achieved.

- The PEM fuel cell is allowed to warm up for about 20 minutes.

- The initial no load value of the voltage is recorded.

- The resistance of the external circuit is controlled by a rheostat. As the rheostat resistance is reduced the different values for voltage and current are recorded.

- Values for current, voltage and temperature are recorded. Power is calculated and graphs are produced.

- Air and hydrogen flow is stopped.

- The fuel cell is disconnected from the test system and disassembled.

- The flow plates are investigated for any damage or anomalies including water blockages.

- The flow plate is replaced with another design and the PEM fuel cell is reassembled.

- The experimental procedure is repeated as above for all variations of flow plate.

Every effort was made to keep parameters constant during the experiments to ensure that the values of resistance, pressure and flow were not changed from one experiment to the next. These parameters were checked throughout the experiment to identify any unwanted errors. The only effect on the efficiency was that of the flow plate design.

Appendix B describes the assembly and disassembly of the PEM fuel cell with standard flow plates and the new PEM fuel cell with open pore cellular foam flow plates.

4.2 Mini Channel Flow Visualisation

From the available literature, as described in Section 2.7, many models exist that help describe water evolution and movement through PEM fuel cell flow plate channels. However it was noticed that few computer models were validated by experiment and the visualisation of large slugs and droplets of water in straight or circular channels of PEM fuel cells was not readily available in literature. Various methods are available to observe water in micro-channels and this is described in Section 2.6. For this study direct optical imaging was performed as it was readily available, cost effective and provided the necessary resolution for flow field investigation. This section describes the background setup and procedure for the mini channel fluid flow visualisation.
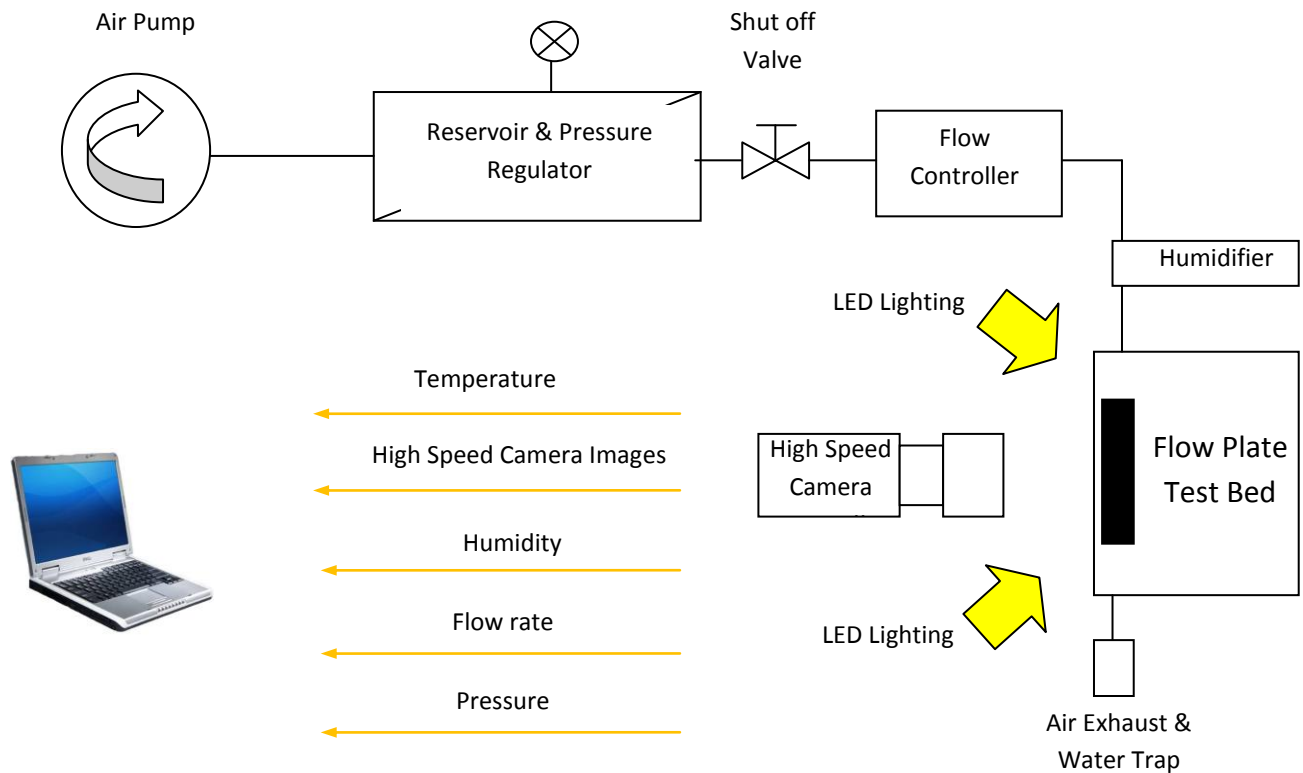
Figure 71 Diagram of experimental apparatus to investigate water slug and droplet flow regimes in ex situ simulated PEM fuel cell channels.

4.2.1 Experimental setup of mini channel

The experiment is to simulate an ex situ operational PEM fuel cell channel operating at a temperature of 55°C and at high current density, flooding is occurring. Only the air side of the fuel cell is simulated as this is the side where the major water management issues occur.

The experimental apparatus is shown in Figure 73. The apparatus is similar in design to Lu et al. [84]. The apparatus includes air feed and air control, (compressor, pressure gauge, flow controller) humidification and a test bed for the flow plate channel that utilises a high speed camera system. The air passes through a volumetric flow controller (Voegtlin red-y series flow controller). The flow controller is calibrated for air. The flow controller is controlled by the data acquisition (DAQ) software (Lab View).

The air is humidified using an in house temperature controlled humidifier. Saturator temperature was set equal to the fuel cell temperature to ensure full gas humidification. The humidified air stream was passed through the channel until the temperature of the fuel cell steady stated. During testing humidification was kept constant; therefore not affecting the experiments.

A hole was drilled at the centre of the back plate of the test bed to position the K-type thermocouple as close to the centre of the channel as possible. The thermocouple was placed into the test bed, against the flow plate, and the temperature values recorded through the DAQ system. The location of

the thermocouples indicated that the channel was between 55 °C and 60 °C for all experiments. This was chosen to be a steady state region and fluctuations were minimised.

The rig was designed to be as simple as possible and to be automated to reduce the amount of human interaction with the experiment. The test bed has room for one 38 mm x 38 mm flow plate to be viewed at any one time.

Figure 72 Flow plate background test set ups.

A transparent (clear polycarbonate) cover is placed over the flow plate to seal it from the outside environment but also for visualisation purposes to allow imaging of the channel. The channel interior colour was modified during testing to find out which contrast gave the best images, see Figure 72. White backgrounds, black channels and normal (grey) channel colours were imaged. It was concluded that the channels would not be modified as this would affect the true surface of the channels which would affect the results and a good enough contrast between the water and the normal (grey) channel was achieved. Three high speed cameras were used in different experiments. These are described in Table 10.

Table 10 High speed cameras used.

High speed camera name	Observation	Frames per second (fps)	Image size (pixels)
JAI M40	Testing	60 -233	546x325
Citius Imaging	Slug movement	1000	344 x 1024
Microtron	Slug formation	2000	512 x416
Microtron	Slug interaction	3000	1024 x 1024

The high speed, high resolution camera observes the fluid behaviour, through specific flow plate channels. The camera's position is fully adjustable. Lighting was provided by high luminous LEDs. Images of water droplet formation and growth on the GDL and slug formation, growth and transport through the flow plate channels were viewed. In addition observations of the flow regime of fluid through different flow plate designs were recorded. Post processing work including droplet

interactions and speed of slugs through the cell, with sensor information about humidity, pressure and temperature, can be very useful in determining the flow plate effectiveness of flooding mitigation. In addition the data can be used to help assess other experiments completed and help validate computer simulations.

Figure 73 High speed camera set up.

A syringe pump was fist conceived to place the droplet into the channel to replicate the movement of water from the GDL to the surface of the GDL as shown by Zhu et al. [136]. However, initial modelling results showed that if a syringe was introduced to the channel it would disrupt the flow of gas and not resemble a real channel activity. Instead, drops or slugs of fluid were placed into the channels and the interaction with the gases was analysed. The definition of a slug in this study is a large water droplet that adheres to either the GDL or channel wall and moves in air flow. Each drop or slug was placed between 3mm and 5mm from the inlet and each had a diameter of between 0.3mm and 0.9mm. The experiment represents an operational PEM fuel cell flow field after approximately 80 minutes of fuel cell operation (according to Ous and Arcoumanis [102]).

4.2.2 Mini channel flow visualisation experimental procedure

- The LEDs and air compressor are turned on.
- The air pressure is set to the required pressure.
- The flow controller is set to 50ml/min (approx 1m/s).
- A drop or slug of water is placed into the channel at a specific location.
- The camera recording is started and the air valve is set on.
- The drop or slug movement is recorded for about two seconds.
- All sensor information is recorded by the DAQ system and time stamped.
- All information is fed back to a computer for post processing.

Please refer to Chapter 5, Section 5.3.2 for all the experimental results and Chapter 6 for a full discussion of these results and the comparison of the results to the developed models.

5

Chapter 5 – Model Development, Simulation & Experimental Results

5.1 Model Development, Simulation & Experiments

This Chapter is concerned with innovative flow plate development; from idea evolution to model building and satisfactory simulation results through to experimental validation. From the knowledge gathered in the literature review, new flow plate concepts, ideas and designs were conceived and then investigated through modelling and simulation. The predictions, conclusions and results obtained from the model simulations are validated from literature and by experiment. The most promising or most suitable flow plate designs that give the best results, after the modelling and simulation process is complete, were manufactured and then experimented in an operational PEM fuel cell (the experimental setup is detailed in Chapter 4).

Model development and evolution and the corresponding simulation results are detailed in section 5.2:

- Section 5.2.1 details the flow plate and flow field development and CFD results.
- Section 5.2.2 details the mini channel CFD VOF results.
- Section 5.2.3 details the open pore cellular foam model development and CFD results
- Section 5.2.4 details the 3-D PEM fuel cell electrochemistry model development and simulation results.

The experimental results are detailed in section 5.3:

- Section 5.3.1 details the experimental PEM fuel cell electrochemistry results for all manufactured flow plate designs.
- Section 5.3.2 details the experimental PEM fuel cell electrochemistry results for the open pore cellular foam flow plate designs.
- Section 5.3.3 details the experimental mini channel visualisation results.

A complete discussion of all the simulation and experimental results is presented in Chapter 6.

5.2 Model development & Simulation Results

CFD programs can accurately predict flow patterns and regimes, velocity analysis and pressure results in parts of some fuel cell components or through full flow plates and flow fields. All flow plate designs presented in this thesis have to cover an active area of 14.45cm^2, as this is the active area of the MEAs used by the operational PEM fuel cell.

Some of the key areas which are important to address when designing a flow plate channel layout are the distribution of pressure on the GDL and membrane, pressure drop in and through the flow plate, distribution of temperature on the GDL and membrane, maintained reactant concentration over the entire active area of the GDL and membrane, membrane hydration and the mitigation of flooding as discussed throughout the literature review in Chapter 2.

Section 5.2.1 describes the flow plate and flow field development and corresponding CFD simulation results; flow regime, pressure analysis and velocity analysis, of some flow plate designs that are in literature and a many designs that were conceived during the course of this work.

Section 5.2.2 describes the models developed and the CFD simulation results using VOF method. Two phase flow regime, pressure analysis, velocity analysis and time sequenced interaction of water droplets and slugs in PEM fuel cell channels (straight and circular) and material surfaces are shown.

Section 5.2.3 describes the development of the open pore cellular foam Representative Unit Cell Structure (RUCS) model and the corresponding CFD simulation results. Flow regime, pressure analysis and velocity analysis, of open pore cellular foam from 10ppi to 100ppi are described.

Section 5.2.4 describes the CFD electrochemistry & I-V model results of a PEM fuel cell with a standard double channel flow plate and a PEM fuel cell with open pore cellular foam flow plates. Species concentration along the flow fields including water production and oxygen and hydrogen distribution and utilisation. Current density is calculated and I-V graphs are plotted.

A full discussion on the developed flow plate designs and all these simulation results are presented in Chapter 6.

5.2.1 Flow Plate & Flow Field Design, Model Development & Simulation Results

CFD modelling allowed for fast trial and error design mythologies to be used to assess and compare suitable flow plate designs, modified from literature or conceived from brainstorming sessions.

5.2.1.1 Serpentine flow plate CFD model

From literature it was recognised that the serpentine flow plate has been intensively investigated and is now an industrial standard flow plate design. Most fuel cell producers use this default design in

their PEM fuel cells, as it is an established design that allows full active area coverage of gas at reasonable pressure losses. The double serpentine channelled flow plate with ribs and channels 1mm wide and deep, as shown in Figure 74, is the most common configuration of this design.
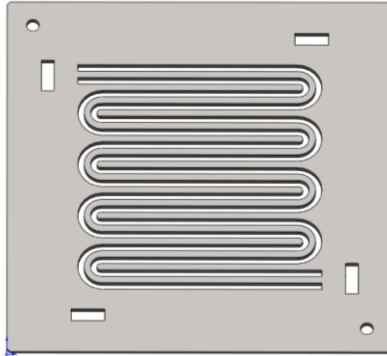
Figure 74 Double serpentine flow plate design.

This flow plate was modelled and analysed using CFD to view its operation and to gain a knowledge base for the proceeding designs. This enabled a better understanding of fluid flow in flow plates and results could be easily correlated to literature. Problems with this design could be identified; new ideas could be employed into new flow plates that could improve the PEM fuel cell performance.

5.2.1.2 Serpentine flow plate simulation results

Figure 75 and Figure 76 show an even distribution a velocity through the flow plate. This velocity insures that the full area of the MEA is supplied with the gas (hydrogen or air).
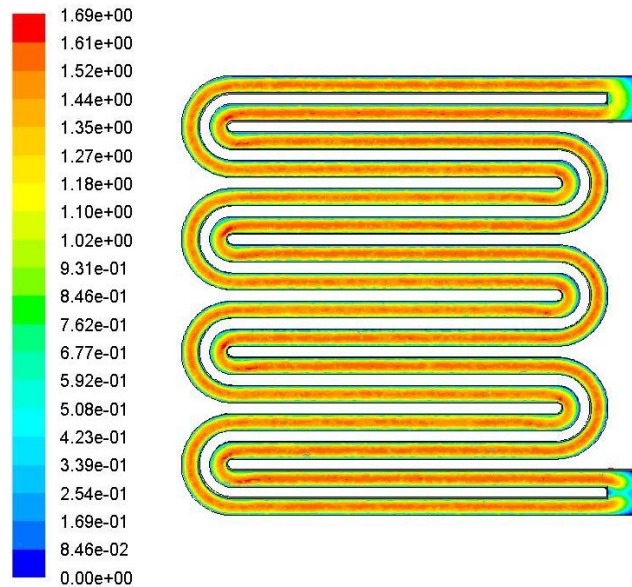
Figure 75 Velocity (m/s) through the serpentine flow plate model.

The double serpentine flow field can ensure velocity flow within the PEM fuel cell is constant (1.5m/s), as shown in Figure 75, this can aid in water product removal.
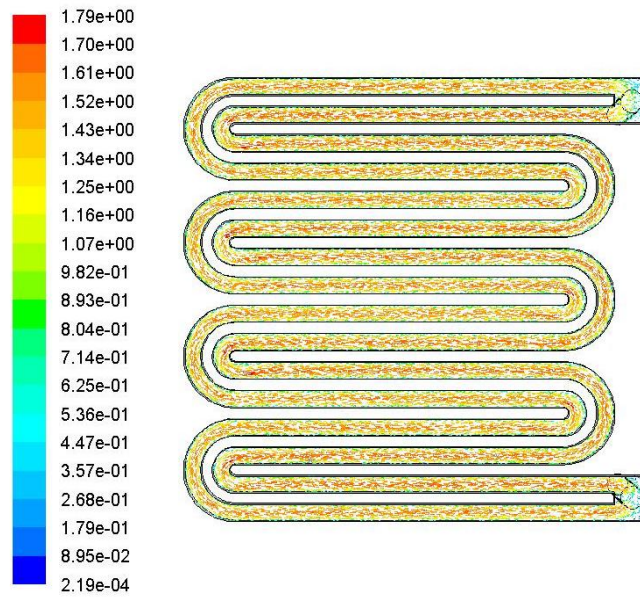
Figure 76 Velocity vectors (m/s) at the outlet.

The continuous fluid flow from inlet to outlet would ensure blockages of water would be moved quickly to the outlet. No dead zones or circulation eddies are visible in the flow path using this design. However boundary layers of lower velocity fluid flow (1.0m/s) is noticed at the channel edges. This can lead to water films being moved to the channel walls, creating annular flow.
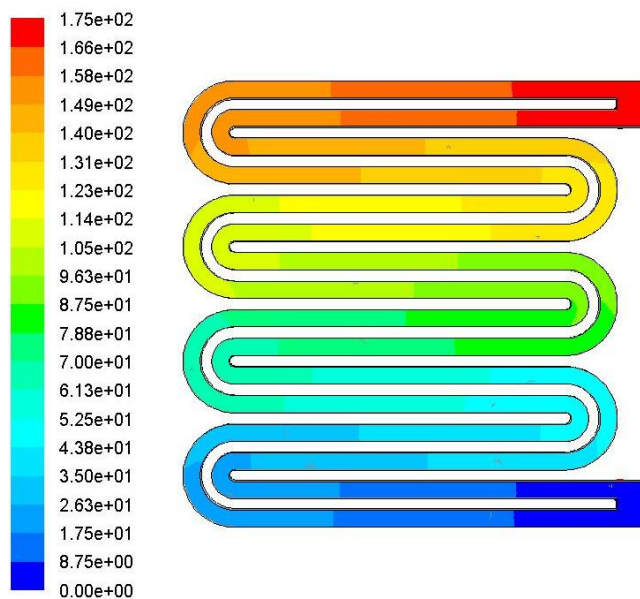
Figure 77 Pressure (pa) through the serpentine flow plate model.

The pressure distribution shown in Figure 77 indicates that there is a high inlet pressure on the first few inlet channels (175 Pa) but this quickly decreases to a low pressure in the exiting channels (8 Pa). This would show that pressure towards the MEA decreases from inlet to outlet and this may have consequences to the mass transport and PEM fuel cell performance.

5.2.1.3 Modified double serpentine flow plate CFD model

The modified double serpentine flow plate (developed during this thesis) is an adaptation of the double serpentine flow plate. More channels were introduced into the design so that a better flow of fuel and oxidant could be achieved throughout the flow plate, as shown in Figure 78. Normal serpentine flow plates have an issue with a decrease in concentration of hydrogen or oxygen from inlet to outlet, due to the long channels. The extra, 1mm, inlet channels could improve gas delivery to the full active area of the PEM fuel cell and reduce the concentration gradient, improving the current density of the cell; however fuel utilisation might be reduced. This design may not affect the extraction of water from the PEM fuel cell, as this introduces no extra channel to the outlet where water could gather, however fully humidified gases could condense in the inlet channels, which may cause flooding issues. This concept evolved many times and Figure 78 shows the best variation of the concept.

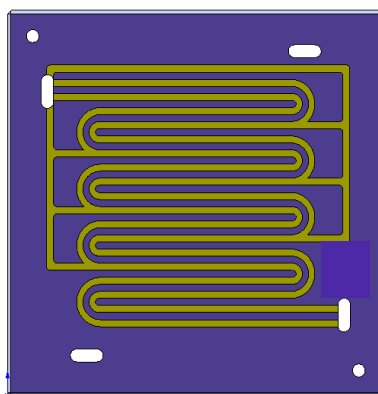**Figure 78 Modified serpentine flow plate design.**

5.2.1.4 Modified double serpentine flow plate simulation results

Figure 79 (a) shows the velocity distribution within the flow plate with high flow rates evident at the last 5 channels of the flow field.
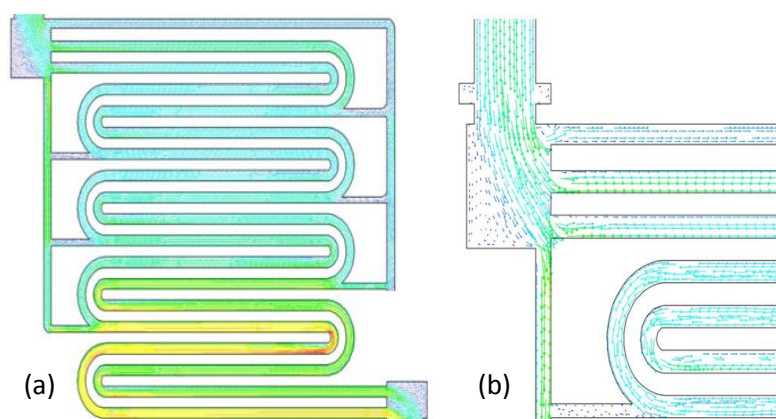

(a)   (b)

Figure 79 (a) Velocity (m/s) through the modified serpentine flow plate model (b) Velocity vectors (m/s) at the inlet.

Figure 79 (b) shows that inlet gas flows the least resistant path to the exit, neglecting the main flow paths. Most fluid flow does not spread over the active area of the MEA. The additional channels seem to have a disadvantage to the utilisation of the gases.
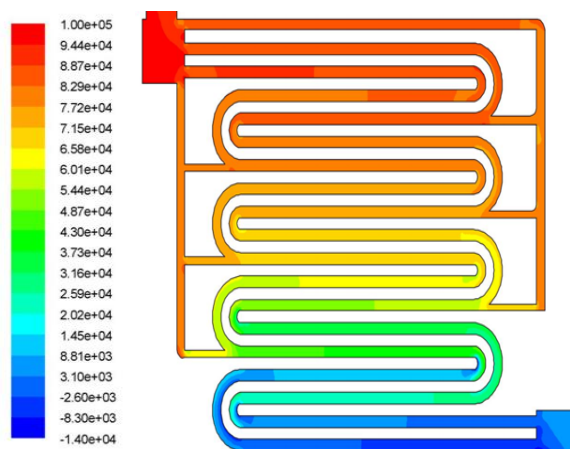
Figure 80 Pressure (pa) through the modified serpentine flow plate model.

The pressure distribution is shown in Figure 80 compliments the velocity distribution result. As the pressure decreases through the internal flow channels, the external flow channel still retains a high pressure thus forcing a higher velocity through this channel as opposed to the internal flow channels. The overall pressure distribution is slightly more even but there remain issues with this flow plate design. This flow plate was assigned for manufacture to draw conclusive results from experimentation, detailed in Section 5.3.1.1 of this chapter.

5.2.1.5 Parallel flow plate CFD model

From literature it was recognised that the parallel flow plate is also an industrial standard. An analysis of the standard parallel flow plate design would enable a better understanding of fluid flow in flow
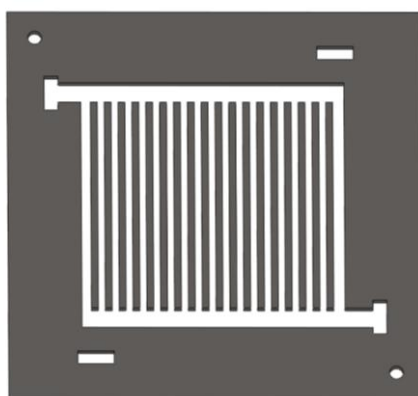
Figure 81 Parallel flow plate design.

plates and information could be easily correlated to literature, identifying problems with the design and enabling new ideas and innovative designs to be produced, that could improve the performance of the flow plate and PEM fuel cell. This design mainly aims at the water extraction and an equal

distribution of the gases throughout the flow plate in order to fully utilise the gas diffusion layer. This design should improve the pressure distribution throughout the flow plate because all the channels (1mm wide and deep) have equal access to the input gas channel as shown in Figure 81.

5.2.1.6 Parallel flow plate simulation results

Figure 82 shows an uneven distribution a velocity through the flow plate. Fluid flow is confined to the right hand side of the flow plate with possible dead zones and water accumulation on the left hand side of this flow plate.
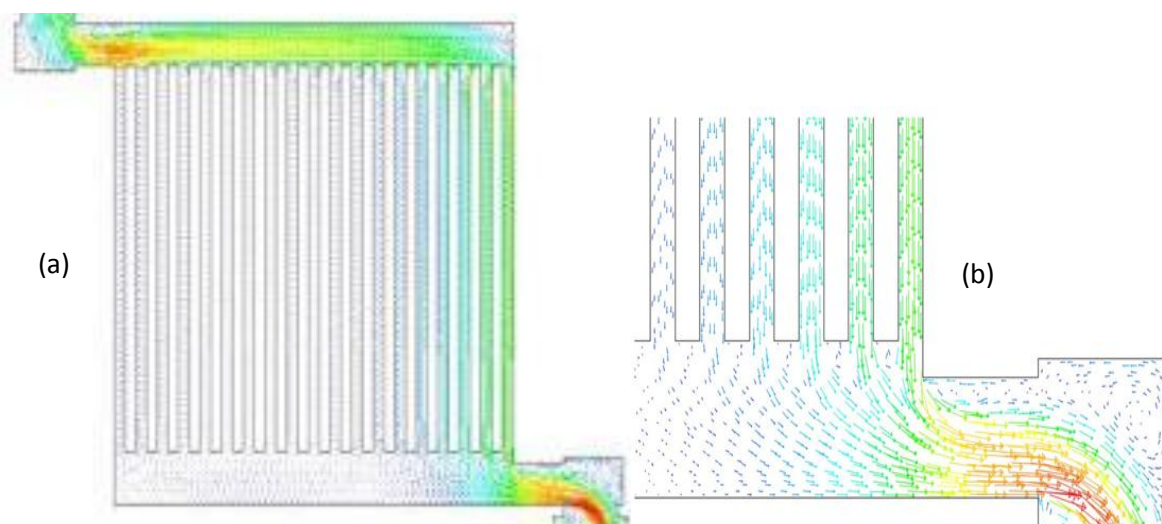
Figure 82 (a) Velocity (m/s) through the parallel flow plate model (b) Velocity vectors (m/s) at the outlet.

This would dramatically reduce the performance of the fuel cell as only one third of the active area of the cell would have convective air flow.
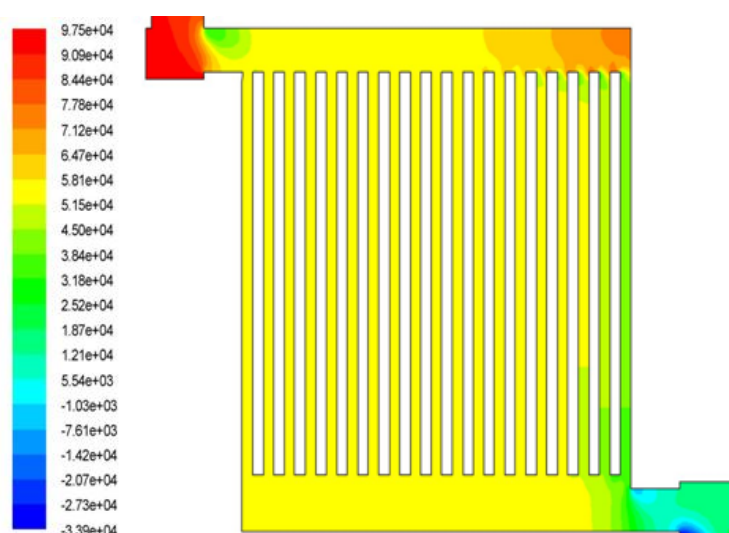
Figure 83 Pressure (pa) through the parallel flow plate model

The pressure distribution, shown in Figure 83, indicates that there is a high inlet pressure low out put pressure and even pressure distribution along the central region of the flow plate, corresponding to the

active area of the MEA. This even pressure is promising but the fluid flow velocity is an issue for this flow plate design.

5.2.1.7 Modified parallel flow plate CFD model

From the results of the parallel flow plate CFD analysis, it was noticed that the flow was not equally distributed throughout the channels. Many variations of the parallel design were tried and tested in an attempt to obtain an optimal flow plate design. A modified parallel design (developed during this thesis) with 2mm ribs and 1mm channels (1mm deep) as shown in Figure 84 was modelled and simulated. This design was then modified to allow fluid to distribute more evenly into the flow field by applying a tapered inlet region as shown in Figure 85. The final modified parallel design (developed during this thesis) incorporated had 1mm ribs and 1mm channels (1mm deep) but with steps at the entrance shown in Figure 86. The steps were placed at different levels at the entrance in order to improve the flow distribution throughout the plate.

Figure 84 Modified parallel flow plate design with 2mm ribs.
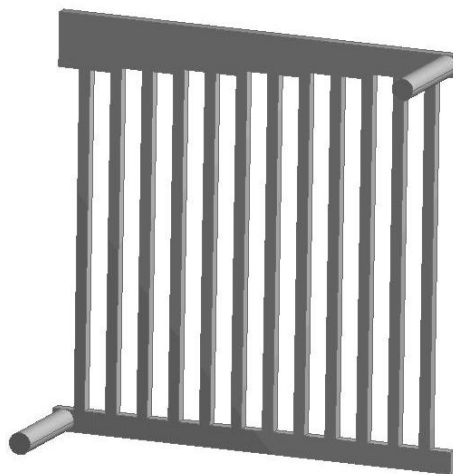
Figure 85 Modified parallel flow plate design with 2mm ribs and tapered inlet.
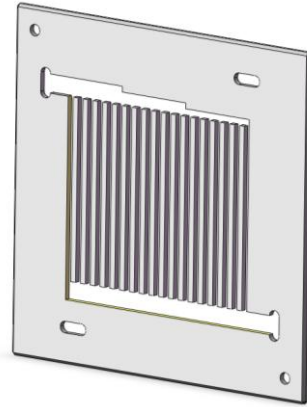
Figure 86 Modified parallel flow plate design with 1mm ribs and channels and inlet steps.

5.2.1.8 Modified parallel flow plate simulation results

The standard parallel flow plate was modified by the addition of steps into the inlet region of the flow field to distribute fluid flow evenly to all channels. This design allowed an even flow of fluid through most of the channels as shown in Figure 87.
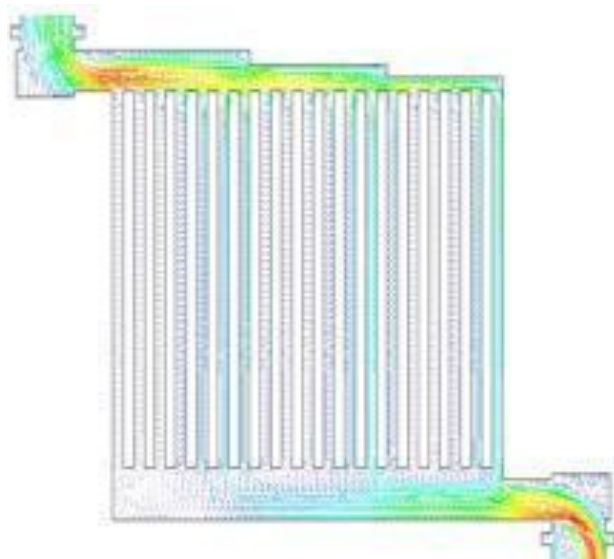
Figure 87 Velocity vectors (m/s) through the stepped parallel flow plate model
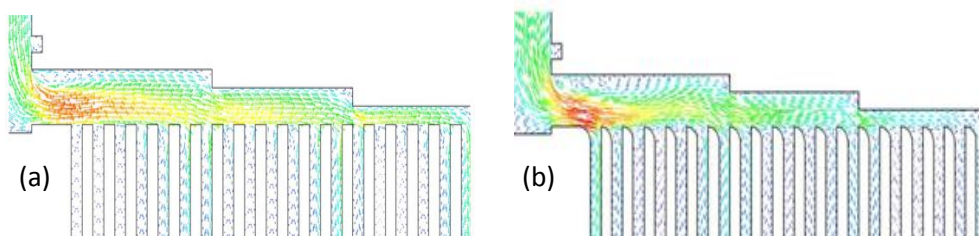
Figure 88 Velocity vectors (m/s) at the inlet (a) Square edges (b) Rounded edges.

The inlet was further investigated and the channel edges modified, left square in Figure 88 (a) and rounded in Figure 88 (b). The rounded edges seem to ensure better flow distribution at the inlet of the channels. However the machining process to achieve these sub millimetre radii could prove difficult.
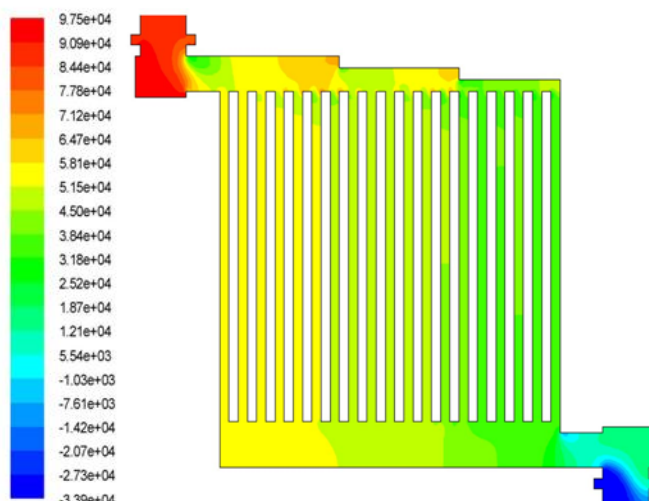
Figure 89 Pressure (pa) through the stepped parallel flow plate model.

Figure 89 highlights the pressure distribution of the stepped parallel flow plate. The pressure distribution is not fully distributed across the flow plate and it is lower than the standard parallel flow plate but a large improvement of this design is the more even flow. This flow plate was assigned for manufacture to draw conclusive results from experimentation, discussed in Chapter 6.

5.2.1.9 Over-flow flow plate CFD model

1mm deep channels, 2mm wide with 0.5mm deep channels 1mm wide were embedded in this flow plate. Figure 90 below shows the CAD design. This over-flow design (developed during this thesis) was modelled and simulated to view the interaction of ribbing on the air flow of the flow plate.
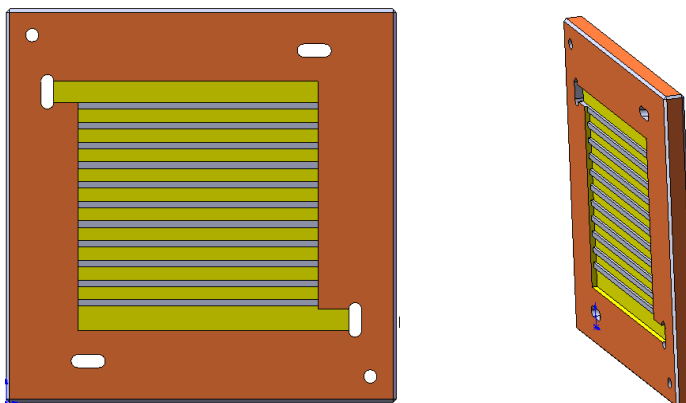
Figure 90 Over-flow flow plate design.

The idea of producing waves along the flow path, caused by the ribs, could force the gases to make better contact with the GDL. Better contact between the gas and the GDL would mean better utilization of the reactant gases. However, it was clear, from the design that, surface contact with the flow plate and the GDL would cause electrical contact issues if this design was manufactured and tested. The question was that whether having a wave path would produce the desired effect.

5.2.1.10 Over-flow flow plate simulation results

This design as shown in Figure 91 was initially conceived to investigate flow in a chamber and observe the interaction of the fluid with channels and ribs. This design had no central channels to make contact to the MEA and so would have given results that would not suit the application of the PEM fuel cell but it did allow information to be gathered to aid in the development of other flow plate designs.
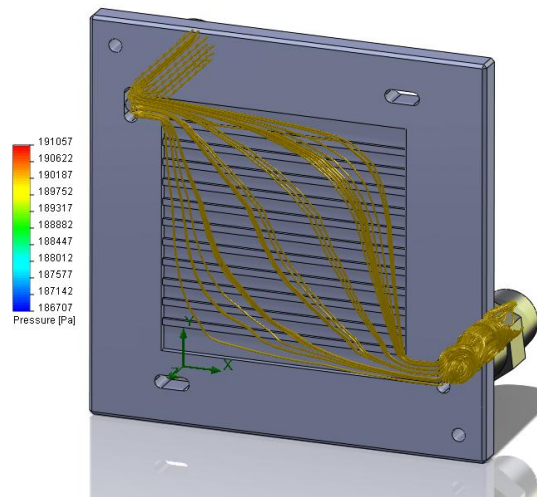
Figure 91 Over-flow flow plate flow.

5.2.1.11 Modified pin flow plate CFD model

This design incorporated a modified version of the pin flow plate from literature. The modified pin flow plate (developed during this thesis) has 2mm pin plates embedded in the flow plate. These wide plates should distribute the fluid evenly through the flow plate and ensure a large contact area with the MEA. Pressure distribution should be more even than other designs proposed.
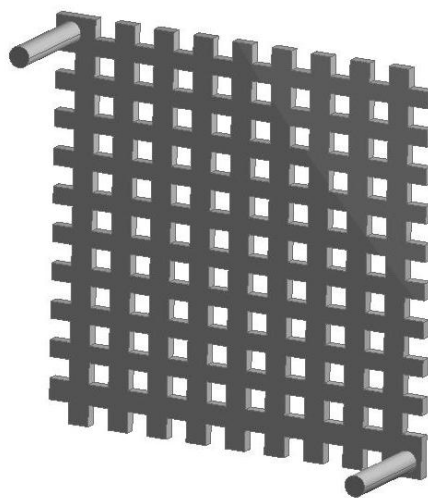
Figure 92 Modified pin flow plate design.

5.2.1.12 Modified pin flow plate simulation results

Figure 93 shows the pressure distribution through the modified pin flow plate model. The pressure distribution is very even with only a 16 Pa pressure drop from inlet to outlet.
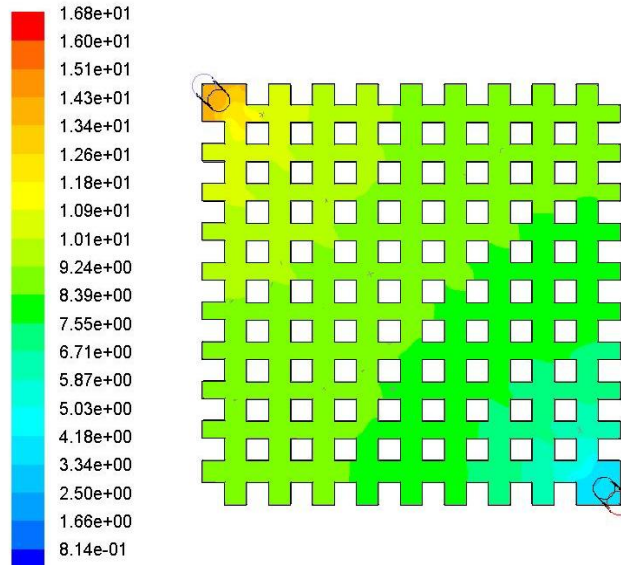
Figure 93 Pressure (pa) through the modified pin flow plate model.

The velocity profile through the modified flow plate is shown in Figure 94. A velocity of 1.7m/s is noticed at the inlet but this is very low compared to other designs and it evens out through the flow plate giving a distributed average flow velocity of about 0.7m/s.
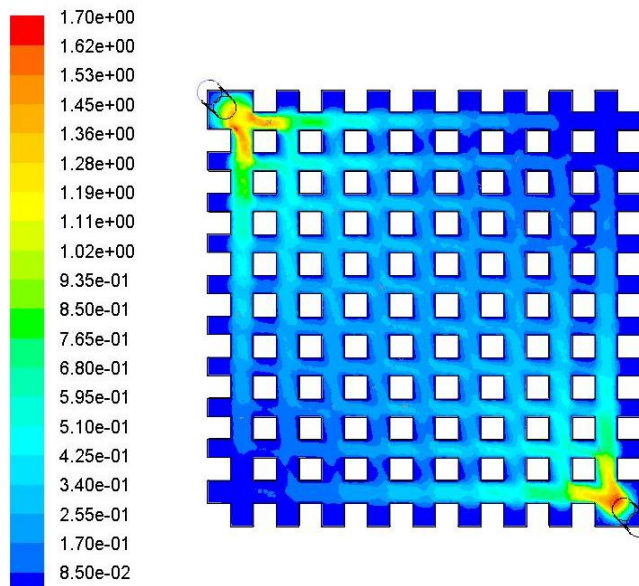
Figure 94 Velocity (m/s) through the modified pin flow plate model.

The velocity vectors, as shown in Figure 95, highlight the areas where there is minimal flow in the flow field. The edges of the flow plate and the opposite corners of the inlet and outlet have minimal flow and this may correspond to stagnant flow areas where water may accumulate and the effective

active area of the MEA could be reduced. This flow plate was not manufactured but future studies could investigate this flow plate design further.
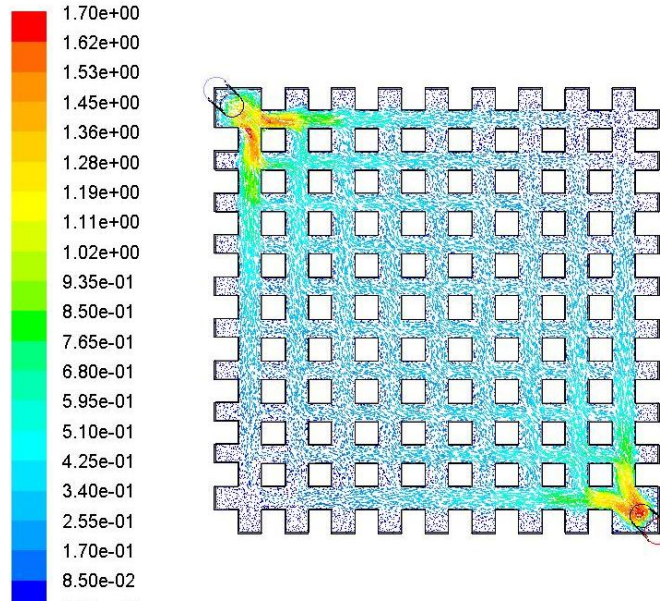
Figure 95 Velocity vectors (m/s) through the modified pin flow plate model.

5.2.1.13 Maze flow plate CFD model

The objective of maze flow plate design (developed during this thesis) is to ensure that there are no dead zones inside the flow plate, maximise contact with the gas diffusion layer to ensure reduced ohmic resistance and efficient extraction of water from the plate while maintaining even distribution of gases and pressure against the GDL. 1mm channels were used and a divergence obstacle was placed at the input, see Figure 96, to ensure distributed flow of inlet gases.
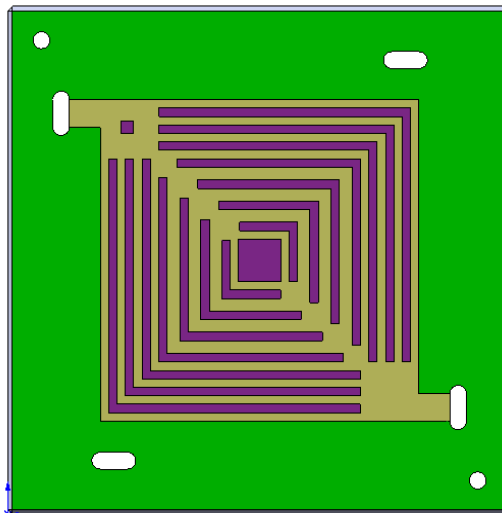
Figure 96 Maze flow plate design.

The central divergence obstacle also distributes the fluid flow and ensures large contact area with the central portion of the cell, where most heat can be generated. This type of design abandons continuous

channels altogether by creating a regular pattern of supporting patches, as shown in Figure 96. This flow plate design could be effective in single cells with the central contact area increased and as it would be difficult to create a bipolar version of this flow plate.

5.2.1.14 Maze flow plate simulation results

The velocity distribution within the flow field is shown in contour and vector plots in Figure 97. A largely even flow of fluid around the outer channels and into the corners of the flow field but the central flow rate is low and unevenly distributed.
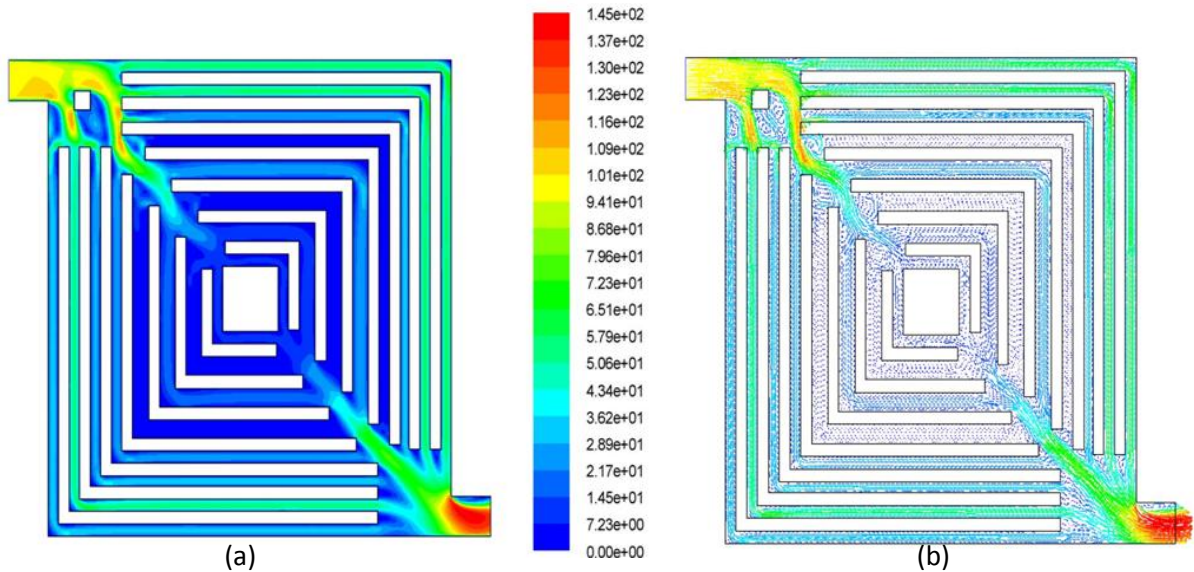
Figure 97 (a) Velocity (m/s) and (b) Velocity vectors (m/s) through the maze flow plate model.
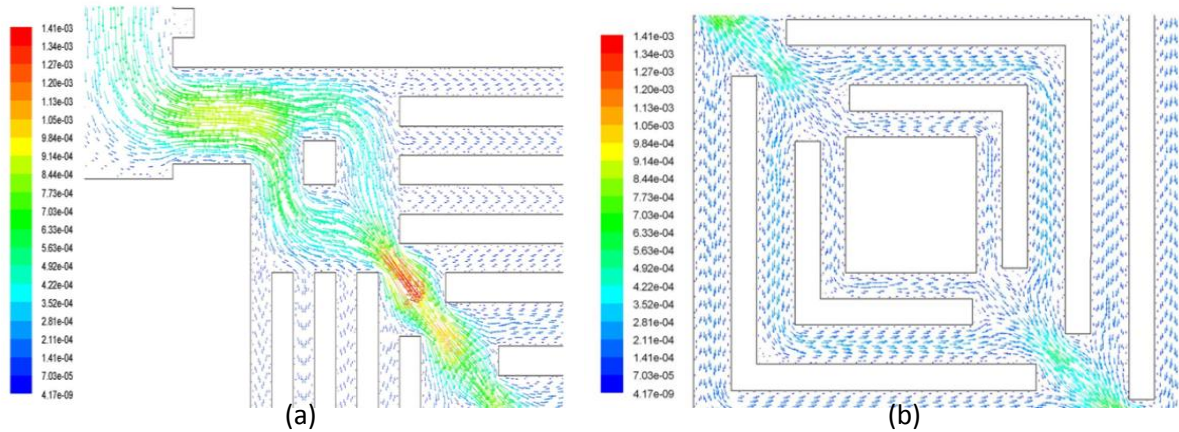
Figure 98 Velocity vectors (m/s) at the (a) inlet and (b) central region of the flow plate.

Figure 98 (a) shows the inlet block that aids the spreading of the fluid to alternative channels and Figure 98 (b) shows the central block that does a similar function to ensure even distribution of fluid through the flow plate.
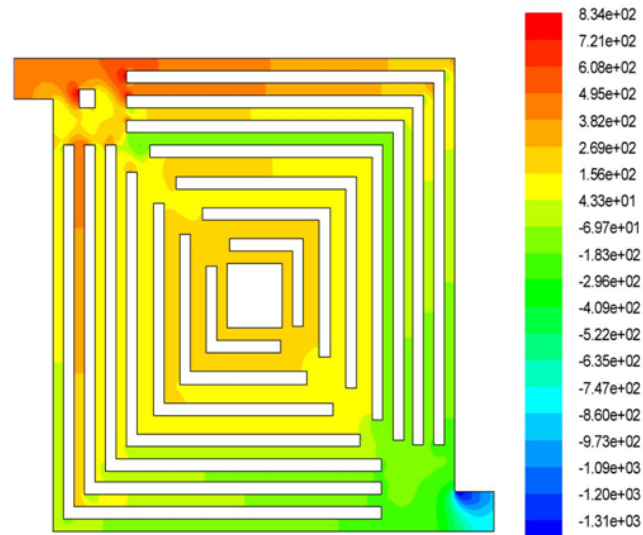
Figure 99 Pressure (pa) through the maze flow plate model.

The outer flow channels have a higher pressure than the inner channels and it is this pressure difference that could drive any water droplets produced in the cell from the flow plate. However there is a large pressure drop from inlet to outlet and the pressure is not distributed evenly within the flow field. This could cause issues such as dehydration of the membrane and GDL and lead to MEA damage. This flow plate was assigned for manufacture to draw conclusive results from experimentation, discussed Chapter 6.

5.2.1.15 Interdigitated flow plate CFD model

The interdigitated flow plate, as shown in Figure 100, has been studied in literature but a full analysis of the operation of this flow plate was not readily available in literature. In the process of understanding the operation of all flow plate designs this flow plate is modelled and simulated and the knowledge gained used to develop other flow plate designs.
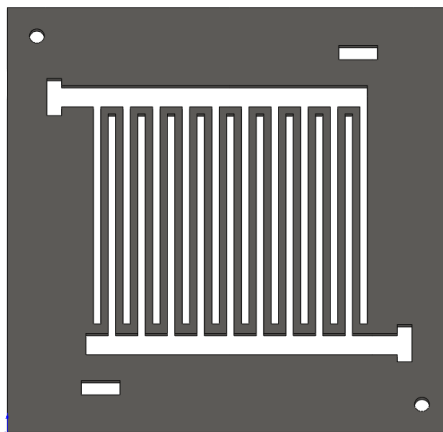
Figure 100 Interdigitated flow plate design.

This interdigitated flow plate design is dead ended flow plate with 1mm ribs and channels (1mm deep). This means that inlet air/hydrogen enters the inlet flow field, the fluid is then forced through

the GDL and then exits the GDL into the outlet flow field and finally the fluid exits the flow plate. For this flow plate to be modelled three separate parts are necessary; the inlet flow field, the GDL and the outlet flow field. The three of these parts are assembled as shown in Figure 101. To ensure a realistic model the GDL is modelled as a porous media with a permeability of $10e^{-10}m^2$ [53].
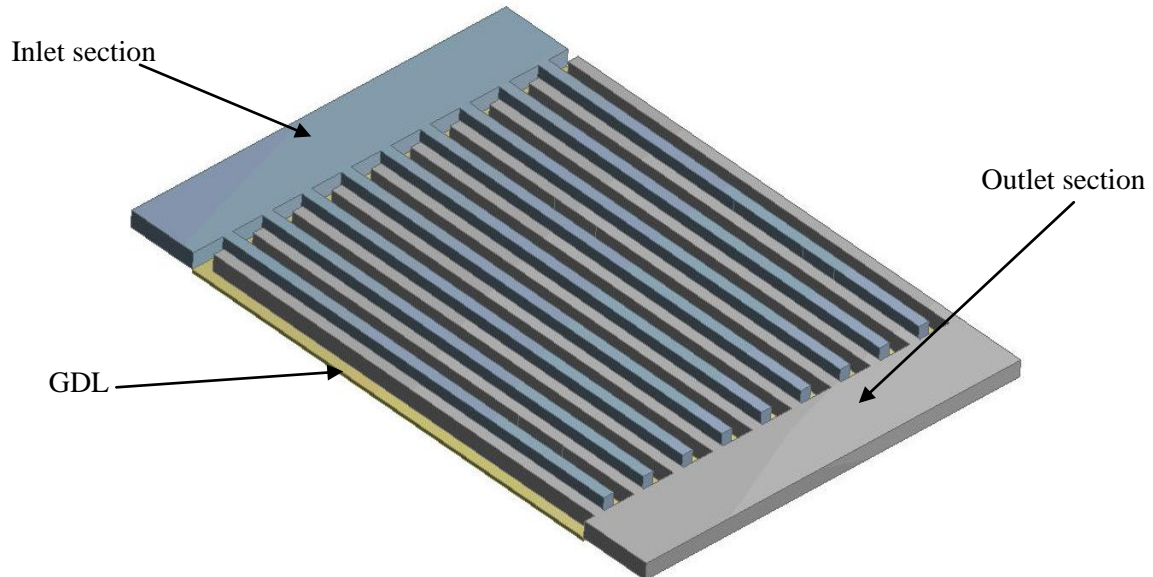
Figure 101 Interdigitated flow plate model assembly.
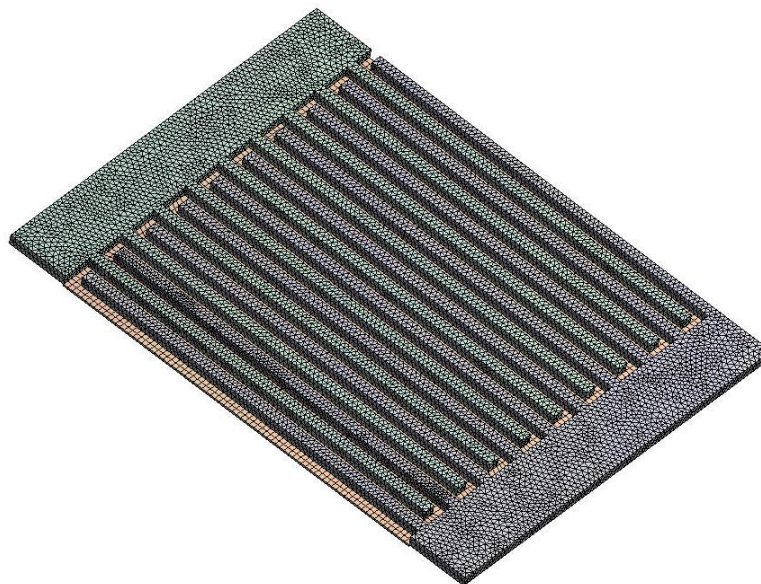
Figure 102 Interdigitated flow plate model assembly mesh.

The inlet pressure of the interdigitated model is expected to be high compared to the outlet channel pressure due to the flow of fluid through the GDL and not just through channels as in the previous models.

5.2.1.16 Interdigitated flow plate simulation results

The pressure at the inlet of this model is very large, owing to the air being forced through the GDL. This pressure, as discussed in the literature review, can aid in the removal of water droplets from the flow fields. Pressure variances are evident at the rib/channel and GDL interface.
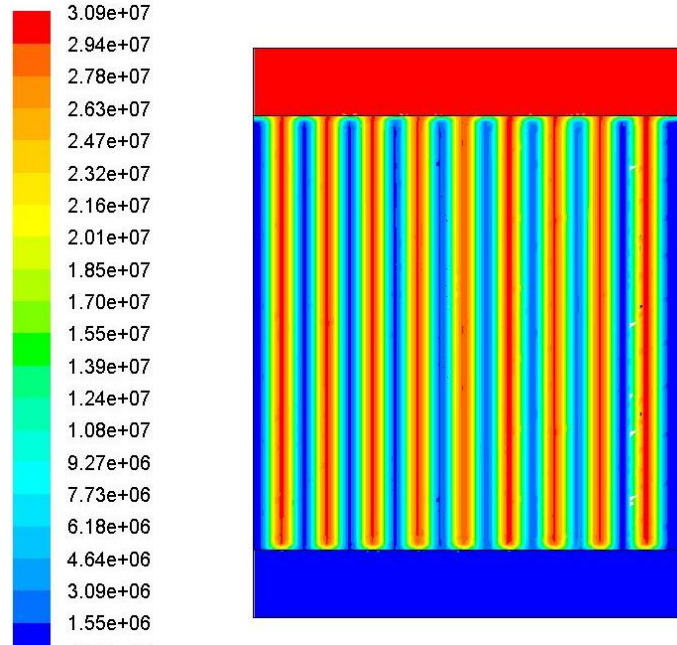
Figure 103 Pressure (pa) through the interdigitated flow plate model.

However large pressure losses can cause parasitic power and efficiency losses in the PEM fuel cell.
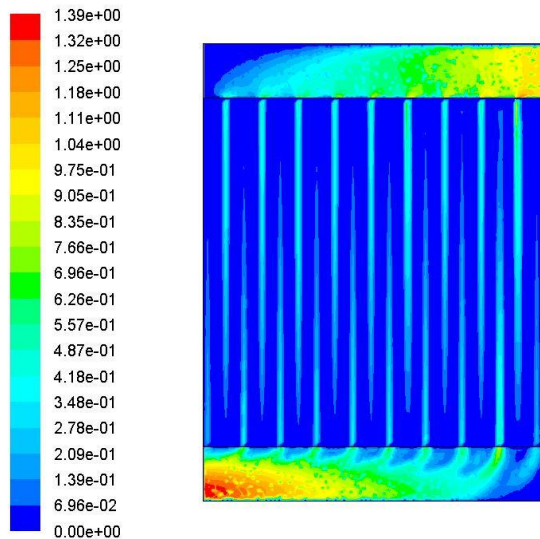
Figure 104 Velocity (m/s) through the interdigitated flow plate model.

Velocity flow is generally low, due to the slow flow of fluid through the GDL. The velocity is also distributed evenly throughout the flow field which can ensure that all channels receive fuel or oxidant.

It is noticed in the velocity vector plot, Figure 105, that this flow plate design ensures fuel or oxidant is effectively received at the central region of MEA. Most convective flow takes place at this region of the flow field. This flow plate was not manufactured but future studies could investigate this flow plate design further.
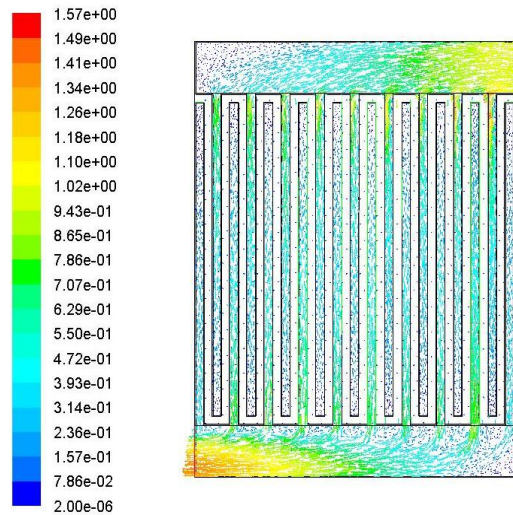
Figure 105 Velocity vectors (m/s) through the interdigitated flow plate model.

5.2.1.17 Modified interdigitated flow plate CFD model

The modified interdigitated flow plate (developed during this thesis) is similar to the normal interdigitated flow plate however the inlet and outlet channels are tapered. Each channel is 2mm wide at the inlet and tapers to 1mm which also reduces the number of channels by two in the flow plate as compared to the normal interdigitated flow plate. This design could ensure a lower inlet pressure which would be advantageous to the PEM fuel cell. The same modelling and simulation procedure was followed as with the interdigitated flow plate model.

(a)   (b)
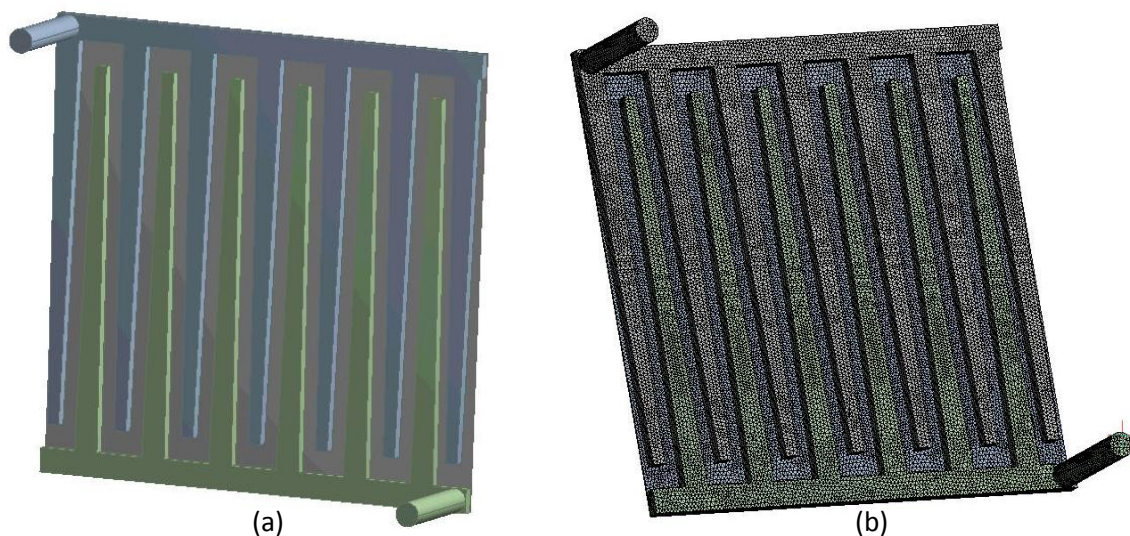
Figure 106 Modified interdigitated flow plate design (a) Model (b) Meshed model.

5.2.1.18 Modified interdigitated flow plate simulation results

The inlet pressure in Figure 107 is much lower than that of the normal interdigitated flow plate. It is also noticed that the pressure gradient from inlet to outlet is more evenly distributed than that of the normal interdigitated flow plate.
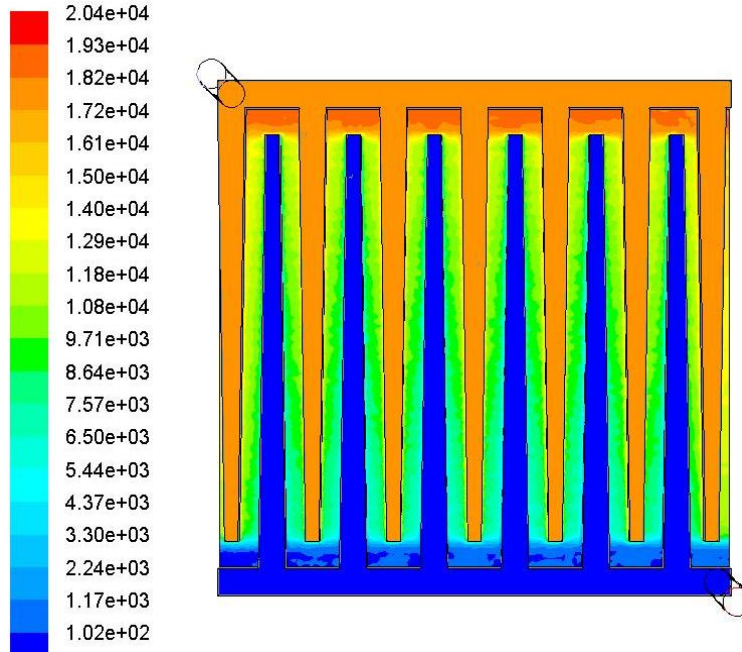
Figure 107 Pressure (pa) through the modified interdigitated flow plate model.

Velocity flow is low, due to the slow flow of fluid through the GDL, but higher than that of the normal interdigitated flow plate. The velocity is also distributed evenly throughout the channels which can ensure that all channels receive fuel or oxidant.
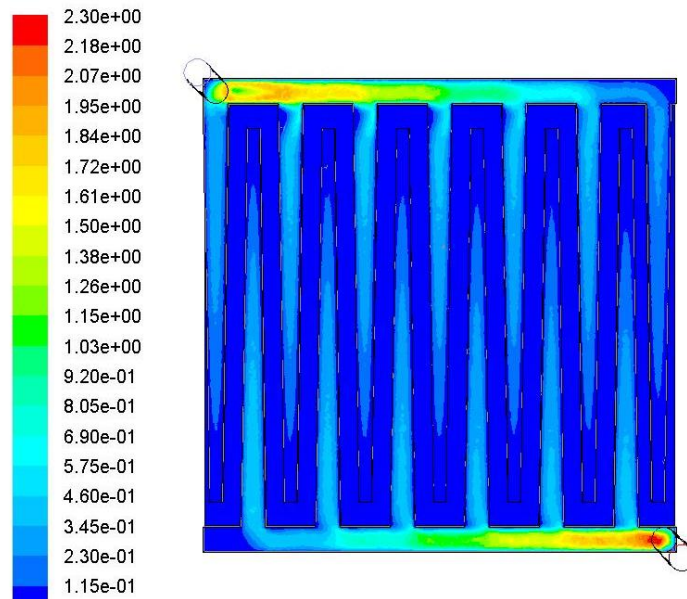
Figure 108 Velocity (m/s) through the modified interdigitated flow plate model.

Unlike the normal interdigitated flow plate, the modified/tapered interdigitated flow plate has a more even distribution of velocity flow in the full flow field, not necessarily the central region of the flow field as shown in Figure 109. This flow plate was not manufactured but future studies could investigate this flow plate design further.
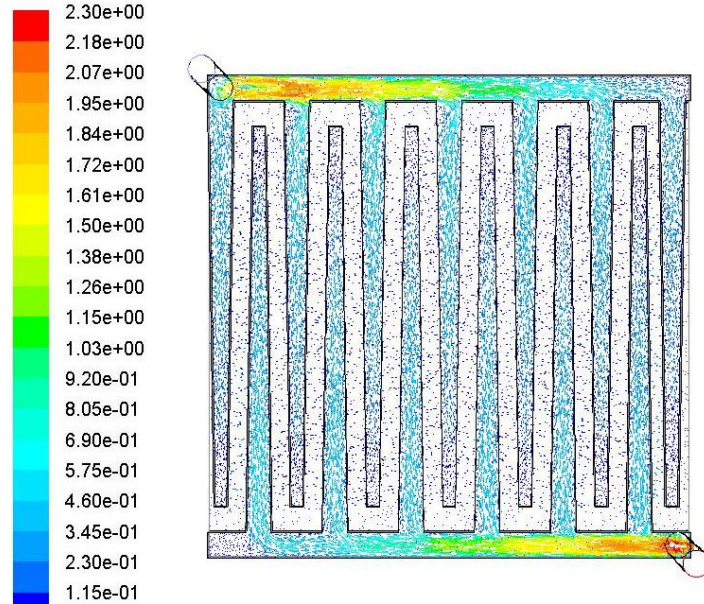
Figure 109 Velocity vectors (m/s) through the modified interdigitated flow plate model.

5.2.1.19 Spiral & vein flow plate CFD models

Figure 110 shows two dead ended flow plate designs. These designs are based on biome metric designs from nature as well as bend designs from the serpentine and channel designs from other flow plates.
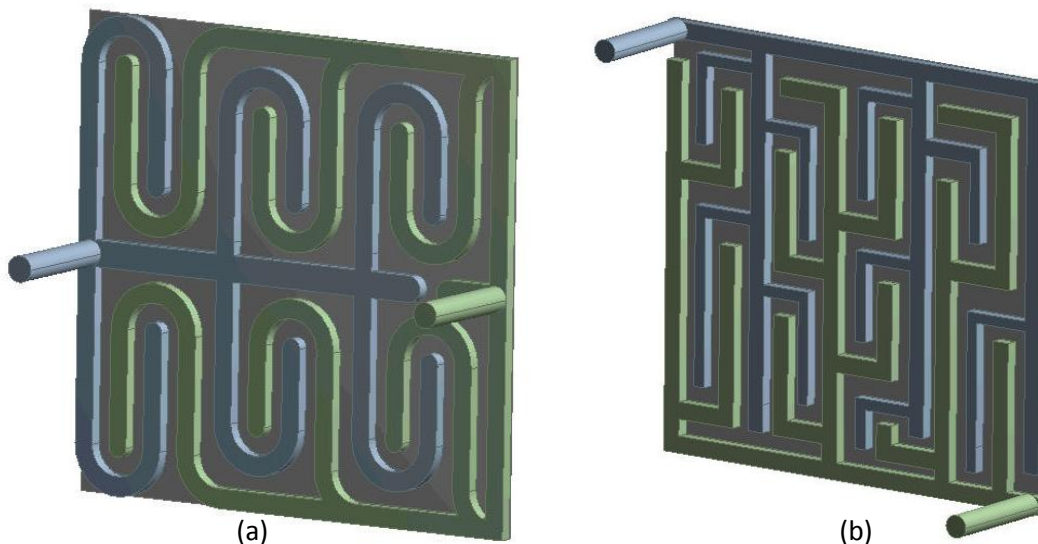
Figure 110 (a) Spiral flow plate design (b) Vein flow plate design.

A large 2mm inlet channel, with 1mm channels and bends branching from it, is incorporated into the spiral flow plate design. The vein design has branches of long and short 1mm channels to help ensure

even pressure and flow across the MEA. These dead ended designs could ensure low pressure drop compared to the normal or modified interdigitated flow plate designs. The same modelling and simulation procedure was followed as with the interdigitated flow plate model.

5.2.1.20 Spiral & vein flow plate simulation results

The inlet pressure of the spiral design is higher than that of the modified/tapered interdigitated flow plate and minimal pressure interaction is noticed around the ribs or channels and GDL as compared to the modified/tapered interdigitated flow plate.

The inlet pressure of the vein flow plate is higher than that of the modified/tapered interdigitated flow plate but still low compared to other designs. There is pressure interaction noticed around the ribs or channels and into the GDL.
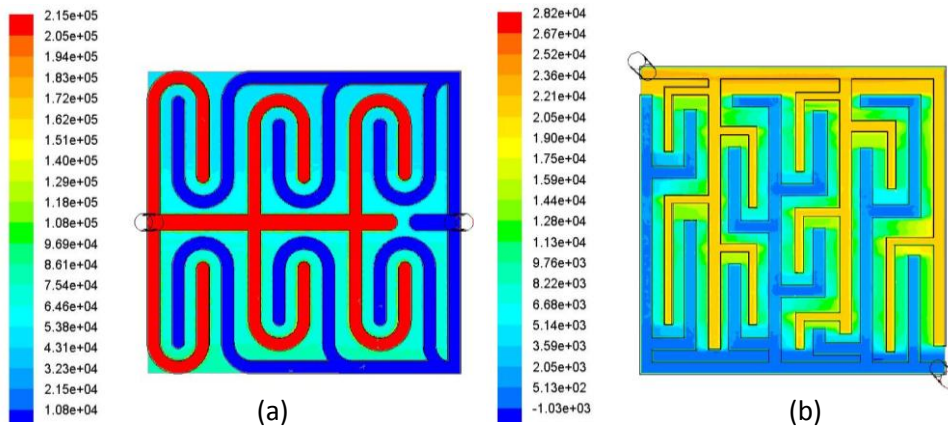
Figure 111 Pressure (pa) through the (a) Spiral flow plate model (b) Vein flow plate model.

The spiral flow plate velocity flow is poor with most of the inlet fluid taking the central channel with minimal distributed flow in the rest of the flow field.

Again the vein flow plate has minimal distributed flow in the flow field with two or three main channels taking all the fluid flow.
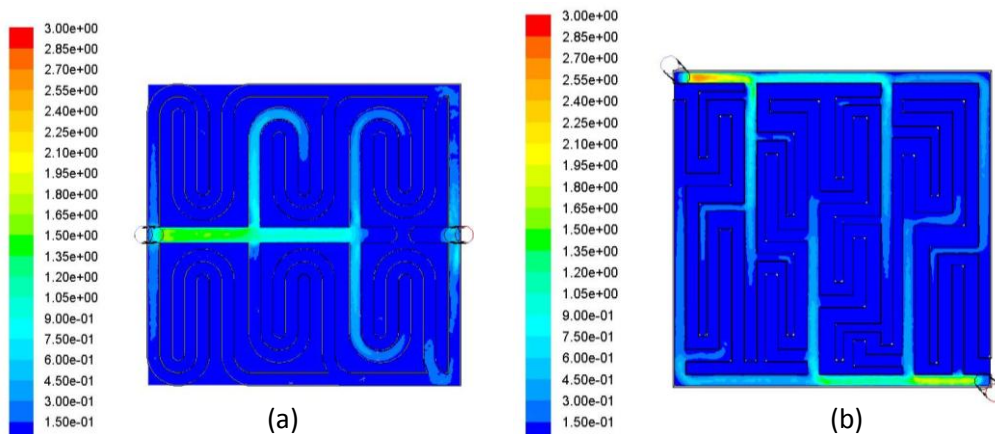
Figure 112 Velocity (m/s) through the (a) Spiral flow plate model (b) Vein flow plate model.

The velocity vectors, in Figure 113, confirm the poor fluid flow distribution. These flow regime and pressure results may not be suitable for a PEM fuel cell. These flow plates were not manufactured but future studies could investigate these flow plate designs further.
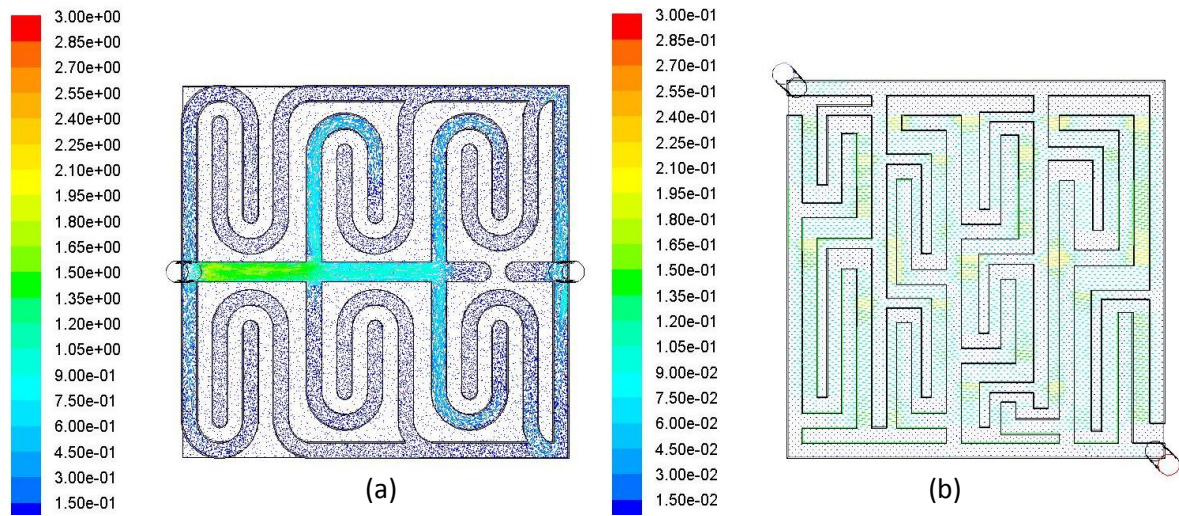
Figure 113 Velocity vectors (m/s) through the (a) Spiral flow plate model (b) Vein flow plate model.

5.2.2 Mini Channel VOF Model Development and Simulation Results

The operational parameters of a PEM fuel cell affect the degree of which flooding will occur. From literature the focus has been on droplet and micro-droplet release from the GDL or interaction within the flow field channels and due to different operational parameters there are discrepancies between models and experimental work performed by different researchers. However to ensure the correct approaches and methods are used to design effective flow channels, to aid the mitigation of water flooding, large water droplets after emergence from the GDL must be investigated and analysed.

In this study, two-phase flow models are developed and the coalescence of droplets and movement of slugs in flow field mini channels are investigated. The definition of a slug in this study is a large water droplet that adheres to either the GDL or channel wall and moves in air flow. A CFD analysis using the VOF method was carried out on various channel and bend designs of PEM fuel cell flow plates. Each simulation took about between 2 and 15 hours to complete, depending on the number of elements in each model. All models converged in fewer than 100 iterations. Flow regime, pressure analysis, velocity analysis and time sequenced interaction of water droplets and slugs in PEM fuel cell channels (straight, circular, parallel and connected) and material surfaces are recorded.

In addition with the aid of imaging techniques, visualisation of water droplets and slugs are recorded in an ex situ flow channels to ensure a realistic model. These results are shown in Section 5.4. The development of suitable models and the corresponding simulation results showing the implication of flow plate design on slugging and PEM fuel cell performance are described and viewed the following sections and the discussion is presented in Chapter 6.

5.2.2.1 2-D & 3-D straight channel model development

A model with a straight channel (1mm x 1mm x 20mm), as shown in Figure 114, was initially simulated in 2-D to investigate the flow of water droplets or slugs hydrophobic and hydrophilic GDLs or channels and the effect they may have on PEM fuel cell mass transport.
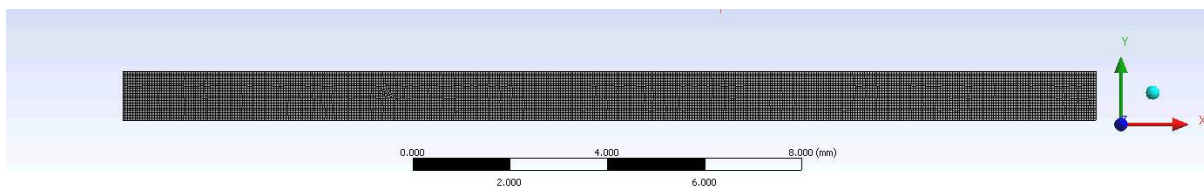
Figure 114 2-D model with a straight channel 1mm x 1mm x 20mm.

Grid independence was completed and these are shown in Figure 115 and Figure 116 and the correspondence of results in the CFD and experimental analysis matched very well.
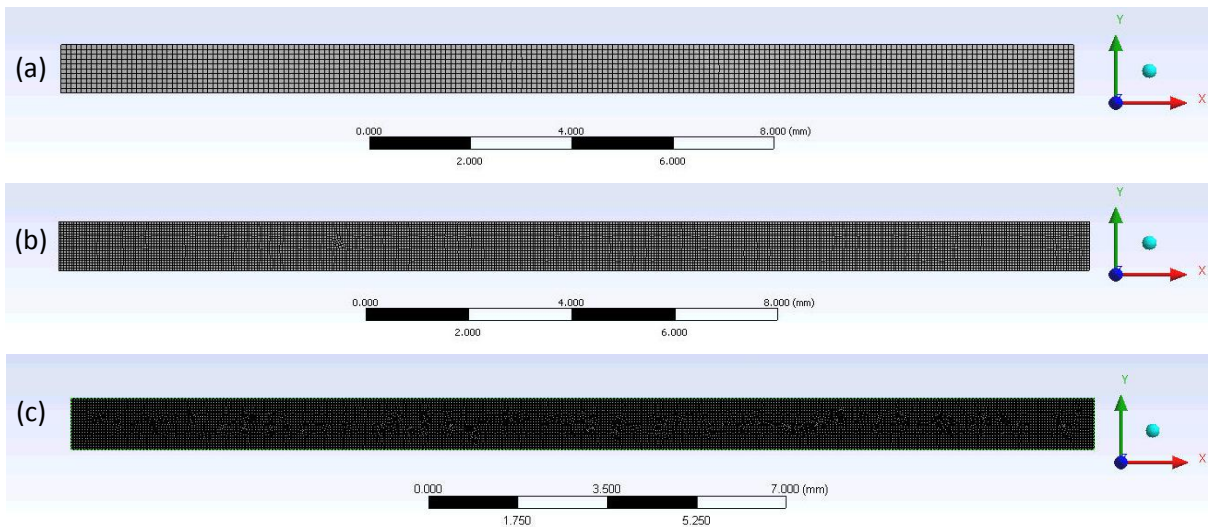
Figure 115 Grid independence of 2-D straight channel model (a) 2k 0.1mm grid (b) 8k 0.05mm grid (c) 33k 0.025mm grid.
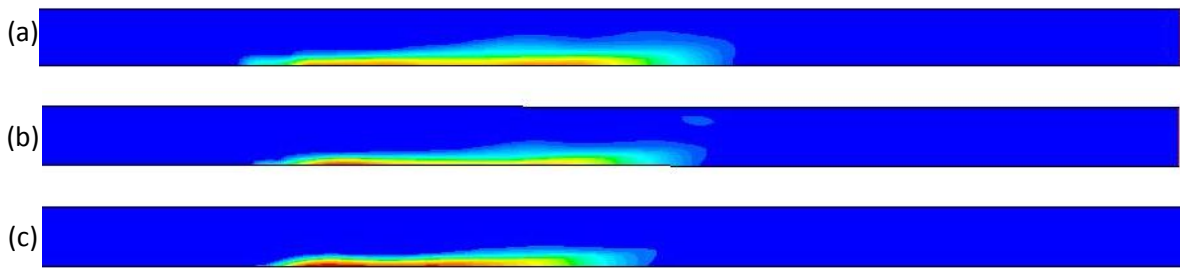
Figure 116 Grid independence results of 2-D straight channel model (a) 2k grid (b) 8k grid (c) 33k grid.

2-D models give limited detailed view of the water movement and the shapes and potential problem areas in the third dimension. A 3-D straight model and a 3-D double bend model were used to view the interaction of slugs and droplets more accurately. Figure 117 shows the schematic structure of the 3-D model with a straight channel used in the study. A grid independence study was conducted for the 3-D models as shown in Figure 118.
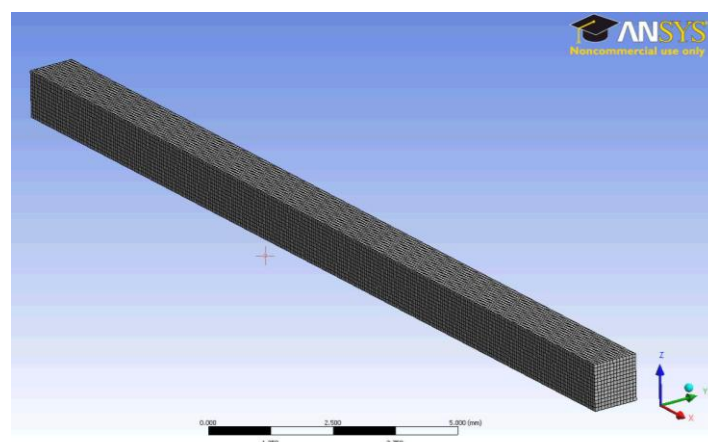
Figure 117 3-D straight channel model
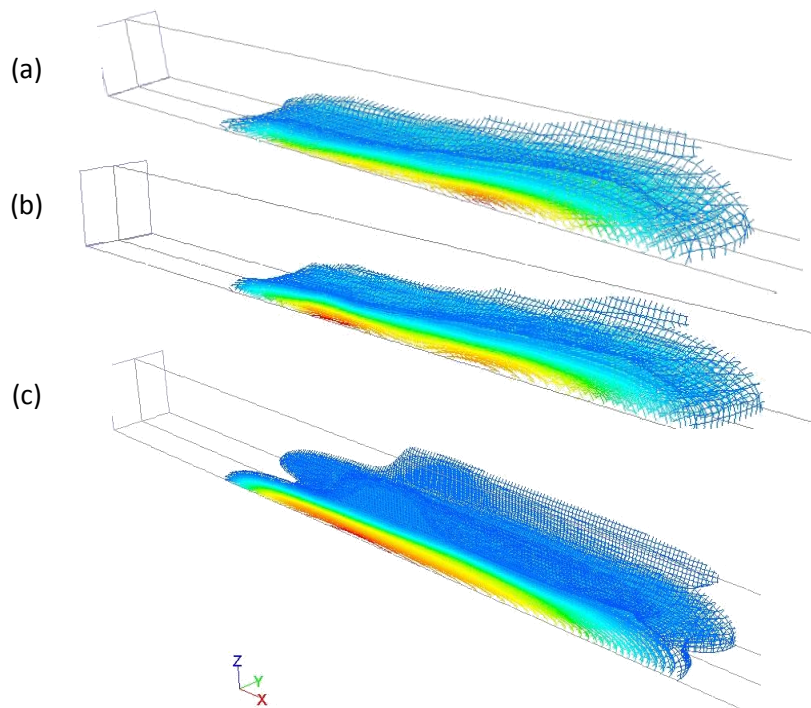
Figure 118 Grid independence results of 3-D straight channel model (a) 20k 0.1mm grid (b) 50k 0.05mm grid (c) 160k 0.025mm grid.

5.2.2.2 2-D & 3-D hydrophobic GDL simulation results

From literature hydrophobic and hydrophilic GDLs have many different advantages and disadvantages in relation to water mitigation in the PEM fuel cell.
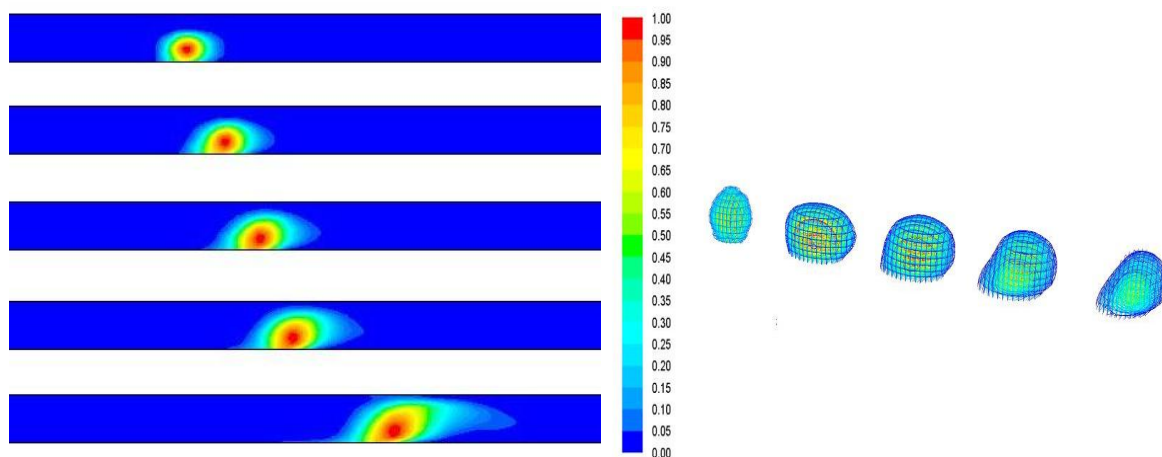
Figure 119 (a) 2-D & (b) 3-D time sequenced droplet (volume fraction) movement results on a hydrophobic GDL.

Figure 119 shows a 2-D and a 3-D time sequenced movement of a single water droplet in a straight channel (1mm x 1mm x 20mm) on a hydrophobic GDL (contact angle 20°). Both models show very similar results of droplet movement but with more accurate structure evident in the 3-D model Figure

119 (b). The 2-D model, Figure 119 (a), has a front trail but this is not as clear in the 3-D model or in observations, clarifying more accurate results can be obtained from the 3-D model.
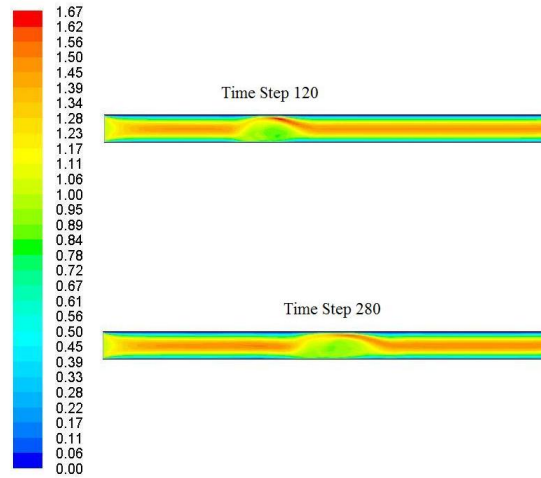
Figure 120 Velocity magnitude (m/s) in a straight channel with a droplet on a hydrophobic GDL at different time steps.

The fluid velocity was viewed in the 3-D model around the region where the droplet is positioned. A maximum velocity of 1.67m/s was highlighted over the droplet, but a calm 1.17 to 1.45m/s is seen in the rest of the channel at time step 280 (0.0056 sec), as the droplet is moved further down the channel its shape is altered and this increases or decreases the flow around it. One observation is that the droplet structure remains intact and no trail is seen where it has moved from. Once this droplet starts to moved it will be exhausted out of the cell quickly.

5.2.2.3 2-D & 3-D hydrophilic GDL simulation results

(a) (b)
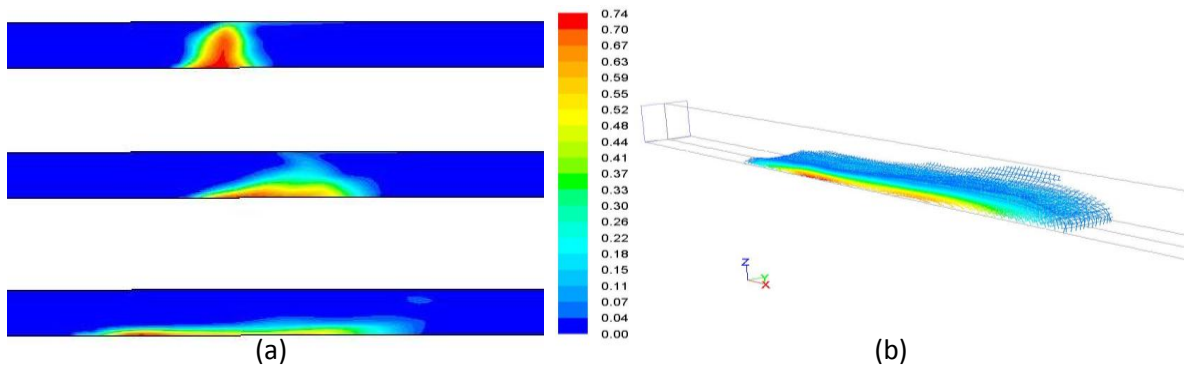
Figure 121 (a) 2-D (b) 3-D time sequenced droplet movement results on a hydrophilic GDL.

Figure 121 (a) shows a 2-D time sequenced movement of a single water droplet in a straight channel (1mm x 1mm x 20mm) on a hydrophilic GDL (contact angle 150°). Both models show very similar results of droplet movement but with more accurate structure evident in the 3-D model Figure 121 (b). The 2-D model, Figure 121 (a), has an undefined surface compared to the 3-D model or in observations, clarifying more accurate results can be obtained from the 3-D model.
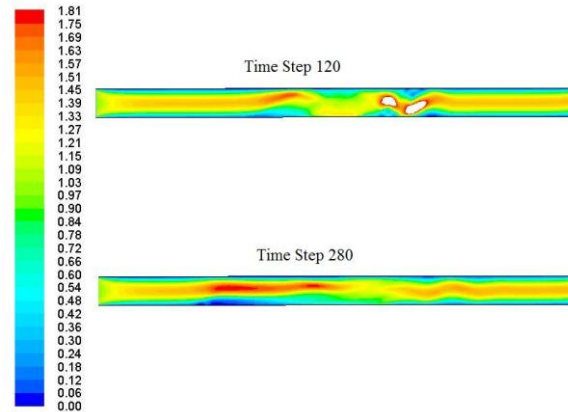
Figure 122 Velocity magnitude (m/s) in a straight channel with a droplet on a hydrophilic GDL at different time steps.

The fluid velocity was viewed in the 3-D model around the region where the droplet is positioned. A maximum velocity of 1.81m/s was highlighted over the droplet and a velocity of 1.1 to 1.6m/s is seen in the rest of the channel at time step 280 (0.0056 sec), as the droplet is moved further down the channel its shape begins to flatten towards the GDL. An interesting observation is that the droplet slows down as it flattens. And it leaves a trail of water behind it. This can be seen to accumulate at the edges of the channels in 3-D model, Figure 121 (b). This water can severely affect the mass transport of gases into the MEA in this area.

5.2.2.4 2-D & 3-D double serpentine flow field model development

A double serpentine flow field was chosen for the simulation and experimental investigations. The serpentine flow field is a common flow channel and reported on well in literature. The advantage of this flow field is that it investigates the straight portion of the mini-channel (1mm^2) and the bend region of a mini-channel. In addition, the parallel channels will detect if a problem in one channel can affect the adjacent parallel channel.

The computation domain consists of a double serpentine flow channel with inlet and outlet and boundary wall specified to be hydrophobic or hydrophilic. The domain is patched with a drop or slug of water, volume fraction one. Each drop or slug was placed between 3mm and 5mm from the inlet and each had a diameter of between 0.3mm and 0.9mm. The model represents an operational PEM fuel cell flow field after approximately 80 minutes of fuel cell operation (according to Ous and Arcoumanis [102]).

A 2-D double serpentine model with separate inlet and outlets (1mm x 1mm x 20mm), shown in Figure 123, was initially used to view water and slug movement through the straight channel and bend channel regions.
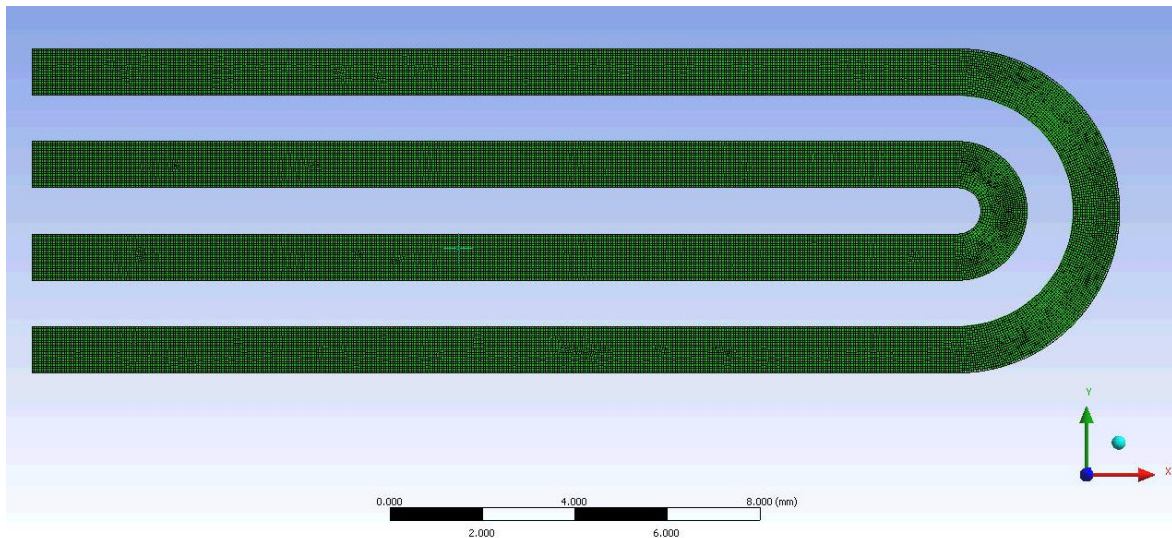
Figure 123 2-D double serpentine model with separate inlet and outlet.

A 3-D double serpentine model with separate inlet and outlets, as shown in Figure 124 was then developed. The 3-D model should allow a more accurate, time sequenced view of the droplet and slug formation and structure than the previous 2-D model.
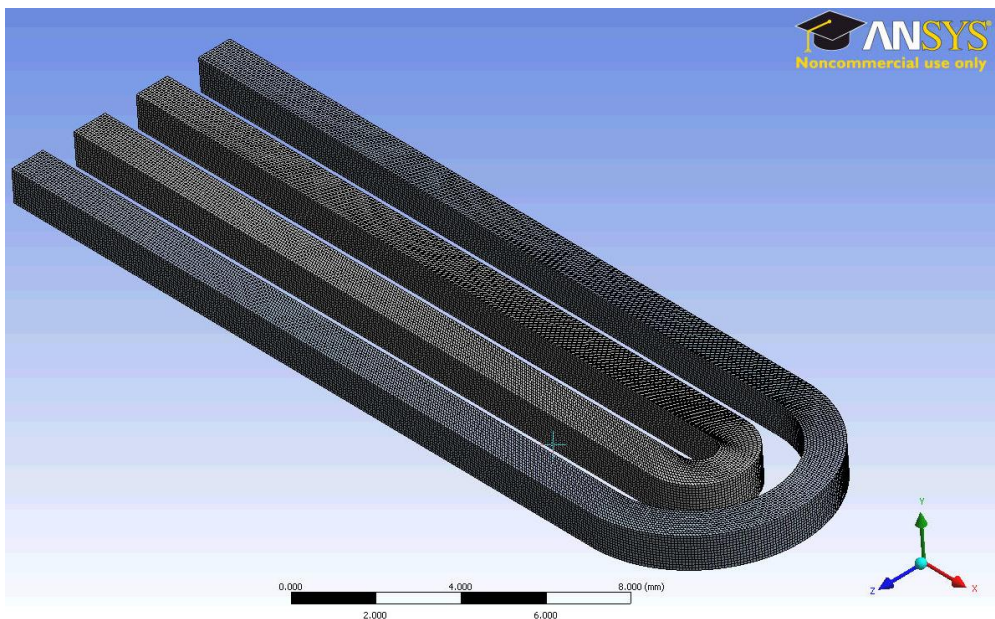
Figure 124 3-D double serpentine model with separate inlet and outlet.

5.2.2.5 2-D & 3-D double serpentine with separate inlet and outlet simulation results

The following simulation results show droplet movement using VOF 2-D and 3-D models in 1mm x 1mm x 20mm double serpentine channels with separate inlets and outlets.
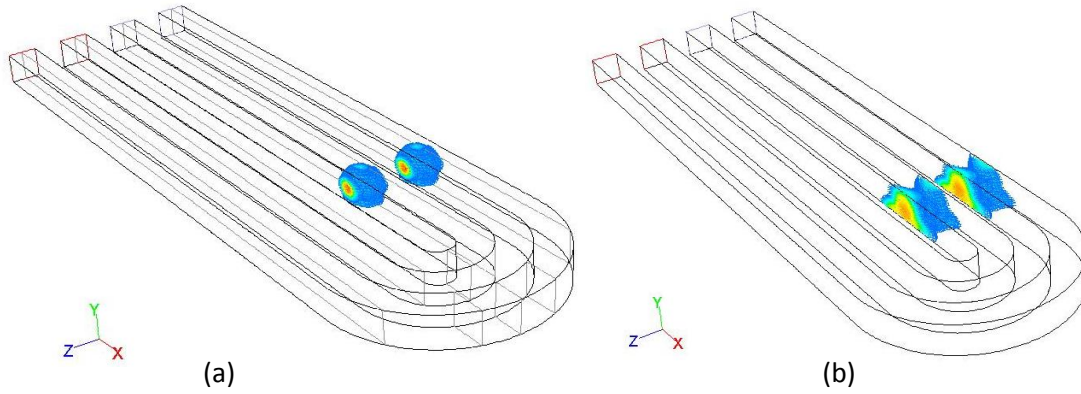
Figure 125 Droplet movement in channels at (a) 0.0002sec and (b) 0.0014sec.

Figure 125 shows the droplet movement from 40 to 280 time steps. The air flow distorts the droplet and flattens it toward the GDL. The GDL was made hydrophilic to view this phenomenon.
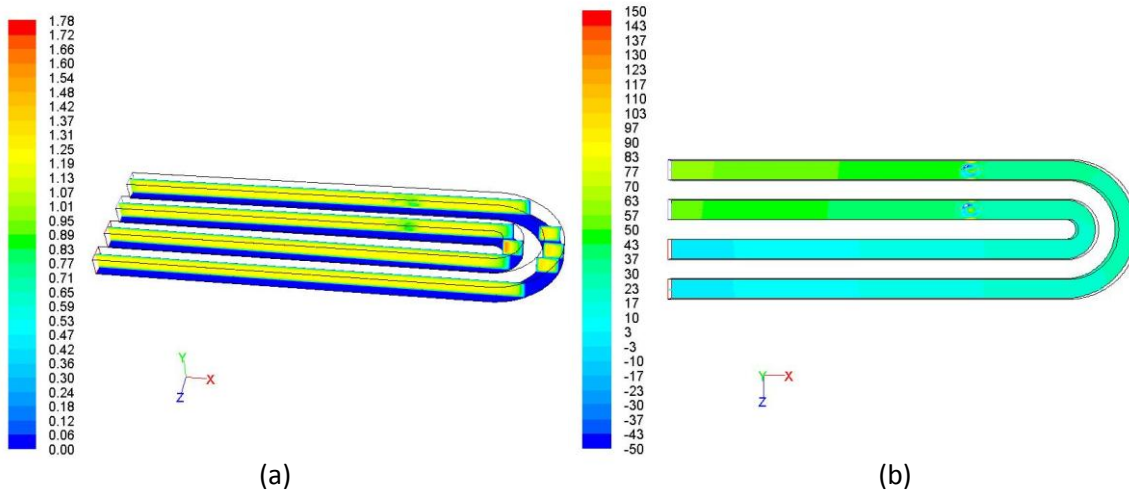
Figure 126 Droplet movement in channels & bends (a) Pressure (pa) (b) Velocity (at 2e^{-4}sec)

Figure 126 shows the pressure and velocity within the channel at time step 40 (0.0002sec). It was observed that pressure remained constant throughout the simulation, with no major blockages evident, even at the bend regions, Figure 127.
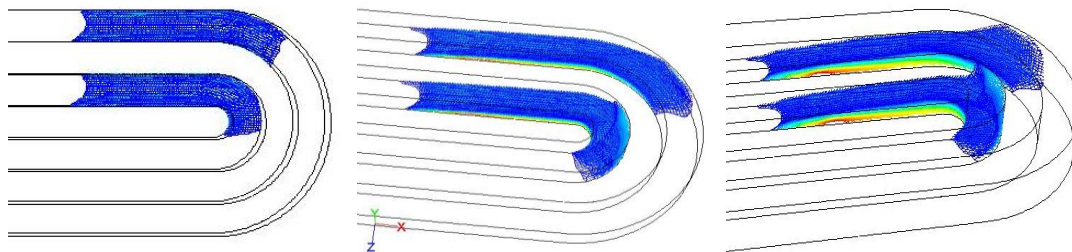
Figure 127 Different views of the same droplet after flattening in channels at 0.012sec (0.2 to 0.6 volume fraction).

The followings simulation results show droplets after forming and joining into a slug. This slug is viewed using VOF 2-D and 3-D models in a 1mm x 1mm x 20mm double serpentine channels with separate inlets and outlets.
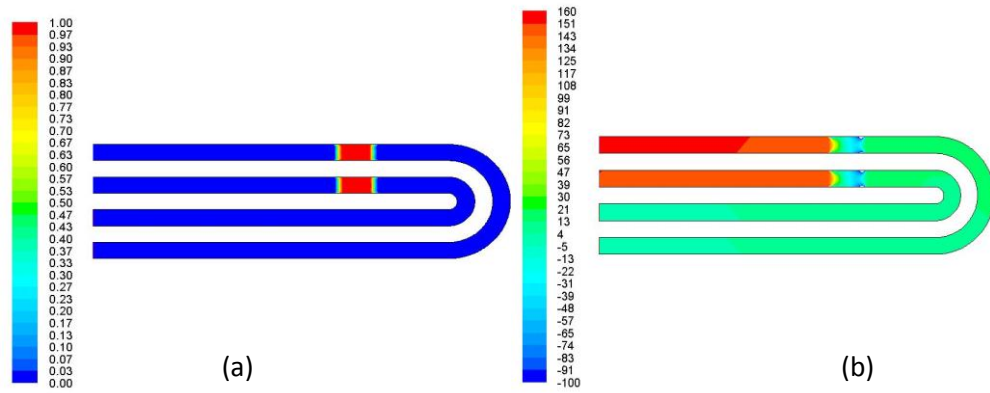
Figure 128 Slug movement in channels & bends (a) Volume fraction of water (b) Pressure (pa).
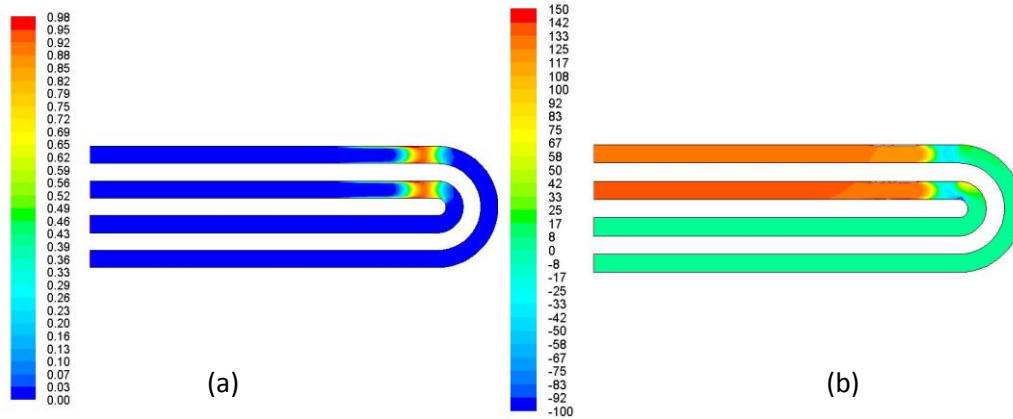
Figure 129 Slug movement in channels & bends (a) Volume fraction of water (b) Pressure (pa).
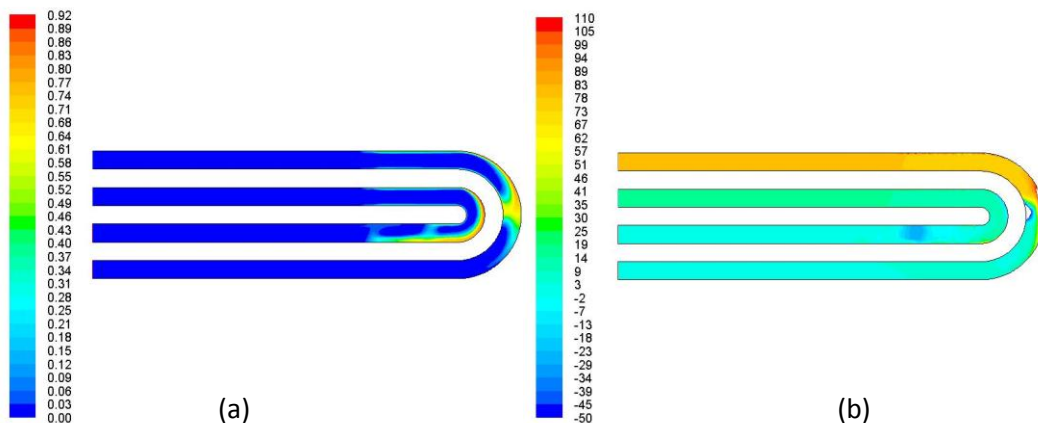
Figure 130 Slug movement in channels & bends (a) Volume fraction of water (b) Pressure (pa).

Figure 131 Slug movement in channels & bends (a) Volume fraction of water (b) Pressure (pa).

From the sequence of images from Figure 128 to Figure 131 it is evident that when a blockage such as the joining of droplets into slugs as above occurs, pressure can suddenly build up in the channels before the blockage and pressure can be very low after the blockage. This then drags the slug towards the outlet very fast, in the order of milliseconds. With the serpentine channel the bend causes an uneven movement of the water slug as shown in Figure 129 (a) in the small inner channel. One side of the slug stretches towards the bend, which allows fluid flow to move past the slug. The slug stretches further flowing down the channel as seen in Figure 130 (a). This in turn, relieves the pressure in the channel as shown in Figure 130 (b). Eventually the same happens to the larger outer channel.

5.2.2.6 3-D double serpentine model layout with mutual inlet and outlet

The model in Figure 132 simulates a double serpentine flow field channel with mutual inlets and outlets. The interaction between droplets and slugs in parallel channels and bends with relation to velocity and pressure measurements should be visible with this model.
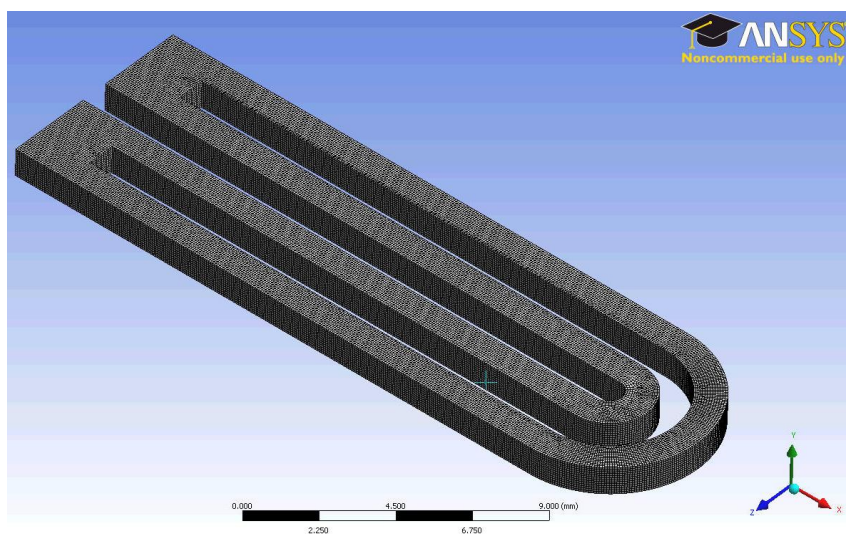
Figure 132 3-D double serpentine model with mutual inlet and mutual outlets.

The total number of cells used in the complete double serpentine model was about 268,000 and each simulation took about five hours to complete. The model converged in fewer than 65 iterations. Grid independence was completed. Please refer to Table 11 for model boundary conditions.

Table 11 Data used for double serpentine flow field model set up.

Multiphase model	**VOF**
Model design	**Double serpentine**
Computation grid	**20 x 1 x 1 mm**
Grid size	**0.05mm**
Scheme	**Explicit**
Phase 1	**Air**
Phase 2	**Water**
Solver type	**Pressure -based**
Time	**Transient**
Temperature (constant)	**328K**
Gas phase	**Ideal mixture**
Fluid flow	**Laminar**
Gravity	**(z) -9.81ms^{-1}**
Number of time steps	**2000**
Time step	**0.00001 sec**
Drop radius	**0.5 mm**
Initial drop position	**(x, y, z) = (2, 0.1, 0.5)**
Inlet velocity	**1 ms^{-1}**
Inlet pressure	**2 bar Gauge**
Outlet Pressure	**0 Bar Gauge**
6 Pixels	**1 mm**
Wall wet	**150**
Wall no Wet	**20**
Interface Representation	**PLIC**
Surface tension	**0.073Nm**

5.2.2.7 3-D double serpentine model layout with mutual inlet and outlet simulation results

The following model investigated the movement of a droplet into a second droplet that is positioned on the channel wall. When both join a slug is formed as shown in Figure 133 (c). The effect of mutual inlet and outlet channels on the flow field is observed.
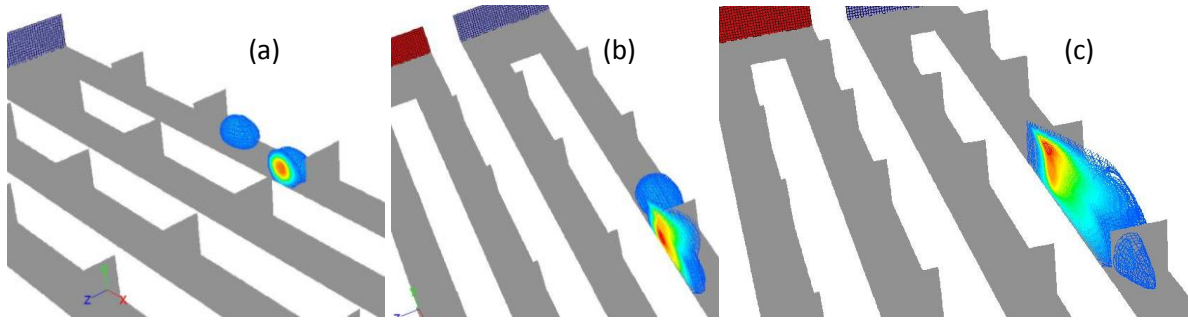
Figure 133 Droplets movement (a) Droplets move (Time step 40) (b) Droplets join (Time step 120) (c) Slug formed (Time step 200)

Figure 134 Droplets movement (a) Velocity (m/s) (b) Pressure (pa) (Time step 40).

Figure 135 Droplets movement (a) Velocity (m/s) (b) Pressure (pa) (Time step 120).

From the time sequence analysis of velocity and pressure in Figure 134, Figure 135 and Figure 136, velocity increases around the droplets but also in the unblocked channel. Pressure builds up at first

and then as the droplets join and the channel blocks. Low pressure is then observed in the blocked channel, after the blockage.
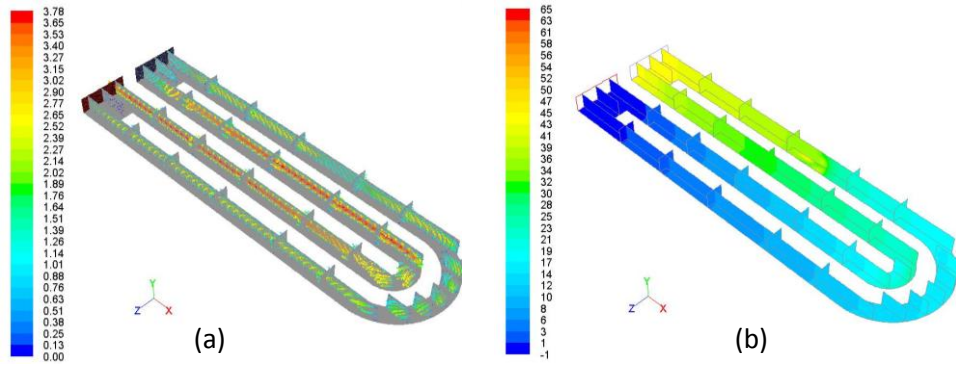
Figure 136 Droplets movement (a) Velocity (m/s) (b) Pressure (pa) (Time step 200).

What seems to occur is that due to the mutual inlet, the fluid in the blocked channel uses the other channel as a relief channel, increasing velocity and decreasing pressure across both channels. With increased velocity in the free channel pressure normalises as shown in Figure 136.

Three similar investigations were performed. Figure 137 shows the model with one side drop and one full drop in one channel and then with one drop in the parallel channel to investigate the fluid flow. Similar results were obtained from this model as shown in Figure 138.
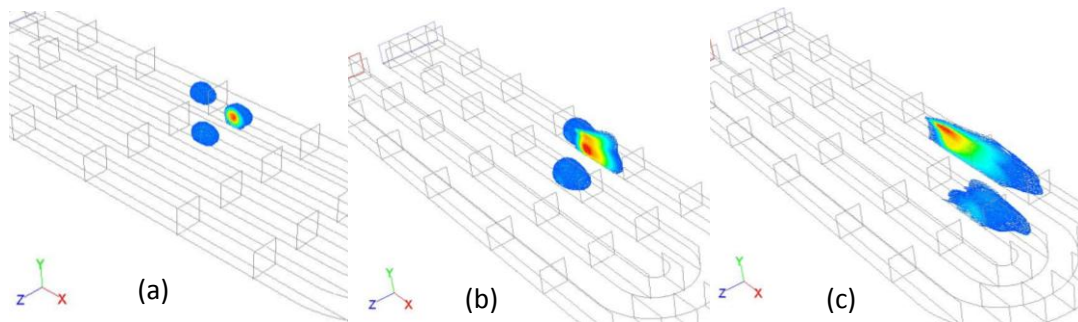
Figure 137 Droplets movement (a) Droplets move (Time step 40) (b) Droplets join (Time step 120) (c) Slug formed (Time step 200)
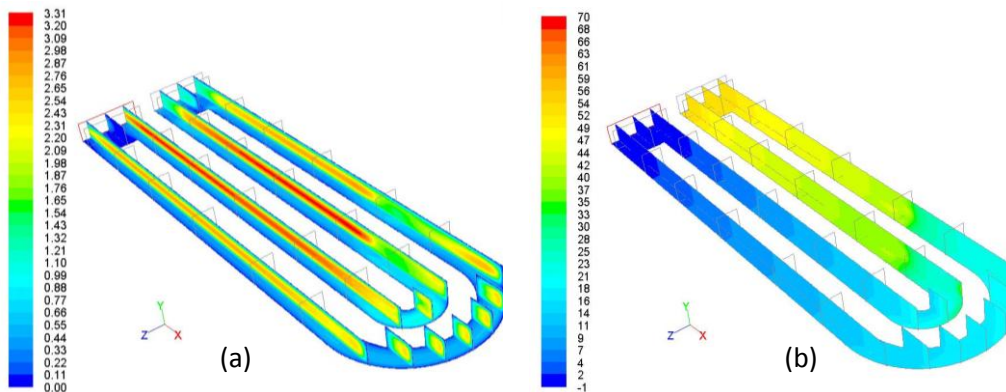
Figure 138 Droplets movement (a) Velocity (m/s) (b) Pressure (pa) (Time step 200).

Figure 139 shows the model with one large slug and one small slug in the other channel. Similar results were obtained from this model as shown in Figure 140. However, a larger pressure was noticed at the start of the sequence. Eventually the smaller slug burst due to the pressure. This increased the flow rate in this channel and relieved the pressure in the entire model as shown in Figure 140.
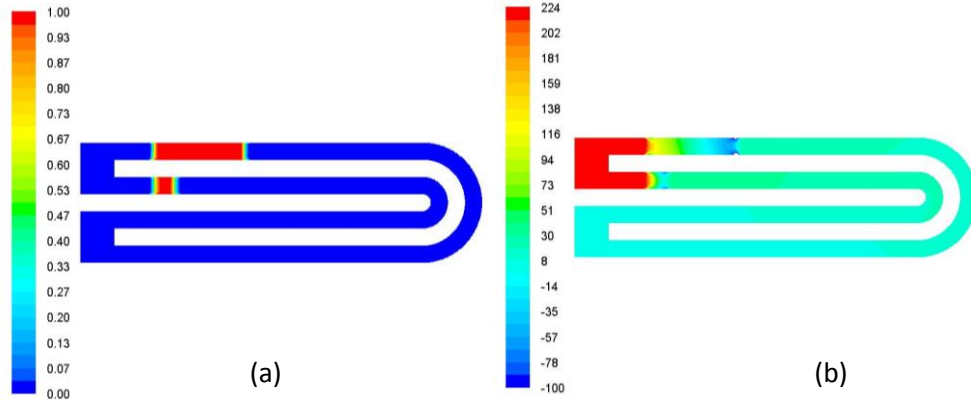
Figure 139 Slug movement in channels & bends (a) Volume fraction of water (b) Pressure (pa) (Time step 40).
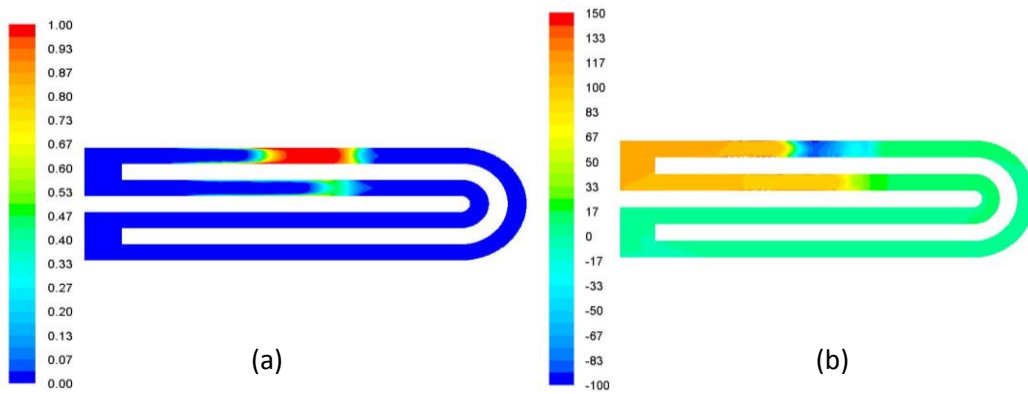
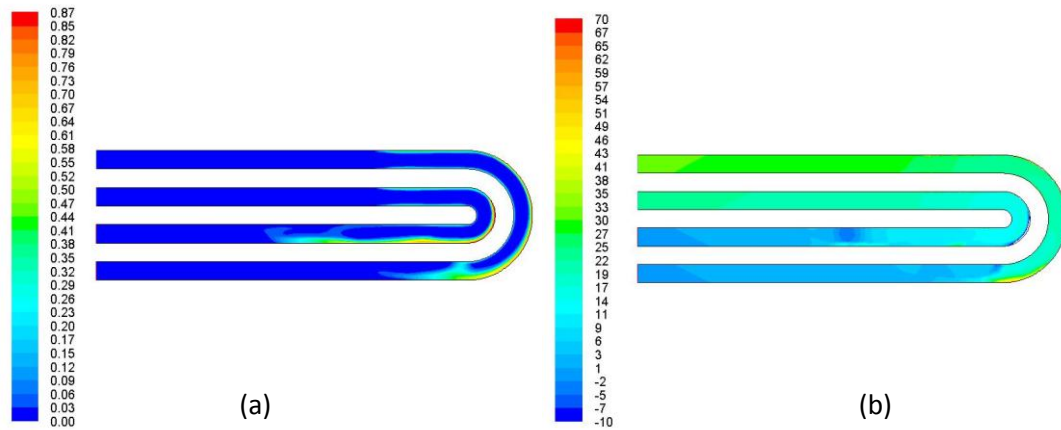**Figure 140 Slug movement in channels & bends (a) Volume fraction of water (b) Pressure (pa) (Time step 200).**
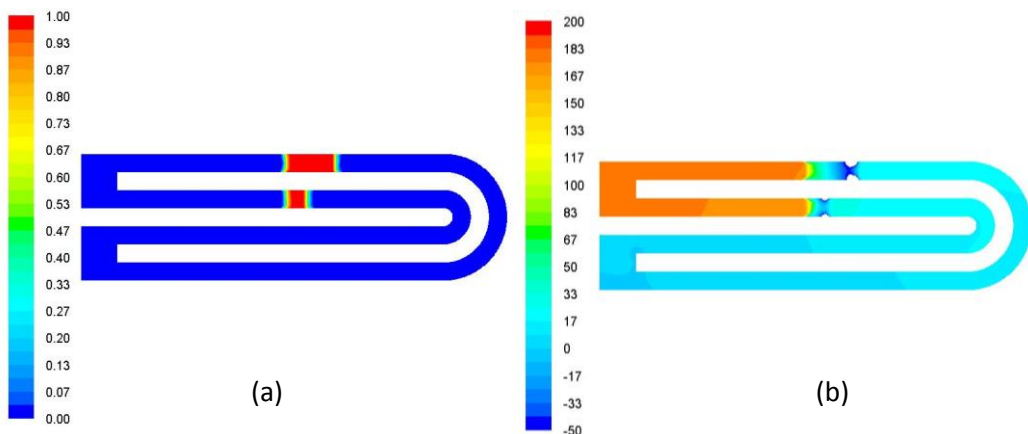
Figure 141 Slug movement in channels & bends (a) Volume fraction of water (b) Pressure (pa) (Time step 40).

Figure 141 shows the model with one medium slug and one small slug in the other channel. Similar results were obtained from this model as shown in Figure 142 with a larger pressure noticed at the start of the sequence. Eventually the smaller slug burst due to the pressure. This increased the flow rate in this channel and relieved the pressure in the entire model as shown in Figure 142.
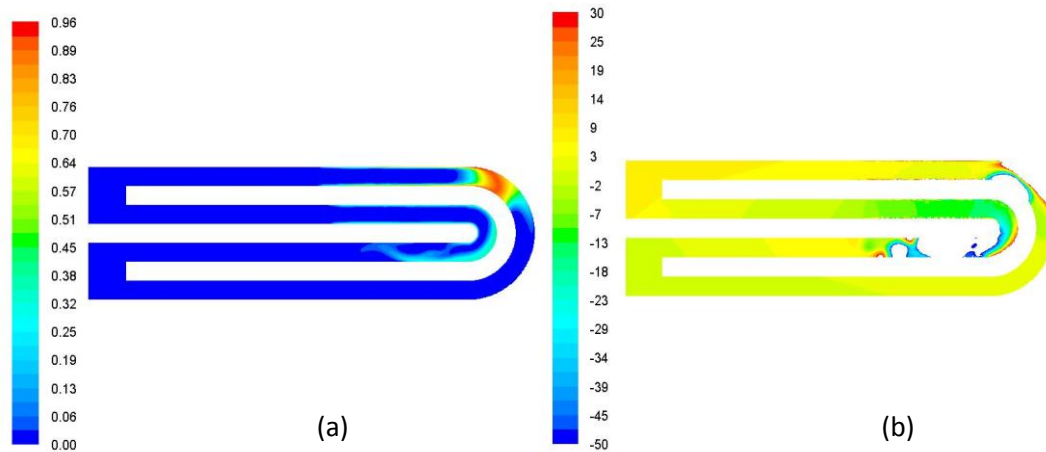
Figure 142 Slug movement in channels & bends (a) Volume fraction of water (b) Pressure (pa) (Time step 280).

5.2.2.8 3-D double serpentine model with mutual inlet and separate outlets development

The final model as shown in Figure 143 was designed to investigate if separate inlet and outlets of the double serpentine/ double parallel cause an issue with fluid flow or pressure build up or velocity of the fluid in each channel. The model also had a wider inlet as would be in a real PEM fuel cell inlet. These changes were created to investigate if the pressure balance from the outlet had an effect on the pressure and velocity of the channels and ensure the previous model results were correct. In addition this model had a hydrophilic flow plate top channel and a hydrophobic GDL, as described by Buie et al. [124] and Jiao et al. [125]
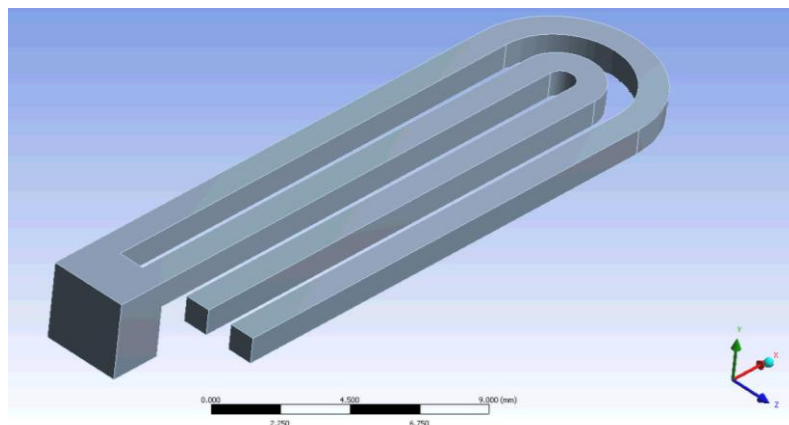
Figure 143 3-D double serpentine model with mutual inlet and separate outlets.

5.2.2.9 3-D double serpentine model with mutual inlet & separate outlets simulation results
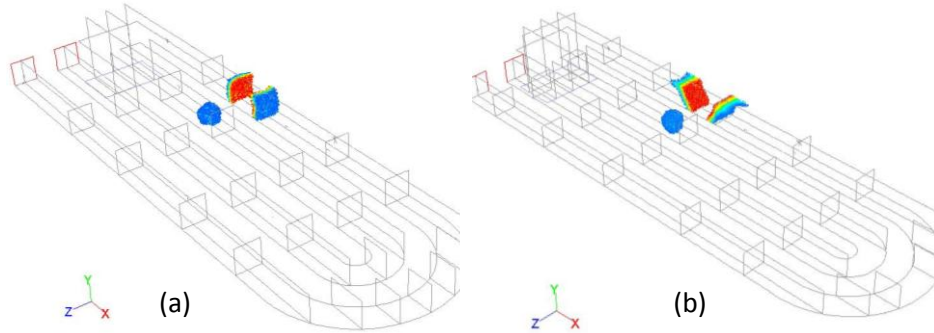
Figure 144 Droplets movement (a) Droplets (Time step 0) (b) Droplets (Time step 40)

A large droplet was positioned in one channel and a smaller drop was positioned on the surface of the GDL in the second channel as shown in Figure 144 (a). The first thing to notice is that due to the hydrophilic nature of the flow plate and the hydrophobic nature of the GDL the droplets move away from the GDL as shown in Figure 144 (b).
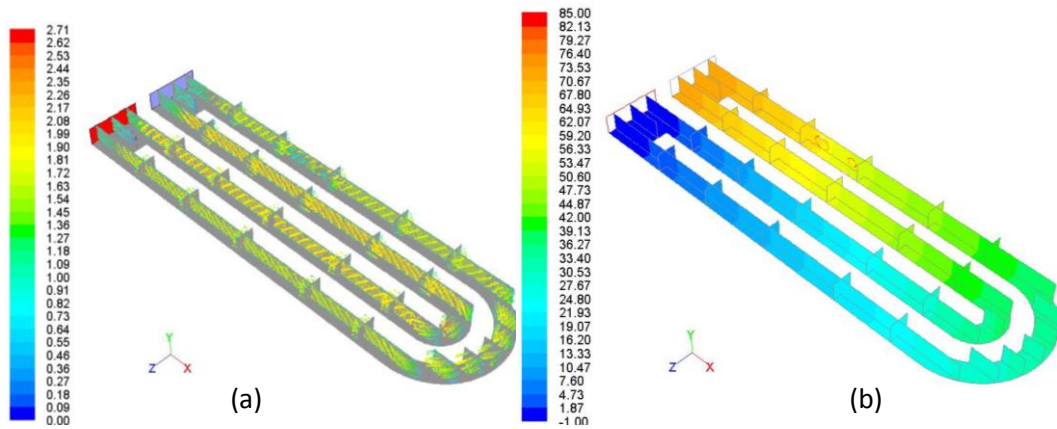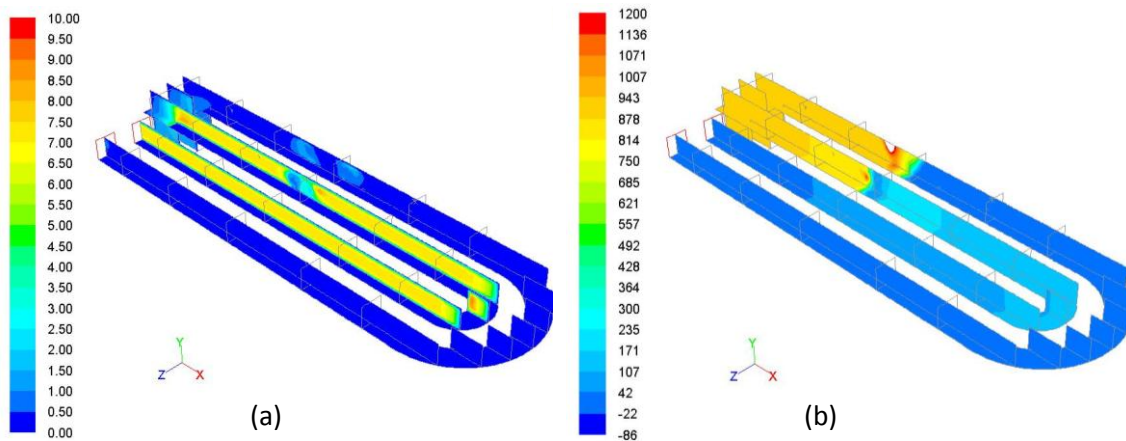

Figure 145 Droplets movement (a) Velocity (m/s) (b) Pressure (pa) (Time step 40).
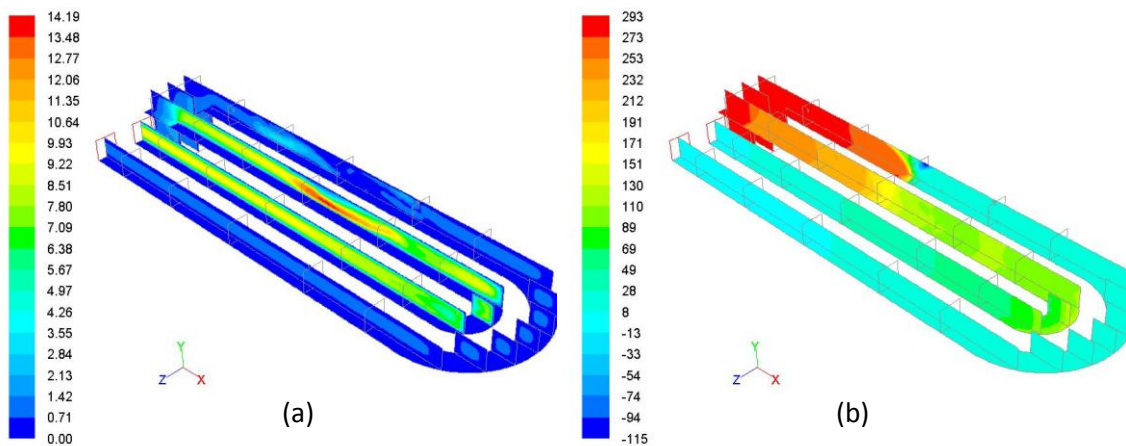
Figure 146 Droplets movement (a) Velocity (m/s) (b) Pressure (pa) (Time step 280).
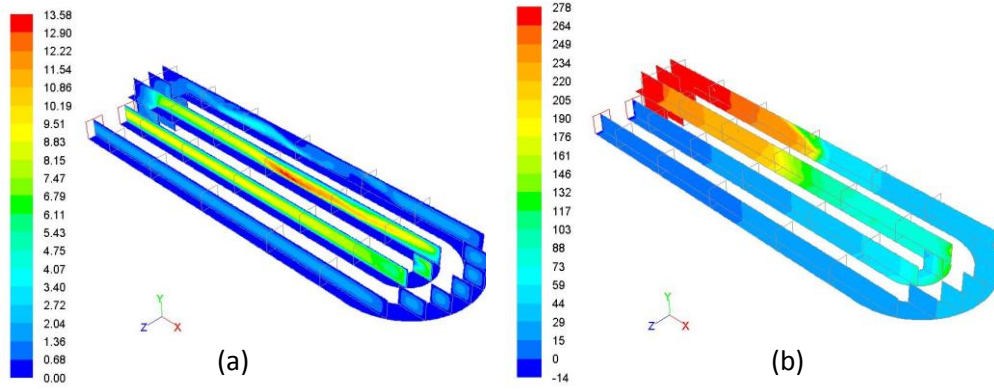
Figure 147 Droplets movement (a) Velocity (m/s) (b) Pressure (pa) (Time step 480).

From the time sequence as shown in Figure 145, Figure 146 and Figure 147 similar results were obtained from this model as compared to the previous model. Pressure builds up due to the slug in the channel blocking fluid flow in this channel. Fluid flow in the other channel with the small droplet increases and is very high around the drop. Figure 146 (b) shows the pressure decreasing in the blocked channel and increasing in the other channel, however, over time the pressure evens out over both channels similar to the previous models.

A further model was completed with small droplets as shown in Figure 148 and similar results were obtained as shown in Figure 148, Figure 149 and Figure 150.
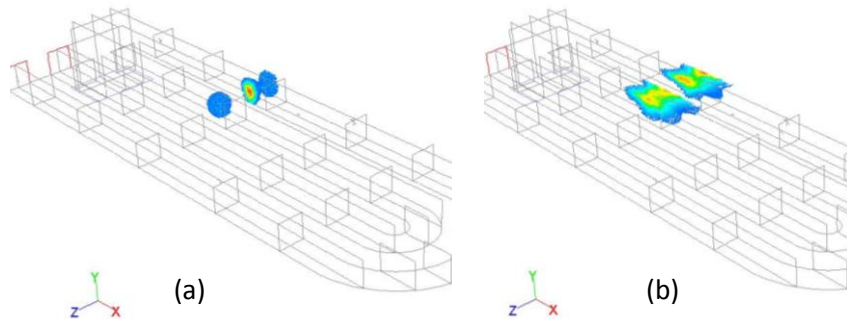
Figure 148 Droplets movement (a) Droplets (Time step 40) (b) Droplets (Time step 280)

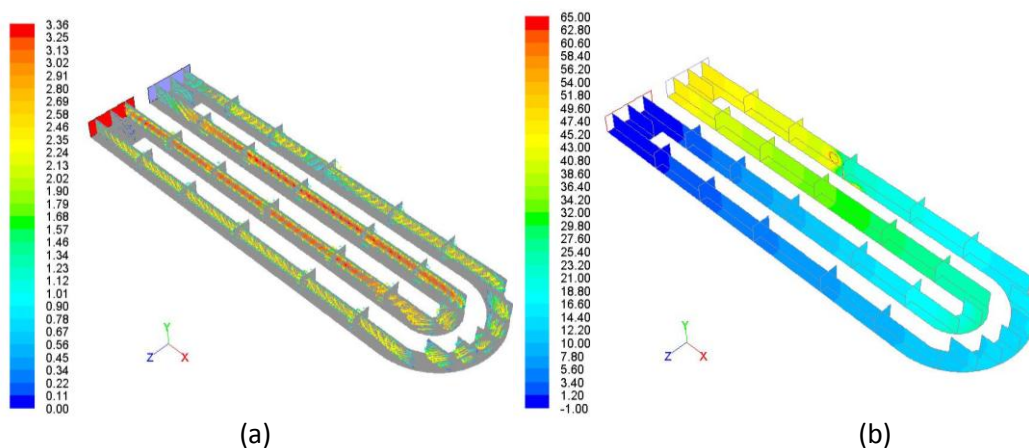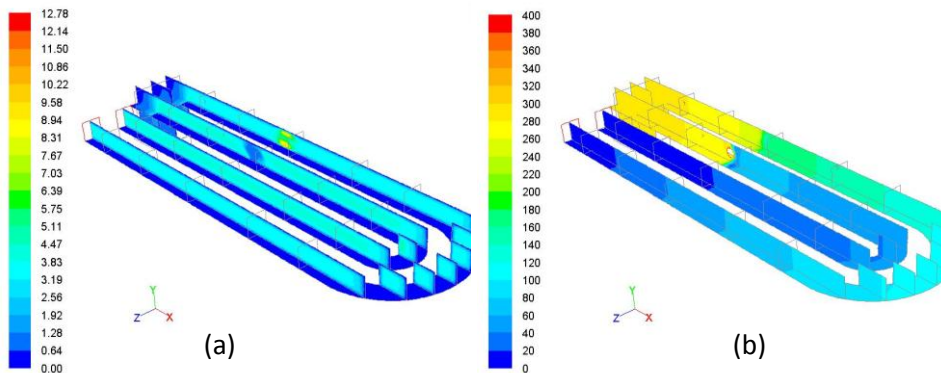**Figure 149 Droplets movement (a) Velocity (m/s) (b) Pressure (pa) (Time step 40).**
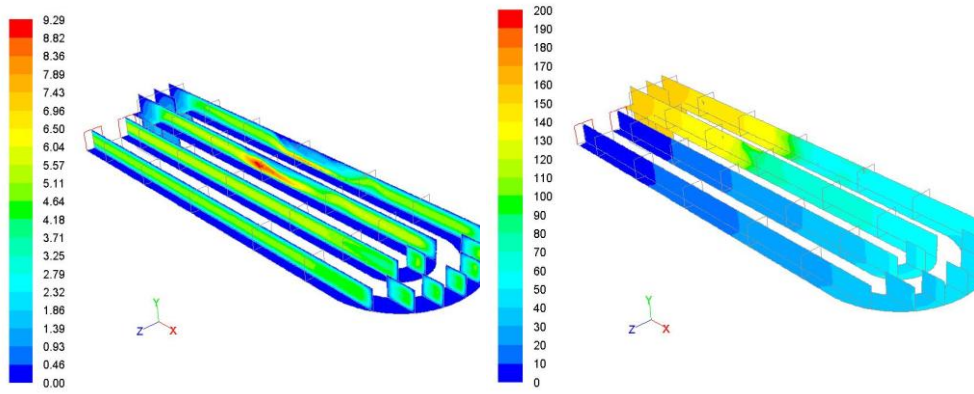
Figure 150 Droplets movement (a) Velocity (m/s) (b) Pressure (pa) (Time step 280).

Please refer to Chapter 6 for a full discussion of these results.

5.2.3 Open Pore Cellular Foam Model Development & Simulation Results

From literature open pore cellular foam material was identified as a possible suitable material for new innovative flow plates. Open pore cellular foam samples were obtained from ERG Aerospace Inc. [159] and initial testing was completed. However, a Representative Unit Cell Structures (RUCS) of open pore cellular foams was not been satisfactorily identified, modelled or simulated in literature and the advantages of open pore cellular foams material for flow plates in PEM fuel cells had not been analysed. This section develops a RUCS model and performs a CFD analysis on 10, 20, 30, 40, 45, 80 and 100ppi open pore cellular foams with relation to pressure drop and velocity flow in PEM fuel cell flow plates.

(Note: 40ppi metal foam has been used in the following calculations.)

5.2.3.1 Open pore cellular foam model development

Flows in porous media may be modelled using a macroscopic approach, where volume-averaged semi-empirical equations are used to describe flow characteristics, or a microscopic approach, where small scale flow details are simulated by considering the specific geometry of the porous medium [175]. In the first approach, small scale details are ignored and the information that could be lost, is represented in the governing equations using an engineering model.
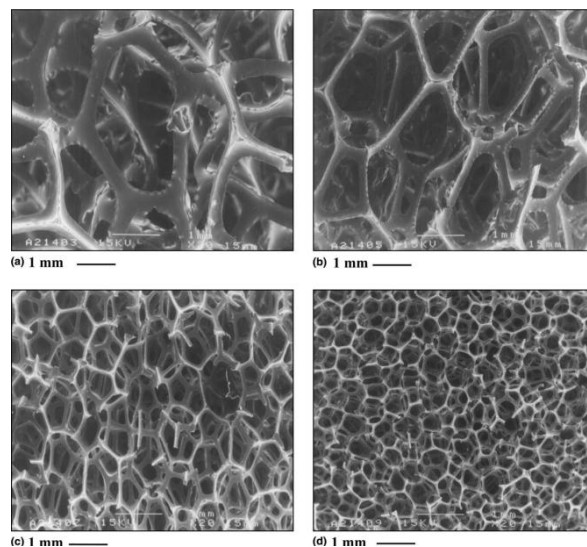
Figure 151 SEM micrograph of metal or RVC foam material [156]**.**

In the second, the intricate geometry of the porous structures, which may cause unpredictable flow patterns to develop and alter the outcome of an engineering model, is accounted for and the transport through these structures is computed. This approach is computationally expensive if the entire physical domain were to be simulated. However, if this approach is adopted a closer model to reality can be created and multi-physical phenomena can be viewed with greater precision and flow and mass

transfer predictions can be made more accurately. This study used a microscopic approach to model open pore cellular foams.

5.2.3.1.1 Representative unit structure development for open pore cellular foam

To aid the development of an idealised structure to represent the open pore cellular foam materials a review of literature was completed to view existing models and gaps in literature, please refer to Chapter 2. From this analysis many current idealised cell structures or Representative Unit Cell Structures (RUCS) were considered including, cylinders, spheres and the fourteen sided tetrakaidecahedron cell. Many of these models have had much analysis work already completed and their properties have been studied in depth but even with this knowledge some models have up to a 25% error between simulation pressure results and actual experimental results [179]. The discrepancy between the two sets of data may be attributed to the design of the RUCS, the design of the model, the simulation parameters, wall effects not accounted for or discrepancies in velocity and boundary conditions in the simulations. As outlined in the objectives in Chapter 1 and to fill an open gap in literature as outlined in Chapter 2, it is the aim of this thesis to design a RUCS for open pore cellular foam materials, develop this into a model and simulate the model to characterise these relatively new materials for future designers and modellers with application to PEM fuel cells.

Researchers such as Ozmat et al. [167] have noted that the isotropic open pore cellular foam consists of randomly oriented polygon shaped cells that could be approximated by a dodecahedron Figure 152. SEM images produced by Friedrich et al. [156] also show the dodecahedron shape Figure 151. This idealised structure has not been mentioned adequately or modelled satisfactorily in literature. To that end the dodecahedron has been used as an idealised structure to represent the foam cells in the following analysis of these materials.
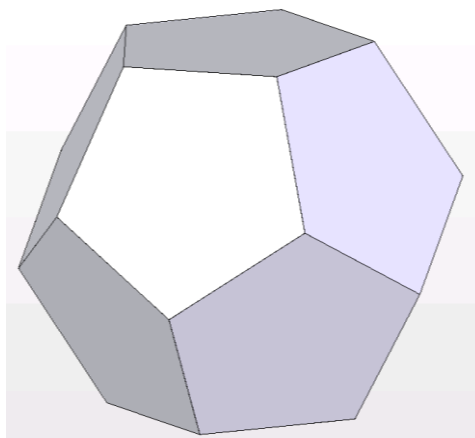
Figure 152 Dodecahedron idealised structure to represent the foam cells.

5.2.3.1.2 Open pore cellular foam model development

A dodecahedron was chosen to best fit the foam cell or 'pore' geometry. A dodecahedron may be divided into 12 identical pyramids having a pentagon shaped base. When assembled, the vertexes of

these pyramids meet at the centroid of the dodecahedron. To produce the solid dodecahedron fourteen pyramids were constructed in commercially available Solid Works as shown in Figure 153 (a). Next the pyramids are joined together to form a solid dodecahedron as shown in Figure 153 (b).
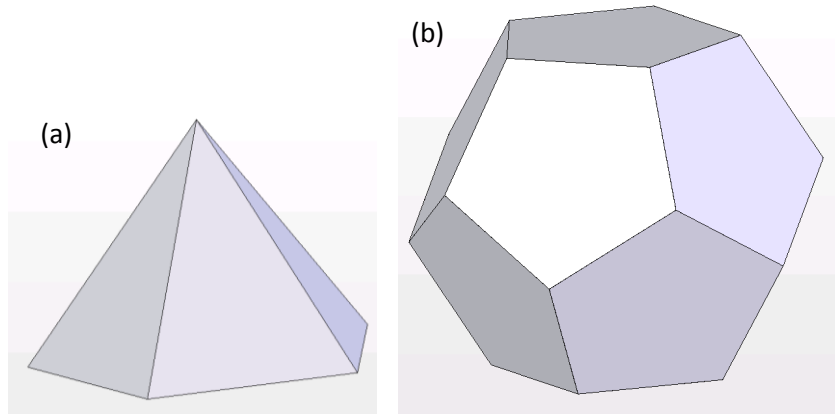
Figure 153 Pyramid (a) used to create dodecahedron (b).

A solid dodecahedron allows the estimation of surface area and pore volume characteristics. The dimensions of the pyramid of the 40ppi foam sample are shown in Table 12. The mathematical formulae that were used to construct these pyramids & the dodecahedron are discussed in Appendix F.

Table 12 Pyramid properties (40ppi example)

Pyramid Type	Pentagonal
Sides	5
Side Length (mm)	0.254
Height (mm)	0.3175
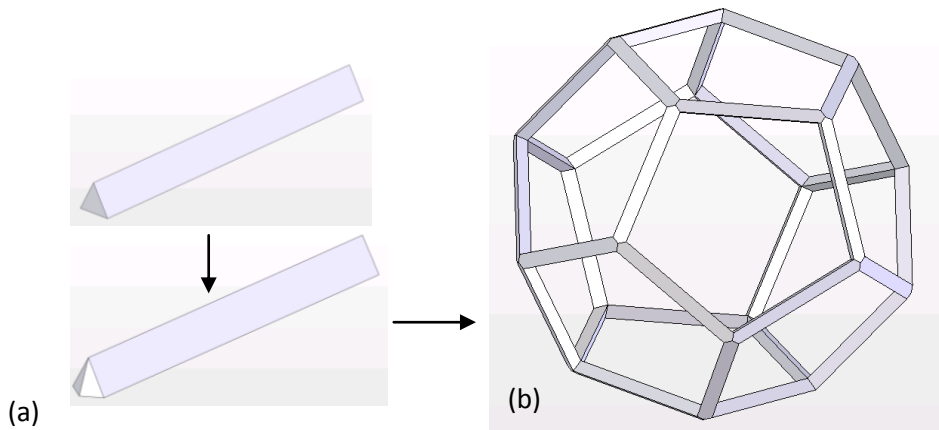
Figure 154 Ligaments (a) are used to create the structure of dodecahedron 'Pore' RUCS (b).

The structures that form pores and connect pores to each other in open pore cellular foam are called ligaments. These have been shown by many researchers such as Ozmat et al. [167] to have an

equilateral triangular cross section. Ligaments were constructed in commercially available Solid Works as shown in Figure 154 (a). These ligaments are joined together to make another dodecahedron or a 'pore' as shown in Figure 154 (b). The dimensions for the ligaments of the 40ppi foam sample are shown in Table 13. The mathematical formulae that were used to construct these ligaments and the dodecahedron are discussed in Appendix F.

Table 13 Ligament properties (40ppi example)

Type	Equilateral Triangle
Triangular Side Length (mm)	0.0236
Inner Length of Ligament (mm)	0.254
Total Length of Ligament (mm)	0.236
Angle of Plane (degrees)	20.9
Angle to side (degrees)	120
Qty of ligaments in a Dodecahedron	30

A simple comparison was made between the dodecahedron made from the pyramids and the dodecahedron made from the ligaments to ensure that both methods produced the similar geometry. The advantage of making the dodecahedron from ligaments ensured a less complicated model and reduced additional activates to make the solid dodecahedron into a ligament structure as completed by researchers such as Krishnan et al. [163] with their complicated models.

5.2.3.1.3 Comparing model to reality

As can be seen from Figure 155 the dodecahedron ligaments and pore structure created match very
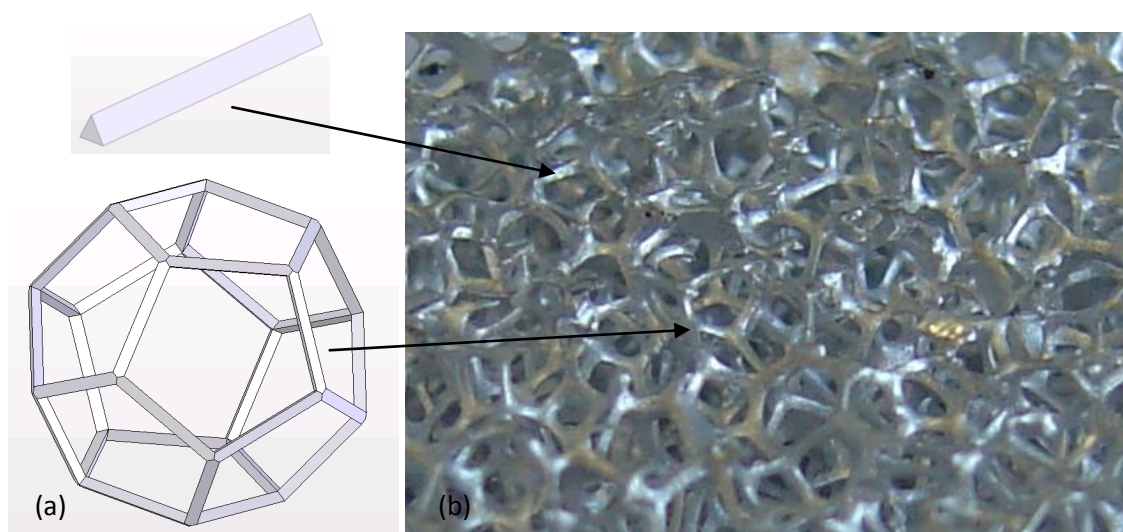
Figure 155 Comparing ligament and pore models (a) to a real open pore foam structure (b).

well to a real sample of similar size open pore cellular foam. Once one dodecahedron, of a certain size

relating to the ppi of the real sample was constructed it could be copied into a large matrix to

represent a section of a real open pore cellular foam material. For a simple comparison of the structure

of the model and a real sample of open pore cellular foam material see Figure 155 and Figure 156.
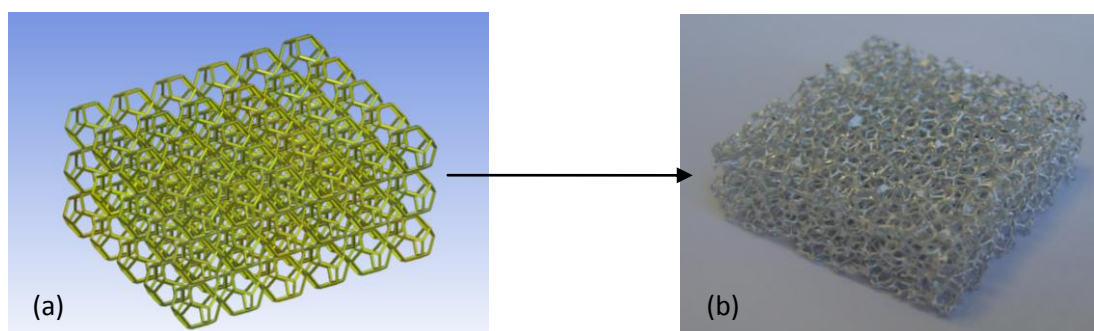
Figure 156 Comparing Open Pore Foam Model (a) to a Real Open Pore Foam Structure (b).

5.2.3.1.4 Model matrix development

To complete a representative model for a section of the real sample the single dodecahedron or 'pore'

or the open pore cellular foam material is patterned into a matrix of pores so that flow analysis and

measurements can be performed for a block of foam material, see Figure 157. This was completed on

commercially available Ansys 12, Design Modeller. The matrix of pores were imported into Ansys 12

and modified to create a fluid volume. The number of pores used and the volume of each model

depended on the ppi of which each model was to represent. Tables of all the relevant information for

all samples of open pore cellular foam can be viewed in Appendix C.
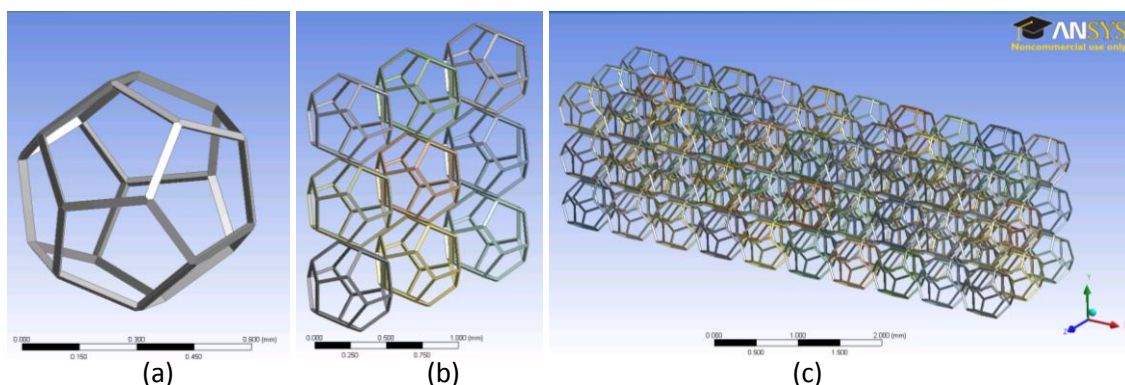
Figure 157 Dodecahedron model matrix development (a) Pore (b) Pore pattern (c) Pore matrix.

The matrix of pores were imported into commercially available Ansys 12, Design Modeller and modified to create a fluid volume. The matrix was contained in a volume and a Boolean operation was used to subtract the matrix from the volume. A closed volume with the pore structure of the dodecahedron pores inside remained as shown in Figure 158.

An inlet region and outlet region is seen in Figure 158. This region was necessary to allow gas time to steady state and to identify a steady inlet region, a porous region (open pore cellular foam region) and an outlet region. Also wall effects were minimised as the matrix protrudes to the edge of the volume. It was noted in literature and visible in early model designs that fluid would take the easier path of skirting around the wall edges to avoid the porous region. This model design avoids this unwanted anomaly.
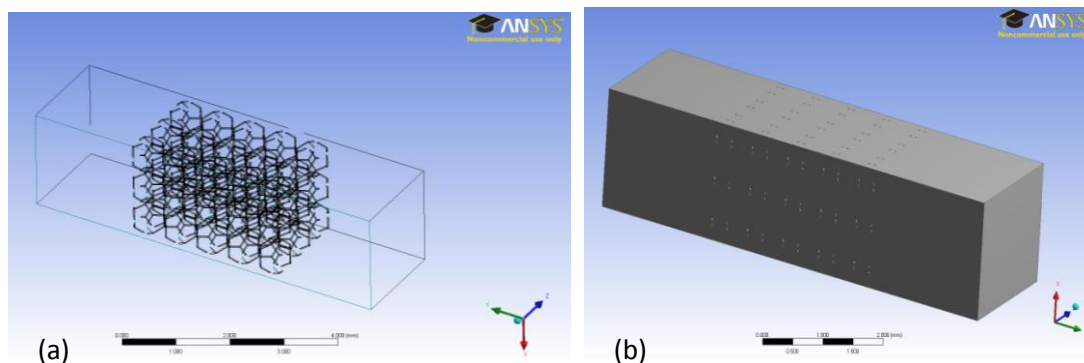
Figure 158 Fluid volume of 40ppi model (a)Wireframe model (b) Complete solid model.

The model was imported in to commercial software Ansys 12, Mesh. Boundary conditions were added to the model and it was meshed using hybrid elements by specifying the minimum edge length, Figure 159. The Fluent software version used in this study can only be used with cases containing less than 512000 elements and so the each model has restrictions on its mesh size. This became very tedious but the final models contained between 300,000 and 500,000 elements course enough not to exceed the limit or computational power or time available but fine enough to give acceptable results, clarified by grid independence analysis. Tables of all the relevant information for all samples can be seen in Appendix F.
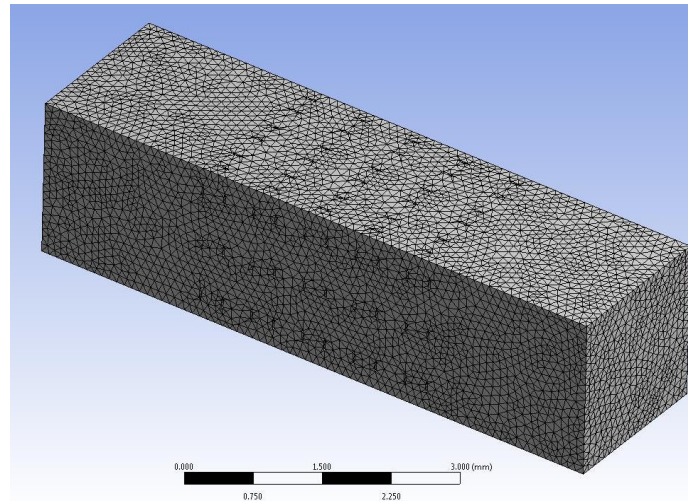
Figure 159 Fluid volume of 40ppi model (Meshed).

The mesh was exported to the commercial code Ansys 12 Fluent which was used to perform CFD analysis on the developed model. Please refer to Chapter 5, Section 5.2.3.2 for all the models CFD results and Chapter 6 for a full discussion of these results.

5.2.3.2 Open pore cellular foam simulation results

A CFD analysis was carried out on open pore cellular foam models. The main results that were investigated were pressure through the model, pressure drop from inlet to outlet, velocity flow through the model and flow regime while observing the interaction of the fluid with the open pore cellular foam and the walls of the model. Each model was examined with five different inlet velocities (1m/s, 3m/s, 6m/s, 9m/s & 12m/s) to examine the fluid flows at different inlet velocities but also to compile results that can be used in post processing to calculate the pressure drop curves of the open pore cellular foam materials.

It is noted that all the following results should be similar, and are similar to each other. As the ppi number increases more pores and smaller pores are in each model and the pressure drop should increase. In the following models only added information is mentioned and the main discussion will be in Chapter 6.

5.2.3.2.1 10ppi model

Due to the constraints of mesh size this model had few pores, as shown in Figure 160 but valid results were obtained from the model.
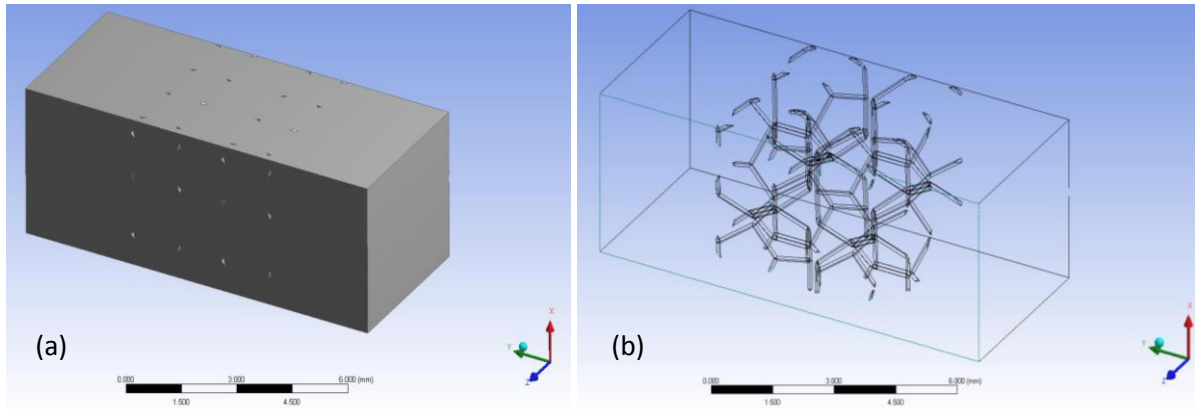
Figure 160 10ppi open pore cellular foam model (a) and wireframe model (b).

The first observation from the results is the fluid flow regime through the models. When the fluid comes in contact with the ligaments, velocity increases and the fluid is diverted around the ligaments creating a convective flow through the porous region, this can be noticed by the orange zones in the velocity profiles for example at 1m/s in Figure 161 (b). A closer look at the arrows of the velocity vectors, Figure 161 (c), of this model at different inlet velocities can show the air flow regime also. As inlet velocity increases, this mixing becomes greater and the velocity at the walls increases also. The pressure drop through this model is small, ranging from 0.5 to 2 Pa at 1m/s inlet velocity as shown in Figure 161 (a) to about 90 Pa at 12m/s inlet velocity as shown in Figure 165 (a).

Figure 161 10ppi inlet velocity 1m/s (a) Pressure (Pa) (b) Velocity (m/s) (c) Velocity vectors (m/s)

Figure 162 10ppi inlet velocity 3m/s (a) Pressure (Pa) (b) Velocity (m/s) (c) Velocity vectors (m/s)

Figure 163 10ppi inlet velocity 6m/s (a) Pressure (Pa) (b) Velocity (m/s) (c) Velocity vectors (m/s)

Figure 164 10ppi inlet velocity 9m/s (a) Pressure (Pa) (b) Velocity (m/s) (c) Velocity vectors (m/s)

Figure 165 10ppi inlet velocity 12m/s (a) Pressure (Pa) (b) Velocity (m/s) (c) Velocity vectors (m/s)
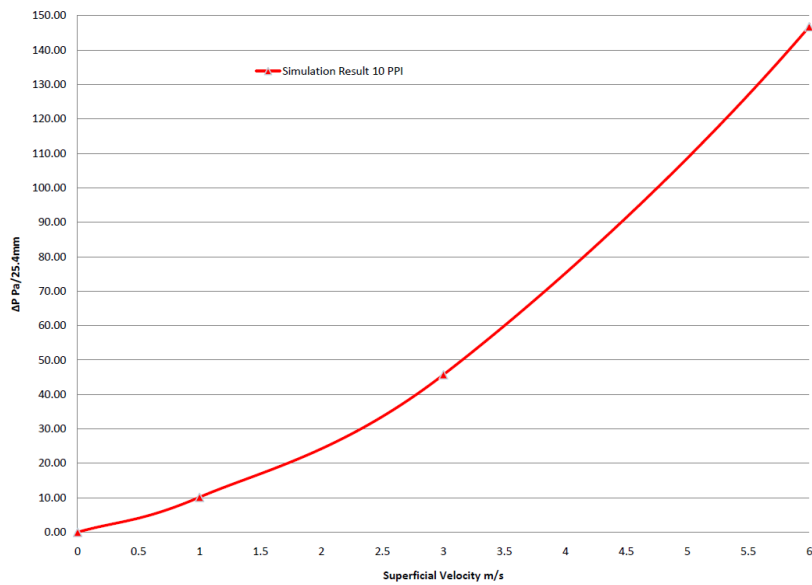
Figure 166 10ppi pressure drop.

Figure 166 shows a normalised pressure drop for the 10ppi model. This graph characterises the 10ppi foam by the curve. Figure 167 shows a comparison of 10ppi model to other mathematical models and

models developed in literature. A good fit to the models is observed. As expected the Darcy (due to high Reynolds number) and the Ergun mathematical models (due to lack of spherical particles) do not align. These results will be discussed further in Chapter 6.
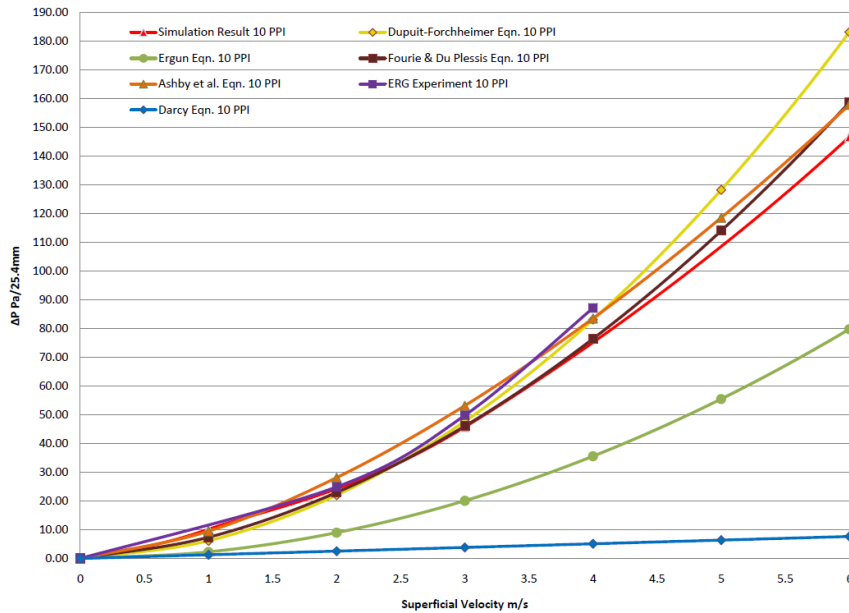
Figure 167 10ppi pressure drop comparison.

5.2.3.2.2 20ppi model

The 20ppi model is shown in Figure 168. Due to the size of this model more pores could be accommodated than the previous model.
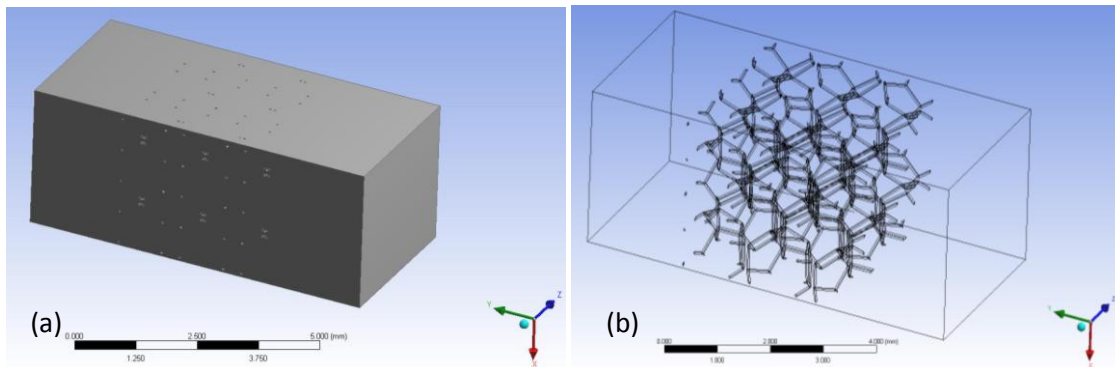
Figure 168 20ppi open pore cellular foam model (a) and wireframe model (b).

The fluid flow regime through the models is observation from the results. When the fluid comes in contact with the ligaments, velocity increases and the fluid is diverted around the ligaments creating a convective flow through the porous region, this can be noticed by the orange zones in the velocity profiles in the diagrams below. As inlet velocity increases, this mixing becomes greater and the velocity at the walls increases also. The pressure drop through this model is small, ranging from 1 to 2 Pa at 1m/s inlet velocity as shown in to about 130 Pa at 12m/s inlet velocity as shown in Figure 173.

Figure 169 20ppi inlet velocity 1m/s (a) Pressure (Pa) (b) Velocity (m/s) (c) Velocity vectors (m/s)

Figure 170 20ppi inlet velocity 3m/s (a) Pressure (Pa) (b) Velocity (m/s) (c) Velocity vectors (m/s)

Figure 171 20ppi inlet velocity 6m/s (a) Pressure (Pa) (b) Velocity (m/s) (c) Velocity vectors (m/s)

(a)   (b)   (c)

Figure 172 20ppi inlet velocity 9m/s (a) Pressure (Pa) (b) Velocity (m/s) (c) Velocity vectors (m/s)

(a)   (b)   (c)

Figure 173 20ppi inlet velocity 12m/s (a) Pressure (Pa) (b) Velocity (m/s) (c) Velocity vectors (m/s)

Figure 174 20ppi pressure drop.

Figure 174 shows a normalised pressure drop for the 20ppi model. This graph characterises the 20ppi foam by the curve. Figure 175 shows a comparison of 20ppi model to other mathematical models and models developed in literature. The simulated pressure drop results are between the other model values. These results will be discussed further in Chapter 6.

Figure 175 20ppi pressure drop comparison.

5.2.3.2.3 30 ppi model

The 30ppi model is shown in Figure 176. The fluid flow regime, pressure, pressure drop from inlet to outlet, velocity flow through the model is observation from the results.

Figure 176 30ppi open pore cellular foam wireframe model.

As inlet velocity increases, this mixing becomes greater and the velocity at the walls increases also. The pressure drop through this model is small, ranging from 3 to 4 Pa at 1m/s inlet velocity as shown in Figure 177 to about 230 Pa at 12m/s inlet velocity as shown in Figure 181.

(a)   (b)   (c)

Figure 177 30ppi inlet velocity 1m/s (a) Pressure (Pa) (b) Velocity (m/s) (c) Velocity vectors (m/s)

(a)   (b)   (c)

Figure 178 30ppi inlet velocity 3m/s (a) Pressure (Pa) (b) Velocity (m/s) (c) Velocity vectors (m/s)

(a)   (b)   (c)

Figure 179 30ppi inlet velocity 6m/s (a) Pressure (Pa) (b) Velocity (m/s) (c) Velocity vectors (m/s)

Figure 180 30ppi inlet velocity 9m/s (a) Pressure (Pa) (b) Velocity (m/s) (c) Velocity vectors (m/s)
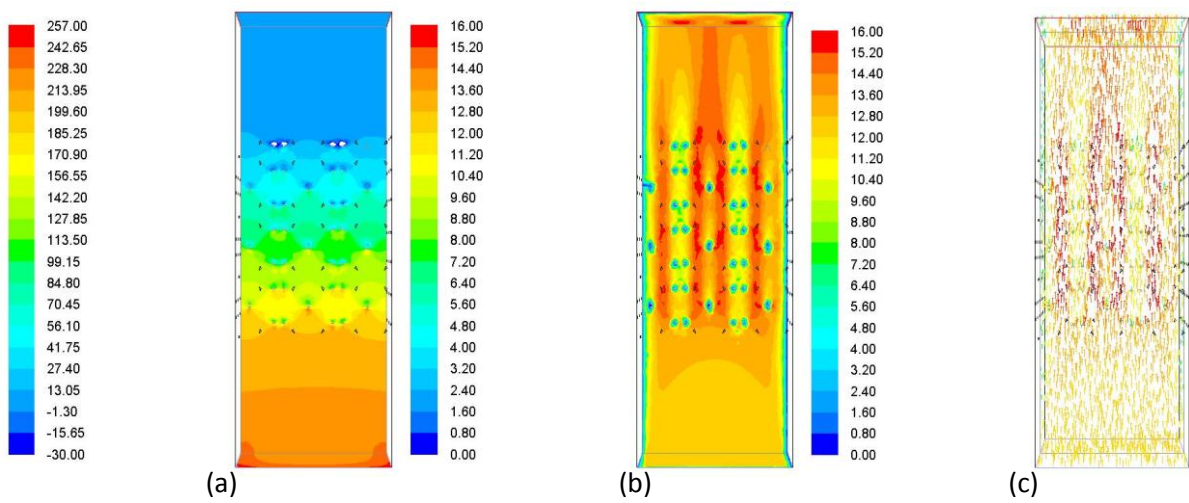
Figure 181 30ppi inlet velocity 12m/s (a) Pressure (Pa) (b) Velocity (m/s) (c) Velocity vectors (m/s)
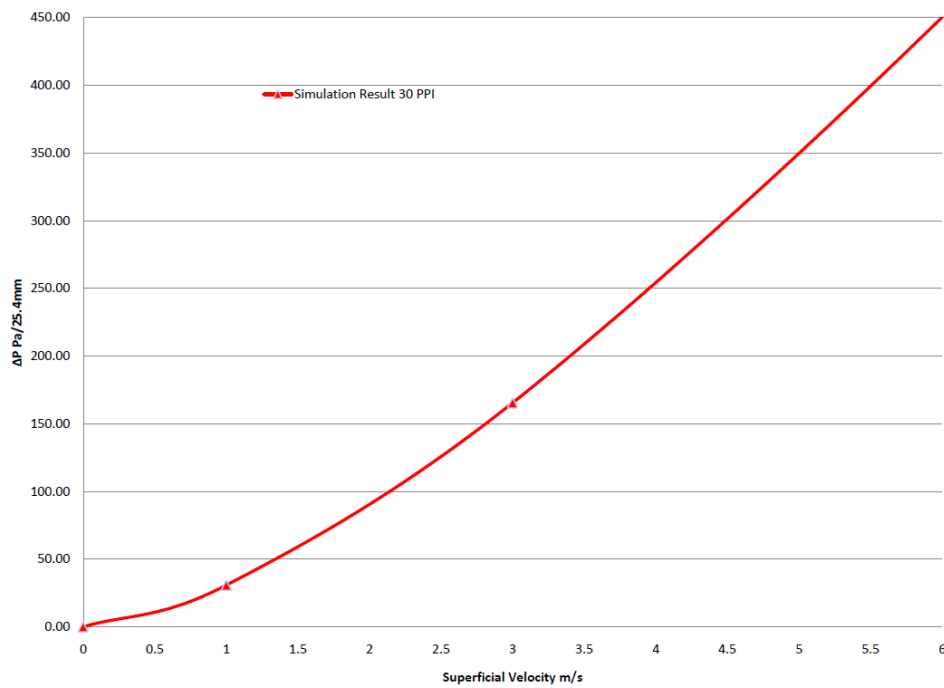
Figure 182 30ppi pressure drop.

Figure 182 shows a normalised pressure drop for the 30ppi model. This graph characterises the 30ppi foam by the curve. Figure 183 shows a comparison of 30ppi model to other mathematical models and models developed in literature. The simulated pressure drop results are between the other model values. These results will be discussed further in Chapter 6.
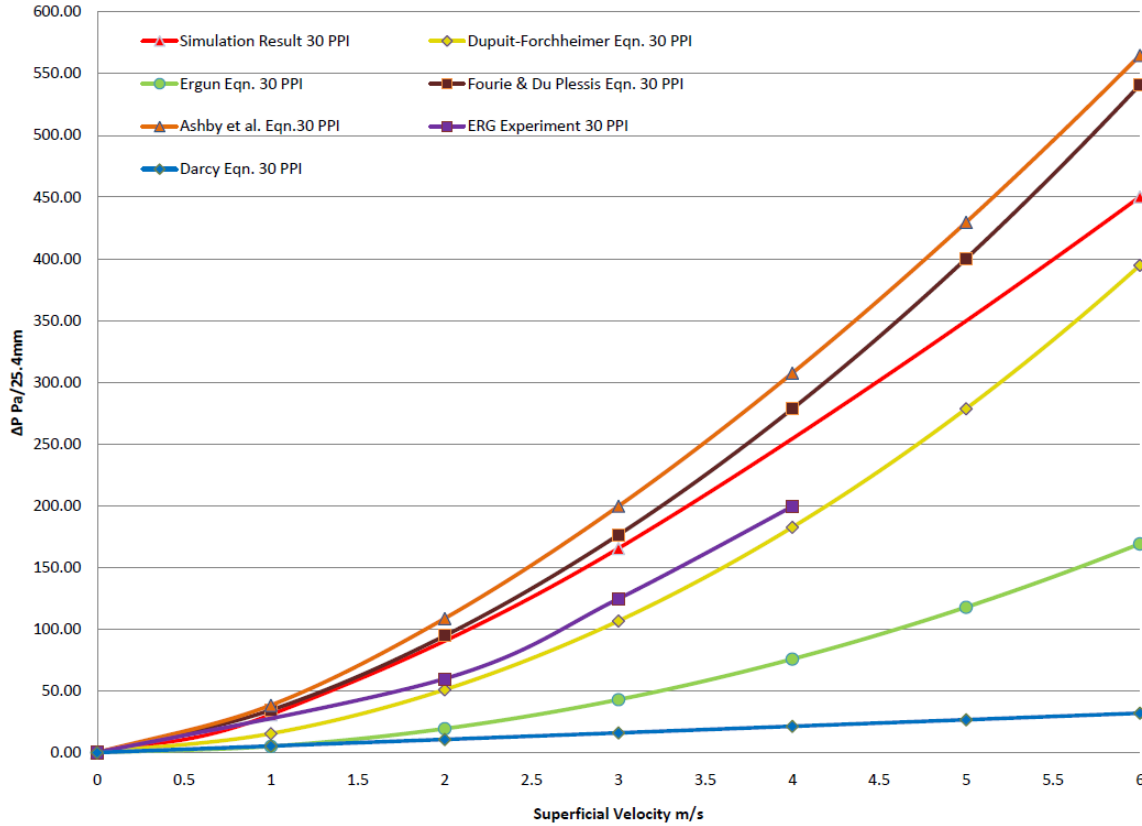
Figure 183 30ppi pressure drop comparison.

5.2.3.2.4 40ppi model

The 40ppi model is shown in Figure 184. The fluid flow regime, pressure, pressure drop from inlet to outlet, velocity flow through the model is observation from the results.

(a) (b)
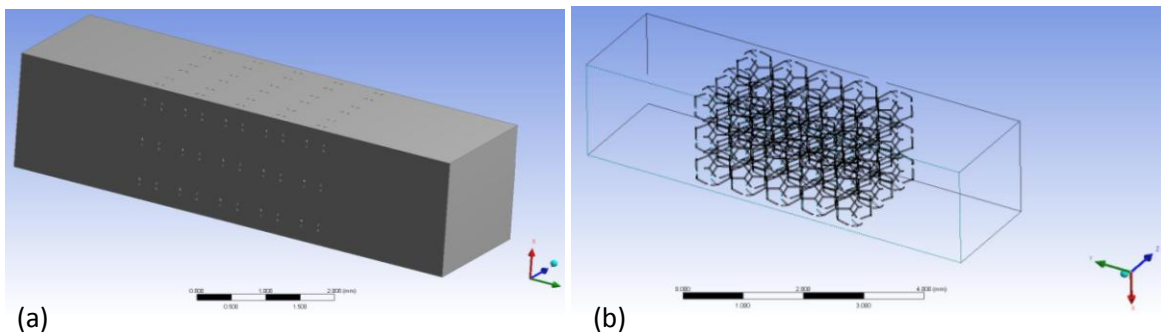
Figure 184 40ppi open pore cellular foam model (a) wireframe model (b).

As inlet velocity increases, this mixing becomes greater and the slow velocity at the walls increases also. The pressure drop through this model is small, ranging from 6 to 8 Pa at 1m/s inlet velocity as shown in to about 330 Pa at 12m/s inlet velocity as shown in Figure 189.
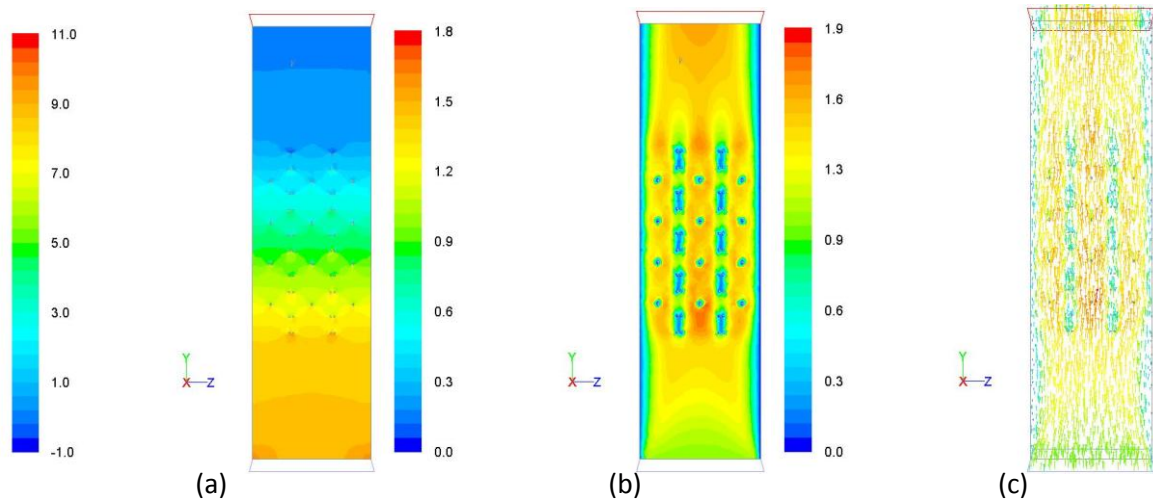
Figure 185 40ppi inlet velocity 1m/s (a) Pressure (Pa) (b) Velocity (m/s) (c) Velocity vectors (m/s)
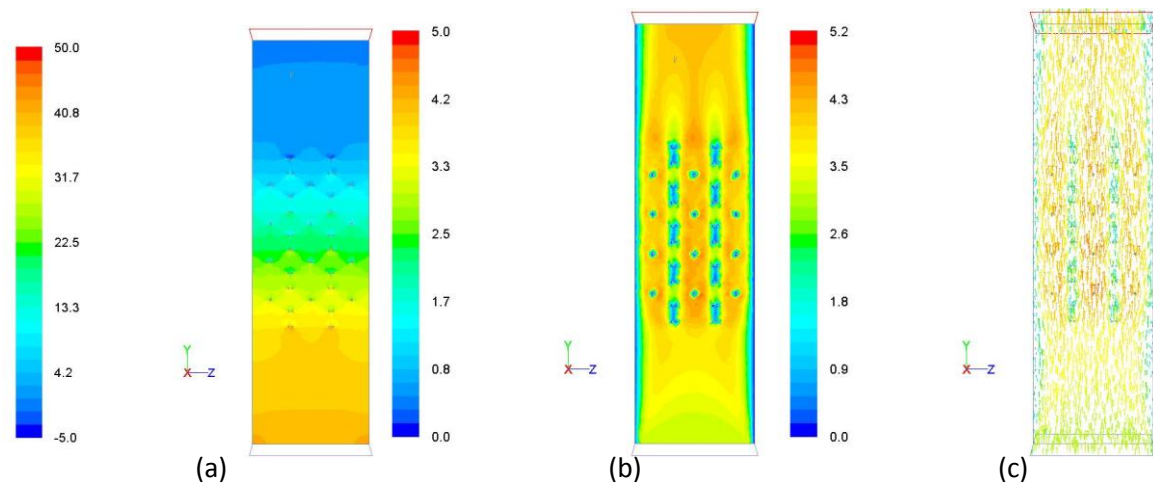
Figure 186 40ppi inlet velocity 3m/s (a) Pressure (Pa) (b) Velocity (m/s) (c) Velocity vectors (m/s)
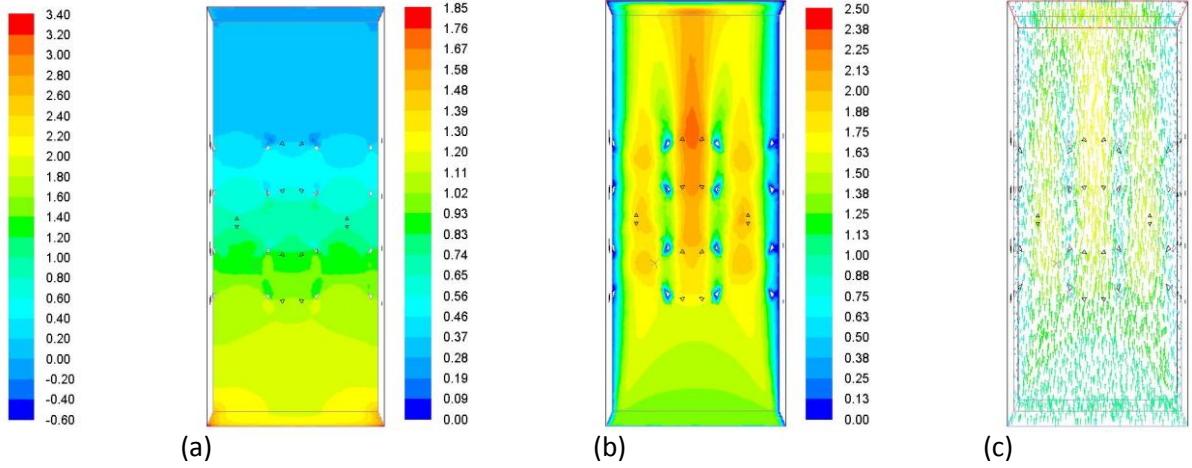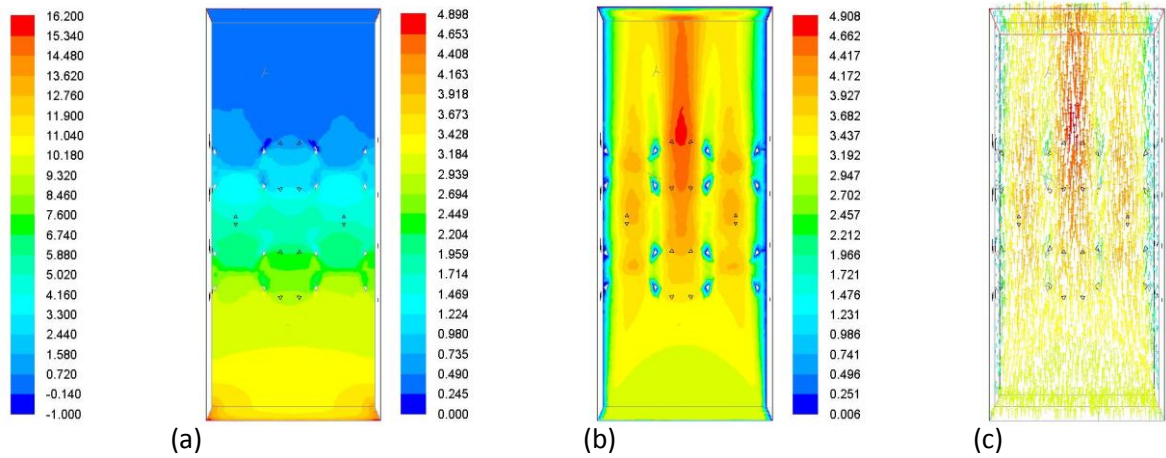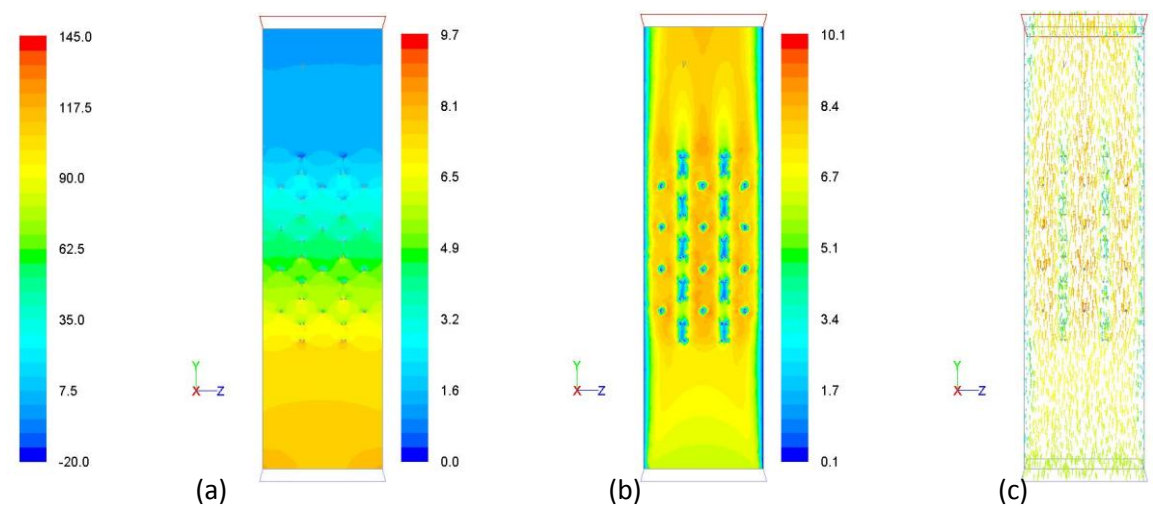

Figure 187 40ppi inlet velocity 6m/s (a) Pressure (Pa) (b) Velocity (m/s) (c) Velocity vectors (m/s)
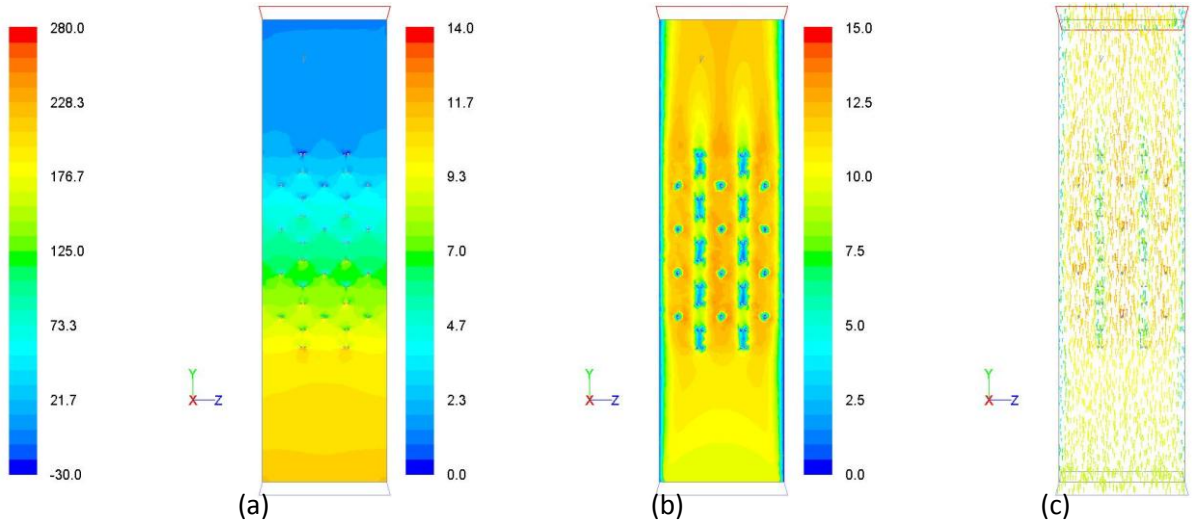
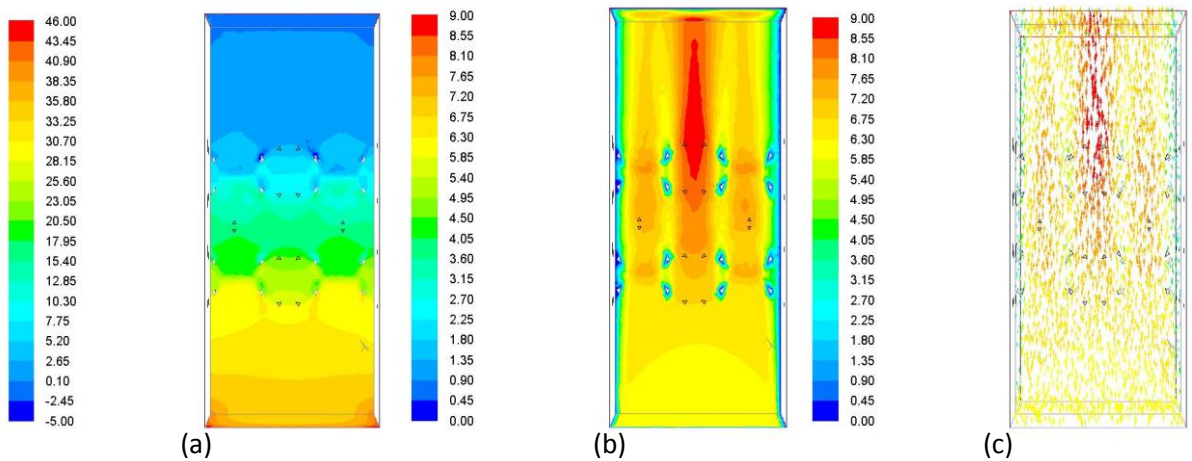**Figure 188 40ppi inlet velocity 9m/s (a) Pressure (Pa) (b) Velocity (m/s) (c) Velocity vectors (m/s)**
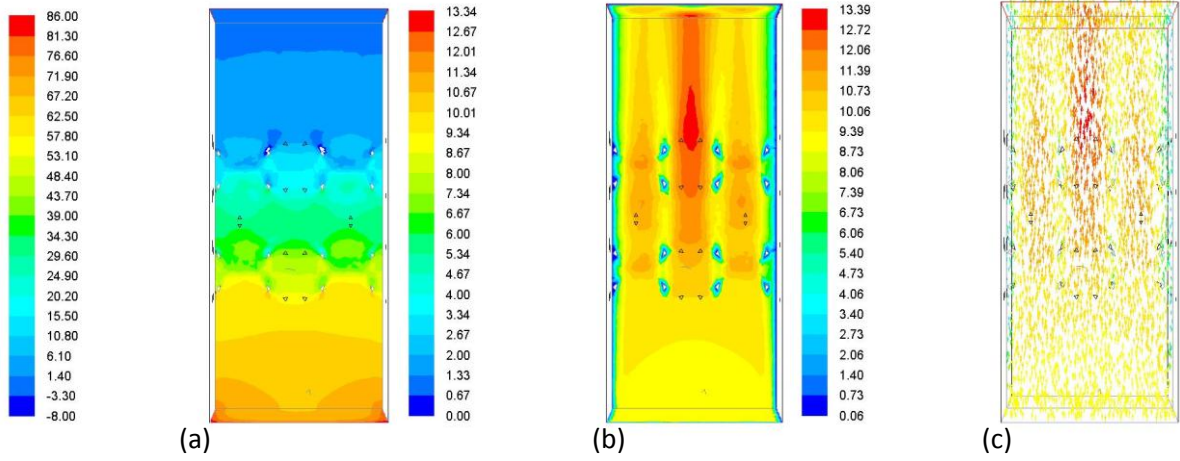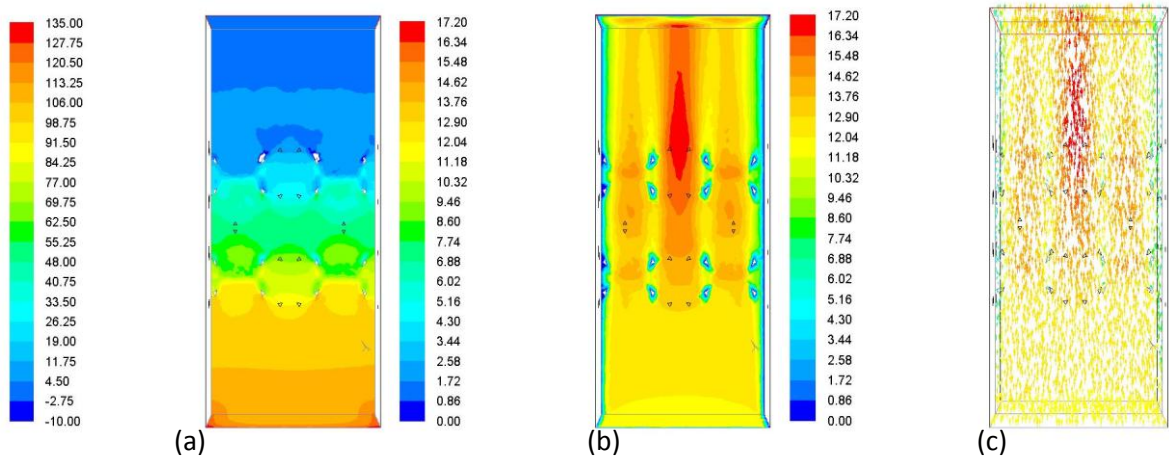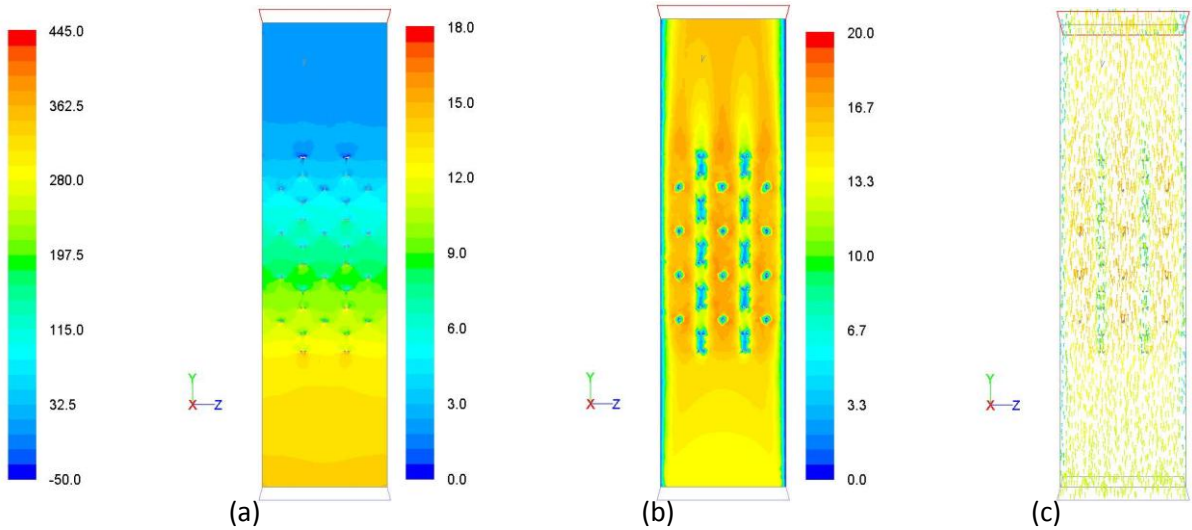

**Figure 189 40ppi inlet velocity 12m/s (a) Pressure (Pa) (b) Velocity (m/s) (c) Velocity vectors (m/s)**
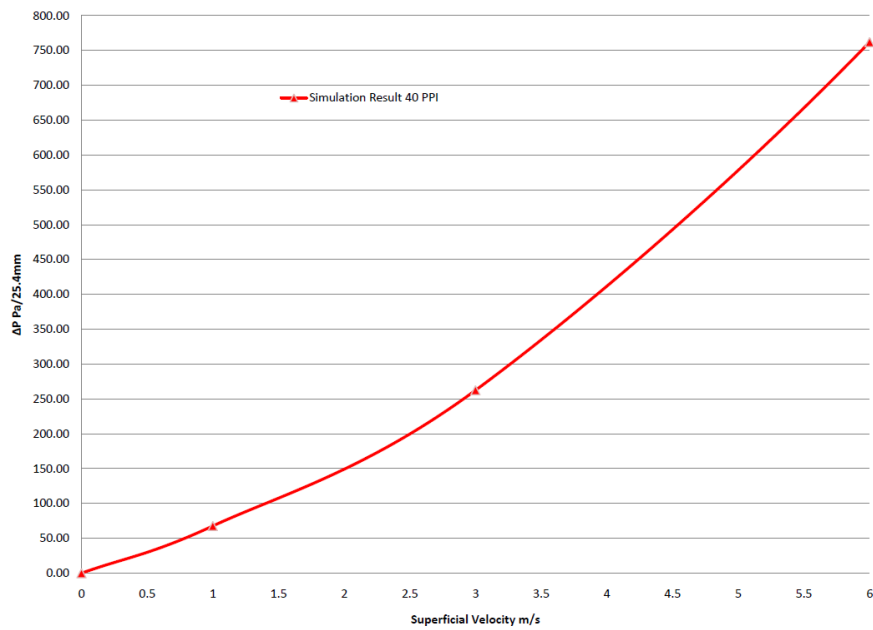
Figure 190 40ppi pressure drop.

Figure 190 shows a normalised pressure drop for the 40ppi model. This graph characterises the 40ppi foam by the curve. Figure 191 shows a comparison of 40ppi model to other mathematical models and models developed in literature. The simulated pressure drop results fit well with Dupuit-Forchheimer and Fourie & Du Plessis but they seem to move away from the experimental ERG model values. These results will be discussed further in Chapter 6.
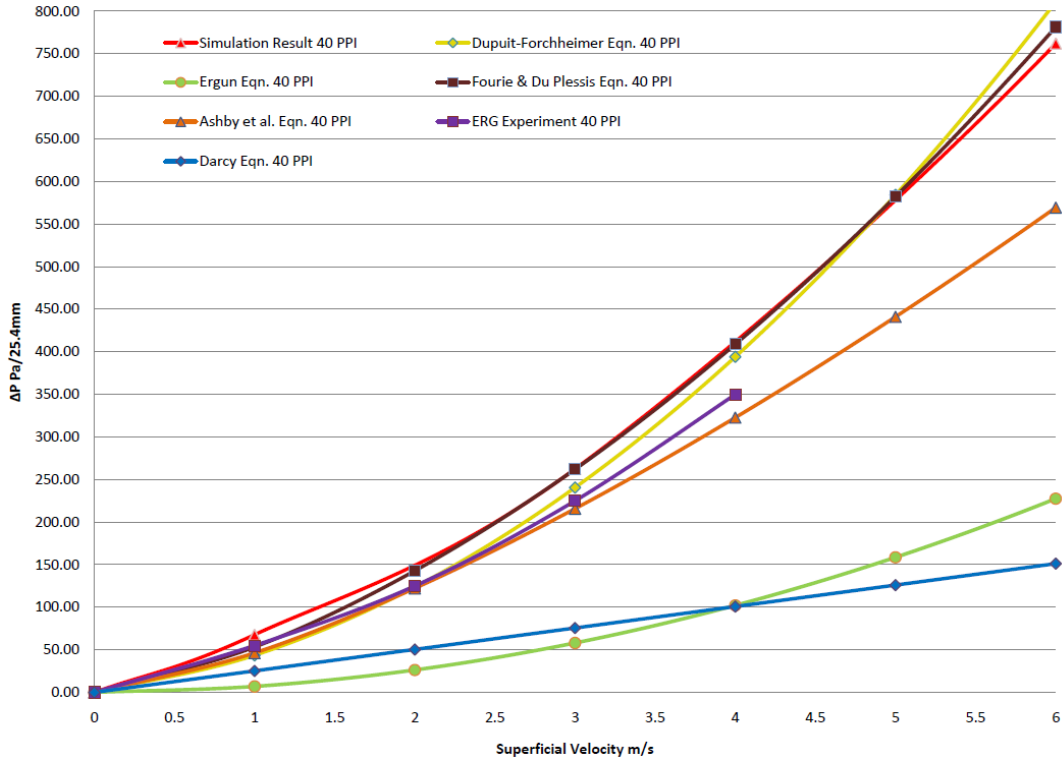
Figure 191 40ppi pressure drop comparison.

5.2.3.2.5 45ppi model

The 45ppi model is shown in Figure 192. The fluid flow regime, pressure, pressure drop from inlet to outlet, velocity flow through the model is observation from the results.
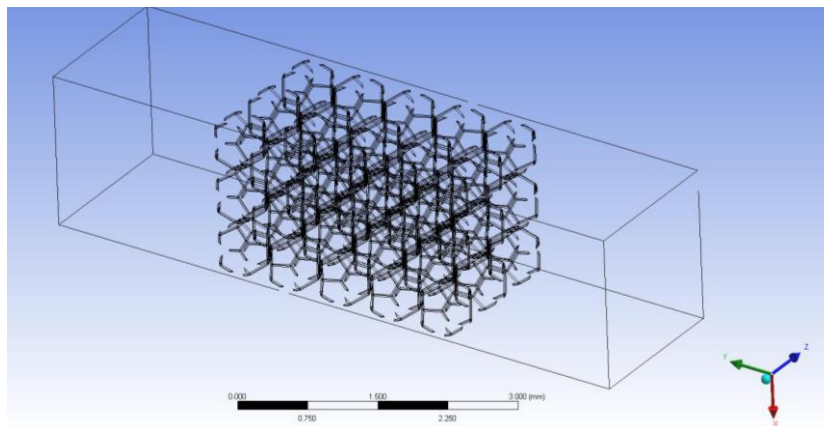
Figure 192 45ppi open pore cellular foam wireframe model.

(a)　　　　　　　　　　(b)　　　　　　　　　(c)
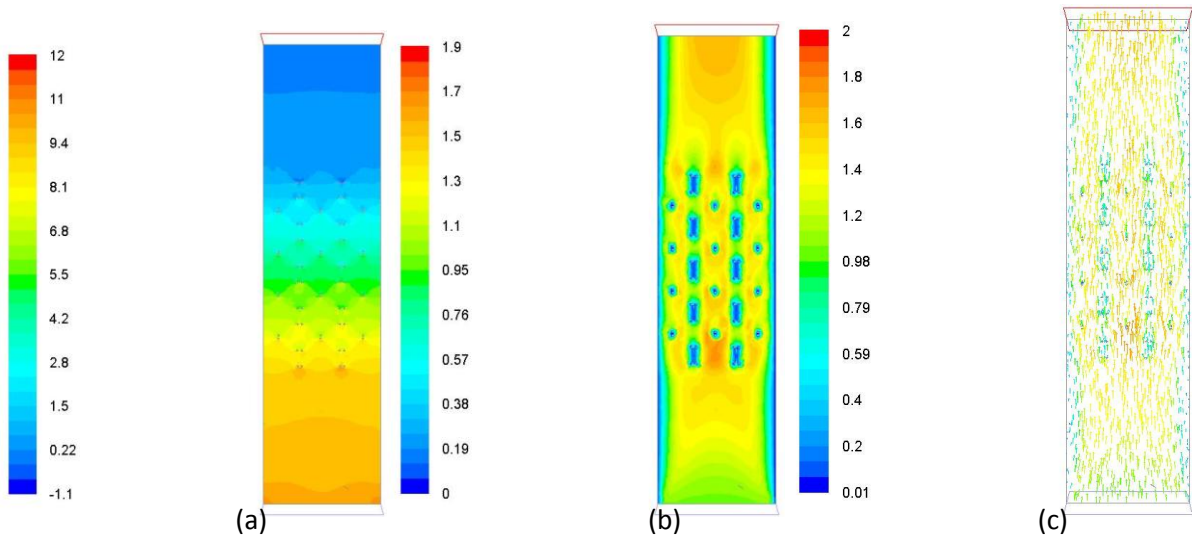
Figure 193 45ppi inlet velocity 1m/s (a) Pressure (Pa) (b) Velocity (m/s) (c) Velocity vectors (m/s)

(a)　　　　　　　　　　(b)　　　　　　　　　(c)
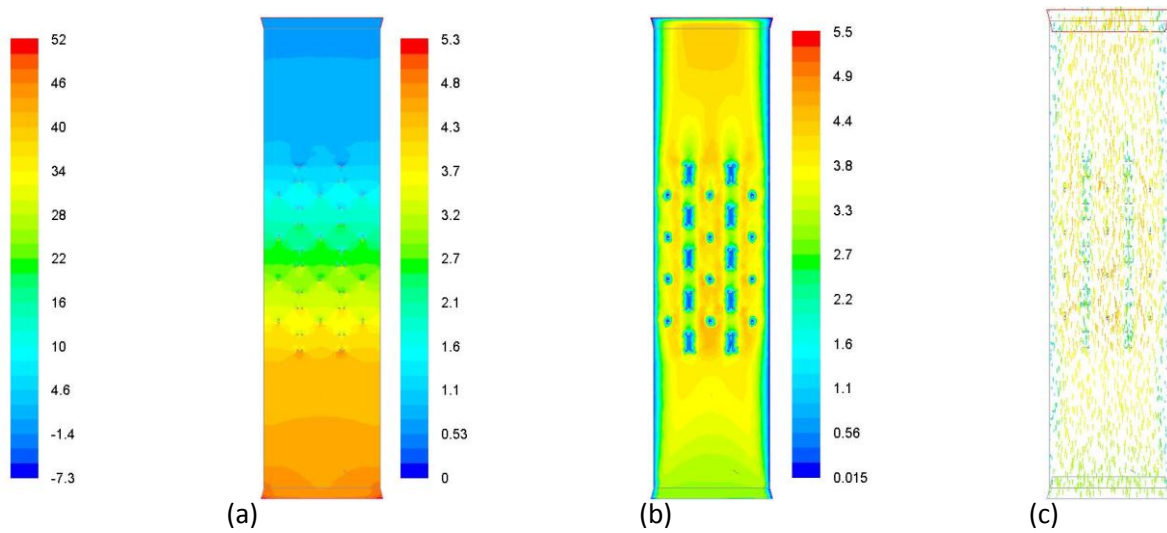
Figure 194 45ppi inlet velocity 3m/s (a) Pressure (Pa) (b) Velocity (m/s) (c) Velocity vectors (m/s)

(a)　　　　　　　　　　(b)　　　　　　　　　(c)
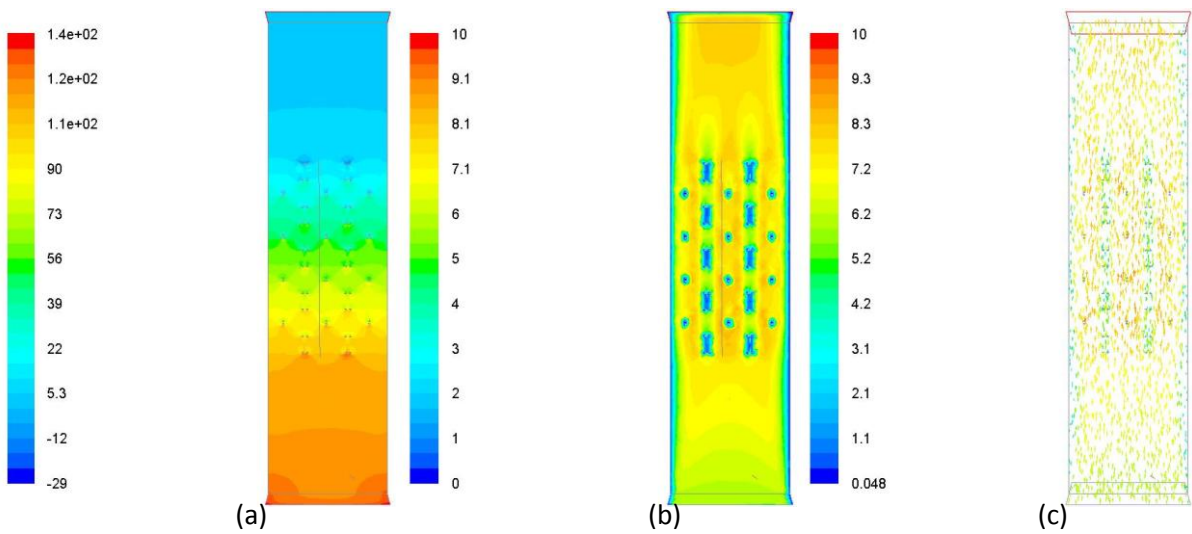
Figure 195 45ppi inlet velocity 6m/s (a) Pressure (Pa) (b) Velocity (m/s) (c) Velocity vectors (m/s)
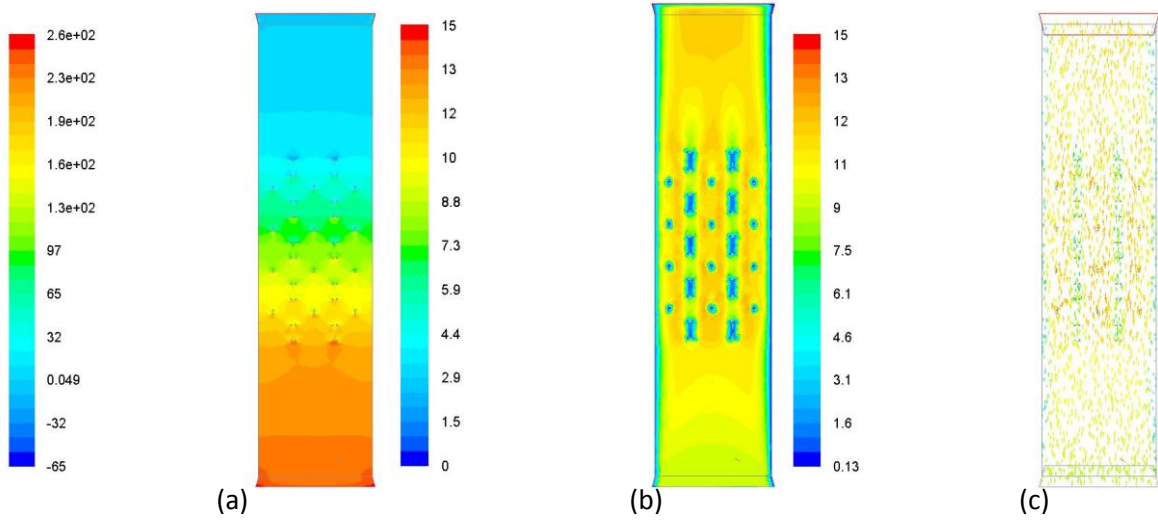
Figure 196 45ppi inlet velocity 9m/s (a) Pressure (Pa) (b) Velocity (m/s) (c) Velocity vectors (m/s)
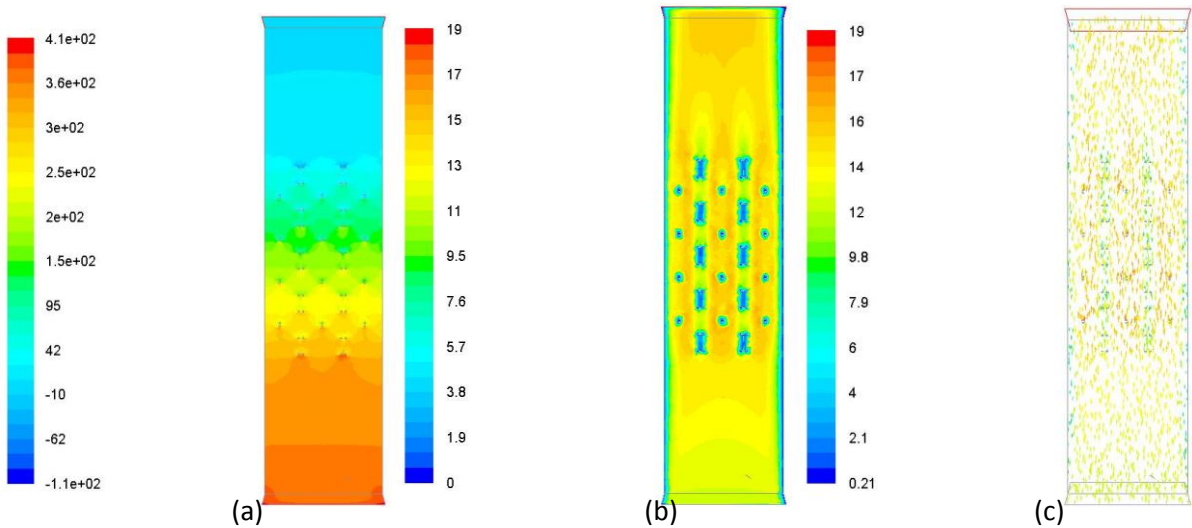
Figure 197 45ppi inlet velocity 12m/s (a) Pressure (Pa) (b) Velocity (m/s) (c) Velocity vectors (m/s)

As inlet velocity increases, this mixing becomes greater and the slow velocity at the walls increases also. The pressure drop through this model is small, ranging from 6 to 8 Pa at 1m/s inlet velocity as shown in to about 330 Pa at 12m/s inlet velocity as shown in Figure 189.

Figure 198 shows a normalised pressure drop for the 45ppi model. This graph characterises the 45ppi foam by the curve. Figure 199 shows a comparison of 45ppi model to other mathematical models and models developed in literature. The simulated pressure drop results are between the other model values but they seem to move away from the experimental ERG model values. These results will be discussed further in Chapter 6.
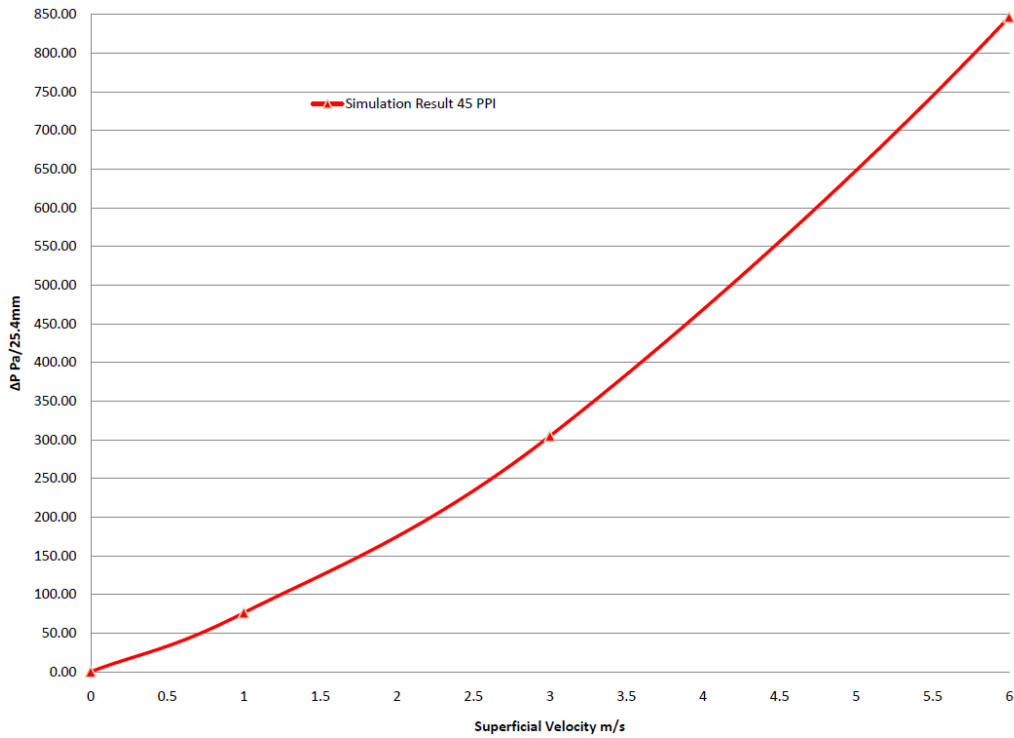
Figure 198 45ppi pressure drop.
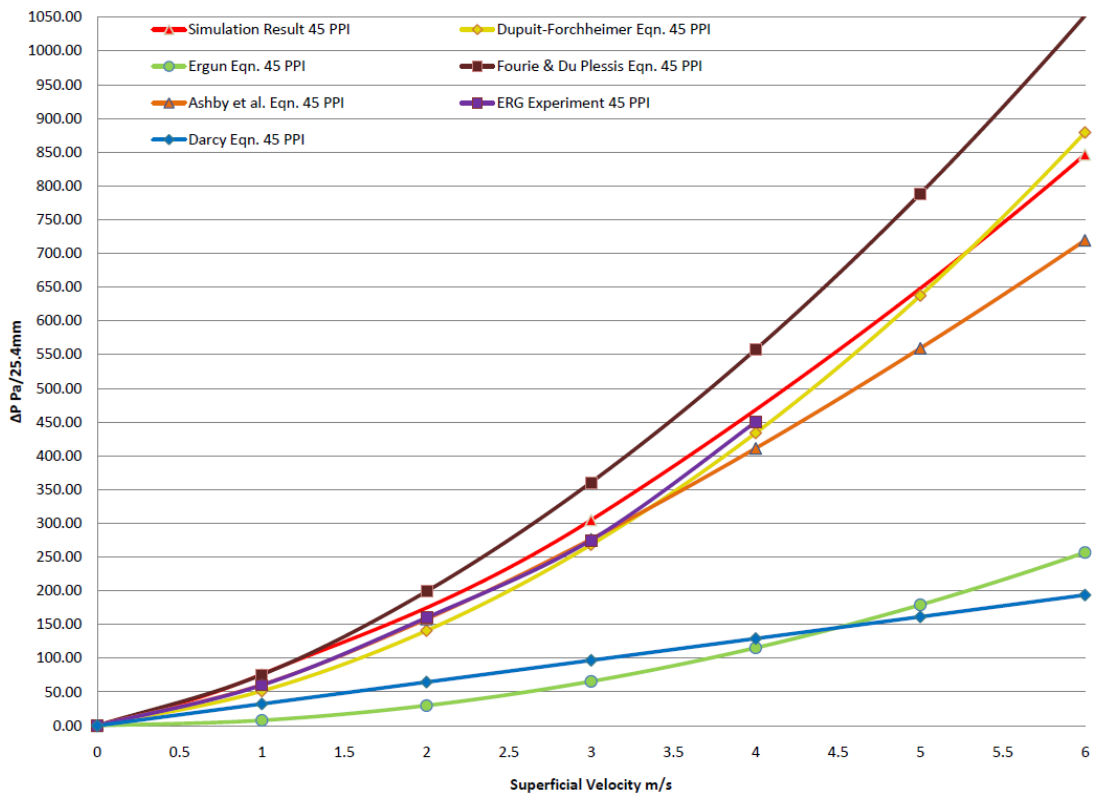
Figure 199 45ppi pressure drop comparison.

5.2.3.2.6 80ppi model

The 80ppi model is shown in Figure 200. The fluid flow regime, pressure, pressure drop from inlet to outlet, velocity flow through the model is observation from the results.
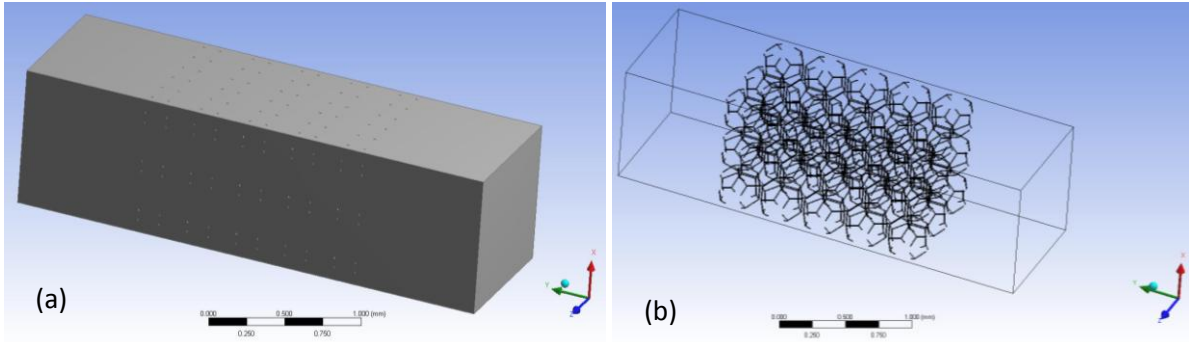
Figure 200 80ppi open pore cellular foam model (a) and wireframe model (b).

As inlet velocity increases, this mixing becomes greater and the slow velocity at the walls increases also. The pressure drop through this model is small, ranging from 1 to 11 Pa at 1m/s inlet velocity as shown in to about 310 Pa at 12m/s inlet velocity as shown in Figure 205.
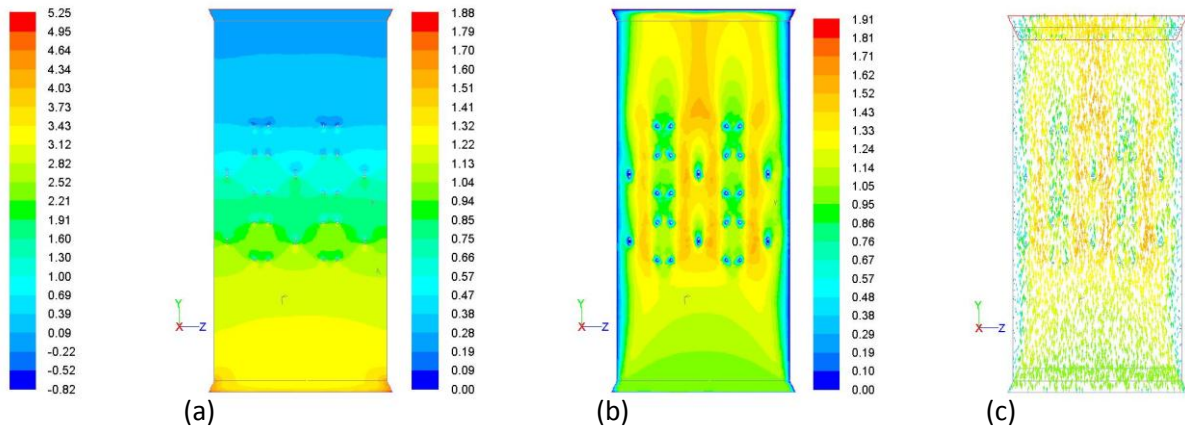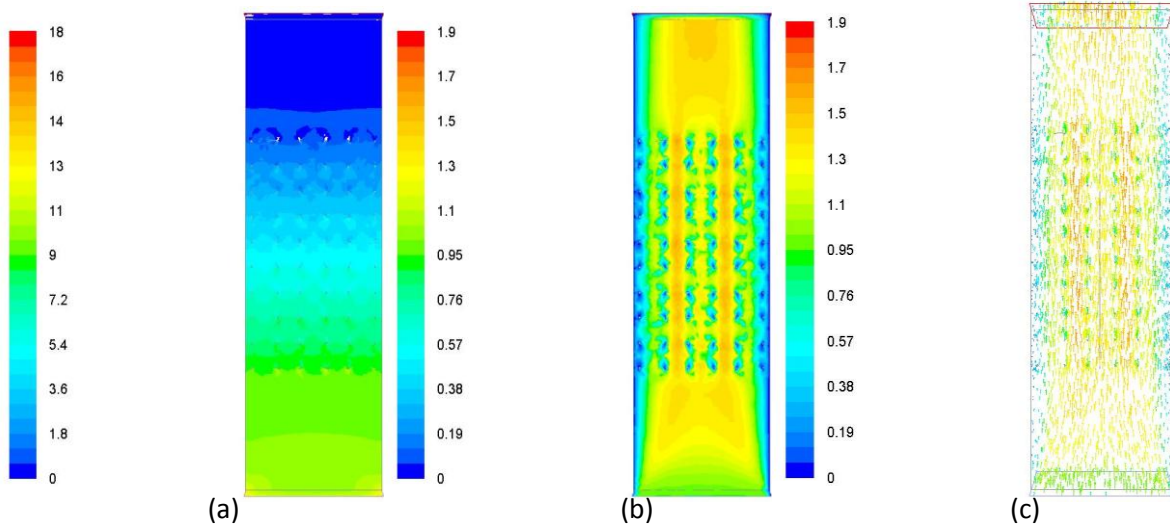

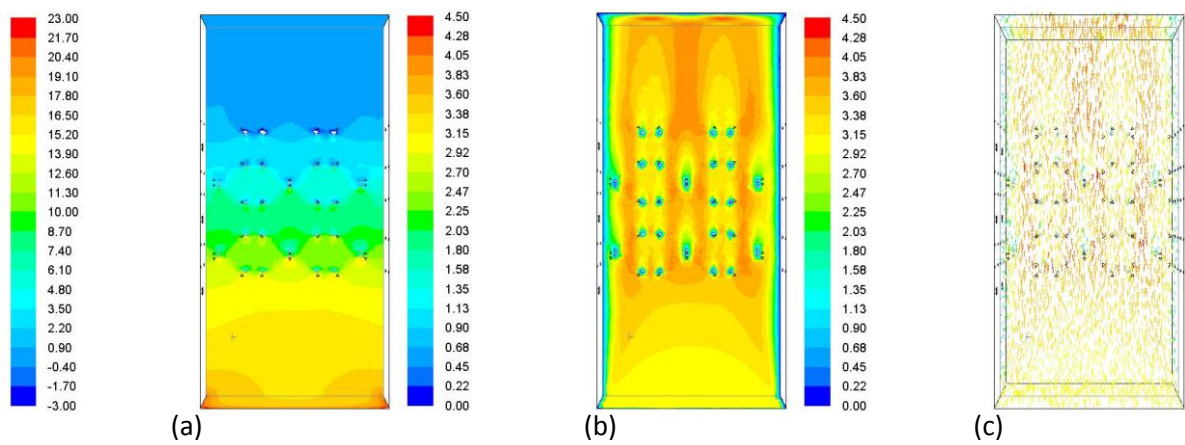**Figure 201 80ppi inlet velocity 1m/s (a) Pressure (Pa) (b) Velocity (m/s) (c) Velocity vectors (m/s)**
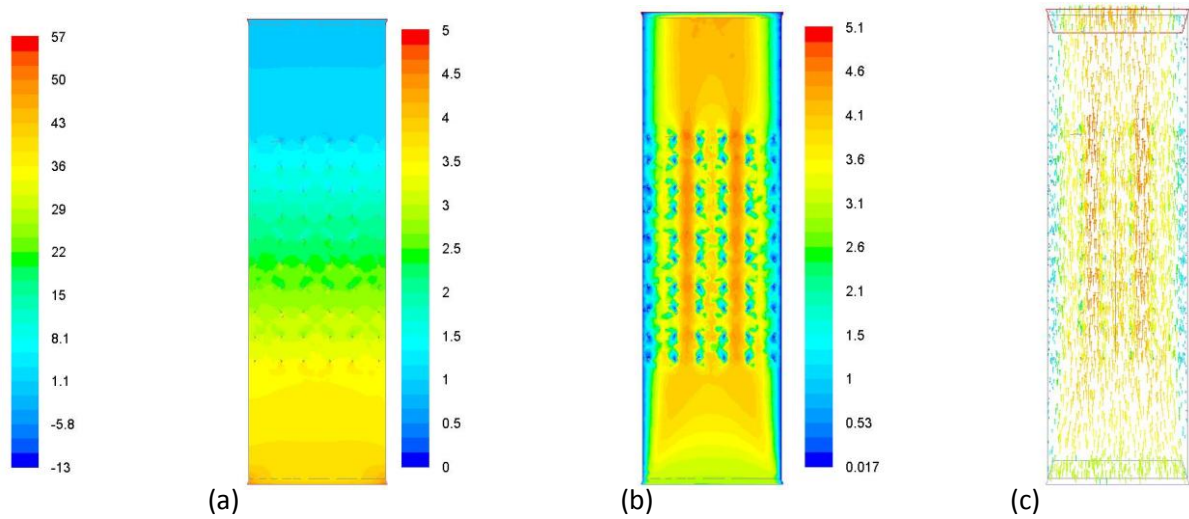
Figure 202 80ppi inlet velocity 3m/s (a) Pressure (Pa) (b) Velocity (m/s) (c) Velocity vectors (m/s)
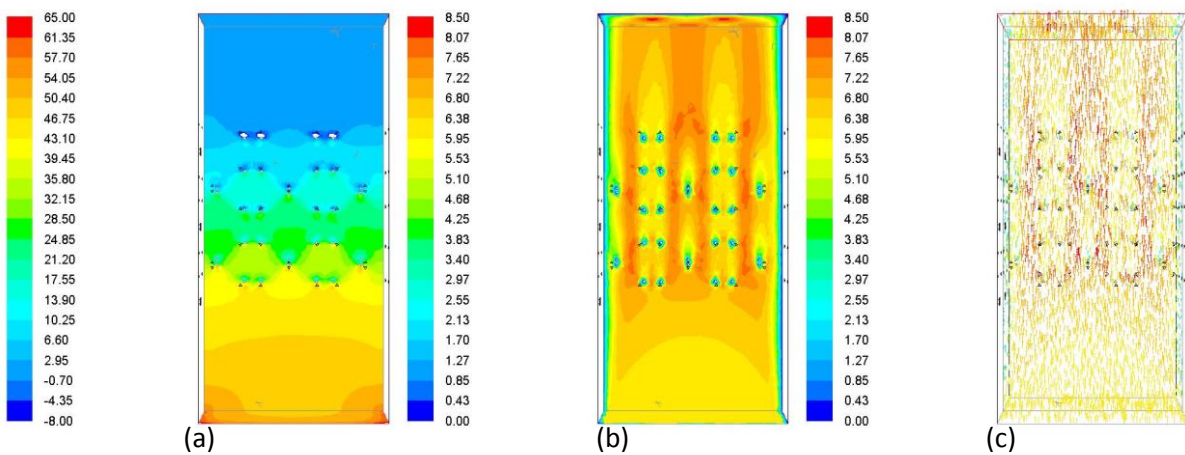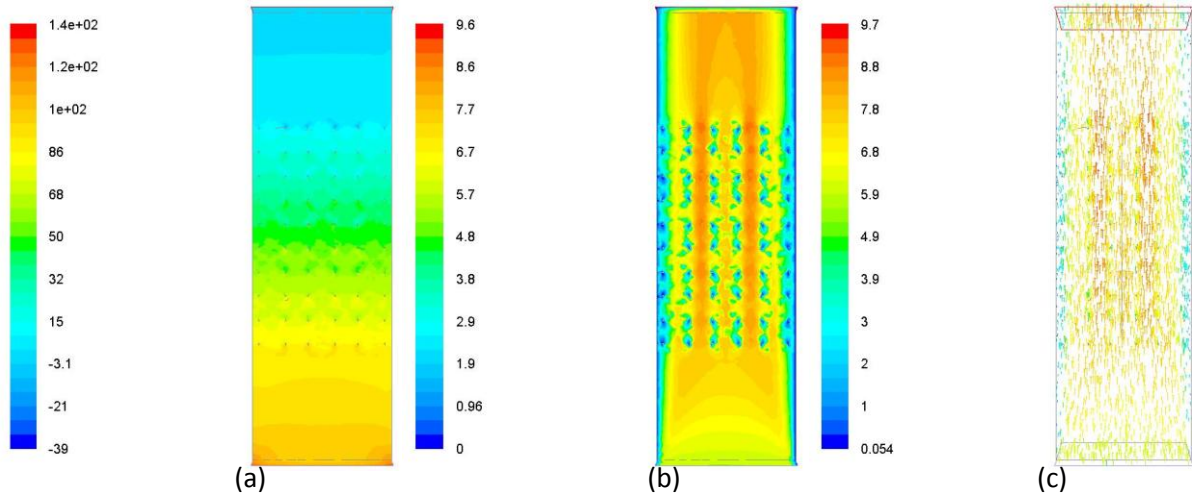
Figure 203 80ppi inlet velocity 6m/s (a) Pressure (Pa) (b) Velocity (m/s) (c) Velocity vectors (m/s)
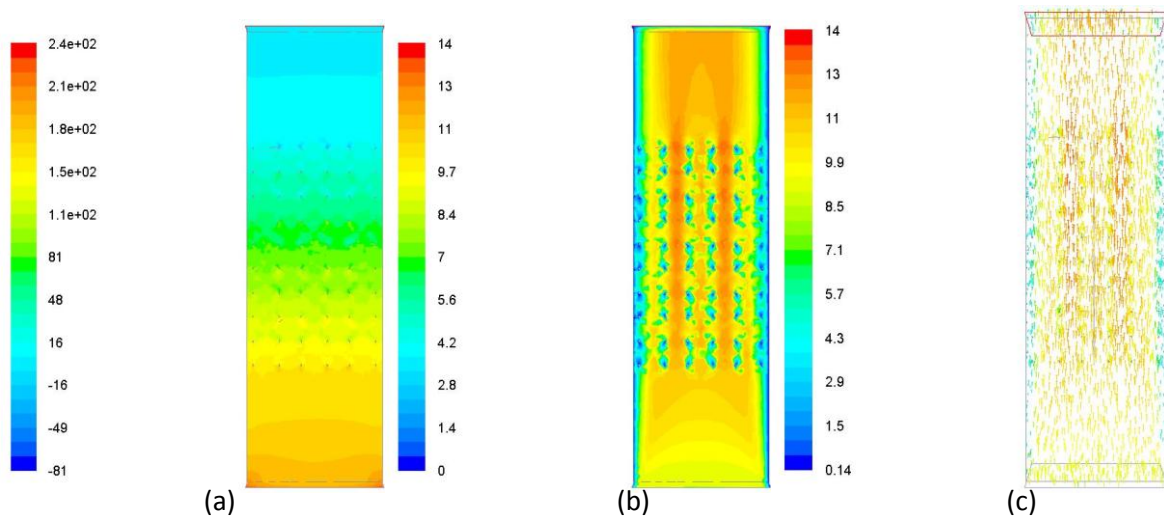
Figure 204 80ppi inlet velocity 9m/s (a) Pressure (Pa) (b) Velocity (m/s) (c) Velocity vectors (m/s)
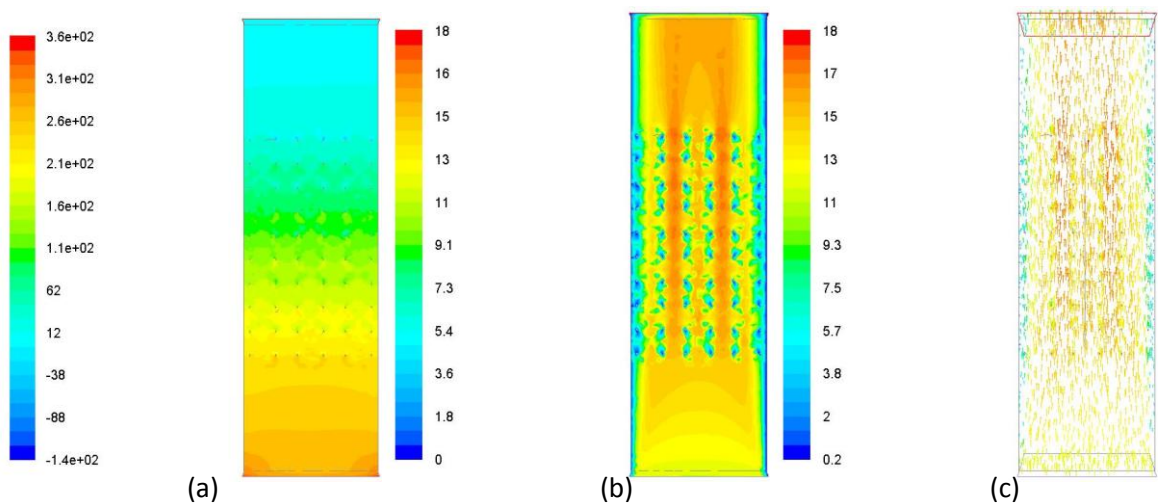
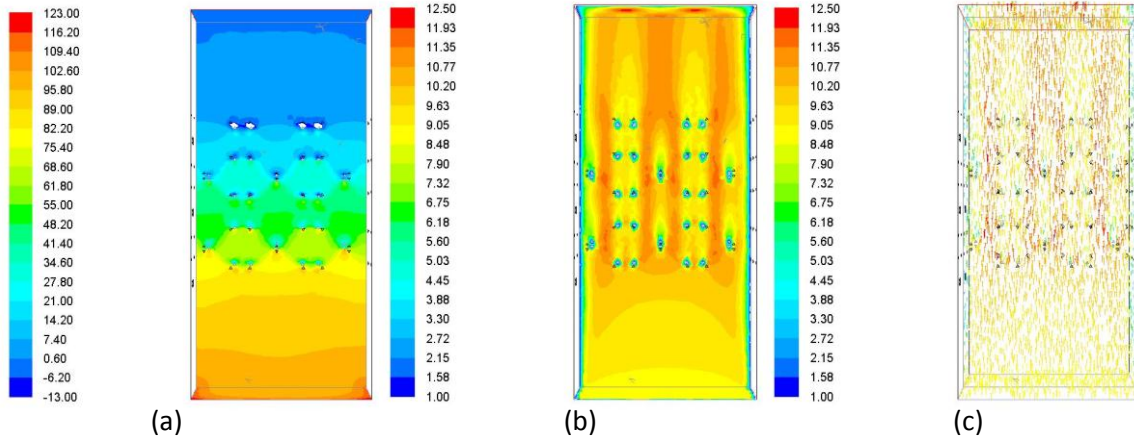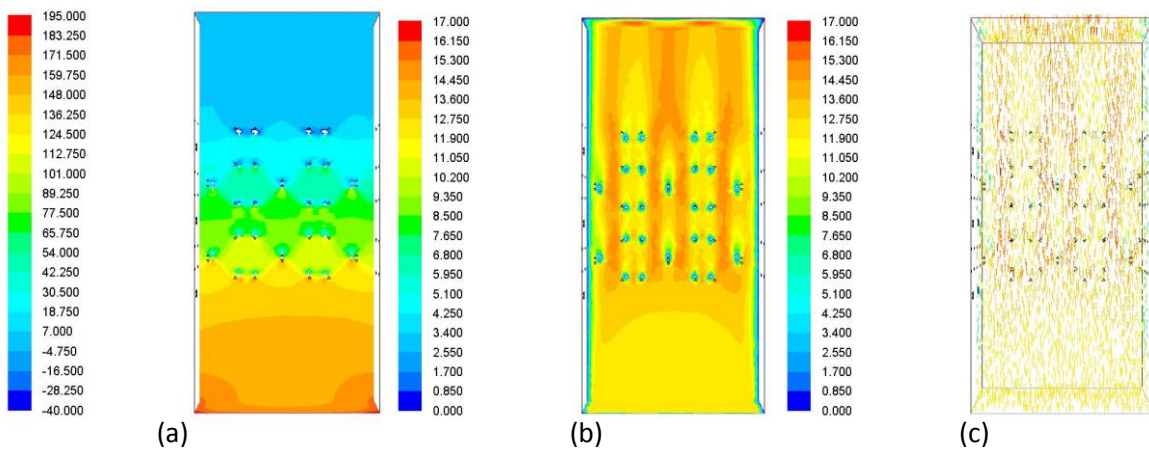**Figure 205 80ppi inlet velocity 12m/s (a) Pressure (Pa) (b) Velocity (m/s) (c) Velocity vectors (m/s)**
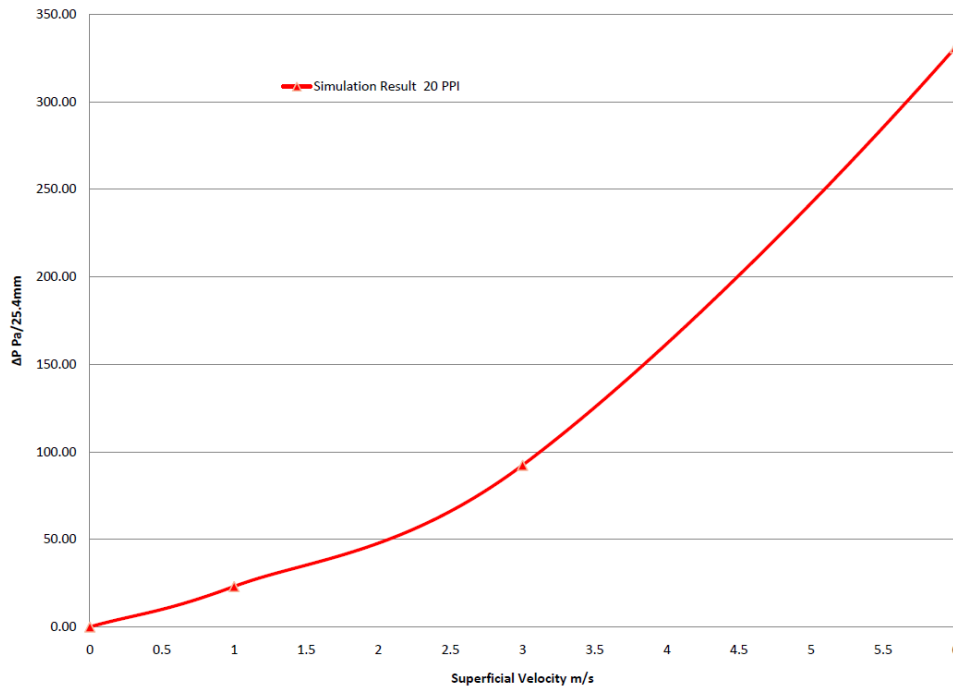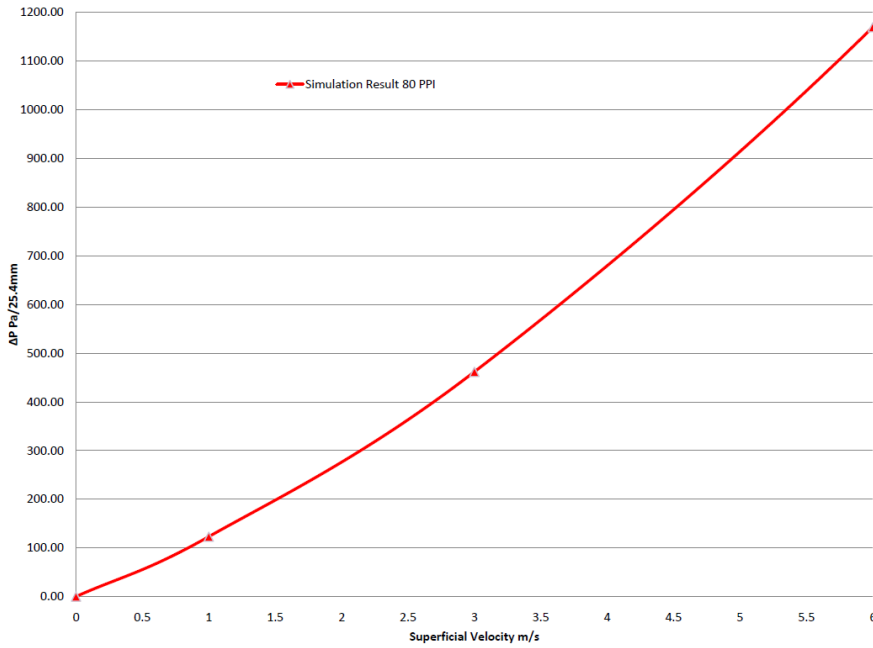
Figure 206 80ppi pressure drop.

Figure 206 shows a normalised pressure drop for the 80ppi model. This graph characterises the 80ppi foam by the curve. Figure 207 shows a comparison of 80ppi model to other mathematical models and models developed in literature. The simulated pressure drop results are between the other model values. These results will be discussed further in Chapter 6.
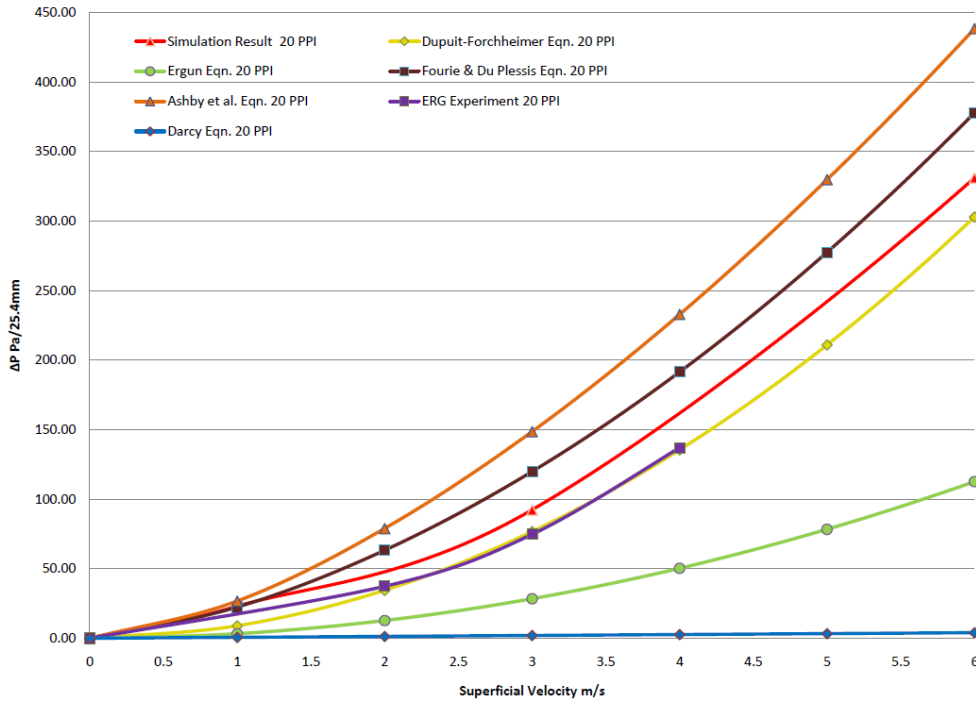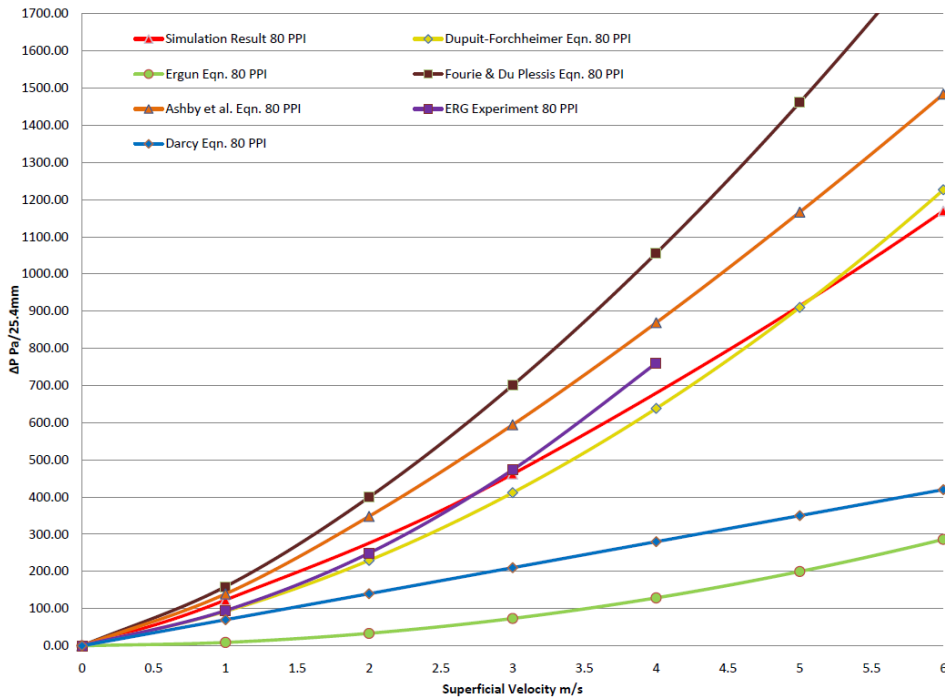

Figure 207 80ppi pressure drop comparison.

5.2.3.2.7 100ppi model

The 100ppi model is shown in Figure 208. The fluid flow regime, pressure, pressure drop from inlet to outlet, velocity flow through the model is observation from the results.
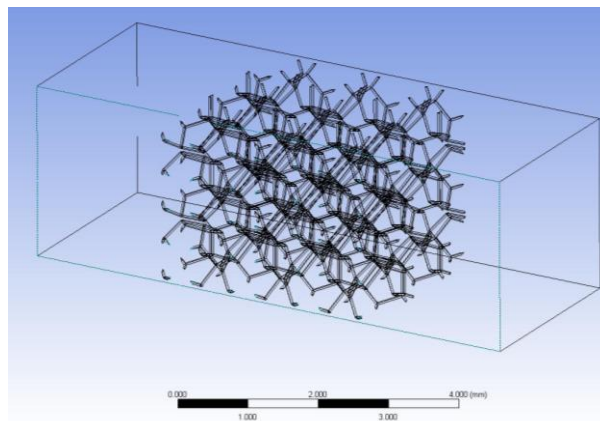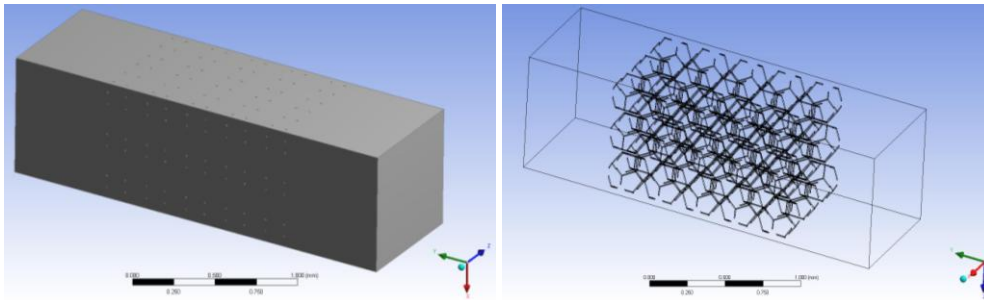

Figure 208 100ppi open pore cellular foam model and wireframe model.

As inlet velocity increases, this mixing becomes greater and the slow velocity at the walls increases also. The pressure drop through this model is small, about 12 Pa at 1m/s inlet velocity as shown in to about 380 Pa at 12m/s inlet velocity as shown in Figure 213.
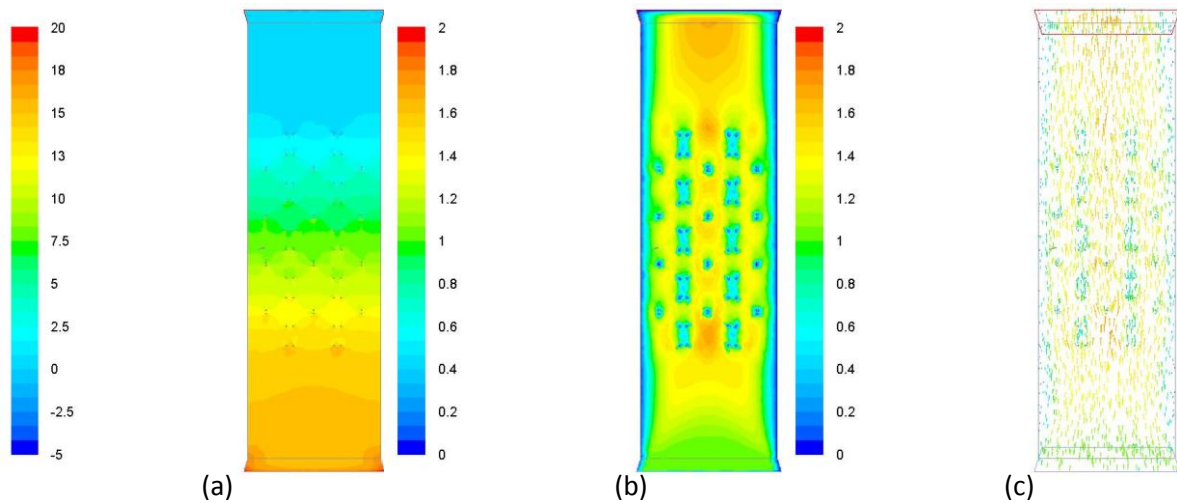
Figure 209 100ppi inlet velocity 1m/s (a) Pressure (Pa) (b) Velocity (m/s) (c) Velocity vectors (m/s)
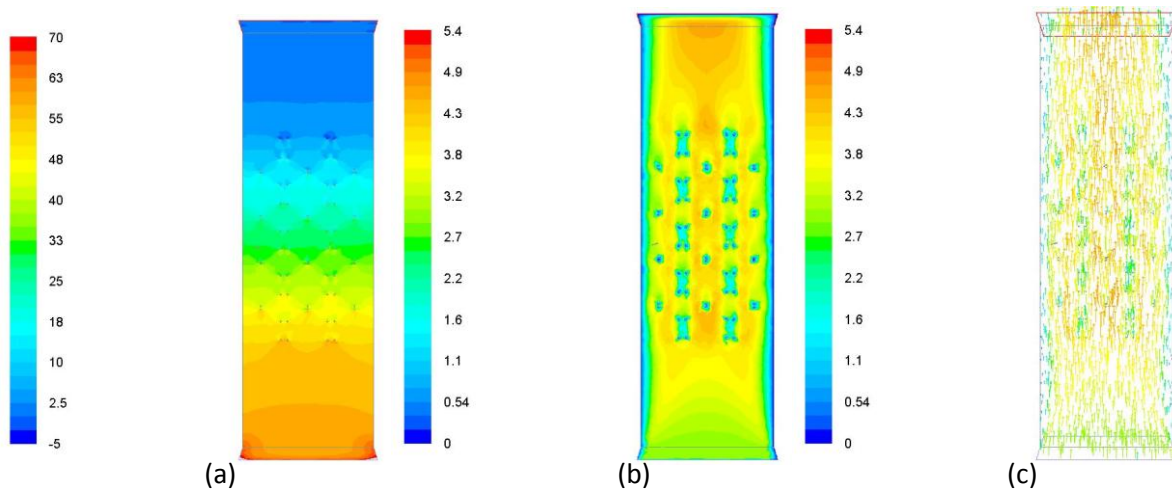
Figure 210 100ppi inlet velocity 3m/s (a) Pressure (Pa) (b) Velocity (m/s) (c) Velocity vectors (m/s)

(a)   (b)   (c)
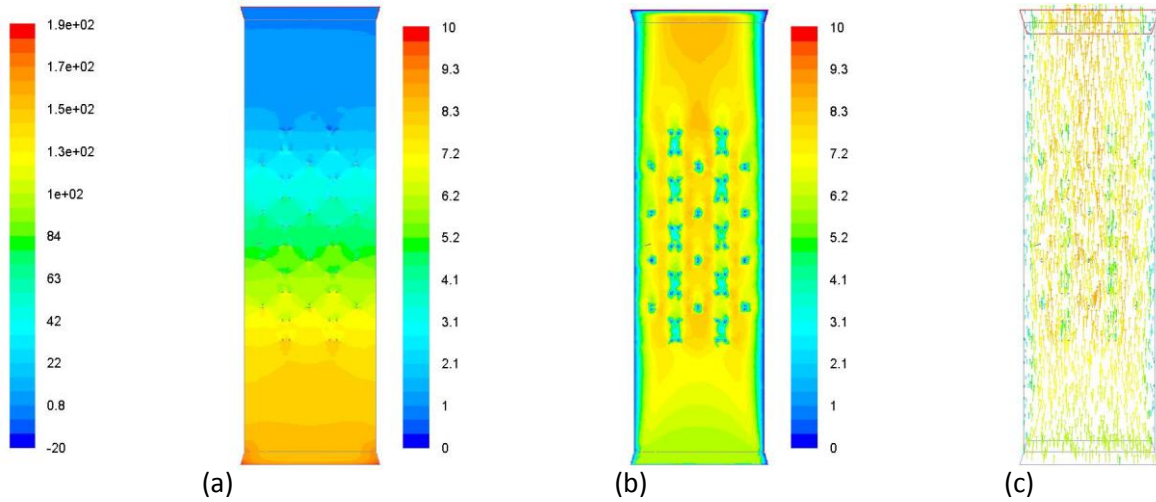
Figure 211 100ppi inlet velocity 6m/s (a) Pressure (Pa) (b) Velocity (m/s) (c) Velocity vectors (m/s)

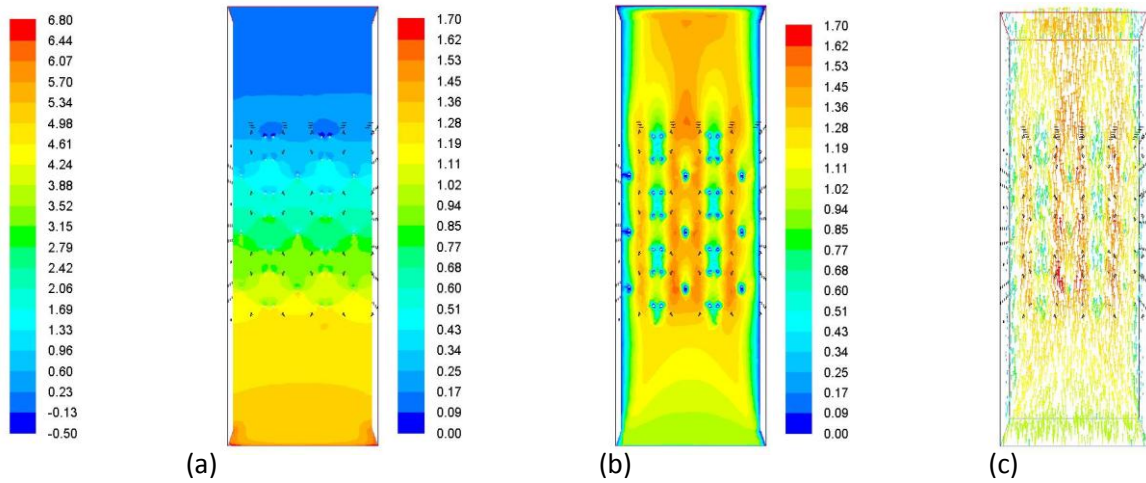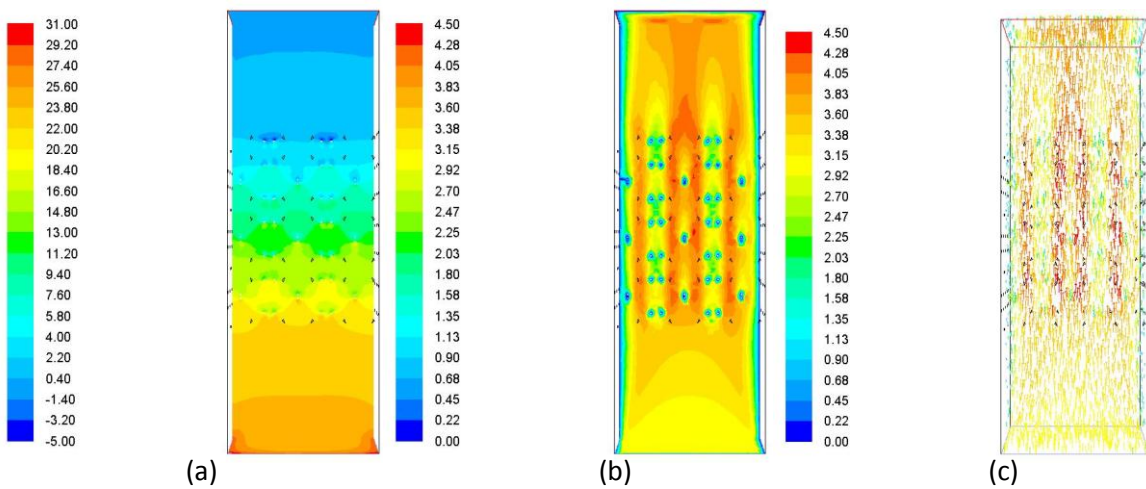(a)   (b)   (c)
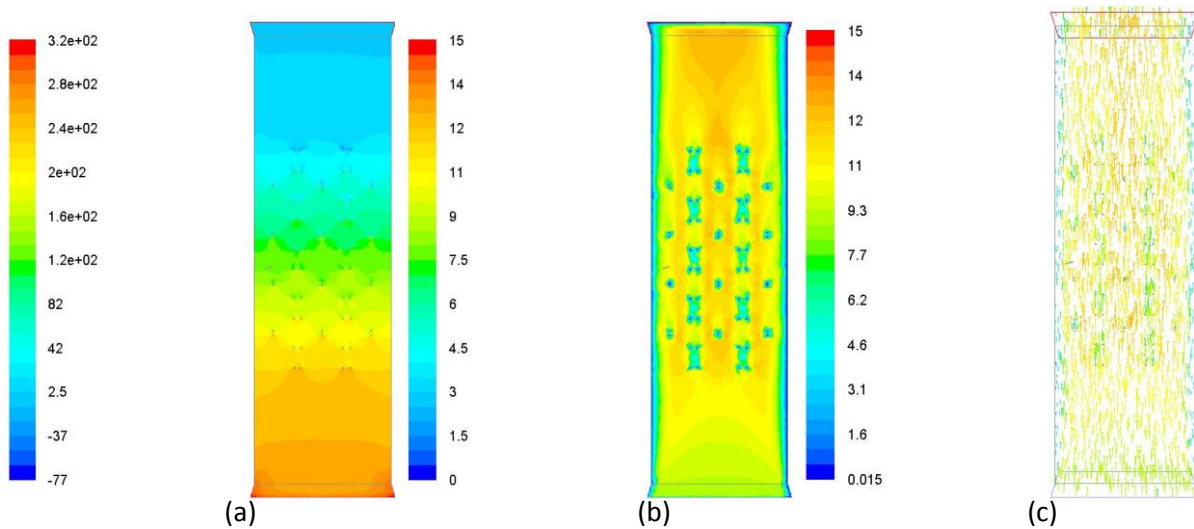
Figure 212 100ppi inlet velocity 9m/s (a) Pressure (Pa) (b) Velocity (m/s) (c) Velocity vectors (m/s)
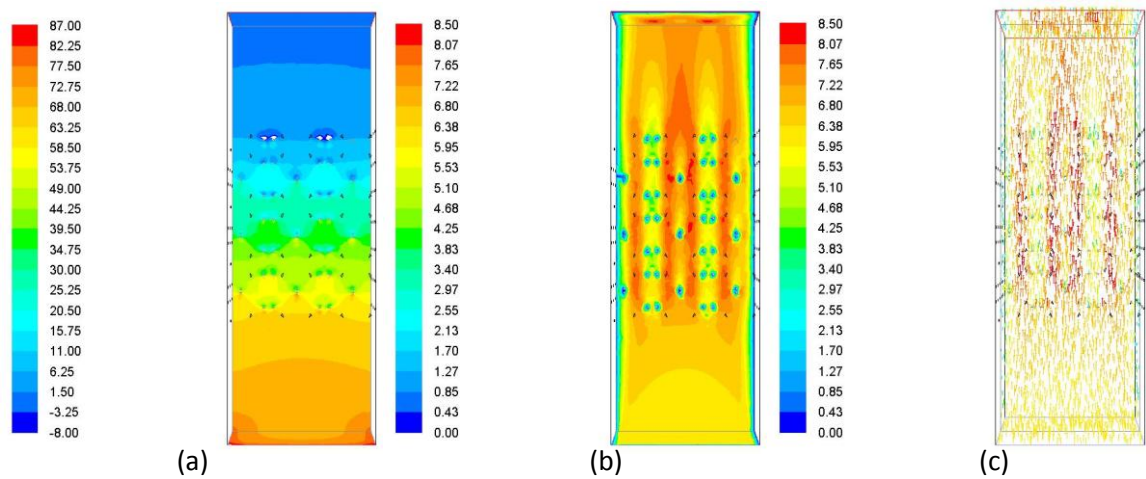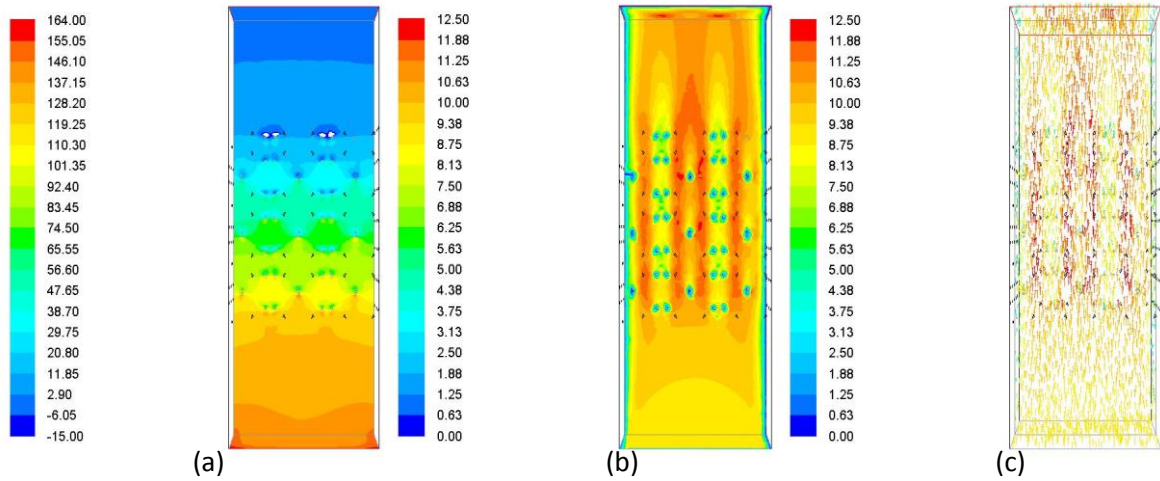

(a)   (b)   (c)
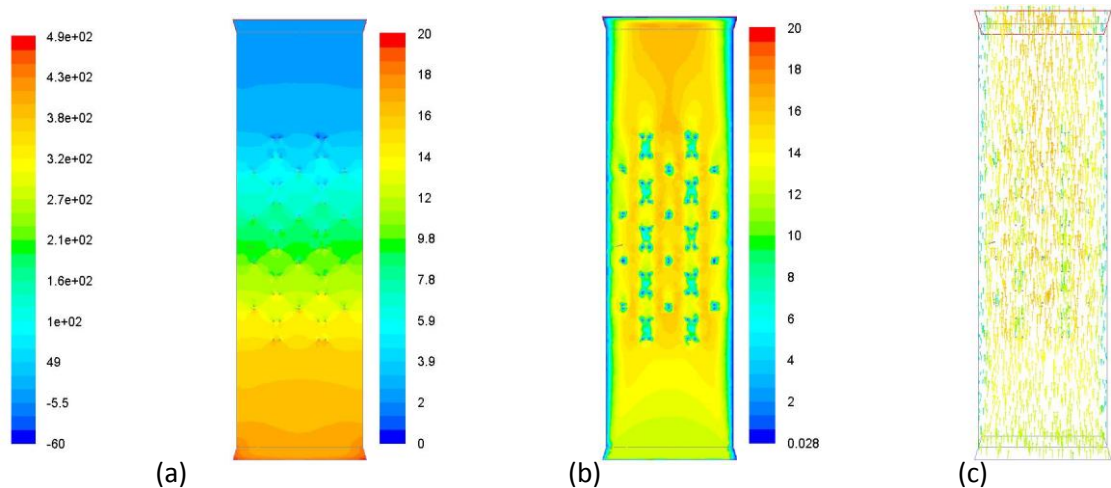
Figure 213 100ppi inlet velocity 12m/s (a) Pressure (Pa) (b) Velocity (m/s) (c) Velocity vectors (m/s)
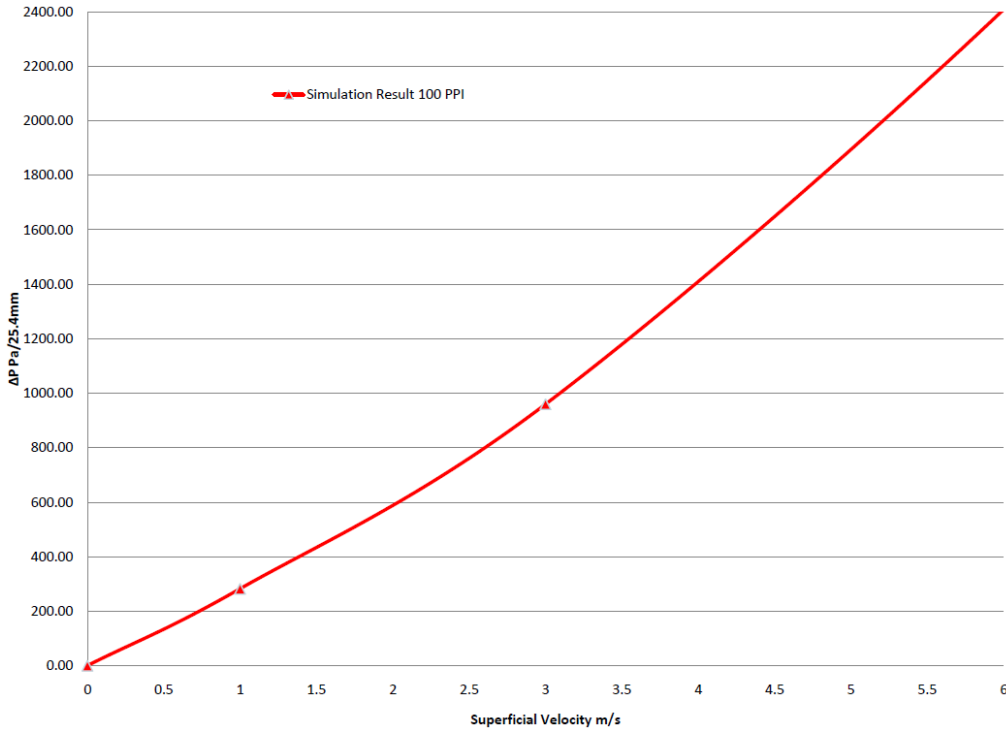
Figure 214 100ppi pressure drop.

Figure 214 shows a normalised pressure drop for the 100ppi model. This graph characterises the 100ppi foam by the curve. Figure 215 shows a comparison of 100ppi model to other mathematical models and models developed in literature. The simulated pressure drop results are between the other model values. It is noticed that the Darcy Model also matches the other models at low velocities. These results will be discussed further in Chapter 6.
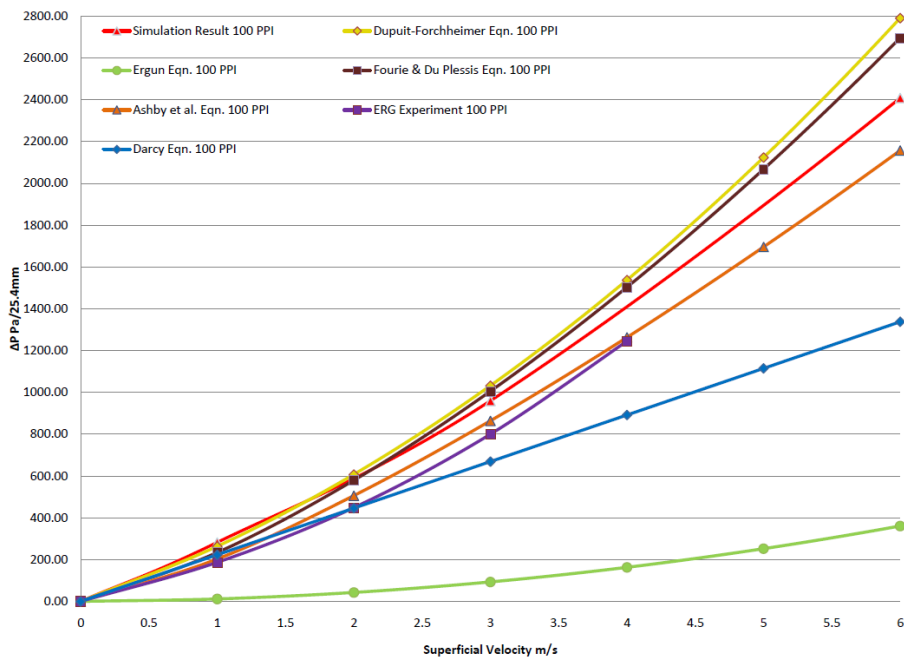
Figure 215 100ppi pressure drop comparison.

5.2.4 3-D Electrochemical Model Development & Simulation Results

3-D electrochemical models take into account all aspects of an operational PEM fuel cell. The model uses many variables and parameters to accomplish its objective, which is to verify if the flow plate designs and configurations proposed in this thesis, are valid and whether they can improve the performance of a PEM fuel cell. The simulation results from the electrochemical PEM fuel cell model simulation will assist in analysing the chemical reactions within the cell. The results will allow for analysis of the effects that cannot be visible during experimentation. Effective flow plate design using open pore cellular foam flow plate designs can be validated or dismissed.

A schematic diagram of the PEM fuel cell model used in this analysis is illustrated in Figure 216. It consists of cathode and anode gas flow channels, catalyst layers, gas diffusion layers and current collectors. This basic scheme is used in both the double channel electrochemical model described in Section 5.2.4.1 and the open pore cellular foam electrochemical model described in Section 5.2.4.2.
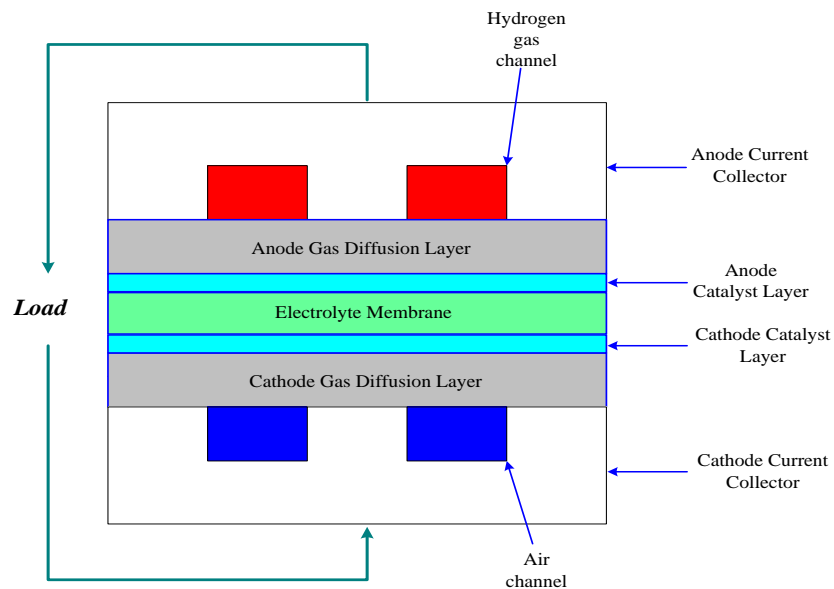
Figure 216 Schematic diagram of the fuel cell model.

In order for the CFD analysis software to recognise the PEM fuel cell model, the zone types must be clearly modelled using Ansys Mesh. Two zone types that need to be specified are boundary and continuum zone types. Boundary-type specifications define the physical and operational characteristics of the fuel cell at those topological entities that represent model boundaries. Continuum zone types define the physical characteristics of the model within specified regions of its domain. For the PEM fuel cell model only the cathode and anode collector are specified as the solid continuum-types, this also simplifies the model [193]. The boundary types are specified as faces while the continuum zone types are the volumes of each component. The boundary zones specified for the double channel electrochemical model and the open pore cellular foam electrochemical model are detailed in the Appendix G.

The analysis is carried out at loading conditions of 0.85V (low current density / low load), 0.75V, 0.65V and 0.55V (high current density / high load) and a polarisation curve (I-V curve) with a power density curve are plotted.

Post possessing involves analysing the data obtained from the simulation; hydrogen utilisation, oxygen concentration, water mass fraction and polarisation or I-V curves. The I-V curves can also be validated and compared to experimental results.

In this study a grid 20% finer than the base grid was used for a comparison analysis of each mesh. A polarisation curves showed no significant difference in performance of the models; therefore the base mesh was used as it reduced the number of nodes saving computational time. (A similar result was obtained from the PEM fuel cell model with open pore cellular foam flow fields.)

5.2.4.1 3-D double channel electrochemical model development

To reduce complexity and computational demand, a section of the complete flow plate is used for the selected computational domain, see Figure 217.
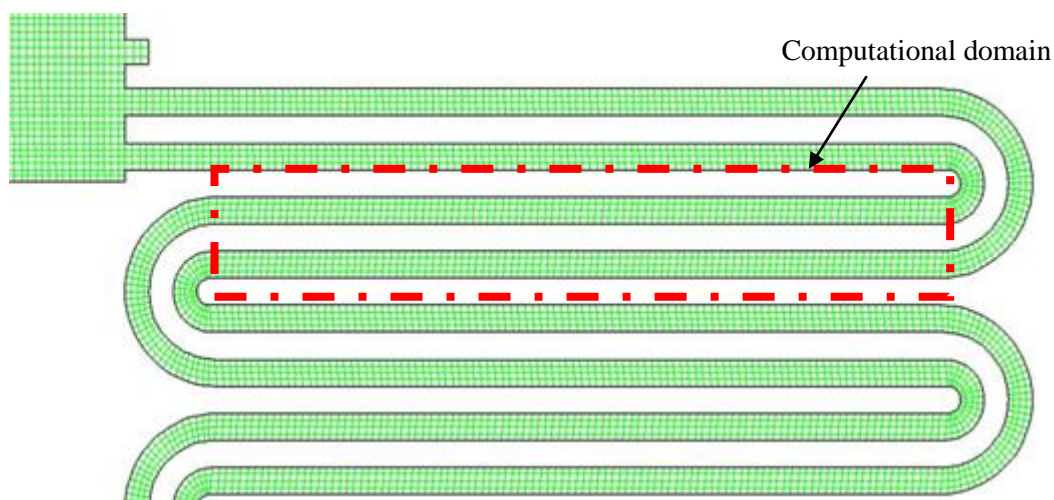
Figure 217 Computational domain for the PEM fuel cell double channel electrochemical model.

The domain consists of two, straight, counter flow, channels, each 1mm x 1mm x 30mm. The dimensions of the full domain are 5.5 mm x 5mm x 30mm in the x, y and z directions, respectively. The cross sectional area of the membrane electrode assembly is consequently 150mm^2, this is the area used in obtaining the current density. Considering that only a section of the full flow plate of the full cell is used in the model, the results of the current density, current per area, can still be related to the current density of an operational PEM fuel cell, which will be used to determine the performance of the flow plate.
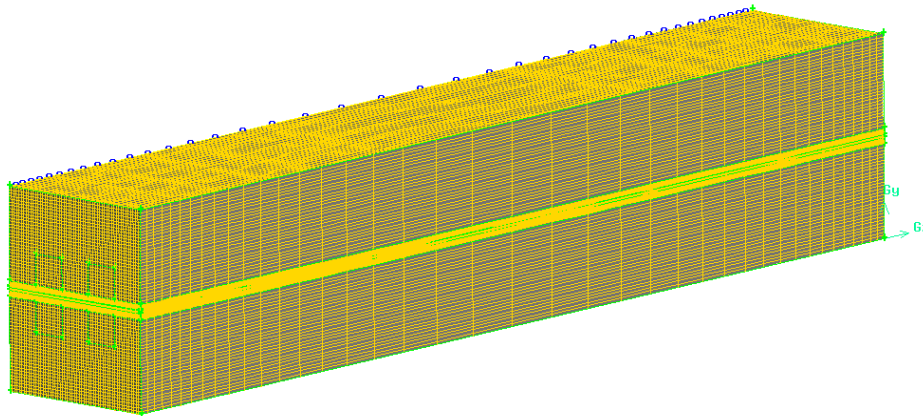
Figure 218 3-D PEM fuel cell with double channel flow plate model mesh.

The 3-D meshed model is shown in Figure 218.The most suitable mesh for the double channel model is the quad submap mesh, which specifies that the mesh includes only quadrilateral mesh elements. The structured grids of mesh elements in each region are generated as seen in Figure 219 for the double channels flow field PEM fuel cell model. This mesh structure is particularly suited for this solution because it increases rate of convergence, increases solution accuracy and reduces the CPU time required.
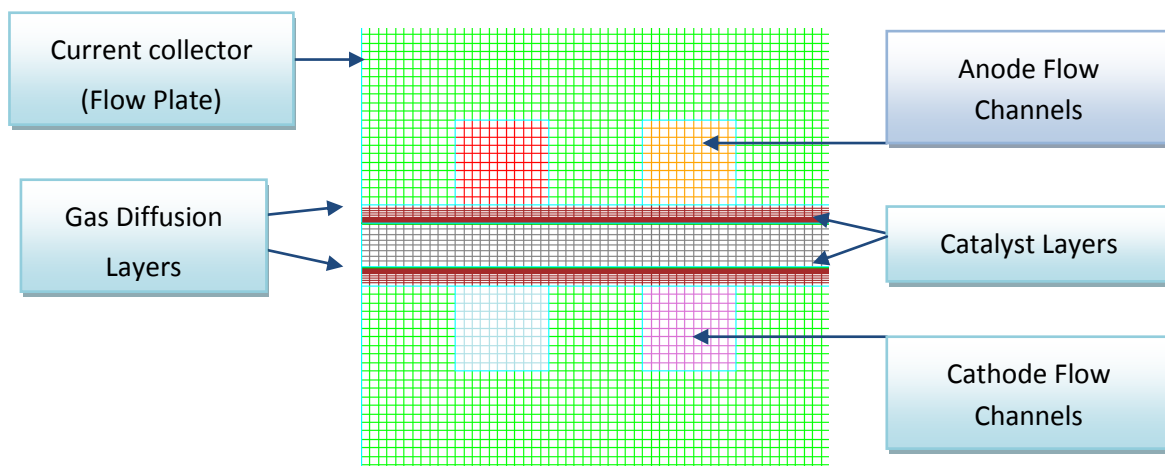
Figure 219 3-D flow channel mesh layout.

With all the zones specified, the mesh is exported ready for analysing. The PEM fuel cell model parameters are set and properties assigned to the relevant regions of the fuel cell before defining the boundary conditions. In order to run the model a minimum number of parameters have to be available to the user. These parameters are obtained from the fuel cell specifications, experimentation, electrochemistry calculations and existing material properties. A full list of the input parameters for all the models is detailed in Appendix G. One of the most important attributes that can be used to validate a PEM fuel cell model simulation is the comparison of the I-V curves of the simulated and experimental results. Please refer to Section 5.2.4.2 for all the models CFD results and Chapter 6 for a full discussion of these results.

5.2.4.2 3-D double channel electrochemical simulation results

Figure 220 shows the model of the PEM fuel cell with double channels having dimensions; 1mm x 1mm x 30mm long with each flow plate 3mm thick. A complete list of the setup and operational parameters of the PEM fuel cell model are listed in Appendix G. To view the results clearly planes (surfaces) are created through different parts of the model, velocity profile is shown in Figure 220 for example. The planes allow for a clearer view of the results.
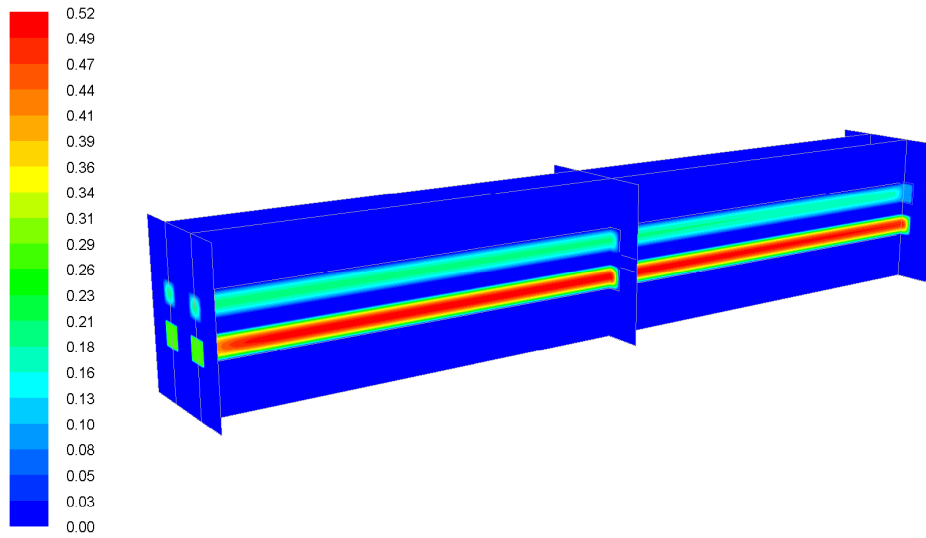
Figure 220 Double channel PEM fuel cell velocity profile (m/s) with planes visible.

5.2.4.2.1 Hydrogen distribution

In Figure 221 the flow in the anode (upper) channel is from right to left. The hydrogen mass fraction decreases in the direction of flow. This is due to water being pulled through the membrane along with hydrogen as it is consumed in the fuel cell.
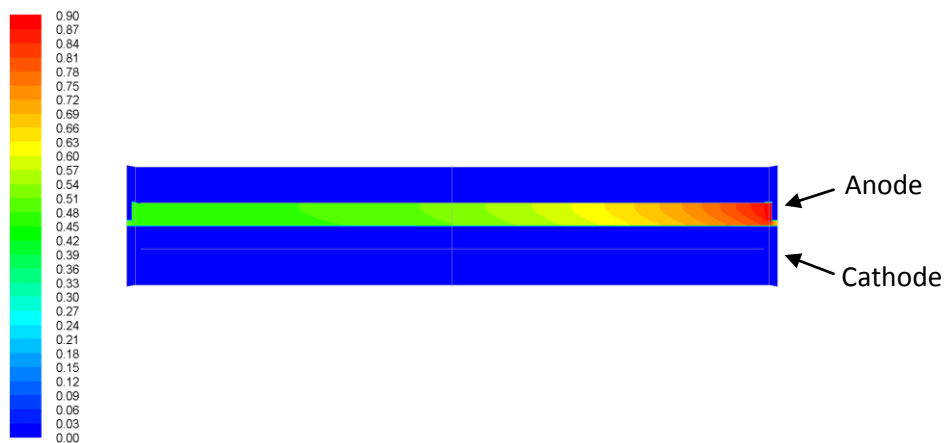
Figure 221 Hydrogen mass fraction at 0.85 volts.
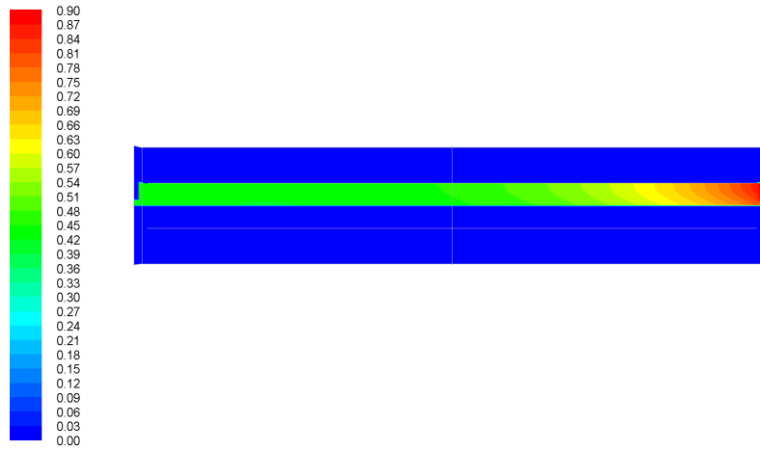
Figure 222 Hydrogen mass fraction at 0.55 volts.

Figure 221 and Figure 222 highlight the hydrogen utilisation at lower (0.85V) and higher (0.55V) loading conditions respectively. A significant difference can be seen in the concentration; the lower loading condition has a higher concentration throughout the channel compared to the higher loading condition. This result signifies that consumption of hydrogen increases with an increase in current drawn from the cell.

5.2.4.2.2 Oxygen distribution

Figure 223 shows the resulting mass fraction of the oxygen at the cathode side, the flow in the cathode (lower) channel is from left to right. The oxygen concentration decreases gradually from the inlet to the outlet due to the consumption of oxygen and the producing of water.
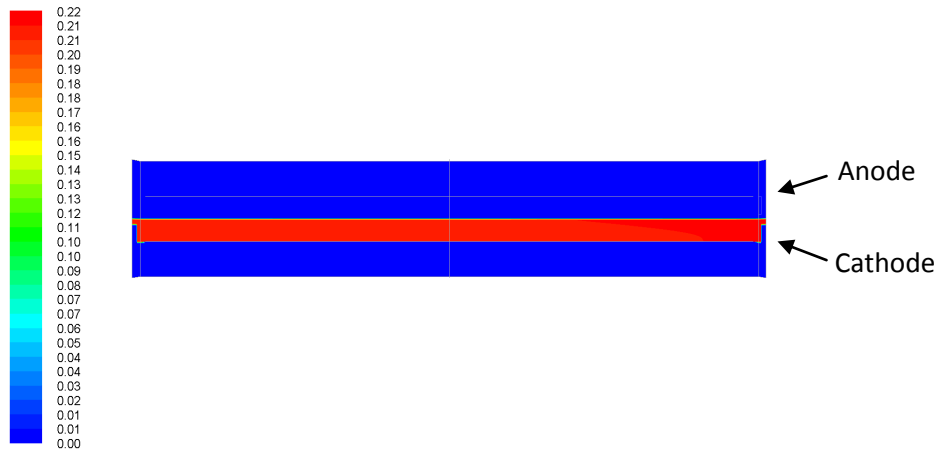
Figure 223 Oxygen mass fraction at 0.85 volts.
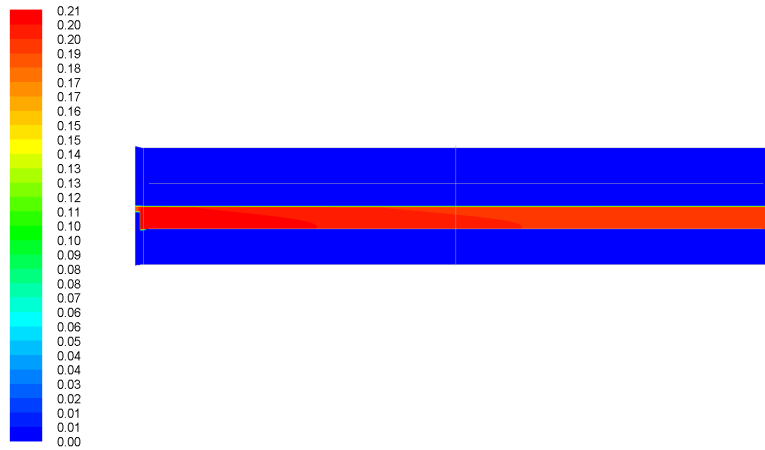
Figure 224 Oxygen mass fraction at 0.55 volts.

When the current density is increased, less oxygen reaches the catalyst layer as shown in Figure 224. Figure 225 shows a clearer view of hydrogen and oxygen consumption in the anode and cathode flow channels. From inlet to outlet hydrogen consumption stabilises, even at high current densities. This is not the case for oxygen at high current densities with the concentration of oxygen decreasing rapidly from inlet to outlet. This indicates that at high current densities the amount of oxygen that can diffuse through the electrode and the amount being consumed by the electrochemical reaction decreases, causing possible mass transport issues.
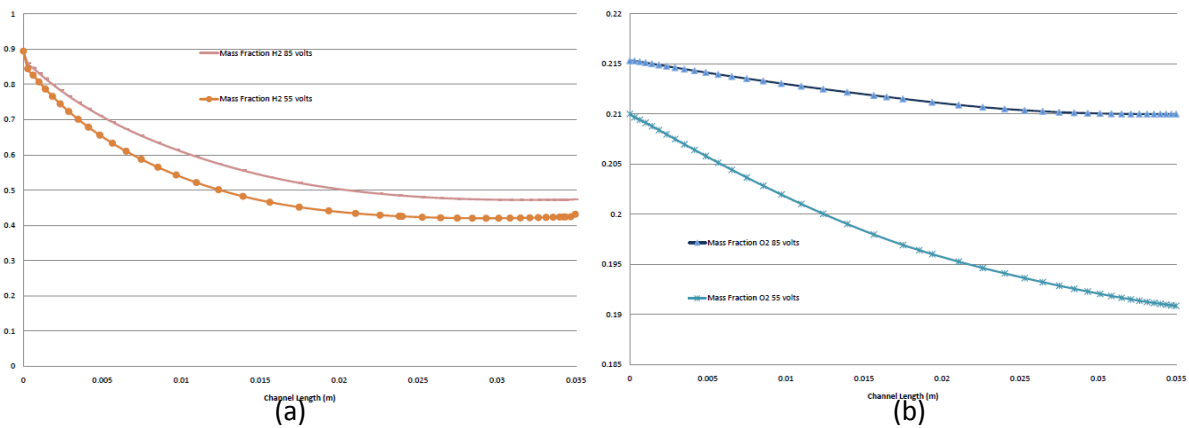
Figure 225 Hydrogen (a) & Oxygen (b) mass fraction at 0.85 volts & 0.55 volts.

5.2.4.2.3 Water distribution

This model does not take into account the phase change and two-phase flow of the water through the channels; therefore these results only show the liquid water activity within the cell. The potential of flooding is shown in Figure 226, Figure 227 and Figure 228. The results show that the water distribution is highest in the cathode side since most reduction reaction to form water occurs in this channel. The concentration increases in the direction of flow in both anode and cathode sides at high current densities.
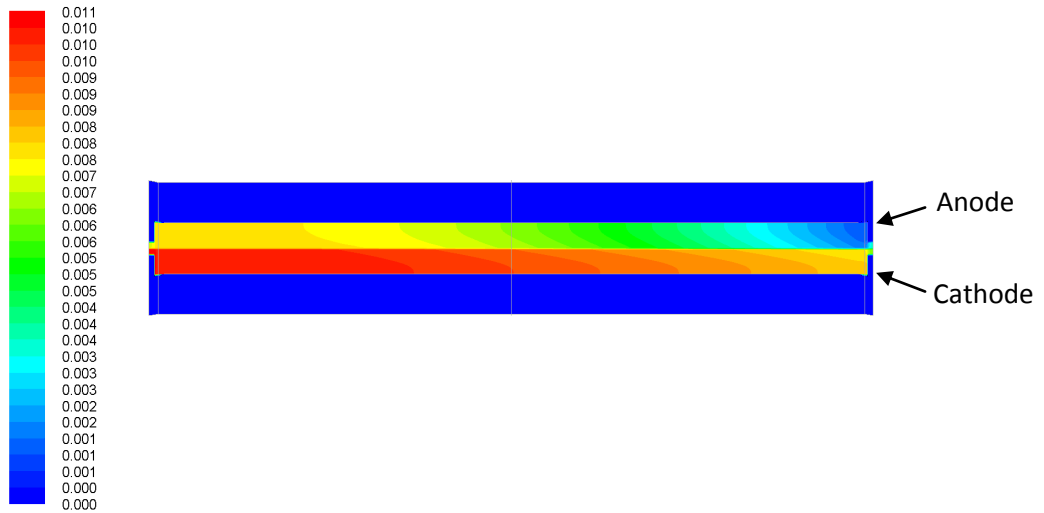
Figure 226 Water distribution at 0.85 volts.
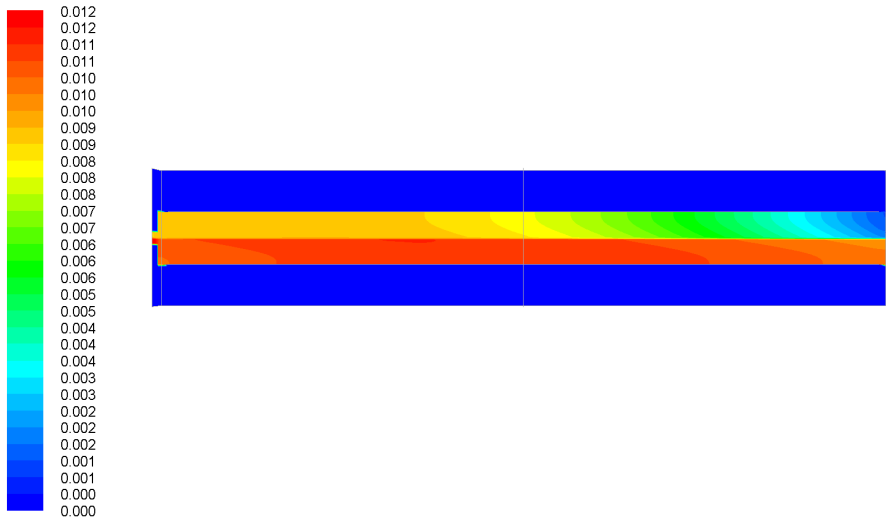
Figure 227 Water distribution at 0.55 volts.
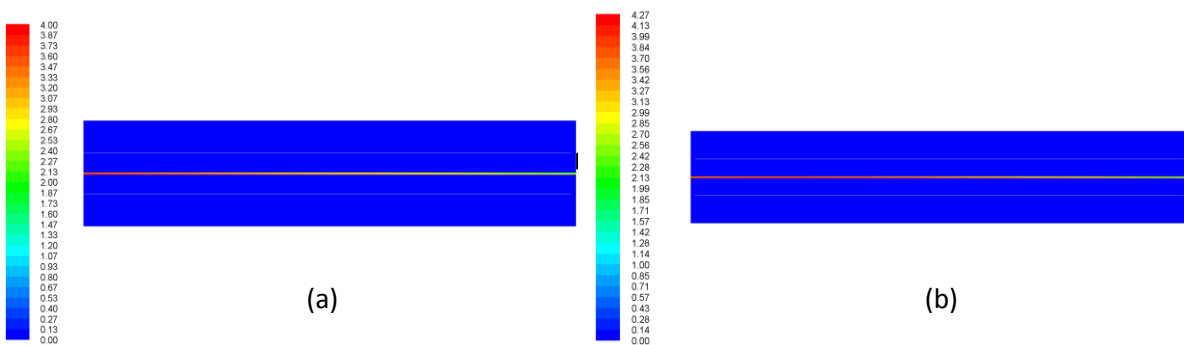
Figure 228 Water distribution in the MEA (a) 0.85 volts (b) 0.55 volts.
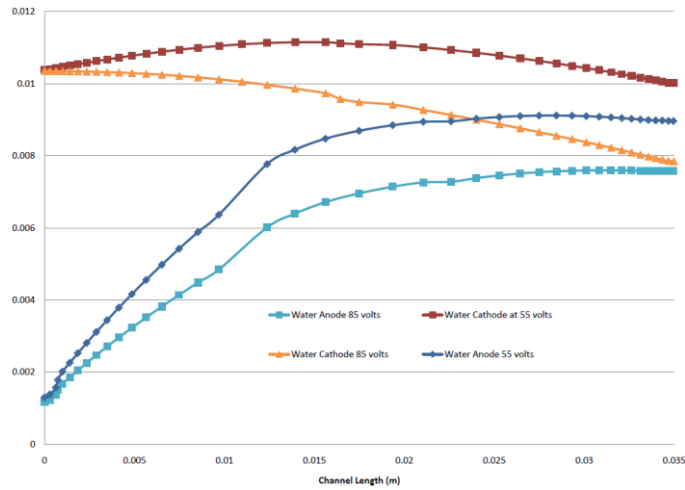
Figure 229 Water distribution in anode and cathode at 0.85 volts & 0.55 volts.

Figure 229 shows a clearer view the water distribution in the anode and cathode flow channels. At the anode water increases from inlet to outlet and then stabilises at low current densities. In the cathode the content of water decreases and is seen to match the anode side as expected. This can be associated to back diffusion which is sufficient to counteract the electro-osmotic drag. Under high current density the electro-osmotic effect dominates back diffusion. These phenomena can result in a drier anode as seen with the slight decrease of water toward the end of the channel in the anode. At the cathode water increases very quickly at high current densities. This then begins to reduce and level off possibly due to water flooding affecting the fuel cell.

5.2.4.2.4 Temperature distribution

The highest temperatures are located at the centre of the PEM fuel cell, slightly higher at the cathode than the anode. The temperature distribution in the fuel cell at low load condition is almost the same as the nominal temperature are shown in Figure 230.
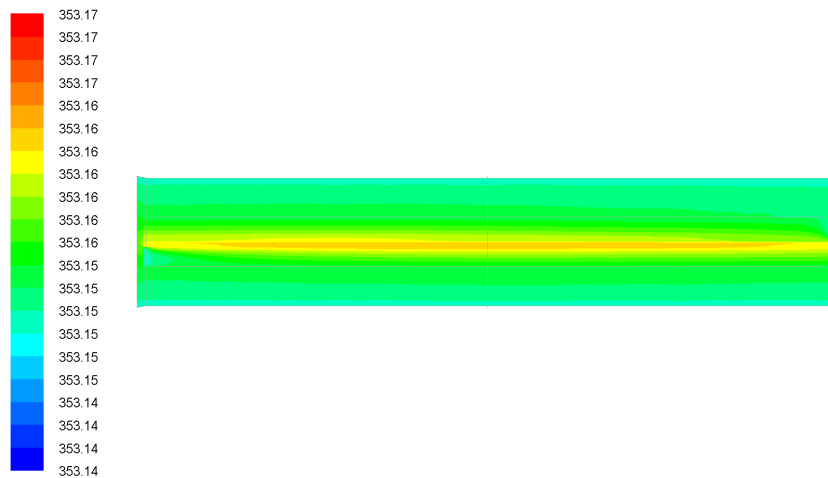
Figure 230 Temperature at 0.85 volts.
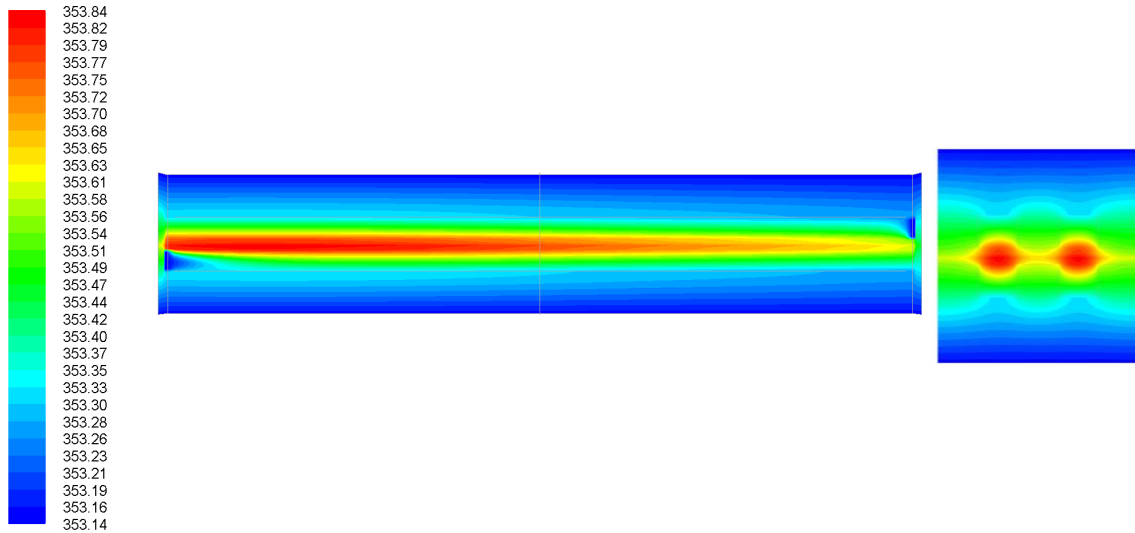
Figure 231 Temperature at 0.55 volts.

The temperature distribution inside the cell is dependent on the loading conditions. At the high load condition the temperature is very close to nominal but slightly higher due to higher current densities as shown in Figure 231.

5.2.4.2.5 Current density

The current density is affected by the oxygen, hydrogen and activation over potential within the membrane. The distribution of oxygen and hydrogen should therefore reflect on the current density distribution. The balance of oxygen and hydrogen occur at the midsection of the model therefore the maximum current density occurs in the centre region of the model. Figure 232 shows the current flux at centre of the z-axis. The concentration is mainly on the gas diffusion layer and the area between the flow channels.

(a)   (b)
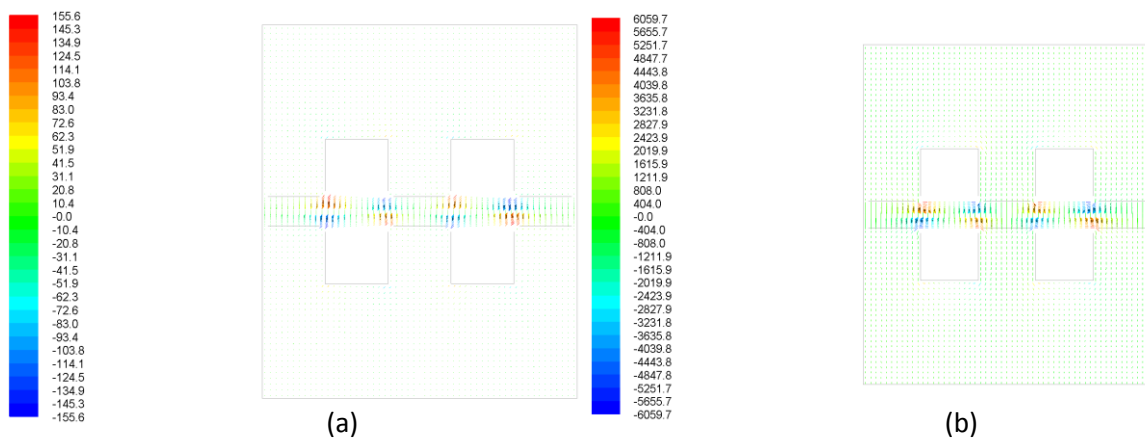
Figure 232 Current Flux (a) 0.85 volts (b) 0.55 volts.

Higher current flux densities are observed at higher loading, this justifies the oxygen concentration results since current flux densities are a directly related to the oxygen concentrations. The current flux

density distribution shows that operating the fuel cell at a higher load increases its efficiency, since the electrochemical reactions are increased at the catalyst layers.

Figure 233 shows the I-V curve results for the double channel simulation and also the experimental result of the operational PEM fuel cell. The results match very well. These results will be discussed further in Chapter 6.
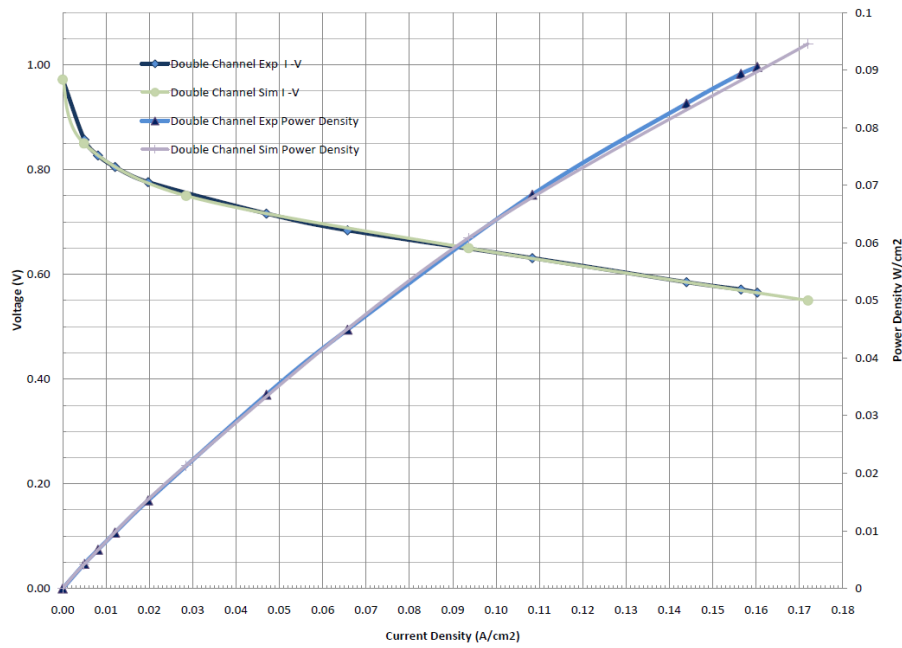
Figure 233 Double channel simulation and experimental polarisation curve.

5.2.4.3 3-D Open pore cellular foam channel electrochemical model development

The 40ppi open pore cellular foam flow plate performed satisfactorily in the initial CFD modelling and so it was decided to model this flow plate. To reduce complexity and computational demand, a section of the complete flow plate is used for the selected computational domain, see Figure 234.

Computational domain of the 40ppi open pore cellular foam model
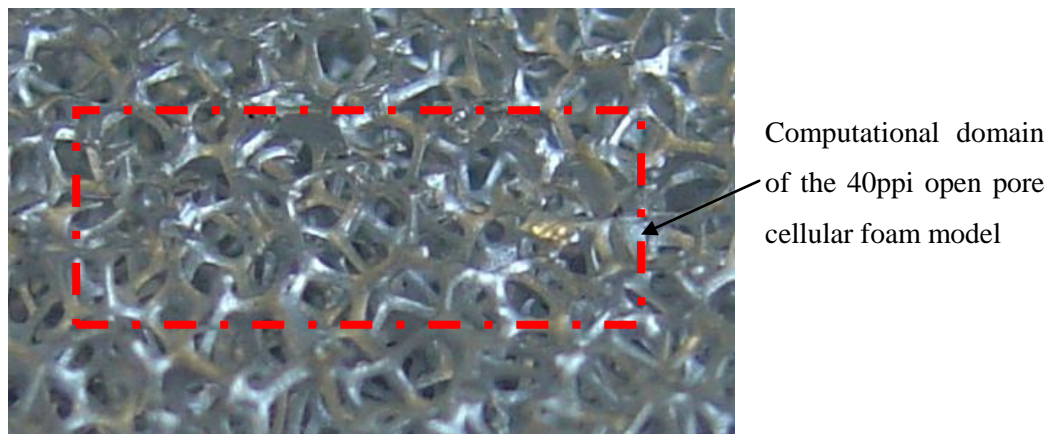
Figure 234 Computational domain for the PEM fuel cell open pore foam flow plate

The flow plate domain consists of the open pore cellular foam flow plate, consisting of 6 pores long by 3 pores wide equating to 2mm x 4mm x 0.62mm. The hydrogen and oxygen are supplied co-flow.

The dimensions of the full domain are 2mm x 2.19mm x 4.5mm in the x, y and z directions, respectively. The cross sectional area of the membrane electrode assembly is consequently 9mm^2, this is the area used in obtaining the current density. Considering that only a section of the full flow plate of the full cell is used in the model, the results of the current density, current per area, can still be related to the current density of an operational PEM fuel cell, which will be used to determine the performance of the flow plate.
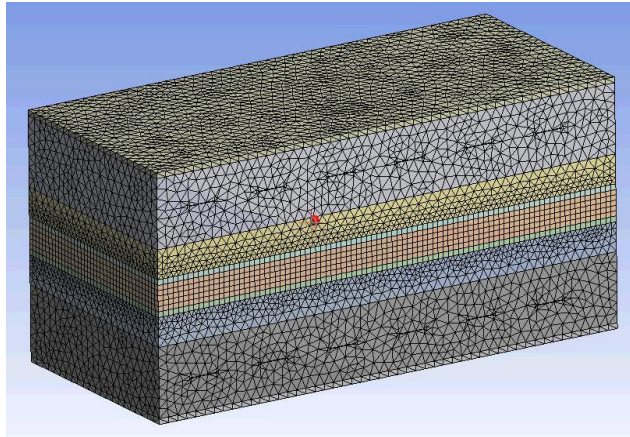
Figure 235 3-D PEM fuel cell with open pore cellular foam flow plate model mesh.

The most suitable mesh for the open pore cellular foam model is a mixed mesh, which specifies that the mesh includes quadrilateral and tetrahedral mesh elements. The structured grids of mesh elements in each region are generated as seen in Figure 235 for the open pore cellular foam flow field PEM fuel cell model. The mesh is quiet complex due to the limitation of 512,000 elements allowed by the software Fluent and the complexity of open pore cellular foam flow plate. The mesh structure is modified to suite this solution and to increases the rate of convergence, reducing the CPU time required, but keeping solution accuracy.
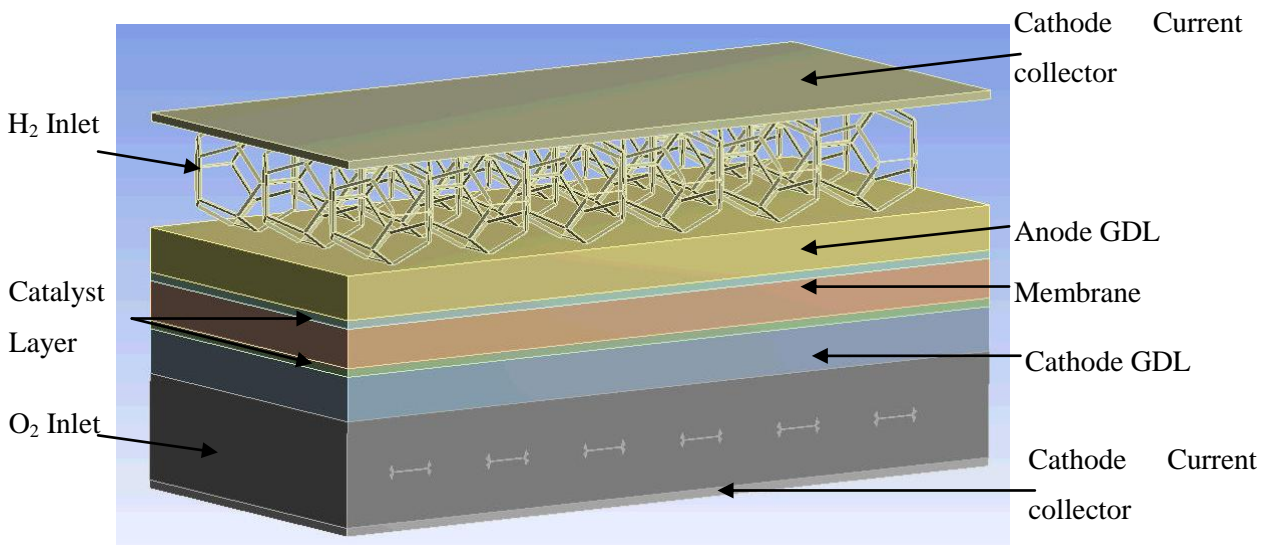
Figure 236 3-D PEM fuel cell model showing open pore cellular foam flow plate.

With all the zones specified, the mesh is exported ready for analysing. The 3-D model is shown in Figure 236 with the hydrogen volume removed, to make the open pore cellular foam flow plate visible. Figure 237 (a) and (b) also gives a detailed view of the PEM fuel cell model showing open pore cellular foam flow plate. The PEM fuel cell model parameters are set and properties assigned to the relevant regions of the fuel cell before defining the boundary conditions. In order to run the model a minimum number of parameters have to be available to the user. These parameters are obtained from the fuel cell specifications, experimentation, electrochemistry calculations and existing material properties. A full list of the input parameters for all the models is detailed in Appendix G. One of the most important attributes that can be used to validate a PEM fuel cell model simulation is the comparison of the I-V curves of the simulated and experimental results. Please refer to Section 5.2.4.4 for all the models CFD results and Chapter 6 for a full discussion of these results.

(a)   (b)
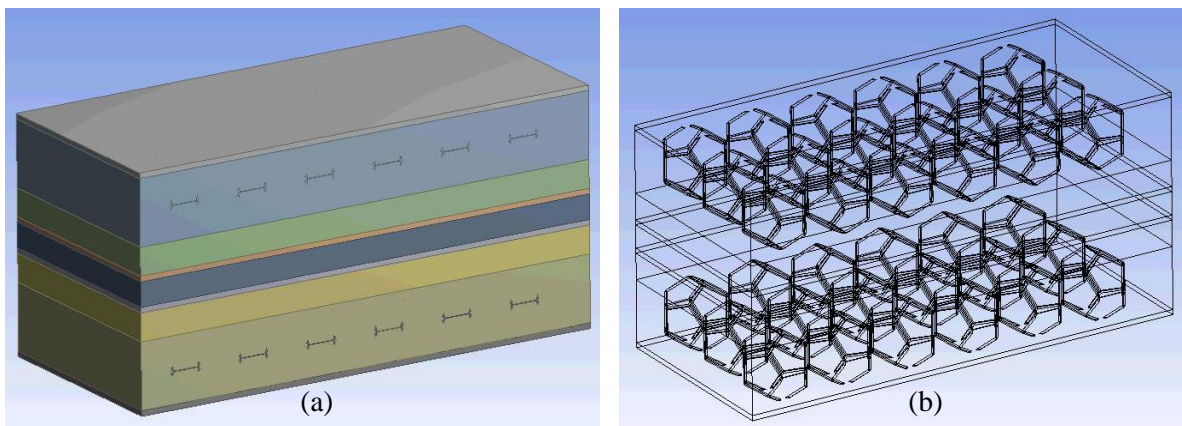
Figure 237 3-D PEM fuel cell model (a) and wireframe (b) with open pore cellular foam flow plate.

5.2.4.4 3-D Open pore cellular foam channel electrochemical simulation results

The setup and operational parameters for the PEM fuel cell model with open pore cellular foam flow plates are listed in Appendix G. To view the results clearly planes (surfaces) are created through different parts of the model, the velocity profile is shown in Figure 238 for example. The planes allow for a 2-D view of the results.
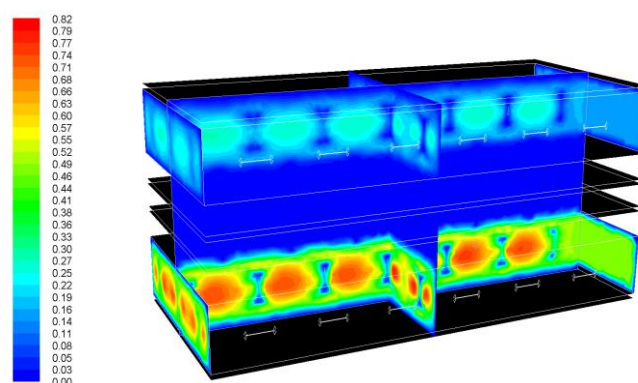
Figure 238 Open pore cellular foam PEM fuel cell velocity profile (m/s) with planes visible.

5.2.4.4.1 Hydrogen distribution

In Figure 239 the flow in the anode (upper) channel is from left to right. The hydrogen mass fraction decreases in the direction of flow. This is due to water being pulled through the membrane along with hydrogen as it is consumed in the fuel cell.
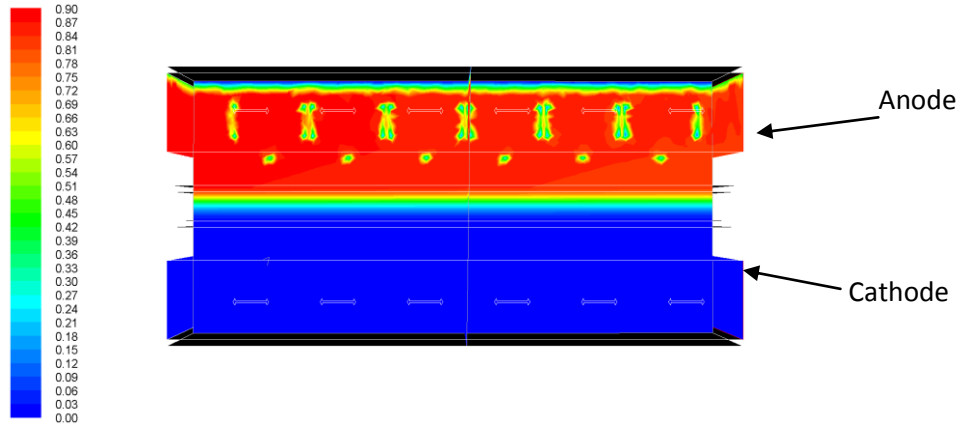
Figure 239 Hydrogen mass fraction at 0.85 volts.
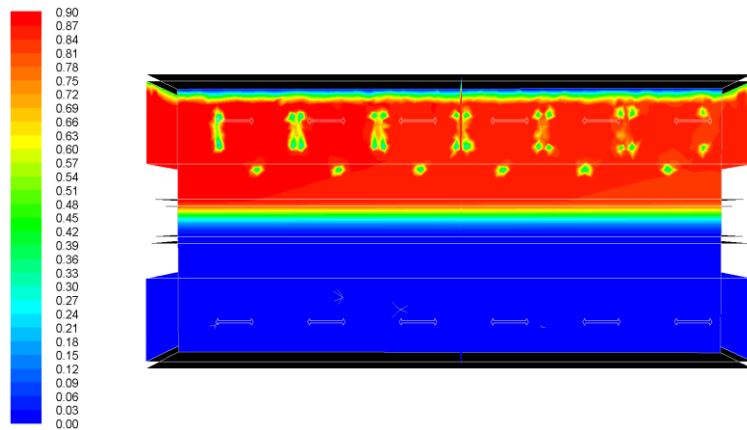
Figure 240 Hydrogen mass fraction at 0.55 volts.

Figure 239 and Figure 240 highlight the hydrogen utilisation at lower (0.85V) and higher (0.55V) loading conditions respectively. The hydrogen concentration decreases gradually from the inlet to the outlet due to the consumption of hydrogen and the producing of current.

5.2.4.4.2 Oxygen distribution

Figure 241shows the resulting mass fraction of the oxygen at the cathode side, the flow in the cathode (lower) channel is from left to right. The oxygen concentration decreases gradually from the inlet to the outlet due to the consumption of oxygen and the producing of water.
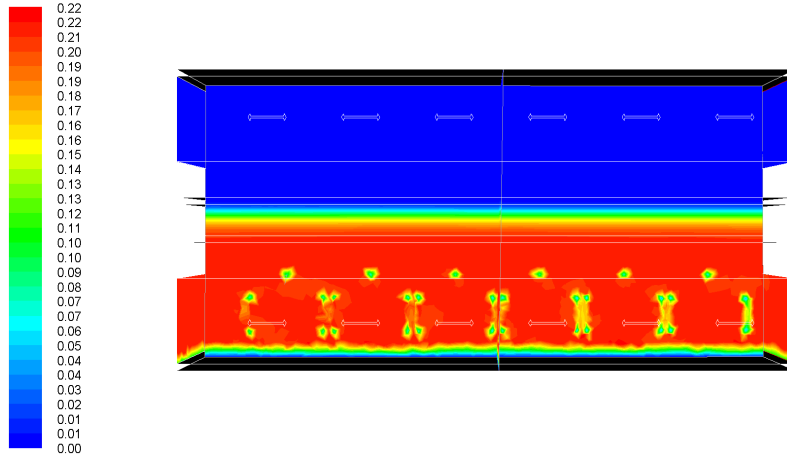
Figure 241 Oxygen mass fraction at 0.85 volts.
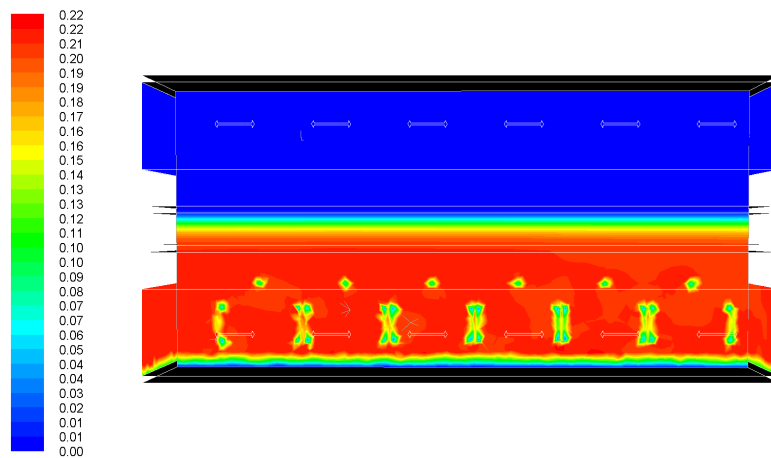
Figure 242 Oxygen mass fraction at 0.55 volts

(a)   (b)
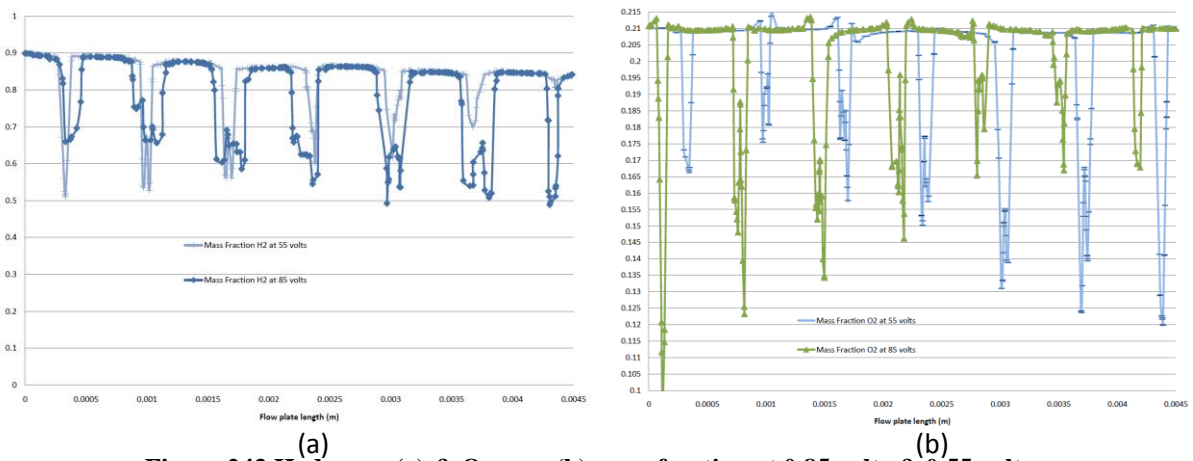
Figure 243 Hydrogen (a) & Oxygen (b) mass fraction at 0.85 volts & 0.55 volts.

Figure 243 shows a clearer view of hydrogen and oxygen consumption in the anode and cathode flow channels. The spikes seen in the graphs are caused by the interaction of the gas with the ligaments of the open pore cellular foam. From inlet to outlet hydrogen consumption decreases but there is very little difference in the low and high loading conditions. At the cathode at low load the oxygen consumption is stable and slightly decreases at the high load condition.

5.2.4.4.3 Water distribution

This model does not take into account the phase change and two-phase flow of the water through the channels; therefore these results only show the liquid water activity within the cell. The potential of flooding is shown in Figure 244, Figure 245 and Figure 246. The results show that the water distribution is highest in the cathode side since most reduction reaction to form water occurs in this channel. The concentration increases in the direction of flow in both anode and cathode sides at high current densities.
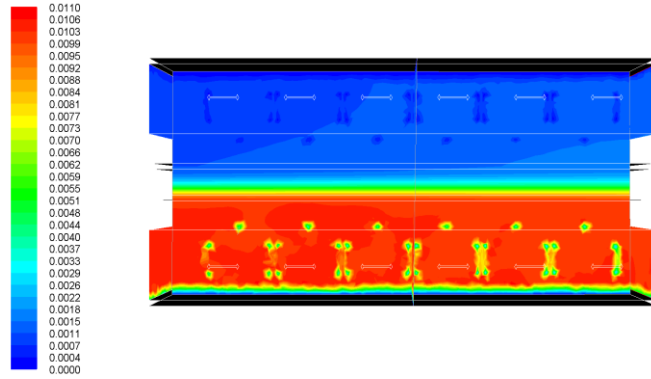
Figure 244 Water distribution at 0.85 volts.
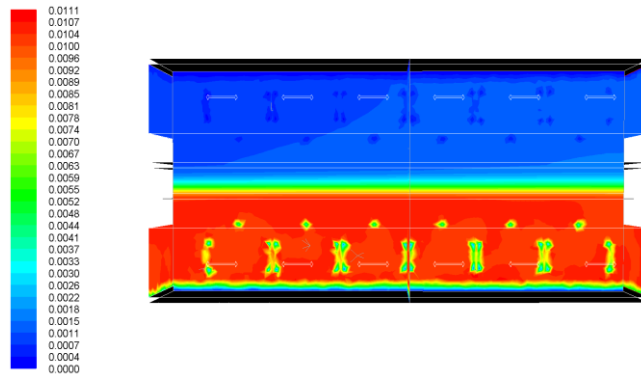
Figure 245 Water distribution at 0.55 volts.
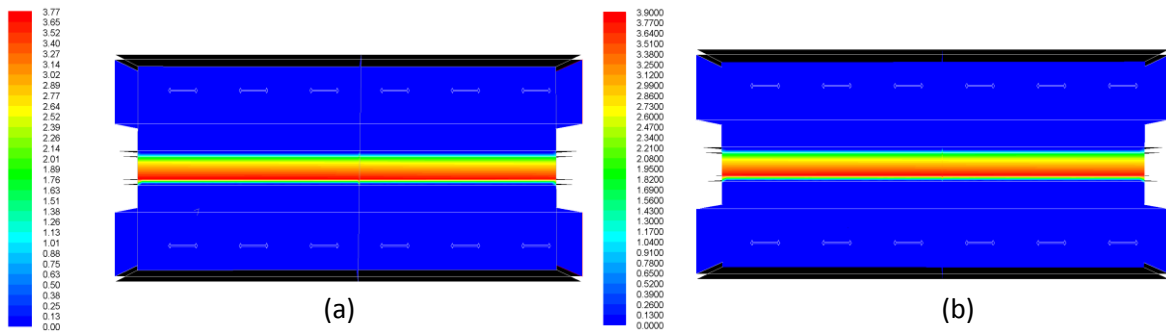
Figure 246 Water distribution in MEA (a) 0.85 volts (b) 0.55 volts.
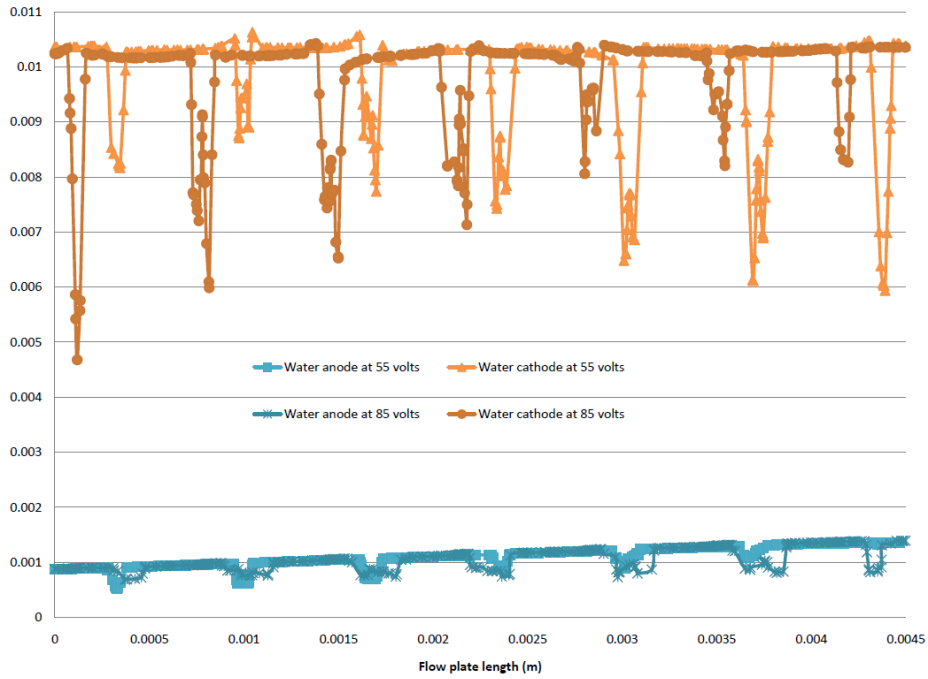
Figure 247 Water distribution in anode and cathode at 0.85 volts & 0.55 volts.

Figure 247 shows a clearer view the water distribution in the anode and cathode flow channels. At the anode water increases from inlet to outlet, at both lading conditions. This can be associated to back diffusion which is sufficient to counteract the electro-osmotic drag. In the cathode the content of water increases slowly and is seen to be only slightly higher at high current density.

5.2.4.4.4 Temperature distribution

At high current density the centre of the PEM fuel cell has a higher distributed heat zone as shown in Figure 248. Heat is then distribution in the cathode and the anode. Patches of hot spots are visible in the anode channel; this may be attributed to the lower flow rate of the hydrogen compared to the air flow rate. The open pore cellular foam may act as a heat sink ensuring that the heat at the core of the fuel cell is distributed to the anode and cathode.
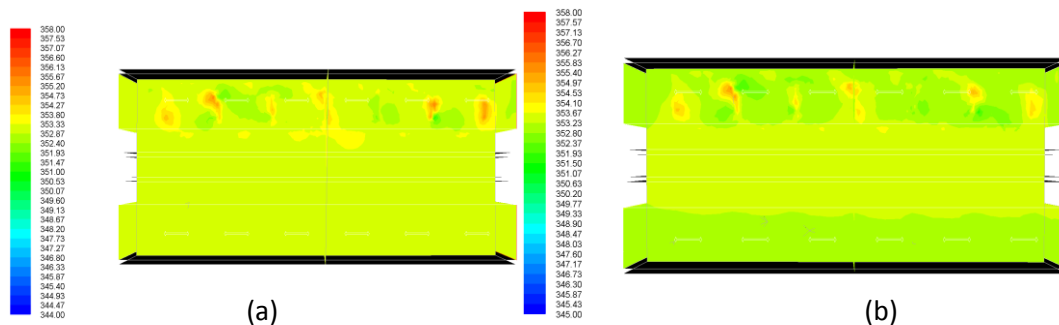
Figure 248 Temperature (a) 0.85 volts (b) 0.55 volts.

5.2.4.4.5 Current density

The current density is affected by the oxygen, hydrogen and activation over potential within the membrane. The distribution of oxygen and hydrogen should therefore reflect on the current density

distribution. The balance of oxygen and hydrogen occur at the midsection of the model therefore the maximum current density occurs in the centre region of the model. Figure 249 shows the current flux at centre of the z-axis. The concentration is mainly on the gas diffusion layer and the area between the flow channels.
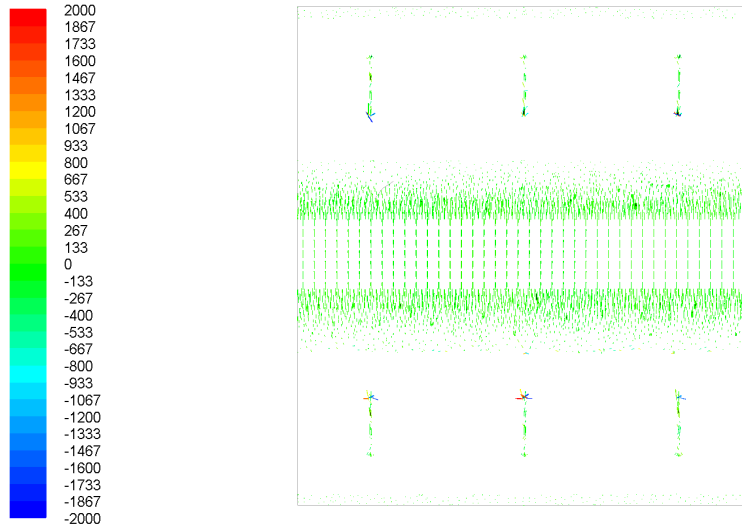
Figure 249 Current Flux at 0.55 volts.

Higher current flux densities are observed at higher loading, this justifies the oxygen concentration results since current flux densities are a directly related to the oxygen concentrations. The current flux density distribution shows that operating the fuel cell at a higher load increases its efficiency, since the electrochemical reactions are increased at the catalyst layers.
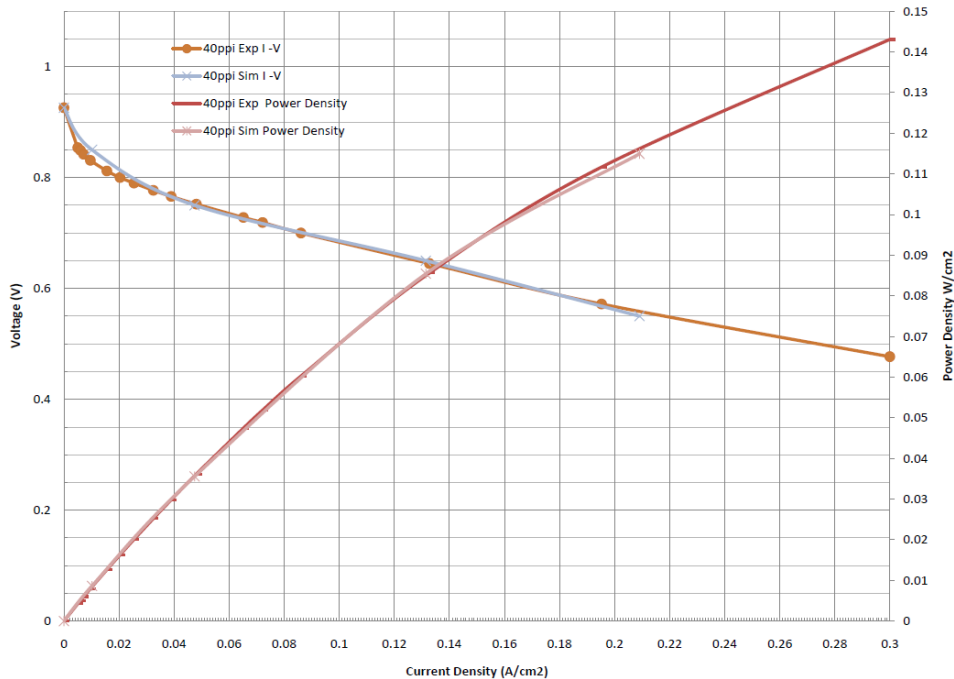
Figure 250 Open pore cellular foam polarisation curve.

Figure 250 shows the I-V curve results for the open pore cellular foam flow plate simulation and also the experimental result of the operational open pore cellular foam PEM fuel cell. The results match very well. These results will be discussed further in Chapter 6.

5.2.4.4.6 Channel electrochemical simulation results comparison
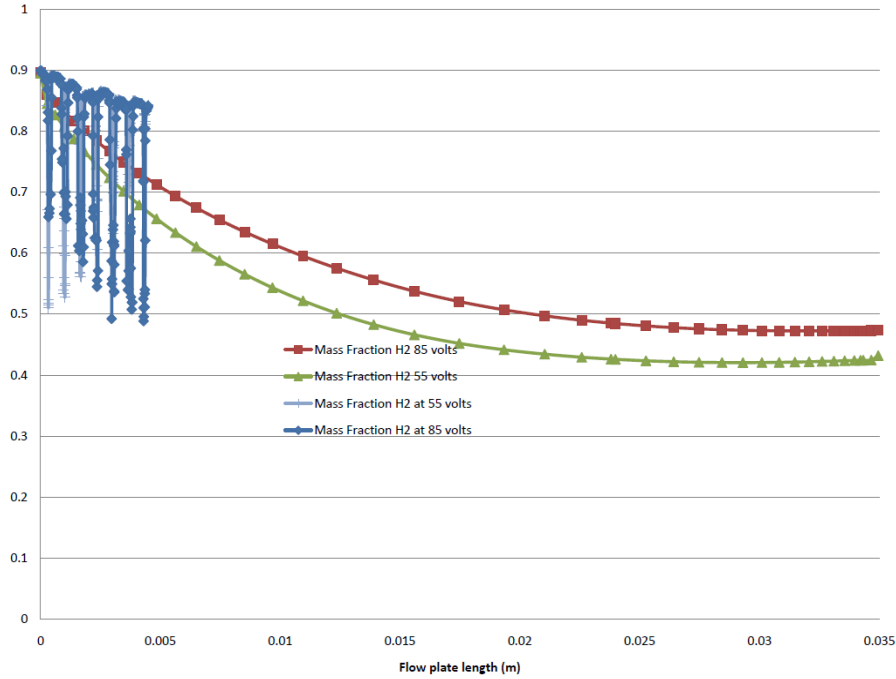
Figure 251 Open pore cellular foam and double channel hydrogen mass fraction comparison at 0.85 volts & 0.55 volts.
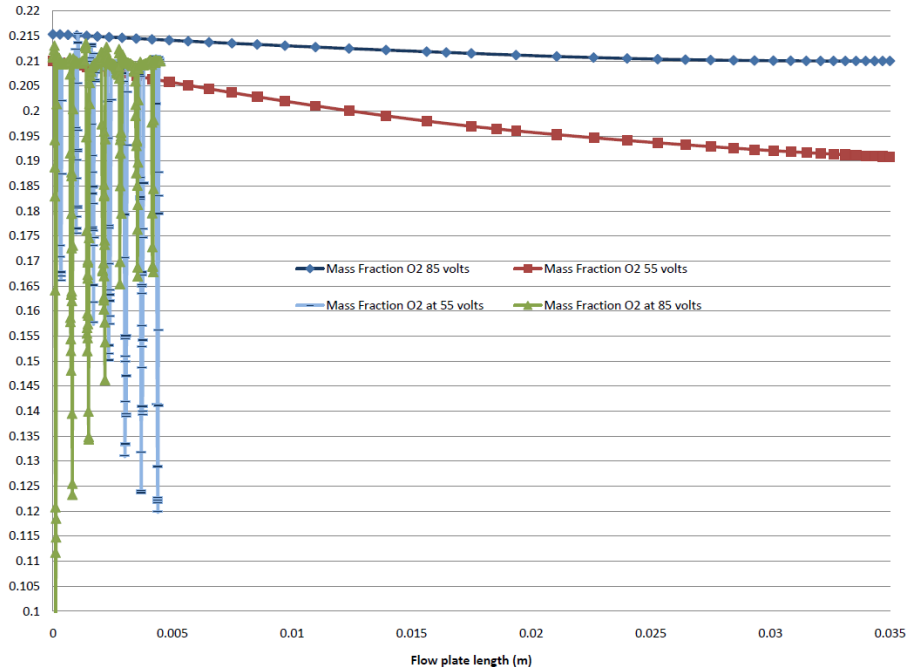
Figure 252 Open pore cellular foam and double channel oxygen mass fraction comparison at 0.85 volts & 0.55 volts.
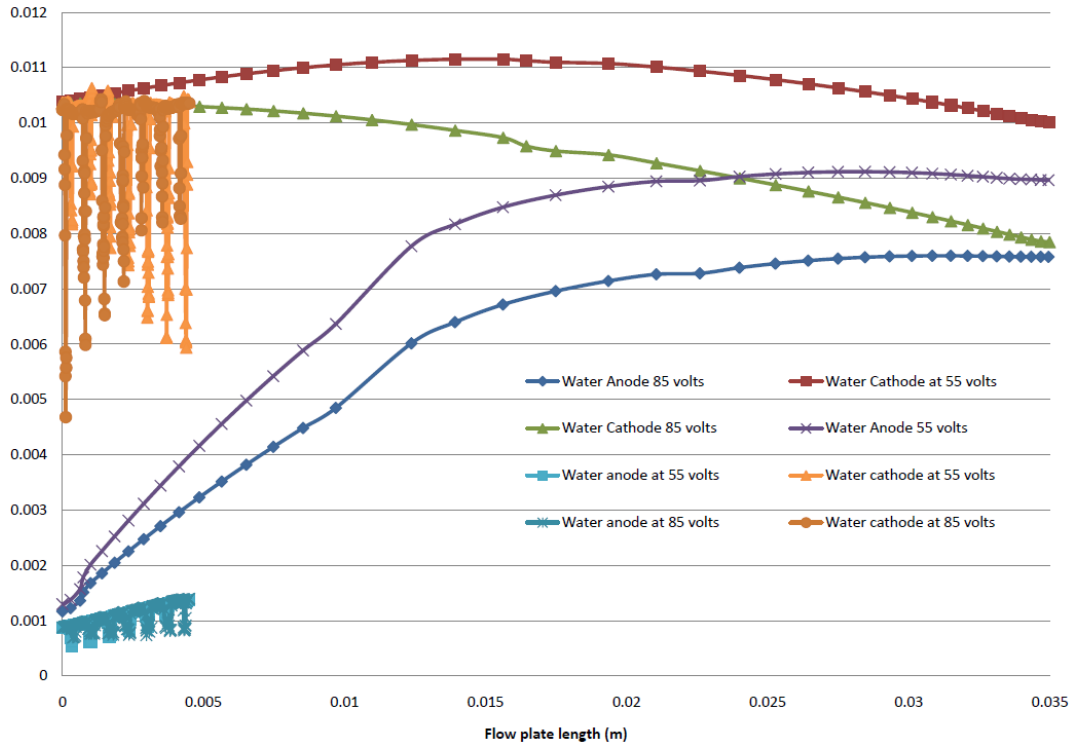
Figure 253 Open pore cellular foam and double channel water distribution in anode and cathode comparison at 0.85 volts & 0.55 volts.
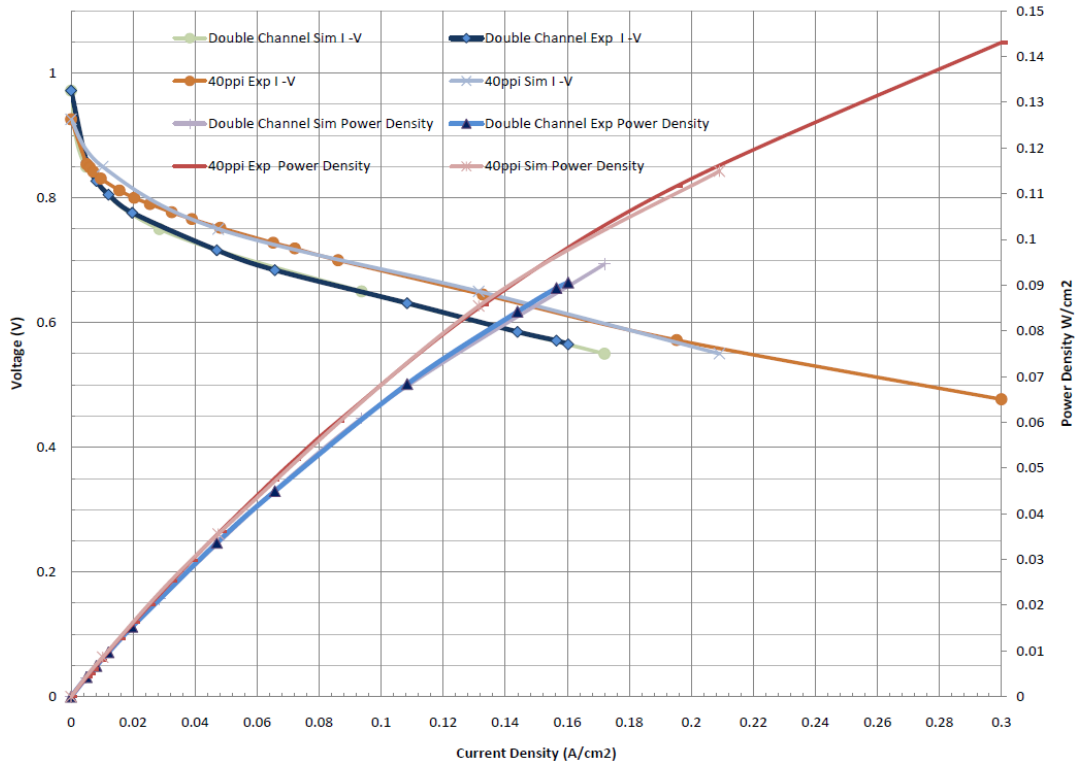
Figure 254 Open pore cellular foam and double channel polarisation curve comparison.

5.3 Experimental Results

The experimental results section is broken into two sections; the PEM fuel cell electrochemistry I-V results (section 5.3.1) and the mini channel high speed camera results (section 5.3.2).

Section 5.3.1 presents the PEM fuel cell characteristic polarisation or I-V results. The characteristic polarisation or I-V curve with an integrated power density curve is used extensively to measure the performance of the PEM fuel cell. The graph consists of direct voltage, current and power measurements taken from the assembled PEM fuel cell as described in Chapter 2, Section 3.

The double serpentine flow plate was tested to ensure a consistent bench mark for all proceeding experiments. The modified double serpentine, modified parallel and maze flow plates were deemed promising to improve PEM fuel cell performance from the simulation results described in Chapter 5, Section 5.2. These flow plates were manufactured and tested the results are presented in section 5.3.1.

Open pore cellular foam, Reticulated Vitreous Carbon (RVC) and Metal Foam (MF) flow plate characteristic polarisation or I-V results are also presented in section 5.3.1. These flow plates have never been tested before in literature and the experiments investigate if they could be used as an alternative flow plate material for PEM fuel cells. At the end of this section the most promising results are graphed together to clearly view comparisons in performance improvement due to flow plate design.

Section 5.3.2 describes the results of the visualisation experiments that view water droplet and slug movement in PEM fuel cell channels. These results will aid in the validation of CFD simulation results, described in Chapter 5, Section 5.2.

Please refer to Chapter 6 for a full discussion of the following results.

5.3.1 PEM Fuel Cell Electrochemistry I-V Results

The PEM fuel cell experimental setup is described in Chapter 3, Section 3. Each flow plate is assembled in to PEM fuel cell (as described in Appendix B) and allowed to heat up for 15 minutes. Voltage and current readings are recorded and temperature readings, from the PEM fuel cell and the humidifiers, are monitored. The double serpentine flow plate is used as a bench mark. Before, during and after each set of tests the double serpentine flow plate is tested and results recorded. This is competed to ensure the MEA is operating correctly and any anomaly or result recorded is due to the design of flow plate used and not any other cause. For each flow plate 15 separate experiments are performed, with the same operational parameters as shown in Table 14. This ensures that the results are consistent and any anomaly or result recorded is due to the design of flow plate used and not any other cause. The average result of all the experiments, for each flow plate design, are shown in the

characteristic polarisation or I-V curve with an integrated power density curve in the following sections.

Table 14 Operating parameters of the PEM fuel cell for all experiments.

Parameter	Anode	Cathode
Inlet fluid	Hydrogen	Air (20% Oxygen)
Inlet flow rate (ml/min)	20	55
Inlet pressure (gauge Pa)	200000	220000
Humidification (% at 55°C)	80-90	80-90
PEM fuel cell Temperature (°C)	50-60	50-60
Back Pressure (gauge Pa)	0	0

5.3.1.1 Conventional PEM fuel cell flow plate experimental results

Please see below all characteristic polarisation or I-V curve with an integrated power density curve results for double serpentine, modified double serpentine, modified parallel and maze flow plate designs. Please refer to Chapter 6 for a full discussion of the following results.
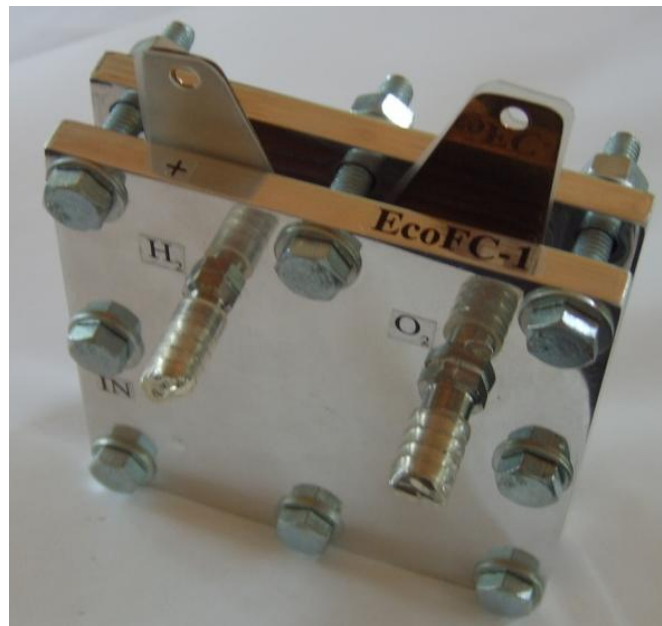
Figure 255 Conventional PEM fuel cell used for experiments.
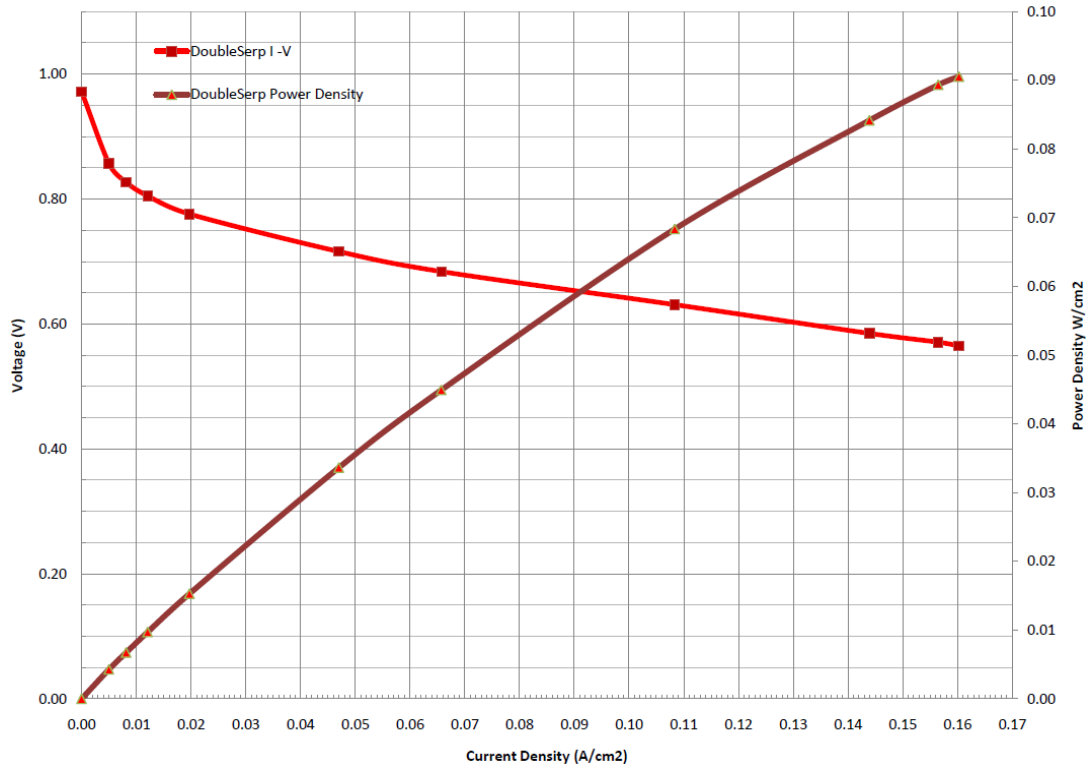
Figure 256 Double serpentine flow plate polarisation curve.
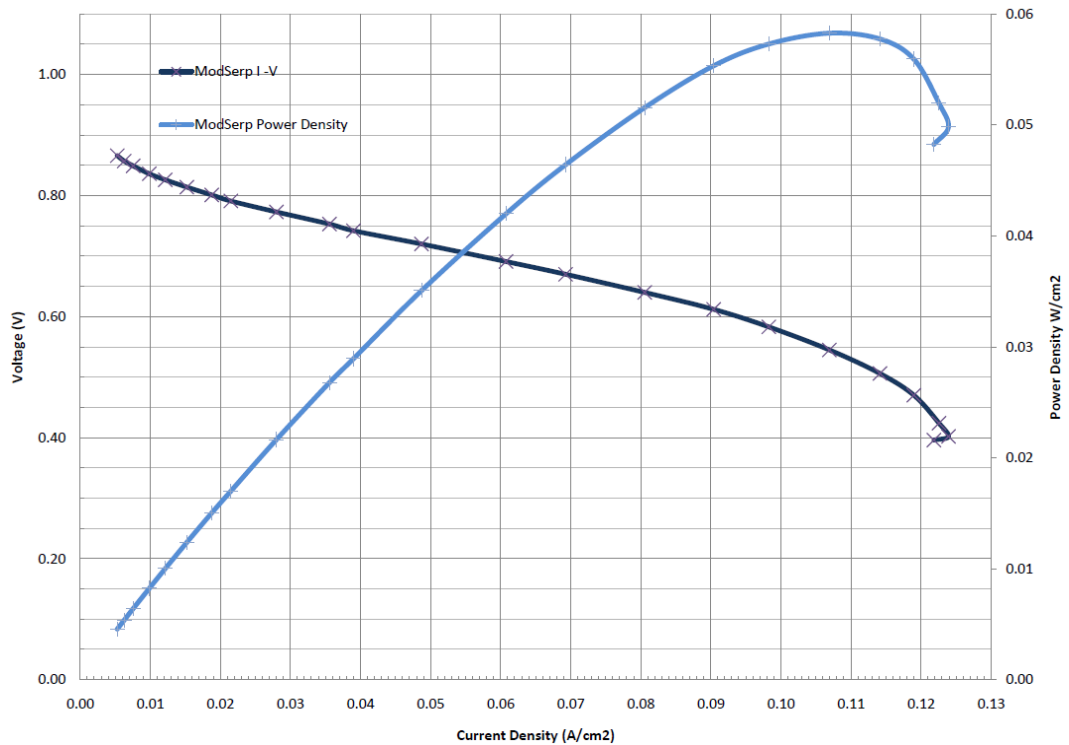
Figure 257 Modified double serpentine flow plate polarisation curve.
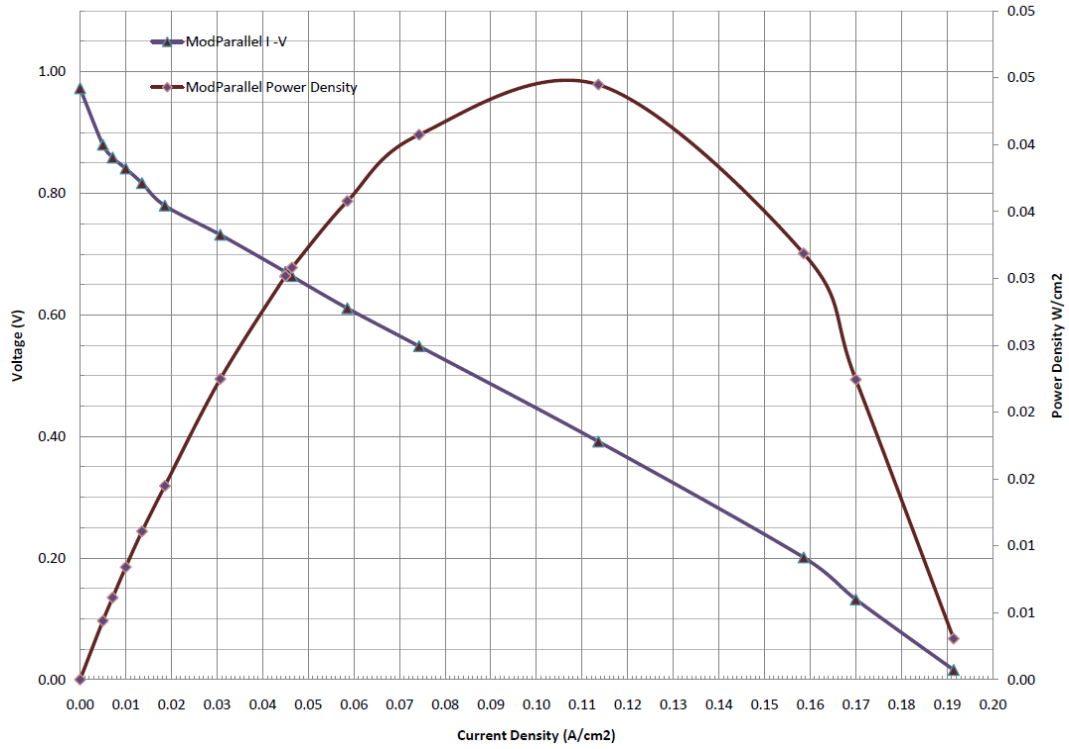
Figure 258 Modified parallel flow plate polarisation curve.
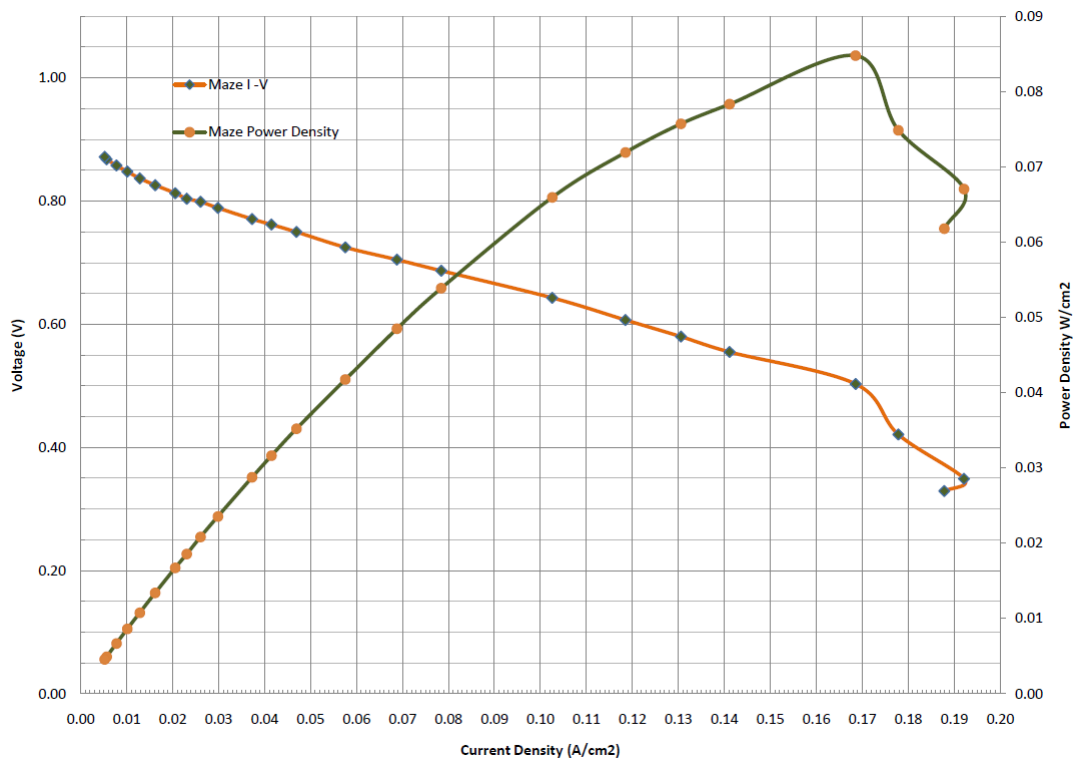
Figure 259 Maze flow plate polarisation curve.
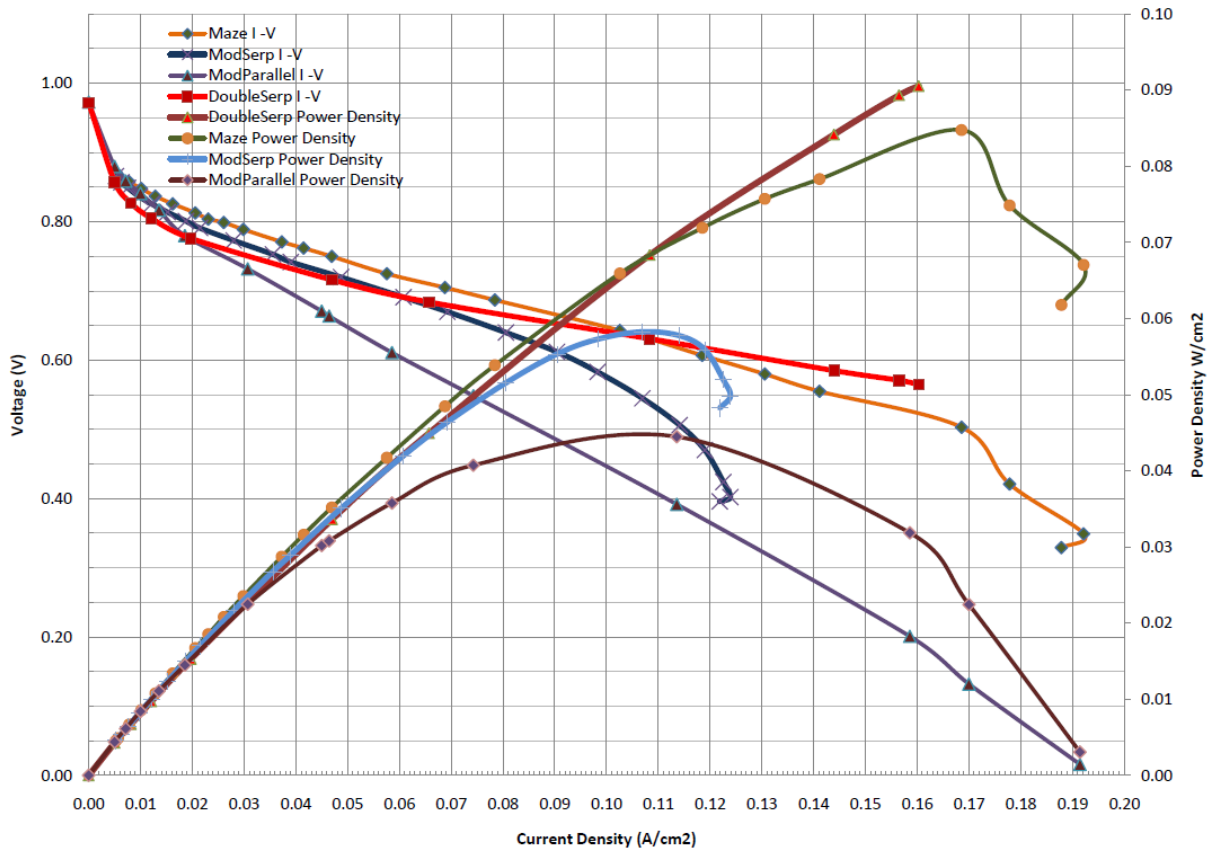
Figure 260 Conventional flow plate polarisation curve comparison.

Please refer to Chapter 6 for a full discussion of the following results.

5.3.1.2 Open pore cellular foam PEM fuel cell flow plate experimental results

Please see below all characteristic polarisation or I-V curve with an integrated power density curve results for 10ppi, 20ppi, 30ppi, 45ppi, 80ppi and 100ppi RVC and 10ppi, 20ppi, 40ppi and 80ppi (dense) MF open pore cellular foam flow plate designs. Please refer to Chapter 6 for a full discussion of the following results.
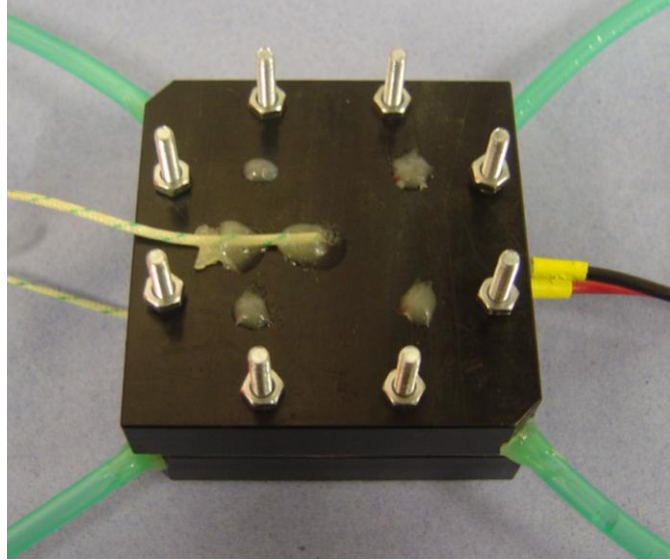
Figure 261Open pore cellular foam PEM fuel cell used for experiments.
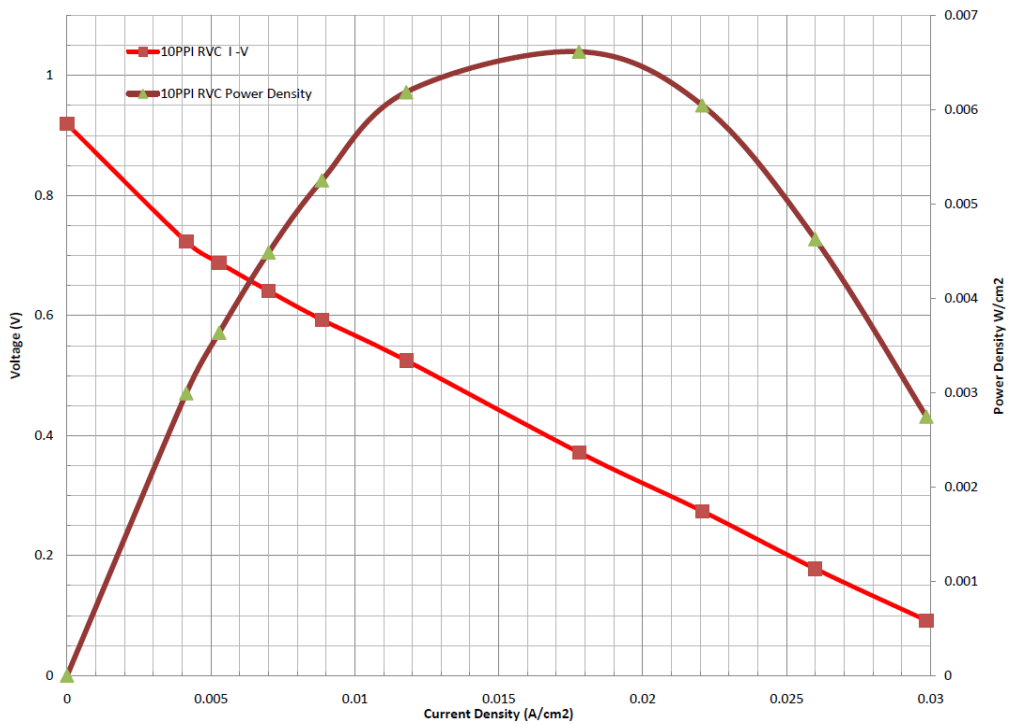
Figure 262 10ppi RVC foam flow plate polarisation curve.
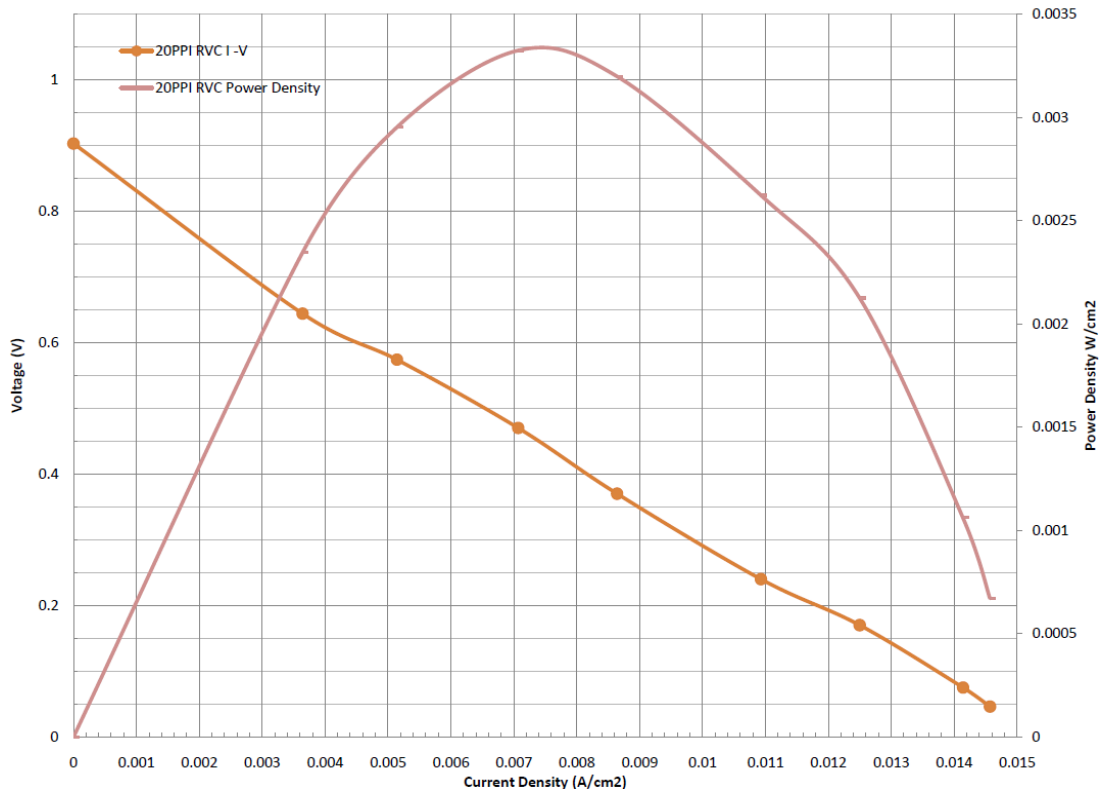
Figure 263 20ppi RVC foam flow plate polarisation curve.
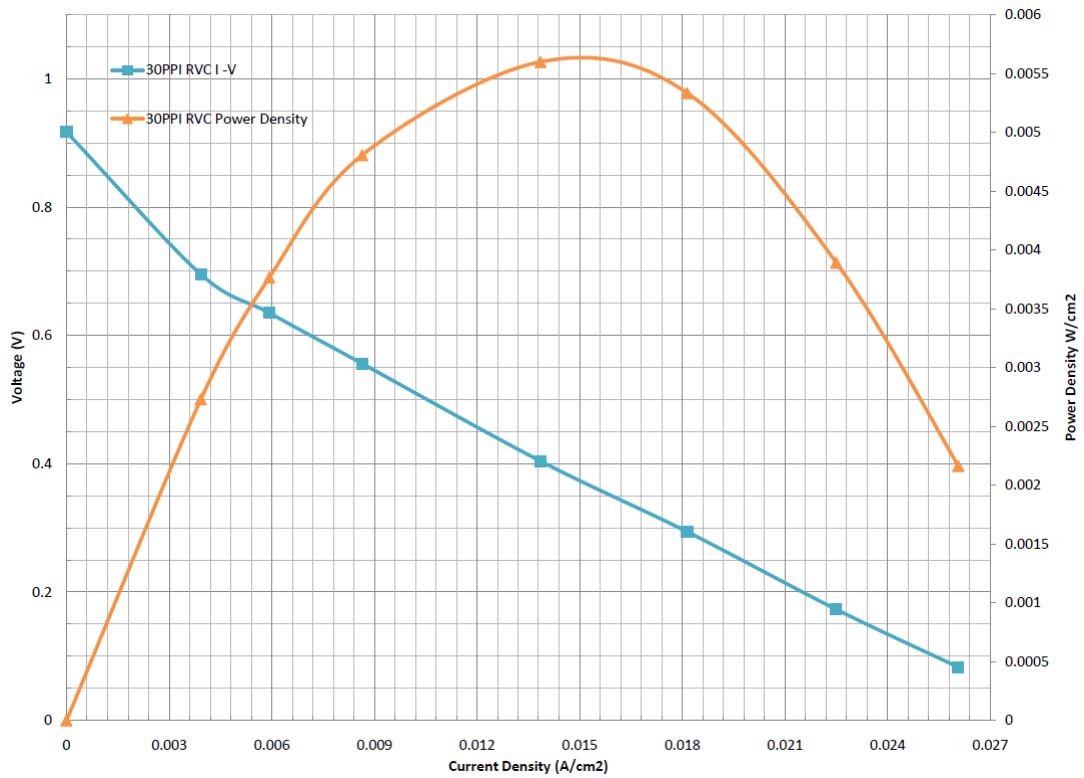
Figure 264 30ppi RVC foam flow plate polarisation curve.
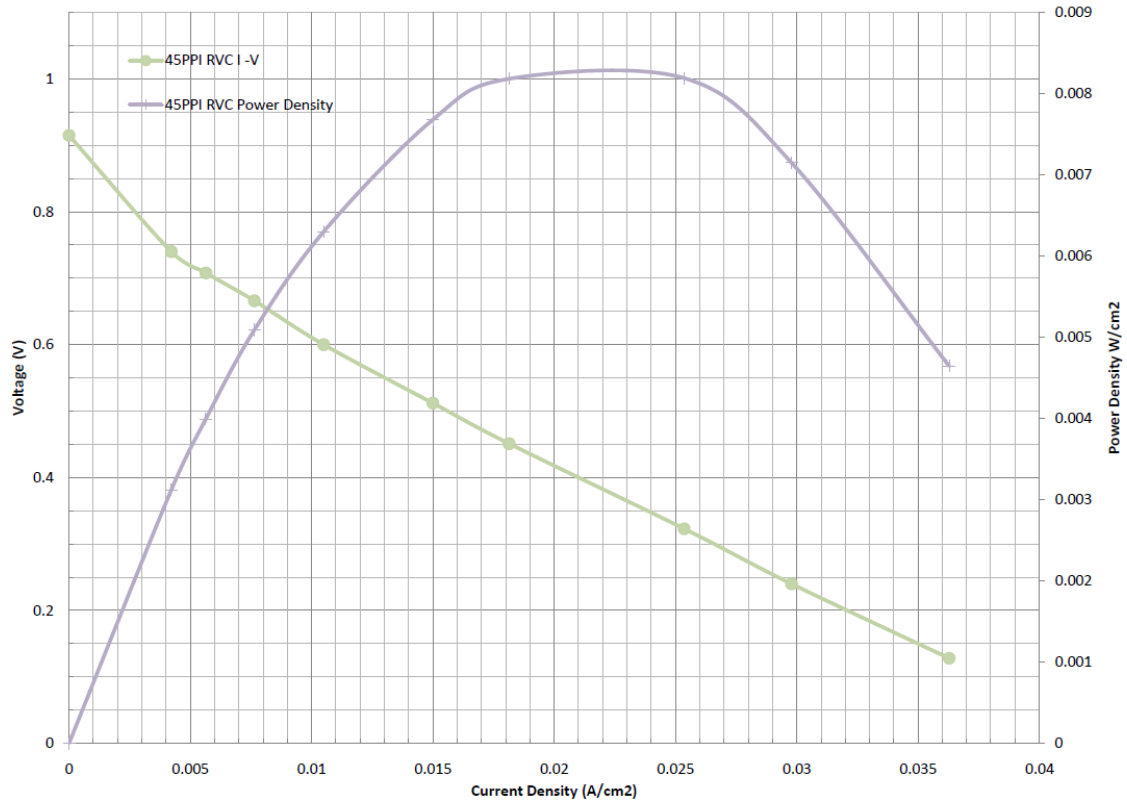
Figure 265 45ppi RVC foam flow plate polarisation curve.
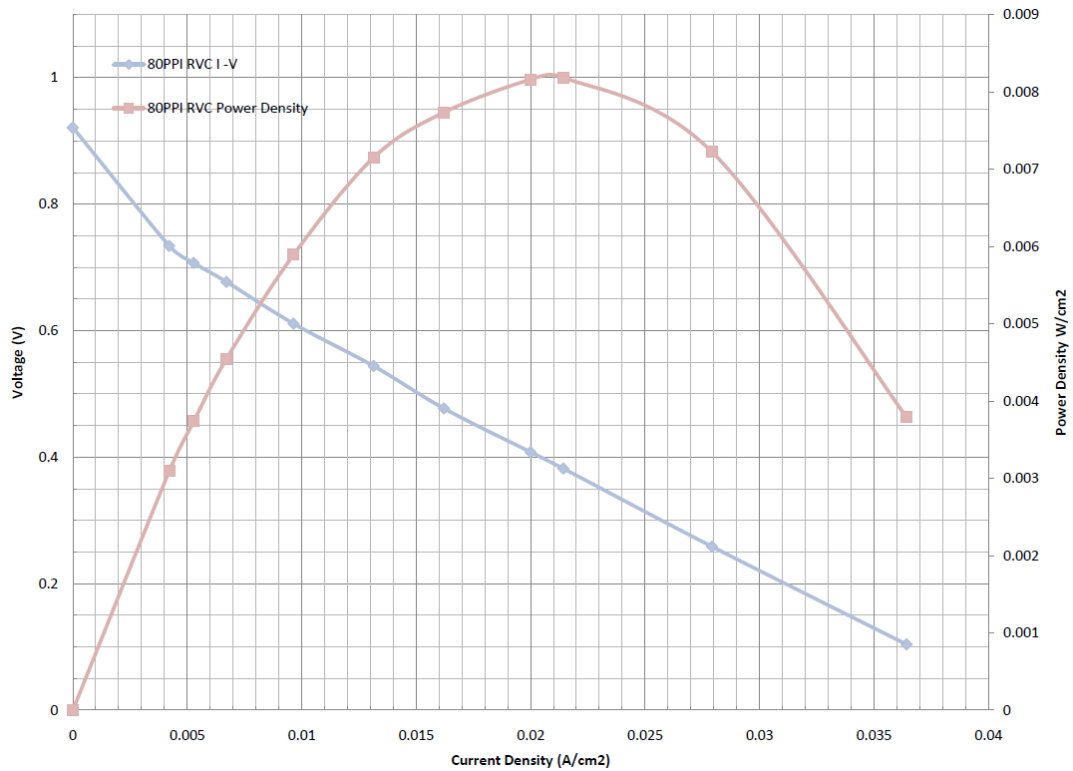
Figure 266 80ppi RVC foam flow plate polarisation curve.
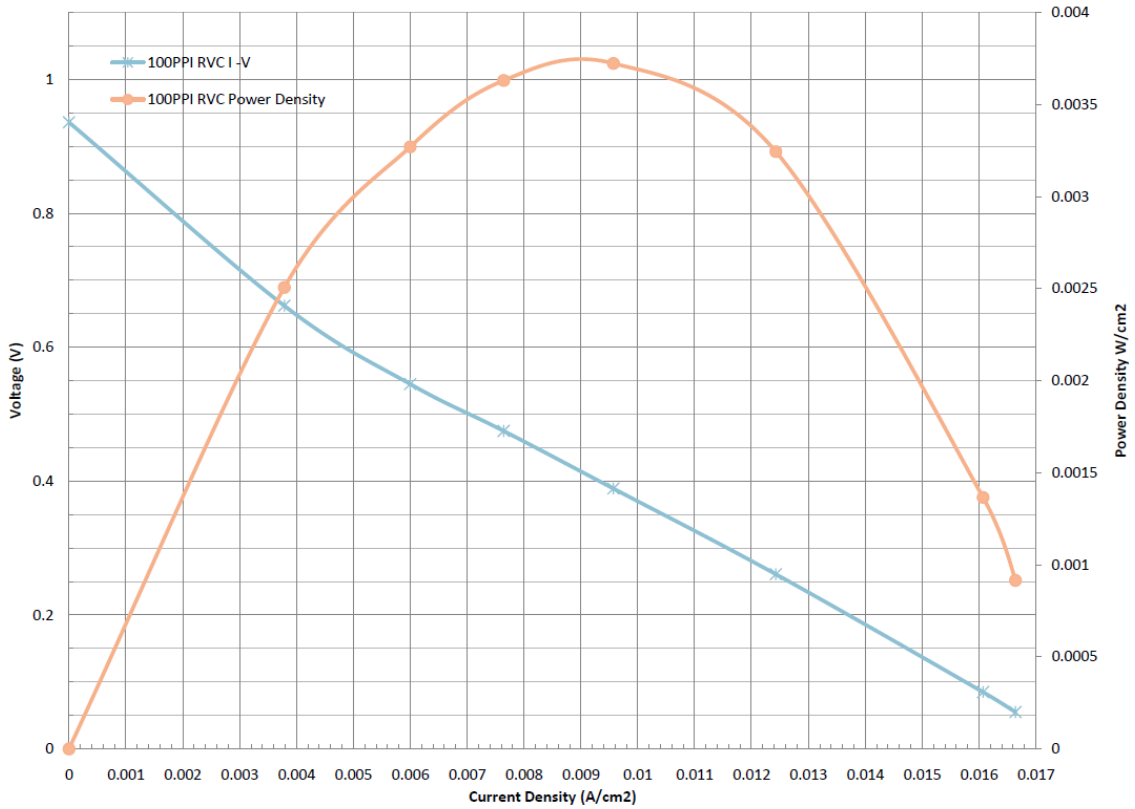
Figure 267 100ppi RVC foam flow plate polarisation curve.
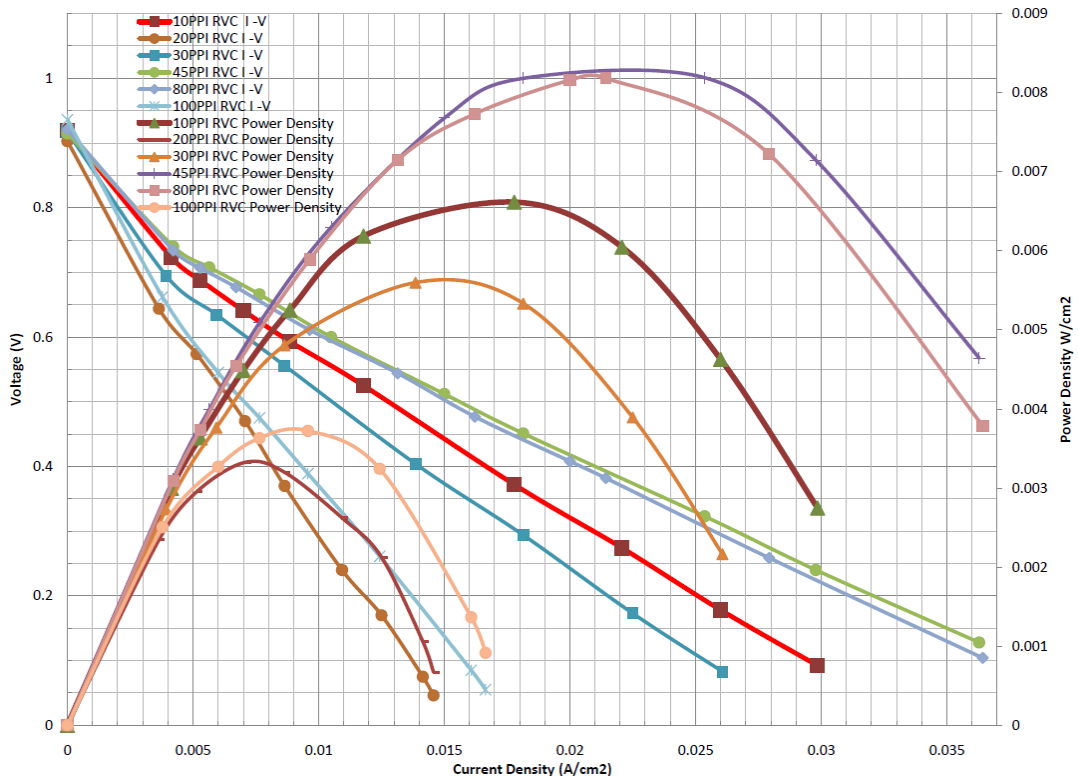
Figure 268 RVC foam flow plate polarisation curve comparison.
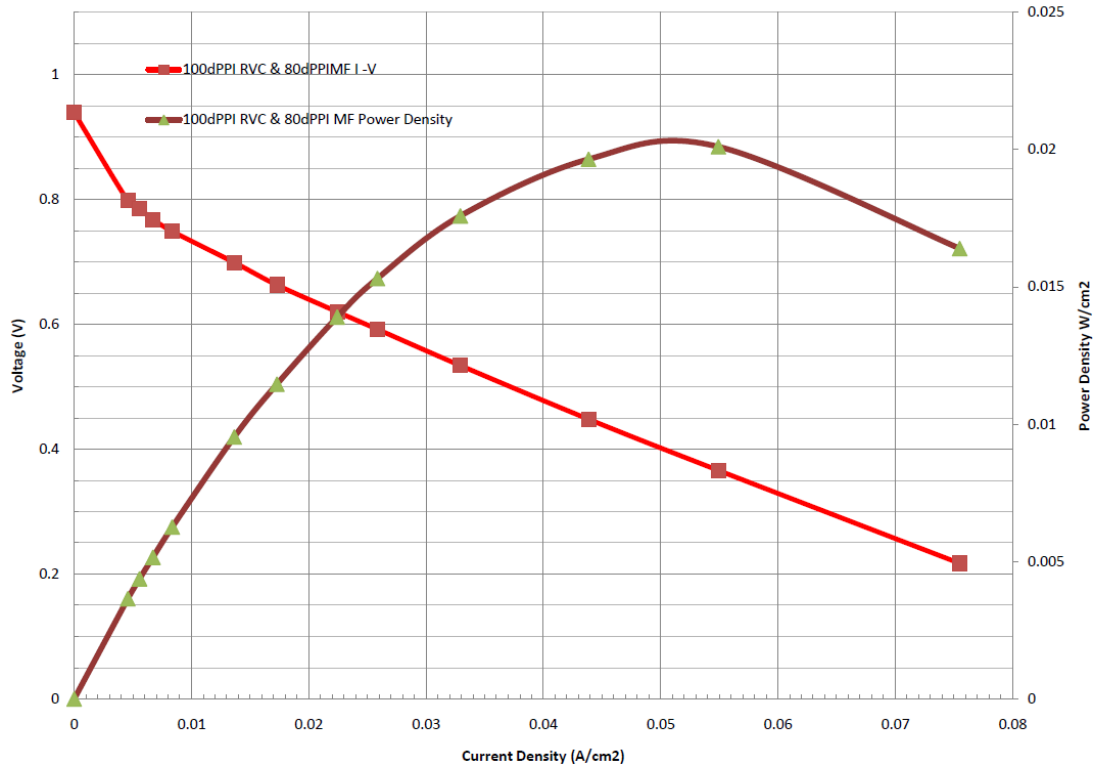
Figure 269 100ppi (dense) RVC & 80ppi (dense) MF flow plate polarisation curve.
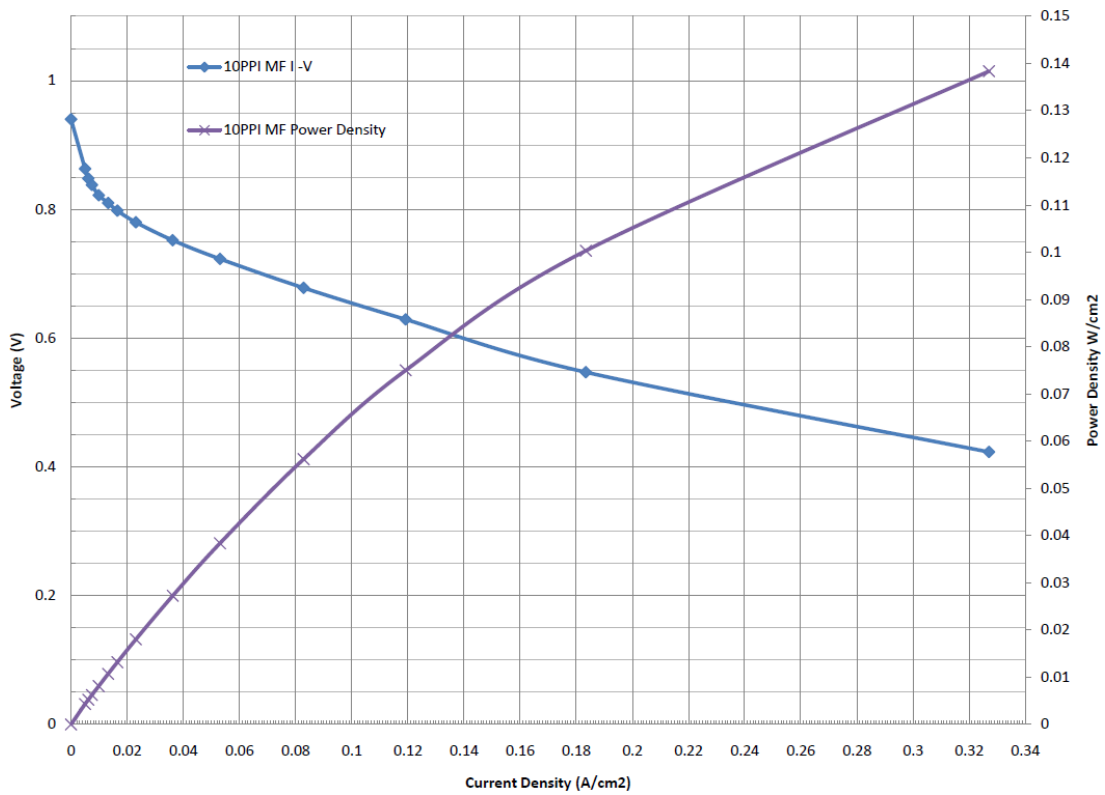
Figure 270 10ppi MF flow plate polarisation curve.
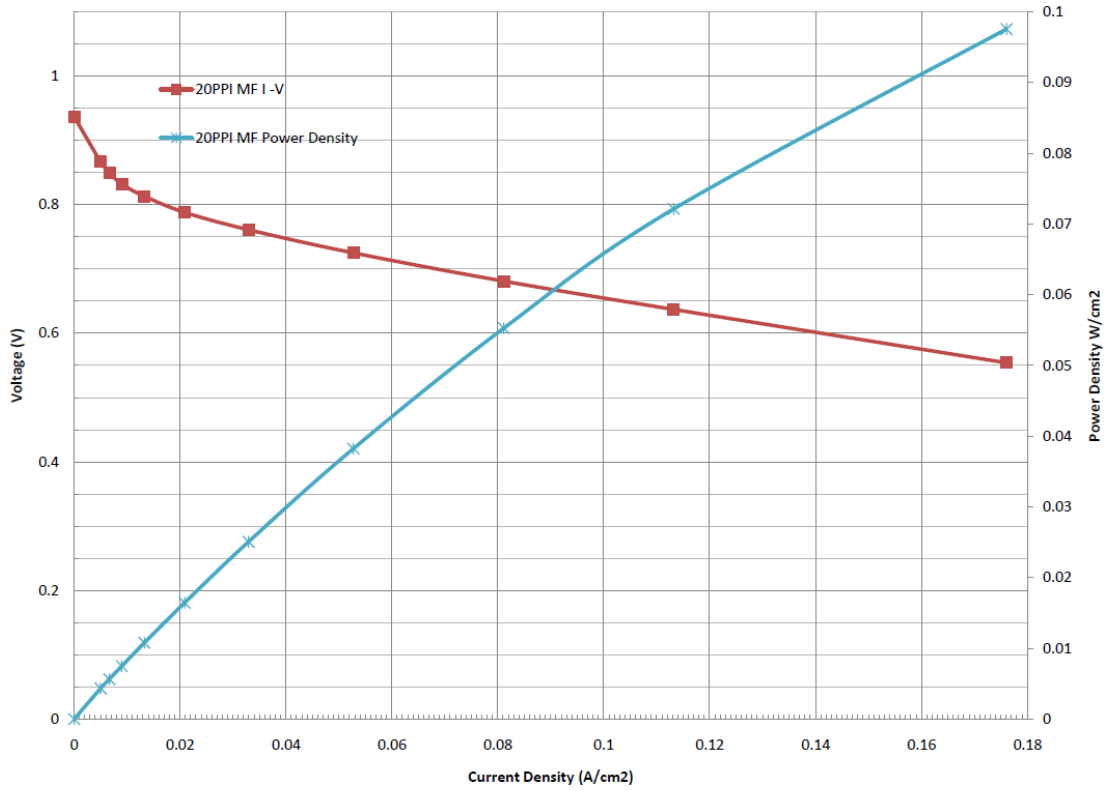
Figure 271 20ppi MF flow plate polarisation curve.
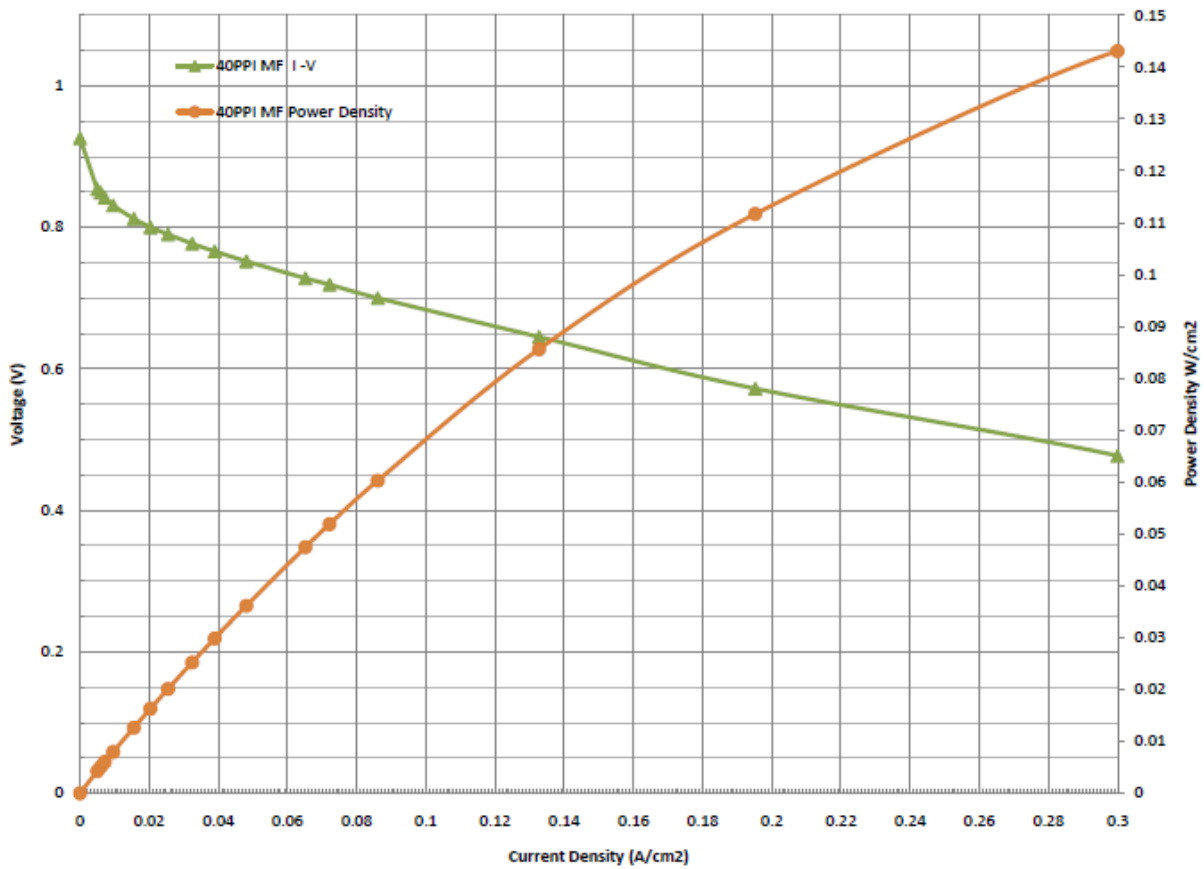
Figure 272 40ppi MF flow plate polarisation curve.
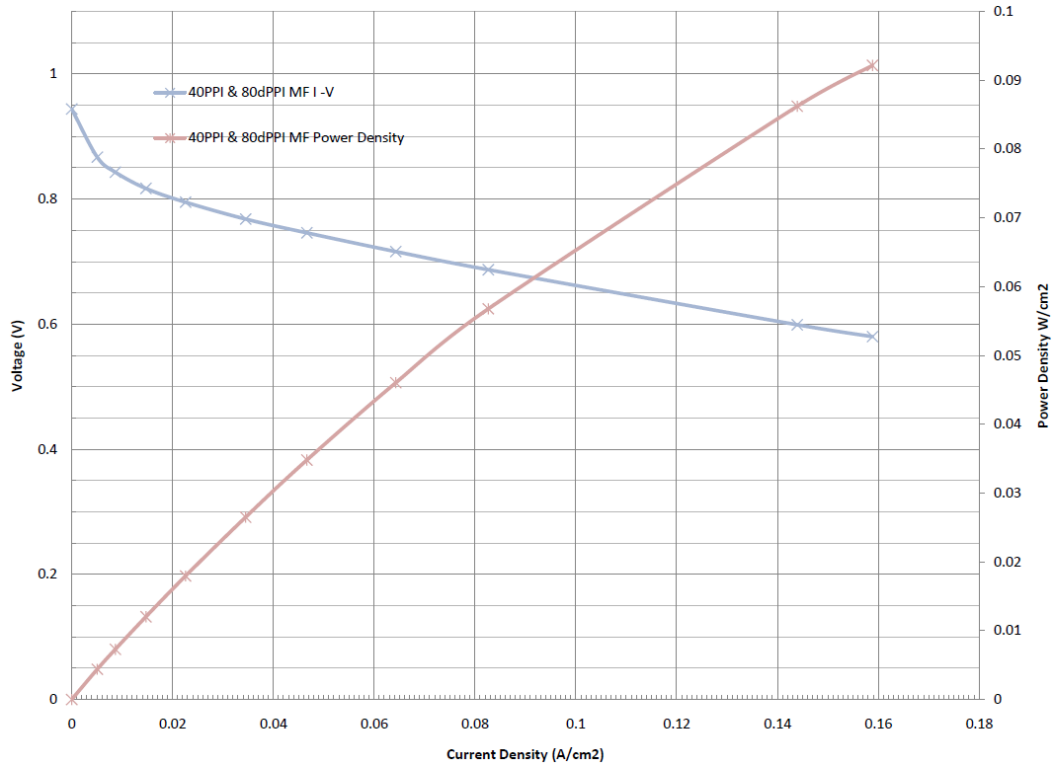
Figure 273 40ppi & 80ppi (dense) MF flow plate polarisation curve.
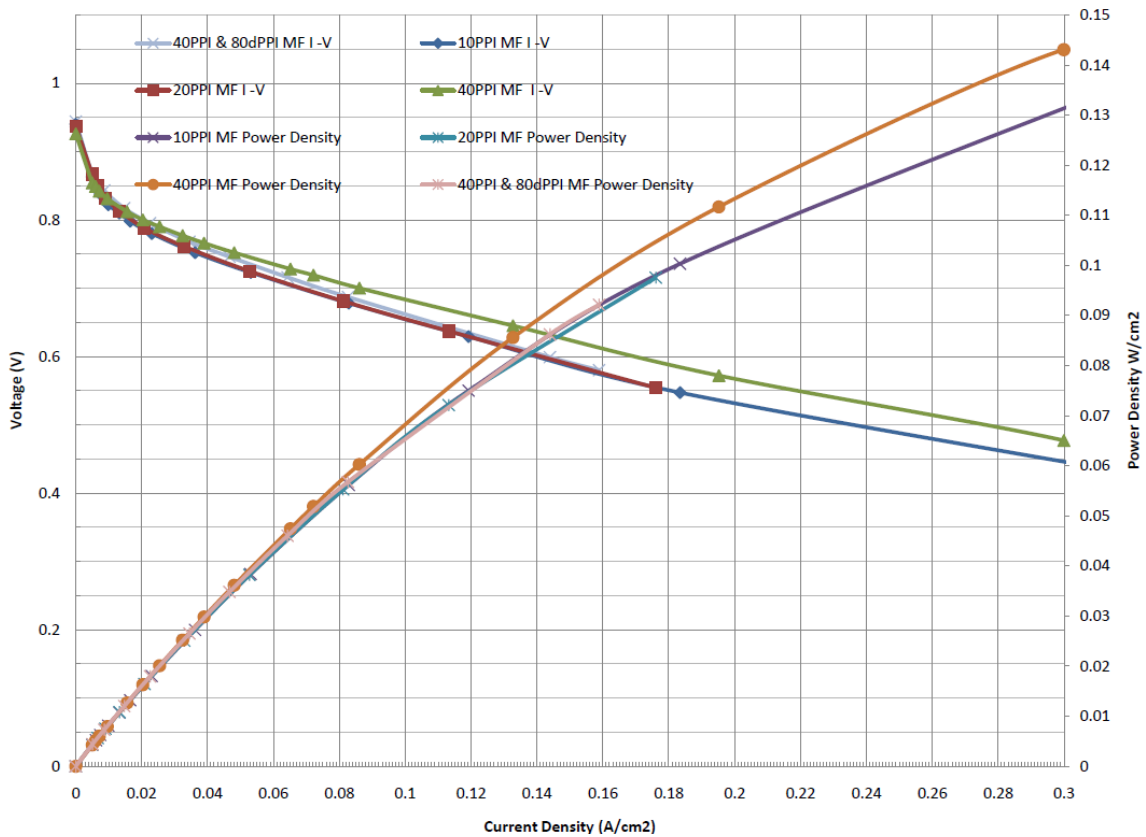
Figure 274 MF flow plate polarisation curve comparison.

Please refer to Chapter 6 for a full discussion of the following results.

5.3.2 Mini Channel High Speed Camera Results

Two-phase flow in mini-channels of PEM fuel cells is complicated due to features unique to fuel cells such as liquid water generation and its influx into the flow channel, presence of the porous GDL, bounding walls with different wetting characteristics, evaporation of water into the gas stream and internal transport of water between the anode and cathode sides. Moreover, presence of multiple channels leads to a non-uniform two-phase flow patterns among channels.

Using an ex situ apparatus, as described in Chapter 3, Section 4.2, observations of fluid flow in channels and around bends of mini channels are recorded and their implications on the PEM fuel cell performance are discussed.

5.3.2.1 Droplet and slug formation and movement in a PEM fuel cell channels

In the first series of experiments the flow plate channel is supplied with 100% humidified air at 30ml/min, while a high speed camera records images at a rate of 2000fps with 512 x 416 pixels. The entire channel is saturated with condensate after about 180 seconds as shown in Figure 275 (a). The first large droplet starts to form within minutes after channel saturation, Figure 275 (b). It is noticed that the droplet formation is at the edge of the channel and micro droplets seem to grow and join, becoming larger and larger as shown in Figure 275 (c) and Figure 275 (d). Two distinct droplets are formed in only 0.062sec and a third is forming, Figure 275 (d) from the initial condensate state of Figure 275 (a). One drop then detaches and moves in the direction of flow along the channel. This droplet may join with more droplets and become a slug. Depending on the surface treatment of the GDL this slug can spread along the GDL or role along the GDL. The fact that these droplets can form so quickly is surprising and it shows that using too much humidification within the PEM fuel cell can cause extensive water flooding very quickly.
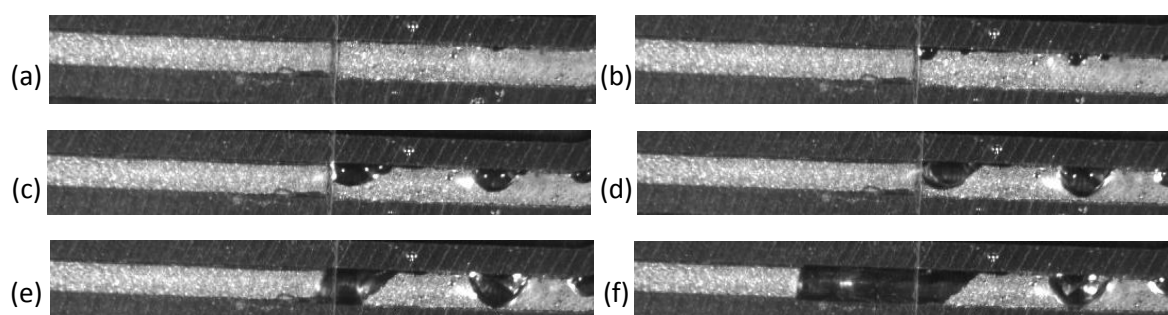
Figure 275 Droplet formation (a) Channel saturation (b) 0.01555sec (c) 0.031sec (d) 0.0465sec (e) 0.062sec (f) 0.0775sec

Slug movement is captured in Figure 276 moving in the direction of flow along the channel. When a droplet detaches from the GDL or channel wall it may join with condensate in the channel or other water droplets, forming a large droplet or slug. Figure 276 captures the slug movement clearly as it wipes up the condensate on the cover wall. Peaks and valleys are noticed in the path of the slug in this condensate, Figure 276 (e). This is from the characteristic movement and deformation of the slug as it

moves along the channel, being pushed by airflow from behind, being squashed by airflow flowing over it and resisting movement by wall affects to the GDL or channel walls, depending on their surface finish or coating.
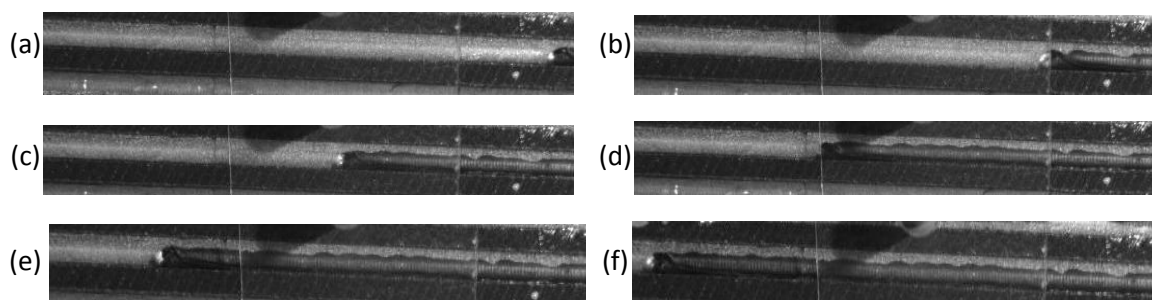
Figure 276 Slug movement (a) 0sec (b) 0.025sec (c) 0.050sec (d) 0.075sec (e) 0.10sec (f) 0.125sec

Figure 277 (a) shows a close up view of a large slug (red outline), almost a cylinder of water, moving from left to right as it approaches two droplets (orange outline) that are attached to the channel wall.
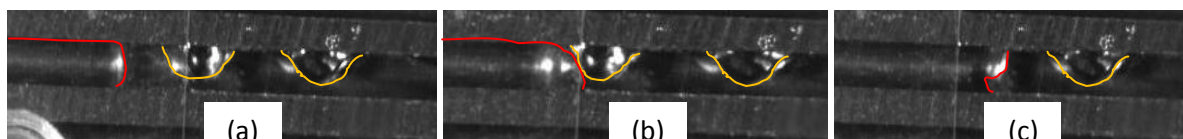
Figure 277 Slug & droplet interaction (a) 0sec (b) 0.01sec (c) 0.02sec

As the slug moves towards the first droplet, the meniscus of the slug is seen to move the droplet, Figure 277 (b), but then the slug and droplet join as shown in Figure 277 (c). All this happens in less than 0.02 seconds.
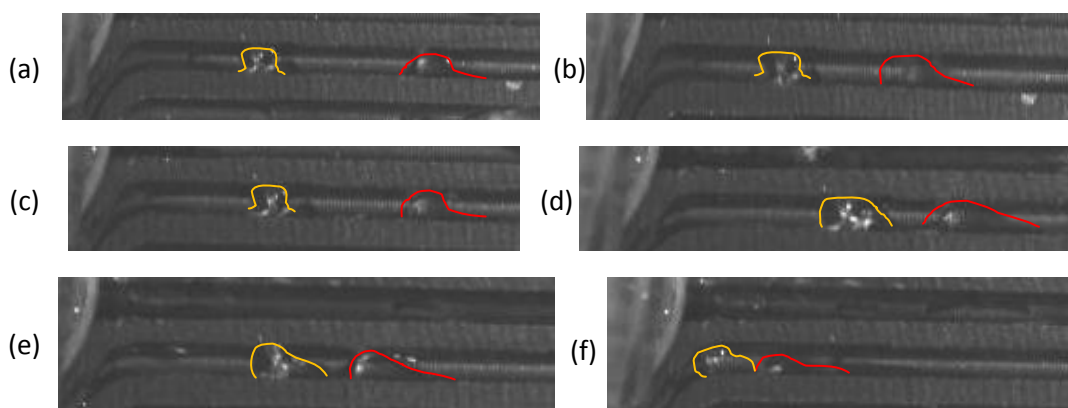
Figure 278 Slug & droplet interaction (a) 0sec (b) 0.016sec (c) 0.033sec (d) 0.050sec (e) 0.066sec (f) 0.0833sec

In the next experiment, droplets are positioned in the channel of a flow plate and air at 50% humidification is supplied to the channel at 30ml/min. A high speed camera records images at a rate of 3000fps with 1024 x 1024 pixels. Figure 278 (a) shows a slug approaching a stationary droplet. Air flow seems to be able to escape around the stationary drop for the first three images. The movement of the slug is again observed, due to the air flow around it. Once the slug comes close to the droplet, airflow becomes more restricted and this begins to deform and then move the droplet as shown in

Figure 278 (d) & (e). The slug however has more momentum and quickly catches the droplet, eventually becoming a bigger slug that would cause profound flooding affects in the PEM fuel cell.

Figure 279 shows a double serpentine flow channel. This experiment highlights an issue with a double channel design. When the cell is operational for a period of time, droplets and slugs will form and accumulate. The orientation of the cell can aid the expulsion of water out of the cell but it can also lead to issues. The serpentine cell should not allow blockages, however Figure 279 shows a worst case scenario for a PEM fuel cell with double serpentine flow channels. The channels are parallel to the force of gravity and any large slugs present will fall to the bottom of the cell and accumulate at the bends. The red line outlines slugs that are stationary over the three images (0.0206sec) in the outer serpentine channel. It is clear that the slugs are completely blocking the air flow in the outer channel, when the PEM fuel cell in positioned in this configuration. The orange line shows the movement of an air bubble in the inner serpentine channel over the three images. It is clear that about 50% of the active area of the MEA is not getting supplied with sufficient gas and this would severely reduce the performance of the PEM fuel cell.
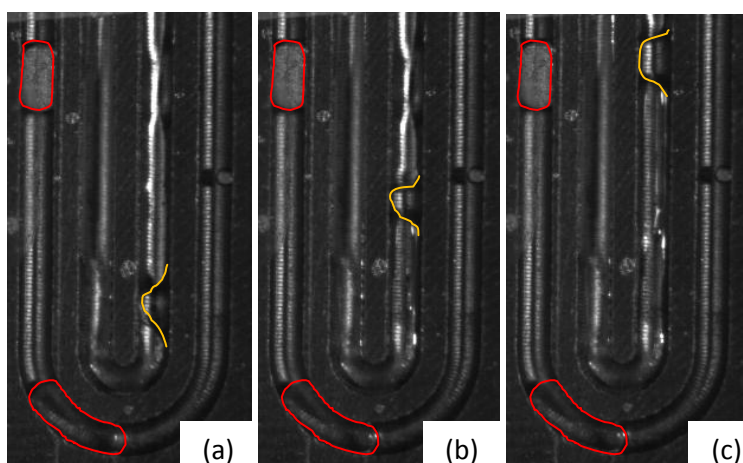
Figure 279 Blocked double serpentine (a) 0sec (b) 0.0103sec (c) 0.0206sec.

In the next set of experiment, droplets and or slugs are positioned in the channel/channels of a flow plate and air at 50% humidification is supplied to the channel at 30ml/min. A high speed camera records images at a rate of 1000fps with 344 x 1024 pixels.

Figure 280 (a) shows a slug positioned in a single straight channel (1mm x 1mm x 25mm) moving with the air flow from left to right. Due to the wetting affect of the hydrophilic surface of the channel, water is streaked behind the slug as it moves with the air flow. As more water is left in the trail the slug looses stability and the air flow is now able to move over it, as shown in Figure 280 (a), leaving the surface with a thin layer of water. Depending on the humidity of the air stream this layer of spread water may evaporate very quickly and may not hinder PEM fuel cell operation for a long period of time.
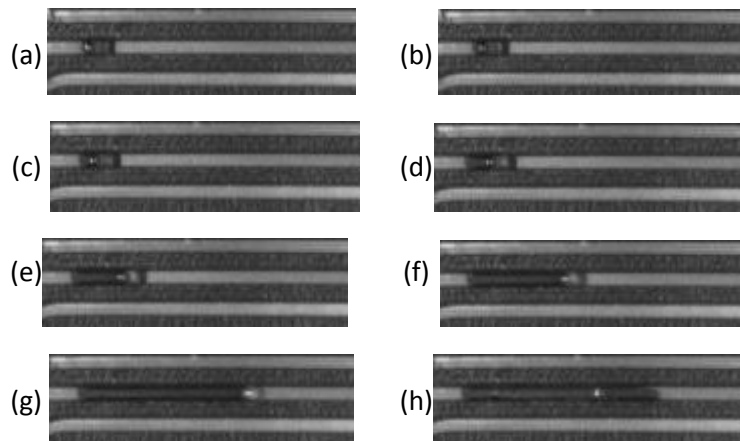
Figure 280 Small slug movement in a single straight channel.

Figure 281 is similar to the above case except with two straight mutual inlet channels each with a slug one bigger than the other. The air flow initially pushes both slugs down the channel, however after just seconds as shown in Figure 281 (c) pressure builds up behind both slugs and the smaller slug starts to move faster. By Figure 281 (d) the smaller slug is seen to move past the larger slug and then in Figure 281 (e) the pressure and velocity of the air becomes large enough to burst the slug, relieving pressure and leaving a small droplet in the channel. This could join with other droplets in the PEM fuel cell and another slug could be formed starting the process again. It is also noticed that when the pressure was relieved in the channel with the small slug, the large slug stopped moving and therefore this channel could now be fully blocked, with most airflow flowing in the inner channel.
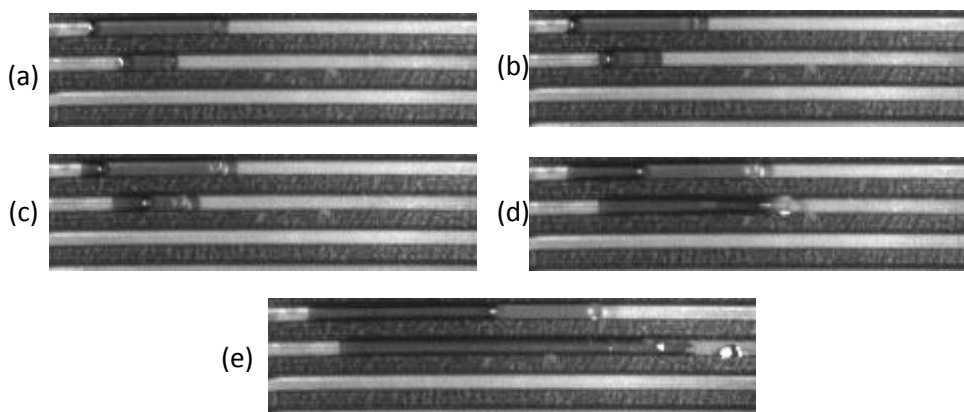
Figure 281 Two slugs movement in double straight channels with mutual inlets.

Figure 282 shows slug movement in a single bend channel while Figure 283 shows slug movement in a double bend channel with mutual inlets. The results are quiet similar with no major difference with the mutual inlets affecting slug movement around bends. This is mostly due to the movement and deformation the slug experiences as it moves around the bend. The inner section of the slug speeds up while the outside slows down.
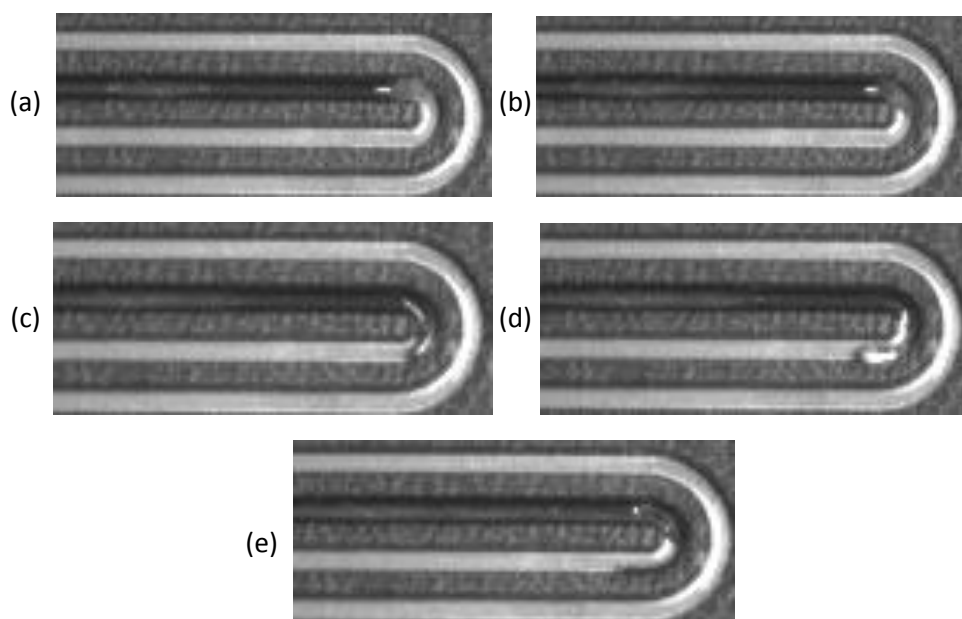
Figure 282 Slug movement in a single bend channel (a)0sec (b)0.001sec (c) 0.003sec (d) 0.006sec (e) 0.032sec.

As the slug approaches the bend it can be seen to be pushed against the side of the wall of the channel. This can encourage the air that may have built up pressure to move around the slug. This movement then makes the slug attach to the channel side as seen in Figure 282 (c) & (d) or Figure 283 (d) instead of the bottom of the bottom of the channel. As the slug deforms with changes in air flow it can burst as shown in Figure 283 (e) leaving droplets of water after the bend areas.
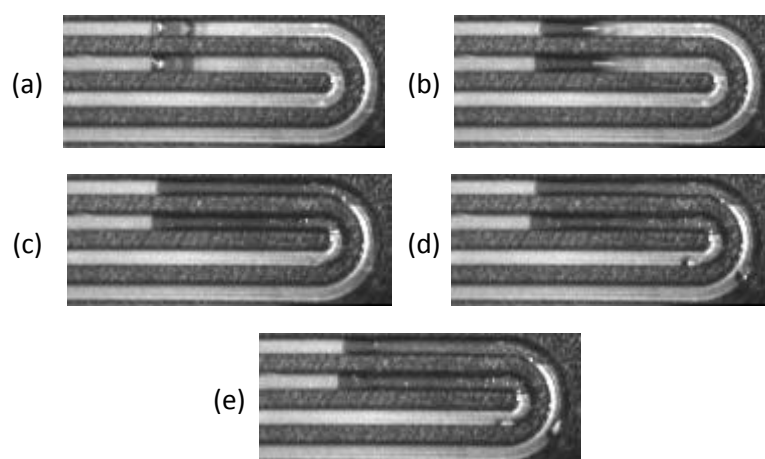
Figure 283 Two slug movement in double bend channels with mutual inlets.

5.3.2.2 Experimental and simulation comparison

A time sequenced VOF model was simulated to view a slug movement in double serpentine channels and bends, examples are shown in Figure 284 (a) and

Figure 285 (a). To ensure that the model matched reality, many experiments were performed to physically view slug movement in double serpentine channels and bends, examples are shown in Figure 284 (a) and

Figure 285 (b).

This simulation and experiment shows two straight mutual inlet channels each with a slug one bigger than the other. The air flow initially pushes both slugs down the channel, however pressure builds up behind both slugs and the smaller slug starts to move faster. By Figure 284 (2) the smaller slug is seen to move past the larger slug and the pressure and velocity of the air becomes large enough to burst the slug. This is visible in both the simulation and visualisation results.
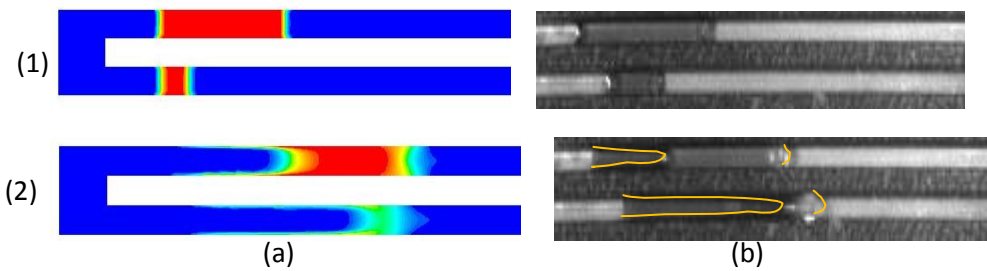
Figure 284 Results comparison (a) Model (b) Experiment (1) Time step 40 (2) Time step 200

This simulation and experiment shows three time instances of the slug movement as shown in

Figure 285. As the slug is pushed with the air it begins to deform

Figure 285 (1). Depending on the surface treatment of the channel and or the GDL, the slug leaves a trail of water behind it, particular evident at the edges of the channels in both the simulation and experiment

Figure 285 (a) &

Figure 285 (b). When the slug approaches the bend it continues forward until it hits the back of the channel bend,

Figure 285 (2). Air begins to escape from around the slug, pushing it against the channel wall. This continues until the air escapes leaving a layer of water towards the bottom of the channel as shown in both the model and experiment results Figure 285 (3).
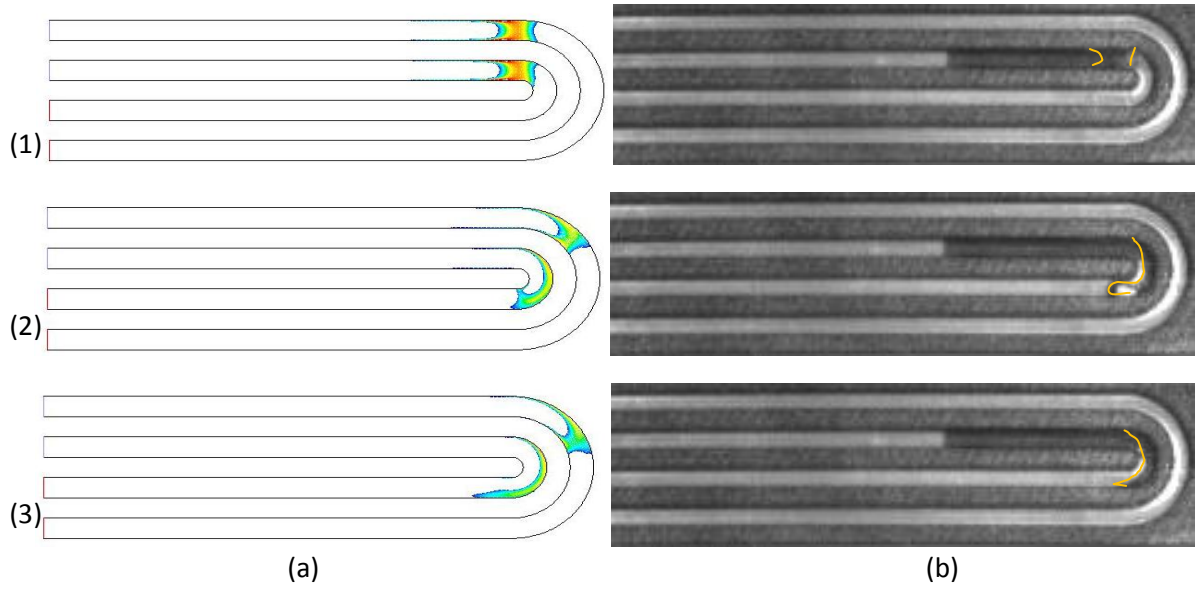
Figure 285 Results comparison (a) Model (b) Experiment (1) 0.0056sec (2) 0.0082sec (3) 0.009sec

From these and other comparisons the simulation and experiment results match well and further simulation analysis proceeded.

BLANK PAGE

6

Chapter 6 - Discussion

Many researchers have been trying to develop new energy technologies in both national and international programmes to meet the challenges of rising oil prices and then climate change since the 1970's [25]. Fuel cell technology is one of the developing technologies.

PEM fuel cells offer several advantages over the use of other fuel cell types; including low temperature operation, high power density, fast start up, system robustness, flexibility of fuel type (with reformer) and no sealing, corrosion, shielding or leaking concerns [8]. PEM fuel cell technology may be a leading candidate technology for the application to portable electronic devices, remote systems including space applications and for light-duty transportation applications as outlined in Chapter 1, Section 1.2.2.

The ultimate goal of this body of work is to improve the performance of PEM fuel cells (i.e. increase the energy efficiency and power density) and in the process, try to simplify their design that could reduce material, manufacturing and assembly costs. This was achieved by the development of low-cost lightweight construction materials, enhanced design, layout, configuration, water mitigation and fabrication methods of PEM fuel cell flow plates.

The effectiveness of each flow plate design, developed in this thesis, was gauged by modelling, simulation and experimental methods. Modelling allowed many flow plate and flow field ideas and designs to be investigated until satisfactory flow plate designs were conceived and complete models developed. (This was in iterative process spanning the duration of this thesis.) Simulation methods were applied to each model, analysing the flow regime, pressure, velocity and viewing gas distribution in the simplest CFD models (Chapter 5, Section 5.2.1 and 5.2.3), viewing two phase flow in the VOF models (Chapter 5, Section 5.2.2) and viewing hydrogen, oxygen, water and current (polarisation curve) in the more complicated electrochemistry models (Chapter 5, Section 5.2.4). Experimental analysis was used to experiment ideas that were not thoroughly concluded by simulation, to validate simulation results and to effectively test new innovative flow plate designs in an operational PEM fuel cell (Chapter 5, Section 5.3). Through electrochemistry simulation and experimentation the PEM fuel cell's performance is summarised with the polarisation curve (I-V curve) of its current and voltage characteristics. An ideal PEM fuel cell will have a constant voltage of

1.23volts, but due to losses, this is not the case for a practical PEM fuel cell. The characteristics of the voltage/current density graph are a result of four major losses (explicitly explained in Chapter 2, Section 2.3.3):

- Activation losses
- Fuel cross over and internal current losses
- Ohmic losses
- Mass transport losses

Activation losses are not attributed to the flow plate design. This loss relates to catalyst which would have been consistent from one simulation or experiment to the next in this thesis; the same MEA, from the same manufacturer, was used for all experiments and the operating temperature and humidification rate were kept constant.

Fuel cross over and internal current losses can be attributed to the flow plate design. However this loss, which is usually minimal, would have been consistent from one simulation or experiment to the next in this thesis; the same MEA with the same seals and closing torque were used in all experiments and leak testing was also performed during testing.

Ohmic losses can be attributed in part to the flow plate or flow field design. This loss is due to the various resistances in the PEM fuel cell restricting the flow of electrons that generates heat. Ohmic losses can be related to the surface contact of the flow plate with the GDL and interconnects to neighbouring cells or connections to the external circuit. In conventional flow plates, such as serpentine or parallel flow plates, ohmic resistance can be affected by the design. To ensure a good surface contact of the flow plate to the GDL, ribs are needed while channels ensure effective gas flow. The conventional flow plates including the double serpentine flow plate used graphite as the flow plate material, the RVCF flow plates used vitreous carbon and the MF flow plates used aluminium.

Mass transport (concentration) losses are mainly attributed to the flow plate design. When the concentration of available fuel or oxidant becomes reduced the voltage and current can drop dramatically. This is usually caused by the cathode. With the build up of water especially at the cathode, particularly at high current densities or during extended fuel cell operation, catalyst sites can become clogged, restricting oxygen access. The flow plate design can add to this loss with concentration gradients from inlet to outlet or due to stagnant air in channels or flow field recirculation zones and unwanted eddy currents present in the flow channels.

Parasitic losses are additional losses related to the operation of the PEM fuel cell. Parasitic losses can affect the PEM fuel cell system efficiency. It is with regard to the power used by the PEM fuel cell to run all the BOP items associated with the operation of the PEM fuel cell. This loss can be affected by the flow plate design. Depending on the PEM fuel cell design high input pressures or high gas flow

rates may be necessary. In conventional dead ended flow plates such as the interdigitated design large input pressures are necessary to push the gases through the flow plates which increase the parasitic losses.

These losses and their effect on flow plate designs developed in this thesis are discussed in the following paragraphs.

The CFD models in Chapter 5, Section 5.2.1 include the double serpentine flow plate (from literature), modified double serpentine flow plate (developed in this thesis), parallel flow plate (from literature), modified parallel flow plate (developed in this thesis), modified pin flow plate (developed in this thesis), maze flow plate (developed in this thesis), interdigitated flow plate (from literature), modified interdigitated flow plate (developed in this thesis) and spiral and vein flow plates (developed in this thesis). CFD VOF models in Chapter 5, Section 5.2.2 were developed and simulated to view water slug formation as this could cause issues in conventional flow plates. Visualisation experiments were also performed (Chapter 5, Section 5.3.3) to assist and validate the VOF model. From these analysis a few interesting conclusions were drawn and these will be discussed next.

The double serpentine flow plate (from literature) was purchased and used as a bench mark flow plate. The double serpentine flow plate pressure distribution shown in Chapter 5, Section 5.2.1.2, Figure 77 indicates that there is a high inlet pressure on the first few inlet channels (175 Pa) but this quickly decreases to a low pressure in the exiting channels (8 Pa). This would show that pressure towards the MEA decreases from inlet to outlet and this may have consequences to the mass transport and PEM fuel cell performance. No dead zones or circulation eddies are visible in the flow path using this design. However boundary layers of lower velocity fluid flow (1.0m/s) was noticed at the channel edges. This can lead to water films being moved to the channel walls, creating annular flow or even slug flow. Visualisation was used to view this issue which is described in Chapter 5, Section 5.3.2.1. It was noticed that serpentine flow plates, especially double, parallel serpentine flow plates can form slugs of water that can block a channel, reducing the fuel cell's performance by almost 33%, also recognised by Hu et al.[127].

The modified double serpentine flow plate (developed in this thesis), added channels to assist in more even pressure distribution throughout the flow field however this flow plate was assigned for manufacture to draw conclusive results from experimentation.

The parallel flow plate (from literature) caused the fluid flow to take the fastest and easiest path to the exit shown as an uneven distribution a velocity through the flow plate in Figure 82, Chapter 5, Section 5.2.1.6. Many variations of the parallel design were tried and tested in an attempt to obtain an optimal flow plate design. The modified stepped parallel flow plate (developed in this thesis) showed

the most promising pressure and velocity flow profiles from simulation results as seen in Chapter 5, Section 5.2.1.8 and was assigned for manufacture and test.

Modified pin flow plate (developed in this thesis) had slight changes, including wider ribs and input flow, compared to literature. This flow plate gave promising velocity and pressure profiles from simulation results as shown in Chapter 5, Section 5.2.1.12 but it was not manufactured. Future studies could investigate this flow plate design further.

The objective of maze flow plate design (developed during this thesis) was to ensure that there are no dead zones inside the flow plate, maximise contact with the gas diffusion layer to ensure reduced ohmic resistance and efficient extraction of water from the plate while maintaining even distribution of gases and pressure against the GDL. This flow plate gave promising velocity and pressure profiles from simulation results as shown in Figure 97 and Figure 98, Chapter 5, Section 5.2.1.12, and was assigned for manufacture and test.

Dead ended flow plate designs including interdigitated flow plate (from literature), modified interdigitated flow plate (developed in this thesis) and spiral and vein flow plates (developed in this thesis) were all modelled and simulated. The spiral and vein flow plate simulation results were not promising as detailed in Chapter 5, Section 5.2.1.18 and so they were not manufactured or tested further. The interdigitated flow plate gave high input pressures as shown in Chapter 5, Section 5.2.1.16 signifying possible parasitic and mass transport losses. The modified interdigitated flow plate with its tapered channels reduced the inlet pressure by 150% as shown in Figure 107, Chapter 5, Section 5.2.1.18, and gave a more even distribution of flow through the channels, reducing parasitic and mass transport losses. However the high input pressures were seen as a disadvantage and these flow plates were not manufactured. Future studies could investigate this flow plate design further.

Water flooding inside a PEM fuel cell as described in Chapter 2, Section 2.5 and the need for water management, lead to the need to use CFD and VOF to model two phase fluid flow and use high speed cameras to investigate water flooding.

(a)   (b)
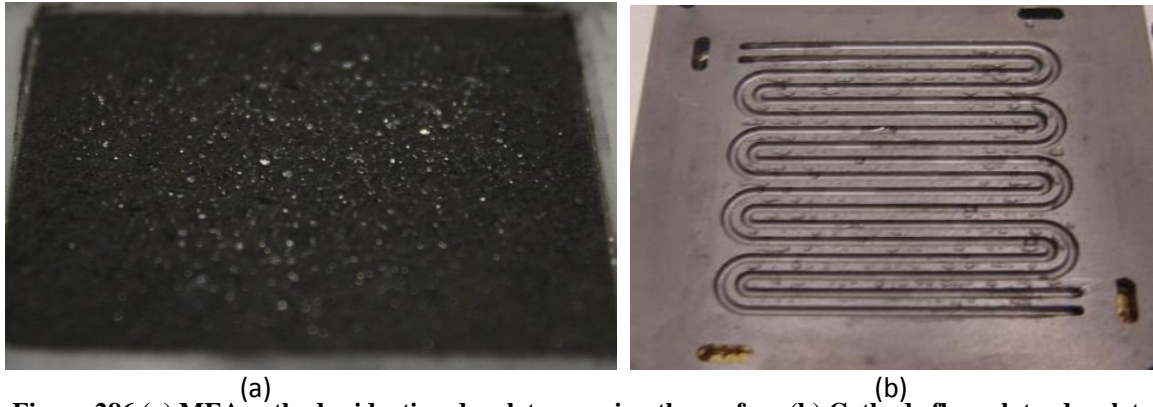
Figure 286 (a) MEA cathode side, tiny droplets covering the surface (b) Cathode flow plate, droplets covering the surface.

Once the PEM fuel cell is disassembled, after use, water is clearly noticed on the GDL in micro-droplet form as shown in Figure 286 (a) and larger droplets are noticed on the flow plate as shown in Figure 286 (b). The water is seen to be mainly on the ribs of the channel rather than in the channel as possibly expected. This is due to water movement from the hydrophobic GDL to the more hydrophilic channel where capillary action ensures it is adhered to the edges of the channel and GDL.

The effect of gravity may assist in the throughput of liquid droplets through the flow plates but capillary action and wetability affects of the GDL and flow plate impact water droplet formation to a greater affect than gravity. Hydrophobic and hydrophilic properties of the GDL and flow channels were highlighted in literature, Chapter 2, Section 2.5, and tested by simulation in Chapter 5, Section 5.2.2. Once droplets start to form on the surface they can wick towards the channel edges, creating films of water. These films can then grow into large drops and then slugs of water as shown experimentally in Figure 275, Chapter 5, Section 5.3.2.1.Once a drop is formed it immediately interacts with the air flow in the channel. This may move the drop towards the exit but it may also join with other droplets forming a slug.

Six distinctly different types of flow regimes were viewed during the visualisation experiments these are shown in Figure 287. Each flow regime occurs due to particular operating conditions of the PEM fuel cell as described by Lu et al. [84] and Hussaini et al. [83].
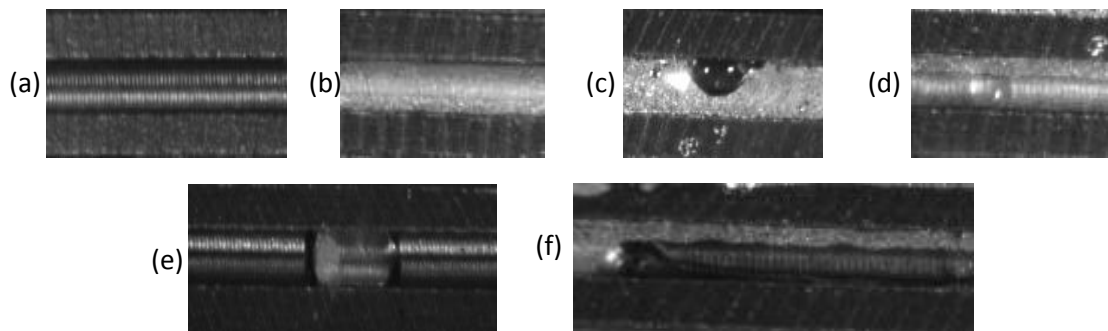
Figure 287 Flow regimes viewed (a) Single phase flow (b) Single phase flow with suspended droplets (mist flow) (c) Droplet attached to channel wall (d) Suspended droplet (e) Stationary slug (f)Moving slug leaving film.

Slug flow and intense annular flow can cause an increased pressure drop due to liquid water build-up and this is a key cause of flow mis-distribution and mass transport losses that dramatically reduces the PEM fuel cell performance and durability.

The CFD VOF model was used to investigate the interaction of the GDL and flow channels with water flooding specifically droplet coalescence and slug formation and movement within channel and bend designs of PEM fuel cell flow plates.

The 3-D double serpentine model layout with mutual inlet and outlet as detailed in Chapter 5, Section 5.2.2.6 was used extensively. Hydrophobic and hydrophilic properties and the flow plate design, flow plate channel or bend region play a major role in the effective mitigation of flooding in flow plates. Once droplets coalesce a large droplet or slug can form in one channel and effectively block the channel, with low pressure observed in the blocked channel, after the blockage. This can reduce the PEM fuel cell's performance by almost 33%, also recognised by Hu et al.[127]. Due to the mutual inlet, the fluid in the blocked channel uses the other channel as a relief channel, increasing velocity and decreasing pressure across both channels. With increased velocity in the free channel pressure normalises as shown in Figure 136, Chapter 5, Section 5.2.2.7 for example. If a second slug begins to form in the second channel, pressure can again build up forcing both slugs to move but most commonly the smaller slug will burst, sending micro droplets down the channel. It is noticed that due to the bend areas in channels slugs become distorted and uneven pressures can effectively burst the largest slugs when carried to the bend region as shown in Figure 142, Chapter 5, Section 5.2.2.7 for example.

Spiegel et al. [69] investigated the performance of a PEM fuel cell with different channel feature sizes. Fuel cell performance improved as the channel feature size decreased and gas flow velocity increased, since the increased flow velocity enhances mass transport. However, it was found that a drawback, of the smaller feature size, is the increased pressure drop in the flow channels. This idea brings us away from conventional PEM fuel cell flow plates to open pore cellular foam materials, that were viewed in literature as discussed in Chapter 2, Section 2.7. To again note, the key issues when

designing a flow plate are: the even distribution of pressure on the GDL and membrane, low pressure drop in and through the flow plate, distribution of temperature on the GDL and membrane, maintained reactant concentration over the entire active area of the GDL and membrane, membrane hydration and the mitigation of flooding as discussed throughout the literature review in Chapter 2. In addition cost and ease of manufacture are also desirable properties of a flow plate. Open pore cellular foam materials seem to have many possible advantages over conventional flow plate materials and designs. These relatively new materials have many interesting combinations of physical, mechanical, electrical, and thermal properties.
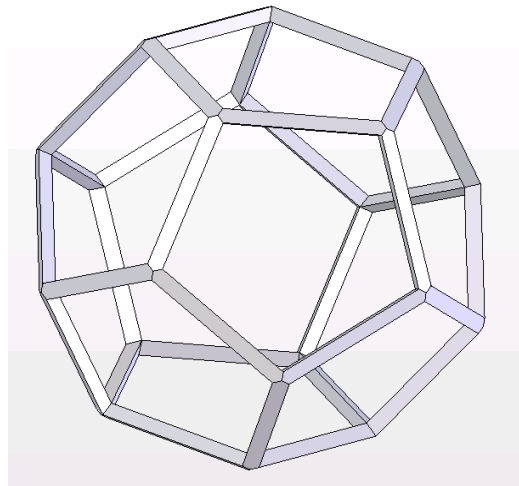
Figure 288 Dodecahedron 'Pore' RUCS

To assess these materials effectively a model had to be developed and simulated, but for a model to be developed a RUCS for open pore cellular foam has to be identified. The RUCS (a dodecahedron as shown in Figure 288) and developed model and CFD simulation results are detailed in Chapter 5, section 5.2.3.

Simulation results include 10, 20, 30, 40, 45, 80 and 100ppi open pore cellular foams with relation to pressure drop and velocity flow in new PEM fuel cell flow plates composed of open pore cellular foam. A key parameter tested was pressure drop through the model of each ppi type. In general pressure drop results matched very well with ERG experimental results, Dupuit-Forchheimer, Ashby and Fourie & Du Plessis mathematical models. As expected the Darcy (due to high Reynolds number) and the Ergun mathematical models (due to lack of spherical particles) do not align as well.

As described in Chapter 2, Section 2.4.2.4 the GDL and flow plate interface is very important in conventional flow fields such as serpentine, the flow is in the direction parallel to the electrode surface. In this configuration the reactant flow to the catalyst layer is predominantly by molecular diffusion through the GDL. This can lead to large concentration gradients across the GDL and mass transfer limitations because of the small channel dimensions, laminar gas flow and the inherent slow

molecular diffusion process. Dead ended flow plate types, as shown in Figure 25, Chapter 2, Section 2.4.2.4, provide convection velocity normal to the electrode surface for better mass transfer and enhanced water removal from the backing layer. This design consists of dead ended flow channels, which are not continuous from inlet manifold to exit, so that the reactant flow is forced under pressure to go through the backing layer. This provides enhanced performance at high current density operation. However large pressure losses and high parasitic power (due to increased gas flow pressure) are characteristics of this dead ended flow field type.

Open pore cellular foam materials reduce the permeability of the gas flow through the flow plate. This result in a more tortuous path parallel to the plates thereby making the flow of reactant gases towards the reaction interface from only diffusion to diffusion plus convection based, unlike conventional flow plates, see Figure 289. In existing flow fields, intricate flow field structures are common but on a much larger scale when compared to open pore cellular foam materials which have sub millimetre pores and ligaments to distribute the air flow. It is noted that permeability reduction with the conventional machined channel design is not possible beyond a particular value (around 10^{-8} m^2), due to difficulty in machining thin cross-section channels [14]. This is not an issue for open pore foam materials with a measured permeability of 10^{-8}m^2 for 40ppi foam for example; with the added benefit of low pressure drop from inlet to outlet, even at high flow rates.
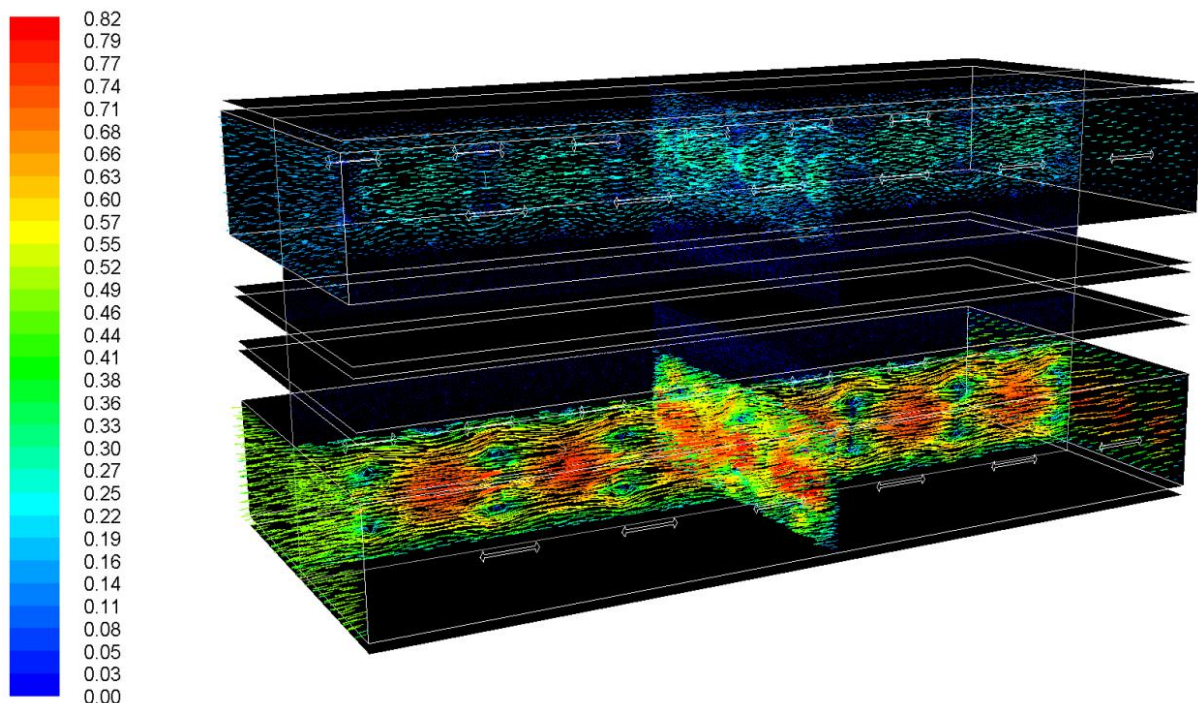
Figure 289 Open pore cellular foam flow plate velocity vectors (m/s)

The GDL and flow plate interaction discussed by Dohle et al. [195] is an important area to consider. In existing flow plates a large area is covered by the channel, affecting fluid and gas flow through the

GDL and flow channel, which is not a concern in foam materials. The large surface area and the high porosity of open pore cellular foam material can achieve high rates of conversion per unit volume. The design of the flow plate with open pore cellular foam material allows for uniform current and potential distribution, low ohmic internal resistance and high rates of mass transport of the electro active species to the electrode surface.

From the development of an electrochemistry model to simulate open pore cellular foam (developed in this thesis) it is possible to compare operational PEM fuel cell simulation results for double channel & open pore cellular foam flow plates. Also polarisation curves were constructed that matched experimental results very well. These results are detailed in Chapter 5, Section 5.2.4.

Figure 251 and Figure 252, Chapter 5, Section 5.2.4.4.6 compares open pore cellular foam and double channel hydrogen and oxygen mass fractions at 0.85 volts & 0.55 volts. It is noticed that even though more power is produced by the open pore cellular foam fuel cell, as shown in Figure 254 (of the same section) the concentration of hydrogen and oxygen is much less than the double channel fuel cell. This can be attributed to the enhanced utilisation of fuel and oxidant and reduced mass transport losses in the open pore cellular foam flow plate.

Figure 253, Chapter 5, Section 5.2.4.4.6, shows the water distribution in the anode and cathode of the open pore cellular foam and double channel PEM fuel cell at 0.85 volts & 0.55 volts. Again the water production is more gradual in the open pore cellular foam fuel cell even at high current densities which would lead to less water flooding issues. This was noted in an experiment by Chen et al. [174] that about 10% water was retained in porous inserts and the inserts featured a self-adjusting capacity for water management in flooding and drying conditions in a fuel cell. Micro porous wicks that are placed on the edges of the channels of a flow plate have been proposed by a number of researchers [196-199]; however this idea adds an extra process to the complicated machining process already used to machine the channels. The open pore cellular flow plate would have many advantages over the placement of additional wick structures.
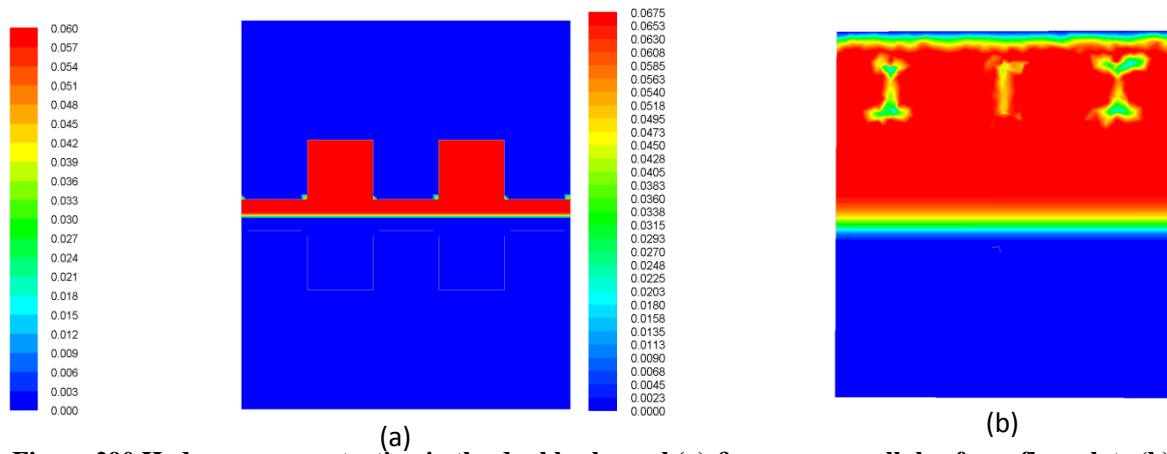
Figure 290 Hydrogen concentration in the double channel (a) & open pore cellular foam flow plate (b) 0.55volts.
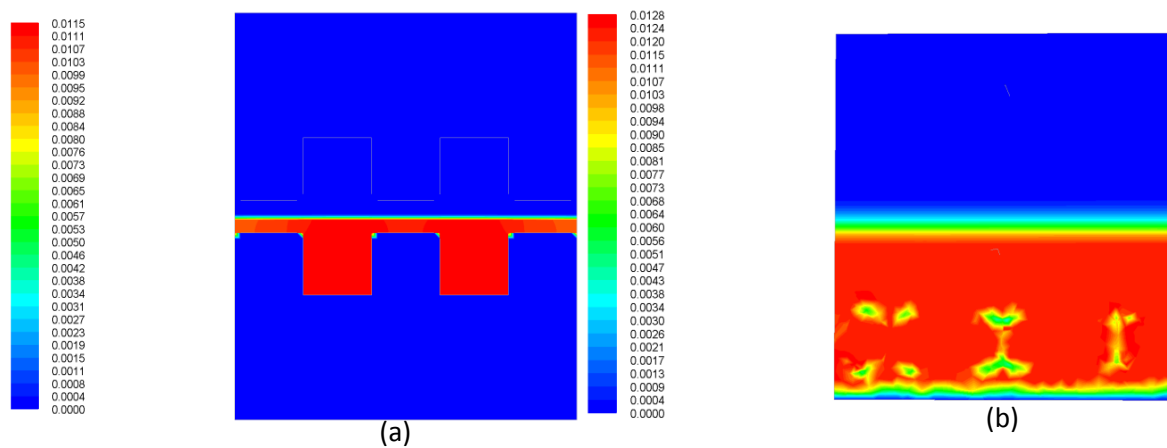
Figure 291 Oxygen concentration in the double channel (a) & open pore cellular foam flow plate (b) 0.55volts.

Looking along the channels, Figure 290 and Figure 291 show the hydrogen and oxygen in the double channel & open pore cellular foam flow plate at 0.55volts. It is clear that the concentration of hydrogen and oxygen is maximum in the channel of the flow channels and reduces to lower concentrations under the ribs of the channels. In the open pore cellular foam flow plate the concentration is even throughout the flow plate due to the matrix design.
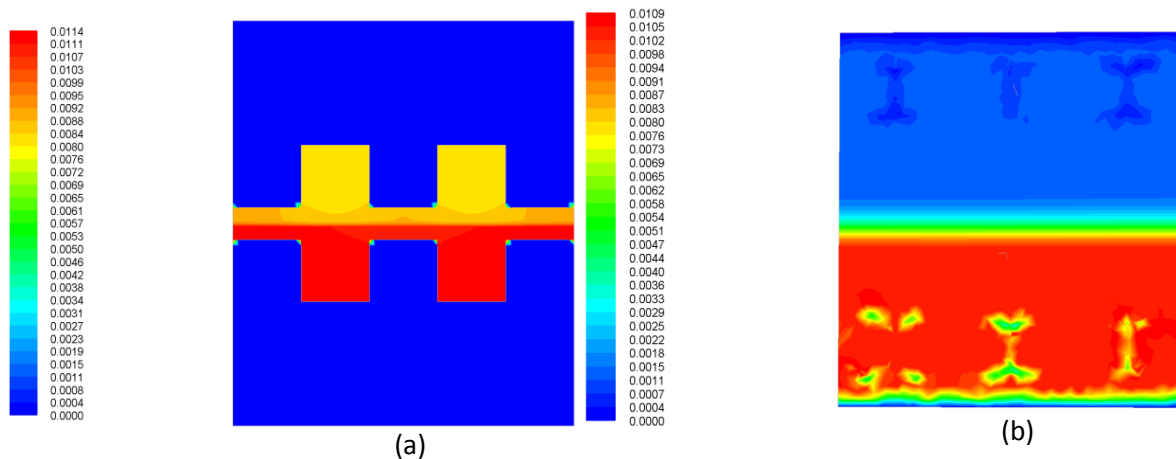
Figure 292 Water concentration in the double channel (a) & open pore cellular foam flow plate (b) 0.55volts
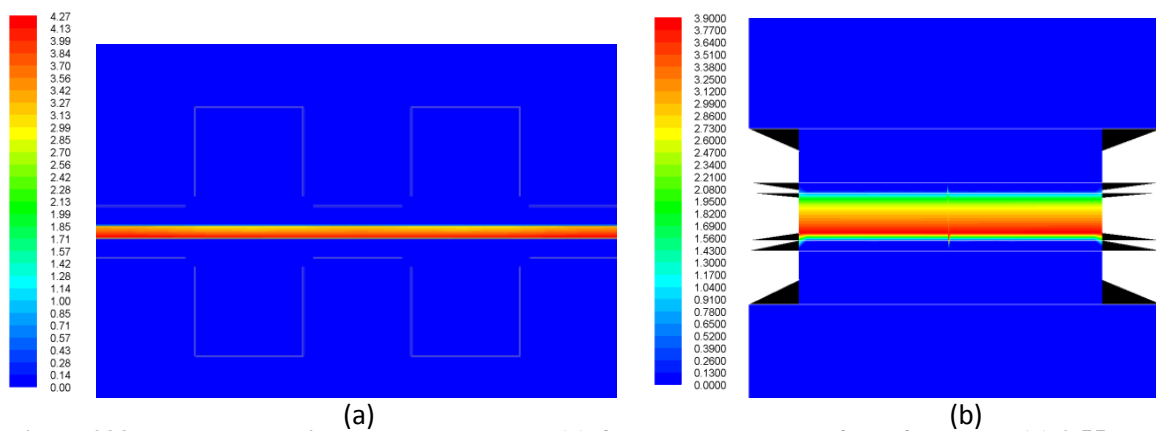
Figure 293 Water content in the double channel (a) & open pore cellular foam flow plate (b) 0.55volts

Figure 292 shows the water concentration and water content in the double channel & open pore cellular foam flow plate at 0.55volts. The water concentration is highest at the cathode, under the ribs of the channels and lowest in the flow channels. This could explain how flooding can hinder the ORR in conventional flow plate designs. A similar result is visible in Figure 293 (a) (magnified to show detail) for water content in the MEA. The open pore cellular foam flow plate has a very even distribution of water concentration in the flow plate and water content in the MEA.

Due to a larger surface contact with the membrane electrode assembly and open structure, excellent heat and electricity conduction and gas diffusion can be achieved through the flow plate. This is evident when comparing the temperature of the models in Chapter 5, the double channel in Figure 231, Section 5.2.4.2.4 and the open pore cellular foam flow plate in Figure 248, Section 5.2.4.4.4, at 0.55 volts.

The intricate designs that are used in traditional graphite flow plates are manufactured by energy intensive and costly CNC machining processes and consequently, alternative materials and concepts are required to fabricate flow plates. In order to save the cost of machining it is proposed to use metal foams as flow plates in PEM fuel cells.

It is also proposed that an open pore cellular foam fuel cell may not need a GDL. In conventional flow plates the GDL's permeability is related to contact resistance of the rib of the flow plate and the compression force holding the cell together. This can reduce GDL pore size if too tight or increase ohmic resistance if too loose. Kumar et al. [14] has suggested that the open pore cellular foam may act as a catalyst support. The open pore cellular foam would have a set permeability, not affected by compression and ensure good contact with the membrane, reducing ohmic resistances further. This idea would there by reduce the number of components in the fuel cell stack simplifying the PEM fuel cell and assembly processes.

Figure 294 is the culmination of the work completed in this thesis. It shows the best performing flow plate polarisation curves with integrated power density curves.

The industrial standard double serpentine flow plate was the bench mark. The purchased fuel cell performed lower than other PEM fuel cells in literature but this did not affect the study as a comparison is performed to investigate the most effective flow plate using optimum input parameters. The industrial standard double serpentine flow plate performed to the manufacturers specifications consistently throughout all experimental work as shown in Figure 294, recording 0.7V at 0.05A/cm^2. The results should be scalable to larger and more efficient fuel cells with different MEA with different platinum loading.

It is clear that the RVCF flow plates did not perform well. The best performing RVCF flow plates were the 45ppi and 80ppi flow plate. This result was expected as the conductivity of RVCF is much less than the MF or conventional flow plates. In addition RVCF is extremely brittle and as it is closed into the fuel cell the compressive forces of closing backing plates noticeably cracked some of the pores in contact with the GDL, increasing ohmic resistance further.

Hybrid assemblies were created with MF and RVCF flow plates such as the 100 dense ppi RVC and the 80 dense ppi MF shown in Figure 294. These flow plates did not perform well either again due to the RVCF material.

Of all the manufactured flow plates the modified serpentine or the modified parallel did not perform well as shown in Chapter 5.The maze flow plate performed better than even the bench mark serpentine fuel cell for low current densities, recording 0.7V at 0.065A/cm^2. However, as the current density increased to about 0.12A/cm^2, the maze flow plate's voltage and power density dropped considerably. This is characteristic to mass transport or concentration losses at the lower voltages. This was an initial concern with this flow plate design, possible compounded by the channel profile and intricate channels prone to water blockage.
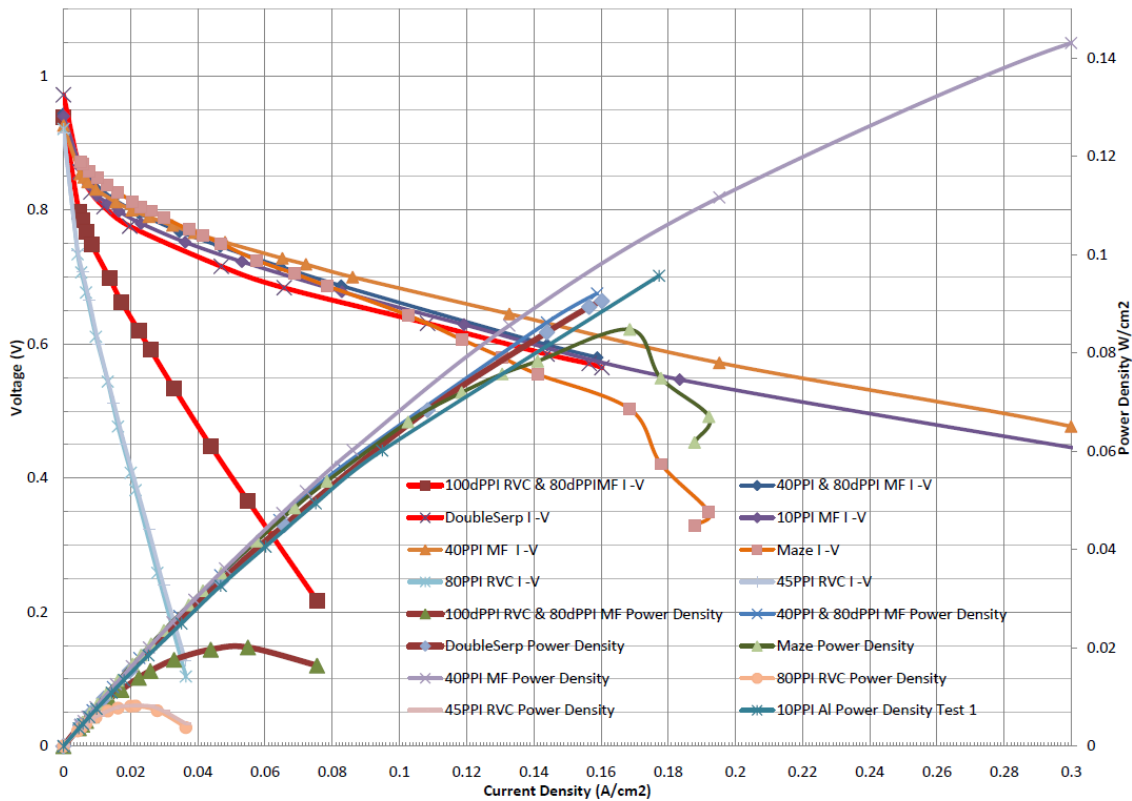
Figure 294 Polarisation curve comparison for the most promising flow plate designs.

Finally the open pore cellular metal foam flow plates are shown in Figure 294. All open pore cellular MF flow plates outperformed all other flow plate designs tested, with the 40ppi MF flow plates consistently performing best in all experiments, recording 0.7V at $0.09A/cm^2$. This in excess of a 55% improvement on the current density of the bench mark double serpentine flow plate under the same operating conditions operating at 0.7 volts.

Interestingly the 10ppi only slightly performed lower than the hybrid 80 dense ppi. The 10ppi foam has large pores and this may reduce the contact area with the MEA shown in the slight reduced ohmic region in Figure 294. However, mass transport or concentration losses at high current densities were not a concern for any open pore cellular MF flow plates, with no sign of these losses in any experiment and the results overshooting the test capabilities. This clarifies the electrochemistry simulation results as discussed in the above paragraphs.

MF materials have issues at present because of the corrosion associated with MF materials in the acidic environment of a PEM fuel cell. Stainless steel or coated foams could be manufactured but these may have added cost or manufacturing processes. Abo El-Enin et al. [67] investigated the use of aluminium, coated with different nickel alloys, as a flow plate instead of graphite in order to reduce the cost and weight and ease the machining. The electroplated nickel alloys on aluminium substrate produced a new metallic flow plate for PEM fuel cell with a higher efficiency and longer lifetime than the graphite flow plate due to its higher electrical conductivity and its lower corrosion rate this idea could be incorporated into open pore cellular metal foam flow plate production.

Table 15 Summary of the disadvantages of conventional flow plate designs and the advantages of open pore cellular foam flow plates.

Disadvantages of conventional flow plates	Advantages of open pore cellular foam flow plates
Gas flow can be parallel to the MEA & mainly by diffusion, which can lead to mass transfer limitations	Gas flow can be diffusion plus convection based minimising mass transfer limitations
Full & even distribution of gas over the active area of the MEA is difficult to achieve	Low resistance to fluid flow and full & even distribution of gas over the active area of the MEA
Concentration gradients of gases from inlet to outlet	Excellent diffusion of gas at low flow rates and pressures
Water production decreases through the length of the flow plate from inlet to outlet due to the concentration gradient; however water blockage increases from inlet to outlet in the flow plate	Low resistance to fluid flow and internal water management can be achieved
Pressure & energy loss can occur due to intricate flow plate design with many turns & bends	Low pressure drop for fluid flow
Depending on the flow plate type; parallel / serpentine / interdigitated; blockages of water and stagnant gas inside the cell can lead to reduced performance	Full & even distribution of gas over the active area of the MEA and porous design reduce the possibility of water blockages and stagnant areas
Water formation from the ORR and other sources channels in the flow plate can become blocked (depending on design & channel dimensions)	Full & even distribution of gas over the active area of the MEA and porous design reduce the possibility of water blockages and stagnant areas
Water droplets condense and drag along the channels: water slug/film formation.	Full & even distribution of gas over the active area of the MEA and porous design reduce the possibility of water blockages and stagnant areas
Water droplets can cover and block the GDL	Foam may be coated with PTFE to resist water cohesion
The permeability of the GDL is strongly influenced by the effect of fibre orientation and contact pressure of the flow plate	The GDL may be incorporated into the foam material.
Small porosity of the GDL results in good electrical conductivity however large pores allows more efficient mass transport	Variable porosity up to 100 ppi & variable density from 3 to 12%
Ohmic losses may be high from contact resistance (effective MEA contact) and material resistance.	Reduce ohmic losses between the flow plate and membrane (metals are better conductors than graphite) Effective surface contact area can be controlled
Temperature must be even and distributed through the MEA; too hot the membrane can dry out and crack, too cold, especially at start up, condensation may occur	Excellent conduction of heat and electricity. Heat management may be controlled easier
Too much humidification causes extra flooding & swelling of the membrane, too little causes the membrane to dry out & crack	Internal humidification may be achieved
Uneven distribution of gases from cell to cell in a stack can occur due to pressure differences or blockage issues	Excellent diffusion of gas at low flow rates and pressures
It may be difficult to re-circulate unused low pressure hydrogen	Low pressure drop for fluid flow
Parasitic losses may occur due to complicated balance of plant systems	Internal humidification may be achieved, reducing flooding issues and balance of plant losses
Conventional flow plates can be brittle and account for 80% of the weight of a stack	Isotropic & rigid geometry with high strength-to-weight ratio. Can significantly reduce weight of flow plate
Graphite can be expensive	Specific MF materials or aluminium foam coated with another material can be tolerant to the corrosive environment of the PEM fuel cell.
Intricate flow plates can increase manufacturing cost	Reduce cost of material & simplify manufacture for flow plates
Conventional electrode designs can limit design applications	Intricate flow plate shapes can be manufactured fast and easily

BLANK PAGE

7

Chapter 7 - Conclusion

7.1 Conclusion

The ultimate goal of this body of work was to improve the performance of PEM fuel cells and in the process try to simplify their design that could reduce material, manufacturing and assembly costs focusing on flow plate development. This thesis conducted a review of PEM fuel cells. An examination of existing flow plates and the issues that continue to persist with these components in PEM fuel cells were highlighted. Open pore foam materials including MF and RVCF were reviewed as a potential flow plate material. Modelling, simulation and experimental methods were all uses together in the design and development stages to evaluate existing and develop new & innovative better performing PEM fuel cell flow plates.

The conclusions resulting from the investigation are summarised as follows:

- Effective water flood mitigation, effective mass transport, increased efficiency, reduced ohmic resistance, weight, cost and complexity of PEM fuel cell stacks can be achieved by optimal flow plate properties and design.

- The CFD VOF model showed the interaction of droplets with the GDL and channels of conventional flow plates. Slugs of droplets (the basis of water flooding) can form inside the intricate flow channels of conventional flow plates causing pressure build up, flow misdistribution and even channel blockages, reducing the fuel cell's performance by almost 33% in some cases. These models were validated by visualisation techniques.

- A satisfactory Representative Unit Cell Structure (RUCS) model for open pore cellular foam material was proposed and developed in this thesis. Pressure drop results matched very well with ERG experimental results, Dupuit-Forchheimer, Ashby and Fourie & Du Plessis mathematical models. As expected the Darcy (due to high Reynolds number) and the Ergun mathematical models (due to lack of spherical particles) do not align as well.

- An electrochemistry PEM fuel cell model demonstrating open pore cellular foam flow plates was developed in this thesis using the RUCS model. The simulation results matched

experimental results. The simulation results were compared to conventional PEM fuel cell flow plate simulation results. The distribution of hydrogen oxygen and water inside the open pore cellular foam flow plates were very much distributed and even from inlet to outlet. The open pore cellular foam flow plates also seemed to distribute the temperature from the MEA more evenly than in conventional flow plates. These advantages of the open pore cellular foam flow plates have huge implications on mitigation of flooding and reduction of mass transport losses increasing the PEM fuel cell performance.

- The experimental analysis of many flow plate designs developed during this thesis clarified that the open pore cellular foam flow plates perform in excess of a 55% improvement on the current density of the bench mark double serpentine flow plate under the same operating conditions, operating at 0.7 volts.

- It is concluded that open pore cellular foam materials can ensure better gas flow through the cell, less pressure drop from inlet to outlet and may have an added benefit of passively managing the water inside the cell. In addition, the resistance of the cell may be reduced not only due to the effective contact area of the foam pores to the GDL but also due to the effective hydration of the membrane that is achieved internally. Finally the need for expensive machining process to manufacture flow plates could be eliminated using open pore cellular foam materials. Once formed, they need only be cut to size for a fuel cell. Improvement in these designs will give lower cost, high efficiency and better power density on both volume and weight basis.

7.2 Future Work Proposed

Further work could include:

- The models developed and validated during the course of this thesis provide a powerful tool for future PEM fuel cell and PEM fuel cell stack development.

- Visualisation of open pore cellular foam was not completed in this study, because of the difficulty of viewing deep inside the pores. Visualisation of porous media using such techniques as NMR can show fluid flow through porous media. This would enhance the knowledge of the flow regimes inside these materials and investigate the proposed water manage ability of open pore cellular foam flow plates.

- Investigation of open pore cellular foam as a catalyst support should be completed. New coating technologies could be used to coat electro-catalysts directly on to open pore cellular foam flow plates. If this study was successful, the proposed idea that the GDL could be removed from a PEM fuel cell using open pore cellular foam flow plates would help propel fuel cell technology forward into market.

- Prototype cells and stacks of innovative Open Pore Cellular Foam PEM fuel cells design, proposed in this thesis, should be manufactured and the application of innovative Open Pore Cellular Foam PEM fuel cells should be employed into a technology demonstration project.

References

[1]O'Hayre R, Cha S, Colella W, Prinz FB. Fuel Cell Fundamentals. USA: John Wiley and Sons;0-471-74148-5, 2006.

[2]Axane. Fuel Cell Typology. US,2009. See Also: http://www.axane.fr/gb/fuel_cell_hydrogen/fuel_cell.html. Accessed Sept 2009.

[3]Lawlor V, Griesser S, Buchinger G, Olabi AG, Cordiner S, Meissner D. Review of the micro-tubular solid oxide fuel cell: Part I. Stack design issues and research activities. J.Power Sources 2009 9/5;193(2):387-399.

[4]S. K. Dong, B. T. Yun and D. K. Lee. Design and numerical study for lkW tubular SOFC APU system. Anonymous Fuel Cell Seminar 2007, October 15, 2007 - October 1912 San Antonio, TX, United states: Electrochemical Society Inc; 2007; 701-706.

[5]Supramaniam S. Fuel Cells: From Fundamentals to Applications New York: Springer Science & business Media; 0-387-25116-2, 2006.

[6]H. R. Haas and M. T. Davis. Electrode and catalyst durability requirements in automotive PEM applications: Technology status of a recent MEA design and next generation challenges. Anonymous 9th Proton Exchange Membrane Fuel Cell Symposium (PEMFC 9) - 216th Meeting of the Electrochemical Society, October 4, 2009 - October 925 Vienna, Austria: Electrochemical Society Inc; 2009; 1623-1631.

[7]Cindrella L, Kannan AM, Lin JF, Saminathan K, Ho Y, Lin CW, et al. Gas diffusion layer for proton exchange membrane fuel cells - a review. J.Power Sources 2009 10/20;194(1):146-60.

[8]Li X, Sabir I. Review of bipolar plates in PEM fuel cells: Flow-field designs. Int J Hydrogen Energy 2005 03;30(4):359-71.

[9]Angstrom Power Inc. Better than batteries. Canada,2010. See Also: http://www.angstrompower.com/. Accessed May 2010.

[10]Toshiba. Methanol Fuel Cell. Japan,2010. See Also: http://www.toshiba.com/. Accessed May 2010.

[11]Carton JG, Olabi AG. Wind/hydrogen hybrid systems: Opportunity for Ireland's wind resource to provide consistent sustainable energy supply. Energy 2010;35(12):4536-4544.

[12]Jason Marcinkoski and Daniel Thomas. Progress in PEM fuel cell activities. Anonymous 136th TMS Annual Meeting, 2007, Febrary 25, 2007 - March 1 Orlando, FL, United states: Minerals, Metals and Materials Society; 2007; 1-10.

[13]Steele BCH, Heinzel A. Materials for fuel-cell technologies. Nature 2001;414(6861):345-352.

[14]Kumar A, Reddy RG. Materials and design development for bipolar/end plates in fuel cells. Journal of Power Sources 2004;129(1):62-67.

[15]Solomon S, Qin D, Manning M, Chen Z, Marquis M, Averyt KB, et al. Intergovernmental Panel on Climate Change. 2007; Available at: AR4, IPCC-2007.

[16]Friedlingstein P, Houghton RA, Marland G, Hackler J, Boden TA, Conway TJ, et al. Update on CO2 Emissions. Nature Geoscience 2010;3:811-812.

[17]IGBP. International Geosphere Biosphere Programme (IGBP) - Climate Change Index. Sweden,2010. See Also: http://www.igbp.kva.se/page.php?pid=504. Accessed Sept 2010.

[18]United Nations. Copenhagen Accord. 2009; Available at: 15, COP15.

[19]United Nations. Kyoto Protocol to the United Nations Framework Convention on Climate Change. 1998; Available at: 1.

[20]Phillips L. EU unveils comprehensive climate and energy package. 2009. See Also: http://euobserver.com/877/25513. Accessed Sept 2010.

[21]Department of Energy Ireland. Carbon Budget 2008. Ireland,2010. See Also: http://www.environ.ie/en/Environment/News/MainBody,18676,en.htm. Accessed Aug 2010.

[22]Department of Energy Ireland. National Renewable Energy Action Plan IRELAND. Ireland,2010. See Also: http://www.dcenr.gov.ie/Energy/. AccessedAug 2010.

[23]S&T Consultants. Hydrogen Pathways Greenhouse Gas Emissions & Energy Use (Prepared for Fuel Cells Canada). Canada,2009. See Also: http://iea-hia-annex18.sharepointsite.net/Public/National%20Documents/Canada/GreenHouseGas-Energy-Use.pdf. Accessed June 2009.

[24]European Commission. Introduction to Hydrogen as an Energy Carrier. 2009. See Also: http://ec.europa.eu/research/energy/pdf/hydrogen_22002_en.pdf. Accessed Aug 2009.

[25]Neef H-. International overview of hydrogen and fuel cell research. Energy 2009 03;34(3):327-33.

[26]Peavey MA. Fuel From Water: Energy Independence with Hydrogen. 11th ed. Louisville KY: Merit Inc; 0-945516-04-5, 2003.

[27]Sigfusson TI. Pathways to hydrogen as an energy carrier. Philosophical Transactions of the Royal Society London, Series A (Mathematical, Physical and Engineering Sciences) 2007 04/15;365(1853):1025-42.

[28]Holladay JD, Hu J, King DL, Wang Y. An overview of hydrogen production technologies. Catalysis Today 2009;139(4):244-260.

[29]Houghton J. Global warming The Complete Briefing. 3rd ed. UK: Cambridge University Press; 2004.

[30]Zeng K, Zhang D. Recent progress in alkaline water electrolysis for hydrogen production and applications. Progress in Energy and Combustion Science 2010;36(3):307-326.

[31]Larry Moulthrop, Jesse Hayes and Mike Spaner. P.E.M. Water electrolyzers in renewable energy capture to hydrogen. Anonymous 2007 AIChE Spring National Meeting, April 22, 2007 - April 27 Houston, TX, United states: American Institute of Chemical Engineers; 2007; .

[32]Balat M. Possible Methods for Hydrogen Production. Energy Sources Part A 2009;31(1):39-50.

[33]Melis A, Happe T. Trails of green alga hydrogen research — from Hans Gaffron to new frontiers. 2005; , 20.

[34]Melis A, Happe T. Hydrogen production. Green algae as a source of energy. Plant Physiol. 2001;127(3):740-748.

[35]F. R. Hawkes, R. Dinsdale, D. L. Hawkes and I. Hussy. Sustainable fermentative hydrogen production: challenges for process optimisation. Anonymous BIOHYDROGEN 200227 UK: Elsevier; 11; 1339-47.

[36]Rechenberg I. Artificial Bacterial Algal Symbiosis (Project ArBAS). 1999; .

[37]Hammerschlag R, Mazza P. Questioning hydrogen. Energy Policy 2005 11;33(16):2039-43.

[38]EG&G Technical Services I. Fuel Cell Handbook. 7th ed. Virginia: U.S. Department of Energy; 2004.

[39]Larminie J, Dicks A. Fuel Cell Systems Explained. Second edition ed. London: John Wiley & Sons Ltd; 2003.

[40]Yu X, Zhou B, Sobiesiak A. Water and thermal management for Ballard PEM fuel cell stack. J.Power Sources 2005;147(1-2):184-195.

[41]G. J. Snyder and Sossina M. Haile. Fuel cell materials and components. Anonymous Advanced Materials for Energy Conversion II, March 14, 2004 - March 18 Charlotte, NC., United states: Minerals, Metals and Materials Society; 2004; 33-41.

[42]Yu HM, Schumacher JO, Zobel M, Hebling C. Analysis of membrane electrode assembly (MEA) by environmental scanning electron microscope (ESEM). J.Power Sources 2005;145(2):216-222.

[43]Zhang S, Yuan X, Wang H, Merida W, Zhu H, Shen J, et al. A review of accelerated stress tests of MEA durability in PEM fuel cells. Int J Hydrogen Energy 2009;34(1):388-404.

[44]Mehta V, Cooper JS. Review and analysis of PEM fuel cell design and manufacturing. J.Power Sources 2003;114(1):32-53.

[45]Suo Jin-ping, Qian Xiao-liang, Yang Hong-qian, Kun C. Development of new proton exchange membranes. Chinese Journal of Power Sources 2003 05;27:238-40.

[46]Keiichi Kaneko, Yuko Takeoka, Masahiro Rikukawa and Kohei Sanui. Syntheses and fuel cell performances of hydrocarbon polymer electrolytes - Durability of polymer electrolytes. Anonymous 54th SPSJ Symposium on Macromolecules, September 20, 2005 - September 2254 Yamagata, Japan: Society of Polymer Science; 2005; 4515-4516.

[47]Jeffrey Gasa, Hengbin Wang, Ryan DeSousa and Ken Tasaki. Fundamental characterization of fullerenes and their applications for proton-conducting materials in PEMFC. Anonymous 7th

Symposium Devoted to Proton Exchange Membrane Fuel Cells - 212th ECS Meeting, October 7, 2007 - October 1211 Washington, DC, United states: Electrochemical Society Inc; 2007; 131-141.

[48]Li H, Tang Y, Wang Z, Shi Z, Wu S, Song D, et al. A review of water flooding issues in the proton exchange membrane fuel cell. J.Power Sources 2008 03/15;178(1):103-17.

[49]Pasaogullari U, Wang C. Two-phase transport and the role of micro-porous layer in polymer electrolyte fuel cells. Electrochim.Acta 2004;49(25):4359-4369.

[50]Ugur Pasaogullari, Chao-Yang Wang and Ken S. Chen. Liquid water transport in polymer electrolyte fuel cells with multi-layer diffusion media. Anonymous 2004 ASME International Mechanical Engineering Congress and Exposition, IMECE, November 13, 2004 - November 19375 Anaheim, CA, United states: American Society of Mechanical Engineers; 2004; 307-315.

[51]Weber AN, J. Effects of Micro Porous Layer in PEM Fuel Cells. Electrochemical Soc. 2005 2005;152(4):667-688.

[52]Jin HN, Kyu-Jin Lee, Gi-Suk Hwang, Charn-Jung Kim, Kaviany M. Microporous layer for water morphology control in PEMFC. Int.J.Heat Mass Transfer 2009 05;52(11-12):2779-91.

[53]Park J, Li X. Multi-phase micro-scale flow simulation in the electrodes of a PEM fuel cell by lattice Boltzmann method. J.Power Sources 2008 03/15;178(1):248-57.

[54]Zhan Z, Xiao J, Zhang Y, Pan M, Yuan R. Gas diffusion through differently structured gas diffusion layers of PEM fuel cells. Int J Hydrogen Energy 2007 12;32(17):4443-51.

[55]Bazylak A. Liquid water visualization in PEM fuel cells: a review. Int J Hydrogen Energy 2009 05;34(9):3845-57.

[56]Al-Baghdadi M. Studying the effect of material parameters on cell performance of tubular-shaped PEM fuel cell. Energy Conversion and Management 2008;49(11):2986-2996.

[57]Benziger J, Nehlsen J, Blackwell D, Brennan T, Itescu J. Water flow in the gas diffusion layer of PEM fuel cells. J.Membr.Sci. 2005;261(1-2):98-106.

[58]Feng-Yuan Zhang, Advani SG, Prasad AK. Performance of a metallic gas diffusion layer for PEM fuel cells. J.Power Sources 2008 01/21;176(1):293-8.

[59]Maheshwari PH, Mathur RB, Dhami TL. Fabrication of high strength and a low weight composite bipolar plate for fuel cell applications. J.Power Sources 2007 11/08;173(1):394-403.

[60]Kakati BK, Mohan V. Development of low-cost advanced composite bipolar plate for proton exchange membrane fuel cell. Fuel Cells 2008 02;8(1):45-51.

[61]Fuel Cell Markets Ltd. Fuel Cell Bipolar plates. UK,2009. See Also: http://www.fuelcellmarkets.com/fuel_cell_markets/bipolar_plates/4,1,1,2564.html. Accessed Aug 2009.

[62]Watkins D, Dircks K, Epp D, inventors. Watkins D, Dircks K and Epp D, assignees. Fuel cell fluid flow field plate. US patent 51088491992.

[63]Watkins D, Dircks K, Epp D, inventors. Watkins D, Dircks K and Epp D, assignees. Fuel cell with a fluid flow field plate. EU patent 04157331991.

[64]Kakati BK, Mohan V. Development of low-cost advanced composite bipolar plate for proton exchange membrane fuel cell. Fuel Cells 2008 02;8(1):45-51.

[65]Maheshwari PH, Mathur RB, Dhami TL. Fabrication of high strength and a low weight composite bipolar plate for fuel cell applications. J.Power Sources 2007 11/08;173(1):394-403.

[66]Peng L, Lai X, Liu D, Hu P, Ni J. Flow channel shape optimum design for hydroformed metal bipolar plate in PEM fuel cell. J.Power Sources 2008 03/15;178(1):223-30.

[67]El-Enin SAA, Abdel-Salam OE, El-Abd H, Amin AM. New electroplated aluminum bipolar plate for PEM fuel cell. J.Power Sources 2008 2/15;177(1):131-136.

[68]Li X, Sabir I, Park J. A flow channel design procedure for PEM fuel cells with effective water removal. J.Power Sources 2007 01/01;163(2):933-42.

[69]Spiegel CS, Agarwal R, Bhansali S. Comparison of microchannel dimensions for air-breathing polymer exchange membrane microfuel cells. J.Power Sources 2008 08/01;182(2):603-8.

[70]Carton JG, Olabi AG. Design of experiment study of the parameters that affect performance of three flow plate configurations of a proton exchange membrane fuel cell. Energy 2010;35(7):2796-2806.

[71]Xiao-Dong Wang, Yuan-Yuan Duan, Wei-Mon Yan, Xiao-Feng Peng. Local transport phenomena and cell performance of PEM fuel cells with various serpentine flow field designs. J.Power Sources 2008 01/03;175(1):397-407.

[72]Kloess JP, Wang X, Liu J, Shi Z, Guessous L. Investigation of bio-inspired flow channel designs for bipolar plates in proton exchange membrane fuel cells. J.Power Sources 2009 3/1;188(1):132-140.

[73]Le AD, Zhou B. A generalized numerical model for liquid water in a proton exchange membrane fuel cell with interdigitated design. J.Power Sources 2009;193(2):665-683.

[74]Kazim A, Liu HT, Forges P. Modelling of performance of PEM fuel cells with conventional and interdigitated flow fields. J.Appl.Electrochem. 1999 12;29(12):1409-16.

[75]Lin J, Chen W, Su Y, Ko T. Effect of gas diffusion layer compression on the performance in a proton exchange membrane fuel cell. Fuel 2008;87(12):2420-2424.

[76]Lai X, Liu D, Peng L, Ni J. A mechanical-electrical finite element method model for predicting contact resistance between bipolar plate and gas diffusion layer in PEM fuel cells. J.Power Sources 2008 07/15;182(1):153-9.

[77]Hassan NSM, Daud WRW, Sopian K, Sahari J. Water management in a single cell proton exchange membrane fuel cells with a serpentine flow field. J.Power Sources 2009;193(1):249-257.

[78]Jin HN, Kaviany M. Effective diffusivity and water-saturation distribution in single- and two-layer PEMFC diffusion medium. Int.J.Heat Mass Transfer 2003 11;46(24):4595-611.

[79]Djilali N, Litster S, Sinton D. Ex situ visualization of liquid water transport in PEM fuel cell gas diffusion layers. J.Power Sources 2006 03/09;154(1):95-105.

[80]Holmstrom N, Ihonen J, Lundblad A, Lindbergh G. The influence of the gas diffusion layer on water management in polymer electrolyte fuel cells. Fuel Cells 2007;7(4):306-13.

[81]Wills J. Imaging water in PEM fuel cells. Fuel Cell Review 2005;2(5):27-29.

[82]Xiao-Dong Wang, Xin-Xin Zhang, Wei-Mon Yan, Duu-Jong Lee, Su A. Determination of the optimal active area for proton exchange membrane fuel cells with parallel, interdigitated or serpentine designs. Int J Hydrogen Energy 2009 05;34(9):3823-32.

[83]Hussaini IS, Wang C. Visualization and quantification of cathode channel flooding in PEM fuel cells. J.Power Sources 2009;187(2):444-451.

[84]Lu Z, Kandlikar SG, Rath C, Grimm M, Domigan W, White AD, et al. Water management studies in PEM fuel cells, Part II: ex situ investigation of flow maldistribution, pressure drop and two-phase flow pattern in gas channels. Int J Hydrogen Energy 2009 05;34(8):3445-56.

[85]Cheng L, Ribatski G, Thome JR. Two-phase flow patterns and flow-pattern maps: Fundamentals and applications. Appl.Mech.Rev. 2008;61(1-6):0508021-05080228.

[86]Pasaogullari U, Wang CY. Liquid water transport in gas diffusion Layer of polymer electrolyte fuel cells. J.Electrochem.Soc. 2004 03;151(3):399-406.

[87]J. S. Yi and T. V. Nguyen. The effect of the flow distributor on the performance of PEM fuel cells. Anonymous Proceeding of the First International Symposium on Proton Conducting Membrane Fuel Cells 1 Pennington, NJ, USA: Electrochem. Soc; 8 Oct. 1995; 66-75.

[88]Curtin DE, Lousenberg RD, Henry TJ, Tangeman PC, Tisack ME. Advanced materials for improved PEMFC performance and life. J.Power Sources 2004;131(1-2):41-48.

[89]J. S. Spendelow, R. Mukundan, J. R. Davey, et al. High resolution neutron radiography imaging of operating PEM fuel cells: Effect of flow configuration and gravity on water distribution. Anonymous Proton Exchange Membrane Fuel Cells 8, PEMFC - 214th ECS Meeting, October 12, 2008 - October 1716 Honolulu, HI, United states: Electrochemical Society Inc; 2008; 1345-1355.

[90]Khrapitchev AA, Stapf S, Callaghan PT. NMR visualization of displacement correlations for flow in porous media. Physical Review E (Statistical, Nonlinear, and Soft Matter Physics) 2002 11;66(5):51203-1.

[91]Bhaga D, Weber ME. Bubbles in viscous liquids: shapes, wakes and velocities. J.Fluid Mech. 1981 04;105:61-85.

[92]Harirchian T, Garimella SV. Effects of channel dimension, heat flux, and mass flux on flow boiling regimes in microchannels. Int.J.Multiphase Flow 2009 04;35(4):349-62.

[93]Bazylak A, Heinrich J, Djilali N, Sinton D. Liquid water transport between graphite paper and a solid surface. J.Power Sources 2008;185(2):1147-1153.

[94]Kumbur EC, Sharp KV, Mench MM. Liquid droplet behavior and instability in a polymer electrolyte fuel cell flow channel. J.Power Sources 2006 10/20;161(1):333-345.

[95]Tüber K, Pócza D, Hebling C. Visualization of water buildup in the cathode of a transparent PEM fuel cell. J.Power Sources 2003 11/24;124(2):403-414.

[96]Ge S, Chao-Yang Wang. Liquid water formation and transport in the PEFC anode. J.Electrochem.Soc. 2007 10;154(10):B998-B1005.

[97]Advani SG, Spernjak D, Prasad AK. Experimental investigation of liquid water formation and transport in a transparent single-serpentine PEM fuel cell. J.Power Sources 2007 07/10;170(2):334-44.

[98]Erin Kimball, Tamara Whitaker, I. G. Kevrekidis and J. B. Benziger. Drops, slugs and flooding in PEM fuel cells. Anonymous 7th Symposium Devoted to Proton Exchange Membrane Fuel Cells - 212th ECS Meeting, October 7, 2007 - October 1211 Washington, DC, United states: Electrochemical Society Inc; 2007; 725-736.

[99]Yang XG, Zhang FY, Lubawy AL, Wang CY. Visualization of liquid water transport in a PEFC. Electrochemical and Solid-State Letters 2004 11;7(11):408-11.

[100]Hakenjos A, Muenter H, Wittstadt U, Hebling C. A PEM fuel cell for combined measurement of current and temperature distribution, and flow field flooding. J.Power Sources 2004;131(1-2):213-216.

[101]Gao B, Steenhuis TS, Zevi Y, Parlange J-, Carter RN, Trabold TA. Visualization of unstable water flow in a fuel cell gas diffusion layer. J.Power Sources 2009;190(2):493-498.

[102]Ous T, Arcoumanis C. Visualisation of water droplets during the operation of PEM fuel cells. J.Power Sources 2007 11/08;173(1):137-48.

[103]Weng F, Su A, Hsu C, Lee C. Study of water-flooding behaviour in cathode channel of a transparent proton-exchange membrane fuel cell. J.Power Sources 2006 7/3;157(2):674-680.

[104]Liu Z, Mao Z, Wang C. A two dimensional partial flooding model for PEMFC. J.Power Sources 2006 8/25;158(2):1229-1239.

[105]Pletser V. Short duration microgravity experiments in physical and life sciences during parabolic flights: The first 30 ESA campaigns. Acta Astronaut. 2004;55(10):829-854.

[106]J. C. Xie, H. Lin, J. F. Zhao, W. R. Hu, A. V. Ivanov and A. Y. Belayev. Investigation on two-phase flow regimes in microgravity. Anonymous Proceedings First International Symposium on Microgravity Research and Applications in Physical Sciences and Biotechnology1 Noordwijk, Netherlands: ESA; 10-15 Sept. 2000; 63-8.

[107]Valota L, Kurwitz C, Shephard A, Best F. Microgravity flow regime data and analysis. Int.J.Multiphase Flow 2007 11;33(11):1172-85.

[108]Weislogel MM, Thomas EA, Graf JC. A novel device addressing design challenges for passive fluid phase separations aboard spacecraft. Microgravity Sci Technol 2009;21(3):257-268.

[109]S. W. K. Yuan and T. H. K. Frederking. Non-linear vapour-liquid phase separation including microgravity effects. Anonymous Space Cryogenics Workshop27 UK; 01; 27-33.

[110]Luciani S, Brutin D, Le Niliot C, Rahli O, Tadrist L. Flow boiling in minichannels under normal, hyper-, and microgravity: local heat transfer analysis using inverse methods. Journal of Heat Transfer 2008 10;130(10):101502 (13 pp.).

[111]Zhao J. Two-phase flow and pool boiling heat transfer in microgravity. Int.J.Multiphase Flow 2010;36(2):135-143.

[112]R. Balasubramaniam, V. Nayagam, M. M. Hasan and I. Khan. Analysis of heat and mass transfer during condensation over a porous substrate. Anonymous Interdisciplinary Transport Phenomena in Microgravity and Space Sciences IV Oxford, UK: Blackwell Publishing; 7-12 Aug. 2005; 459-70.

[113]Chen Y, Melvin III LS, Weislogel MM, Jenson RM, Dhuey S, Nealey PF. Design, fabrication, and testing of microporous wicking structure. Microelectronic Engineering 2008;85(5-6):1027-1030.

[114]Guo H, Wu F, Ye F, Zhao J, Wan S, Lu C, et al. Two-phase flow in anode flow field of a small direct methanol fuel cell in different gravities. Science in China, Series E: Technological Sciences 2009;52(6):1576-1582.

[115]Guo H, Zhao JF, Ye F, Wu F, Lv CP, Ma CF. Two-phase flow in fuel cells in short-term microgravity condition. Microgravity Sci Technol 2008;20(3-4):265-269.

[116]Guo H, Zhao J, Liu X, Ye F, Wan S, Ma C. Experimental study of performance of proton exchange membrane fuel cells in short-term microgravity condition. Kung Cheng Je Wu Li Hsueh Pao/Journal of Engineering Thermophysics 2009;30(8):1376-1378.

[117]Guo H, Zhao J, Lu C, Wan S, Wu F, Ye F, et al. Experimental study of fuel cells performance in short term microgravity condition. Kung Cheng Je Wu Li Hsueh Pao/Journal of Engineering Thermophysics 2008;29(5):865-867.

[118]Jianfu Z, Hang G, Fang Y, Shixin W, Minggang W, Feng W, et al. Experimental study on two-phase flow and power performance of DMFC utilizing the drop tower Beijing. Chinese Journal of Space Science 2008 01;28(1):17-21.

[119]Chen S, Wu Y. Gravity effect on water discharged in PEM fuel cell cathode. Int J Hydrogen Energy 2010 4;35(7):2888-2893.

[120]Michael Pien, Marvin Warshay, Steven Lis and Radha Jalan. PEM fuel cell with dead-ended operation. Anonymous Proton Exchange Membrane Fuel Cells 8, PEMFC - 214th ECS Meeting, October 12, 2008 - October 1716 Honolulu, HI, United states: Electrochemical Society Inc; 2008; 1377-1381.

[121]Wu Yu-hou, Chen Shi-zhong, Hong S, Yu W. Experimental study on gravity effect on performance of PEM fuel cell. Renewable Energy Reources 2007;25(2):66-9.

[122]Jay Benziger, Tamara Whitaker, Erin Kimball and I. G. Kevrekidis. Liquid water transport in PEM fuel cells. Anonymous Fuel Cell Seminar 2007, October 15, 2007 - October 1912 San Antonio, TX, United states: Electrochemical Society Inc; 2007; 67-79.

[123]Gurau V, Zawodzinski Jr. TA, Mann Jr. JA. Two-phase transport in PEM fuel cell cathodes. Journal of Fuel Cell Science and Technology 2008;5(2).

[124]Buie CR, Posner JD, Fabian T, Cha S, Kim D, Prinz FB, et al. Water management in proton exchange membrane fuel cells using integrated electroosmotic pumping. J.Power Sources 2006;161(1):191-202.

[125]Jiao K, Zhou B. Effects of electrode wettabilities on liquid water behaviours in PEM fuel cell cathode. J.Power Sources 2008 01/03;175(1):106-19.

[126]Li X, Park J. An experimental and numerical investigation on the cross flow through gas diffusion layer in a PEM fuel cell with a serpentine flow channel. J.Power Sources 2007 01/01;163(2):853-63.

[127]Hu M, Zhu X, Gu A. Simulation of the internal transport phenomena for PEM fuel cells with different modes of flow. Chin.J.Chem.Eng. 2004;12(1):14-26.

[128]J. M. Hyman. Numerical methods for tracking interfaces. Anonymous Proceedings of the Third Annual International Conference of the Centre for Nonlinear Studies12D Netherlands; 07; 396-407.

[129]G. Cerne, S. Petelin and I. Tiselj. Shape and stability of the bubble moving through the viscid incompressible fluid. Anonymous Proceedings of International Conference on Nuclear Energy in Central Europe '98 Ljubljana, Slovenia: Nucl. Soc. Slovenia; 7-10 Sept. 1998; 211-18.

[130]Van SA, Deen NG, Kuipers JAM. Numerical simulation of gas bubbles behaviour using a three-dimensional volume of fluid method. Chemical Engineering Science 2005;60(11):2999-3011.

[131]F. Lai, C. Sanchez and M. Sanchez. Numerical Simulation of Thermocapillary Pumping Using the Volume of Fluid Method. Anonymous Oklahoma Science86 Oklahoma; 2006; 75-83.

[132]Theodorakakos A, Ous T, Gavaises M, Nouri JM, Nikolopoulos N, Yanagihara H. Dynamics of water droplets detached from porous surfaces of relevance to PEM fuel cells. J.Colloid Interface Sci. 2006;300(2):673-687.

[133]Horvath A, Jordan C, Lukasser M, Kuttner C, Mararuk A, Harasek M. CFD Simulation of Bubble Columes using the VOF method:Comparision of commercial and Open Source Solvers with and Experiment. Chemical Engineering Transactions 2009;18(1):605-610.

[134]Fei K, Chen TS, Hong CW. Direct methanol fuel cell bubble transport simulations via thermal lattice Boltzmann and volume of fluid methods. J.Power Sources 2010;195(7):1940-1945.

[135]Du W, Zhang L, Bi XT, Wilkinson D, Stumper J, Wang H. Two-dimensional simulations of gas-liquid two-phase flow in mini channels of PEM fuel cell flow field. International Journal of Chemical Reactor Engineering 2010;8.

[136]Zhu X, Sui PC, Djilali N. Dynamic behaviour of liquid water emerging from a GDL pore into a PEMFC gas flow channel. J.Power Sources 2007;172(1):287-295.

[137]Zhu X, Liao Q, Sui PC, Djilali N. Numerical investigation of water droplet dynamics in a low-temperature fuel cell microchannel: effect of channel geometry. J.Power Sources 2010 02/01;195(3):801-12.

[138]Zhou B, Quan P, Sobiesiak A, Liu Z. Water behavior in serpentine micro-channel for proton exchange membrane fuel cell cathode. J.Power Sources 2005 12/01;152:131-45.

[139]Quan P, Ming-Chia Lai. Numerical study of water management in the air flow channel of a PEM fuel cell cathode. J.Power Sources 2007 01/10;164(1):222-37.

[140]V. R. Dushin, O. E. Ivashnyov, V. F. Nikitin, et al. Viscous fingering in porous media. Anonymous 58th International Astronautical Congress 2007, September 24, 2007 - September 281 Hyderabad, India: International Astronautical Federation, IAF; 2007; 438-450.

[141]Dushin V, Nikitin V, Philippov Y, Smirnov N. Two phase flows in porous media under microgravity conditions. Microgravity Sci Technol 2008;20(3-4):155-160.

[142]Scovazzo P, Illangasekare TH, Hoehn A, Todd P. Modeling of two-phase flow in membranes and porous media in microgravity as applied to plant irrigation in space. Water Resour.Res. 2001;37(5):1231-1243.

[143]Guo B, Holder DW, Carter L. Distribution of flowing fluids in a confined porous medium under microgravity conditions. Phys.Fluids 2004 08;16(8):3045-50.

[144]Lakehal D, Narayanan C. Two-phase flow and heat transfer in microtubes under normal and microgravity conditions. Multiphase Science and Technology 2009;21(4):279-295.

[145]Vesna Stanic, Robert Wynne, Paul Borthwick and Mark Hoberecht. Gravitational effect on PEM fuel cell water management. Anonymous 3rd International Energy Conversion Engineering Conference, August 15, 2005 - August 183 San Francisco, CA, United states: American Institute of Aeronautics and Astronautics Inc; 2005; 1424-1435.

[146]Djilali N. Computational modelling of polymer electrolyte membrane (PEM) fuel cells: Challenges and opportunities. Energy 2007 04;32(4):269-80.

[147]Bernardi DM, Verbrugge MW. Mathematical model of a gas diffusion electrode bonded to a polymer electrolyte. AICHE J. 1991;37(8):1151-1163.

[148]Bernardi DM, Verbrugge MW. A mathematical model of the solid-polymer-electrolyte fuel cell. J.Electrochem.Soc. 1992;139(9):2477-91.

[149]Wang ZH, Wang CY, Chen KS. Two-phase flow and transport in the air cathode of proton exchange membrane fuel cells. J.Power Sources 2001 02/15;94(1):40-50.

[150]T. Berning, D. M. Lu and N. Djilali. Three-dimensional computational analysis of transport phenomena in a PEM fuel cell. Anonymous 7th Grove Fuel Cell Symposium, Grove VII, September 11, 2001 - September 13106 London, United kingdom: Elsevier; 2001; 284-294.

[151]Le AD, Zhou B. A general model of proton exchange membrane fuel cell. J.Power Sources 2008;182(1):197-222.

[152]Anh DL, Zhou B. A general model of proton exchange membrane fuel cell. J.Power Sources 2008 07/15;182(1):197-222.

[153]Girlich D. Open Poer Metal Foam. 2008; Available at: 1.

[154]Wang J. RETICULATED VITREOUS CARBON - A NEW VERSATILE ELECTRODE MATERIAL. Electrochim.Acta 1981;26(12):1721-1726.

[155]Knippenberg WF, Lersmacher B. CARBON FOAM. Philips Technical Review 1976;36(4):93-103.

[156]Friedrich JM, Ponce-de-Leon C, Reade GW, Walsh FC. Reticulated vitreous carbon as an electrode material. J Electroanal Chem 2004;561(1-2):203-217.

[157]Donald E. Floyd II, Mark J. Topolski and Jeff Darabi. Design and evaluation of copper metal foams in cold plates. Anonymous 2006 ASME International Mechanical Engineering Congress and

Exposition, IMECE2006, November 5, 2006 - November 10 Chicago, IL, United states: American Society of Mechanical Engineers; 2006; .

[158]E. Gyenge, J. Jung and B. Mahato. Electroplated reticulated vitreous carbon current collectors for lead-acid batteries: opportunities and challenges. Anonymous LABAT'02113 Switzerland: Elsevier; 01/27; 388-95.

[159]ERG Materials and Aerospace Corp. Material Specific Properties of Metal Foam. US,2009. See Also: http://www.ergaerospace.com/. Accessed July 2009.

[160]A. Braun, M. Bartsch, F. Geiger, et al. A study on oxidized glassy carbon sheets for bipolar supercapacitor electrodes. Anonymous Symposium Warrendale, PA, USA: Mater. Res. Soc; 5-8 April 1999; 369-80.

[161]Scott K, Cotlarciuc I, Hall D, Lakeman JB, Browning D. Power from marine sediment fuel cells: The influence of anode material. J.Appl.Electrochem. 2008;38(9):1313-1319.

[162]Cheng TT, Gyenge EL. Direct methanol fuel cells with reticulated vitreous carbon, uncompressed graphite felt and Ti mesh anodes. J.Appl.Electrochem. 2008;38(1):51-62.

[163]Shankar Krishnan, Suresh V. Garimella and Jayathi Y. Murthy. Simulation of thermal transport in open-cell metal foams: Effect of periodic unit cell structure. Anonymous 2006 ASME International Mechanical Engineering Congress and Exposition, IMECE2006, November 5, 2006 - November 10 Chicago, IL, United states: American Society of Mechanical Engineers; 2006; .

[164]Blaedel WJ, Wang J. FLOW ELECTROLYSIS ON A RETICULATED VITREOUS CARBON ELECTRODE. Anal.Chem. 1979;51(7):799-802.

[165]Krishnan S, Murthy JY, Garimella SV. A two-temperature model for solid-liquid phase change in metal foams. Journal of Heat Transfer 2005;127(9):995-1004.

[166]Davidson JH, Kulacki FA, Savela D. Natural convection in water-saturated reticulated vitreous carbon foam. Int.J.Heat Mass Transfer 2009;52(19-20):4479-4483.

[167]Ozmat B, Leyda B, Benson B. Thermal applications of open-cell metal foams. Mater.Manuf.Process. 2004;19(5):839-62.

[168]Grigoriev SA, Millet P, Volobuev SA, Fateev VN. Optimization of porous current collectors for PEM water electrolysers. Int J Hydrogen Energy 2009 06;34(11):4968-73.

[169]El-Deab M, Saleh MM. Electrocatalytic production of hydrogen on reticulated vitreous carbon. Int J Hydrogen Energy 2003 11;28(11):1199-206.

[170]Ultramet. Refractory Open-Cell Foams. US,2009. See Also: http://www.ultramet.com/refractoryopencells.html. Accessed July 2009.

[171]Jung S. Yi, Jonathan Puhalski and Constance King. Porous flow plate with interdigitated flow fields for PEM fuel cells. Anonymous Proton Conducting Membrane Fuel Cells III - Proceedings of the International Symposium, October 21, 2002 - October 23PV 2002-31 Salt Lake City, UT, United states: Electrochemical Society Inc; 2002; 174-182.

[172]Litster S, Santiago JG. Dry gas operation of proton exchange membrane fuel cells with parallel channels: Non-porous versus porous plates. J.Power Sources 2009;188(1):82-88.

[173]Kumar A, Reddy RG. Polymer Electrolyte Membrane Fuel Cell with Metal Foam in the Gas Flow-Field of Bipolar/End Plates. Journal of New Materials for Electrochemical Systems 2003;6(4):231-236.

[174]Chen J. Experimental study on the two phase flow behavior in PEM fuel cell parallel channels with porous media inserts. J.Power Sources 2010;195(4):1122-1129.

[175]Shankar Krishnan, Jayathi Y. Murthy and Suresh V. Garimella. Direct simulation of transport in open-cell metal foam. Anonymous 128: American Society of Mechanical Engineers793-799.

[176]Lu TJ, Stone HA, Ashby MF. Heat transfer in open-cell metal foams. Acta Materialia 1998 06/12;46(10):3619-35.

[177]Du Plessis P, Montillet A, Comiti J, Legrand J. Pressure drop prediction for flow through high porosity metallic foams. Chemical Engineering Science 1994;49(21):3545-3553.

[178]Fourie JG, Du Plessis JP. Pressure drop modelling in cellular metallic foams. Chemical Engineering Science 2002;57(14):2781-2789.

[179]Boomsma K, Poulikakos D, Ventikos Y. Simulations of flow through open cell metal foams using an idealized periodic cell structure. Int J Heat Fluid Flow 2003;24(6):825-834.

[180]Lemlich R. A theory for the limiting conductivity of polyhedral foam at low density. J.Colloid Interface Sci. 1978 3/15;64(1):107-110.

[181]Dharmasena KP, Wadley HNG. Electrical conductivity of open-cell metal foams. J.Mater.Res. 2002;17(3):625-631.

[182]Ma X, Peyton AJ, Zhao YY. Measurement of the electrical conductivity of open-celled aluminium foam using non-contact eddy current techniques. NDT&E International 2005 07;38(5):359-67.

[183]Ashby MF, Evans AG, Fleck NA, Gibson LJ, Hutchinson JW, Wadley HNG. Metal Foams: A design Guide. 1st ed. Massachusetts: Butterworth-Heinemann; 2000.

[184]Medraj M, Baril E, Loya V, Lefebvre L. The effect of microstructure on the permeability of metallic foams. J.Mater.Sci. 2007;42(12):4372-4383.

[185]Dukhan N. Correlations for the pressure drop for flow through metal foam. Exp.Fluids 2006 10;41(4):665-72.

[186]Wilson L, Narasimhan A, Venkateshan SP. Permeability and form coefficient measurement of porous inserts with non-darcy model using non-plug flow experiments. 2006; . Accessed 3, 128.

[187]Stone HA, Evans AG, Bastawros AF. Evaluation of cellular metal heat transfer media. 1998; , MECH 325.

[188]Medraj M, Baril E, Loya V, Lefebvre L-. The effect of microstructure on the permeability of metallic foams. 2007; . Accessed 12, 42.

[189]David P. Haack, Kenneth R. Butcher, T. Kim and T. J. Lu. Novel Lightweight Metal Foam Heat Exchangers. Anonymous 2001 ASME International Mechanical Engineering Congress and

Exposition, November 11, 2001 - November 166 New York, NY, United states: American Society of Mechanical Engineers; 2001; 141-147.

[190]Dukhan N, Minjeur II CA. A two-permeability approach for assessing flow properties in metal foam. 2010:1-8.

[191]Cavallini A, Mancin S, Rossetto L, Zilio C. AIR flow in aluminum foam: Heat transfer and pressure drops measurements. Exp.Heat Transfer 2010;23(1):94-105.

[192]Aachen University. Hydrogen & Fuel cells in industrial & Commercial Stationary Applications. Germany,2009. See Also: http://www.ika.rwth-aachen.de/r2h/index.php/Hydrogen_and_Fuel_Cells_in_Industrial_and_Commercial_Stationary_Applications. Accessed Aug 2009.

[193]Fluent Inc. Fluent Manual & Tutorials. U.S.,2010. See Also: http://my.fit.edu/itresources/manuals/fluent6.3/help/. Accessed Aug 2010

[194]Grace JR. Shapes and velocities of bubbles rising in infinite liquids. Transactions of the Institution of Chemical Engineers 1973 04;51(2):116-20.

[195]Dohle H, Jung R, Kimiaie N, Mergel J, Muller M. Interaction between the diffusion layer and the flow field of polymer electrolyte fuel cells - Experiments and simulation studies. J.Power Sources 2003;124(2):371-384.

[196]Shan-Hai Ge, Xu-Guang Li, Hsing I-. Water management in PEMFCs using absorbent Wicks. J.Electrochem.Soc. 2004;151(9):523-8.

[197]Ge S, Li X, Hsing I-. Internally humidified polymer electrolyte fuel cells using water absorbing sponge. Electrochim.Acta 2005;50(9):1909-1916.

[198]Strickland DG, Litster S, Santiago JG. Current distribution in polymer electrolyte membrane fuel cell with active water management. J.Power Sources 2007 11/22;174(1):272-81.

[199]Strickland DG, Santiago JG. In situ-polymerized wicks for passive water management in proton exchange membrane fuel cells. J.Power Sources 2010;195(6):1667-1675.

[200]I.E.A. Hydrogen & Fuel Cells:Review of National R&D Programs. 2004; Available at: 4, ISBN 92-64-108-831.

[201]Elsevier Inc. Journal Archive Data Base. U.S.,2010. See Also: www.engineeringvillage.com. Accessed Sept 2010.

Appendices

Appendix A

Research in Hydrogen & Fuel Cells

There are six different technologies and more than twenty countries around the world undertaking intensive research into fuel cells. In the last decade, a research and industry community in the field of hydrogen energy and fuel cell technologies has been formed across the EU. Some countries within the EU also have their own targets. A detailed source of funding for institutions and governments can be found in the international energy agency's review of national R&D programs [200].
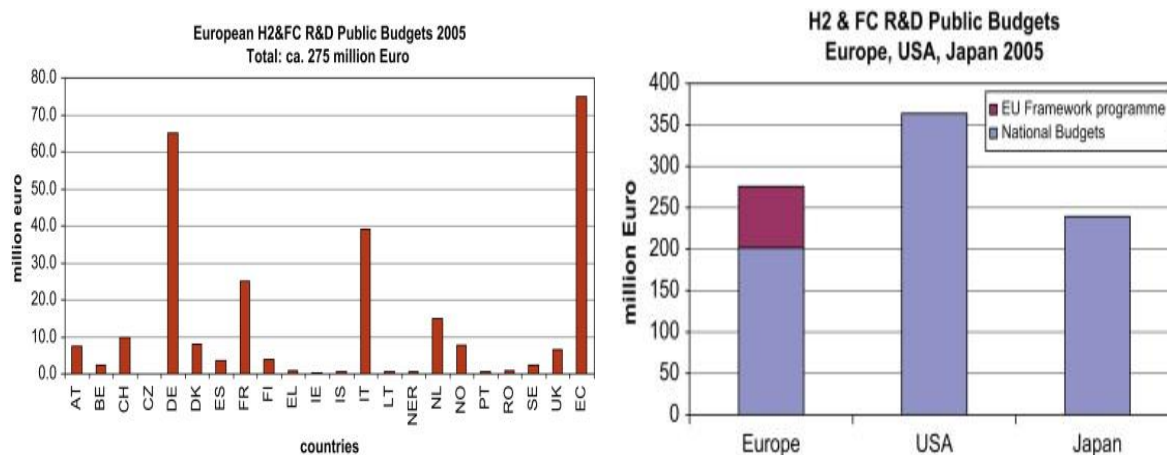
Figure 295 (a) Hydrogen & fuel cell R&D public budgets in Europe (b) Comparison of hydrogen & fuel cell R&D public budgets Between Europe, America and Japan [25]**.**

In pursuit of the long-term goals, Snapshot 2020 has been set by the European Hydrogen & Fuel Cell Technology Platform. 2020 has been chosen because it encourages challenging targets, whilst helping to test for practicality and feasibility. SET-Plan & Fuel Cells and Hydrogen Joint Technology Initiative (FCH JTI) is the initiative proposing a public-private partnership for research to development in fuel cell and hydrogen technologies. The aim of the International Energy Agency (IEA) Advanced Fuel Cells Program and the International Partnership for the Hydrogen Economy (IPHE) are to advance the state of understanding of all contracting parties in the field of advanced fuel cells.

Figure 296 The main players known to be active in industrial and commercial applications of hydrogen & fuel cell systems [192]**.**

Internationally there is a whole range of universities and research institutions that would be considered key players in the fuel cell technologies. However, only a limited number of companies successfully exploit niche markets and, as yet, only to a very limited extent. Fuel Cell systems require much further development and have only made a tiny impression in the dominance of existing energy generation technologies. One of the current leaders in developing these fuel cells is Ballard Power Systems, a Canadian company, which has recently formed an alliance with DaimlerChrysler and Ford to develop the next generation of fuel cell powered vehicles. Other companies are also developing their own PEM fuel cells including United Technologies, Siemens, General Motors, Toyota, Mazda, Toshiba and Heliocentris, while Johnson-Matthey have been very much involved with the development of catalysts and other components. An overview of some companies to be developing fuel cell systems for commercial and industrial applications is presented in Figure 296.

Level of research in PEM fuel cells

To view and try to analyse the quantity of research in PEM fuel cells the Compendex database on the web based information service Engineering Village was used [201]. Engineering Village offers a data base of a wide range of quality scientific and engineering publications, from the most popular journals around the world, for specialists, professionals and researchers working in the applied science and engineering fields.

Using different inclusion and exclusion parameters in the advanced search engine in the database, publications in a specific field can be identified and sorted very effectively. It can, on the onset, seem a crude approach to reviewing PEM fuel cell research but the method is very effective for a macro scale view of current and past research and it is beneficial to view research trends. The following

results were identified from the database which had 'proton exchange membrane fuel cell' or 'PEM fuel cell' in their abstracts, titles or subject fields and then further refined to give more detailed results. This data was accessed in November 2010 and ranges from 1995 to 2010 inclusive.
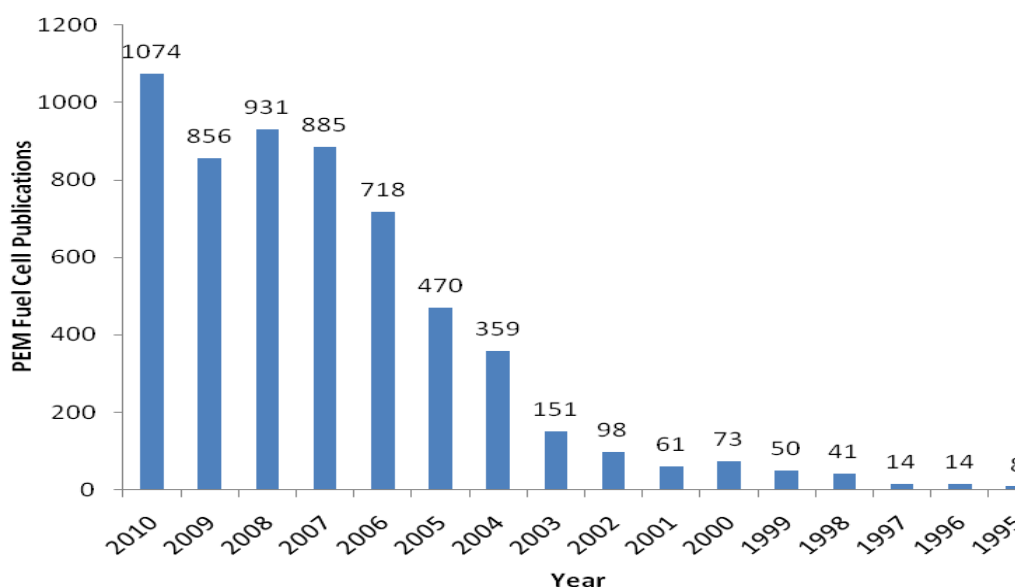
Figure 297 PEM fuel cell publications 1995 to 2010.

It is clear that there has been a recent surge in the interest in general PEM fuel cell research in the last decade, as shown in Figure 297. Before 1995 PEM fuel cell research is sparse and has not got a foot hold in the scientific or research community. However, from the early '00's research has been intensified and has grown most years since, to over one thousand publications in 2010.

Table 16 Publications per country.

Country	2010	2009	2008	2007	2006	2005	2004	2003	2002	2001	2000	1999	1998	95-'97
U.S.	266	171	186	212	170	115	107	57	38	13	31	26	13	12
U.K.	39	27	21	26	10	13	5	6	4	4	2	2	0	3
China	225	144	154	164	165	79	59	16	5	2	0	2	0	1
Korea , Rep. of	100	85	89	50	44	17	34	8	5	3	3	1	2	0
Canada	93	70	91	68	69	44	29	14	7	8	12	4	6	4
Japan	83	59	73	90	46	32	21	6	6	5	2	1	2	2
Germany	39	55	50	38	40	31	25	8	3	12	11	7	11	4
Spain	31	41	16	25	11	14	4	2	1	1	2	0	0	0
Italy	41	35	47	37	19	10	10	5	3	4	0	0	0	0
France	64	33	51	35	30	19	14	1	1	0	3	1	7	2
Taiwan	58	52	66	58	50	25	10	6	2	0	0	0	0	0
India	32	26	29	29	10	7	7	3	0	0	0	1	0	0

The database can be categorised by country and this is presented in Table 16 & Figure 298. The U.S. has being ahead with most publications per year since the mid '90's but Germany, Canada and the U.K. consistently produce many publications per year.
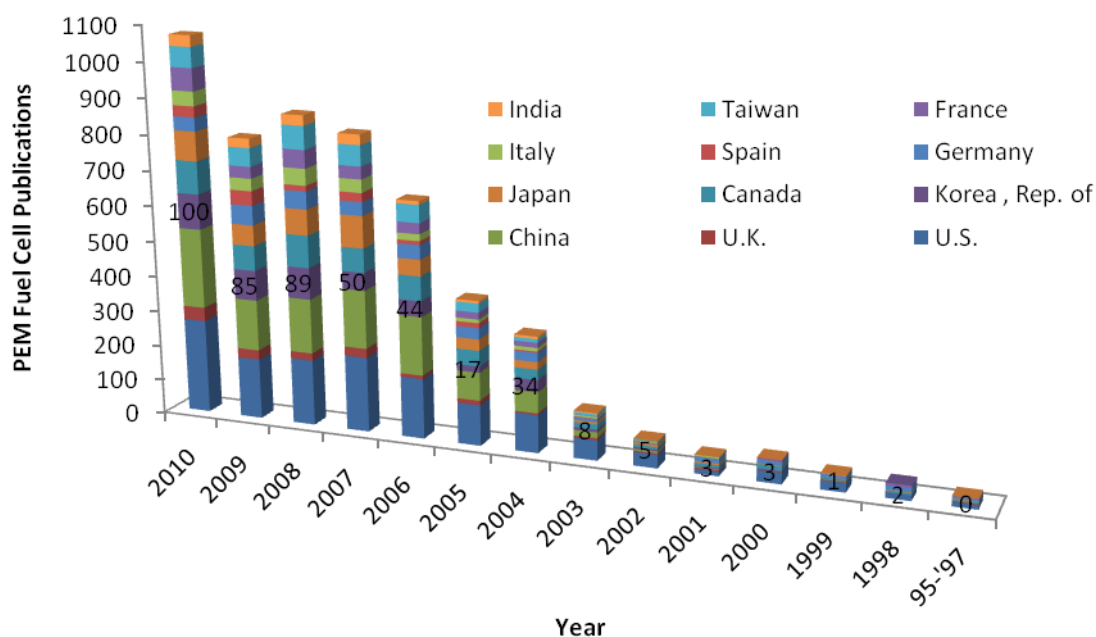
Figure 298 Break down of the search results in to the countries of origin of the major contributors.

It is evident, for example with Taiwan, Japan, Spain, Italy or China with the sudden surge of research publications, that research programs must have been created in the early '00's to promote PEM fuel cell research in these countries. The Republic of Korea's publications are highlighted in Figure 298. It is clear from this plot that the Republic of Korea seem to be continually expanding their research. This country had minimal publications up until the early '00's and in 2010 their publications on PEM fuel cells has increased to about one hundred. This can show that a small country can have a huge impact in any field if it sets its focus in that direction.

Table 17 Breakdown of PEM fuel cell research.

Keyword	2010	2009	2008	2007	2006	2005	2004	2003	2002	2001	2000	1999	1998	95-'97
Electrolyte	453	414	375	334	226	169	139	61	31	27	34	16	17	9
Electro-catalyst	324	271	270	302	236	152	130	52	38	20	26	15	16	10
Gas Diffusion Layer	159	98	126	109	105	37	35	9	4	4	3	3	4	2
Modelling & Simulation	118	122	123	121	110	75	57	17	7	4	8	2	3	4
Water Management	65	64	85	50	53	24	23	8	7	5	4	0	1	2
Flow Plate	30	29	29	26	25	15	19	8	2	2	3	2	1	1

In relation to the current focus of this thesis keywords were selected and searched within the publication. These keywords and the number of publications of each per year are listed in Table 17 and Figure 299. There is a slight over estimation of the quantity of papers published per year as compared to Figure 297 because a single publication could include several topics such as electrolyte and electro catalyst, for example. From the simple over view it is clear that research has gained momentum in the last decade with most publication or research focusing in the electrolyte and electro catalyst areas. The area of interest in relation to this thesis work is in flow plate design, water management and modelling and simulation. There is less publications in these areas, even though they encompass vast fields of the design of PEM fuel cells, compared to other areas.
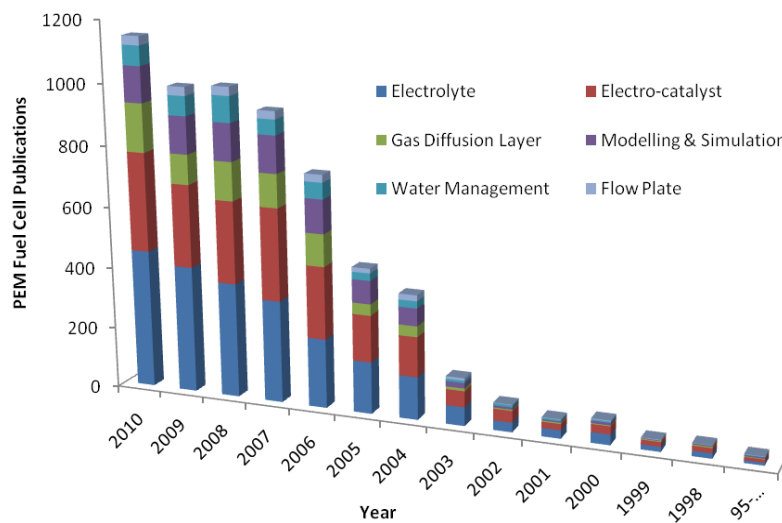
Figure 299 Breakdown of PEM fuel cell research.

Appendix B

Planar PEM Fuel Cell Assembly/Disassembly Procedure

Planer PEM fuel cell assembly

The following section describes the assembly of the PEM fuel cell.

Figure 300 Assembled PEM fuel cell.

Note: It is recommended that the stack is disassembled in an environment at room temperature and with 80% humidity. (The Nafion membrane can dry out and shrink, this may damage the MEA. The MEA may be placed or stored in a zip locked bag with a damp piece of cotton.)

The backing plate is placed horizontal and in a flat position, sitting on blocks to accommodate the in/out pipe fittings.
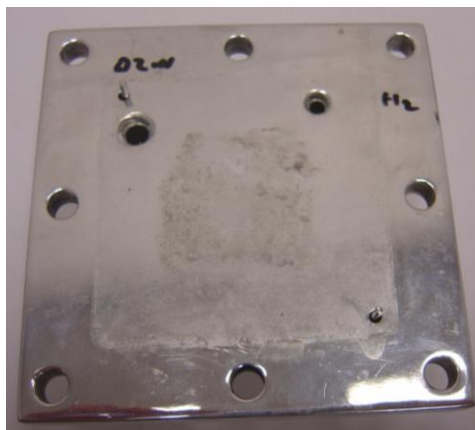
Figure 301 Backing plate placed horizontal.

The gasket (which is needed to separate the current collector from the metal backing plate) is placed onto the plate. The holes of the gasket correspond to the holes of the backing plate.

Figure 302 Gasket placed on backing plate.

The current collector (metallic plate which collects electrons from the carbon flow plates) is placed onto the gasket. The holes of the current collector correspond to the holes of the gasket and backing plate.
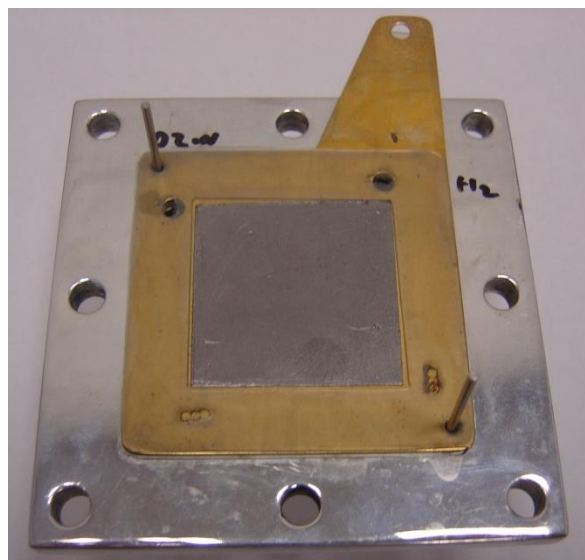
Figure 303 Current collector placed into position.

Location pins are placed into the backing plate as shown in Figure 303. These pins are vital for correct alignment of all the layers of the planner PEM fuel cell. These pins also help with orientation of the parts for assembly. The pins aid in a fool proof method or Poke okay way of the assembly process.

Note: The current collector has an inner square section (the same size as the flow plate) made of a soft carbon conductive material. The plate aids with electrical contact from the flow plate to the current collector. A gasket surrounds the layer.
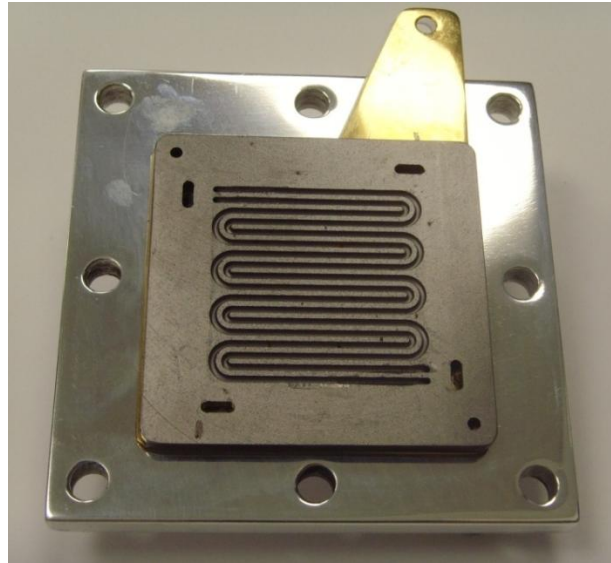
Figure 304 Flow plate placed into position.

The first flow plate is aligned and placed on the previous parts. The air and hydrogen holes are ensured to be free from blockages. The channels of the flow plate are cleared of water or dirt.

The next component placed into position is the membrane electrode assembly (MEA). The gas diffusion layers (GDL) are placed on to each side of the MEA and slots into rubber gaskets each side of the MEA. The GDL can also come attached to the MEA depending on the supplier of the components.

(a)

(b)

Figure 305 Gas diffusion layer (GDL)

(a)

(b)
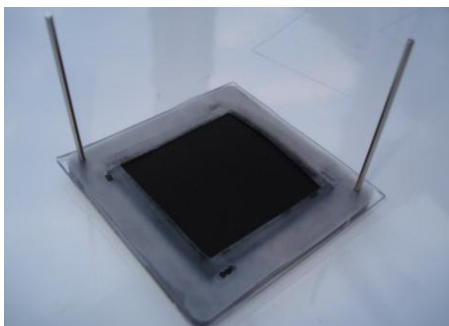
Figure 306 (a) MEA (b) Gasket.
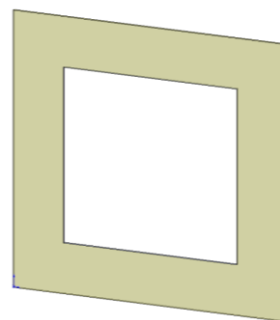
The MEA with the GDL's attached are orientated correctly and placed onto the flow plate. The cathode side, if indicated on the MEA faces the oxygen/air flow plate (Cathode to oxygen / Anode to hydrogen). The air and hydrogen holes are ensured to be free from blockages. The channels of the flow plate are cleared of water or dirt.
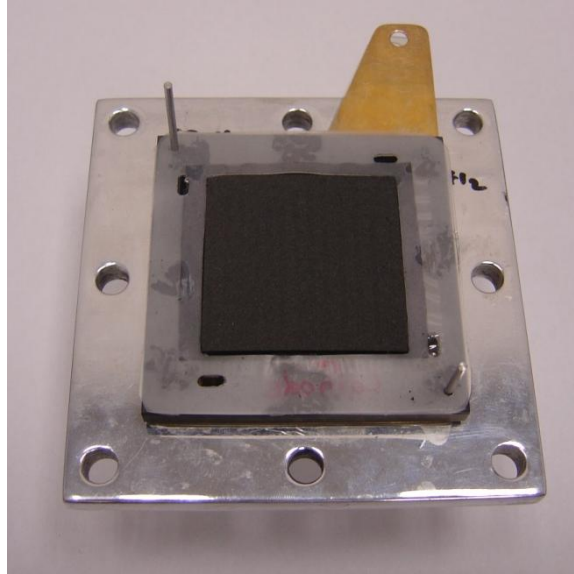
Figure 307 MEA positioned correctly.

Next the second flow plate is placed onto the MEA, channels towards the MEA and the second current collector is placed onto the flow plate.

(a)   (b)
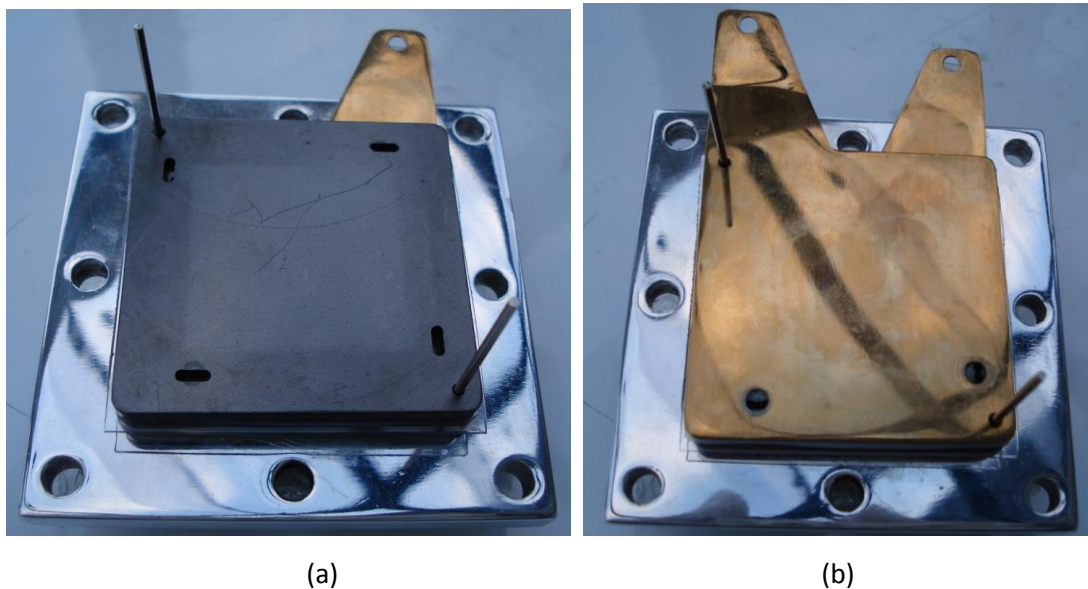
Figure 308 Flow plate (a) and current collector (b) are positioned.

The gasket is placed on the current collector, held in place by the pins. Bolts may be placed into the bottom backing plate. The air and hydrogen holes are ensured to be free from blockages.
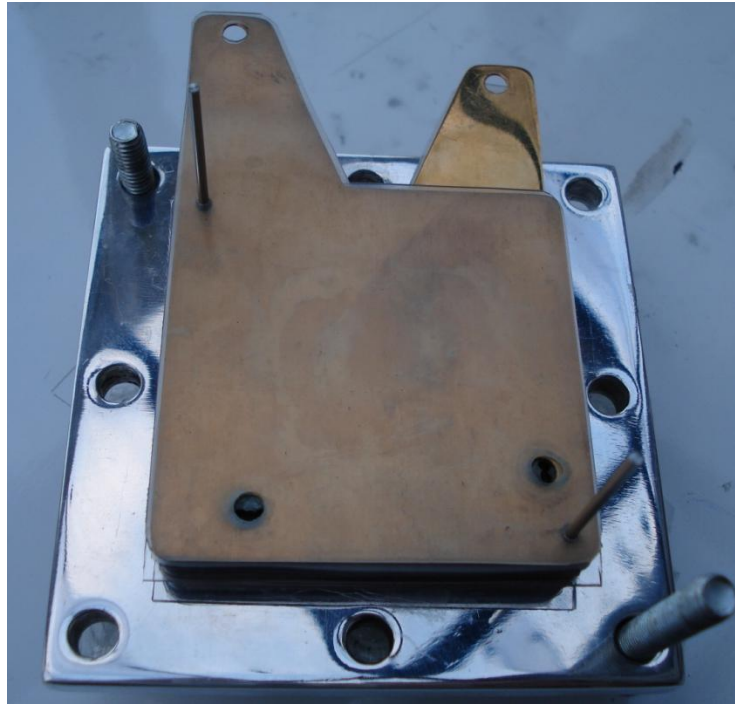
Figure 309 The final gasket is placed into position.

The backing plate is placed onto the rest of the components and aligned with the pins. The washers and nuts are placed onto the bolts. The bolts are tightened alternating and evenly to give an even spread of force over the fuel cell. The bolts are torque to 4Nm. Finally, the alignment/location pins are removed from the assembly. The pins may cause shorting within the cell if they were left in. For reassembly of the stack put back the removed components of the stack in the reverse sequence.

(a)
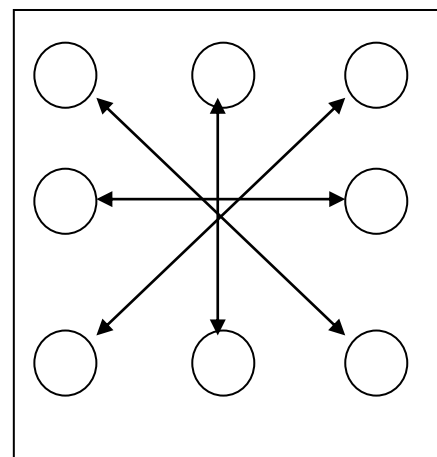
(b)

Figure 310 (a) Backing plate secured into position (b) Bolts tightened alternating.

Figure 311 Assembled PEM fuel cell.

A leak test can be performed to ensure the PEM fuel cell is sealed correctly.

- Seal the oxygen/air inlet and hydrogen outlet.

- Connect a tube to the oxygen / air outlet and put it inside a glass with water.

- Feed pure nitrogen or inert gas to the hydrogen inlet with a pressure of one bar.

- No bubbles should come out from the oxygen outlet inside the glass of water.

- If bubbles appear the stack is not tightened correctly or the MEA is punctured.

- The cell should not be run if the MEA is punctured.

Planer PEM fuel cell disassembly

Note: It is recommended that the stack is disassembled in an environment at room temperature and with 80% humidity. (The nafion membrane can dry out and shrink, this may damage the MEA. The MEA may be placed or stored in a zip locked bag with a damp piece of cotton.)

After disconnecting the fuel cell from the gases follow the procedure below:

- Pass pure humidified nitrogen (or inert gas) at a flow rate of 1-3l/min into both hydrogen and oxygen/air channels for about 15 minutes.

- To avoid short circuits test the voltage on the current collectors with a volt meter. The volt meter should read mV. If it reads higher repeat the previous step.

- Place the guide pins into the location pin holes.

- Start gradually loosening the bolts and nuts. When one bolt is being loosened, loosen the opposite bolt as shown in Figure 310.

- The gasket or graphite foil may become stuck to the current collector. If this happens it is recommended not to remove it from the current collector.

- All of the above should be done extremely carefully and slowly in order to avoid damaging the MEA.

- Do not touch the black catalyst layer.
- Immediately after removing the MEA from the stack put it inside a plastic zip-lock bag together with a small wet cotton gause.
- The electrodes on the MEA are pre-treated to handle the corresponding gases; incorrect gas supply may cause irreversible damage to the stack.

PEM Fuel Cell Assembly/Disassembly Procedure with Open Pore Cellular foam Flow plates

The following section describes the assembly of the PEM fuel cell.

The primary difference with the planer PEM fuel cell with normal flow plates and the PEM fuel cell with open pore cellular foam flow plates is the need use of a housing as shown in Figure 312. The housing incorporates the inlet and outlet pipes, the conductive current collector and the thermocouples. The particular open pore cellular foam flow plates is placed inside the housing and bolts are placed through the housing as shown in Figure 313. A gasket is then placed into position as shown in Figure 313.
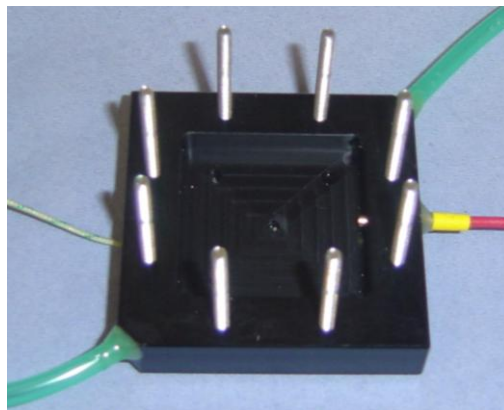
Figure 312 Housing of PEM fuel cell with open pore cellular foam flow plates.
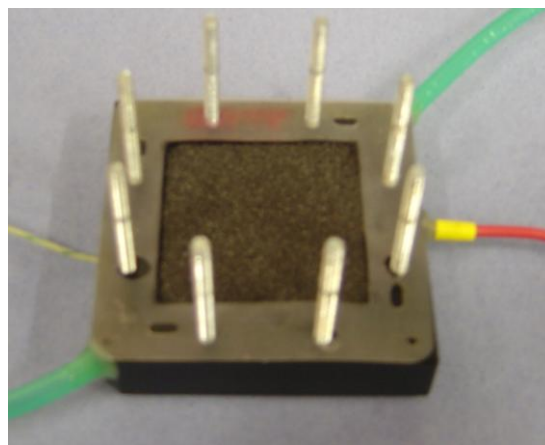
Figure 313 Housing with open pore cellular foam flow plate, bolts and gasket in position.

The MEA is then assembled as described with the planer PEM fuel cell. It is noted that the same safety and precautionary measures are employed to the storage, handling and installation of the MEA as with the planer PEM fuel cell. The MEA is positioned onto the housing as shown in Figure 314.
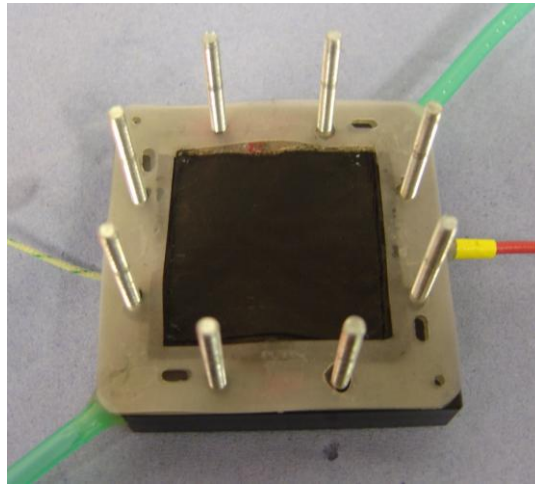
Figure 314 Housing with bolts and gasket in position.

A second gasket is then placed onto the MEA as shown in Figure 314.

A second open pore cellular foam flow plate is placed into a second housing. The second housing is then placed onto the bolts of the first housing as shown in Figure 315. The MEA and gasket positions are checked and both housings are closed. Nuts are placed on the bolts and they are tightened.
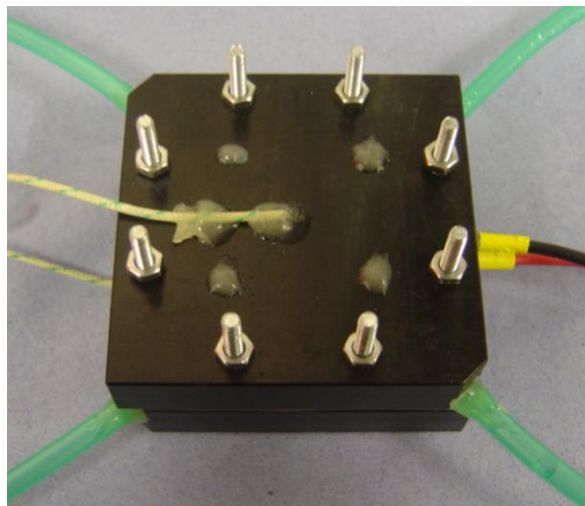
Figure 315 Assembled PEM fuel cell with open pore cellular foam flow plates.
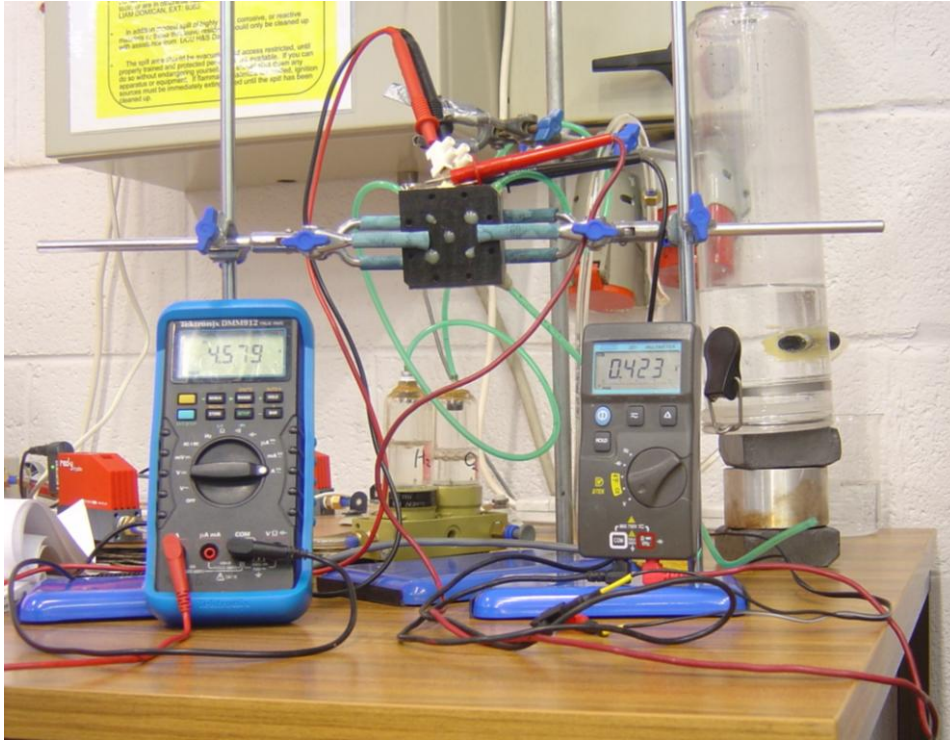
Figure 316 Operational PEM fuel cell with open pore cellular foam flow plates.

It is noted that the same safety and precautionary measures are employed to the disassembly procedure of the PEM fuel cell with open pore cellular foam flow plates as with the planer PEM fuel cell.

To disassemble the reverse of the assembly procedure is followed.

Appendix C

PEM Fuel Cell DAQ System

LabView is programmed with set of icons that represents controls and functions, available in the menu of the software. Such a programming is called visual programming. The user interface, which is called a Virtual Instrument (VI), consists of two parts, a front panel and a diagram. This is similar to that of an instrument where a front panel is used for an input, output controls, and to display the data whereas the circuit resides on the circuit board. Similarly you can bring the buttons, indicators and graphing and display functions on the front panel.

When Data Acquisition (DAQ) is performed, the software needs to know the following information:

- Device number
- Channel
- Sampling rate

This information is changed using the DAQ assist menu as shown in Figure 317.
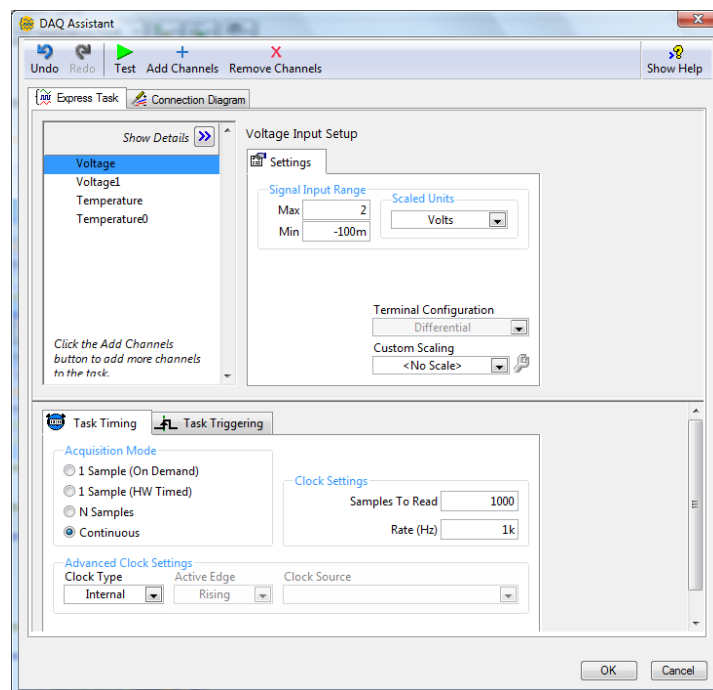
Figure 317 DAQ assist tool.

Often LabView is used to perform system simulations, since it contains many commonly used filter, digital signal processing, and statistical functions. LabView compiles almost as fast as C or Mat lab and therefore one can perform complete simulation within a VI. In addition to data input, output Lab View can access serial ports, parallel ports and GPIB cards to read data from instruments that have a GPIB interface.

The DAQ unit supplied by National Instruments has the ability to capture analogue and digital inputs and outputs. The DAQ unit is plugged into the computer via a USB cable. This both powers the unit and carries data to and from the computer.
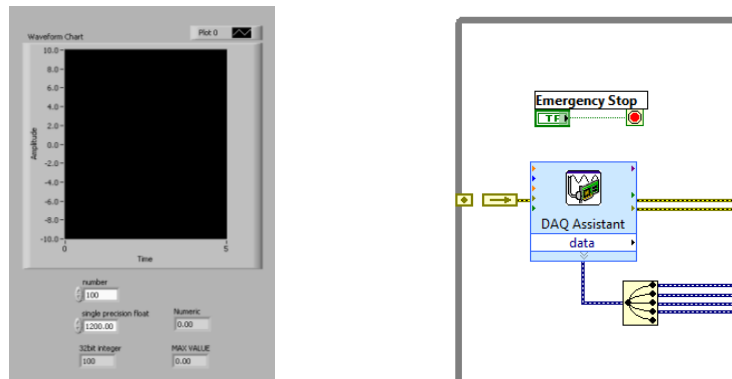
Figure 318 Initial interface Screen of data capture program.

Figure 318 shows the first VI completed in LabView. The tutorials assisted in the construction of this initial VI and the lab view help assisted in the knowledge of the specific channels and sample rate of the signal. A six volt input was used with a 50Ω potentiometer connected to it. The input was see on the graph of the control panel and when the resistance of the potentiometer was chanced the signal in the graph would rise or fall accordingly. Additional functions were added to give max and min values of the analogue input.

For the PEM fuel cell test system LabView is used to control the flow of hydrogen and oxygen and to obtain the current, voltage and temperature produced by the cell.

Figure shows the electronic setup needed to capture voltage and current values from the fuel cell. A rheostat is used to act as a load for the test fuel cell. The rheostat has a maximum resistance of 12.6 Ω and is rated at 50 watts.
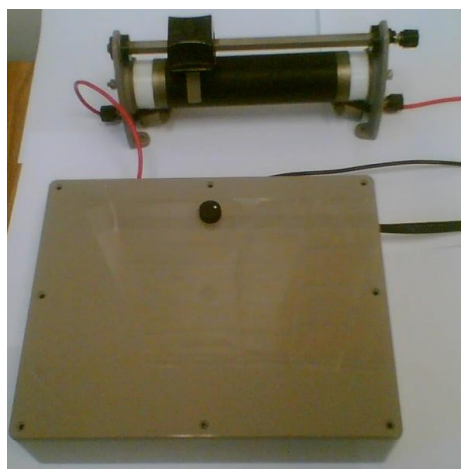
Figure 319 Experimental Setup of Fuel Cell testing apparatus.

The voltage output from the fuel cell is hardwired to the DAQ unit. The current was initially measured directly by the DAQ unit however this proved inconsistent and anomalies were noticed. Finally current was measure by measuring a voltage drop. These results were verified by an amp meter. The temperature measurements were taken using thermocouples and these were wired directly to the DAQ unit. Calibration equations were designed for the thermocouples in the software to ensure a correct scale.

Figure   shows the voltage input program that was designed to capture the voltage from the PEM fuel cell. The captured signal is filtered and values are recorded. The software then sends all the data to an excel file where later post processing can be completed.
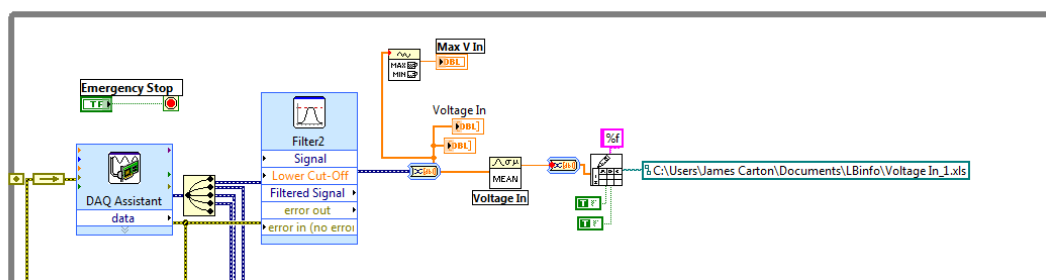
Figure 320 User interface Screen of data capture program.

Figure 321 shows the complete Lab View user screen. The temperature of the cell can easily be seen. Voltage and currents can be seen and anomalies identified.

Figure 322 shows the full DAQ program screen. Voltage, current and temperature programs are all identified. All the information is sent a excel files, an example is seen in Table 18. Voltage and current plots are then produced and conclusions about the experiment can then be discussed.
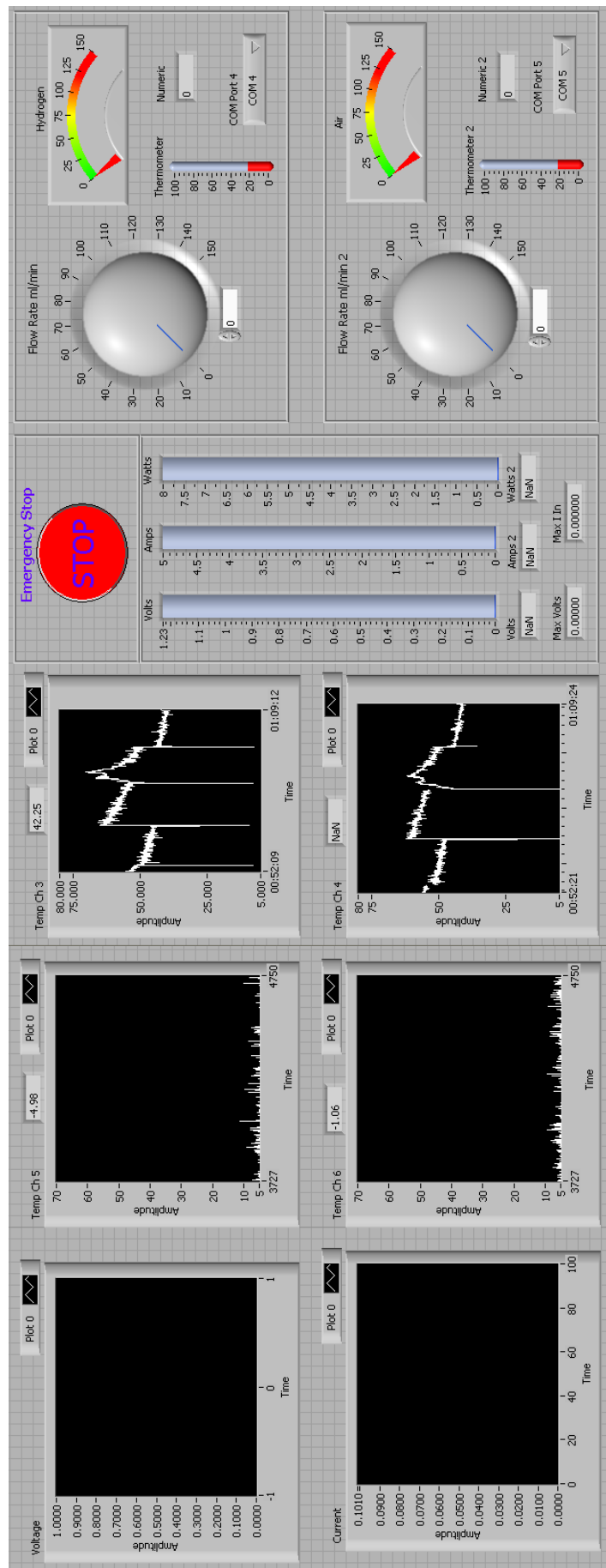
Figure 321 Complete user interface Screen of data capture program.
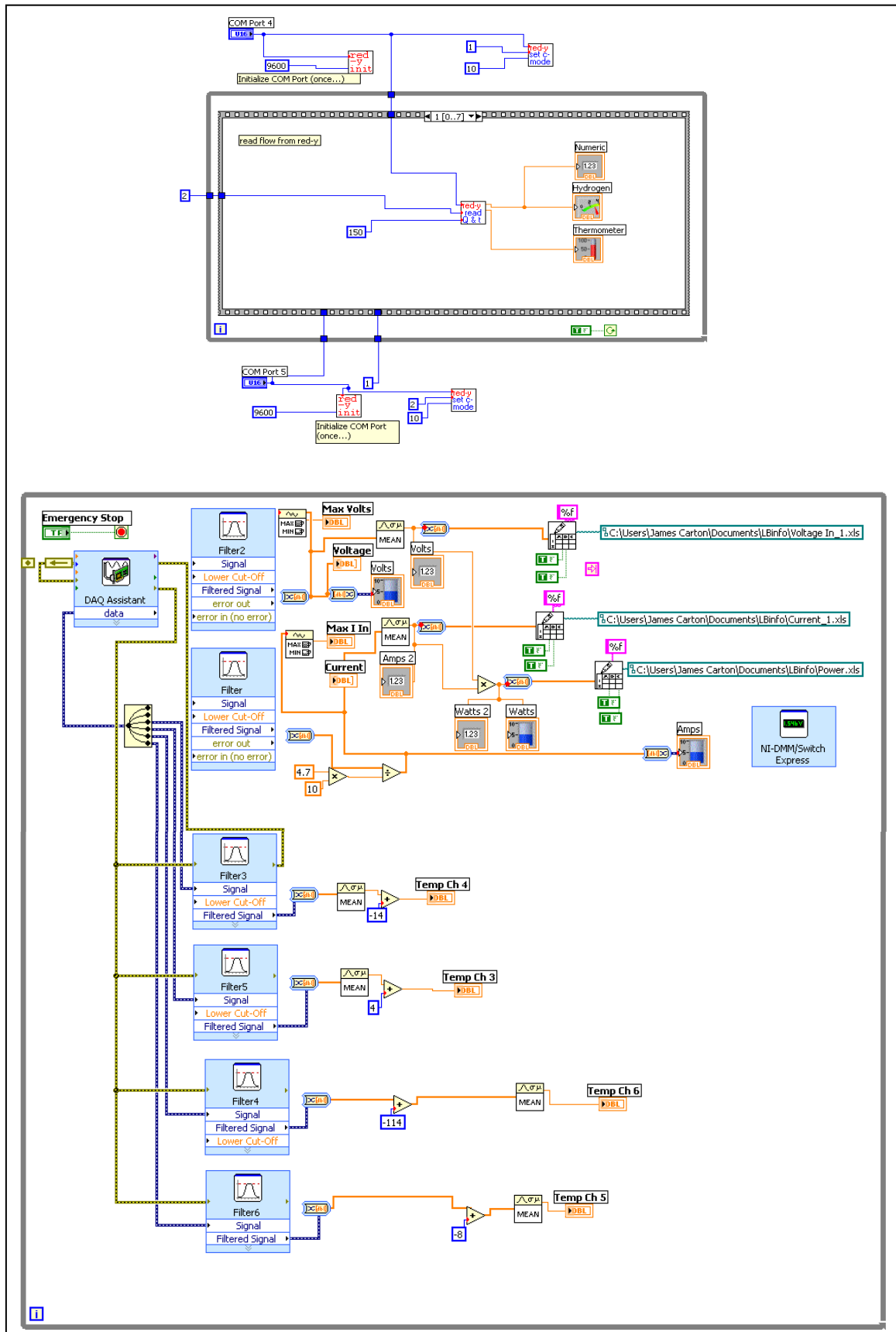
Figure 322 Complete screen of data capture program.

Table 18 Example of compiled results from LabView program.

Current (A)	Current Density (A/cm^2)	Voltage (V)	Power (W)	Power Density (W/cm^2)
1.4640000	0.1013149	0.3570000	0.5226480	0.0361694
1.3370000	0.0925260	0.3920000	0.5241040	0.0362702
1.2480000	0.0863668	0.4160000	0.5191680	0.0359286
1.0990000	0.0760554	0.4550000	0.5000450	0.0346052
0.9610000	0.0665052	0.4910000	0.4718510	0.0326540
0.7900000	0.0546713	0.5350000	0.4226500	0.0292491
0.6720000	0.0465052	0.5670000	0.3810240	0.0263684
0.5710000	0.0395156	0.5960000	0.3403160	0.0235513
0.5110000	0.0353633	0.6140000	0.3137540	0.0217131
0.4200000	0.0290657	0.6390000	0.2683800	0.0185730
0.3640000	0.0251903	0.6570000	0.2391480	0.0165500
0.3140000	0.0217301	0.6720000	0.2110080	0.0146026
0.2700000	0.0186851	0.6870000	0.1854900	0.0128367
0.2250000	0.0155709	0.7040000	0.1584000	0.0109619
0.2050000	0.0141869	0.7110000	0.1457550	0.0100869
0.1590000	0.0110035	0.7270000	0.1155930	0.0079995
0.1250000	0.0086505	0.7400000	0.0925000	0.0064014
0.0880000	0.0060900	0.7550000	0.0664400	0.0045979
0.0650000	0.0044983	0.7680000	0.0499200	0.0034547
0.1400000	0.0096886	0.7270000	0.1017800	0.0070436
0.1070000	0.0074048	0.7440000	0.0796080	0.0055092
0.0750000	0.0051903	0.7550000	0.0566250	0.0039187

Appendix D

Flow Control**Error! Reference source not found.**To successfully and correctly measure all the information from the PEM fuel cell, it was important to be able to measure the flow of hydrogen flowing in to the fuel cell accurately. Accurate measurement devices, volumetric flow meters/controllers (Voegtlin red-y series flow controller), had to be installed at this point so that the correct information could be collected. Each hydrogen rated and air rated flow controller was calibrated for each gas and each flow controller was controlled by the data acquisition (DAQ) software (Lab View).

Figure 323 Hydrogen & Oxygen/Air flow meters/controllers.

The red-y mass flow meter has a constant heating power and ensures a temperature difference that is directly proportional to the gas flow rate. Inside the flow channel of the flow controller a temperature measurement is followed by a heater and then a temperature measurement again. Figure 324 below illustrates this process.
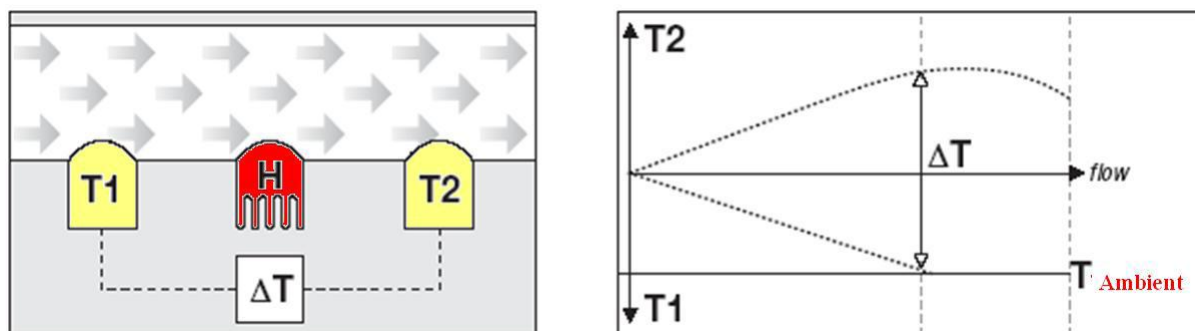
Figure 324 Method of measuring the flow rate in the mass flow controllers.

If there is no gas flowing through the controller the heater —H‖ uniformly distributes the heat, and the temperature difference T1-T2 equals zero. The mass flow rate is proportional to the temperature difference between T1 and T2. This means that the faster the gas flows through the controller, the

greater temperature of difference between T1 and T2 as seen in Figure 324 (right). This type of controller has an advantage over volumetric principles of measurement because pressure and temperature do not have to be additionally measured to obtain an accurate flow rate.
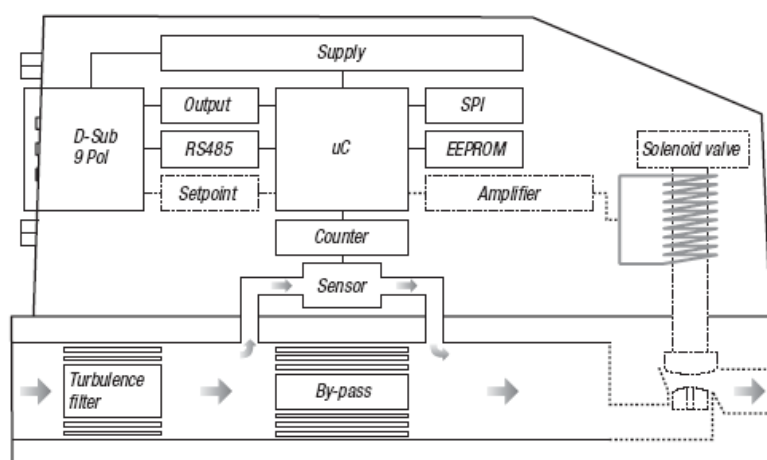
Figure 325 A schematic of the components inside the flow controllers

The flow controllers use a CMOS semi conductor chip that allows high sensor precision, as well as digital intelligence, reliability, a dynamic measuring range and a fast response time. CMOS is a standard technology for the manufacture of integrated circuits. With the CMOS technology, the sensor element, the amplifier and the A/D converter form a unit on the same silicon chip. The digital intelligence linked to the CMOS sensor permits the emission of a fully calibrated temperature-compensated output signal.

Table 19 Flow controller specifications.

Type:	GSC-A9SA-BB22	GSC-A9SA-BB21
Range:	16.67-500 mln/min	16.67-500 mln/min
Accuracy:	+/-1.5% f.s.	+/-1.5% f.s.
Medium:	O2	H2
Temperature:	20 °C	20 °C
P inlet:	2 bar a	2 bar a
P outlet:	1.001 bar a	1.001 bar a
Fitting:	G1/4"	G1/4"
Body:	Aluminium	Aluminium
Seal:	FKM	FKM
Power supply:	+24 Vdc	+24 Vdc
Setpoint:	RS485 + 4-20 mA	RS485 + 4-20 mA
Output:	RS485 + 4-20 mA	RS485 + 4-20 mA
Automatic Valve:	0.2 mm (85%)	0.1 mm (94%)
Documentation & calibration on CD:	Provided	Provided

Appendix E

Visualisation Technique Tested

Visualisation was used in this thesis to view water droplet movement in mini channels of PEM fuel cells. Air flow drives the water droplet and the speed at which the droplet moves can be between 0.1m/s to 1m/s, depending on the surface of the mini channel, speed of the air flow and size of droplet or shape of the droplet (slug or suspended drop). Visualisation is a relatively cheap method but high speed cameras can still cost anywhere between ten to thirty thousand Euro.

At the early stages of research it was difficult to acquire a high speed camera to use for the visualisation. Two cameras were eventually sourced, a camera with 30fps with reduced resolution with 500fps. These cameras however did not show droplet movement in the channels as the speed of the droplets were faster. It was calculated that an 800fps to 1500fps camera would be most beneficial to capture the necessary evolution of the droplets in mini channels of PEM fuel cells.

A problem was apparent, a 1000fps camera was necessary to view the droplets but the best camera available was a 500fps camera at reduced resolution. This sparked new ideas of how to use the low fps camera to acquire images similar to that of a higher fps camera. This could be achieved by pulsing the light source, a pulsed visualisation technique. The light would have to pulse about thirty times as fast as the 30fps camera to capture 1000fps image quality on just 30 frames. Each picture would have 30 image movements of the droplet.

A rotating light blade as shown in Figure 326 was initially used to allow light to dim and illuminate the channel that was being viewed. This method proved unsuccessful as it was difficult to control and shadows were visible on the images.

Figure 326 Rotating blade.

The final method tested was to pulse the LED lights to a very accurate and controllable frequency. This was achieved by designing and building a microcontroller to turn on and off the LEDs at any desired frequency, set by the user.
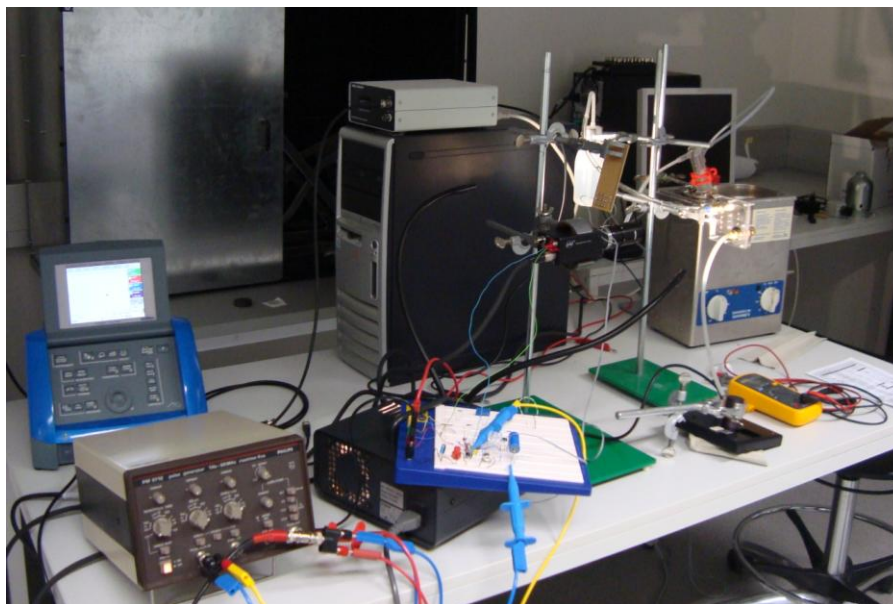
Figure 327 High speed camera set up using pulsed visualisation technique.

Tests were carried out using paper arrays as shown in Figure 328. This was moved in front of the camera to examine if the method worked.
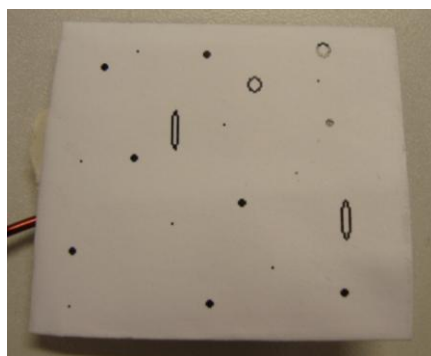
Figure 328 Array of shapes.

Figure 329 shows the first images taken by the camera, the single frame with four distinct images of the dot and circle.

Figure 329 Object taken with pulsed visualisation technique.

Figure 330 shows an image where the object is too slow leaving a ghost trail of the dots and circles. Cross over of the object being viewed, depends on the size of the object see Figure 331. The small dot at the top of the image, in red, is viewed well and the increase in speed of the object can be seen with the dot moving further away from the first image to the fifth. The larger dot has slight cross over but it

still can be defined well. However, the circle images are on top of themselves and this could be difficult to distinguish during post processing.
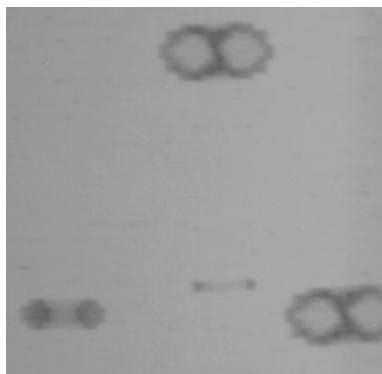
Figure 330 Object too slow for pulse.
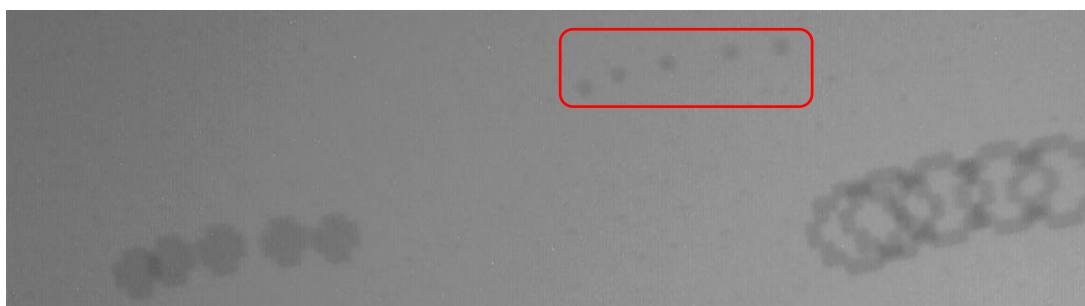
Figure 331 Cross over depending on object size.

The final test was to investigate if droplets in channels could be viewed. Figure 332 shows the first attempts of the pulsed visualisation technique. The white inside the red boxes is the reflection of the water droplet. Two distinct images are visible in the first image and six images are seen in the second image.
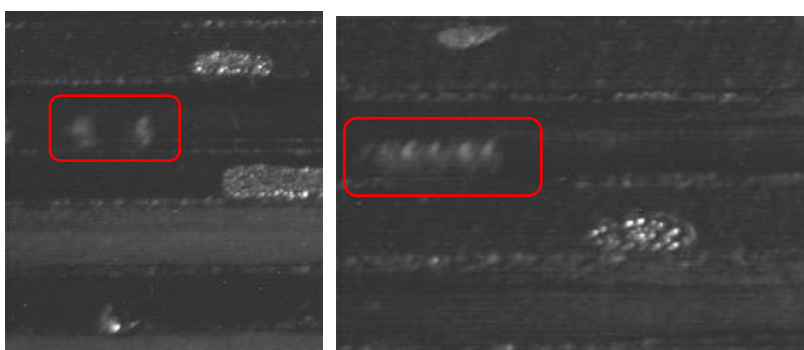
Figure 332 First attempts to capture droplet movement in channel.

Figure 333 shows another image with five distinct images of the one droplet of water in the mini channel.
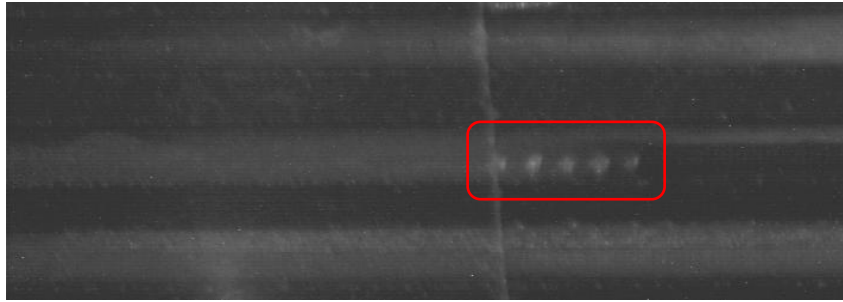
Figure 333 Droplet movement in channel captured.

Figure 334 shows the movement of a slug in a PEM fuel cell mini channel, with six distinct images of the slug at different times viewed on a single image.
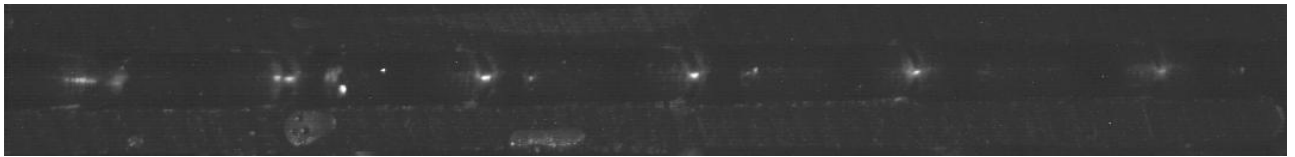
Figure 334 Slug movement in channel captured.

The pulsed visualisation technique described here has mush potential for low cost visualisation applications. For this thesis a high speed camera was eventually sourced and all results described in this thesis used the high speed camera and not the pulsed visualisation technique. One disadvantage for the current research was that the speed of the droplets being viewed was not constant, and droplets in PEM fuel cells can join and grow and this was very difficult to view using the pulsed visualisation technique. This information is mentioned in this thesis as it was explored and was found to be quiet useful but not particularly applicable to droplet visualisation in PEM fuel cell mini channels. A dedicated study could be completed into this method and its applications and limitations could be explored.

Figure 335 Cameras used in the visualisation process.

Appendix F

Dodecahedron Construction

Note: 40ppi metal foam has been used in the following calculations. Open cellular foam samples were obtained from ERG Inc. [159]
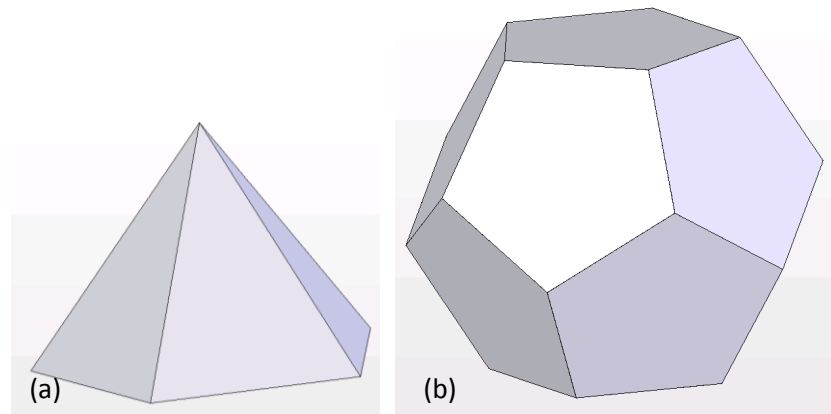
Figure 336 Pyramid (a) used to create dodecahedron (b).

A dodecahedron consists of twelve pentagonal based pyramids. The apex and base angles of the five isosceles triangles of the pentagon shaped faces are 72° and 54° respectively. The angle between a base pyramid and the plane of the adjacent pyramid Ψ is:

$$\Psi = cos^{-1}(Cos\ \theta\ /\ 1 + Cos\ \theta) \qquad\qquad Eqn.\ (1)$$

which equates to 63.43494882°.
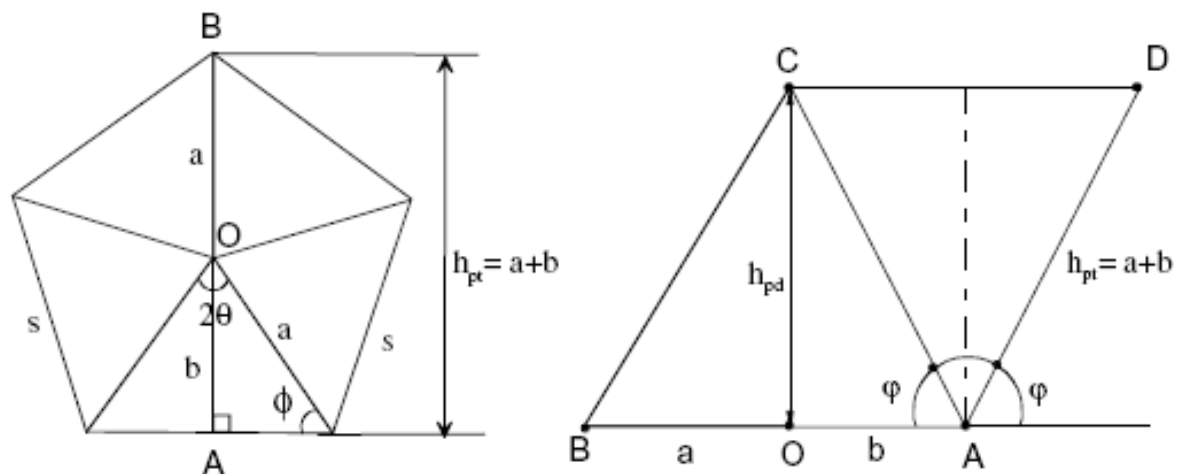
Figure 337 Geometric features of a dodecahedron [167]**.**

The average dimension of a dodecahedron is related to the cell density α of the open pore cellular foam given as pore per inch (ppi):

$$1/\alpha = (h_{dmax} + h_{dmin}/2) \qquad\qquad Eqn.\ (2)$$

which is approximately equal to 2.5s where s is the ligament cell edge length. For the 40ppi open pore cellular foam this equates to 0.254mm. The height of the dodecahedron h_{davg} is related to ligament cell edge length s by 2.5 and for the 40ppi open pore cellular foam this is 0.635mm.

The volume of the dodecahedron is twelve times the volume of a single pyramid which is approximately equal to $7.66s^3$. For the 40ppi open pore cellular foam this equates to $0.12552451mm^3$.

The mass of a single pore of the open pore cellular foam is related to the volume of the pore (without compression) and the density of the material.

$$M_{pore} = \rho * V_{pore} \qquad\qquad Eqn.\ (3)$$

but M_{pore} is also equal to:

$$M_{pore} = L_{side}{}^2 * A - A^3 * B \qquad\qquad Eqn.\ (4)$$

where A and B are constants related to the cell density α. The cross section of the ligaments of a dodecahedron is assumed to be equilateral triangle. From equation 3 and 4 the ligament side dimension can be calculated. For the 40ppi open pore cellular foam this equates to 0.023mm.

Open pore cellular foams have a high specific surface area compare to other materials. The specific surface area S_o is calculated by:

$$S_o = (L_{side} * C + D\,L_{side}{}^2/3) / 100 * \rho * V_{pore} \qquad\qquad Eqn.\ (5)$$

where C and D are constants related to the cell density α. For the 40ppi open pore cellular foam this equates to $1600m^2/m^3$.
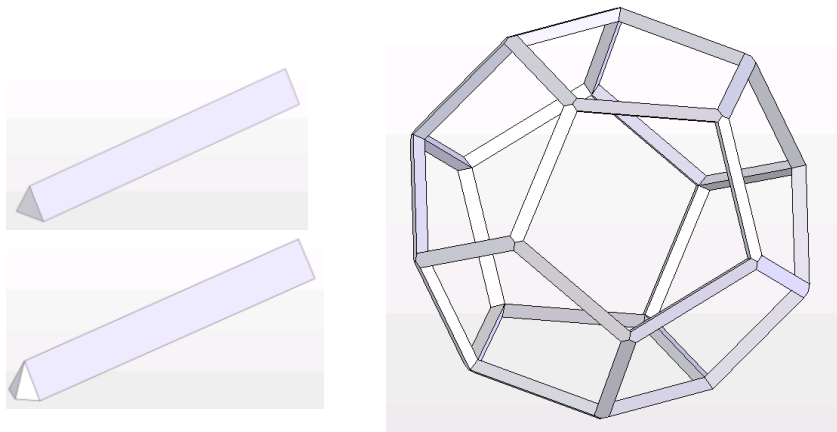
Figure 338 Ligaments used to create structure of dodecahedron 'Pore'.

Table 20 shows the main characteristics calculated for all open pore cellular foam materials used in this thesis. Please refer to Ozmat et al. [167] for a more information about the equations detailed here.

Table 20 Open pore cellular foam characteristics.

Cell density α (ppi)	10	20	30	40	45	80	100
Ligament edge length (mm)	1.016	0.508	0.338	0.254	0.225	0.127	0.1016
Pore diameter (mm)	2.54	1.27	0.85	0.635	0.564	0.318	0.254
Pore volume (mm^3)	8.034	1.004	0.2975	0.1255	0.08816	0.01569	0.00803
Ligament triangular side (mm)	0.15	0.048	0.033	0.023	0.0154	0.00712	0.005347
Specific surface (m^2/m^3)	900	1266	1447	1600	1705	1795	1854
Cell porosity (%)	0.08	0.08	0.08	0.08	0.08	0.08	0.08

Appendix G

Extra Simulation Results

Modified parallel flow plate simulation results
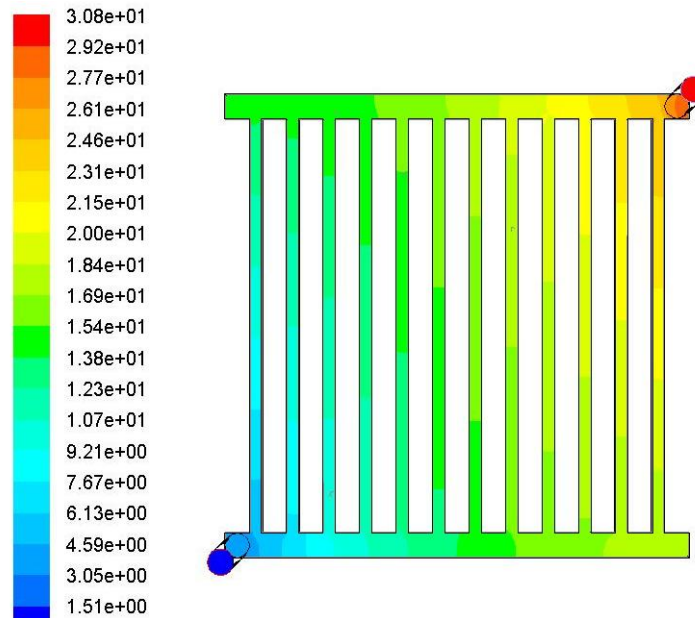
Figure 339 Pressure (pa) through the modified parallel flow plate model with 2mm ribs.
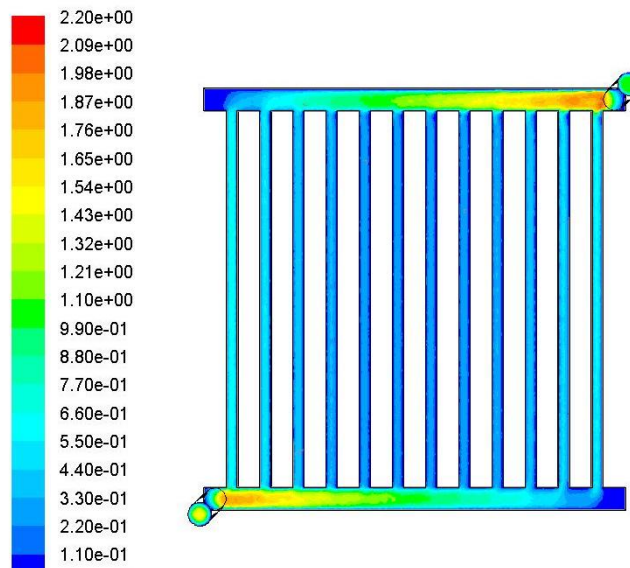
Figure 340 Velocity (m/s) through the modified parallel flow plate model with 2mm ribs.
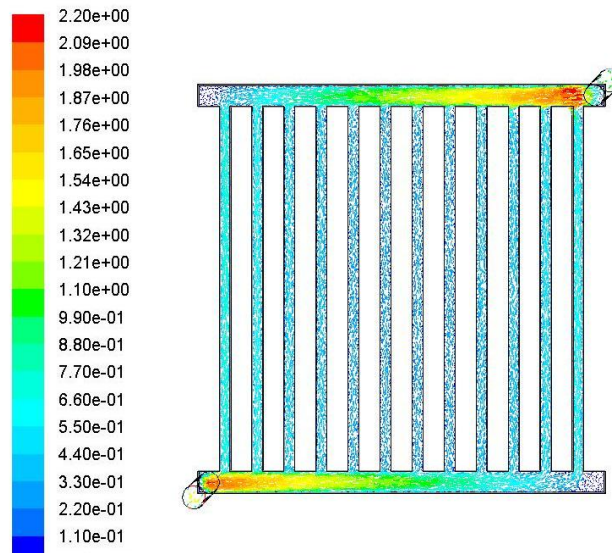
Figure 341 Velocity vectors (m/s) through the modified parallel flow plate model with 2mm ribs.
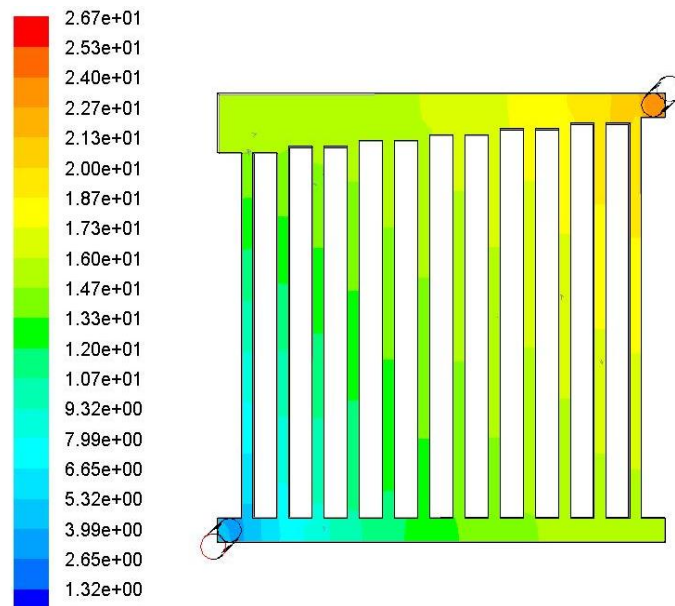
Figure 342 Pressure (pa) for the modified parallel flow plate model with 2mm ribs and tapered inlet.
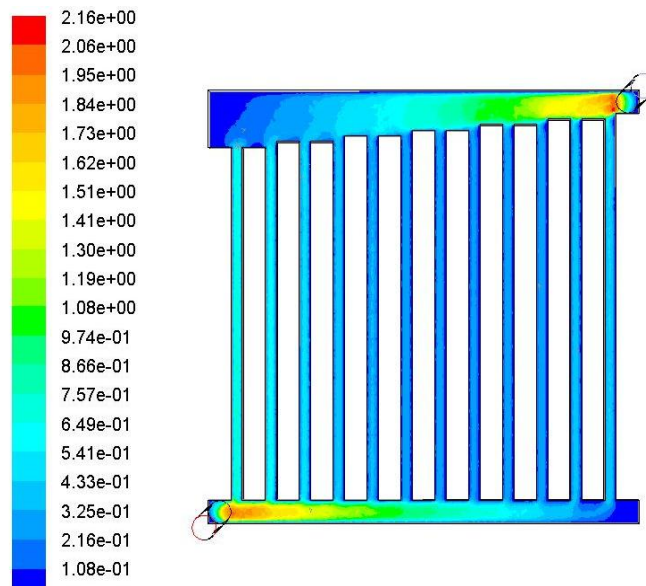
Figure 343 Velocity (m/s) through the modified parallel flow plate model with 2mm ribs and tapered inlet.
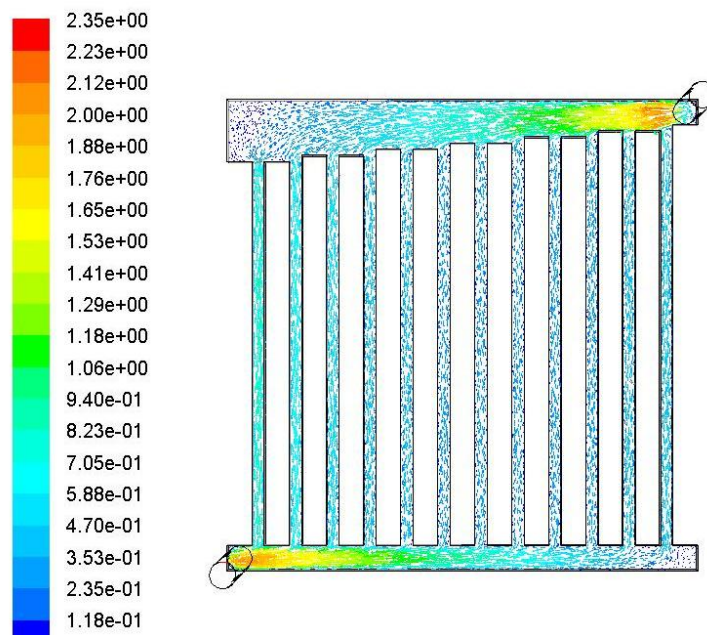
Figure 344 Velocity vectors (m/s) for the modified parallel flow plate model with 2mm ribs & tapered inlet.

Information Tables

Table 21 Purchased PEM fuel cell operational parameters.

Cell open circuit voltage (V)	**0.9**
Cell operational voltage (V)	**0.65**
Cell power (W)	**3.5**
Cell Efficiency (%)	**50**
Active Area (cm^2)	**14.45**
Hydrogen pressure maximum (Pa)	**200000**
Hydrogen flow rate (ml/min)	**20**
Oxygen pressure maximum (Pa)	**200000**
Oxygen flow rate (ml/min)	**150**
Humidification (%)	**60 -100**
Temperature (°C)	**40 – 80**
Sensitive to	**CO, SO$_2$, H$_2$S**

Table 22 PEM fuel cell model zones

Zone	Description	Type	Notes
Anode current collector	Conducts current	Solid	0 volts Aluminium
Anode flow channel	Hydrogen gas flow	Fluid	Hydrogen & water vapour
Anode gas diffusion layer	Carbon cloth	Fluid	Default GDL material
Anode catalyst layer	Platinum coating layer	Fluid	Default catalyst material
Membrane layer	Active membrane	Fluid	Default membrane material
Cathode catalyst layer	Platinum coating layer	Fluid	Default catalyst material
Cathode gas diffusion layer	Carbon cloth	Fluid	Default GDL material
Cathode flow channel	Air (oxygen) gas flow	Fluid	Oxygen, nitrogen & water vapour
Cathode current collector	Conducts current	solid	Fixed voltage Aluminium

Table 23 PEM fuel cell gas flow rates.

	Air mass flow rate (kg/s)	Air velocity (m/s)	Air flow rate (ml/min)	Hydrogen mass flow rate (kg/s)	Hydrogen velocity (m/s)	Hydrogen flow rate (ml/min)
Standard exp.	1.103e-6	0.917	55	2.997e-8	0.334	20
Model channel	1.103e-6	0.917	55	2.997e-8	0.334	20
Model foam	1.103e-6	0.917	55	2.997e-8	0.334	20

Table 24 PEM fuel cell input parameters for electrochemistry simulations.

Parameter	Value	Units
Operating pressure	201325	Pa
Gravity	0	m/s
Temperature	353.15 (80)	K (°C)
Electrochemically active area	9.0 E-06 / 19.25 E-06	m²
Anode Thickness	0.00005	m
Cathode Thickness	0.00005	m
Electrolyte Thickness	0.00023	m
Anode exchange current density	10000000	A/m^3
Anode reference concentration	1	kmol/m^3
Anode concentration exponent	0.5	-
Anode exchange coefficient	2	-
Cathode exchange current density	50000	A/m^3
Cathode reference concentration	1	kmol/m^3
Cathode concentration exponent	1	-
Exchange coefficient	2	-
Diffusivity hydrogen	0.00006	m²/s
Diffusivity oxygen	0.00035	m²/s
Diffusivity water vapour	0.00006	m²/s
Diffusivity other gases	0.00008	m²/s
Multiphase saturation exponent	2	(for pore blockage)

Table 25 PEM fuel cell model parameters for electrochemistry simulations.

PEM Fuel Cell model	**On**
Surface energy source	**On**
Disable CO electrochemistry	**Off**
Volumetric energy	**Off**
Solver type	**Pressure based**
Pressure	**standard**
Pressure-velocity coupling	**SIMPLE**
Formulation	**Implicit**
Time	**Steady**
Velocity formulation	**Absolute**
Gradient option	**green gauss cell based**
Porous formulation	**superficial velocity**
Energy equation	**on**
Viscous model	**laminar**
Species sources	**On**
Species model	**Species transport**
Species options	**diffusion energy source**
Mixture species	**O2 N2 H2O H2**

Table 26 PEM fuel cell solution parameters for electrochemistry simulations.

Residual criteria	
Continuity	2.20E-05
x-velocity	1.00E-06
y-velocity	1.00E-06
z-velocity	1.00E-06
energy	1.00E-07
do-intensity	1.00E-06
h20	1.00E-06
o2	1.00E-06
h20	1.00E-06
uds-0	1.00E-08
Under relaxation factors	
Pressure	0.3
Density	0.7
Body forces	0.7
Momentum (First order upwind)	0.4
H20 (First order upwind)	1
02 (First order upwind)	1
H2 (First order upwind)	1
Energy (First order upwind)	1
Discrete Ordinates (First order upwind)	1
User Scaler 0 (First order upwind)	1

Table 27 Flow plate simulation parameters 1.

Flow Plate	Double serpentine	Modified serpentine	Parallel	Modified stepped parallel	Modified tapered parallel	Over flow
Modeller	Ansys DM	Ansys DM	Ansys DM	Ansys DM	Ansys DM	Ansys DM
Mesher	Ansys Meshing	Ansys Meshing	Ansys Meshing	Ansys Meshing	Ansys Meshing	Ansys Meshing
Mesh	Mixed Tet & Quad	Mixed Tet & Quad	Mixed Tet & Quad	Quad	Mixed Tet & Quad	Quad
Size function	Fixed	Fixed	Fixed	Fixed	Fixed	Fixed
Smoothing	medium	medium	medium	medium	medium	medium
Transition	Slow	Slow	Slow	Slow	Slow	Slow
Nodes	74827	39735	46848	34535	49471	30555
Elements	324244	110250	199560	108655	214077	105251
Solver	Fluent 3-D Double Precision	Fluent 3-D Double Precision	Fluent 3-D Double Precision	Fluent 3-D Double Precision	Fluent 3-D Double Precision	Fluent 3-D Double Precision
Solver type	Pressure based	Pressure based	Pressure based	Pressure based	Pressure based	Pressure based
Model	Laminar	Laminar	Laminar	Laminar	Laminar	Laminar
Fluid	Air	Air	Air	Air	Air	Air
Solid	Al	Al	Al	Al	Al	Al
Temperature	Constant	Constant	Constant	Constant	Constant	Constant
Porous GDL	N/A	N/A	N/A	N/A	N/A	N/A
Viscous resistance (m-2)	N/A	N/A	N/A	N/A	N/A	N/A
Inertial resistance	N/A	N/A	N/A	N/A	N/A	N/A
Porous Body	N/A	N/A	N/A	N/A	N/A	N/A
Viscous resistance (m-2)	N/A	N/A	N/A	N/A	N/A	N/A
Inertial resistance	N/A	N/A	N/A	N/A	N/A	N/A
Inlet velocity (m/s)	1	1	1	1	1	1
Pressure outlet relative (Pa)	0	0	0	0	0	0
Scheme	Simple	Simple	Simple	Simple	Simple	Simple
Gradient	least squares cell based	least squares cell based	least squares cell based	least squares cell based	least squares cell based	least squares cell based
Pressure	Standard	Standard	Standard	Standard	Standard	Standard
Momentum	Power law	Power law	Power law	Power law	Power law	Power law
Compute from	Inlet	Inlet	Inlet	Inlet	Inlet	Inlet
Monitors	Mass flow Continuity Velocity	Mass flow Continuity Velocity	Mass flow Continuity Velocity	Mass flow Continuity Velocity	Mass flow Continuity Velocity	Mass flow Continuity Velocity
Iterations	100	100	100	100	100	100
Manufactured parts	Yes	Yes	No	Yes	No	Yes

Table 28 Flow plate simulation parameters 2.

Flow Plate	Pin	Maze	Interdigitated	Tapered interdigitated	Spiral	Vein
Modeller	Ansys DM	Ansys DM	Ansys DM	Ansys DM	Ansys DM	Ansys DM
Mesher	Ansys Meshing	Ansys Meshing	Ansys Meshing	Ansys Meshing	Ansys Meshing	Ansys Meshing
Mesh	Mixed Tet & Quad	Quad	Mixed Tet & Quad	Mixed Tet & Quad	Mixed Tet & Quad	Mixed Tet & Quad
Size function	Fixed	Fixed	Fixed	Fixed	Fixed	Fixed
Smoothing	medium	medium	medium	medium	medium	medium
Transition	Slow	Slow	Slow	Slow	Slow	Slow
Nodes	80651	37961	38043	88326	83685	91074
Elements	364240	108251	119876	384432	362672	311420
Solver	Fluent 3-D Double Precision	Fluent 3-D Double Precision	Fluent 3-D Double Precision	Fluent 3-D Double Precision	Fluent 3-D Double Precision	Fluent 3-D Double Precision
Solver type	Pressure based	Pressure based	Pressure based	Pressure based	Pressure based	Pressure based
Model	Laminar	Laminar	Laminar	Laminar	Laminar	Laminar
Fluid	Air	Air	Air	Air	Air	Air
Solid	Al	Al	Al	Al	Al	Al
Temperature	Constant	Constant	Constant	Constant	Constant	Constant
Porous GDL	N/A	N/A	GDL	GDL	GDL	GDL
Viscous resistance (m-2)	N/A	N/A	1.00E+12	1.00E+12	1.00E+12	1.00E+12
Inertial resistance	N/A	N/A	N/A	N/A	N/A	N/A
Porous Body	N/A	N/A	N/A	N/A	N/A	N/A
Viscous resistance (m-2)	N/A	N/A	N/A	N/A	N/A	N/A
Inertial resistance	N/A	N/A	N/A	N/A	N/A	N/A
Inlet velocity (m/s)	1	1	1	1	1	1
Pressure outlet relative (Pa)	0	0	0	0	0	0
Scheme	Simple	Simple	Simple	Simple	Simple	Simple
Gradient	least squares cell based	least squares cell based	least squares cell based	least squares cell based	least squares cell based	least squares cell based
Pressure	Standard	Standard	Standard	Standard	Standard	Standard
Momentum	Power law	Power law	Power law	Power law	Power law	Power law
Compute from	Inlet	Inlet	Inlet	Inlet	Inlet	Inlet
Monitors	Mass flow Continuity Velocity	Mass flow Continuity Velocity	Mass flow Continuity Velocity	Mass flow Continuity Velocity	Mass flow Continuity Velocity	Mass flow Continuity Velocity
Iterations	100	100	100	100	100	100
Manufactured parts	No	Yes	No	No	No	No

Table 29 Permeability (K) & Inertial resistance or form coefficient (C) values.

	100 PPI	80 PPI	45 PPI	40 PPI	30 PPI	20 PPI	10 PPI
A	20.176	11.2	9.522	9.1656	9.92	8.17	4.799
B	222.94	70	32.279	25.193	10.47	1.314	2.5139
ρ	1.225	1.225	1.225	1.225	1.225	1.225	1.225
t	0.0254	0.0254	0.0254	0.0254	0.05	0.05	0.05
μ	1.84E-05	1.84E-05	1.84E-05	1.84E-05	1.84E-05	1.84E-05	1.84E-05
1/k (Viscous resistance)	4.78E+08	1.50E+08	6.92E+07	5.40E+07	1.14E+07	1.43E+06	2.74E+06
K (Permeability)	2.09E-09	6.67E-09	1.45E-08	1.85E-08	8.77E-08	6.99E-07	3.65E-07
C (Inertial resistance)	1.30E+03	7.20E+02	6.12E+02	5.89E+02	3.24E+02	2.67E+02	1.57E+02

Appendix H

Housing Design for Open Pore Cellular Foam Flow Plate

Vertical design
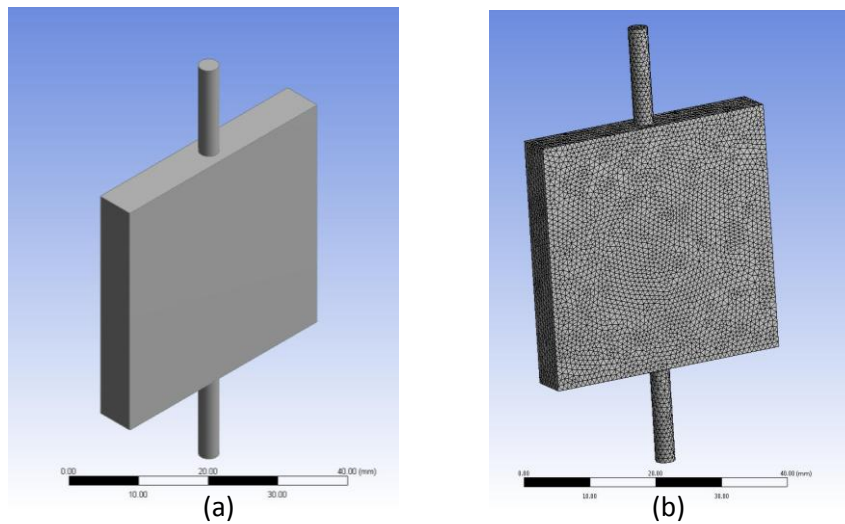
Figure 345 (a) Vertical flow model (b) Vertical flow mesh.
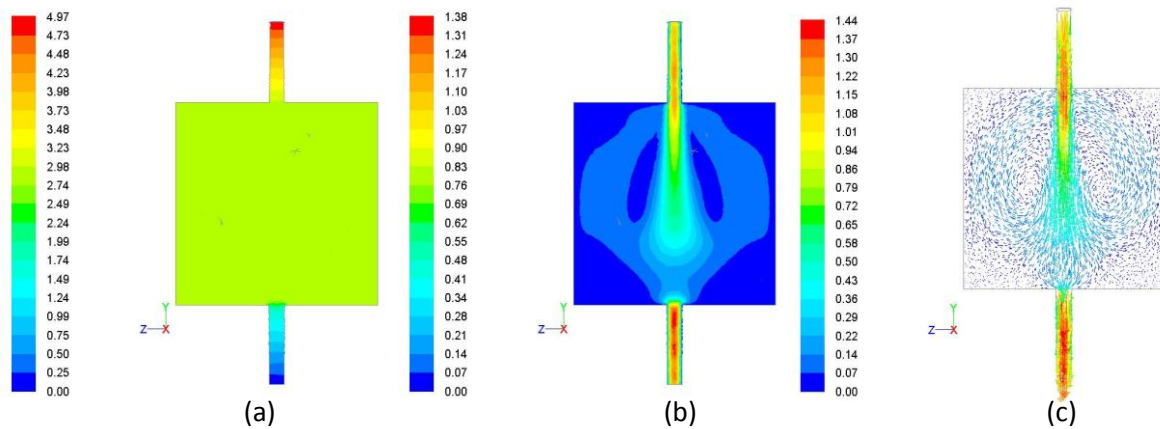
Figure 346 Vertical flow (a) Pressure Pa (b) Velocity m/s (c) Velocity vectors m/s.

Diagonal design
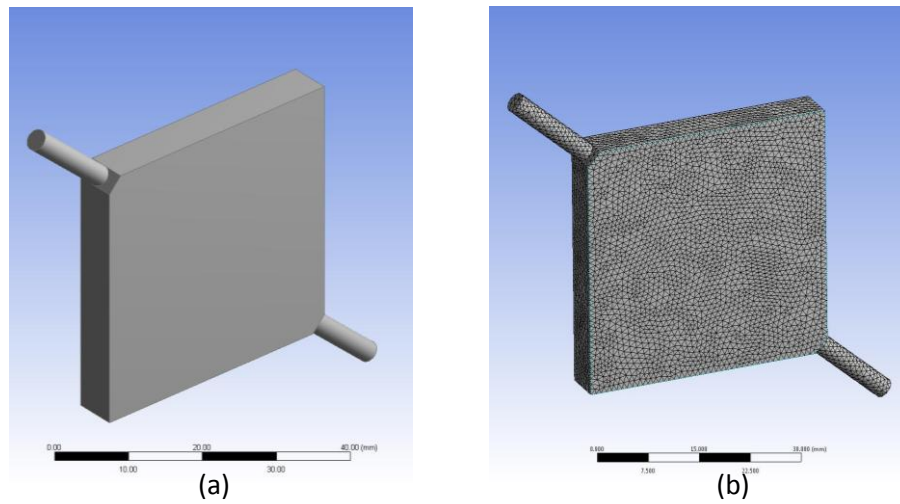
Figure 347 (a) Diagonal flow model (b) Diagonal flow mesh.
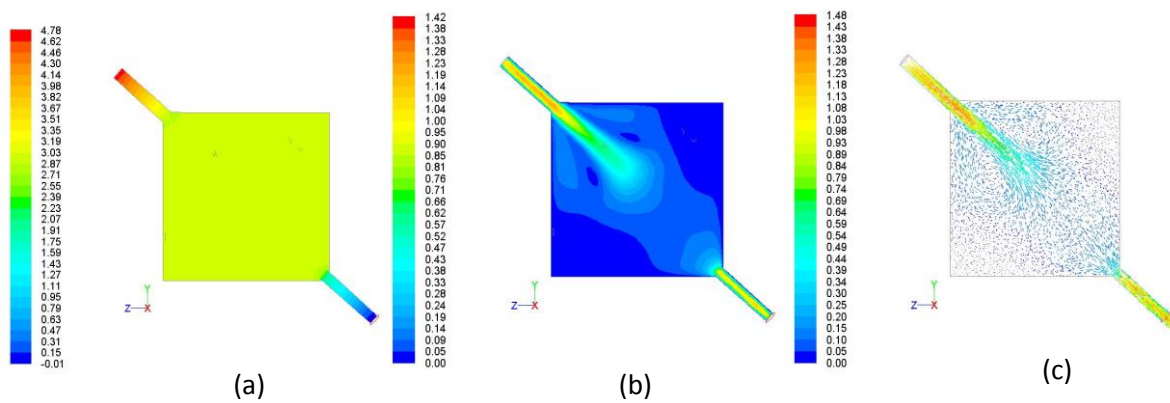
Figure 348 Diagonal flow (a) Pressure Pa (b) Velocity m/s (c) Velocity vectors m/s

Appendix I

Drawings

Manufactured flow plate designs

All channels and wall between them
are equally spaced at a distance of
1.10 mm.
corners have the same radius value
as the radius of the tool.

Drawing 1 — Modified Serpentine C2

Dimensions (left side): 0, 4, 8.50, 9.60, 11, 14.24, 21.70, 30.50, 39.30, 40.40, 52.66, 54.66, 60

Top: 0, 5.34, 7.34, 11, 45.76, 49, 54.55, 60

Right side: 0, 5.34, 7.34, 42.50, 45.76, 49, 56

Bottom: 6.24, 14.24, 52.66, 54.66, 56

+2
4–0.50
1

4 x1 THRU
R3.85
2 Ø2 THRU

All channels and wall between them
are equally spaced at a distance of
1.10 mm
corners have the same radius value
as the radius of the tool.

UNLESS OTHERWISE SPECIFIED
DIMENSIONS ARE IN MILLIMETRES
SURFACE FINISH N5
TOLERANCES: +/– 0.02
LINEAR
ANGULAR

DEBUR AND BREAK SHARP EDGES
DO NOT SCALE DRAWING   REVISION

DCU
School of Mechanical and
Manufacturing Engineering

DRAWN James Carton SIGNATURE JC DATE 09/09/2008
CHK'D
APP'D
MFG
QA

MATERIAL: Graphite

TITLE: Modified Serpentine C2

DWG NO. FP-001-C2-00   A4

WEIGHT   SCALE 1:1   SHEET 1 OF 1

Drawing 2 — Stepped Parallel H2

Top: 0, 11, 14.24, 25, 38, 52.66, 54.66, 56, 60

Left side: 0, 5.34, 7.34, 11, 12, 13, 14.30, 45.76, 49, 56, 60

Right side: 0, 11, 14.24, 45.76, 49, 52.66, 54.66

Bottom: 0, 5.34, 7.34, 45.76, 1, 49

+2
4–0.50
1

2 Ø2 THRU
4 x1 THRU

All channels and wall between them
are equally spaced at a distance of
1.00 mm
corners have the same radius value
as the radius of the tool.

UNLESS OTHERWISE SPECIFIED
DIMENSIONS ARE IN MILLIMETRES
SURFACE FINISH N5
TOLERANCES: +/– 0.02
LINEAR
ANGULAR

DEBUR AND BREAK SHARP EDGES
DO NOT SCALE DRAWING   REVISION

DCU
School of Mechanical and
Manufacturing Engineering

DRAWN James Carton SIGNATURE JC DATE 09/09/2008
CHK'D
APP'D
MFG
QA

MATERIAL: Graphite

TITLE: Stepped Parallel H2

DWG NO. FP-002-H2-00   A4

WEIGHT   SCALE 1:1   SHEET 1 OF 1

All channels and wall between them
are equally spaced at a distance of
1.00 mm
corners have the same radius value
as the radius of the tool.

DCU
School of Mechanical and
Manufacturing Engineering

UNLESS OTHERWISE SPECIFIED
DIMENSIONS ARE IN MILLIMETRES
SURFACE FINISH N5
TOLERANCES +/- 0.02
LINEAR
ANGULAR

DEBUR AND
BREAK SHARP
EDGES

DO NOT SCALE DRAWING   REVISION

TITLE: Stepped Parallel C2

MATERIAL: Graphite

DWG NO: FP-002-C2-00   A4

SCALE:1:1   SHEET 1 OF 1

DRAWN James Carton JC 09/09/2008

All channels and wall between them
are equally spaced at a distance of
1.00 mm
corners have the same radius value
as the radius of the tool.

DCU
School of Mechanical and
Manufacturing Engineering

UNLESS OTHERWISE SPECIFIED
DIMENSIONS ARE IN MILLIMETRES
SURFACE FINISH N5
TOLERANCES +/- 0.02
LINEAR
ANGULAR

DEBUR AND
BREAK SHARP
EDGES

DO NOT SCALE DRAWING   REVISION

TITLE: Maze Flow Plate H2

MATERIAL: Graphite

DWG NO: FP-003-H2-00   A4

SCALE:1:1   SHEET 1 OF 1

DRAWN James Carton JC 09/09/2008

All channels and wall between them are equally spaced at a distance of 1.00 mm
corners have the same radius value as the radius of the tool.

School of Mechanical and Manufacturing Engineering

UNLESS OTHERWISE SPECIFIED DIMENSIONS ARE IN MILLIMETERS
SURFACE FINISH N5
TOLERANCES +/- 0.02
LINEAR
ANGULAR

DEBUR AND BREAK SHARP EDGES

DO NOT SCALE DRAWING | REVISION

TITLE
Maze Flow Plate C2

MATERIAL: Graphite

DWG NO. FP-003-C2-00 | A4

SCALE:1:1 | SHEET 1 OF 1

The bumps are 0.5 mm high, placed in a depth of 1.00 mm.

School of Mechanical and Manufacturing Engineering

UNLESS OTHERWISE SPECIFIED DIMENSIONS ARE IN MILLIMETERS
SURFACE FINISH N5
TOLERANCES +/- 0.02
LINEAR
ANGULAR

DEBUR AND BREAK SHARP EDGES

DO NOT SCALE DRAWING | REVISION

TITLE
Over Flow Flow Plate H2

MATERIAL: Graphite

DWG NO. FP-004-H2-00 | A4

SCALE:1:1 | SHEET 1 OF 1

The bumps are 0.5 mm high, placed in a depth of 1.00 mm.

UNLESS OTHERWISE SPECIFIED: DIMENSIONS ARE IN MILLIMETERS SURFACE FINISH: N5 TOLERANCES: +/- 0.02 LINEAR ANGULAR	DCU School of Mechanical and Manufacturing Engineering		DEBUR AND BREAK SHARP EDGES	DO NOT SCALE DRAWING	REVISION
	NAME	SIGNATURE	DATE		
DRAWN	James Carton	JC	03/03/2009	TITLE: Over Flow Flow Plate C2	
CHKD					
APPV'D					
MFG					
QA			MATERIAL: Graphite	DWG NO. FP-004-C2-00	A4
			WEIGHT	SCALE:1:1	SHEET 1 OF 1

Open pore cellular foam housings

Visualisation test bed

ITEM NO.	PART NUMBER	DESCRIPTION	QTY.
1	KFH08U-02	1/4" X 6MM PIPE FITTING	2
2	Bolt	M3 HEX HD	10
3	Base	BASE HOLDER	1
4	Cover	CLEAR COVER	1

TITLE:

Test Viewer

DRAWN .JC 27/5/10

UNLESS OTHERWISE SPECIFIED:
DIMENSIONS ARE IN MM
TOLERANCES:
DIMENSIONS: ±0.05 MM
ANGULAR: ± 1 DEGREE

INTERPRET GEOMETRIC
TOLERANCING PER:
MATERIAL
A/R
FINISH

FOR REFERENCE ONLY

SIZE **B** DWG. NO. TestViewer Assem REV

SCALE: 1:1 WEIGHT: SHEET 1 OF 1

NEXT ASSY USED ON APPLICATION DO NOT SCALE DRAWING

CHECKED
ENG APPR.
MFG APPR.
Q.A.
COMMENTS:

Dedication

This thesis is dedicated to my family especially my father and mother whose inspiration and constant support allowed me to come up to this success. They are a symbol of love, trust and greatest personality. To my friends who have helped me along the way. To my colleagues, who have inspired me and helped with this research. And finally this thesis is dedicated to my girlfriend, Tina, whose support has been amazing and whom I love dearly.

Biography

James Carton was born in Wexford in the snow of January 1982. He attended secondary education at the Christian Brothers School in Enniscorthy until 2000. In 2005 he obtained a second class honours BS. Eng. in Manufacturing Engineering at Bolton St. Dublin Institute of Technology. In 2006 he started his Ph.D. research in Dublin City University under the supervision of Dr. A. G. Olabi. His work focused on the research, design and development of PEM fuel cell technology, as described in this thesis.

James' interests encompass many areas of engineering, science, technology and nature. He has a flare for cutting edge technology and an amazement of nature's workings. James has a huge interest in astronomy & space exploration and completed a seven month internship in 2009 at the J.F.K. Kennedy Space Centre and also has completed other design projects for the European Space Agency.

James is a social outgoing, highly motivated, skilled & innovative individual who aims to work with or set up a progressive, exciting company working on interesting design and development projects and products.

Publications Arising from this Research

Journal Publications

Carton JG, Olabi AG. Design of experiment study of the parameters that affect performance of three flow plate configurations of a proton exchange membrane fuel cell. Energy 2010;35(7):2796-2806.

Carton JG, Olabi AG. Wind/hydrogen hybrid systems: Opportunity for Ireland's wind resource to provide consistent sustainable energy supply. Energy 2010;35(12):4536-4544.

Journal Publications in Review

J. G. Carton, V. Lawlor, A. G. Olabi, C. Hochenauer, G. Zauner – Water droplet accumulation and motion in PEM fuel cell mini-channels – In review in Energy Journal.

J. G. Carton, V. Lawlor, A. G. Olabi – Open Pore Cellular Foam as Flow Plate Material for Proton Exchange Membrane Fuel Cells: Part 1 – To be submitted to journal.

J. G. Carton, V. Lawlor, A. G. Olabi – Open Pore Cellular Foam as Flow Plate Material for Proton Exchange Membrane Fuel Cells: Part 2 – To be submitted to journal.

Journal Publications as Co-Author

Lawlor V, Zauner G, Hochenauer C, Mariani A, Griesser S, Carton JG, et al. The Use of a High Temperature Wind Tunnel for MT-SOFC Testing-Part I: Detailed Experimental Temperature Measurement of an MT-SOFC Using an Avant-Garde High Temperature Wind Tunnel and Various Measurement Techniques. Journal of Fuel Cell Science and Technology, 2010; 12;7(6):061016.

Achour H, Carton JG, Olabi AG. Estimating vehicle emissions from road transport, case study: Dublin City. Applied Energy, 2011; 88, (5):1957-1964.

V. Lawlor, J. G. Carton, C. Hochenauer, A. Mariani, G. Zauner, S. Griesser, A. Olabi, K. Klein, S. Kuehn, S. Cordiner, D. Meissner, G. Buchinger, A Micro Tubular SOFC and Stack Testing Apparatus – Submitted to Energy Journal.

Journal Publications in Review (Non Thesis Related)

J. G. Carton, D. Clifford, et al. – A novel mission concept for upper air water vapour, aerosol and cloud observations using Integrated Path Differential Absorption LiDAR Limb Sounding – In review in Remote Sensing Journal.

Proceeding Publications

J. G. Carton & A. G. Olabi, Developments of Fuel Cell Technology, IMC24, Manufacturing: Focus on the Future, Volume 1, Page 273. Aug 2007.

J. G. Carton & A. G. Olabi, A study of the future transport industry; Fuel Cells Vs ICE's, Proceedings of EFC2007, European Fuel Cell Technology and applications Dec 2007, Volume 1, Page 187.

J. G. Carton & A. G. Olabi, Optimisation of a Proton Exchange Membrane Fuel Cell: Flow Plate Design & Testing, Agmet, Energy and Irish climate harnessing the Irish Climate for Energy, The National Botanic Gardens Dublin, Feb 2008, Page 29.

J. G. Carton & A. G. Olabi, Optimisation of a PEM Fuel Cell, IMC25, Manufacturing & Design: The Next Generation, Sept 2008, Volume 2, Page 511.

J. G. Carton & A. G. Olabi, Developing Energy storage & a fuel cell system in conjunction with renewable energy systems, SEEP 2009, Sustainable Energy Beyond 2020, Volume 2, Page 14.

J.G. Carton, A.G. Olabi, V. Lawlor, Metal & Reticulated Vitreous Carbon Foams as Bipolar Flow Plate Material for Proton Exchange Membrane Fuel Cells, SEEP 2010, Bari Italy, July 2010.

J.G. Carton, A.G. Olabi, V. Lawlor, Metal Foam Material; Effective Bipolar Plate Material for PEM Fuel Cells, Fuel Cells Science & Technology Conference, Barcelona Spain, Oct 2010

J.G. Carton, A.G. Olabi, V. Lawlor, Open Pore Cellular Foam; Effective Materials for Fuel Cells, Sustainable Development of Energy, Water & the Environment, Dubrovnik, October 2011, Conference paper accepted.

Presentations & Workshops

J. G. Carton, COST 542 Super Capacitors, Workshop, Berlin, Dec 2006.

J. G. Carton, Cost 542 Fuel Cells; Design, Applications and Future Developments, Workshop, Genoa, Sept 2007.

J. G. Carton, Cost 542 Super Capacitors & Fuel Cells, Workshop, Gdansk, Dec 2007.

J. G. Carton & A. G. Olabi, Optimisation of a proton exchange membrane fuel cell: flow plate design & testing, Dundalk, May 2008.

J. G. Carton & A. G. Olabi, Optimisation of a proton exchange membrane fuel cell, Symposium for Mechanical Engineering Research and Practice (SMERP), Dublin City University, May 2008.

J. Carton, Design, Analysis & Final Testing & Verification of the Advanced Biological Research System (ABRS), Workshop, SLSL, Kennedy Space Centre, April 2009.

J. Carton, Design, Analysis & Final Testing & Verification of the Advanced Biological Research System (ABRS) at the Kennedy Space Centre, SMERP, Dublin City University, June 2009.

J. G. Carton, Advanced fuel cell flow manifolds for automotive applications, Design and Production of Vehicles and Infrastructure, YEAR2010; The Young European Arena of Research, http://year2010.fehrl.org/?m=24&mode=view&id=303, June 2010.

BLANK PAGE